FOREWORD

This is Report No. 16 (Final Report) on Armour Research Foundation (ARF) Project 8203 covering the period of June 1960 through October 1961, on Contract No. Af33(616)-7465. This contract was initiated under Project 7350, Task No. 735001, "Refractory Inorganic Non-Metallic Materials". This contract is under the direct supervision of the Ceramics and Graphite Branch, Metals and Ceramics Laboratory, Directorate of Materials and Processes, Aeronautical Systems Division (ASD) with Lt. J. B. Blandford and Mr. J. D. Latva as the ASD Technical Monitors.

This program is under the overall direction of N. A. Weil, Project Manager. The specific Tasks are identified by numbers, titles and principal investigators as follows:

Task 1 - Effect of Structural Size; "The Zero Strength"
S. A. Bortz, Armour Research Foundation

Task 2 - Effect of Strain Rate
H. R. Nelson, Armour Research Foundation

Task 3 - Effect of Non-Uniform Stress Fields
N. A. Weil, I. M. Daniel, Armour Research Foundation

Task 4 - Effect of Microstructure
P. R. V. Evans, Armour Research Foundation

Task 5 - Internal Friction and Lattice Defects
P. D. Southgate, Armour Research Foundation

Task 6 - Effect of Surface Energy in Brittle Fracture
N. J. Petch, University of Durham, England

Task 7 - Fracture Mechanisms
E. Orowan, Massachusetts Institute of Technology

Task 8 - Impurity Influences
I. B. Cutler, University of Utah

Task 9 - Static Fatigue; Delayed Fracture
R. J. Charles, General Electric Company

Task 10 - Effect of Thermal-Mechanical History
R. J. Stokes, Minneapolis-Honeywell Res. Labs

Task 11 - Surface Active Environments
G. T. Murray, Materials Research Corporation

Tasks 6, 7, 9 and 11 are monitored by N. A. Weil, while Task 8 is under the supervision of L. M. Atlas, and Task 10 is monitored by W. Rostoker. Project Engineers and contributing personnel are listed in the respective Task contributions.

ABSTRACT

Extensive research on factors influencing the behavior of brittle non-metallic ceramics was undertaken. General information on the forms of Al_2O_3 and MgO studied and preliminary work on the effect of porosity on the fracture strength of Lucalox (Al_2O_3) are presented. Individual problem areas were attacked on separate task programs.

Task 1 - Effect of Structural Size: "The Zero Strength"

Task 2 - Effects of Strain Rate

Task 3 - Effect of Non-Uniform Stress Fields'

Task 4 - Effect of Microstructure

Task 5 - Internal Friction Measurements

Task 6 - Surface Energy on Brittle Behavior

Task 7 - Fracture Mechanisms

Task 8 - Impurity Influences

Task 9 - Static Fatigue: Delayed Fracture

Task 10 - Effect of Thermal-Mechanical History

Task 11 - Surface Active Environments

PUBLICATION REVIEW

This report has been reviewed and is approved.

FOR THE COMMANDER:

W. G. Ramke
Chief, Ceramics and Graphite Branch
Metals and Ceramics Laboratory
Directorate of Materials and Processes

TABLE OF CONTENTS

LIST OF ILLUSTRATIONS

PART IV

APPENDIX A

LIST OF TABLES

I. INTRODUCTION

Unlike metals, inorganic nonmetallic refractories can exist in two fundamentally different forms: crystalline and amorphous. A polycrystalline aggregate of a pure ceramic phase in planar section appears very much like a metal, with a cellular network of interfaces at the junctures of grains or subgrains of different crystallographic orientation. Each grain is, in fact, a single crystal in terms of uniqueness of orientation, the only absence of regular atomic lattice development occurring at the interfaces by virtue of the orientation disregistries. This zone is generally narrow, and seldom exceeds five atomic spacings.

Many nonmetallic materials—pure materials as well as homogeneous "alloys"—freeze on cooling to a solid state without crystallization. The solid state remains amorphous and is regarded as a subcooled liquid. Such structures are basically metastable; crystallization can sometimes be induced by annealing at elevated temperatures, although the kinetics of such transformations vary widely. In selected systems it is possible to study not only the limiting states (crystalline and amorphous) but also a phase mixture of these.

The crystalline and amorphous states operate under different mechanisms for the initiation of fracture. Equal importance must be attached to each, because at the present time there is no basis for predicting which structural configuration offers the better expectation of strength. Indeed, a material consisting of a phase mixture of both structures may ultimately present the most promising solution, but this can be appreciated only from a fundamental understanding of the character of the individual types of composite structures.

In research aimed at developing such understanding of fundamentals, it is customary to regard the mechanical behavior of solids as being either brittle or ductile. Such sharp definitions are gradually losing ground, owing to the discovery that most "brittle" materials,

Manuscript released by authors February 1961 for publication as an ASD Technical Report.

such as metals, metaloids, intermetallics and isometric closely-packed ionic crystals, are capable of limited amounts of deformation by the mechanism of dislocation mobility and the development of slip planes.

Unfortunately, most nonmetallic solids behave in ways which are quite unlike those of metals or "ductile" ceramics. Because their behavior is irregular, they are seldom investigated. Failure to study less simple structures, such as multicrystalline or multi-phase systems, is usually defended by pointing to the difficulties of achieving adequate reproducibility or purity in them. Recent years, however, have brought a gradual realization of the importance of these problems, with the result that an increasing amount of research is being devoted to the determination of the basic mechanisms governing the mechanical and electrical properties of structurally anisotropic, multicrystalline, multiphase inorganic refractory materials.

This intensified attention focused on factors affecting the strength of "brittle" substances, fostered by the need for being able to live with this brittleness in structural applications, has resulted in intensified research effort yielding an increased store of knowledge regarding the phenomenological properties and behavior of these substances. Some phenomena are quite well understood today, others have been repeatedly found to fit empirically postulated rules so well that the basis or adequacy of these formulations is seldom questioned.

Space does not permit to review here the current state of understanding regarding the fundamentals of brittle fracture; a reasonable review of this subject has been presented recently[1], resulting from work performed on this program. Since Reference 1, however, is likely to be published as a classified document, an updated version of this paper will be issued within four months, as an addendum to this report. Suffice it to mention that the initiation of cracks is generally accepted as being due to the mobilization of dislocations, which are rather uniformly dispersed, even in pure substances, at something like

100 atomic distances apart. These defects may take many forms, the most common disarrays being those of a complete row (edge dislocation) or a cylindrically climbing mismatch (screw dislocation). These dislocations, or vacancies, are held firm in their surrounding "atmospheres" by the excess energy attendent to the disturbance in the ordered atomic lattice. However, if this energy is overcome, either by temperature or by applied stress, the dislocations can be mobilized. The energy required to achieve this mobility is called the activation energy, and the stress at which this energy level is attained, the friction stress of dislocations.

Once the dislocations are activated, they continue to run until a natural obstacle is encountered. This physical motion of atoms (or ions) leaves steps behind in an initially smooth surface, giving rise to dislocation glide bands. The bands are generally associated with areas of residual stresses, enhancing stress corrosive attack. Etchants will attack these areas preferentially, generating etch-pits which provide tell-tale tracks allowing for the detection of the passage of dislocations.

The barrier to further motion of dislocations is most often provided by a grain boundary, or sometimes, by another dislocation glide band already activated in the material. At these barriers the dislocations pile up; if this occurs for sufficient numbers of dislocations a microcrack will form. This mechanism, then, is the one that leads to crack initiation in the material.

This description implies that the mobilizing of dislocations is invariably associated with irreversible displacement. Conditions that enhance the mobility of dislocations promote ductility (but generally lower the strength); factors retarding the mobility of dislocations will, in turn, lead to poorer ductility. The more these influences manifest themselves, the greater the degree of brittleness of the material; in the extreme, when dislocations are either completely absent (pure atomic lattice) or locked rigidly in place, the material will exhibit

purely elastic behavior and fail without a trace of plastic deformation at very high strength values. In fact, the failure stress corresponding to this condition is called the theoretical strength of the material.

Foreign ions (doping elements) in the host lattice, precipitate at the grain boundary, certain types of thermal or mechanical treatment, high rates of straining, or the application of multiaxial stress fields, all generally serve to increase the activation energy of dislocations. The result of these factors, in short, will be an embrittling effect accompanied by increased strength. This is also the case when dislocation mobility is hampered by an increased number of barriers in the glide path, as is the case for a closer spacing of grain boundaries; smaller grains also lead to higher strength, but reduced ductility.

The above discussion assumed tacitly that the material is dense and contains no gross flaws. In many cases the material contains numerous internal flaws which become operative at crack nucleation mechanisms long before dislocation activation can be induced to act as the crack initiation source. Such is the case with materials that contain finely dispersed flaws, inclusions, or vacancies in the form of pores. Under these circumstances the material may fail at stresses far lower than those required to overcome the friction force of individual dislocations.

Whatever the crack initiation mechanism, failure will not ensue until the "worst flaw" becomes capable of self-propagation under the imposed state of stress. A good deal is understood about crack propagation, there being two somewhat complementary theories dealing with this subject. One theory is deterministic in nature, postulating that a flaw can propagate provided its extension is accompanied by a net liberation of strain energy in the material. This concept was first formulated by Griffith, based upon the work of Inglis, and was proved to hold for amorphous and completely brittle substances (such as glass) in numerous investigations. The Griffith criterion entails only one arbitrary constant, the crack depth, and bases the energy required

to create new surfaces upon the theoretical surface energy of the substance. Experiments soon showed that the surface energy required to allow for crack propagation in crystalline materials was far higher than that derivable from purely elastic considerations. Hence, the theory was amended by Orowan to include in the surface energy term the plastic deformation energy dissipated in a narrow band underlying the fracture surfaces. However, this induces a second arbitrary factor into the Griffith-Orowan theory, since the "effective surface energy" term must be deduced from observed test results rather than being known a priori.

Subsequent work extended the utility of the Griffith criterion to the case of multiaxial stresses and non-uniform stress fields; in fact, the theory has been applied with some success to account for strain-rate effects and to predict conditions under which a running crack may be halted or decelerated. At the same time, the Griffith theory cannot explain size effects, different strengths corresponding to various loading conditions, or account for the effect of grain size and porosity influences (other than by an artificial variation of the surface energy term).

The second failure theory is probabilistic in nature. Proposed by Weibull, it is not concerned with the influence of a single crack on fracture strength, but considers that a random distribution of flaws exists in the material. Considering then the density and severity of existing cracks, the theory assigns a certain probability of failure to the body depending upon its size and the state of stress existing in it. The Weibull theory also contains (in its simplest form) two arbitrary constants: the stress level below which cracks simply cannot be propagated (the "zero strength") and a constant descriptive of flaw distribution and severity in the material. This statistical approach to fracture can directly account for the variation in strength with volume, state of stress or manner of loading. Regarding, however, such parameters as temperature, grain size, porosity, skin effects or stress gradients,

the theory is reduced to a condition of requiring arbitrary adjustments in the empirical constants contained in it. When it comes, lastly, to such considerations as strain rate effects or delayed fracture, the Weibull theory is simply incapable to render a satisfactory account of observed phenomena.

This oversimplified account of the current state of understanding of fracture phenomena shows that, while a few items are understood, many more require elucidation. Recognizing the need for a carefully planned approach to this area of research, the Aeronautical Systems Division decided to fund a broad study, allowing for a well-planned and soundly organized approach to a fundamental investigation of the parameters influencing the strength and failure characteristics of inorganic non-metallic ceramics.

In selecting the research areas most worthwhile to explore on this program, it was evident from the outset that, even as large a program as this one could not resolve all of the challenging problems requiring attention; the gaps in knowledge were too wide, the fundamentals sometimes questionable, and the specific results pertaining to structural ceramics too few. Therefore, it appeared desirable to combine research areas ranging from the very fundamental to the highly applied, in order to achieve a maximum degree of utility for the overall program.

It was decided early in the preparation for this effort that a single contractor, even if broadly diversified, could not develop the maximum possible returns from this program; an effort concentrated solely within one organization, no matter how gifted its personnel, would suffer from the stultifying effects of drawing only upon ideas available "in house". Therefore, it was resolved to divide the program into individual Task investigations, and to subcontract about half of the Tasks to other leading industrial or academic research organizations in order to obtain a large cross-fertilization of ideas and approaches to the central problem.

The question of selection of suitable research areas for individual Tasks posed a considerable problem. Some 14 major factors having an effect upon the strength of brittle materials are discussed in Reference 1 and this list is, by no means, exhaustive. The decision for initial areas of investigation was largely based upon the importance of information sought, coupled with the possible degree of success for attaining the stated goals of the program. These considerations resulted in selecting 11 areas of research to be explored on separate Tasks, whose brief identification by title is given below.

Task	Brief Title
1	Size Effects; "Zero Strength"
2	Strain Rate Effects
3	Non-Uniform Stress Fields
4	Effect of Microstructure
5	Internal Friction and Lattice Defects
6	Surface Energy Determinations
7	Fracture Mechanisms
8	Impurity Influences
9	Static Fatigue; Delayed Fracture
10	Effect of Thermal-Mechanical History
11	Surface Active Environments

A more comprehensive breakdown of the nature of the Tasks, giving an overall presentation of the complete program scope as well, is presented in Table I. Of the total of 11 Tasks undertaken on this program, five are conducted at Armour Research Foundation, while six are carried out under subcontract in keeping with the philosophy of general principles for this program as explained.

At the risk of oversimplification, one may generalize the nature of individual research areas by observing that Tasks 1, 2, 4, 9 and 11 seek to inquire into factors whose effect on the strength of brittle substances has been already explored to some degree for metals or other materials displaying brittle behavior (plastics, glass, plaster of paris, natural rocks), but whose qualitative or quantitative influence on the strength of carefully prepared ceramic oxides was never explored in any detail. Conversely, the information sought from Tasks 3, 5, 6,

Table I

Task	Research Organization	Principal Investigator	ARF Coordinator	Ceramic Material	Experimental Technique	Temperature	Environment	Type of Specimen	Measured Quantity
1. Size Effects; "Zero	Armour Research Foundation	S. A. Bortz		MgO, Al_2O Polycryst. Lucalox	Rupture, Surf. Exam.	R. T. to	Neutral, Oxidizing, Saturated	Dogbone	Strength, Deformation, Fracture Source
2. Effect of Strain Rate	Armour Research Foundation	H. R. Nelson		Al_2O_3 Polycryst. Graphite	Rupture, Surface Exam.	R. T. Elevated	Neutral, Oxidizing	Dogbone	Strength, Strain Rate, Fracture Surface
3. Non-Uniform Stress Field	Armour Research Foundation	I. M. Daniel N. A. Weil		CR-39, Graphite, Plexiglas, Al_2O_3 Polycryst.	H. S. Photog. Photoelasticity Rupture	R. T.	Air	Disc, Theta, Beam, Dogbone	Stress Gradient, Strength
4. Microstructure	Armour Research Foundation	P. R. V. Evans		MgO, Lucalox	Electro. Micro, Crystallo., Crushing	R. T. to 2000°C	Air	Solid cylinder	Grain Size, Strength, Deformation
5. Internal Friction, Lattice Defects	Armour Research Foundation	P. D. Southgate		MgO, Single Crystals	Rupture, log. decremt.	Subatmos. to 800°C	Vacuum	Cleaved Single crystal Beam	Internal Friction Dislocation Pile-up Crack Nucleation
6. Surface Energy	University of Durham	N. J. Petch	N. A. Weil	Al_2O_3 Polycryst.	Electro. Micro. Crystallo., Rupture	R. T. to near melting	Air Vacuum	Thin plate, Rod, Single Crystal	Strength, Dislocation Density, Surf. Energy
7. Fracture Mechanisms	Massachusetts Inst. of Tech.	E. Orowan	N. A. Weil	MgO, KCl, NaCl Single Cryst.	Birefringence Surface Exam. Etch-pit X-ray backscat.	Various	Inert Air Vacuum	Single crystal, Compression	Dislocation Glide Bands, Crack Nucleation, Strength
8. Impurity Influences	University of Utah	L. B. Cutler	L. Atlas	Al_2O_3, MgO Polycrys.	Crystallo., Etching	Elevated and R. T.		Disc Beam	Grain Size Impurities Strength
9. Static Fatigue; Delayed Fracture	General Electric Research	R. J. Charles	N. A. Weil	Sapphire, Al_2O_3 Polycryst., Lucalox	Crystallo. Rupture	-19° to 1000°C	Neutral, Oxidizing, Saturated	Thin rod, Beam	Fracture Surface, Time, Strength, Yielding
10. Thermo-Mechanical History	Honeywell Research	R. J. Stokes	W. Rostoker	MgO Single Crystals	Birefringence, Etch-pit, Crystallo.	R. T. to 2000°C	Air	Cleaved, Single crystal	Time, Strength, Dislocation Density
11. Surface Active Environments	Materials Research	G. T. Murray	N. A. Weil	MgO, CaF_2, Al_2O_3 Single Crystals	Etch-pit, Crushing, Rupture	R. T. to 600°C	Neutral, Oxidizing	Cleaved, Single crystal,	Surf. Residue, Fracture Surface, Time, Strength, Yielding

7, 8 and 10 represents a novel departure, not previously investigated in a searching manner.

Another aspect governing the planning for this program was that, insofar as possible, the same materials be selected for experiments conducted on each Task, to afford ready comparisons and provide background data for the individual research undertakings. Observing this requirement, Al_2O_3 and MgO were selected as the principal materials to be studied on this program, because of their comparatively ready availability both as single crystals and multicrystals in reasonably large sizes, the particularly simple crystallographic nature (ionic lattice) of MgO, and an extensive amount of prior literature assembled regarding their behavior. In this context, Al_2O_3 and MgO are regarded as "model materials"; if their phenomenologic behavior is satisfactorily explored, it will open the way to an understanding of the anticipated performance of other brittle substances (nitrides, borides, carbides, intermetallics) intended for structural use in ultra-high temperature environments.

For purposes of basic studies, these materials are utilized in three forms: (a) single crystals, (b) polycrystalline material of the best density and purity consistent with commercially practiced fabrication methods, and (c) polycrystals of the highest purity and density attainable with the most demanding fabrication methods known at present, which eliminate the influence of as many extraneous factors (porosity, impurities) as possible. The consideration underlying the utilization of two polycrystalline forms of the materials selected is to extend results obtained with pure forms commercially available substances which, if successfully accomplished, could yield design data of direct applicability.

The proper organization and presentation of the results of a research program as broad as the current one always poses some difficult problems. To maintain the continuity of presentation, and still identify the specific problems attacked on each phase of the program,

it has been decided to assemble general information pertaining to the materials used in this program into a separate section dealing specifically with this subject; this topic comprises Chapter II of the text. The results of research carried out on this program are then summarized in Chapters III and IV, where each Task is described as an individual self-contained item. Thus, each of the Task reports are identified in regard to principal investigator and research organization, and carry their own abstracts and conclusions; their figures, tables and references are identified by a prefix corresponding to the Task number.

In addition to the final Task reports given in Chapters III and IV, Appendix A presents the final report on "Anelastic Phenomena in Polycrystalline Oxide Ceramics" by L. M. Atlas and J. M. Stuart. This report was prepared as a result of an internally sponsored ARF program, and is attached because of its close association with the current work and planned continuation of Task 5 of the parent program.

As with all large research undertakings, the success of attaining the stated goals of the overall program rests in large measure with the guidance given it by the sponsoring agency. It is pleasing to acknowledge in this regard the frequent exchange of helpful information, the supply of reports dealing with related research programs, and the suggestions advanced in the conduct of research by J. B. Blandford and J. D. Latva, the Technical Monitors of this research program, as well as by W. G. Ramke and J. J. Krochmal from the Ceramics and Graphite Branch, Directorate of Materials and Processes of the Aeronautical Systems Division, USAF.

It is also pleasing to report that the research carried out to date on this contract has already resulted in the oral presentation of two technical papers[1, 2]. In addition, E. Orowan has submitted a technical note for publication to Nature and a number of other papers are in preparation presenting the results of research conducted on this program.

REFERENCES

1 Weil, N. A., "Review of Brittle Fracture Criteria in Ceramic Materials", submitted for publication to the M. A. B. - N. A. S. Symposium on Design with Brittle Materials, Washington, D. C., (December, 1960).

2 Durelli, A. J., Morse, S. A., and Parks, V. J., "The Theta Specimen for the Determination of Tensile Strength of Brittle Materials", Ann. Mtg. Am. Cer. Soc., Toronto, Canada (April, 1961).

II. MATERIALS

1. INTRODUCTION

As mentioned, the research carried out on this program is concerned mainly with two oxides, Al_2O_3 and MgO, although other ionic crystals such as KCl, NaCl, KI and CaF_2 are also being used for exploratory purposes by some of the Tasks. In addition, exploratory work for several Tasks also utilized photoelastic materials (CR-39 and Plexiglas), Graphite, plaster of paris and glass.

The magnesium oxide and aluminum oxide used as the principal materials of research are explored as single crystals and in two forms of polycrystalline material: a form whose purity and density is equal to the highest levels attainable in normal commercial operations, and an ultra-high density and purity polycrystalline material fabricated specially for purposes of this investigation. The three varieties of the two oxides, therefore, comprise six materials used throughout the program for experimental purposes. Information regarding these materials, concerning background data of general interest (such as methods of fabrication, compositional analysis and general mechanical properties) is given below.

2. ALUMINUM OXIDE

A. Single Crystals

This material is being supplied by the Crystal Products Section of the Linde Company, a division of Union Carbide Corp. in East Chicago, Indiana. Boules are available in sizes up to 500 carats; centerless ground specimens in maximum sizes of 3 in. length for 1/2 in. diameter, 10 in. length for 1/4 in. diameter and 18 in. length for 1/8 in. diameter. The material is available in four finishes (chemically etched, flame polished, mechanically polished and centerless ground). A representative composition is: Fe 1-10 ppm; Mg and Li 1-10 ppm; Mn, Sn, B undetected (within sensitivity of

measurement of 10 ppm); Ag, Ca, Cr, Cu undetected (within sensitivity of measurement of 1 ppm); balance Al_2O_3.

The material can be supplied with doping oxides up to the following percentages: Cr 4.0; Ni 3.0; Co, Mo and V 2.0; Cu 1.0; Fe 0.75.

B. High-Density Commercial Multicrystals (Wesgo AL995)

This material, and specimens fabricated from it, were supplied by the Western Gold and Platinum Corporation (Wesgo), using a proprietary composition labeled AL995. This material is listed as a 99.5% Al_2O_3 body, with a bulk specific gravity of 3.89 (theoretical = 3.996); the estimated density, therefore, is 97.35% of theoretical, and the porosity does not exceed 3%. Major impurities consist of MgO, SiO_2, CaO and Fe_2O_3; total impurities do not exceed 0.75%. A spectroscopic analysis of this material is presented in Table II.

Table II

SEMI-QUANTITATIVE ANALYSIS OF WESGO AL995 *

Element	Amount present (percent)
Al	Principal Constituent
Mg	0.3
Si	0.3
Ca	0.04
Fe	0.02
Ga	0.01
Ti	0.008
Cr	0.006
Ni	0.002
Cu	0.00005

*By Chicago Spectro-Service Laboratory, Inc.

The Wesgo material is prepared from a starting powder, doped with additives probably used as sintering aids. It is cold-pressed and sintered, the latter operation consisting of firing for three hours

at 1700°C, which produces an Al_2O_3 ceramic with maximum electrical properties, but represents a slight overfiring from viewpoint of optimum mechanical strength. The annealing operation used for some control specimens, consisting of a further three-hour soaking at 1700°C, represents a considerable overfiring of this material.

To examine the grain size characteristics of "as-received" Wesgo AL995, specimens were sectioned and polished, and examined under a monochromatic light using a B & L Metallograph with a calibrated eyepiece. The grain size distribution was found to vary between 16 and 128μ with an average of about 48μ; the distribution curve is slightly skewed toward the larger sizes. The grains show a large variation in shape, ranging from low to intermediate sphericity. The pores, in turn, show little variation in size or shape.

The same material, annealed at 1700°C for three hours, shows a bimodal grain size distribution with maxima at 24 and 64μ, even though the total size range remains within the limits of 16-128μ in the annealed material. The grains continue to have low to intermediate sphericity, the smaller grains being more angular than the large ones. The pores show large variations in size and shape after annealing.

The "as-received" Wesgo material indicated a small amount of secondary grain growth, which became very pronounced in the annealed material. This secondary growth did not affect the strength of the material, except to cause zones of high residual stresses around the holes drilled to admit the loading pins. This led to premature failure in some of the specimens.

C. Ultra-High Density Multicrystals (Lucalox)

This material is a development of the Lamp-Glass Division of General Electric Company which has been trademarked Lucalox. At grain sizes in excess of 20μ, the material is a pure dense aluminum oxide (99.97% theoretical) with an essentially zero porosity and

is largely translucent as compared to the opaque Wesgo AL995. The results of a spectroscopic analysis of Lucalox are listed in Table III.

Table III

SEMI-QUANTITATIVE ANALYSIS OF LUCALOX*

Element	Sample Crushed in Agate Mortar, Amount Present (Percent)	"As Received," Not Mortared Amount Present (Percent)
Al	Principal Element	Principal Element
Fe	0.07	0.002
Mg	0.15	0.15
Ti	0.01	Not Detected
Mn	0.001	Not Detected
V	0.004	Not Detected
Na	0.08	Not Detected
Cu	0.0003	Not Detected
Ni	0.0015	Not Detected
Ca	0.04	0.004
Cr	0.002	Not Detected
Ga	0.003	Not Detected
Si	0.03	0.03

*By Chicago Spectro-Service Laboratory, Inc.

A grain size determination showed a distribution ranging from 32 to 64 μ with an average of approximately 48 μ. The distribution was symmetrical and the grains were of uniform shape, with a few small pores of uniform size and shape distributed evenly in the material.

At grain sizes above 30μ the material approaches the theoretical density for Al_2O_3 (3.996 g/cc); below this grain size the density gradually decreases to about 97.2% theoretical at a grain size of 5μ, as shown in Fig. 1. Lucalox is composed of grains of very uniform size; as anticipated, at a grain size of 5μ a small amount of intergranular porosity is observable, as illustrated in the photomicrograph of Fig. 2. Details of the manufacturing procedures used in the production of Lucalox are proprietary and therefore not available.

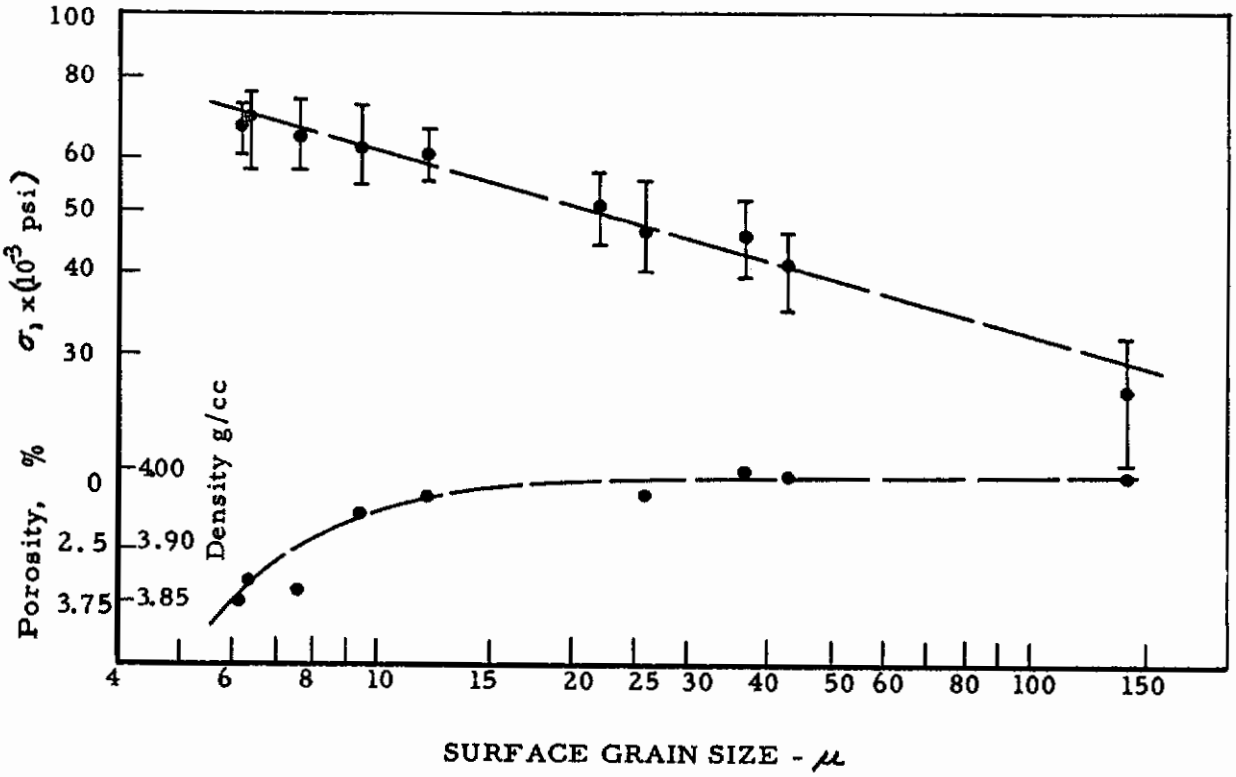

Fig. 1 STRENGTH AND DENSITY OF LUCALOX AS A FUNCTION OF GRAIN SIZE

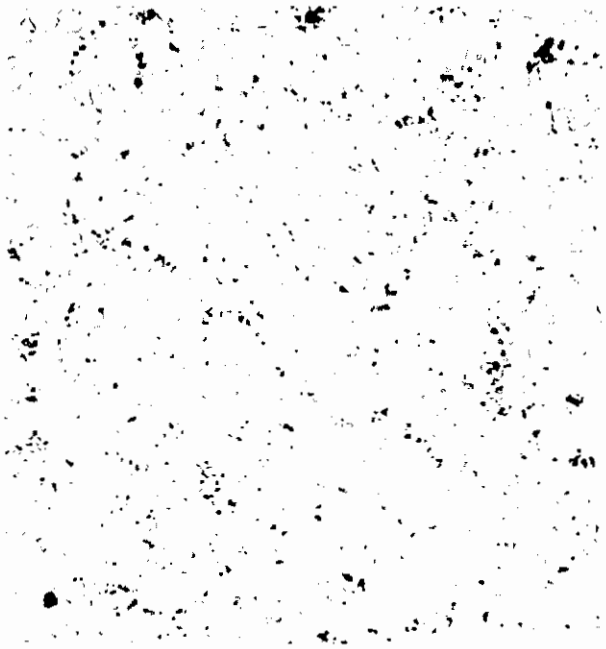

Note small amount of intergranular porosity characteristic of material at this grain size.

Fig. 2 PHOTOMICROGRAPH OF LUCALOX AT 5μ GRAIN SIZE X 250

D. Preliminary Studies on Al_2O_3

Before proceeding with large scale testing of the two grades of Al_2O_3 used in the program, a preliminary study was undertaken to validate information obtained from the sources of supply of the material, and to gain some insight into the anticipated properties of the materials to be used.

Initial information released by the manufacturer of Lucalox indicated a strength of 55, 000 psi. Inquiries made in this regard revealed that the reported data were obtained on highly polished bars, 1/4 in. square in section and 1 in. long, loaded over a 5/8 in. span in three-point bending. Therefore, as-received Lucalox specimens having an average grain size of 48μ, were cut into the shape defined above, and subjected to a three-point loading over a span of 5/8 in. A total of nine bars were used to study the additional effects of surface finish, three bars were left in the as-received condition, three were given a mild polish to remove the gross surface defects, and the last three were given a high polish. A group of three as-received Wesgo AL995 specimens were also tested at the same time. The results of these experiments are given in Table IV. The last line included in Table IV pertains to a set of three "maximum strength" Wesgo specimens tested in the as-received condition. This material is specially processed by the company for outstanding strength properties and costs about 50% more than the normal production materials.

Table IV

ROOM TEMPERATURE BENDING STRENGTHS
OF Al_2O_3 SPECIMENS*

Material and Finish	Extreme Fiber Strength, (10^{-3} psi)			
	Spec. 1	Spec. 2	Spec. 3	Average
Lucalox, As Received	28.4	26.2	27.6	27.4
Lucalox, Semi-Polished	30.9	35.5	29.4	31.9
Lucalox, Polished	34.8	40.5	39.9	38.4
Wesgo AL995, As Received	41.1	31.0	43.5	38.5
Wesgo "Maximum Strength" Al_2O_3 As Received	52.7	55.5	61.8	56.7

*1/4-in. square cross section specimens, tested over 5/8 in. span in 3-point bending.

The average fracture strength obtained for the polished Lucalox is 38, 400 psi, corroborating the strength of 39, 000 psi shown in Fig. 1 for an average grain size of 48μ. The effects of surface finish are seen in the 16.6% increase in rupture strength for semi-polished samples and the 40.2% increase for a highly polished surface. This indicates the sensitivity of the fracture strength of a bending sample to the presence of surface flaws.

A rather unexpected result was the considerably higher strength of the Wesgo material than the Lucalox at comparable grain sizes, despite the higher porosity of the former. This is very likely to have its origin in what can best be termed the "textural properties" of the material. According to the Petch relationship, cracking should clearly initiate in the largest grain subject to a given stress. Since the Wesgo AL995 has, because of its wider grain size distribution, larger grains than those to be found in Lucalox of the same average grain size, crack initiation should require a lower stress in the former. Therefore, one must rule out crack initiation considerations as an explanation of the observed strength relationship, and seek an answer for this apparent anomaly in conditions governing the propagation of already nucleated cracks.

In the case of Lucalox, a crack which has begun to propagate has little in its way to stop it. While it is probable that grain boundaries have some dispersing action on the stress concentration at the tip of the crack, this is apparently not a very effective barrier to continued crack propagation. In contrast, Wesgo AL995 has two textural properties which may be potentially effective crack barriers: pores and very small grains. The crack retarding effect of a small pore is well known and need not be further belabored. However, the possible barrier effect of small grains acting as a matrix between large crystals has not been given much consideration. As is well known, the Griffith propagation theory postulates that the crack is running into a uniform stress field, an assumption which is not particularly applicable to a polycrystalline material. In this case, the stress field is more apt to be fluctuating (because of the influence of grain boundaries and pores), akin to the more periodical fluctuation of the potential field in a crystal lattice. When the fluctuations are far apart, compared to the critical size of a crack needed for propagation, the cracks develop their full velocity and easily jump the grain boundary barriers. However, if a crack initiates in a large grain, but then has to traverse a

series of very small grains with only short distances between the boundaries, its momentum may be much diminished. Consequently it may be brought to a halt at small discontinuities which would not effectively stop a more rapidly propagating crack. These considerations lead to the interesting conclusions that polycrystalline ceramics might, in effect, be strengthened by the presence of a small residual porosity and by a widening of the distribution around the average value of grain size.

Additional evidence of the possibility of this behavior is that while the as-received Wesgo material with an average grain size of 45μ has approximately the same strength as the polished Lucalox, a slightly lower density Wesgo material with an average grain size of 10μ has a strength considerably lower than polished Lucalox specimens having a comparable grain size of 10μ .

E. Influence of Porosity on Strength of Lucalox

Because of the questions raised by the preliminary studies described in the previous section, it was decided to review the available evidence on the influence of porosity and grain size upon the strength of brittle materials.

Without attempting to make a complete review of this problem, it may be mentioned that two general formulations have been proposed to relate the strength of brittle bodies to the porosity contained in them. One is due to Balshin[1] which expresses the strength σ_p of a porous body in the form

$$\sigma_p = \sigma \gamma^m \qquad (1)$$

where σ is the strength of the dense body, γ is the relative density ($\gamma = 1 - p$; p = porosity), and m is a numerical exponent varying between 3 and 6. The second formulation is due to Ryshkewitch[2] who,

in a detailed investigation on polycrystalline Al_2O_3 and ZrO_2, noted that they varied exponentially with a decrease in porosity. This observation was formalized by Duckworth[3] who in a discussion of Ryshkewitch' paper proposed the form

$$\sigma_p = \sigma e^{-bp} \qquad (2)$$

where b is a numerical constant generally varying between 4 and 9.

Actually, both of these formulations must be considered as partial simplifications of more complex phenomena. The effect of porosity on strength should be a composite of two independent influences: the amount of material removed from the material by the pores, and the stress concentration factors attributable to them. The first effect is purely volumetric. The second effect, however, would consider whether the material contains many small voids or a few large pores, and assign different weakening factors to the corresponding textural effects. Additional considerations may involve the uniformity of size and distribution of pores, which must be attacked by statistical considerations.

As long as pores are roughly proportional in size to the void ratio and grain size, these parameters will not manifest themselves separately, but will be submerged into expressions that take into account only the influence of grain size and porosity on the strength of the material. This, in fact, is frequently the case with polycrystalline materials. For these conditions, Eq. 1 and 2 will then be quite representative; the choice between them must then be made on the basis of correlations with experimental results after, of course, suitable allowance is made for the inclusion of the grain size effect into the corresponding equations.

Tests appear to indicate that the Ryshkewitch relationship is a better description of observed phenomena; this expression has, therefore, found rather wide acceptance. A detailed study on this subject has been recently carried out by Knudsen[4] who, after careful examination of the

available theoretical and experimental evidence, suggested the adoption of Eq. 2, combined with a strength-grain size relationship of

$$\sigma = k\, d^{-a} \qquad (3)$$

where d is the grain size, while a and k are constants. The complete form of the relationship proposed by Knudsen, therefore, reads

$$\sigma_p = k\, d^{-a}\, e^{-bp} \qquad (4)$$

and its applicability was shown to hold for a wide variety of materials, with values of a ranging between 0.2 and 0.9. Further confirmation of this relationship has been given in a recent paper by Spriggs and Vasilos[5] who, for Al_2O_3, found a = 1/3. They further proposed a relationship similar to Eq. 2 for the modulus of elasticity of the material, in the form

$$E_p = E\, e^{-Bp} \qquad (5)$$

where E_p and E are the moduli of elasticity pertaining to the porous and dense material, respectively. The value of the constant B in Eq. 5 was found to be 4.5 for both Al_2O_3 and MgO.

A possible objection to the relationship embodied in Eq. 3 is that it predicts a vanishing strength with increasing grain size. If used beyond the limits of its intended range, this could be construed to imply that single crystals would have virtually no strength of their own. One way of circumventing this is to replace Eq. 3 with the strength relationship proposed by Petch[6], in the form

$$\sigma = \sigma_o + k\, d^{-1/2} \qquad (6)$$

where σ_o is the Peierls-Nabarro friction stress causing dislocation locking. The complete strength relationship would then become

$$\sigma_p = (\sigma_o + k\, d^{-1/2})\, e^{-bp} \qquad (7)$$

To investigate the adequacy of these predictions, a careful review was made of the strength versus grain size and density relationship for the materials used on this program. At the time of this writing, such information was available only for Lucalox, derived as part of the work performed on Task 9 of this program, using rods 0.070 in. in diameter with a carefully controlled grain size under 4-point bending. This is presented in Fig. 1.

A careful analysis of these data was made by Knudsen[7] who found that the results presented in Fig. 1 could be well represented by Eq. 4, with numerical values of k = 150,000, a = 0.35 and b = 4 for the constants appearing in that relationship. In developing these values, a reference line was established for the strength versus grain size relationship of Eq. 2, by drawing a straight line through the least porous (highest grain size, porosity about 0.1%) specimens shown in Fig. 1. This construction is presented in Fig. 3.

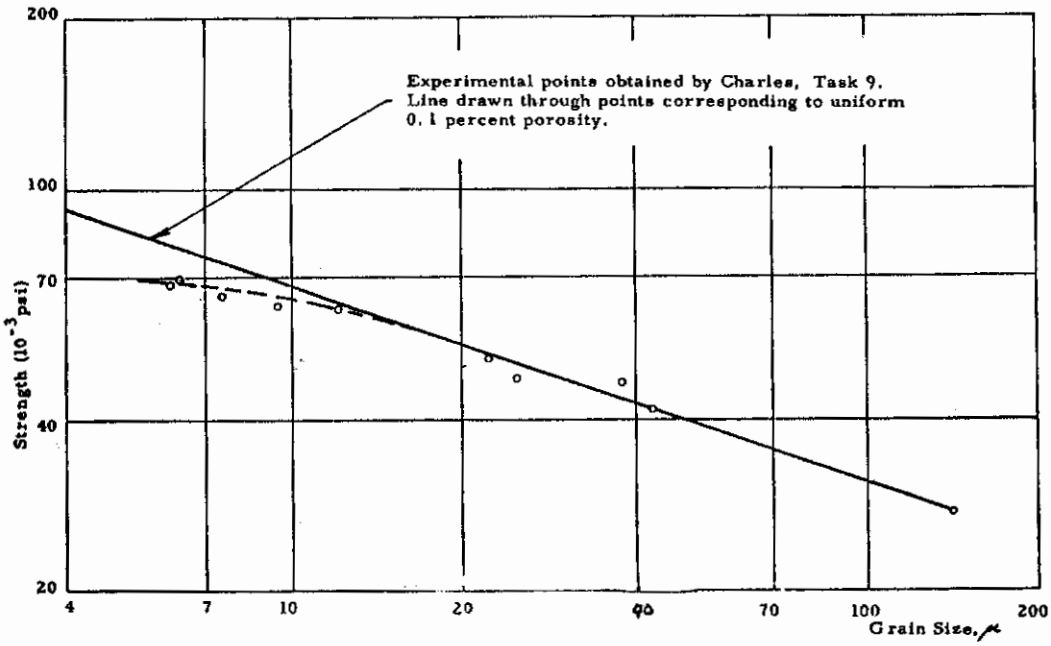

Fig. 3 MODIFIED STRENGTH VS. GRAIN SIZE RELATIONSHIP FOR LUCALOX AT CONSTANT POROSITY[7]

The fit of the resulting equation of

$$\sigma_p = 150,000\, d^{-0.35}\, e^{-4p} \qquad (8)$$

to the experimental data is shown in Table V. As can be seen, the agreement is rather good, the average absolute difference between predicted and observed results being 2.6%

Table V

FIT OF KNUDSEN EQUATION TO DATA ON LUCALOX[7]

Observed Strength (10^{-3} psi)	Calc. Strength, Eq. 8, (10^{-3} psi)	Percent Deviation*
68.0	68.58	+0.9
70.0	69.06	-1.3
65.0	69.43	-0.9
63.0	64.63	+2.6
62.0	59.62	-3.9
47.0	47.09	+0.2
46.0	41.94	-8.8
41.0	40.05	-2.3
27.0	26.37	-2.3
Average of Absolute Deviations: 2.6%		

*Percent Deviation $= \dfrac{\sigma_{calc.} - \sigma_{obs}}{\sigma_{obs}}\, 100$

A similar study was carried out to examine the adequacy of the proposed Eq. 7. In order to do this, the data of Fig. 1 were first replotted in a Petch-type form, shown in Fig. 4. Next, a graph was prepared, with p on the abscissa and log (σ_p/σ) on the ordinate as shown in Fig. 5, where values of σ were derived from the previous

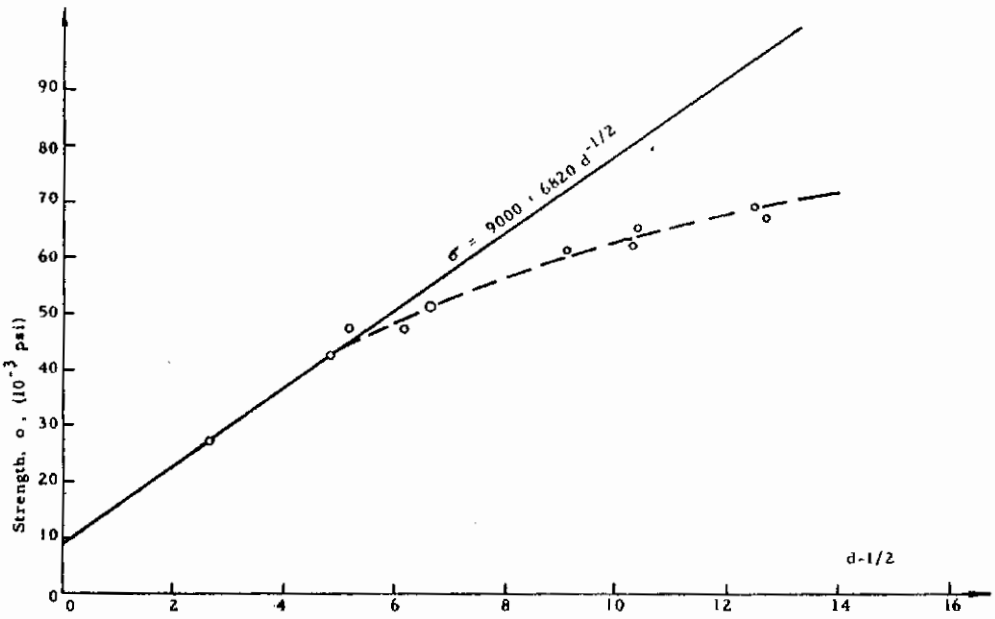

Fig. 4 PETCH-TYPE RELATIONSHIP FOR DEPENDENCE OF STRENGTH ON GRAIN SIZE IN LUCALOX

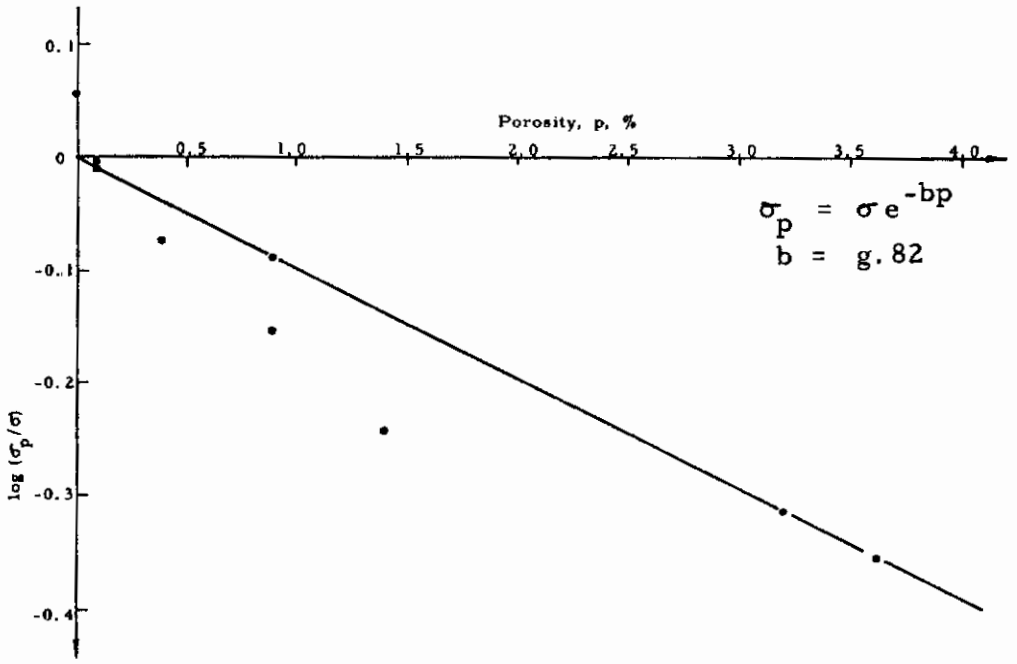

Fig. 5 DEPENDENCE OF STRENGTH ON POROSITY IN LUCALOX

figure. The resulting numerical values were σ_o = 9,000 psi, k = 6,820 and b = 9.82 with relation to Eq. 7, which then becomes

$$\sigma_p = (9,000 + 6,820\ d^{-1/2})\ e^{-9.82p} \qquad (9)$$

The fit of calculated and experimental data resulting from this relationship is presented in Table VI; as can be seen, the agreement is satisfactory, although the average of absolute deviations is somewhat higher at 3.9%.

Table VI

CALCULATED STRENGTH OF LUCALOX AS FUNCTION OF GRAIN SIZE AND POROSITY, BASED ON EQ. 9

Grain Size, d (mm)	Observed Strength σ_{exp} (ksi)	Porosity, (absolute) p	Calculated Strength at 0 Porosity σ_o (ksi)	$\sigma_p = \sigma e^{-bp}$ calculated strength for porous material (ksi)	Deviation 100 $\frac{\sigma_p - \sigma_{exp}}{\sigma_{exp}}$ (percent)
.0062	67.0	0.036	95.6	67.0	0.0
.0064	69.0	0.032	94.2	68.8	-0.3
.0077	65.0	0.034	79.8	57.3	-10.8
.0094	62.0	0.014	79.3	69.2	+11.6
.012	61.0	0.009	71.1	65.1	+6.8
.022	51.0	0.004*	54.9	52.8	+3.5
.026	47.0	0.009	51.2	46.9	-0.2
.037	47.0	0	44.4	44.4	-5.5
.042	42.0	0.001	42.2	41.8	-0.5
.140	27.0	0.001	27.2	27.0	0.0

Average of absolute deviation: 3.9%

*Estimated value

One limitation in making effective comparisons at this time is that Lucalox is an extremely dense material, whose porosity variation is too narrow to permit a detailed investigation of this problem; all that can be

said with data available at present is that both Eq. 4 and 7 apparently are quite satisfactory in predicting the strength of ceramics having different grain sizes and varying levels of porosity. A more detailed investigation of this entire problem area is planned during the continuation phase of this research, at which time ceramic substances with a far wider variation of porosities will be drawn under scrutiny.

3. MAGNESIUM OXIDE

A. Single Crystals

This material is being procured from two sources. One source is the Norton Company, Worcester, Massachusetts, whose single crystal MgO is obtained as a by-product of their "Magnorite" operations. Upon completion of the thermal fusion process for Magnorite, the contents of the retort are dumped out and crushed with sledgehammers. The yield of crystals, as much as 1000 lb, is therefore broken up into pieces ranging up to about 3 in. in size.

The resulting single crystals of MgO vary in shape, size and color, and level of contaminants. Their color may range from totally colorless to a faint brown, yellow or green tint indicating increased levels of impurities. Also, the pieces may vary from completely transparent to barely translucent. Some crystals contain white "clouds", thought to be the result of incipient fissuring induced by thermal stresses accompanying cooling.

The maximum total impurities present in the Norton material may range up to 1.0%. Their composition varies widely. A spectrochemical analysis of three samples, excerpted from Task 5, is reproduced in Table VII.

The second source of MgO single crystals is Semi-Elements, Inc., Saxonburg, Pennsylvania. Their manufacturing methods are aimed at the direct production of crystals grown from a pure MgO starting

Table VII

QUANTITATIVE SPECTROCHEMICAL ANALYSIS OF SINGLE CRYSTAL MgO SPECIMENS*

Material Source		Impurity (ppm)							Max. total Impurity (percent)
		Al	Ca	Cr	Cu	Fe	Mn	Si	
Norton Co.	Range for 3 spec.	200-1000	600-1500	60-100	2	600	30-40	5-10	0.6
	Aver.	600	900	73	2	600	37	7	
Semi-Elements, Inc.		200	200	80	2	400	30	5	0.3

*by Chicago Spectro-Service Laboratory, Inc.

powder; the crystals are supplied with a cleaved, chemically-polished or ground finish up to 1-1/2 in. sizes. The composition varies, but the impurity levels are generally lower than those found in the Norton material. This is also shown in Table VII, where the values shown are based upon the analysis of a single specimen. The chemical analysis supplied by Semi-Elements for their material is given as: SiO_2 - 0.05%; Fe_2O_3 - 0.03%; PbO - 0.001%; Al_2O_3 - 0.015%; CuO - 0.0005%; NiO - 0.001%; CaO - 0.15%; MnO - 0.01%; Na_2O - 0.005%; K_2O - 0.001%; balance MgO; total impurities: less than 0.3%. These results compare reasonably well with those listed in Table VII.

B. High Density Sintered MgO

Whenever possible, the materials used were purchased from commercial suppliers. These companies were required to produce the specimens from one batch of material and with one kiln firing after the specimens had been randomly spaced in the kiln. No commercial source was found who could produce the MgO specimens

required within the time and funding allotted to this task. The Foundation personnel developed a process by which high-density multicrystalline MgO was produced easily and rapidly. While several systems have been tried and reported, the technique presented below was found to be best for mass producing the required samples.

The process consists of preparing a solution by dissolving 1.5 wt. percent of Acryloid B-72 resin (100% solids, Rohm & Haas Co., Philadelphia Pa.) and 3 wt. percent stearic acid in carbon tetrachloride and mixing in an equal weight of Mallinckrodt AR Grade magnesium oxide powder to form a slurry. This slurry is then mixed and kneaded while the carbon tetrachloride evaporates until little solvent remains. The solid mass is then ground to pass a 30-mesh screen. The resulting powder is pressed from both sides in a die at 9000 psi for one minute to form the required specimen shape. The green body is then removed and placed in a drying oven at 100°C to drive off the last traces of carbon tetrachloride and to harden the specimen. After drying the specimens are kept in a desiccator until firing.

The specimens are stacked six high on dense alumina bricks covered with carefully leveled fine alumina grain. A light dusting of MgO between each specimen provides a parting surface for easy separation. The bricks and specimens are placed in an alumina sagger and fired in a Remmey air/gas laboratory kiln. Depending on size, 75 to 90 specimens are fired from room temperature to 1700°C in 20 hours, held at temperature for 3 hours, and then slowly cooled in the furnace. Two firings can be made in a 40-hour time period.

The Mallinckrodt MgO powder has a bulk density of 0.1-0.2; after mixing with the carbon tetrachloride solution, the resulting powder has a bulk density of 0.8-1.0. Density of the green specimen is 1.7-1.9, or approximately a 2:1 compaction ratio which is the result of addition of Acryloid resin to the MgO powder. The resin greatly improves strength and hydration resistance of the green specimen.

The fired MgO specimens have a bulk density ranging between 3.39 and 3.42, or approximately 95 percent of theoretical (3.58). They are white and partially translucent, although not to the same degree as Lucalox. A spectrographic analysis of this material is given in Table VIII. A grain size determination using the Smith-Guttman[9] technique indicated a range from 10 to 100 μ with the average size at about 25 μ. The grains are highly spherical with a few small scattered pores being visible.

Table VIII

SEMI-QUANTITATIVE ANALYSIS OF COLD-PRESSED AND SINTERED MgO*

Element	Amount Present, (percent)
Mg	Principal Constituent
Al	0.05
Si	0.03
Ca	0.04
Fe	0.005
Cr	0.0003
Cu	0.0002

*Chicago Spectro-Service Laboratory, Inc.

To date, this material was used exclusively for the experiments conducted on Task 1 of this program. However, facilities have been established at sufficient production rates to satisfy the needs of all other Tasks, and the incorporation of this material into experiments of other Task programs is planned in the future.

C. Hot-Pressed (Ultra-High Density) Polycrystalline MgO

High density polycrystalline MgO specimens for the program have been manufactured at ARF using the hot pressing techniques.

The MgO used was Fisher's USP light powder (Cat. No. M49) to which 0.5 percent LiF was added to aid the sintering process and thereby produce material of high density. It was not thought that the LiF addition would significantly influence the trend of the experimental data; the presence of porosity would be far more undesirable.

Some 120 specimens have been produced with densities within the range 3.56 - 3.57 g/cc, i.e., 99.4 - 99.7 percent of theoretical: In the hot-pressed condition, the material was relatively fine grained. The manufacturing procedure, based on the initial work of Tinklepaugh[8], is briefly outlined below.

(1) Magneisum oxide powder together with 5 wt percent LiF was ball milled in batches of 250 in one-gallon jars for 72 hours. Rubber stoppers were used as balls. In addition to thoroughly mixing the MgO and LiF, this operation reduced the volume of the light, fluffy as-received powder. It should be noted that the LiF was premixed with about 37 g MgO and panned through a NBS No. 35 sieve several times to blend the powders before adding to the bulk of the MgO. This stage helped considerably in producing a homogeneous mixture of the two powders on subsequent milling.

(2) Hot-pressing was carried out in a 12 in. high x 4 in. diam. graphite mold containing a 1/2 in. diam. center hole into which the blended MgO powder was charged. A 1/4 in. hole drilled from the top to a depth of 6 in. and parallel to the die cavity was used for the optical temperature measurements.

(3) The mold was filled by pouring in 14 g of powder (enough to make one cylinder about 1 in. tall x 1/2 in. diam.) lightly cold pressed to allow the top punch to move into the mold, and transposed to the hot pressing apparatus. Both top and bottom punches were made of grade 580 graphitized carbon.

(4) The mold was heated by a 30-kw Ajax induction unit, the temperature being brought up to 1600-1700°F before any measurable load was applied. At this temperature the pressure was gradually increased, reaching a maximum of about 3000 psi at 2000°F. The temperature was then raised to 2350°F, and held there for 20 min; subsequently the pressure was released and the mold unit removed from the apparatus.

(5) The mold was then quickly immersed in vermiculite and allowed to cool slowly to room temperature before ejecting the MgO compact.

(6) On removal from the mold, the MgO specimens are encrusted with carbon picked up from the graphite die during hot-pressing. Decarburization was effected by heating the specimens to 1200°C for 168 hours in air, which removed the carbon by oxidation. Thus, high density, single phase, polycrystalline MgO was produced, a typical microstructure is shown in Fig. 6. In the pressed condition, the grain size was about 27μ, as determined by the Smith-Guttman[9] technique. A microscopical examination of a number of longitudinal sections showed the pressings to be homogeneous in both grain size and distribution of microporosity. Furthermore, there was no evidence of laminations in the structure.

Prior to testing the specimens were centerless ground and the end faces ground square to the cylindrical axis. In all grinding operations water coolant was used to avoid thermal cracking.

Production of hot-pressed MgO specimens was limited to cylindrical bodies, used to date exclusively for purposes of experiments conducted on Task 4 of this research program.

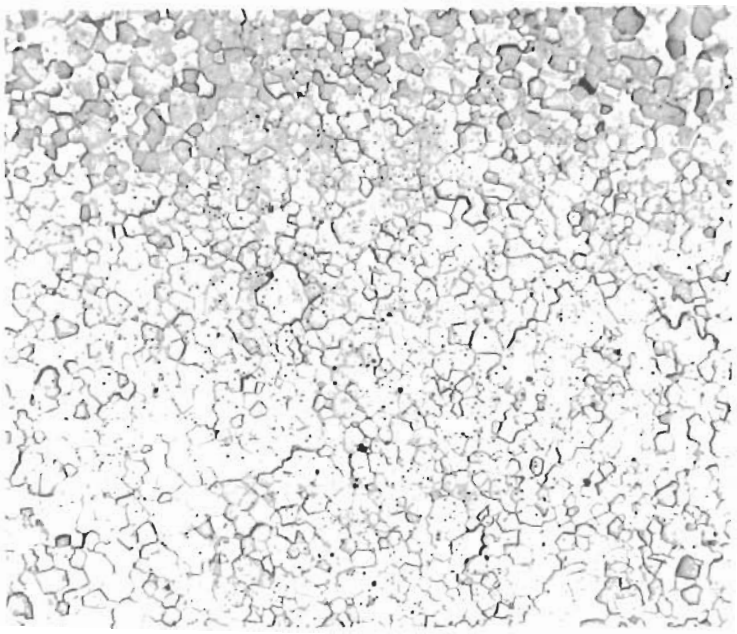

Fig. 6 PHOTOMICROGRAPH OF HOT PRESSED AND DECARBURIZED MgO X 100
Grain size: 27μ ; No etchant

4. REFERENCES

1. Balshin, M. Y., Doklady Akad. Sci., USSR, 67, 831 (1949).

2. Ryshkewitch, E., J. Am. Cer. Soc., 36, 65 (1953).

3. Duckworth, W., Discussion to Ref. 2, J. Am. Cer. Soc., 36, 68 (1953).

4. Knudsen, F.P., J. Am. Cer.S oc., 42, 376 (1959).

5. Spriggs, R.M. and Vasilos, T., "Effect of Grain Size and Porosity on the Transverse Bend Strength and Elastic Modulus of Hot Pressed Alumina and Magnesia", presented at the 63rd Ann. Mtg., Am. Cer. Soc., Toronto (April 1961).

6. Petch, N. J., Phil. Mag., 1, 866 (1956). Also Br. J., Iron and Steel Inst., 174, 25 (1953).

7. Knudsen, F.P., Private Communication to N. A. Weil, (August 1961).

8. Tinklepaugh, J.R., Contract AF 33(616)-3798, Rept. No. 11, Wright Air Development Division (July 1960).

9. Smith. C.S. and Guttman, L., Trans. AIME, 197, 81 (1953).

III. FINAL REPORTS ON IN-HOUSE TASK PROGRAMS

TASK 1 - EFFECT OF STRUCTURAL SIZE; THE "ZERO STRENGTH"

Principal Investigator: S. A. Bortz
Armour Research Foundation

ABSTRACT

A detailed program was undertaken to determine the applicability of statistical fracture theories to inorganic ceramic material, and to define the major parameters affecting fracture strength. Specimen shapes were developed, adaptable to a broad range of loading conditions and volumetric variations.

A rather complete experimental problem was carried out on Wesgo AL995, investigating the effect of five variables: prior thermal history, specimen finish, test temperatures, environment, and specimen size. Of these parameters, specimen size, testing temperature, surface treatment and thermal history were found to have a primary influence on fracture strength. Environmental effects (moisture content) were found to be significant only for ground specimens tested at 20° C; at 1000° C all environmental influences became negligible.

Fracture in Wesgo AL995 at room temperature is governed purely by surface induced failure mechanisms. Both Weibull constants, the "flaw density parameter", m, and the "zero strength", σ_u, are highly sensitive to surface treatment and thermal history. Specifically, grinding increases the value of m but leaves σ_u unaltered; annealing increases m while also dropping the value of σ_u to zero. Both conditions act to weaken the material. This weakening effect is particularly pronounced in the case of annealed specimens; this is thought to be ascribable to the destruction of a beneficial residual stress distribution originally existing in the material due to the subsequent annealing treatment.

Similar trends are indicated for Lucalox and MgO, but data in hand at present are insufficient to permit firm conclusions to be drawn.

TASK 1 - EFFECT OF STRUCTURAL SIZE; THE "ZERO STRENGTH"

1. INTRODUCTION

The statistical nature of fracture in brittle materials is a comparatively well established fact; both theories and experimental studies have shown that conventional concepts of elastic theories do not suffice to explain the behavior of brittle materials, unless the underlying aspects of the random variability of their strength is fully taken into account.

Theories dealing with the statistical distribution of the strength of brittle substances are generally based on the concept of the "weakest-link" as the source of fracture initiation, as reviewed in greater detail in the report prepared for Task 3 of this program. These theories, in their simplest form, entail two material parameters, the stress level that the material can withstand with an absolute assurance of freedom from failure (σ_u, the "zero strength"), and a constant descriptive of the flaw density and severity existing in the material (m, the "flaw density constant"). Apart from requiring a knowledge of these two material parameters, the theories are at a satisfactory state of development to handle problems associated with the size of the structural object, its geometrical shape and the stress distribution existing in the body.

The general aspects of such theoretical investigations have been confirmed by experiment. Thus, it has been shown that brittle materials display a random statistical variation of strength, adequately described in most cases by the comparatively simpler concepts of theoretical formulations. However, the brittle materials used in these studies were generally those inexpensively procured and easily fabricated; thus, plaster of paris, concrete, hydrostone, and glass were the general objects of previous experimental work. Inorganic ceramics, because of their cost and fabrication problems, were seldom employed.

Furthermore, little attention was paid to the true nature of the material "constants" descriptive of statistical theories. While one investigation on graphite did show that the value of m varies with temperature, seldom was any attempt made to explore this subject fully, or to investigate the effect of other parameters, such as environmental conditions, thermal history or surface treatment, upon the resulting variations in material "constants" entering the formulation of statistical strength theories.

In view of these considerations, the purpose of this research had two main objectives. First, to investigate the applicability of statistical theories of fracture to the ceramic oxides selected as general materials to be used throughout this program and to derive values of the statistical material parameters, as well as to confirm the effect of specimen size in these materials. The second objective consisted of determining the constancy or variability of basic material descriptors entering statistical formulations, and to examine the specific effects that temperature, atmospheric environment, surface finish, and heat treatment may have upon the values of σ_u and m for these substances.

2. SPECIMEN DESIGN

To investigate the fracture properties of the materials, studies were conducted using both tension and bending test specimens. Initial experiments were performed in cooperation with the personnel of Task 3, utilizing photoelastic methods to observe whether contemplated configurations produced critical stress concentrations which would cause fractures to occur in areas other than the desired gage section. These experiments were performed using Columbia resin CR-39, a very brittle plastic excellently suited to photoelastic studies.

A. Flexural Specimens

To study size effects the specimens would require a controlled gage section to be loaded in pure bending. This requirement could

best be met using a 4-point loading system. However, Frocht[1-1] points out the difficulty of producing a stress pattern of pure bending of known bending moment. One of the major problems is the loading conditions themselves.

If the external loads are applied to the extreme fibers, friction forces are developed which tend to reduce the applied bending moment and shift the position of the neutral axis. On the compression side of a beam (Fig. 1-1) there are two factors which tend to shorten the distance AB on the beam; the compressive strain and the deflection. Thus, loads applied at A and B tend to move toward the end of the beam, generating friction forces F_1 which act as shown in Fig. 1-1. Strains developed on the tension side tend to increase the length of CD, while the deflection tends to shorten the horizontal distance between CD. Experiments, as indicated in Fig. 1-2 and 1-3, show that the effect of these friction forces is to reduce the applied moment. Accordingly, the forces F_2 act opposite to F_1 . Each friction force thereby generates an axial force and a couple opposite in sign to that of the applied bending moment.

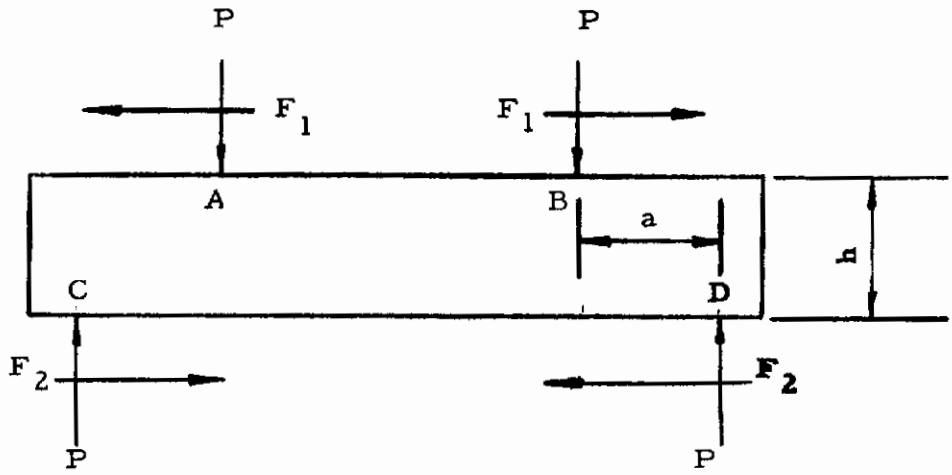

Load Points: A, B
Support Points: C, D

Fig. 1-1 EFFECT OF FRICTION FORCES ON PURE BENDING

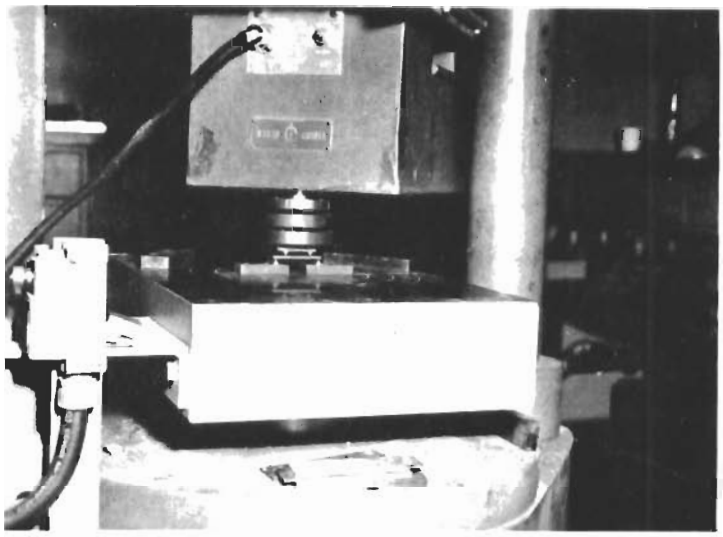

Fig. 1-2 4-POINT BENDING WITH FIXED LOAD POINTS AND SUPPORTS

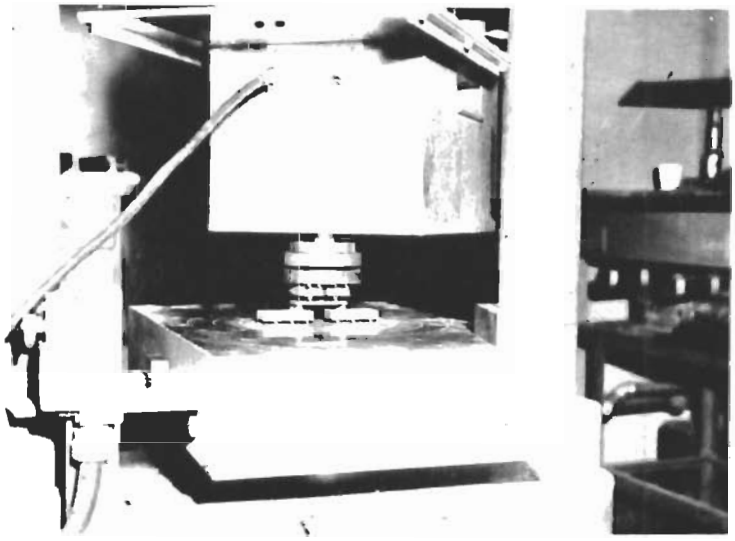

Fig. 1-3 4-POINT BENDING TEST, LOAD POINTS AND SUPPORTS MOUNTED ON ROLLERS

If μ is the coefficient of friction at all points of load contact, the friction forces in Fig. 1-1 are

$$F_1 \leq \mu_1 P \quad \text{and} \quad F_2 \leq \mu_2 P \tag{1-1}$$

The stresses in the gage section resulting from the forces acting as shown in Fig. 1-1 are

$$\sigma = \frac{M}{S} \tag{1-2}$$

$$M = Pa - (F_2 h/2 + F_1 h/2) \tag{1-3}$$

where M is the internal moment and S is the section modulus of the cross section. The total stress over the central part of the beam, therefore, becomes

$$\sigma_f = \frac{F_2 - F_1}{bd} \pm \frac{6}{bd^2} \left[Pa - (F_2 h/2 + F_1 h/2)\right] \tag{1-4}$$

For the same friction coefficients at all contact points, Eq. 1-4 reduces to

$$\sigma_f = \pm \frac{6P}{bd^2} (a - \mu h) \tag{1-5}$$

To determine the magnitude of error entailed in using load points that allow for the development of frictional forces, the Eq. 1-5 must be compared with the equation for stress neglecting friction.

$$\sigma = \pm \frac{6\,Pa}{bd^2} \tag{1-6}$$

so that

$$\frac{\sigma_f}{\sigma} = \frac{(a - \mu h)}{a} \tag{1-7}$$

Table 1-I gives the results of a friction study made, using graphite specimens.

Table 1-I

FRICTION FORCES IN BEND TESTS ON GRAPHITE

Loading	Fracture Load (lb)			Average Load (lb)
	1	2	3	
Fixed load points and supports	47.5	51	42.5	47
Movable load points and supports	53	62	47.5	54.2

The coefficient of friction between the load jig and specimen was determined as 0.4. The specimens were 1/8 in. thick, and the length as shown in Fig. 1-1 was 0.4375 in. Since the fracture load is proportional to fracture stress for specimens of the same dimensions, there results

$$\frac{P_f}{P} = \frac{\sigma_f}{\sigma} = \frac{(a - \mu h)}{a} = 0.885 \qquad (1\text{-}8)$$

The experimental results presented in Table 1-I yield

$$\frac{P_f}{P} = \frac{47}{54.2} = 0.87 \qquad (1\text{-}9)$$

in good agreement with theory.

The results of these experiments led to the use of circular holes on the neutral axis of the beam, with loads applied through pins passing through these holes. This procedure eliminated the possibility

of errors being introduced when the fracture strengths of different depth beams were compared for size effects.

Furnace requirements limited specimen lengths to 4 in. for the bending tests. To keep down fabrication costs, the basic bending specimen shape was also to be used for the tensile specimens; a minimum transition radius of 2 in. was chosen for this purpose. To ensure uniformity of denseness and reduce body flaws during pressing and sintering a flat coupon type body was decided upon. Several shapes were subjected to detailed experimentation; the final shape selected was a "dogbone" configuration which met the requirements of this study. Figure 1-4 presents a view of a photoelastic pattern made during the dogbone investigation. The fringe pattern indicates that pure bending occurs in the gage section, and shows that stress concentrations around the pin holes are not large enough to cause premature failure at these points.

The various dogbone shapes adapted for this program are shown in Fig. 1-5. The volume ratios are 1:4: 8.35 from the smallest to the largest gage section.

B. Tension Specimens

Studies were undertaken to determine an effective technique for axial tension loading of the basic dogbone design used as a flexure specimen. Experiments with a pin connection were unsuccessful, although modifications were made in accordance with photoelastic data obtained by Frocht[1-2], as shown in Fig. 1-6. These failures were due to the limitation on the sample sizes.

Studies were made using end grips instead of pins through the samples. Although swivel attachments were used in the pull-heads, photoelastic experiments indicated that bending was occurring in the gage section. Further investigation with end grips of various shapes

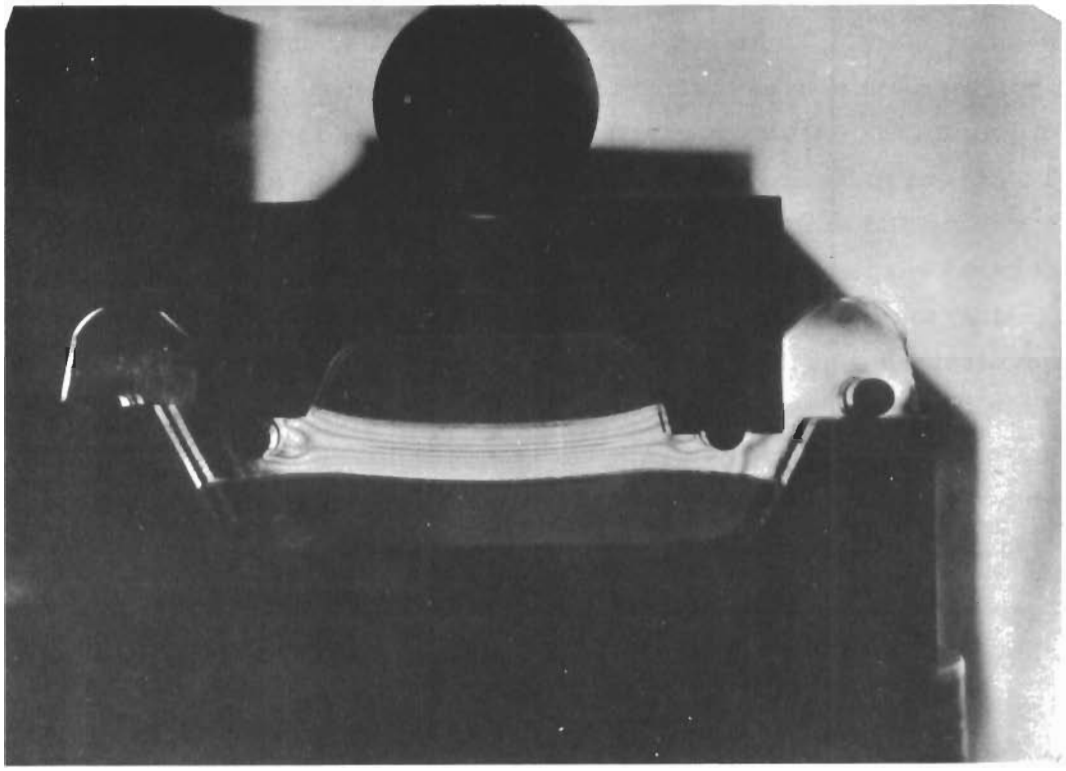

Fig. 1-4 PHOTOELASTIC PATTERN SHOWING UNIFORM BENDING IN THE DOGBONE SPECIMEN

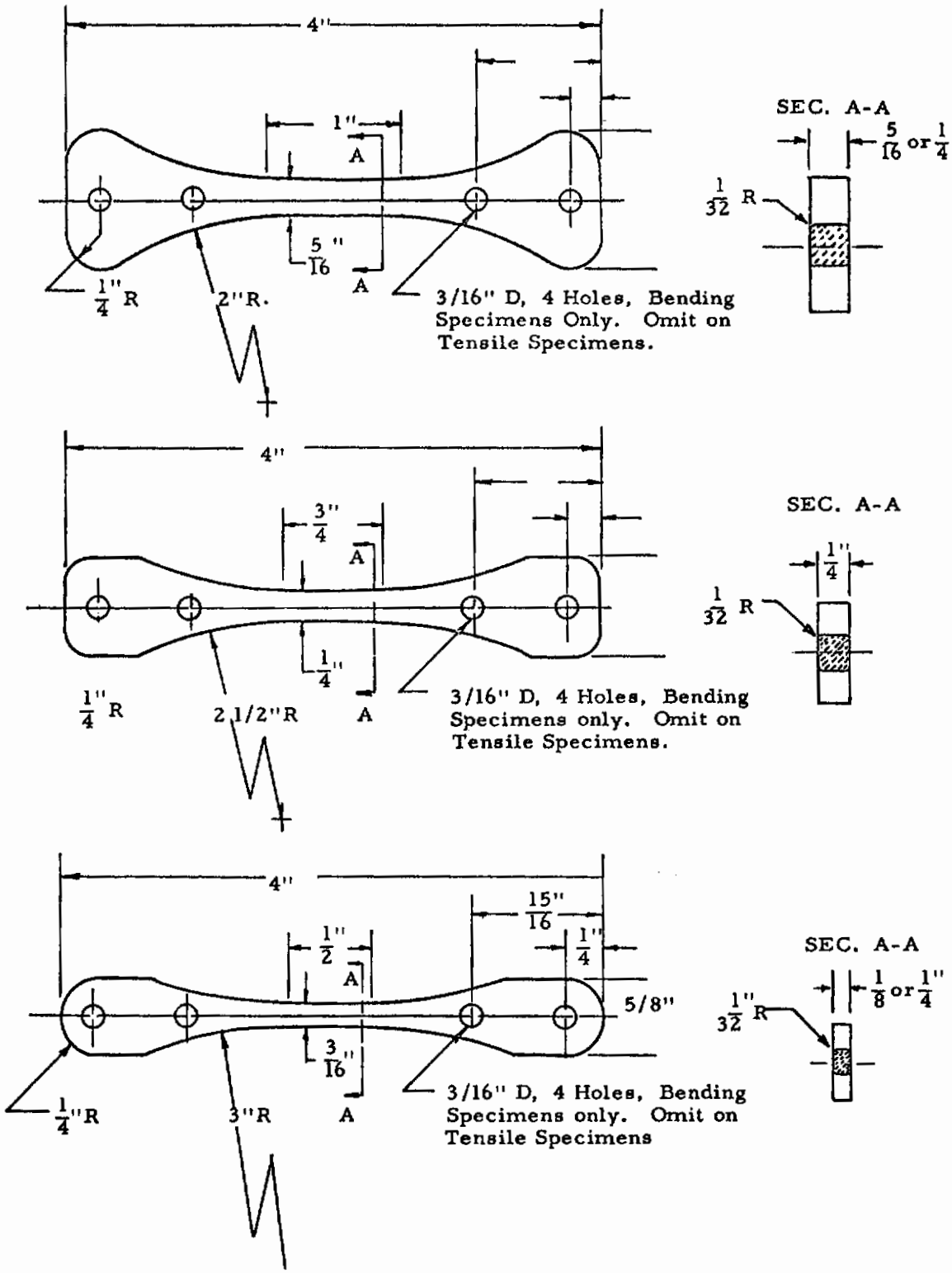

Fig. 1-5 DETAILS OF MULTICRYSTALLINE DOGBONE SPECIMENS FOR TENSION AND BENDING

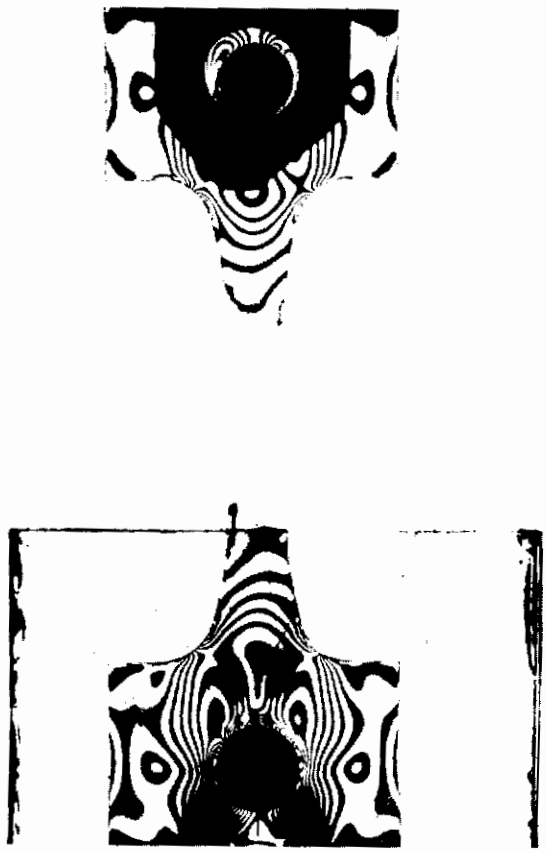

Fig. 1-6 PHOTOELASTIC PATTERN IN PINNED TENSION SPECIMENS SHOWING SMALL ECCENTRICITY OF LOADING

led to the adoption of an open snug fitting grip with a double clevis pin connection, shown in Fig. 1-7. Photoelastic patterns, presented in Fig. 1-8, exhibited uniform axial loading for this arrangement. Subsequent experiments using SR-4 strain gages displayed some bending component in the ceramic specimens. However, with careful alignment of the specimen in the grips and the use of crushable shims, the bending strain shown by the gages could be kept below 10% of the total strain at failure.

3. EQUIPMENT

A two-bay 30, 000-lb hydraulic universal testing machine, equipped with a hydraulic ram, load cell with scales and small proving rings which allow accurate reading from 0. 5-30, 000 lbs, was used in the experiments. Recorders can be attached which will plot stress-strain automatically. The ram and load cell are mounted so that furnaces can be set up in both bays and the loading mechanism can be easily moved from one side to the other. This reduces the lag time for sample placement, time to reach test temperature and actual loading. Load can be preset and held indefinitely or cycled from tension to compression. Ram rate varies from 0 to 3 in. /min at maximum. Figure 1-9 presents a view of this equipment, showing the control panel with the load recorder in operation.

An induction heating furnace has been designed and built for operation in the range of 1750°C which is the upper limit of the contemplated high temperature tests using this loading machine. Induction heating was chosen because of the rapidity of reaching operating temperature and the wide range of temperatures which can be attained. A schematic drawing of this furnace is shown in Fig. 1-10. The upper temperature is limited by the formation of carbides between the carbon susceptor and the oxide tube, which becomes very rapid above 1800°C.

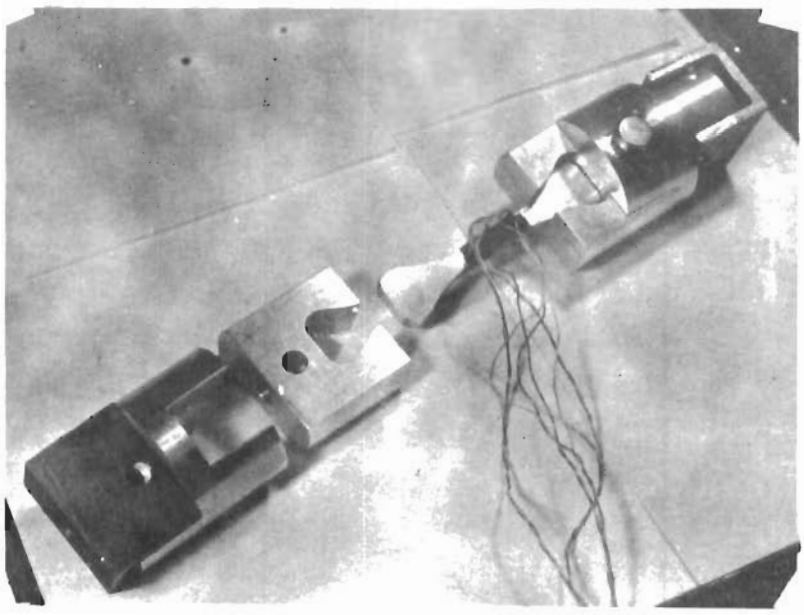

Fig. 1-7 TENSION GRIPS AND SR-4 INSTRUMENTED SAMPLE

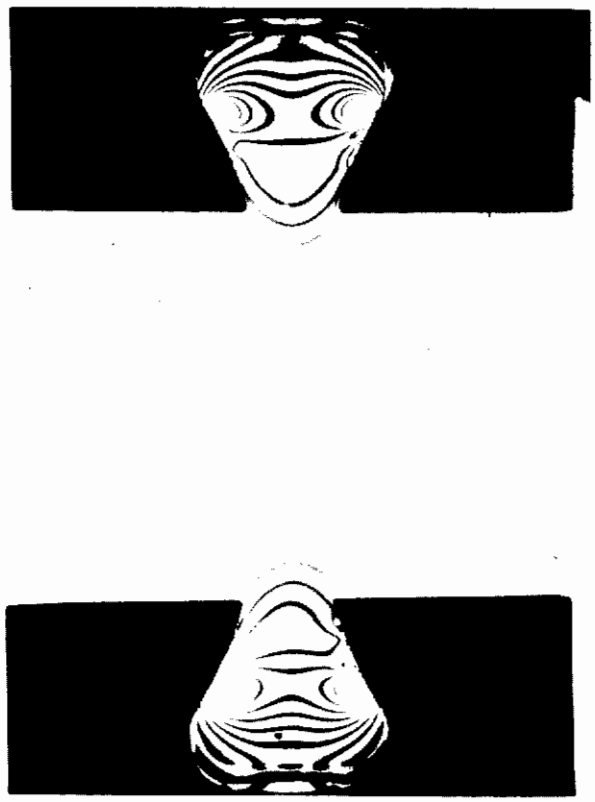

Fig. 1-8 AXIAL LOADING OF SPECIMEN USING SNUG GRIP AND PIN CONNECTION

Fig. 1-9 TWO-BAY 30,000 lb UNIVERSAL TESTING MACHINE

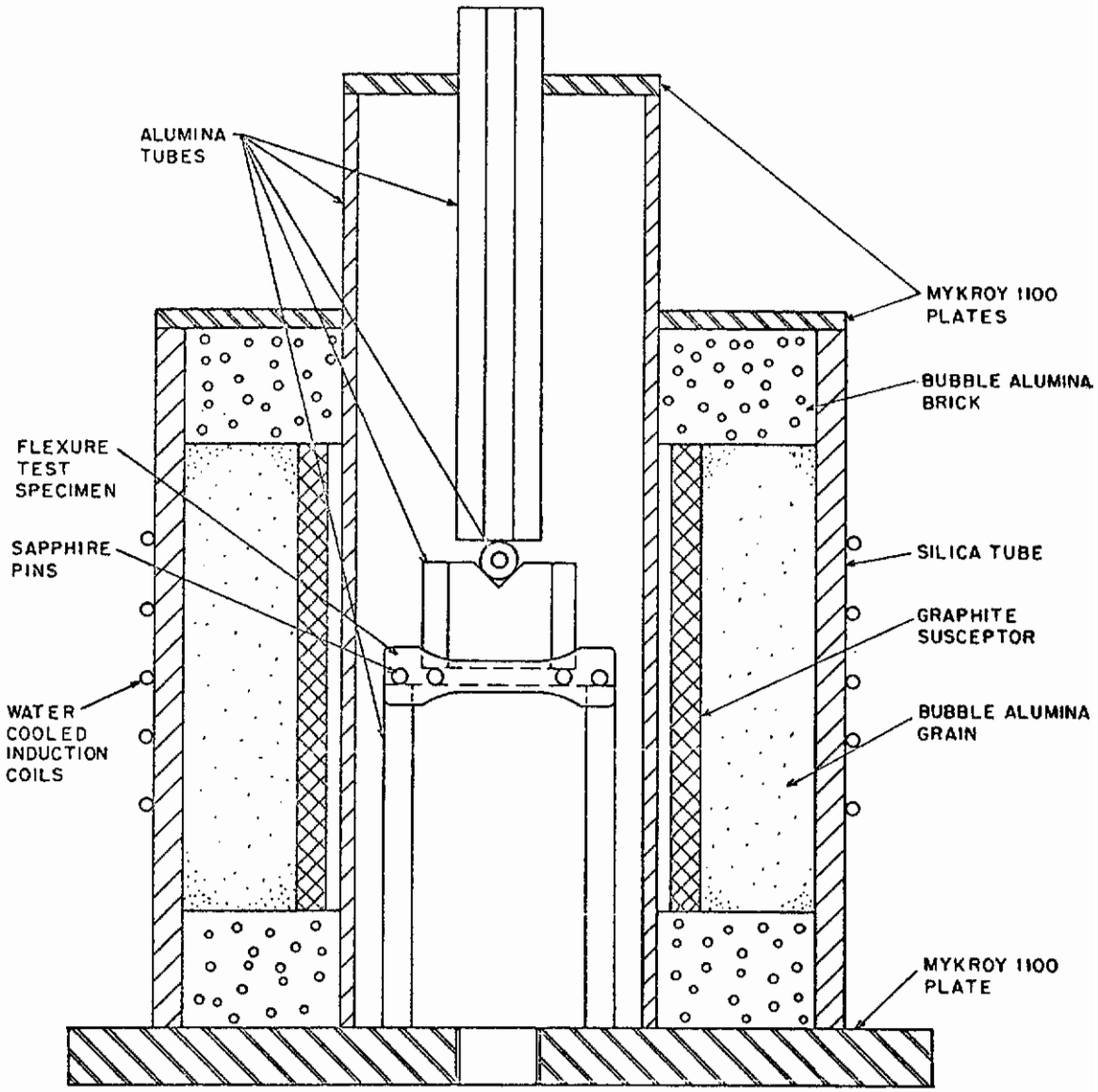

Fig. 1-10 SCHEMATIC OF HI-T FURNACE TO 1750°C WITH FLEXURE TEST FIXTURE FOR AIR OR INERT ATMOSPHERE

The susceptor is isolated from the test chamber by an alumina tube. This allows the susceptor to be protected by passing an inert gas around it, while maintaining an oxidizing atmosphere in the test chamber. A 10-kc power input, low-frequency generator was utilized for this furnace. The use of low-frequency power makes for good impedance matching and good coupling between coil and susceptor, and also allows the use of the best thermal insulation while minimizing power loss from electrical radiation.

To expedite experimental work on this program, an intermediate temperature (1000°C) furnace was also fabricated. The same furnace design as shown in Fig. 1-10 was used. The susceptor was replaced by a resistance heating element of Kanthal wire.

Both furnaces are suitable for use in air, reducing atmospheres, inert atmospheres, and vacuum, if diaphragms are used to seal the loading ports.

The flexural testing jig is shown in Fig. 1-11. This fixture is fabricated of Inconel for room temperature and 1000°C studies; for higher temperatures, Al_2O_3 is used. A set of typical bending fractures obtained with different materials is shown in Fig. 1-12.

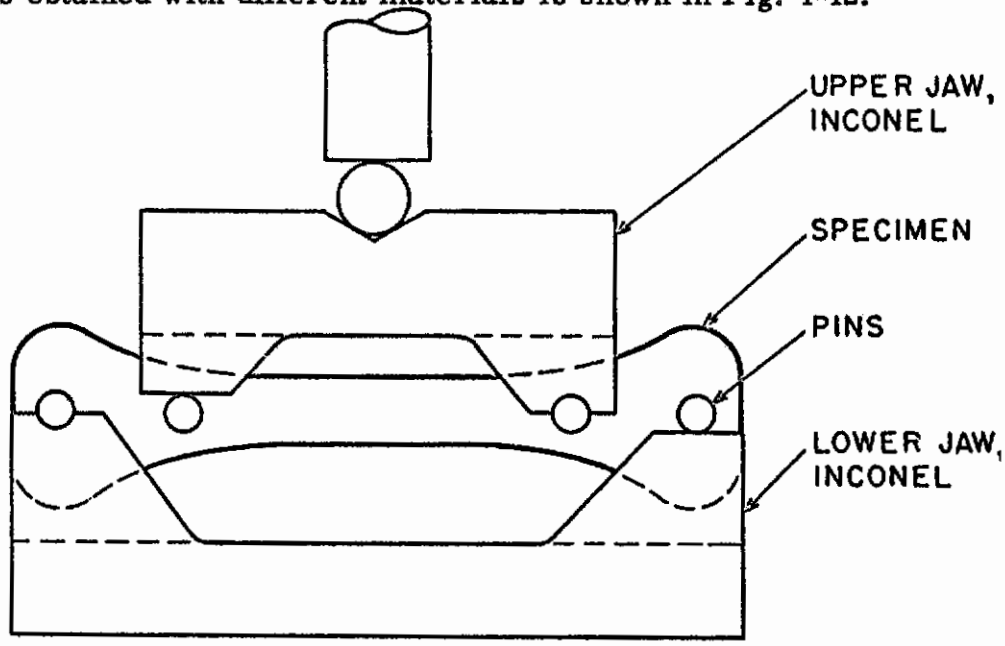

Fig. 1-11 FLEXURE TEST FIXTURE

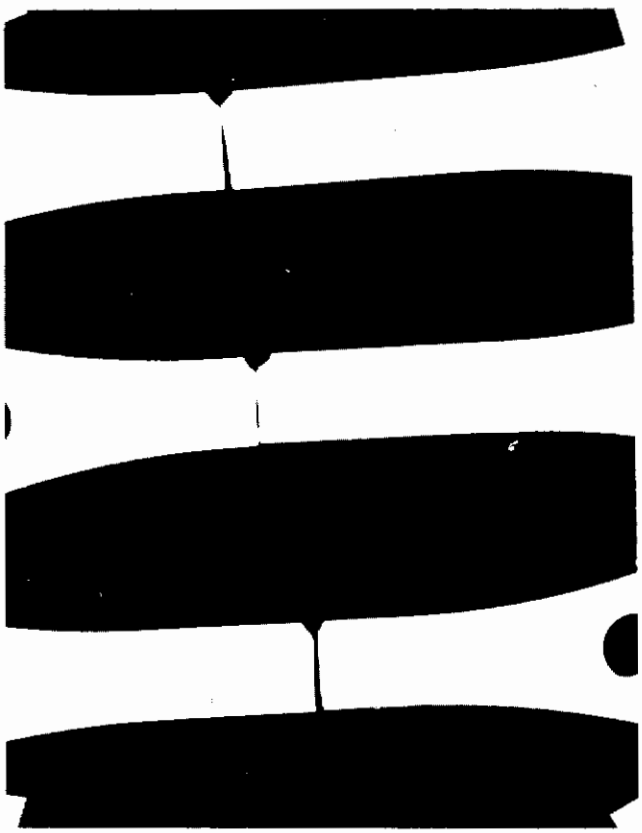

Fig. 1-12 TYPICAL BENDING FRACTURES

4. THEORETICAL CONSIDERATIONS

A. Flaw Constants

The Weibull theory[1-3, 1-4] is based on the concept that brittle materials contain a large number of flaws, which greatly lowers the fracture stress of a material from its theoretical rupture stress. These flaws are assumed to be of random size and distribution throughout the body, and are assumed to be the cause of the scatter observed in the failure of a ceramic material. It is further assumed that when the stress at the worst flaw contained in the specimen becomes large enough to propagate it into a running crack, the entire body fails (weakest-link theory of failure).

In developing his theory, Weibull assumed a normal distribution function relating the probability of fracture, S, to the actual stress observed at fracture, σ, in the form

$$S = 1 - \exp\left[- V \left(\sigma / \sigma_o\right)^m\right] \qquad (1\text{-}10)$$

In this function, σ_o and m are constants of the material, with σ_o being the classical strength of a "flawless" specimen and m being representative of the flaw density in the body; V is the volume of the component subjected to tensile stresses. Weibull only considers tensile stresses as contributing to the fracture of a brittle component. As the number of flaws per unit volume increases, so does the probability that there will be a flaw of maximum severity which will cause fracture at a given stress; at the same time, with an increased number of flaws (m) the distribution curve becomes narrower and the fracture scatter becomes smaller.

The relationship embodied in Eq. 1-10 requires a zero value of fracture stress, σ, for the probability of fracture, S, also to reach zero. This, in turn, implies the extreme statement that absolute

safety from fracture can be achieved only in the total absence of applied (or internal) loads, which is in obvious contradiction with observed behavior. To correct this overstatement of his theory, Weibull proposed subsequently a semi-empirical distribution function of the form

$$S = 1 - \exp\left[-V\left(\frac{\sigma - \sigma_u}{\sigma_o}\right)^m\right] \qquad (1\text{-}11)$$

where the new symbol, σ_u, is the lower limit stress (below which fracture cannot occur), while all other symbols retain their previous meaning. Since the probability of fracture corresponding to an applied stress of σ_u is $S = 0$, σ_u is frequently referred to as the "zero fracture probability stress" or, briefly, the "zero strength".

If one rewrites Eq. 1-11 in the form, using Briggs' logarithms,

$$\log\log\frac{1}{1-S} = m\log(\sigma - \sigma_u) - m\log\sigma_o + \log V + \log\log e \qquad (1\text{-}12)$$

the plot of the distribution function will be linear in a system where $\log\log\frac{1}{1-S}$ is the ordinate and $\log(\sigma - \sigma_u)$ is the abscissa. The slope of the distribution function will determine m, and the intercept on the abscissa will yield σ_o. This method assumes that the constant σ_u is known, which is usually not the case.

The discussion to this point has been concerned with the functions for the uniaxial state of stress. The equations change somewhat for a bending specimen. Starting with the expression for probability of fracture

$$S = 1 - e^{-B}$$

the "risk of rupture", B, for a beam of rectangular cross section (b x 2h) subjected to pure bending over a length, ℓ, is

$$B = \int_V f(\sigma)\, dV = \frac{b\ell}{\sigma_o^m} \int_{h_u}^{h} \left[\sigma \frac{y}{h} - \sigma_u\right]^m dy$$

$$= \left[\frac{V}{2(m+1)\,\sigma_o^m}\right] \left[\frac{(\sigma - \sigma_u)^{m+1}}{\sigma}\right] \qquad (1\text{-}14)$$

where V = volume of beam under pure bending, σ = bending stress at the extreme fiber, and $h_u = \sigma_u\, h/\sigma$.

The semi-empirical distribution for bending specimens is of the form

$$\log\log \frac{1}{1-S} = \log B + \log\log e$$

$$\log B = (m+1)\log(\sigma - \sigma_u) - \log\sigma + \log \frac{V}{2(m+1)\,\sigma_o^m} \qquad (1\text{-}15)$$

where N = total number of specimens, and logarithms are Briggs'.

The probability of fracture, S, corresponding to a particular stress level, σ_n, can be calculated from the expression

$$S = \frac{n}{N+1} \qquad (1\text{-}16)$$

where N is the total number of samples tested in the series, and n is the specimen serial number listing the fracture stresses in an increasing order from 1 to N, with σ_n being the nth fracture stress. By Eq. 1-16 therefore

$$\log\log \frac{1}{1-S} = \log\log \frac{N+1}{N+1-n} \qquad (1\text{-}17)$$

and Eq. 1-15 takes the form

$$\log\log\frac{N+1}{N+1-n} = (m+1)\log(\sigma - \sigma_u) - \log\sigma + \log\frac{V}{2(m+1)\,\sigma_o^{\,m}}$$

Several methods are now available for determining the constants of the distribution function, the most common (and also most practical) being an iterative graphical method based on Eq. 1-12. By this approach, first a test plot is made assuming $\sigma_u = 0$. If the plot follows a straight line σ_u is indeed equal to 0; if the test plot is a curved line, a trial value is taken for $\sigma_u = 0$. If the curve reverses itself, the trial value of σ_u is too high and a new value is chosen. This process may be iteratively continued until a reasonably straight line plot is obtained.

To obtain the values of m, σ_u and σ_o graphically for bending, a plot is prepared for

$$\log\log\frac{N+1}{N+1-n} + \log\sigma \text{ versus } \log(\sigma - \sigma_u)$$

The value of σ_u is determined by trial and error; the correct value is again the one that results in a straight line plot. For the correct value of σ_u, m + 1 will define the slope of the straight line, and σ_o is determined from the intercept of this line on the vertical axis.

For the special case where $\sigma_u = 0$

$$\log\log\frac{N+1}{N+1-n} = m\log\sigma + \log\frac{V}{2(m+1)\,\sigma_o^{\,m}} \qquad (1\text{-}18)$$

and the constants are obtained by plotting $\log\log\frac{N+1}{N+1-n}$ versus $\log\sigma$ as in the case for tensile specimens.

B. Size Effects

After determining the material constant, m, the theoretical effect of volume on the flexural specimens can be calculated and

compared to the test data. For the special case where $\sigma_u = 0$, Weibull's expression for the mean fracture strength, σ_b, is

$$\sigma_b = \int_0^\infty \sigma \, dS \tag{1-19}$$

where σ is the state of stress in a body and S is the probability of fracture occurring at that stress. If the distribution of stresses in the body is arbitrary, the risk of fracture is

$$B = \int_{-\infty}^{\infty} n(\sigma) \, dY \tag{1-20}$$

where the function $n(\sigma)$ is the material function.

The probability of rupture is

$$S = 1 - e^{-B} \tag{1-21}$$

The expression for fracture strength of a body under a non-uniform stress is

$$\sigma_b = \int_0^\infty e^{-B} \, d\sigma \tag{1-22}$$

The material function, $n(\sigma)$ can also take the form

$$n(\sigma) = K \sigma^m$$

where K is a constant and m is the material flaw constant. Weibull further shows that the risk of fracture of a point in a body subjected to a polydimensional stress is of the form

$$B' = 2K \int_0^{\pi/2} \int_{-\phi}^{+\phi} \cos^{2m+1} \phi \, (\sigma_x \cos^2 \phi + \sigma_y \sin^2 \phi)^m \, d\phi d\psi \tag{1-23}$$

where φ and ψ are the angles the normal stress makes with the principal stresses.

In a rectangular beam of width b and height 2h subjected to a pure bending stress, the stress increases as a linear function of the distance from the neutral axis according to the relation $\sigma = \sigma_b\, y/h$. The risk of rupture B'_b for the length ℓ is

$$B'_b = \frac{V_b}{2(m+1)} K \sigma_b^{\,m} \qquad (1\text{-}24)$$

Combining these concepts with Eq. 1-21 the following fracture formula is obtained for the bending strength of a rectangular cross section

$$\sigma_b = \frac{I_m}{\left[\frac{KV_b}{2m+2}\right]^{1/m}} \qquad (1\text{-}25)$$

where σ_b is the fracture strength in bending, K a constant, V_b the volume of the gage section, m the material flaw constant, and I_m a constant depending on the value of m. From Eq. 1-24 it can be seen that the strengths of the flexural samples are a function of the volume of the samples.

This principal can be used to compare the ratio of fracture strength of the different sized samples since, by Eq. 1-25

$$\frac{\sigma_{b1}}{\sigma_{b2}} = \left[\frac{V_{b2}}{V_{b1}}\right]^{1/m} \qquad (1\text{-}26)$$

where σ_{b1} and σ_{b2} are the mean strengths of two groups of samples having volumes of V_{b1} and V_{b2}, and m is the material flaw constant.

If the value of the material function m is known, along with the equations for the risk of rupture for a particular stress state, and $\sigma_u = 0$, the Weibull theory can also be used for predicting the strength in one stress state from the known strength value corresponding to another stress system. Equation 1-24 provides the relation for the risk of rupture in bending of a rectangular beam and solving Eq. 1-20 for the case of pure tension, the equation for the risk of rupture pertaining to the latter system becomes

$$B_t' = V_t K \sigma_t^m \tag{1-27}$$

At identical fracture probabilities in bending and tension ($B_b' = B_t'$), the ratio of the ultimate strength in bending to that of tension, using Eq. 1-20 and Eq. 1-27, is given by

$$\frac{\sigma_b}{\sigma_t} = \left[\frac{(2m + 2)\ V_t}{V_b}\right]^{1/m} \tag{1-28}$$

5. EXPERIMENTAL WORK AND DISCUSSION

A. Test Conditions and Data

The following factors have been investigated for possible effects on the fracture strength of the ceramic materials:

(a) Prior Thermal History
  (1) As received
  (2) Annealed at 1700°C

(b) Specimen Finish
  (1) As fired
  (2) Fine ground surface

(c) Test Temperature
  (1) 20°C (room temperature)
  (2) 1000°C

(d) Atmosphere
  (1) Room air
  (2) Saturated air or steam
  (3) Dry argon

(e) Specimen Size (Dogbone shape)
  (1) Small (1/8 x 3/16 x 1/2-in. gage section) gage volume = 0.0117 $in.^3$
  (2) Medium (1/4 x 1/4 x 3/4-in. gage section) gage volume = 0.0469 $in.^3$
  (3) Large (5/16 x 5/16 x 1-in. gage section) gage volume = 0.0977 $in.^3$

Initially, five specimens were to be tested for all combinations of factors in each category. However, as data were collected this number was found to be too small to define accurately the Weibull material parameters. The room temperature data for the Wesgo AL995 is listed in Table 1-II. The intermediate volume specimens were used for the analysis of the Weibull parameter to determine flaw constants and size effects.

A statistical approach was used to analyze and group the data. An analysis of variance was made for the effect of atmosphere for the medium volume specimens at room temperature; this showed that for the as-received material environmental atmosphere had no significant effect at room temperature range investigated; however, for specimens with a ground surface environment turned out to be a significant factor. A test for size effects indicated that volume differences had a significant effect on breaking strength at the 99 percent level. It should be noted that statisticians usually take the 95 percent level of significance as the criterion for dividing the same mean population. The data analyzed were either well above or below this dividing line.

Table 1-II

FLEXURE STRENGTH OF WESGO AL995 SPECIMENS AT 20°C

Atmosphere	Condition	Volume, ($in.^3$)	No. of Tests	Ave. Failure Stress (10^{-3} psi)	Standard Deviation, (10^{-3} psi)	Coefficient of Error, (percent)
Wet air	as-received	0.047	9	26.2	2.97	11.3
Ambient	ground	0.012	5	39.1	1.27	3.1
Ambient	ground	0.047	19	26.7	2.60	9.7
Ambient	ground	0.098	8	24.3	2.03	8.4
Dry argon	ground	0.012	3	24.1	1.42	5.9
Dry argon	ground	0.047	5	23.6	2.12	9.0
Dry argon	ground	0.098	5	26.3	1.19	4.5
Saturated steam	ground	0.012	4	19.2	2.56	11.7
Saturated steam	ground	0.047	9	21.7	1.09	5.0
Saturated steam	ground	0.098	6	18.8	3.50	18.6
Ambient	annealed and unground	0.012	5	34.6	3.50	10.1
Ambient	annealed and unground	0.047	36	31.0	3.62	11.7
Ambient	annealed and unground	0.098	5	27.0	7.91	34.2
Ambient	annealed and ground	0.012	5	25.6	2.82	11.0
Ambient	annealed and ground	0.047	30	28.6	2.44	8.5
Ambient	annealed and ground	0.098	4	27.8	2.74	9.9

A study of the effect of surface treatment on the fracture strength of the intermediate size specimens revealed that annealing and surface grinding influenced the observed results separately and in combination The influence of surface treatment upon fracture strength, ranked in the order of the most to the least significant effect, is as follows: (a) unground annealed, (b) ground annealed, (c) unground unannealed, and (d) ground unannealed.

A similar analysis was used to compare rupture data as functions of atmosphere, specimen treatment, and size at 1000°C. Size was significant at the 99 percent confidence level while the other factors were not. The values for each size and temperature were combined and analyzed; both were important, the former at the 99 percent level and the latter at the 99.5 percent level.

A series of tests (Table 1-IV) were made using Wesgo material which was ground to one-half the thickness of the specimens listed in Tables 1-II and 1-III. Specimens identified "as-received" in Table 1-IV were symmetrically ground on both side faces to one-half of their original thickness; however, their bottom surface (the locus of fracture origination), was left in the original condition. Specimens identified "ground" had a thin layer removed on the top and bottom surfaces as well, to yield the same reduced volume. The principal purpose of this part of the work was to eliminate possible changes ascribable from the study of size effects. Because of time limitations no effort was made to carry out a complete analysis of the results obtained; however, the data are presented here and the analysis will be performed as part of a future program.

The data for both Lucalox and MgO specimens are listed in Table 1-V. Time limitations confined the effort to the determination of the Weibull parameters for the intermediate volume specimens at room temperature under ambient conditions.

Table 1-III

FLEXURE STRENGTH OF WESGO AL995 SPECIMENS AT 1000°C

Atmosphere	Condition	Volume, (in.^{3})	No. of Tests	Ave. Failure Stress (10^{-3}psi)	Standard Deviation (10^{-3}psi)	Coefficient of Error %
Ambient	as-received	0.012	4	22.3	1.37	6.1
Ambient	as-received	0.047	5	23.8	2.19	9.2
Ambient	as-received	0.098	5	19.7	3.60	18.3
Dry argon	as-received	0.012	5	17.6	1.98	11.3
Dry argon	as-received	0.047	5	22.3	3.32	14.9
Dry argon	as-received	0.098	5	17.7	3.82	21.6
Saturated steam	as-received	0.012	5	18.8	2.11	11.2
Saturated steam	as-received	0.047	8	18.2	1.92	10.5
Saturated steam	as-received	0.098	5	17.0	1.68	9.9
Ambient	ground	0.012	5	22.5	1.30	5.8
Ambient	ground	0.047	5	23.5	0.75	3.1
Ambient	ground	0.098	5	23.5	1.71	7.3
Dry argon	ground	0.012	4	22.2	2.23	10.0
Dry argon	ground	0.047	5	19.9	1.65	8.3
Dry argon	ground	0.098	5	19.6	1.92	9.8
Saturated steam	ground	0.012	5	23.5	2.69	11.5
Saturated steam	ground	0.047	5	20.9	0.40	1.9
Saturated steam	ground	0.098	5	20.1	0.42	2.1
Dry argon	annealed and unground	0.012	5	18.0	2.04	11.3
Dry argon	annealed and unground	0.047	5	19.2	1.07	5.5
Dry argon	annealed and unground	0.098	5	17.5	1.78	10.2
Saturated steam	annealed and unground	0.012	5	17.5	1.98	11.3
Saturated steam	annealed and unground	0.047	5	18.7	1.63	8.7
Saturated steam	annealed and unground	0.098	5	16.1	1.63	10.2
Ambient	annealed and ground	0.012	4	18.7	0.40	2.1
Ambient	annealed and ground	0.047	5	17.2	0.81	4.7
Ambient	annealed and ground	0.098	5	16.3	0.90	5.5

Table 1-IV

20°C FLEXURE STRENGTH OF WESGO AL995 SPECIMENS GROUND TO ONE-HALF OF ORIGINAL THICKNESS

Atmosphere	Condition	Volume, (in.^{3})	No. of Tests	Average Failure Stress (10^{-3} psi)	Standard Deviation (10^{-3} psi)	Coefficient of Error (percent)
Ambient	as-received	0.006	5	24.3	2.63	10.8
Ambient	as-received	0.024	5	21.6	2.14	9.9
Ambient	as-received	0.049	5	23.5	0.77	3.3
Ambient	ground	0.006	5	38.4	3.70	9.6
Ambient	ground	0.024	5	22.9	1.14	5.0
Ambient	ground	0.049	5	26.1	2.23	8.6

Table 1-V

20°C FLEXURE STRENGTH OF LUCALOX AND MgO SPECIMENS

Material	Atmosphere	Condition	Volume, (in.^{3})	No. of Tests	Average Failure Stress (10^{-3} psi)	Standard Deviation (10^{-3} psi)	Coef. of Error (percent)
Lucalox	Ambient	as-received	0.012	2	25.5		
Lucalox	Ambient	as-received	0.049	26	26.5	3.62	13.6
Lucalox	Ambient	as-received	0.098	2	25.9		
Lucalox	Ambient	annealed	0.049	2	32.6		
MgO	Ambient	as-received	0.049	60	16.6	1.94	11.7

The results of annealing Lucalox show an interesting increase in strength but the sample size is not large enough to permit firm conclusions to be drawn at this time. The results of room temperature as-received Wesgo AL995 tension tests are shown in Table 1-VI.

Table 1-VI

20°C TENSION DATA: WESGO AL995 SPECIMENS

(Air Environment)

Gage Volume ($in.^3$)	No. of Tests	Average Tensile Strength, (10^{-3} psi)	Standard Deviation, (10^{-3} psi)	Coefficient of Error, (percent)
0.012	5	24.4	3.7	15.2
0.047	5	27.0	3.6	13.3
0.098	5	19.1	2.7	14.2

B. Data Analysis and Discussion

Figures 1-13 to 1-16 present distribution plots of the intermediate size flexure specimens tested at room temperature for as received, as received and annealed, ground, and ground and annealed conditions. The as-received plot is normal in appearance while the others are skewed toward the lower strengths and, in general, indicate a narrower distribution range. The distribution curve for specimens of the same size tested at 1000°C is shown in Fig. 1-17. This curve was obtained by combining the data of unground specimens for the different atmospheres and annealed samples. This combining of high temperature data was admissible because previous statistical analysis indicated that these variables had no effect on the fracture stress of specimens

Fig. 1-13

DISTRIBUTION CURVE OF FRACTURE STRENGTHS OF AS-RECEIVED WESGO AL995 AT 20°C

$N = 54$

$\bar{x} = 26,300$ psi

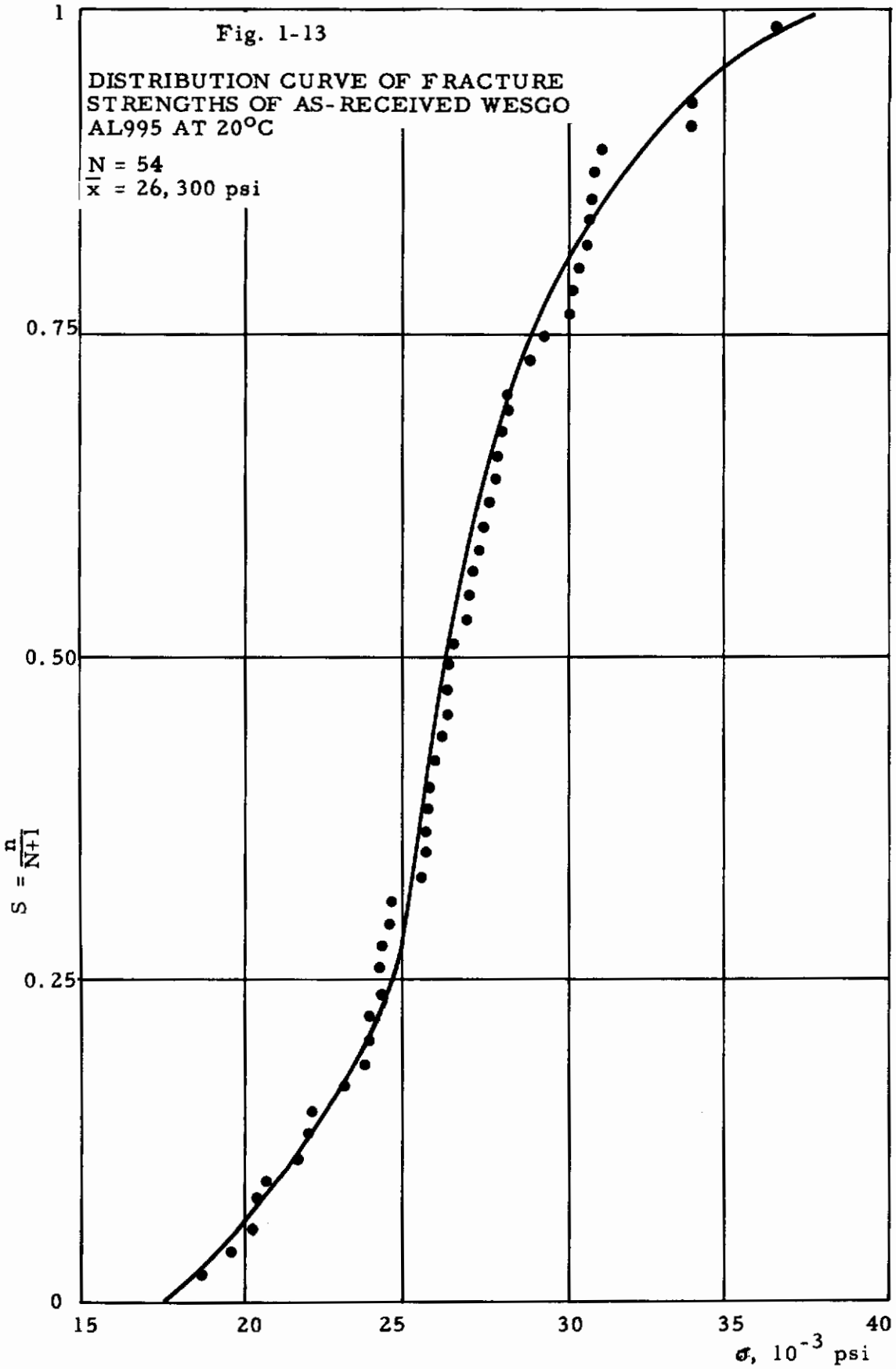

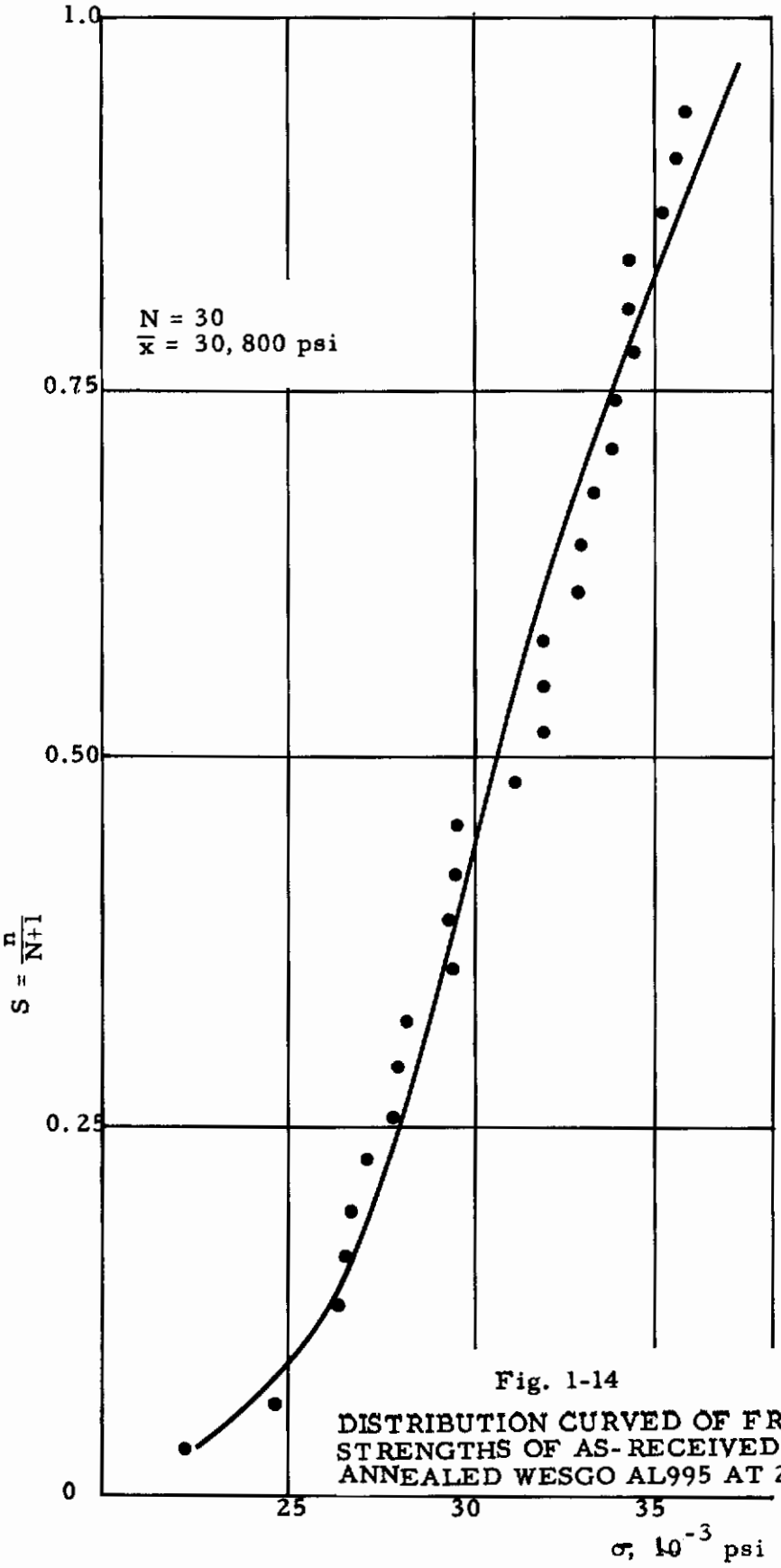

Fig. 1-14

DISTRIBUTION CURVED OF FRACTURE STRENGTHS OF AS-RECEIVED AND ANNEALED WESGO AL995 AT 20°C

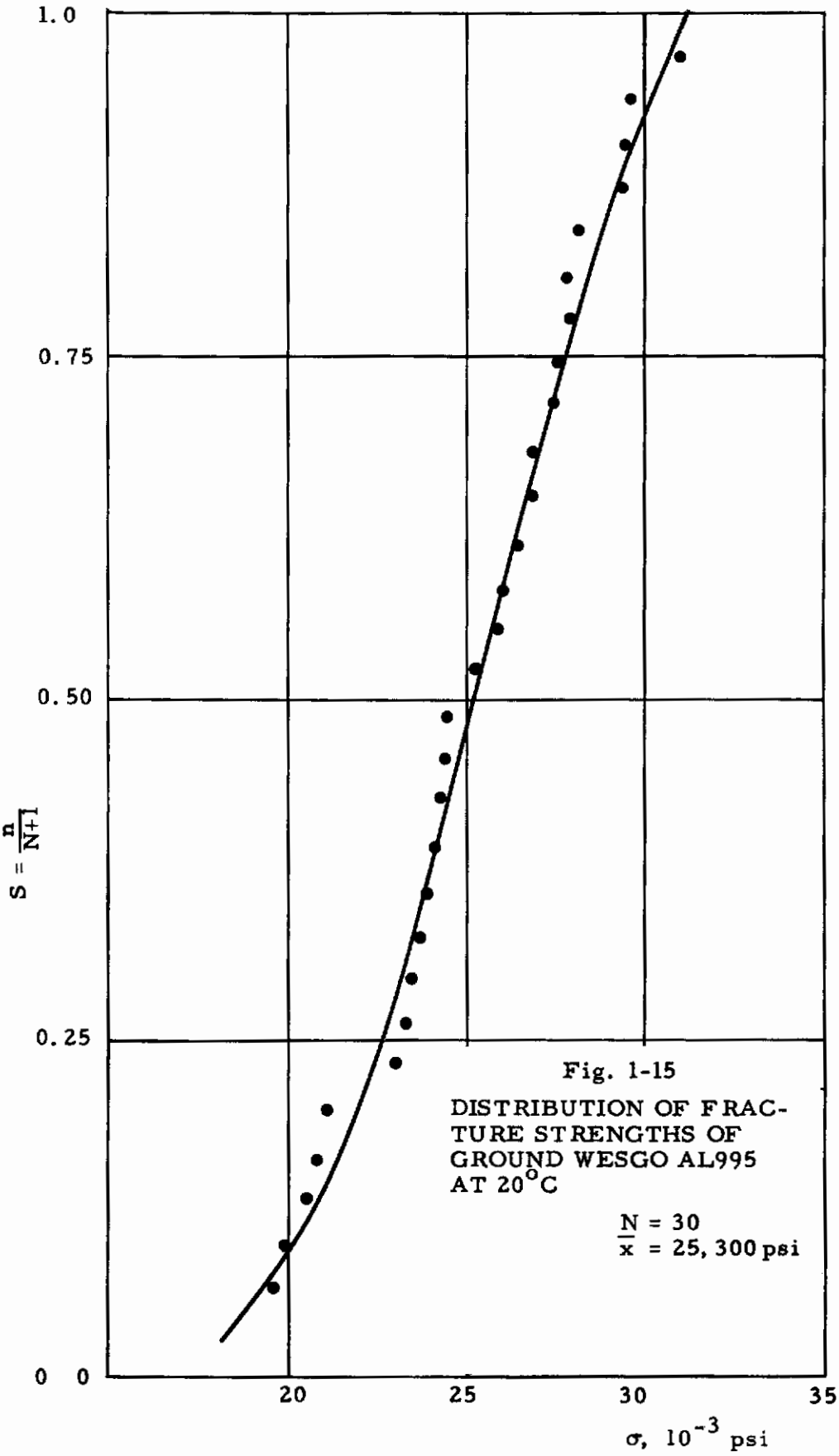

Fig. 1-15

DISTRIBUTION OF FRACTURE STRENGTHS OF GROUND WESGO AL995 AT 20°C

$N = 30$

$\bar{x} = 25,300$ psi

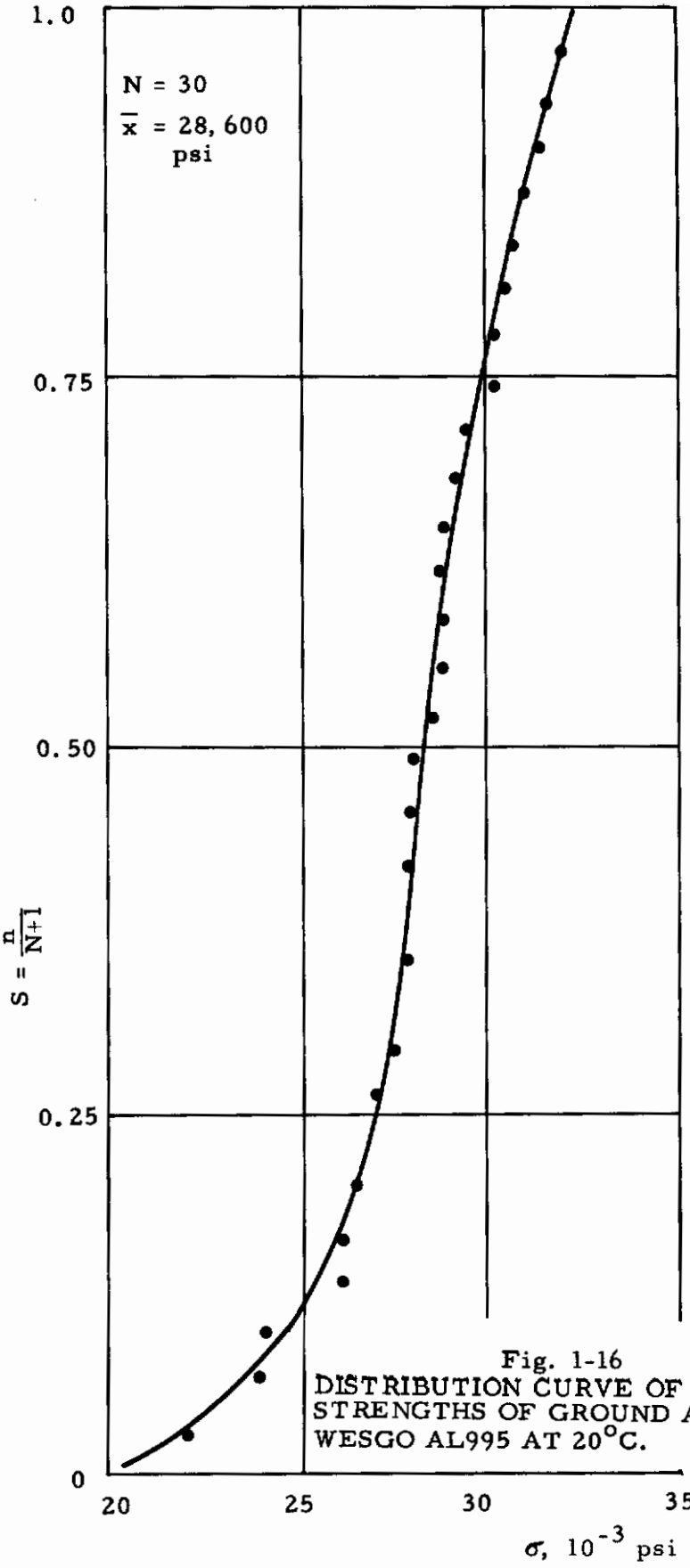

Fig. 1-16
DISTRIBUTION CURVE OF FRACTURE STRENGTHS OF GROUND AND ANNEALED WESGO AL995 AT 20°C.

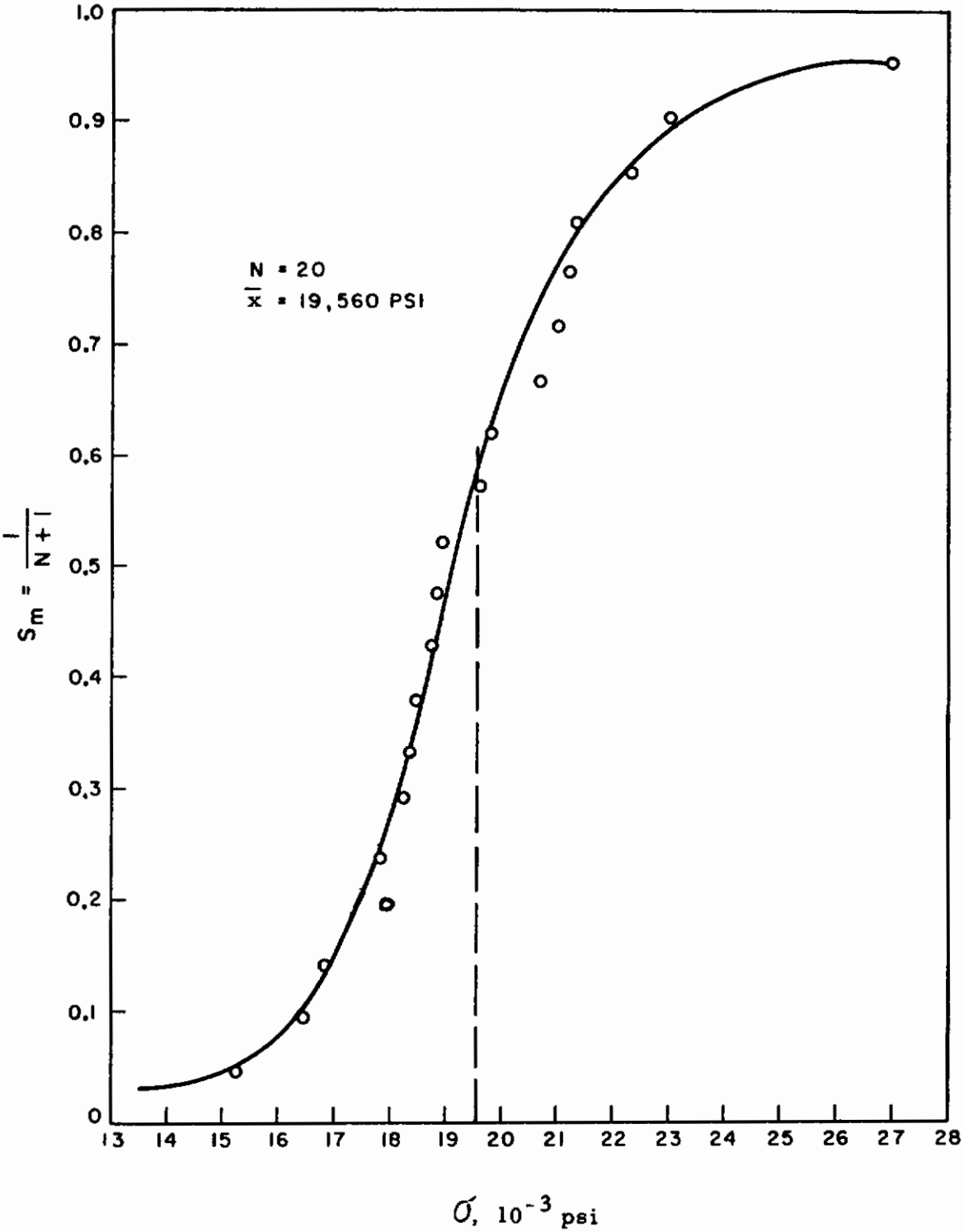

Fig. 1-17 DISTRIBUTION CURVE OF FRACTURE STRENGTHS OF WESGO ALUMINA AT 1000°C

of the same size. This plot is displaced somewhat toward the higher stresses.

The distribution curves for the intermediate size Lucalox and MgO flexure specimens are shown in Fig. 1-18 and 1-19. While a smooth regular curve has been fitted to the Lucalox data, the points appear to show a more complicated distribution. The plot as shown is skewed toward the higher strengths. The MgO appears to have a normal distribution curve. It may be mentioned that skewed distribution curves are more typical of the materials under investigation than the normal distribution.

The logarithmic distribution curves of fracture stresses are shown in Fig. 1-20 to 1-23. These curves are plotted first on basis of the assumption that $\sigma_u = 0$, as explained by the definition of the methodology in Section IIIA. As can be seen, the plots for the unannealed Wesgo material (both as-received and ground) shown in Fig. 1-20 and 1-21 are concave downward, indicating that $\sigma_u \neq 0$ for these conditions. The annealed Wesgo AL995 specimens, both unground and ground, on the other hand, result in straight lines, as seen in Fig. 1-22 and 1-23. For these conditions, therefore, σ_u is truly equal to zero.

For the "as-received' Wesgo AL995 tested at 1000°C, as well as for the Lucalox and MgO tested at room temperature, once again downward concave plots result (Fig. 1-24, 1-25 and 1-26). Hence, for these materials, σ_u again assumes a finite rather than a vanishing value.

To determine the correct value of σ_u for cases where initial plots based on the $\sigma_u = 0$ assumption yielded concave downward curves, the iterative trial and error method described in Section IIIA was employed. This was continued until a straight line resulted, with the manner of plotting employing the coordinate values shown before.

The replotted curves corresponding to Fig. 1-20, 1-21, 1-25 and 1-26 are presented in Fig. 1-27, 1-28, 1-29 and 1-30, respectively,

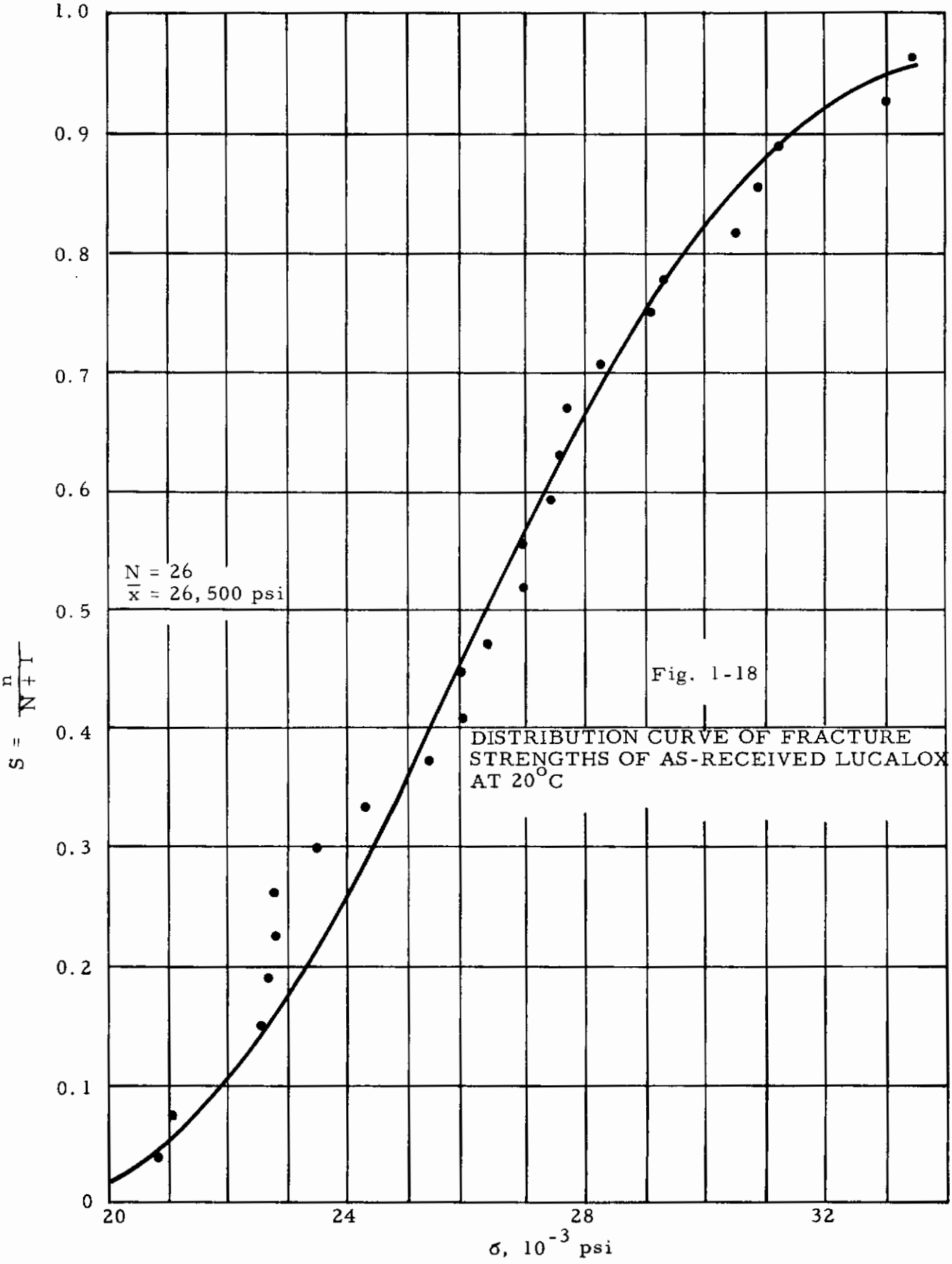

Fig. 1-18

DISTRIBUTION CURVE OF FRACTURE STRENGTHS OF AS-RECEIVED LUCALOX AT 20°C

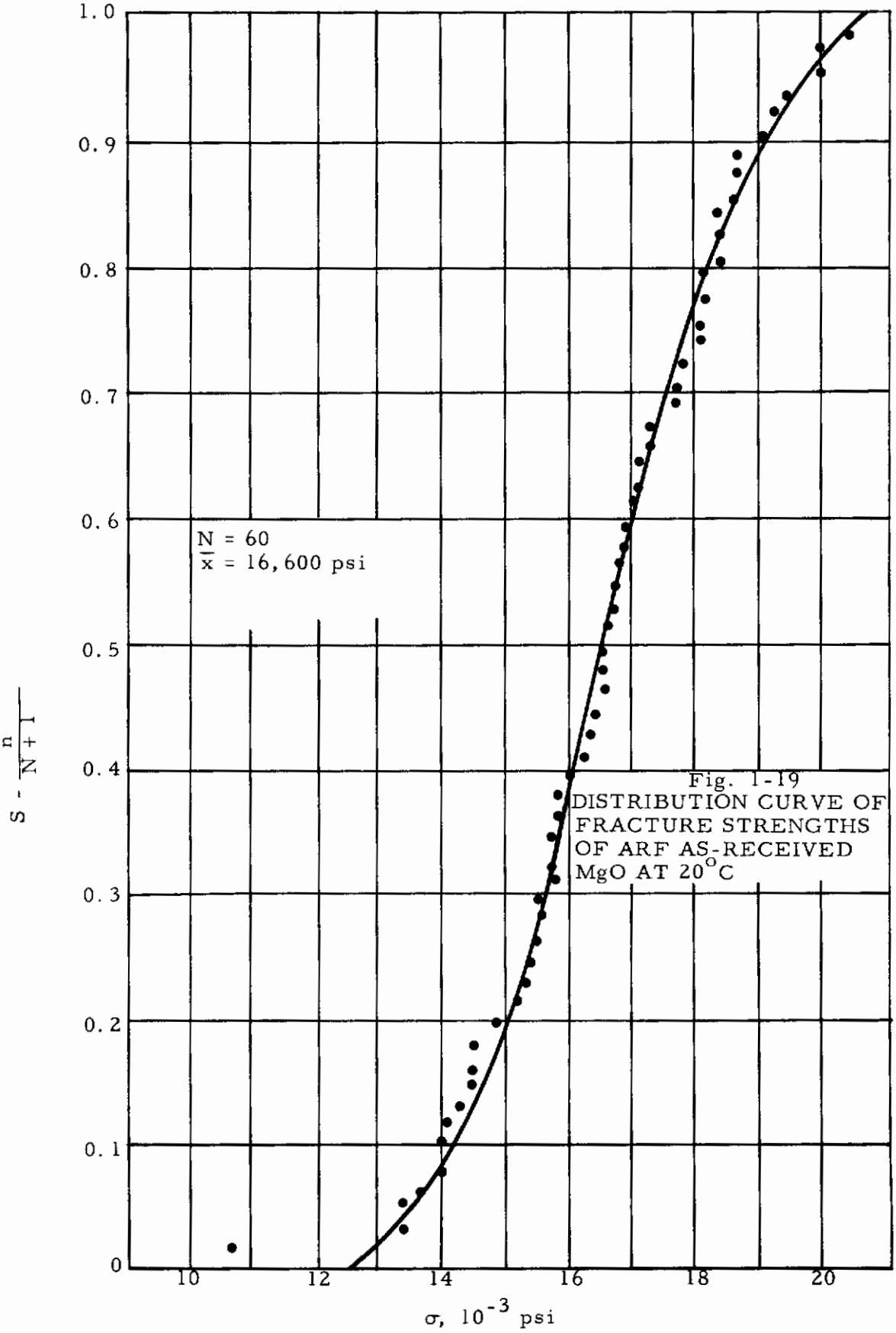

Fig. 1-19
DISTRIBUTION CURVE OF FRACTURE STRENGTHS OF ARF AS-RECEIVED MgO AT 20°C

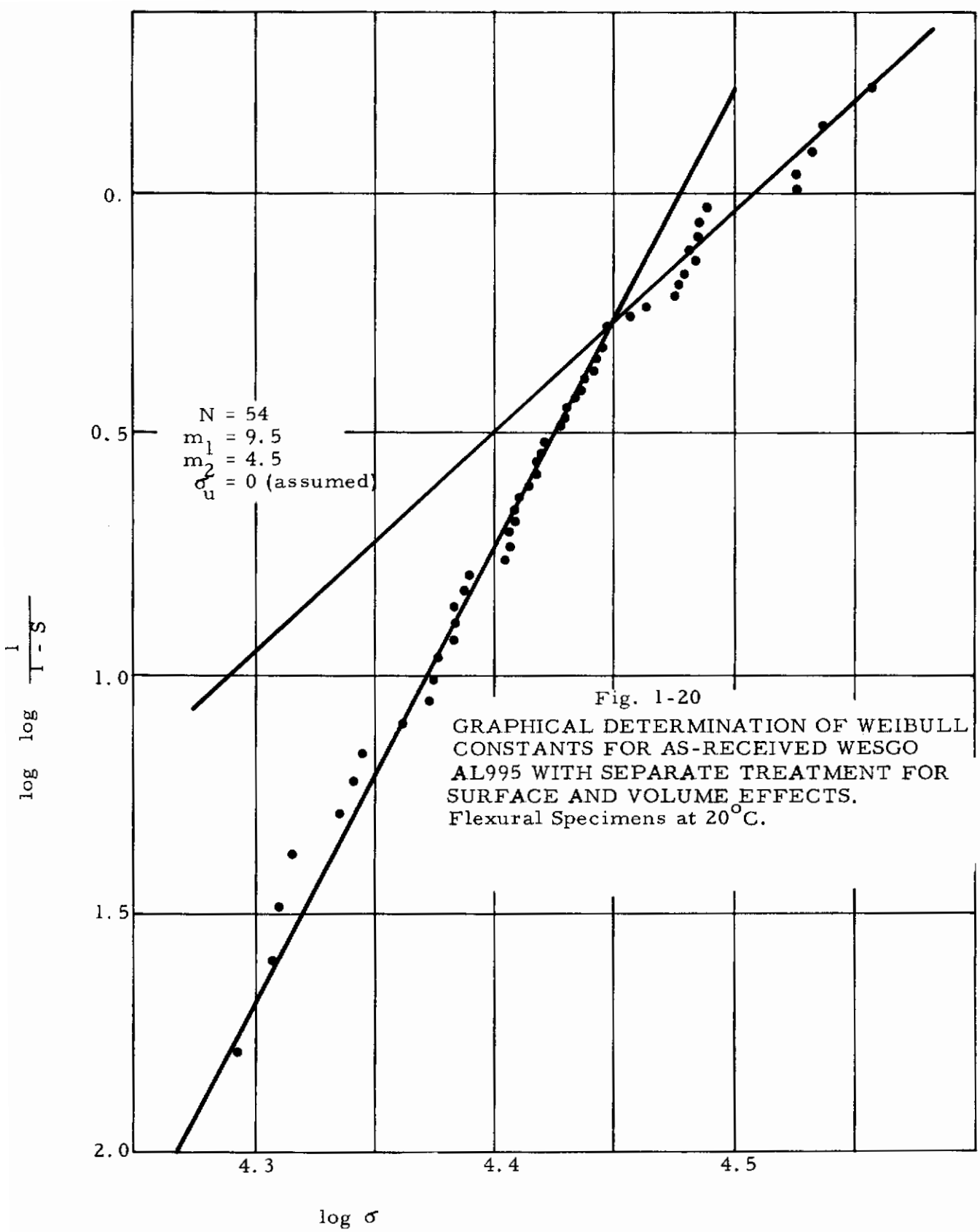

Fig. 1-20
GRAPHICAL DETERMINATION OF WEIBULL CONSTANTS FOR AS-RECEIVED WESGO AL995 WITH SEPARATE TREATMENT FOR SURFACE AND VOLUME EFFECTS.
Flexural Specimens at 20°C.

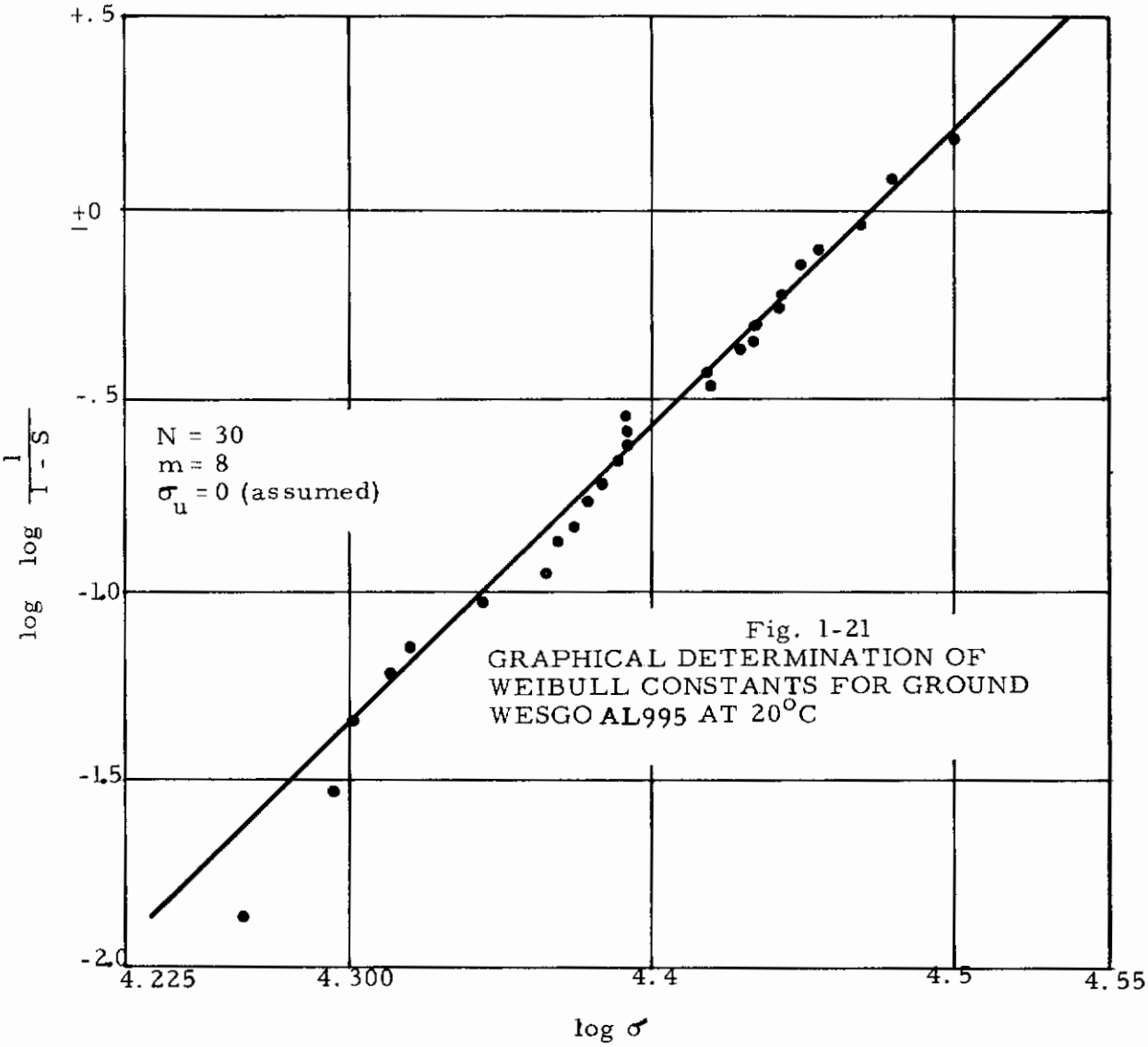

Fig. 1-21
GRAPHICAL DETERMINATION OF WEIBULL CONSTANTS FOR GROUND WESGO AL995 AT 20°C

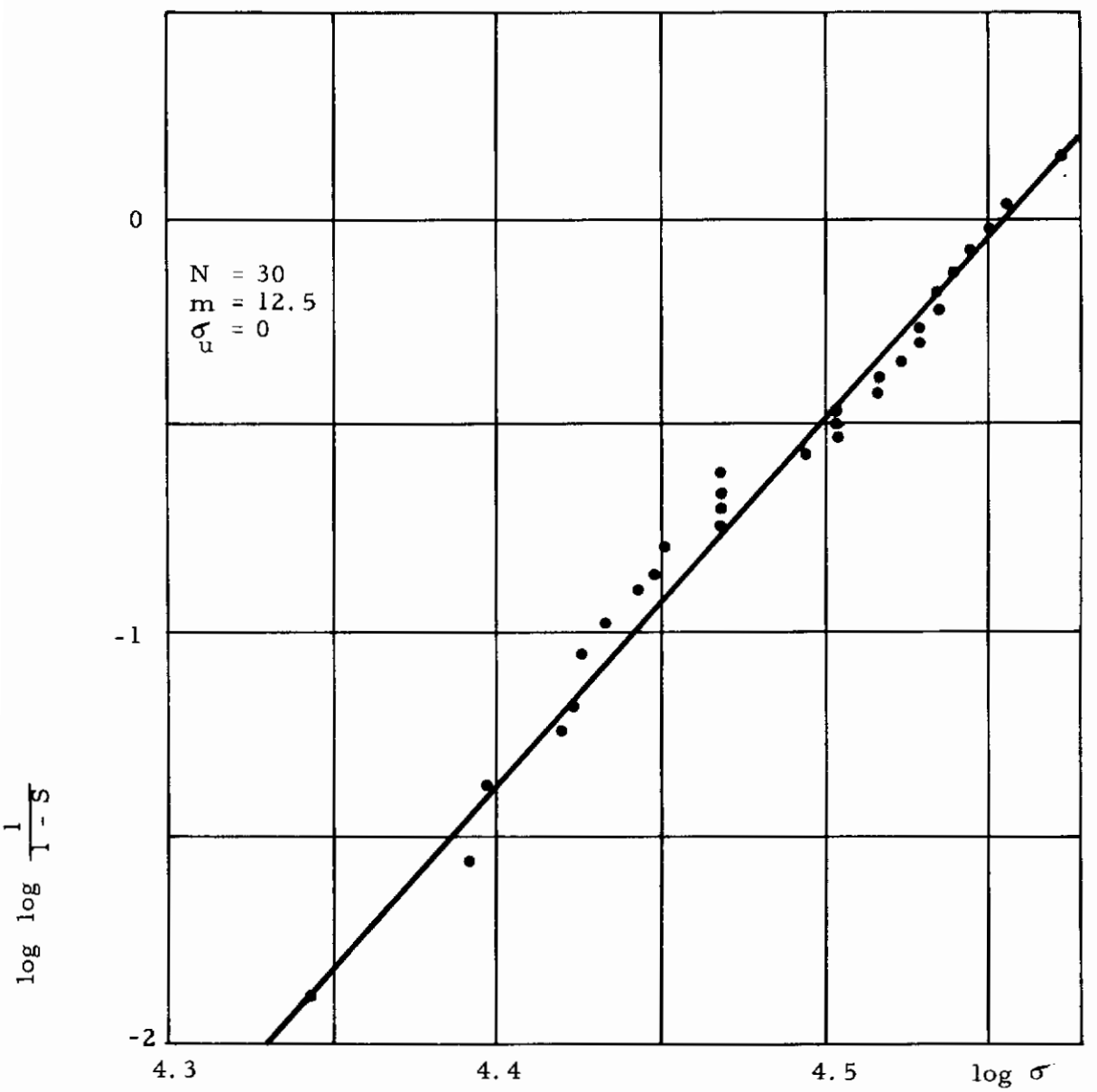

Fig. 1-22
GRAPHICAL DETERMINATION OF WEIBULL CONSTANT FOR AS-RECEIVED AND ANNEALED WESGO AL995 AT 20° C

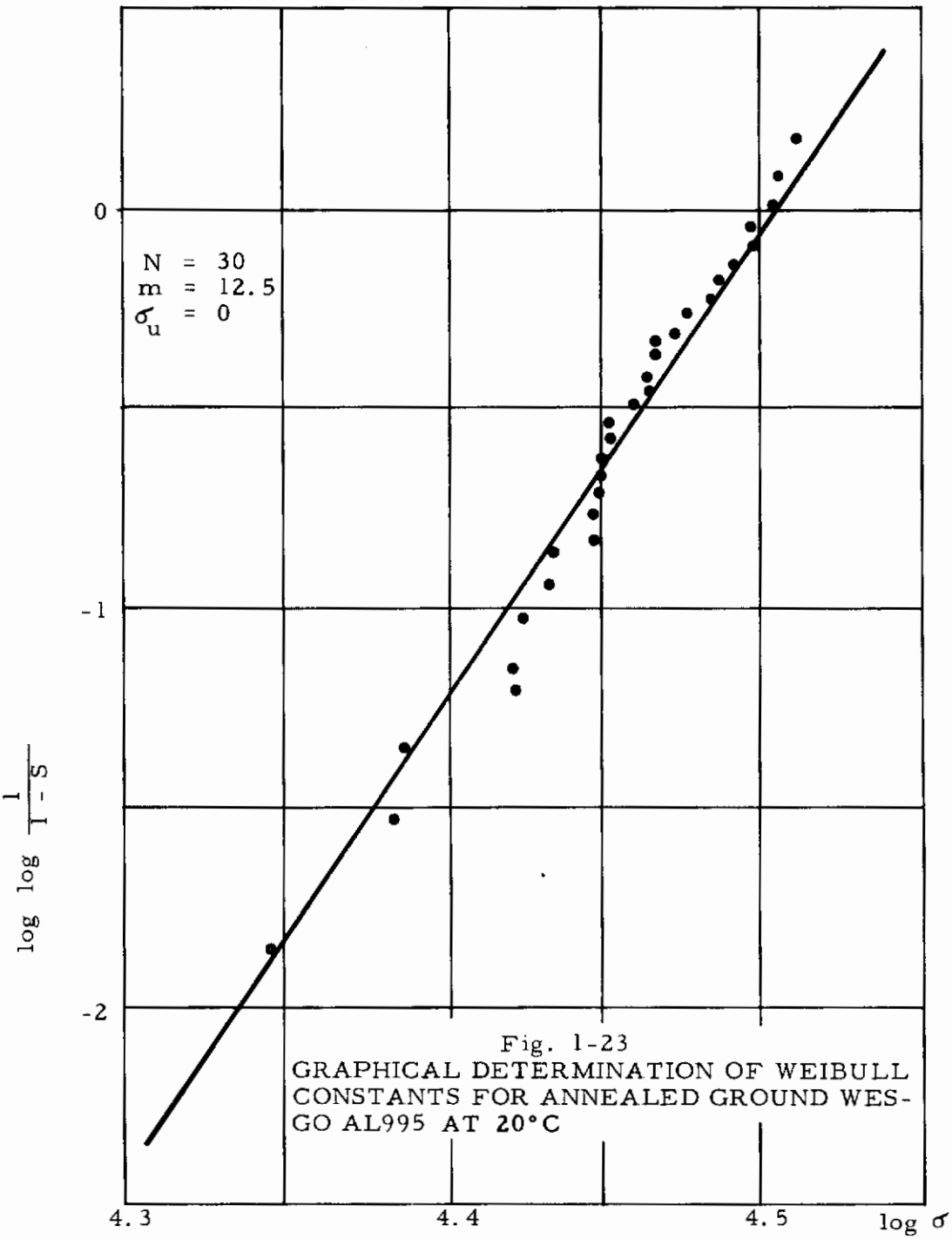

Fig. 1-23
GRAPHICAL DETERMINATION OF WEIBULL CONSTANTS FOR ANNEALED GROUND WESGO AL995 AT 20°C

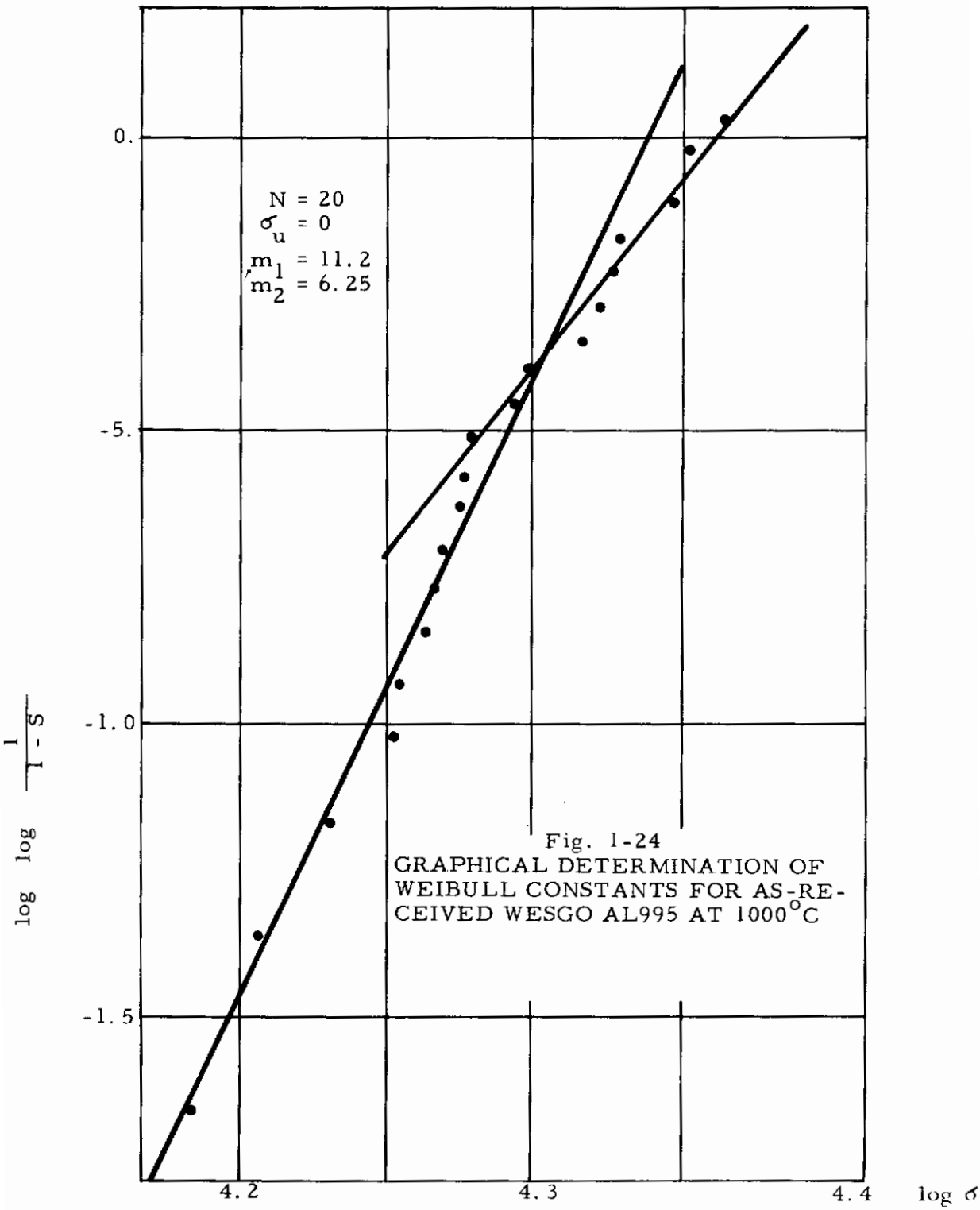

Fig. 1-24
GRAPHICAL DETERMINATION OF WEIBULL CONSTANTS FOR AS-RECEIVED WESGO AL995 AT 1000°C

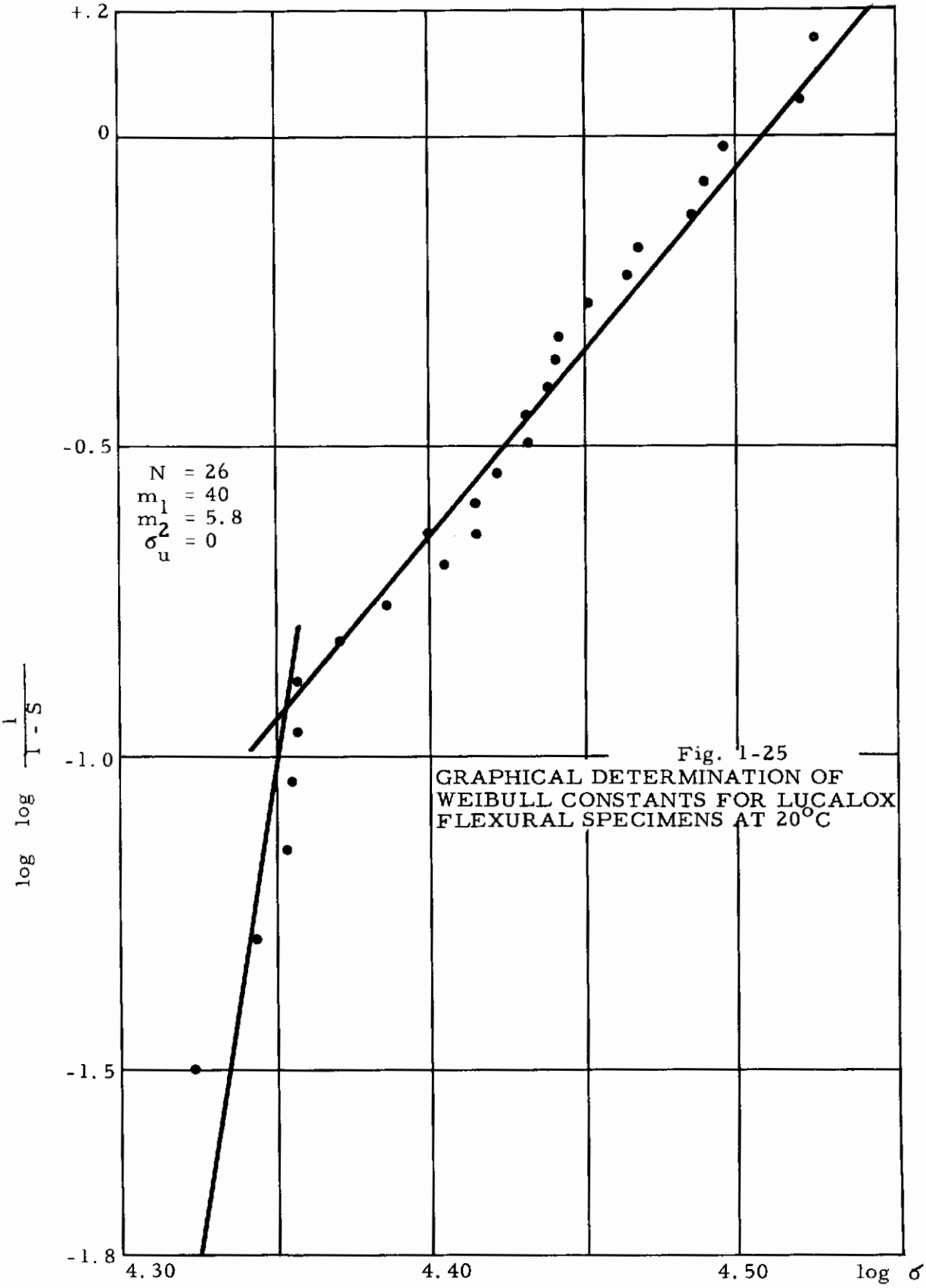

Fig. 1-25
GRAPHICAL DETERMINATION OF WEIBULL CONSTANTS FOR LUCALOX FLEXURAL SPECIMENS AT 20°C

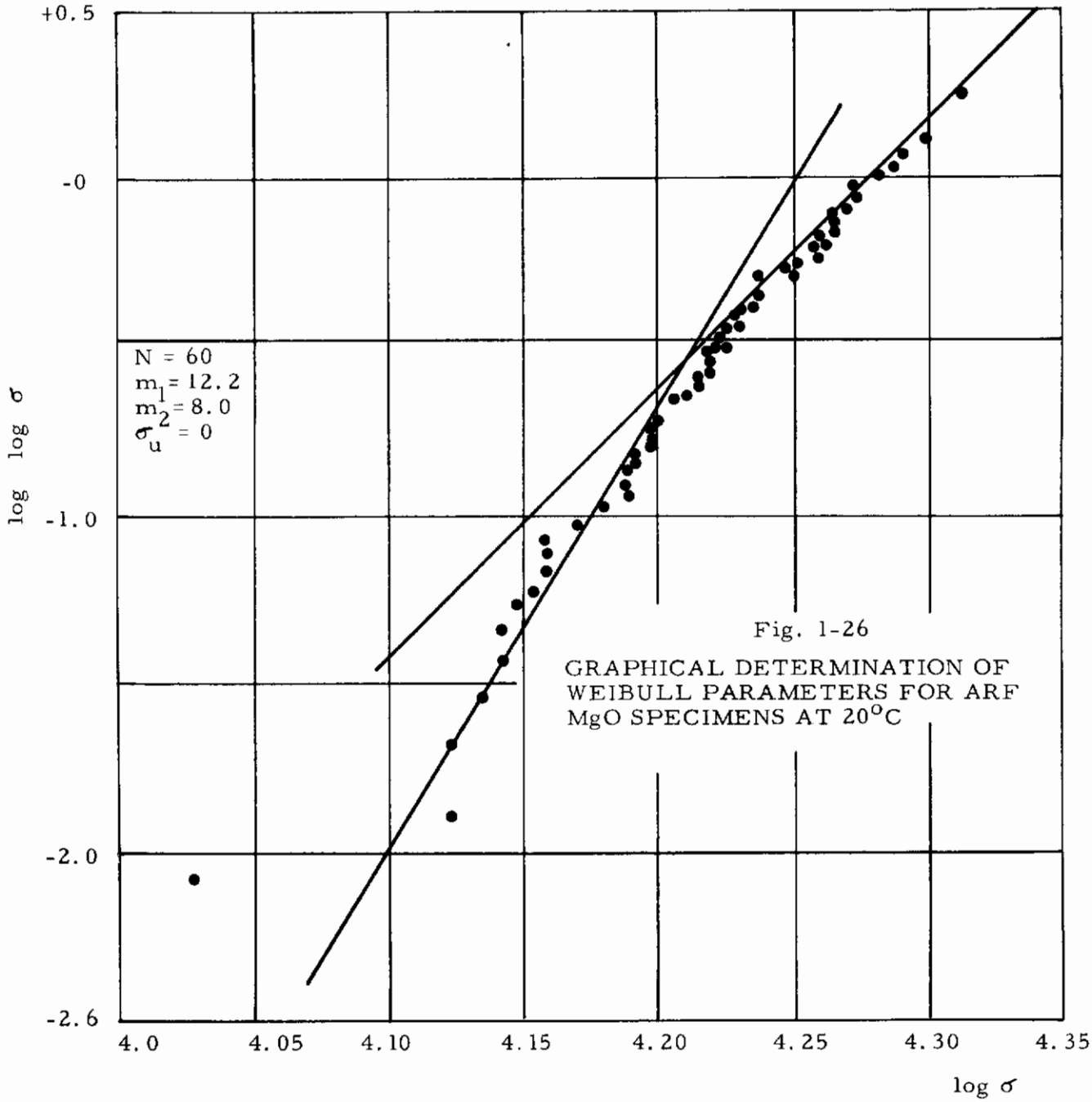

Fig. 1-26

GRAPHICAL DETERMINATION OF WEIBULL PARAMETERS FOR ARF MgO SPECIMENS AT 20°C

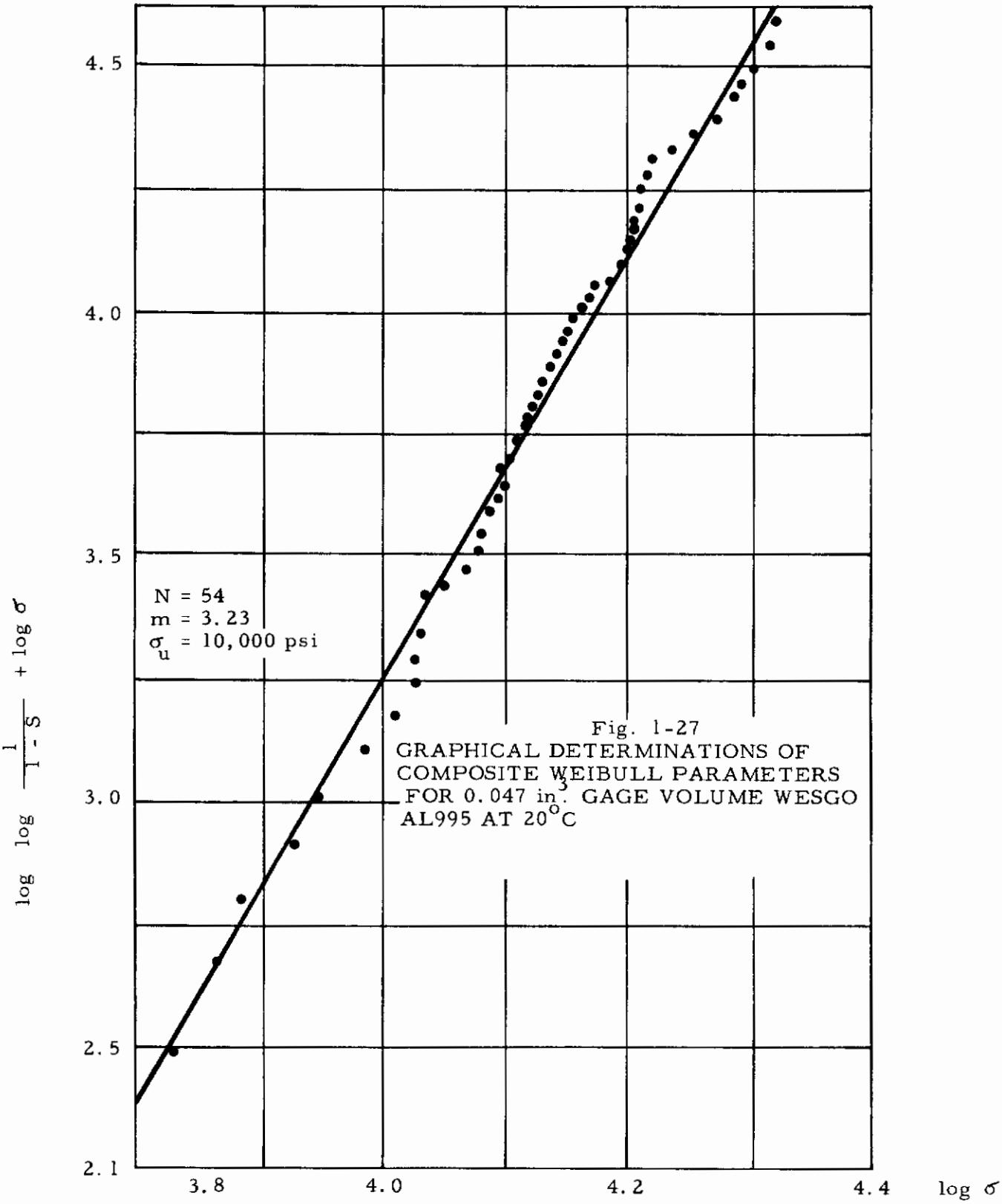

Fig. 1-27
GRAPHICAL DETERMINATIONS OF COMPOSITE WEIBULL PARAMETERS FOR 0.047 in^3. GAGE VOLUME WESGO AL995 AT 20°C

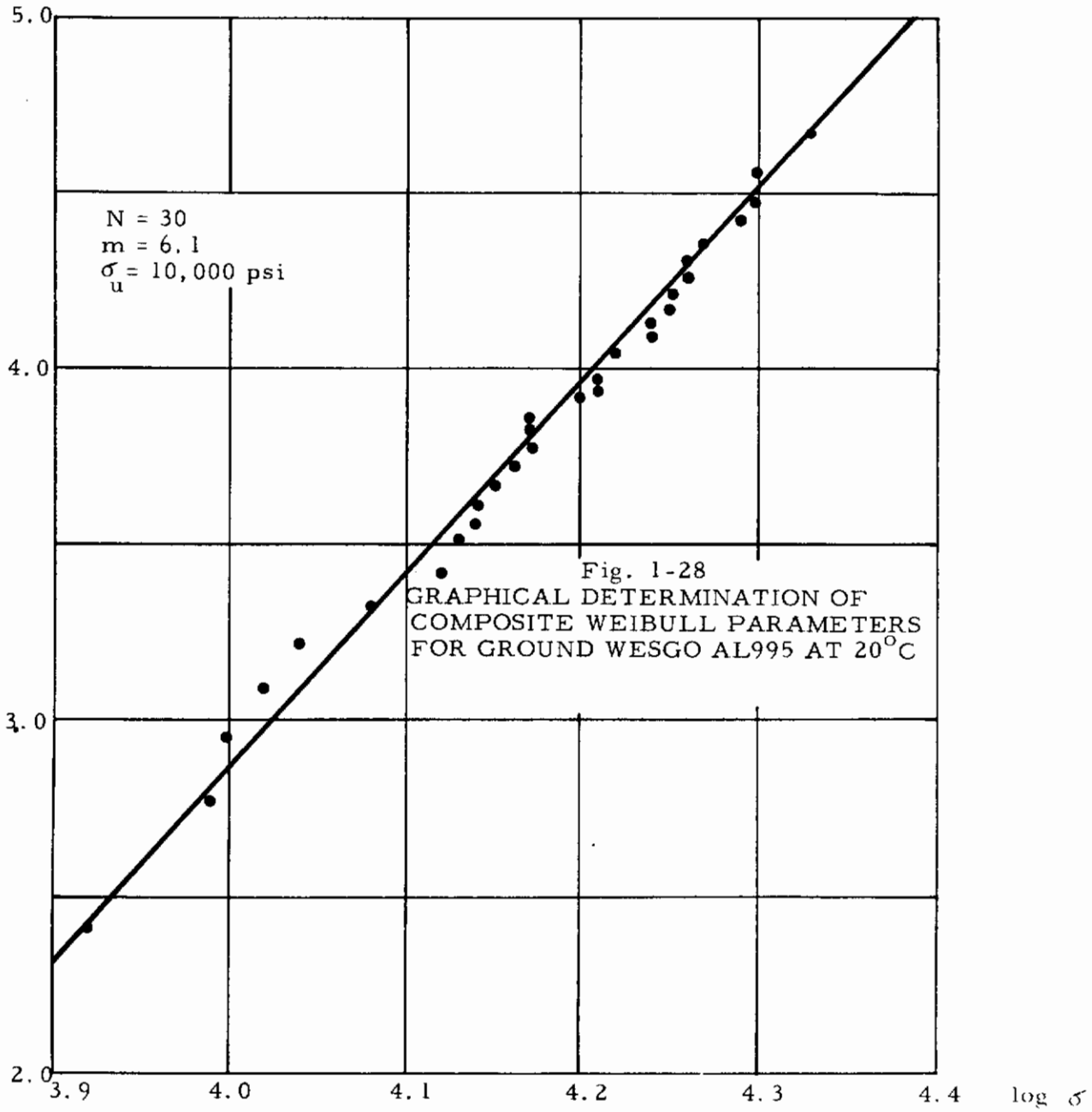

Fig. 1-28
GRAPHICAL DETERMINATION OF COMPOSITE WEIBULL PARAMETERS FOR GROUND WESGO AL995 AT 20°C

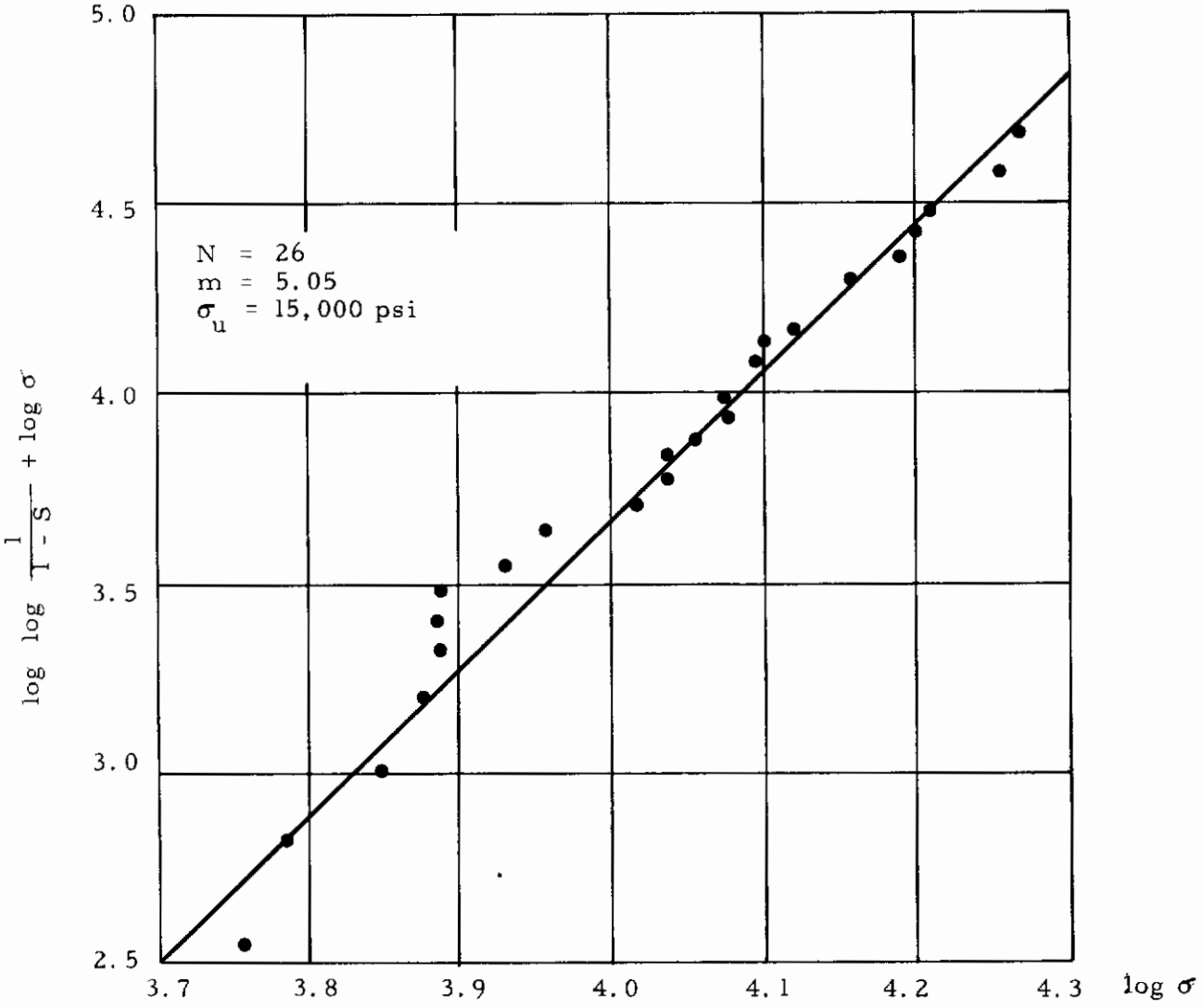

Fig. 1-29 GRAPHICAL DETERMINATION OF COMPOSITE WEIBULL PARAMETERS FOR AS-RECEIVED LUCALOX FLEXURAL SPECIMENS AT 20°C

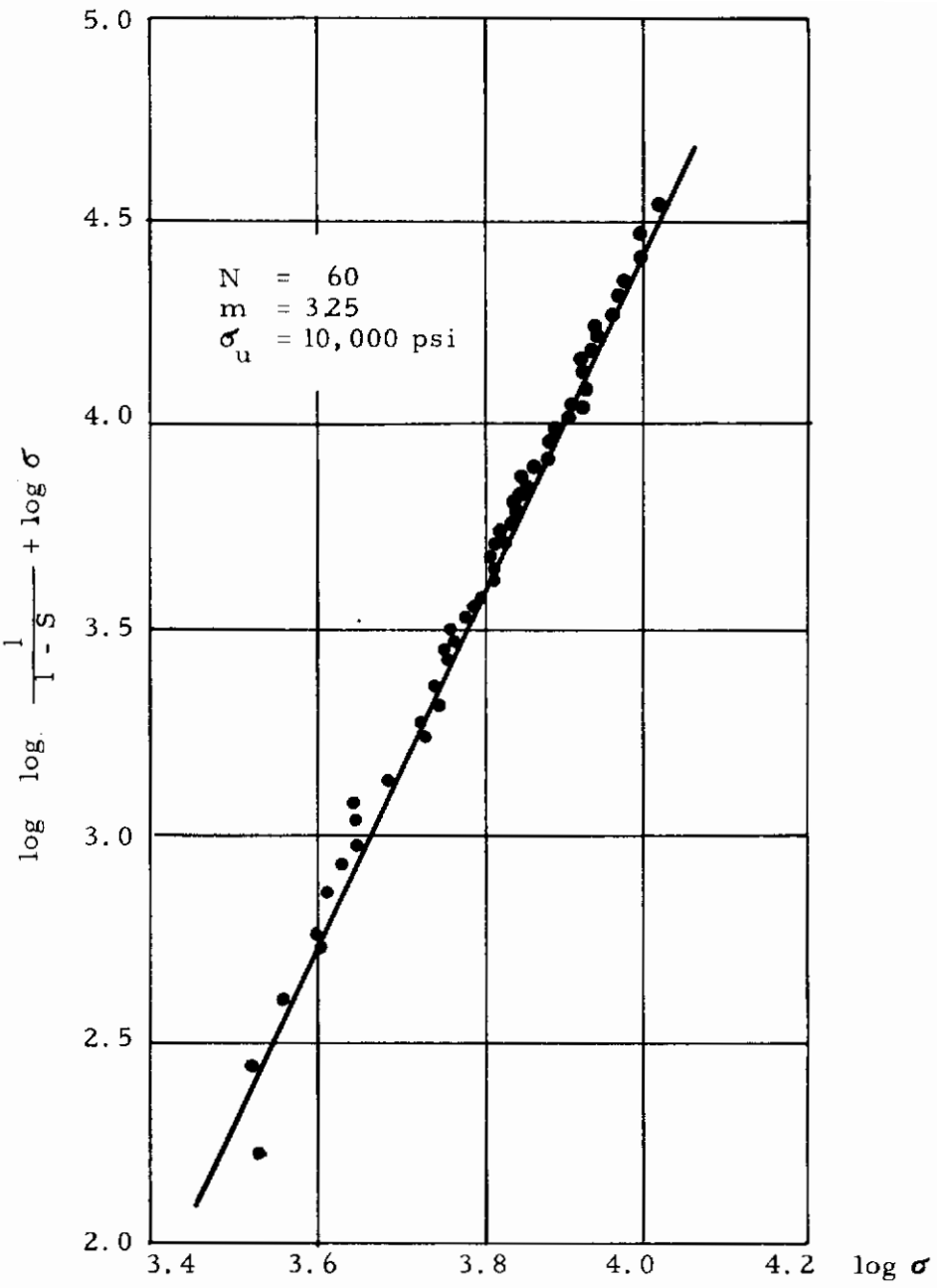

Fig. 1-30 GRAPHICAL DETERMINATION OF COMPOSITE WEIBULL PARAMETERS FOR ARF MgO FLEXURAL SPECIMENS AT 20°C

for "as-received" and ground Wesgo AL995, Lucalox and MgO tested at 1000°C (Fig. 1-24) which also showed a zero-strength value different from zero, have not yet been fully analyzed as yet.

The cumulative results excerpted from these graphs (Fig. 1-22 1-23, 1-27, 1-28, 1-29 and 1-30) are summarized in Table I-VII. Examination of this table, and the curves upon which it is based, indicates that both of the Weibull constants are highly dependent upon the surface condition and heat treatment of the material. Specifically, it can be seen from values listed for the Wesgo material in Table I-VII, that the Weibull "constants" are not constants at all, but fluctuate highly with the thermal and mechanical history of the specimen.

Both grinding and annealing change the values of the Weibull constants. While annealing may affect both surface distributed flaws or volumetrically dispersed sources of crack nucleation, grinding can affect only the former. This proves that the fracture of Wesgo specimens is, beyond any doubt, a surface induced phenomenon. This raises another complication, notably that the fracture probabilities and Weibull constants were all evaluated here on premise of a volumetrically distributed flaw density, as indicated by the derivation entailed in equations 1-1 to 1-9. Although this mathematical treatment is far more rigorous than that commonly employed in the literature, in the sense that no attempt was made here to envoke the simplifying assumption* of $\sigma_u = 0$, the fact is that the entire analysis of data should have been based on a surface distributed flaw density theory, rather than a volumetric one. Such a derivation, unavailable in the literature, is now in progress, and the data will be reexamined on basis of this theory, which will in all likelihood entail changes in the values of the Weibull constants shown here.

---

*The literature, in fact, contains no treatment of the fracture data by the Weibull theory when $\sigma_u \neq 0$. In this regard the derivations and method of plotting presented here are original contributions.

Table 1-VII

SUMMARY OF WEIBULL MATERIAL CONSTANTS FOR VARIOUS MATERIALS USING USING GRAPHICAL SOLUTION

All Tests at Room Temperature

Material	Surface Treatment	Heat Treatment	Weibull Constants	
			"Flaw Density Constant" (m)	"Zero Strength" σ_u, (10^{-3} psi)
Wesgo AL995	as-received	none	3.23	10.0
	ground	none	6.10	10.0
	as-received	annealed	10.0	0
	ground	annealed	12.5	0
Lucalox	as-received	none	5.05	15.0
ARF MgO	as-received	none	3.25	10.0

Beyond this remark, it is interesting to note that grinding definitely weakens the material. This can be seen by the fact that σ_u remains unchanged while m increases for the ground specimens, which indicates that the strength of the as-received specimen is somewhat larger for any failure probability value other than zero (at S = 0, the strengths are equal at σ_u).

Annealing, however, induced significant reductions in strength, as shown by the fact that m acquires even higher values while the value of σ_u drops to zero. The former effect is anticipated in a sense, since increasing m values indicate a greater uniformity of flaw distribution. However, the "flaw healing effect" frequently associated with annealing treatments is totally absent; the annealed specimens are weaker at all fracture probability levels than their unannealed counterparts. While no firm proof can be cited at this time, it is hypothesized that this effect is attributable to the destruction of a beneficial residual stress distribution (compressed skin layer existing in the "as-received" specimens) during annealing.

Somewhat similar results were obtained previously by Anthony and Mistretta[1-5] who, working with ATJ graphite, found "m" values of 7.5, 7.3, 14.5 and 7.8 at temperatures of 70°; 2000°F, 2500°F and 2750°F, respectively. While they did not attempt to evaluate the influence of surface flaw density distributions and volumetric effects separately, their findings of a nearly two-fold variation of m over the comparatively narrow temperature range of 2000-2750°F is remarkable, and parallels in a measure some of the results reported here. This either means that statistical flaw density parameters cannot be regarded as a true material constant or that some new mechanism enters to affect the fracture probability at different temperatures, rendering (in the referenced case) the distribution of critical flaws far more uniform in graphite at the particular temperature of 2500°F.

It should be noted that the σ_u values for the Wesgo AL995 show the same zero strength, 10, 000 psi, regardless of surface treatment. Future work in this area will be done to clarify the significance of this finding.

Combining the 20°C Wesgo data into individual size groups, and using the average value of m = 11 (representative of the annealed materials listed in Table 1-VII) along with $\sigma_u = 0$, predictions were made for fracture strength. The average strength of the intermediate volume specimen (27, 460 psi) was used as the base and the strength of the small and large specimens were predicted. The predicted strength for the small volume specimens is 31, 000 psi, as compared with the actual average strength of 31, 400 psi. The predicted strength for the large specimens is 25, 700 psi and the actual value is 25, 890 psi. As can be seen, predicted values are in excellent agreement with experimental results. Similarly satisfactory results were obtained in tests performed at 1000°C for the large specimens; here, 18, 900 psi was predicted and 18, 700 psi obtained in actual experiments; the correlation, however, is less favorable for the small specimens, a predicted value of 23, 000 psi corresponding to 20, 100 psi obtained in actual experiments.

6. CONCLUSIONS

The purpose of this Task of the overall program dealing with fundamental studies of the fracture of brittle inorganic materials

to develop as much understanding as possible regarding the statistical nature of failure strengths of Al_2O_3 and MgO, the two ceramic materials selected for use throughout the program.

To make specimens adaptable to a variety of loading conditions, a detailed study was undertaken on the stress concentration effects, frictional disturbances and failure modes of a number of possible configurations. As a result of these studies, various dogbone-shaped specimens were evolved as standard specimens, which were also utilized in investigations conducted on companion Tasks.

A review of the Weibull theory of statistical failure was undertaken, and formulations were established applicable to the conditions of the experimental work carried out on the program.

Detailed experimental studies were conducted on one material, a commercial grade high-density Al_2O_3 supplied by Wesgo, with the principal purpose of determining the material constants (m, the flaw density parameter; and σ_u, the zero strength) and the volume effects entailed in the Weibull statistical theory. These parameters were determined as influenced by the variation of five factors, including (a) prior thermal history, (b) specimen finish, (c) test temperature, (d) environmental atmosphere, and (e) specimen size. Preliminary work has also been carried on Lucalox and multicrystalline MgO, and initial results pertaining to these materials are also reported. Data obtained were analyzed by statistical methods to determine the significance of various effects investigated. The principal conclusions can be summarized as follows:

(a) Environmental effects for Wesgo AL995 at room temperature are significant only for specimens having a ground surface; as-received specimens are not significant affected by environmental conditions. At 1000°C, all environmental effects tend to vanish, in confirmation of results obtained by Charles on Task 9.

(b) Specimen volume has a significant effect on fracture strength at the 99 percent confidence level; however, the size effect observed is not explained adequately by the simple Weibull distribution function.

(c) Meaningful comparisons at this time can be made only for the behavior of the Wesgo AL995 tested at room temperature. This shows that fracture in this ceramic is definitely a surface induced phenomenon, indicating that all investigations based upon the volumetrically distributed Weibull flaw criteria are in error. This probably covers virtually all technical papers presented in the literature on this subject.

(d) The previous comment is based upon results obtained with "as-received" and ground specimens. Grinding lowers the strength of Al_2O_3 for all fracture probabilities other than zero, through an increase of the flaw density constant m. This implies a greater density and uniformity of flaws at the surface, which is a natural consequence of the grinding operation. Grinding, however, leaves the value of the zero strength unaffected at 10, 000 psi for Wesgo AL995. This finding is not fully understood, and is thought to be coincidental at this time.

(e) Annealing induces a drastic weakening of the Wesgo material, accompanied by a drop in the value of σ_u to zero. Thus, annealing cannot be said to have any beneficial "flaw healing effects" for the case investigated. It is assumed that the severe weakening effect of annealing is ascribable to the destruction of a beneficial residual stress distribution, whose compressive skin-layer effect imparts added strength to the unannealed specimens.

(f) Preliminary results indicate that similar conditions will be found to be operative in Wesgo alumina tested at 1000°C; however, data in hand at this time are too few to permit firm conclusions.

As general observations, it may be noted that the primary factors influencing the fracture of the Wesgo AL995 are the specimen size, testing temperature, surface treatment and prior thermal history of the material; secondary factors are represented by the moisture content of the environment and the duration of exposure. Preliminary results obtained with Lucalox and MgO appear to show similar trends for these materials, but data available at this time are insufficient to permit firm conclusions to be established. Such data including information on Wesgo AL995 tested at 1000°C, are expected to be gathered during the continuation phase of this Task of the overall program.

7. CONTRIBUTING PERSONNEL

Contributing personnel include L. M. Atlas, S. A. Bortz, I. M. Daniel, R. Firestone, H. Nagao, V. J. Parks and N. A. Weil.

8. REFERENCES

1-1 Frocht, M. M., "Photoelasticity," Vol. 1, pp. 380-81, Wiley and Sons, N. Y. (1951).

1-2 Frocht, M. M., "Photoelasticity," Vol. 2, pp. 174-201, Wiley and Sonz, N. Y. (1951).

1-3 Weibull, W., "A Statistical Theory of the Strength of Materials," Ing. Vetenskaps Akard Handl, No. 151, Stockholm (1939).

1-4 Weibull, W., "The Phenomenon of Rupture in Solids," Ing. Vetenskaps Akard Handl. No. 153, Stockholm (1939).

1-5 Anthony, F. M. and Mistretta, A. L., "Leading Edge Design with Brittle Materials," Paper No. 61-151-1845, IAS-ARS Meeting, Los Angles (June 1961).

8. BIBLIOGRAPHY

Duckworth, Schwope, "Mechanical Property Tests on Ceramic Bodies," WADC TR 52-67.

Salmassy, Duckworth, and Schwope, "Behavior of Brittle State Materials," WADC TR 53-50, Pt. I and II.

Kies, J. A., "Strength of Glass," NRL Report 5098 (April 3, 1958).

Kao, John H. K., "A Graphical Estimation of Mixed Weibull Parameters in Life-Testing of Electron Tubes," Technometrics, 1, No. 4, (November 1959).

Epstein, Benjamin, "Statistical Aspects of Fracture Problem", J. Appl. Phys. 19 (February 1948).

Bernbaum and Brodie, "Measurement of Tensile Strength of Brittle Materials," Brit. J. Appl. Phys., 10 (June, 1959).

TASK 2 - EFFECT OF STRAIN RATE

Principal Investigator: H. R. Nelson
Armour Research Foundation

ABSTRACT

The goal of this task was to investigate the effect of strain rate upon the fracture strength of ceramic materials. Since direct methods of recording high strain rates on the specimen proper were beyond the state of the art for the brittle materials used in this research, extensive studies were undertaken to develop suitable fixtures, specimen preparation techniques and recording methods.

Recording techniques were developed, suitable for strain rates up to 10^2 sec^{-1} and the problem of specimen loading for bending has been resolved. The manner of gripping the specimens in tension is still under review. Special equipment was developed for low strain rates in the 10^{-5} sec^{-1} to 10^{-1} sec^{-1} range and an intermediate rate device was constructed for use up to 10^2 sec^{-1}; equipment has also been designed to conduct experiments at higher strain rates.

TASK 2 - EFFECT OF STRAIN RATE

I. INTRODUCTION

The project effort on the effect of strain rate on the fracture strength of brittle materials had four objectives:

(a) Design and development of tensile and transverse bend test equipment which would develop strain rates of 10^{-5}, 10^{-3}, 10^{-1}, 10^{1}, and 10^{3} sec^{-1}.

(b) Development of a measuring and recording system for the determination of nominal stress-nominal strain behavior of brittle materials strained at the above rates.

(c) Development of elevated temperature facilities which would neither interfere with strain measurement nor place any hindrances on the use of special test equipment developed.

(d) Determination of the tensile and bend behavior of polycrystalline Al_2O_3 and MgO, at the strain rates specified.

The problems encountered in achieving objectives (a), (b) and (c) could be solved by relatively straightforward, though complex, means. The problems encountered in meeting objective (d) proved far more difficult of solution. Collection of reliable, reproducible test data from specimens known to have an ultimate tensile strain of less than 0.1 per cent demanded an accuracy of axial strain distribution that far exceeded the present state-of-the-art. Therefore, activities in connection with objective (d) became largely concerned with the prerequisite to its attainment, - an improvement in the state-of-the-art of mechanical testing. The following sections described the techniques used, and the progress made, in attaining these objectives.

2. DEVELOPMENT OF EQUIPMENT TO PRODUCE DESIRED STRAIN RATES

A. Low Strain Rate Machine

A standard Riehle universal testing machine, equipped with a Thyratron speed control, was used as the basic equipment for this part of the program. This machine originally possessed two crosshead speed ranges, 0.2 - 2.0, and 1.0 - 10 in./min respectively. Insertion of a transmission train with interchangeable pulleys and a 400:1 gear reducer made it possible

to achieve crosshead speeds in the desired 10^{-5} to 10^{-1} in./sec range. Care was taken to select gear and pulley ratios which would permit attainment of a specific crosshead speed when the motor drive pulley was rotating at no less than 10% of its rated rpm. This assured reproducibility of Thyratron control action. The various pulley and gear reducer combinations used for given speed ranges are shown in Table 2-1.

The ability of the machine crosshead screws to transmit a uniform crosshead motion at the slowest speed, 4.18×10^{-6} in./sec was checked on a 4-in. wide steel tensile bar. This calibration specimen showed a uniform strain rate over a period of four minutes, twice the time of the longest planned test when using brittle specimens.

Table 2-I

PULLEY AND SPEED REDUCER COMBINATIONS FOR GIVEN SPEED RANGES

Motor-Drive Pulley Ratio	400:1 Speed Reducer	Low Speed Range, (in./sec)	High Speed Range, (in./sec)
2:1	no	3.33×10^{-3}	1.67×10^{-2}
		3.33×10^{-2}	1.67×10^{-1}
4:1	no	1.67×10^{-3}	8.35×10^{-2}
		1.67×10^{-2}	8.35×10^{-1}
2:1	yes	8.58×10^{-4}	4.18×10^{-5}
		8.58×10^{-3}	4.18×10^{-4}
4:1	yes	4.18×10^{-6}	2.09×10^{-4}
		4.18×10^{-5}	2.09×10^{-3}

A 4-range electric tachometer for measuring and indicating the tensile machine drive motor speeds was installed, and calibration curves were prepared, enabling strain rates to be read directly from the tachometer meter.

B. Intermediate Strain Rate Loading Device

The machine designed and constructed for this purpose is shown in Fig. 2-1. The unit consists of a steel tube, a compression spring, an end adapter, and a sear arrangement for triggering the unit to release the compressed spring. Loading velocities could be varied as a function of the amount of spring preload. Figure 2-2 shows the arrangement for specimen and end grips and adapters used in the tube of the spring loading fixture. Figure 2-3 shows the spring loaded fixture mounted in the testing machine.

Determinations of average ram velocity by measurement of the anvil traverse time over a fixed distance showed that values of up to 380 in./sec could be achieved. Assuming constant acceleration of the extended spring, a maximum striking velocity of approximately 760 in./sec could be obtained.

C. High Strain Rate Loading Device

A strain rate loading device capable of loading specimens at 1000 in./sec was designed. A schematic diagram of the device is shown in Fig. 5-4. Angular velocity of the steel flywheel is controlled by a d-c variable speed motor. The specimen is mounted in the machine between an upper and lower platen, both of which are rigidly affixed to the machine base. For the tension loading shown, the specimen is suspended from the upper platen through a water-cooled load cell link connected to a double pin-and-clevis specimen grip. At the lower end of the specimen, the same type double pin-and-clevis is used for connection to a water-cooled loading bolt. The entire assembly is then freely suspended. The loading bolt and load applicator cage move vertically in line-bored holes to prevent misalignment.

Specimen loading is accomplished by rapid transfer of energy from a high mass rotating flywheel to the specimen through a quick acting wrapped wire spring brake. The diameter of the wrapped spring is smaller than the flywheel diameter, and is held open in a cocked position by a sear. When the desired speed is reached, the sear is released, and the wrapped spring

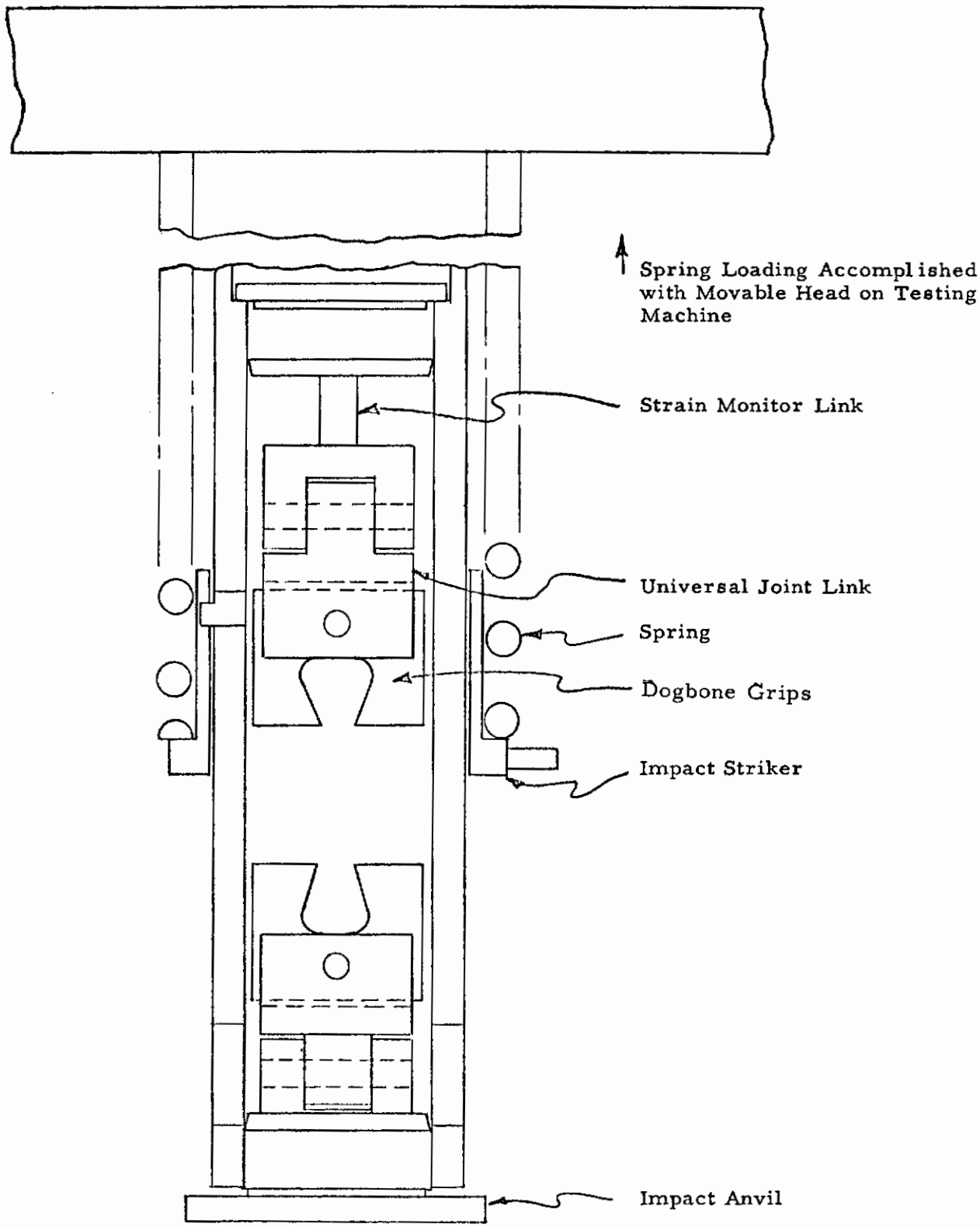

Fig. 2-1 SPRING LOADED DEVICE FOR MEDIUM-HIGH STRAIN RATE EXPERIMENTS

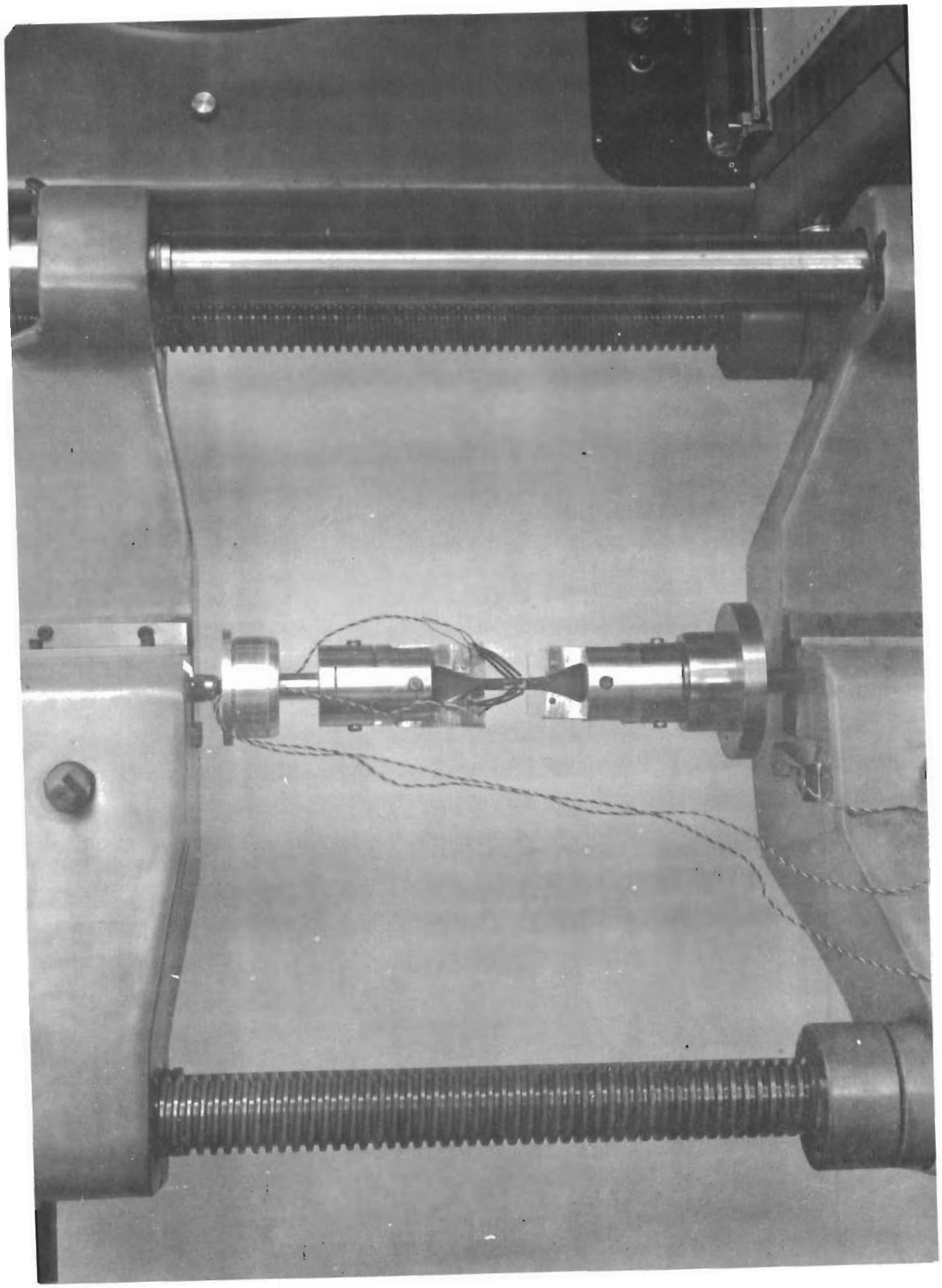

Fig. 2-2 STRAIN GAGE INSTRUMENTED SPECIMEN MOUNTED IN END CONNECTORS FROM SPRING LOADED IMPACT DEVICE

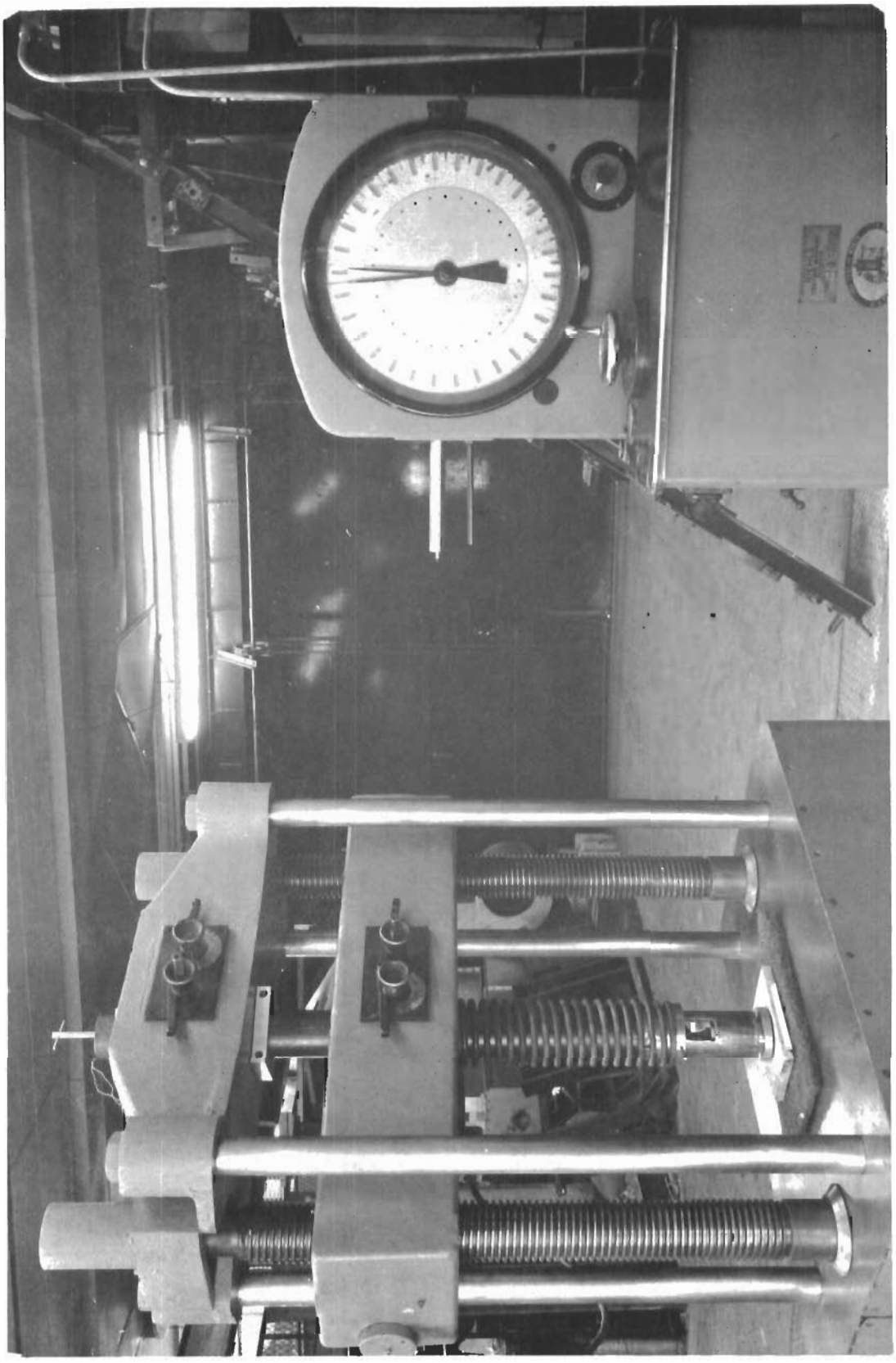

Fig. 2-3 INSTALLATION OF SPRING LOADED DEVICE IN TESTING MACHINE

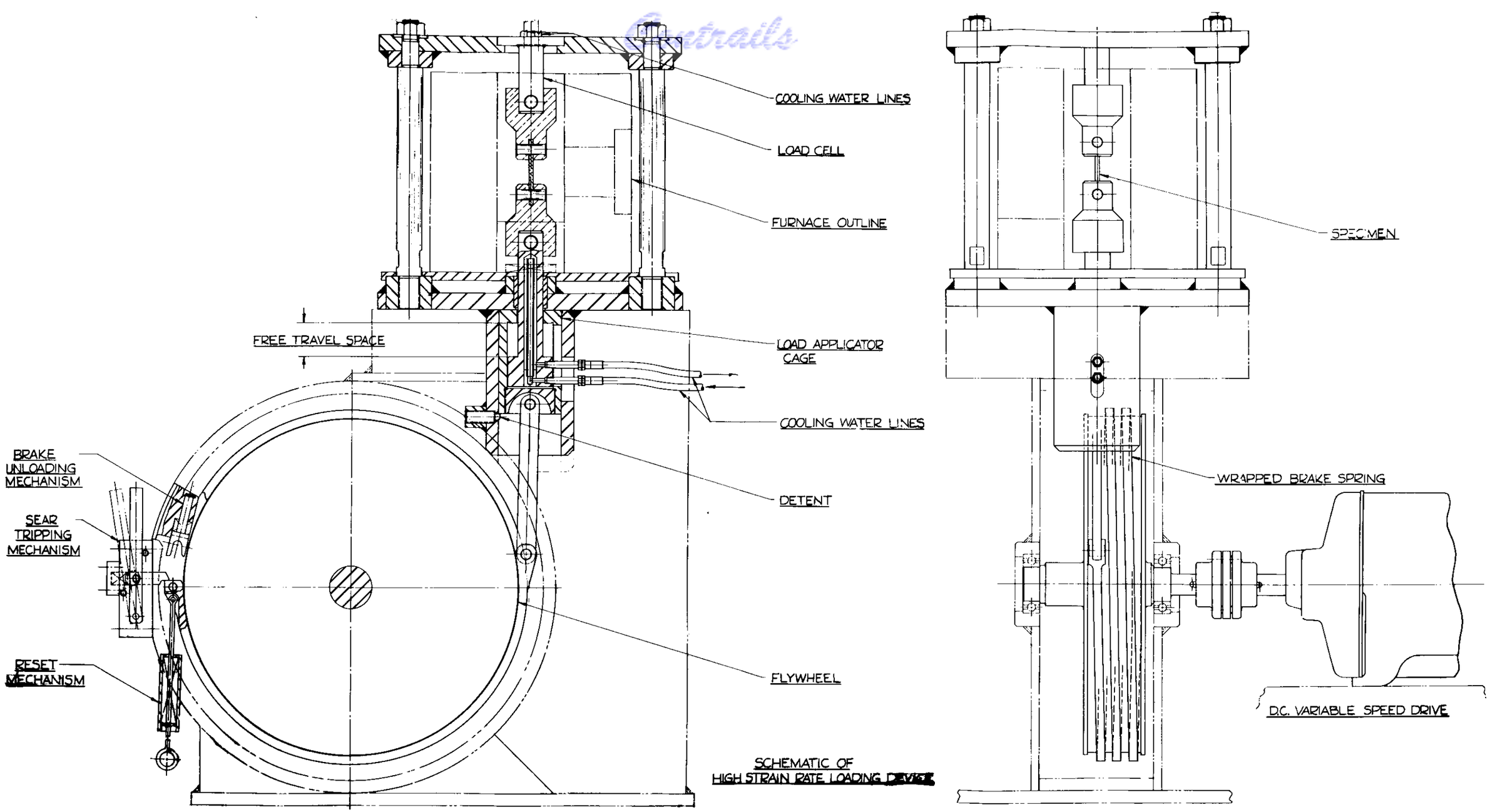

Fig. 2-4 SCHEMATIC OF HIGH STRAIN RATE LOADING DEVICE

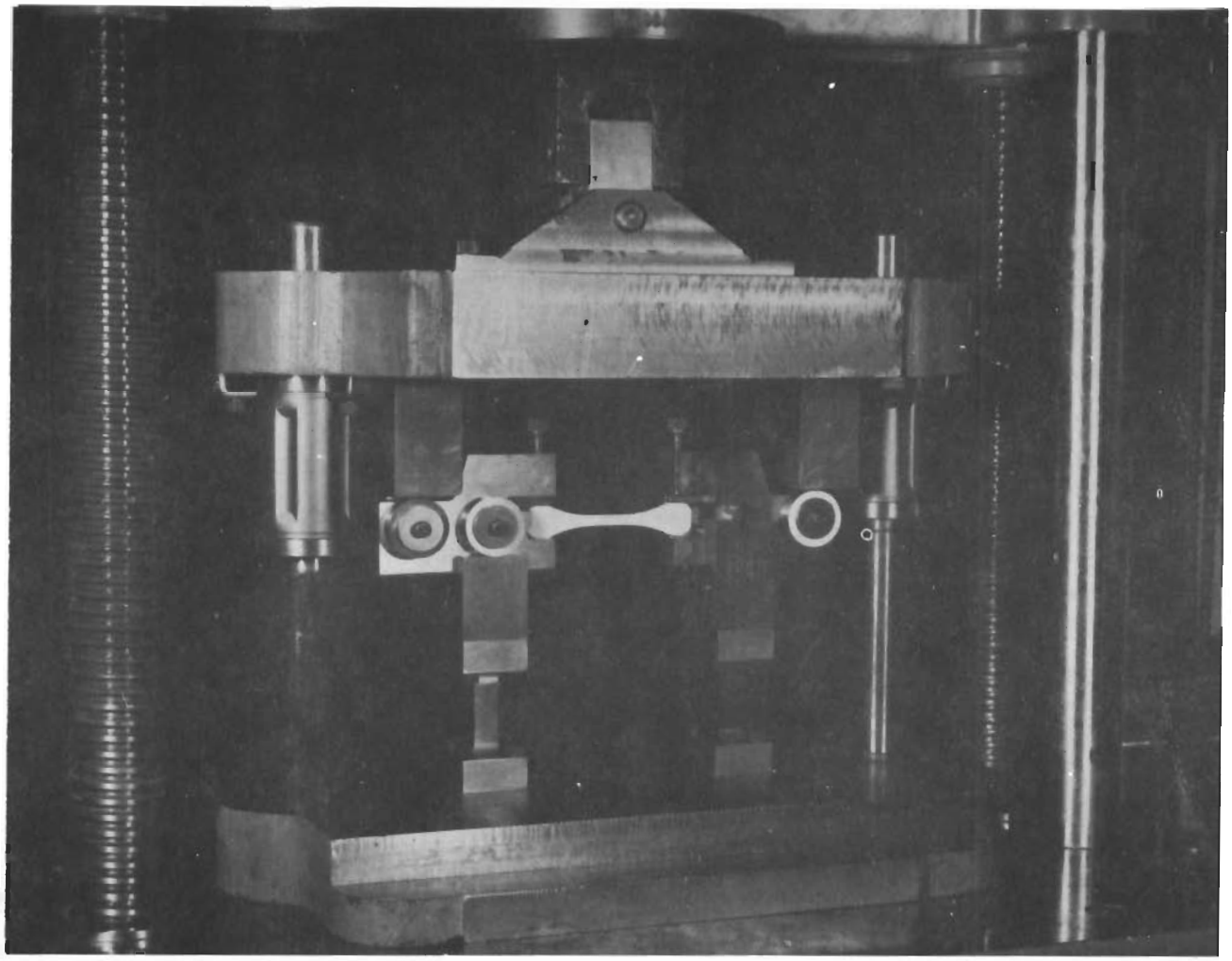

Fig. 2-5 CLOSE-UP VIEW OF SPECIMEN BEND FIXTURE

collapses on the periphery of the wheel. The collapsed spring then starts to rotate with the flywheel, and transmits its motion through a link to the load applicator cage. The load applicator cage is restrained from movement when the brake is first energized by a detent, to assure that no movement occurs until the spring brake has been fully engaged by the flywheel. A 2-in. separation is maintained between the brake and the loading bolt of the test assembly, to permit the loading cage velocity to approach wheel velocity before impacting the specimen.

Construction of this equipment was deferred when it was established both by experiments (with the medium strain rate machine) and calculation that tensile loading rates in excess of 385 in./sec would generate a stress wave which would fracture the specimen outside the gage length. Nonetheless, such a device would be most useful on high-speed deformation studies of more ductile materials.

3. DEVELOPMENT OF TRANSVERSE BEND TEST EQUIPMENT

Photoelastic studies had indicated that uniform specimen bending could be produced by 4-point loading. The load connection was established by drilling 4 holes through the specimen, and placing pins in the holes. Outer holes were connected to the upper crosshead of a tensile machine, inner holes to the lower crosshead. Gimbals were used between each pin and the appropriate crosshead to compensate for the possible lack of parallelism of loading holes in the specimen.

This system, although suitable for metals, did not develop uniform bending in the ceramic specimens. Therefore, a high-precision bend test unit had to be constructed; the severe difficulties encountered in this task focussed particular attention, in turn, on the problems associated with achieving uniaxial tensile loading.

The reasons for lack of uniform bending in test specimens were found to lie in the limit of machining accuracy, and in the ability of gimbal sets to compensate for machining deviations. The highest degree of accuracy presently attainable for the hole centerline, is a tolerance of $\pm$0.0001 in. from true perpendicular to the specimen surface, at a specimen thickness of 0.250 in. If the axis is horizontally inclined, the gimbal will compensate for the misalignment; however, if the hole is vertically inclined, the gimbal

is useless. If the vertical deviation of two adjacent holes is in opposite direction, a 0.0004-in. twisting strain will be superimposed on the bending strain. At a failure strain of less than 0.001 in. in bending, the twisting strain becomes at least 40 per cent of the bending strain, and the test loses all validity. Unfortunately, photoelastic strain determinations were not sufficiently sensitive to detect this difficulty.

When these difficulties became fully appreciated, a special fixture was designed and constructed which placed the specimen in bending without the need for any holes. Figures 2-5 and 2-6 show details of the operating parts and its method of mounting on the tensile machine. The posts supporting the roller pedestals are machined to $\pm$0.0001 in. for use as load cell members. High-sensitivity semi-conductor strain gages (not shown) were mounted on the right hand post. This member has a compressive load applied to its centerline at all times, due to anchoring of the right hand roller assembly. The left hand roller assembly is left free to move laterally, in order to prevent buildup of any axial stresses in the specimen subjected to the bending load. Linear bearing races were used to minimize friction between the upper head of bend tester and alignment posts. Loading posts, attached to the upper section of the fixture, and all rollers, were machined to a tolerance of $\pm$0.0001 in.

The rugged construction of this fixture (250-lb approximate weight), permits its use with fast loading devices.

4. DESIGN OF THE MEASURING AND RECORDING SYSTEM

Since experiment and calculation had shown that tensile strain rates in excess of approximately 300 in./sec would cause specimen fracture outside the gage length due to stress wave propagation, it was decided to hold the maximum strain rate to approximately 200 sec^{-1}. This, in turn, fixed the minimum total test time at 10^{-5} sec for a strain of 0.001 in./in. The recording system would then have to possess a full-scale deflection time, or rise time, of 5×10^{-7} sec in order to assure its ability to follow variations in the stress-strain curve during loading. Strain resolution limit was fixed at 5×10^{-6} in., to provide a resolution of 0.5 per cent of estimated strain, using specimens possessing a gage length of 1 in.

Selection of an appropriate load cell was relatively simple. A 5000-lb strain gage load cell of $\pm$0.25 per cent accuracy, with suitable dynamic response characteristics, and adequate for use with the strongest material, was selected as a stress transducer.

A detailed review was made of the advisability of using either indirect or direct strain measurement. Indirect methods measure strain induced in some portion of the tensile grip, using an extrapolation function to determine the state of strain in the specimen proper. This process has the advantage of utilizing non-expendable strain transducers which, moreover, would not require attachment to the specimen, disturbing thereby the local strain distribution. This disadvantage of this method lies in the difficulty of an accurate determination for the correct extrapolation function. Since the latter depends both upon temperature and strain rate, direct and indirect strain measurements would have had to be obtained over the entire temperature and strain rate range of the tests. Because of the inherent uncertainties involved in this approach, indirect measurements were eliminated from further review, and only direct strain measurements were considered.

A search of the literature concerning the state-of-the-art of direct measurement devices disclosed only two applicable techniques, notably optical gages or strain gages.

Strain gages have a high degree of strain resolution; their disadvantages lie in the economics of their use, and their lack of reliability at elevated temperatures. Gages for operation at 1800°F cost between $15 and $20 each, compared with room temperature gages at $2 to $3 each; at least one gage must be mounted on every specimen tested. The cost of labor expended in mounting the gages is also considerable. Furthermore, problems concerned with a drift in the value of gage factors and creep in cements have been encountered at temperatures in excess of 1000°F, ruling out the use of these devices for static tests, and posing some difficulties in strain gage bridge calibration even for dynamic tests.

Although the disadvantages to the use of strain gages were not prohibitive, they appeared sufficiently great to make evaluation of optical strain measurement devices worthwhile.

The ideal optical system would scan the distance between fiducial marks on the specimen; associated instrumentation would then determine distance between marks as a function of scanning rate, and appropriate time markers. Such a system has the advantage of avoiding use of any expendable sensors. The disadvantage of commercially available systems is their relatively poor degree of strain resolution. Although manufacturers of such equipment were initially optimistic about their ability to improve the resolution of the devices to acceptable limits, such hopes turned out to be unattainable. Therefore, it was decided to construct the strain recording instrumentation based upon the utilization of strain gages, making provision for drift and calibration adjustment immediately before running elevated temperature dynamic tests.

For a maximum rate of response, strain gage bridge current must be d-c, requiring d-c amplifiers to generate a usable output signal.

The maximum output of a strain gage bridge is approximately 20 mv; therefore, a high gain amplifier is required to develop a sufficiently strong signal to drive an oscilloscope. The frequency band pass of high gain amplifiers is small, 300 kc representing about the maximum frequency such amplifiers can handle. This, in turn, limits the oscilloscope trace speed to between 0.5 and 1.0 μ sec/cm. Assuming a 10-cm wide screen, the fastest trace that can be obtained will be between 5 and 10 μ sec. Hence, the band-pass characteristics of the strain gage amplifier, or oscilloscope amplifier, will limit the recordable strain rate to about 10^2 sec^{-1} for a total extension of 0.001 in.

The slowest strain rate used, 10^{-5} sec^{-1}, strains the specimen to destruction in 100 seconds. In this case, output signals from the load cell and the strain gage bridge could be fed directly to the two arms of an X-Y recorder, affording a direct plot of the stress-strain curve.

An X-Y oscilloscope was procured for all other higher strain rates. The oscilloscope trace was photographed by a polaroid camera; superposition of the illuminated oscilloscope graticule on the film enabled stress-strain data to be read directly from the film.

Suitable correction for change in strain gage factor in elevated temperature tests was accomplished by first placing a load known to cause a given strain on the specimen, then adjusting the gage factor control knob

(or the gain on the oscilloscope amplifier) until a given beam deflection was noted. Errors resulting from creep of gage cement were minimized by running the test as soon as possible after zero and calibration adjustments were made.

5. DESIGN AND CONSTRUCTION OF A SUITABLE FURNACE FOR TENSILE AND BEND TEST APPLICATION

The design of the transverse bend and tensile test fixture made it mandatory that the furnace heat only the reduced section of the test specimen. Consequently, a small furnace was designed and constructed for use in both tensile and bend test activity. A schematic diagram of this furnace is shown in Fig. 2-7.

Total furnace length is 1 in.; the zone of uniform temperature is substantially in excess of the 1/4-in. specimen gage length. Continuous operating temperature of the furnace is 1850°F. Number 10 Nichrome wire was used for the heating element to assure long element life. Operating current is approximately 45 amps, for a 6-8 volt input.

The furnace is designed to be slipped over the test specimen prior to insertion in the grips and is then supported by an appropriate bracket attached to the testing fixture.

To test the suitability of the furnace, the gage section of an Al_2O_3 specimen, mounted in tensile grips with lead shims, was heated to 1800°F and held at temperature for 5 hours. The lead shims did not soften or melt during this time.

6. LOADING SYSTEMS FOR UNIAXIAL OR PURE BENDING STRAINS IN BRITTLE MATERIALS

A. Uniaxial Loading

Photoelastic studies of several tensile specimens and grip designs of differing geometric configuration, undertaken during the first six months of the project, indicated that a shoulder-type specimen and grip would possess an adequate uniaxial loading characteristic when loaded in tension. This design was also favored because the type of tensile specimen (dogbone) could be easily and relatively economically produced by the ceramic manufacturers. A drawing of this specimen is shown in Fig. 2-8. Succeeding

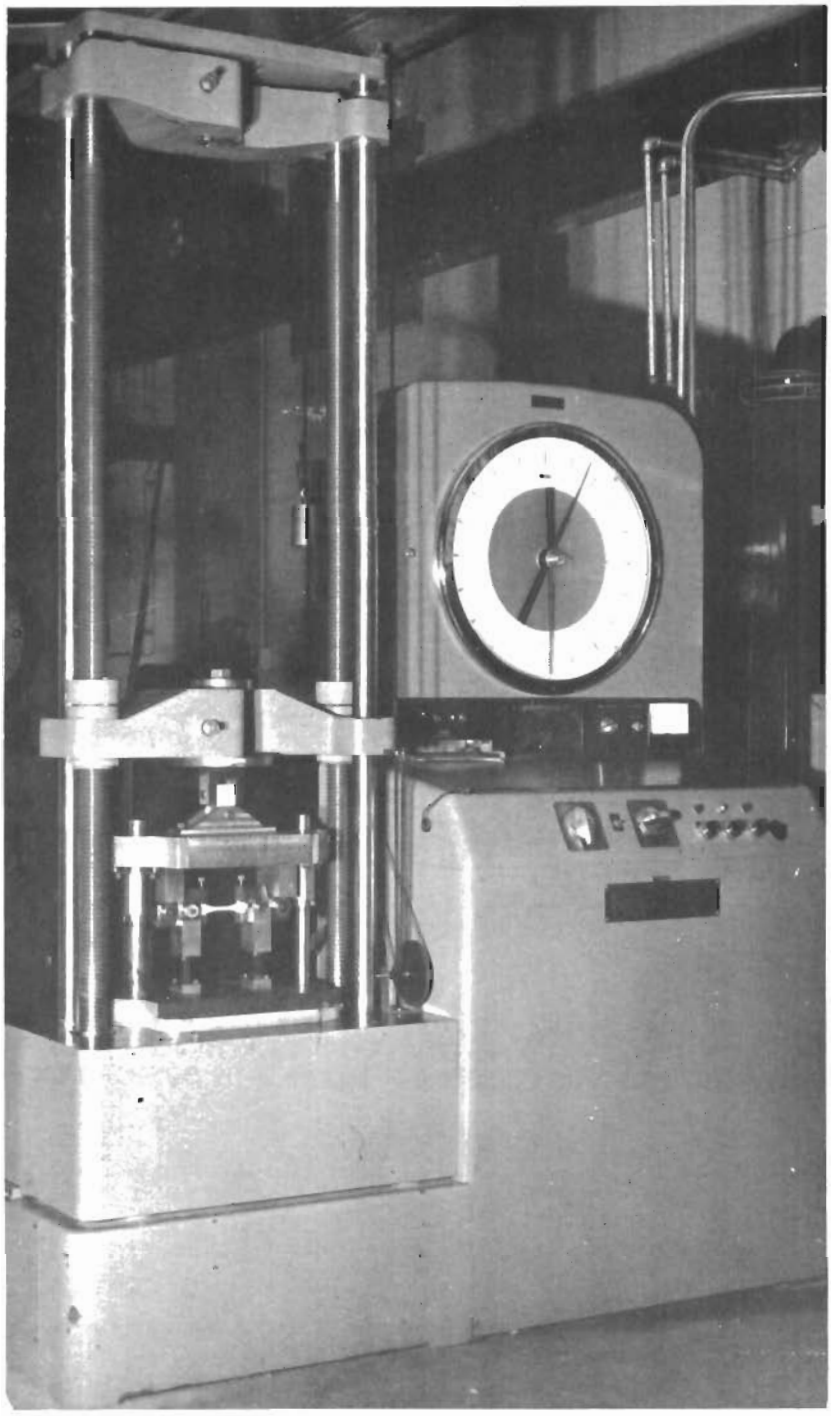

Fig. 2-6 VIEW OF SPECIMEN BEND FIXTURE MOUNTED IN TESTING MACHINE

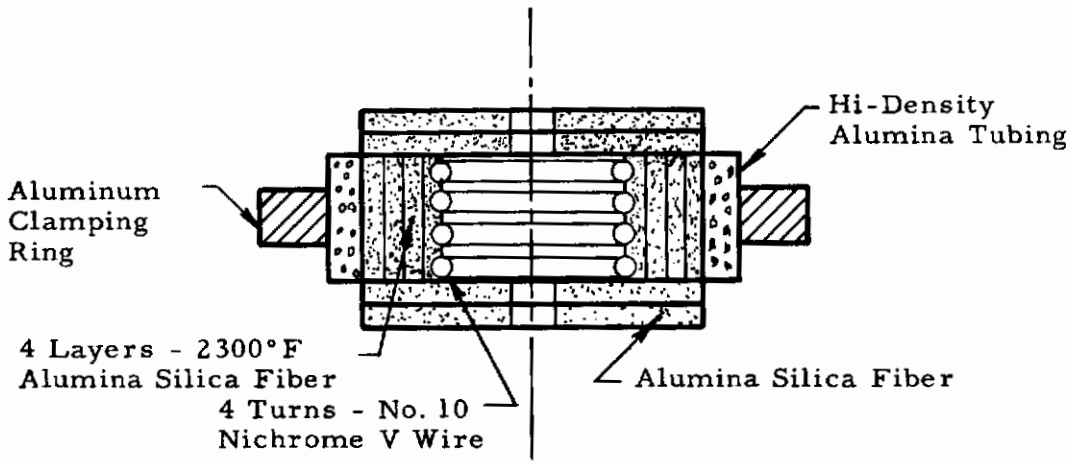

Fig. 2-7 SCHEMATIC OF ELEVATED TEMPERATURE FURNACE FOR TEST SECTION OF DOGBONE SPECIMEN

tensile tests, utilizing this specimen shape for ceramic materials, showed that the plastic birefringent materials used in the initial photoelastic test had not been sufficiently sensitive to indicate the deficiencies of this design. Occasional bending strains amounting to 50 to 60 per cent of the tensile component were determined to be present in ceramic specimens subjected to "pure tension". Use of self-aligning gimbals between specimen grips and tensile machine crosshead did little to reduce this high bending strain.

First efforts to reduce bending were concerned with improvements in the self-aligning test grip gimbals, and a reduction in grip and specimen tolerances. Variations were explored on two basic types of gimbals; a double clevis-double pin type, and a ball swivel type. The latter proved to be superior after many trials. An additional improvement was effected by attaching a low-frequency vibrator to the tensile machine while the test was in progress. Test specimens were ground to the dimensions shown in Fig. 2-8, in an effort to reduce possibilities of unsymmetrical loading. Although these measures were helpful, the bending component occasionally still approached 30 per cent, without any demonstrated test reproducibility. Attention was next centered on grip design.

Further investigation revealed that the remaining eccentricity was due to the inability to control the position of the shoulder contact surfaces between grip and specimen. The radius of curvature of such surfaces could neither be machined nor gaged to the accuracy demanded for uniform reproducible area contact. As a result, the amount and position of the contact surface between specimen and grip became a random function, causing the loading axis to be transposed or angularly misaligned by varying amounts with respect to the specimen centerline, resulting in a random bending component with a maximum value of about one-third of the tensile strain.

The problem of accurate alignment of specimen and grip was approached by use of oversize grips, a standard specimen, a "potting" material, and a jig to maintain specimen-grip alignment while the potting material set. The alignment jig and oversize grips were machined to a tolerance of ± 0.0005 in. Photographs of the precision tensile specimen and gage, and the precision tensile specimen cemented in tensile grips are shown in Fig. 2-9 and 2-10. The grip cavities were milled from a solid block of steel in an effort to make them as rigid as possible.

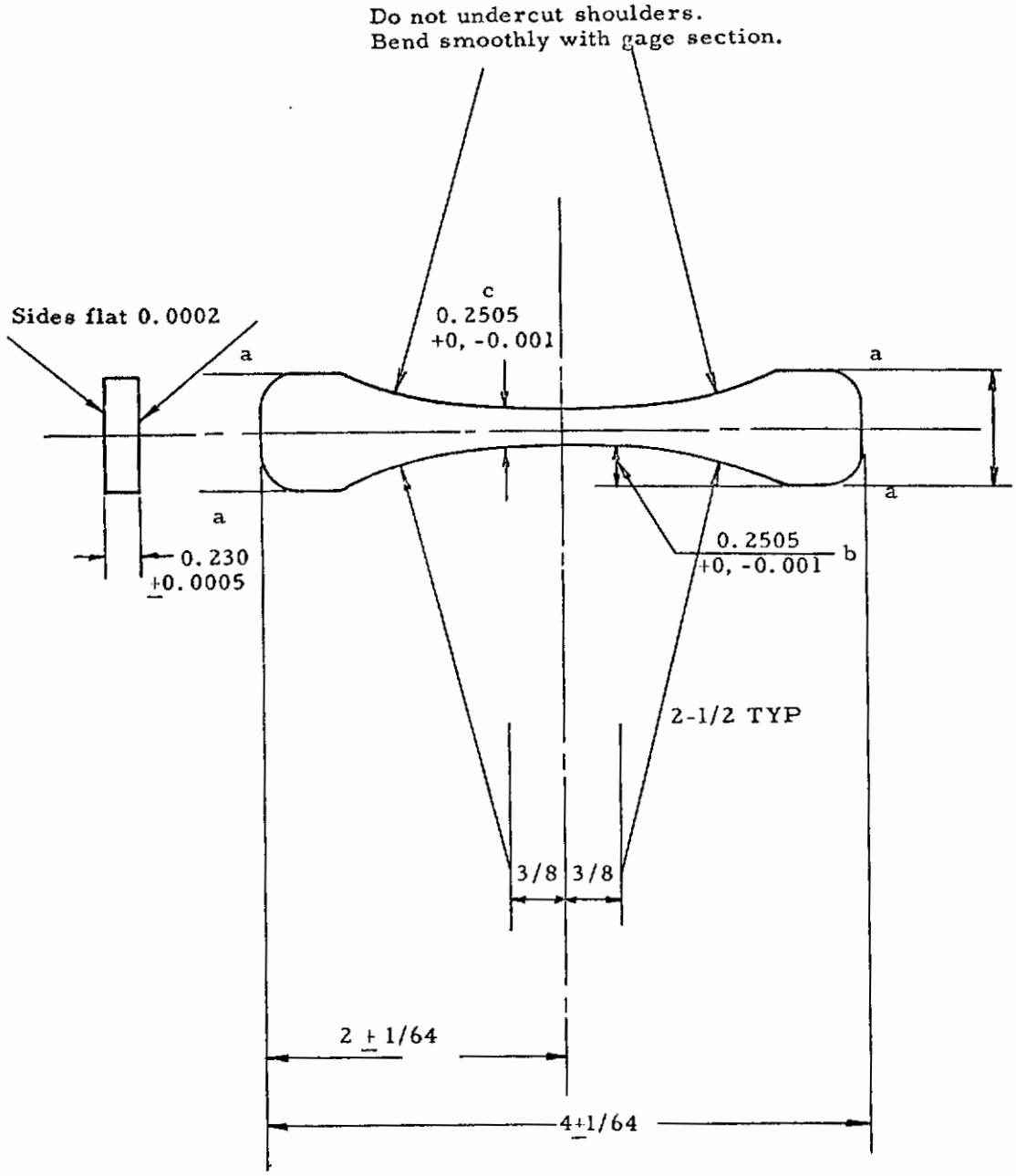

Procedure:
1. a - a Grind flat and parallel.
2. b a - a 0.250 in.
3. Grind 0.250 dim. c
4. Grind d to clean up

Fig. 2-8 CERAMIC TEST SPECIMEN

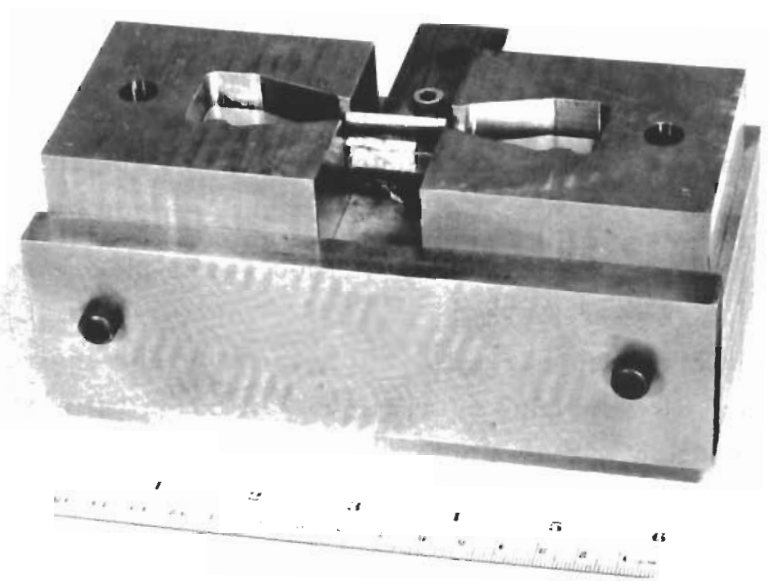

Fig. 2-9 PRECISION TENSILE SPECIMEN AND GAGE

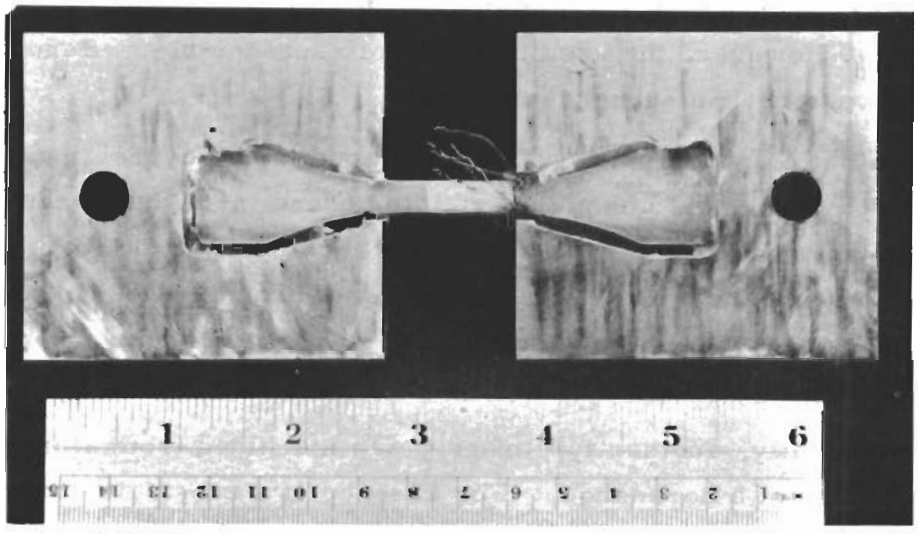

Fig. 2-10 PRECISION TENSILE SPECIMEN CEMENTED IN TENSILE GRIPS

Potting materials were screened according to their ability to fulfill the following requirements:

(a) High yield strength;

(b) Zero or positive linear expansion coefficient on cooling, to assure filling of space between grip and specimen; and,

(c) Relatively low melting temperature to avoid thermal shock to specimen, or softening of steel grip. To satisfy this requirement, an arbitrary limit of 1000°F was placed on the melting point of the potting material.

Two materials appeared to satisfy these three requirements: an epoxy resin and a low melting point alloy. Although little mechanical property information was available on the epoxy resin, it was known that its ultimate tensile strength was in the neighborhood of 8,000 psi, and that it possessed a positive expansion coefficient. The alloy, "cerro-matrix", possessed an ultimate tensile strength of 15,000, a total elongation of only 2 per cent (indicating the yield strength to be near the ultimate strength), and a positive expansion coefficient on cooling. Melting range was 315 to 360°F.

In tests both materials showed considerable yielding at loads over 400 lb. The epoxy material cracked loudly, exhibited discontinuous yielding, and did not reduce the amount of bending component. The metal alloy, in two tests, reduced the bending component to 5 per cent and 3 per cent respectively. However, the results were not reproducible. Bending ran as high as 35 per cent in subsequent tests.

Examination of the potting metal surfaces from several specimens after specimen testing disclosed that yielding of the metal had taken place over a relatively small section of its contact surface, whose location shifted from test to test. Therefore, a random contact process was still occurring, due to the rigidity of the grip which afforded no possibility for any stress relief of the potting material.

Consequently, another type of grip was machined from aluminum, in the general shape of a horseshoe. For absence of a cross-tie, the horseshoe ends were free to open slightly as a tensile pull was exerted on the specimen. The grip was machined oversize, and lead shims were used to fill in the space between specimen and grip. After some experimenting, a shim of approximately 3/32-in. thickness was found to be most effective.

Tensile tests using this grip showed that a 35 to 50 per cent bending component existed when a 100-lb tensile load was placed on the specimen. However, the relative bending strain steadily decreased until, at a 1000-lb load, the bending strain decreased to 15 per cent of the tensile strain; the opening between the grip horseshoe ends increased by 0.015-in. under this load. The test was not carried past this point to avoid a possibility of premature specimen fracture.

As the next step, the thickness of the horseshoe was reduced in steps to determine optimum thickness for reduction of bending component at a minimum tensile load, while preserving adequate strength in the grips for higher loads. Unfortunately, no significant improvement was obtained by this effort. Moreover, test results were not reproducible. Turning the same specimen upside down, or front-to-back, would change the bend component reduction characteristic of the grip.

This effect suggested two remedial possibilities. The first was an increase in the self-alignment properties of the tensile grip-specimen combination; the second, an improvement in the dimensional tolerance of the specimens used in the test. An improvement was attempted in self-aligning properties first. This was accomplished by using several layers of lead shim stock between the specimen and the grip. Experimentation showed that best improvement in uniaxial loading characteristic was secured by the use of 3 lead shims 0.008-in. thick.

Tensile test results showed marked improvement in uniaxial loading characteristics in some cases, no improvement in others. Maximum bending component in some tests, with loads of up to 1200 lb, was 10 per cent, ranging from a 10-μ in. bending strain at a 200-lb load to a 35-μ in. strain at 1200 lb. In other tests, maximum bending components ran as high as 42 per cent. In addition, the deformation and slippage rate of the lead shims did not vary linearly with load, resulting in a variable strain rate even when crosshead velocity remained constant. However, the use of lead shims was not immediately abandoned because of the demonstrated potential of this system in reducing bending strain components to acceptable levels.

Instead, attention was turned to the possibility of uniaxial load improvement through the use of test specimens machined to a closer tolerance than those previously used. The maximum tolerance was reduced by a factor of 5, from $\pm$0.0025 to $\pm$0.0005 in. The dimensions of the low-tolerance specimens produced are shown in Fig. 2-8. This reduction in tolerance represented a 20-fold increase in accuracy in the sections on which a tolerance could be measured, but did not necessarily improve the accuracy of the shoulder radii; no gaging techniques are known to exist which can accurately determine deviations of curvature at all points on the arc.

Comparison of static and dynamic test results obtained from the testing of high-precision specimens with those obtained from the testing of the lower precision specimens showed that the bending component minima and maxima were reduced from 10 per cent to 3 per cent, and from 42 per cent to 19 per cent, respectively, when the higher precision specimens were used. However, successive static tests run on the same high-precision specimen did not yield the same bending component. Direction of bending did not change if specimens were rotated 180° on successive static or dynamic tests. High-precision specimens loaded to fracture broke adjacent to the end of the gage length in an area in which shoulder grinding marks running in one direction intersected gage section grinding marks which ran in another direction. Ultimate tensile strength of these pieces was low, approximately 12,000 psi.

Although this activity did not produce the desired results, four conclusions could be drawn from this data:

(a) An improvement in uniaxial loading characteristic is effected if specimens are ground with a high degree of precision.

(b) Surface finish may have an important effect on tensile strength.

(c) The lead shim is not effective in reducing the bending component with increasing load. This component, in terms of per cent of tensile strain, remains constant.

(d) The amount of bending component appears to be determined by the chance mating of the lead shim and the specimen, when the specimen is inserted in the grip. This is shown by the variation in bending component from test to test on the same specimen.

B. Bend Test Activity

The bend fixture described in Section 3 forestalls the development of any axial loads in the specimen, but the prevention of twisting strains is a more difficult problem. Although the rugged construction of the bend test fixture frame prevents its twisting under the applied load, all four load transmitting posts must contact the load rollers (cf. Fig. 2-5) at the same time to avoid twisting the specimen. Load cell posts, load rollers, and load transmitting posts are all ground to a tolerance of $\pm$0.0001 in. Nevertheless, it is possible for a cumulative tolerance error to cause the load transmitting posts to be in contact with some rollers before others. Furthermore, the bearing-guide pin tolerance can also effect a roller contact height change.

Tests, using both standard and high-precision test specimens, have shown that the fixture was exerting a twisting strain of the specimen, while bending it. The difficulty was found to be due to unequal roller contact height. Three rollers were contacted by the load transmitting posts at virtually the same height; the fourth was not. Distance between the fourth load transmission post and its roller was between 0.0002 and 0.0005 in. Since the "late" roller contact was on the right side, this deviation caused a bending of the load cell post, with a resultant loss of load measurement accuracy. (This post has a 1-lb sensitivity, and a repeatability of $\pm$1 lb. However, load must be compressive if signal output is to be linear.)

Procedures are being investigated for adjustment of the height of the load transmitting posts, using elimination of twist strain as the criterion of proper adjustment.

7. CONCLUSIONS

The problems associated with the design and development of high loading rate equipment for tensile and bend testing of brittle materials, high and low speed data recording, and elevated temperature testing could be solved by utilization of procedures which did not extend beyond the state of the specific art employed. As examples, required machining tolerances, response time and signal sensitivity of the electronic equipment used, and furnace temperatures were all readily attainable, and did not require any research to extend performance ranges. These project objectives were attained during the program period.

However, demands of tensile testing of brittle materials greatly exceeded the present capability of the art. Since the manner of gathering strain data was to use a strain gage on only one specimen face, procurement of meaningful tensile test data demanded that the bending strain be held to less than 5 per cent of the tensile strain. Since the ductility of the specimens tests in no case exceeded 0.001 in.$^{-1}$, this meant that maximum bending strain could not exceed 50 μ in. Conventional machining tolerances are about 2000 μ in., 40 times the maximum bending strain tolerated.

Although improvements in uniaxial loading characteristics were secured by holding machining and grinding tolerances to extremely tight specifications, it became apparent that the techniques being used were too coarse to develop the required loading accuracy.

A similar situation existed with bend test data. However, there were two alleviating conditions, which did not exist in the tensile test activity. First, the specimen could be gripped in an area where its dimensions were accurately known and, second, the bend test fixture was, in reality, a separate machine specifically designed for the testing of brittle materials. Care was taken to avoid development of unwanted specimen stresses by design and precision machining practice.

The improvement in the existent state of the art of meaningful and reproducible tensile testing on brittle materials appears to require more than improved equipment design; it would be necessary to have built-in means of sensitive adjustment, and optical gages of 50 μ in. sensitivity so placed as to determine results secured by adjustment. The use of a specimen possessing extremely close tolerances and axial symmetry would greatly assist in reducing adjustment complexity.

Bend test problems appear nearer of solution with the equipment on hand. Use of optical gages and adjustable-height load transmission posts in conjunction with an improved tensile machine supplying a downward thrust free of horizontal components should develop the necessary precision required for accurate bend testing of brittle materials.

TASK 3 - EFFECT OF NON-UNIFORM STRESS FIELDS

Principal Investigators: I. M. Daniels and N. A. Weil
Armour Research Foundation

ABSTRACT

The purpose of this program is to investigate the effect of non-uniform stress fields upon the fracture characteristics of brittle materials, the principal aim being to determine whether the stress gradient existing at the location of fracture initiation has an independent effect upon the fracture strength.

To study this parameter, specimens were evolved whose effective size ranged over three decades with a stress gradient variation from 0 to 12.5 σ_p/in. (σ_p = peak stress). A special shape, the "theta"-specimen, was developed which generates uniform tension at the locus of fracture initiation, and is comparatively insensitive to the manner of load alignment.

Formulations, based upon existing theories of failure were derived for uniform tension and pure bending, and experiments were carried out on three "sample" brittle materials: Columbia resin (CR-39), plexiglas and graphite. In addition, work with multicrystalline Al_2O_3 has been begun.

Correlations were developed for the effect of stress gradient and the volume of high stress upon fracture strength, and good comparisons were obtained for CR-39 and graphite. Graphite, when analyzed according to existing statistical theories, appears to exhibit a "Weibull-anisotropy", which may indicate that its surface and interior fracture probabilities are governed by different criteria.

TASK 3 - EFFECT OF NON-UNIFORM STRESS FIELDS

1. INTRODUCTION

The principal characteristic of brittle materials which causes conventional methods of working stresses to be inadequate is that their strength is statistically distributed over a comparatively wide range. Because of this, it is insufficient to deal with the mean strength of the objects, and it becomes necessary to determine the variability of strength as a function of material and environmental parameters.

Statistical theories dealing with this subject allow for an adequate prediction of the failure probabilities of simple shapes of brittle materials, and take full account of the volume effect as well as the nature of the stress distribution to which the body is subjected. These predictions were reasonably well confirmed by experiments. However, in existing theories (statistical or deterministic) the stress gradient in the vicinity of the governing stress is not assumed to have an independent effect upon fracture strength, nor have any experiments been carried out to investigate this point. The purpose of this Task, accordingly, is to determine the effect of non-uniform stress fields upon the fracture characteristics of brittle materials, and to examine whether the stress gradient existing at the point of crack initiation has an independent influence upon the fracture strength of the material. Such studies are to be carried out both experimentally and theoretically.

In the simplest case the non-uniformity of a stress field can be described by a single parameter, the stress gradient. A major part of the effort was devoted to selection and evaluation of specimen designs giving known and controllable stress gradients. A wide range of stress gradients was covered by tensile, pure bending, ring and theta-shaped specimens. A large variation in effective size or volume under high stress accompanied the variation in stress gradient. For this reason, the volume under high stress was studied as an additional parameter influencing fracture. Correlations of experimental data obtained with existing statistical theories of failure were made for tensile and pure bending specimens only. The application of such theories to the more complicated stress distributions of the

ring specimens is very involved mathematically, and was not attempted in view of the time limitations of the program.

Since most of the work reported herein is of an exploratory nature, dealing with the selection and evaluation of specimen designs and establishment of experimental procedures, initial experiments were conducted with readily available and relatively inexpensive brittle materials, such as (a) Columbia Resin (CR-39), an amorphous polymeric brittle material with very good birefringent properties, (b) Plexiglas, an amorphous brittle polymer with some birefringent properties and good machinability and (c) Graphite with the properties of brittleness and fairly good machinability. Work on ceramics, such as polycrystalline Al_2O_3 and MgO was initiated but did not progress to the point where significant results could be reported.

Correlations were made between failure stress and each of the two parameters mentioned above, i.e., stress gradient and volume at high stress, treating each one in turn as the only significant parameter. This, of course, is true only when all parameters except the one in question are kept constant. In the present case no effort was made to segregate the effects of stress gradient from that of effective size. A good correlation (especially for CR-39 and graphite) between failure stress and effective size was obtained by arbitrarily defining the effective size as the volume of the specimen subjected to at least 95 per cent of its maximum tensile stress.

2. STATISTICAL THEORY OF BRITTLE FRACTURE

The fracture of completely brittle materials was first examined in detail by Griffith[3-1] who, using the theoretical results of Inglis, predicted that the growth of a crack will become possible when

$$\sigma = (2\gamma E/\pi c)^{1/2}$$

where γ is the surface energy, E is the modulus of elasticity of the material, c the depth of the existing surface crack, and σ the intensity of the applied (uniaxial) stress field. Griffith's theory is based on the balance between the energy liberated from the stress field and that absorbed in creating new surfaces; it also assumes that the crack is infinitely sharp and that its

propagation into the homogeneous material ahead of it is obtained by the parting of atomic bonds at the tip of the penetrating crack. Many questions arise in connection with this representation of fracture stress; as an example, the influence of the surface energy term upon fracture criteria is being investigated in detail on Task 6 of this program.

Of interest here is the fact that, according to Griffith, fracture will be initiated in a material containing a pre-existing flaw c, provided that the applied stress exceeds $\sigma = Kc^{-1/2}$, where K is simply a proportionality constant taking all other physical parameters into account. Moreover, the crack will continue to propagate unless the stress intensity drops below the value postulated above at the existing (increased) depth of the running flaw.

This simple picture of fracture in brittle materials would be adequate, provided one could determine the most significant "flaw" (dislocation pile-up, microscopic or macroscopic cracks, "metallurgical notches", lack of grain boundary fusion, surface attack by corrosive media) existing in the material. This, of course, cannot be done. Instead, one must approach the problem in an inverse sense. By a determination of the fracture strength, one can obtain an indication of the magnitude of governing flaw that existed in the structure.

Such an approach will disclose that the strength of apparently identical specimens is highly variable, because of the different magnitude of significant flaws contained in them. Moreover, the strength will clearly be a function of size: the larger the specimen, the greater the probability that a severe flaw will be contained in it.

The problem must therefore be attacked on a statistical basis, assigning a given probability of failure to a specified stress level. Theories based on this concept postulate that each material contains a random distribution of flaws, whose severity varies from specimen to specimen; fracture will be occasioned by the most severe flaw the piece happens to contain. To allow for analytical formulation, the specimen is visualized as being composed of individual infinitesimal volumes (or "links"), each of which carries a certain failure probability corresponding to the stress level to which it is subjected. When the first such link is ruptured, the shole specimen fails; hence these approaches are designated as the "weakest-link" theories of fracture.

Several formulations of the weakest-link theory of fracture have been proposed[3-2, 3-3], but the most widely accepted is that of Weibull[3-4] who is credited with the suggestion of a special elementary distribution function of wide applicability[3-5]. Epstein[3-6] reviewed the technical literature and formulated the problem of fracture in terms of fundamental mathematical statistics. This paper emphasized that the problem of fracture is that of the distribution of smallest values in samples of a given size (or a given number of flaws). The application of the general theory to a specific problem is a matter of selecting the most suitable distribution function.

In general, the occurrence of a phenomenon is characterized by an underlying or "unit" probability density function $f(x)$ of the variable x. The cumulative distribution function

$$F(x) = \int_{-\infty}^{x} f(x)\, dx \qquad (3\text{-}1)$$

expresses the probability that the event will occur at a value of the variable less than or equal to x. Then, the probability density function in samples of size n is

$$g_n(x) = nf(x) \left[1 - F(x)\right]^{n-1} , \qquad (3\text{-}2)$$

and the associated cumulative distribution function is

$$G_n(x) = \int_{-\infty}^{x} g_n(x)dx = 1 - \left[1 - F(x)\right]^{n} . \qquad (3\text{-}3)$$

The mode of $g_n(x)$ represents the most probable value of x in samples of size n; this also corresponds to the value x_n^* at which the function $g_n(x)$ attains a maximum. By solving for $g_n'(x) = 0$ from Eq. 3-2,

$$f^2(x_n^*)\,(n-1) = \left[f'(x_n^*)\right] \left[1 - F(x_n^*)\right] . \qquad (3\text{-}4)$$

Knowledge of the "unit" probability density function, $f(x)$, enables one to calculate the mode and all other measures of the distribution.

The form of the Weibull distribution function is based on the assumption that the probability of fracture of an infinitesimal element subjected to a known stress is proportional to the volume, so that

$$S_i = \phi(\bar{\sigma})\, dV \tag{3-5}$$

where, S_i is the probability of fracture in infinitesimal element dV for a value of the variable less than or equal to $\bar{\sigma}$, $\phi(\bar{\sigma})$, the function associated with the material, and $\bar{\sigma}$ is the function of stress components at a point used as a criterion of failure. (For a specimen under uniform tensile stress $\bar{\sigma}$, $\bar{\sigma} = \sigma$).

The probability of no-fracture (survival) of a specimen composed of n volume elements dV with respective probabilities of fracture $S_1, S_2, \ldots, S_n$ is

$$1 - S = \prod_{i=1}^{n} (1 - S_i) \tag{3-6}$$

then,

$$\log (1-S) = \sum_{i=1}^{n} \log (1-S_i) \cong - \sum_{i=1}^{n} S_i \tag{3-7}$$

and, if the stress does not exceed $\bar{\sigma}$ in any elemental volume

$$\log (1-S) = - \int_V \phi(\bar{\sigma})\, dV$$

from which

$$S = 1 - \exp \left[- \int_V \phi(\bar{\sigma})\, dV \right] = 1 - e^{-B} \tag{3-8}$$

where B is termed the "risk of rupture".

The requirements on $\phi(\bar{\sigma})$ are that it be a positive and monotonically nondecreasing function. The simplest form of such a function for the case of a specimen under uniform tensile stress is the following one suggested by Weibull:

$$\phi(\sigma) = \begin{cases} \left(\dfrac{\sigma - \sigma_u}{\sigma_o}\right)^m & \text{for } \sigma \geq \sigma_u \\ 0 & \text{for } \sigma < \sigma_u \end{cases} , \tag{3-9}$$

where σ_u, σ_o and m are constants associated with the material. In statistical terminology, the Weibull function gives the cumulative distribution function for a unit volume

$$F(x) = 1 - e^{-\left(\frac{x - x_u}{x_o}\right)^m} \tag{3-10}$$

and the "unit" probability density function, by Eq. 3-1, will be given by

$$f(x) = \frac{d\,F(x)}{dx} = \frac{m}{x_o}\left(\frac{x - x_u}{x_o}\right)^{m-1} e^{-\left(\frac{x - x_u}{x_o}\right)^m} . \tag{3-11}$$

The probability of rupture of a tensile specimen of volume V, by simple integration of Eq. 3-8, is

$$S = 1 - \exp\left[-V\left(\frac{\sigma - \sigma_u}{o}\right)^m\right] \tag{3-12}$$

which becomes zero when $\sigma \leq \sigma_u$ no matter how large the volume V. However, as Kies[3-7] observed, the probability of fracture does not reach unity until σ becomes infinite. In Kies' modification,

$$S = 1 - \exp\left[-V\left(\frac{\sigma - \sigma_u}{\sigma_o - \sigma}\right)^{\alpha}\right] , \tag{3-13}$$

where is an exponent different from Weibull's m, and σ_o is an upper limiting stress of the material.

Weibull's elementary function has the advantage of yielding closed-form solutions for the mean failure stress and standard deviation for certain simple cases of non-uniform stress distribution. It has found experimental corroboration especially in materials where the failure stress is much smaller than the theoretical strength. As far as can be determined, Kies' function has not been applied to the solution of problems involving non-uniform stress fields.

For a simple Weibull distribution, the mean value is given by

$$\bar{\sigma}_m = \bar{\sigma}_u + \int_{\bar{\sigma}_u}^{\infty} e^{-B} \, d\sigma \qquad (3\text{-}14)$$

where

$$B = \int_V \phi(\bar{\sigma}) \, dV \quad ,$$

and the variance by

$$a^2 = \int_{\bar{\sigma}_u}^{\infty} e^{-B} \, d(\bar{\sigma}^2) - \bar{\sigma}_m^2 \quad . \qquad (3\text{-}15)$$

For a specimen of volume V under uniform tensile stress σ,

$$\sigma_m = \sigma_u + \int_{\sigma_u}^{\infty} e^{-V\left(\frac{\sigma - \sigma_u}{\sigma_o}\right)^m} \, d\sigma = \sigma_u + \sigma_o V^{-\frac{1}{m}} \int_o^{\infty} e^{-z^m} \, dz$$

or

$$\sigma_m = \sigma_u + \sigma_o V^{-\frac{1}{m}} \Gamma\left(1 + \frac{1}{m}\right) \quad . \qquad (3\text{-}16)$$

(The gamma function if defined as $\Gamma(y) = \int_o^{\infty} z^{y-1} e^{-z} \, dz$)

The variance is given by

$$a^2 = \sigma_o^2 \, V^{-\frac{2}{m}} \left[\Gamma(1 + \tfrac{2}{m}) - \Gamma^2 (1 + \tfrac{1}{m}) \right] , \qquad (3\text{-}17)$$

and the mode determined by Eq. 3-4 is

$$\sigma_{mode} = \sigma_u + \sigma_o \, V^{-\frac{1}{m}} \left(1 - \tfrac{1}{m}\right)^{1/m} . \qquad (3\text{-}18)$$

These formulas suggest an analytical method of determining the parameters of the Weibull distribution from tensile tests of one size of specimen only. If one determines experimentally the ratio

$$\frac{(\sigma_m - \sigma_{mode})^2}{a^2} = \frac{\left[\Gamma(1 + \frac{1}{m}) - (1 - \frac{1}{m})^{1/m} \right]^2}{\Gamma(1 + \frac{2}{m}) - \Gamma^2 (1 + \frac{1}{m})} , \qquad (3\text{-}19)$$

the corresponding value of m can be found, since the right-hand side of Eq. 3-19 is a function of parameter m only, even for $\sigma_u \neq o$. Then, σ_o can be calculated from Eq. 3-17, and finally σ_u is determined using either Eq. 3-16 or 3-18. In the special case when $\sigma_u = o$, one can determine m by taking the coefficient of variation or relative variance

$$\frac{a^2}{\sigma_m^2} = \frac{\Gamma(1 + \frac{2}{m})}{\Gamma^2 (1 + \frac{1}{m})} - 1 . \qquad (3\text{-}20)$$

A. Multiaxial Stresses

In the theory of brittle fracture, it is assumed that only tensile normal stresses contribute to failure. A tensile normal stress, whether arising from a uniaxial or a polyaxial stress field, is not only a point function, but is also associated with a direction. Therefore, to determine the correct risk of rupture, according to Weibull[3-4], the contributions of all normal tensile stresses at a point must be taken into consideration. The risk of rupture B can be determined as follows:

If $\sigma = \sigma(x, y, z, \theta, \phi)$ is the normal stress at a given point (x, y, z) along a direction defined by the angles θ and ϕ

$$\phi(\bar{\sigma}) = K \int_{\theta} \phi(\sigma)\, d\theta \qquad (3\text{-}21)$$

where θ is the spatial angle of the tensile stress σ. As before

$$B = \int_{V} \phi(\sigma)\, dV$$

The validity of this treatment for multiaxial stresses has been evaluated only in a few isolated cases.

B. Non-Uniform Stress Fields (Uniaxial)

Let the stress at any point be written as

$$\sigma = \sigma_p\, f(x, y, z) \qquad (3\text{-}22)$$

where σ_p is a characteristic stress at an arbitrary point of the specimen, and $f(x, y, z)$ the function of position. The risk of rupture is given by

$$B = \int_{V} \phi(\sigma)\, dV = \int_{V} \phi\left[\sigma_p\, f(x, y, z)\right] dV \quad . \qquad (3\text{-}23)$$

The simplest case of a non-uniform stress field is that in a prismatic beam under pure bending. In the case of a rectangular cross section (b x 2h),

$$\sigma = \sigma_p \frac{y}{h} \quad ; \quad dV = b\ell\, dy \qquad (3\text{-}24)$$

where σ_p here is the extreme fiber stress. Then,

$$B = \int_{V} \left(\frac{\sigma - \sigma_u}{\sigma_o}\right)^m dV = \frac{b\ell}{\sigma_o^m} \int_{h_u}^{h} \left[\sigma_p \frac{y}{h} - \sigma_u\right]^m dy$$

$$= \frac{V}{2(m+1)} \left(\frac{\sigma_p - \sigma_u}{\sigma_p}\right) \left(\frac{\sigma_p - \sigma_u}{\sigma_o}\right)^m \qquad (3\text{-}25)$$

where, ℓ is gage length, $h_u = h\frac{\sigma_u}{\sigma_p}$ and V the volume of gage section of specimen.

The mean failure stress is $\sigma_m = \int_{\sigma_u}^{\infty} e^{-B}\, d\sigma_p$ which for $\sigma_u = o$ becomes

$$\sigma_m = \sigma_o \left[\frac{2m+2}{V}\right]^{1/m} \Gamma\left(1 + \frac{1}{m}\right) . \qquad (3\text{-}26)$$

The mean failure stress for a pure bending specimen and a tensile specimen of the same gage volume for $\sigma_u = o$ have the ratio

$$\frac{(\sigma_m)_b}{(\sigma_m)_t} = (2m+2)^{1/m} . \qquad (3\text{-}27)$$

C. Graphical Determination of Distribution Parameters

Let the total number of specimens tested be N, and assume that upon completion of the experiments are given a serial number n, where $1 \leq n \leq N$ is assigned according to an increasing level of fracture stress. For this system it is obvious that the probability of fracture will be given by

$$S = \frac{n}{N+1} .$$

Combining this with Eq. 3-8 ($1 - S = e^{-B}$), and taking the double logarithm of both sides,

$$\log\log\frac{1}{1-S} = \log\log\frac{N+1}{N+1-n} = \log B + \log\log e \qquad (3\text{-}28)$$

where, the logarithms are Briggs'.

Substituting $B = V\left(\frac{\sigma - \sigma_u}{\sigma_o}\right)^m$ into Eq. 3-28 for the case of tensile specimen, there results

$$\log\log\frac{N+1}{N+1-n} = m\log(\sigma - \sigma_u) + \log V - m\log\sigma_o + \log\log e. \qquad (3\text{-}29)$$

To obtain the numerical values of the parameters, it is most convenient to plot $\log \log \frac{N+1}{N+1-n}$ against $\log (\sigma - \sigma_u)$. For the correct value of σ_u, this plot will be a straight line having a slope of m and an intercept of $\log V - m \log \sigma_o + \log \log e$, which permit the determination of σ_o once m and V are known. The value of σ_u resulting in a linear plot must, of course, be determined by trial and error.

For the case of pure bending, the expression for B from Eq. 3-25 is substituted into Eq. 3-28 yielding

$$\log \log \frac{N+1}{N+1-n} = (m+1) \log (\sigma_p - \sigma_u) - m \log \sigma_o$$

$$- \log \sigma_p + \log \frac{V}{2(m+1)} + \log \log e \qquad (3\text{-}30)$$

It is suggested here for the case where $\sigma_u \neq o$ to plot

$$\left[\log \log \frac{N+1}{N+1-n} + \log \sigma_p \right] \quad \text{versus} \quad \log (\sigma_p - \sigma_u) \ .$$

The value of σ_u is found by trial and error until a straight line plot is obtained. Then, $(m+1)$ is determined as the slope of this line and σ_o is found as in the case of the tensile specimen above.

3. STRESS DISTRIBUTION FACTORS AFFECTING FAILURE

A. Weibull Theory

The Weibull theory presented above is fully capable of predicting failure conditions for the case of non-uniform stress fields subject, of course, to the validity of its underlying assumptions. Each infinitesimal element is still considered to be under uniform stress, and the risk of rupture for a given specimen is found by integrating the risk of rupture of each element over the volume of the specimen. Essentially this is a description based on size effect only, and accounts for the effects of the non-uniformity of stress distribution solely through the consideration of different risks of rupture associated

with the varying stress levels existing in each component element. The effect, if any, of sharp stress concentrations, however, cannot be accounted for with this approach.

Weibull[3-4] hinted that such an effect might exist by suggesting that the material function can be affected and altered in regions of high stress gradients caused by sharp stress concentrations. One way to describe this effect is to consider the material continuously or discontinuously anisotropic (in the Weibull sense) with a variable material function applicable to the differently stressed regions. This explanation, however, is conceptually hard to accept since a material function is expected to depend on the material only. It is hoped that this point will be clarified in future research.

A necessary requirement for the application of the Weibull (or any other statistical) theory to non-uniform stress fields is that the stress-strain relationship to failure be linear. If this is not true, a stress redistribution occurs in the specimen. Then, even in the absence of size effects, one would compute a higher failure stress in cases of non-uniform stress fields than actually exists at failure.

B. Stress Gradient

In non-uniform stress fields, the peak stress generally occurs at a free boundary; stresses decrease as one proceeds towards the interior (Fig. 3-1(a)). A good descriptor of the stress distribution in such a case would be the value of the maximum tensile stress and the stress gradient existing at the boundary. This is normally represented by the slope of the stress vs. position curve at the boundary. General experience shows that failure in the form of a crack would initiate at the boundary, and it has been observed in many materials that the sharper the stress gradient the higher the peak stress at failure.

The Weibull theory, in fact, anticipates that such an effect will occur; in the statistical treatment of fracture probabilities each infinitesimal volume is assigned a given probability of failure depending upon the stress level imposed upon it. The probability of fracture of the entire body is then the integrated value of the failure probabilities of all component volumes.

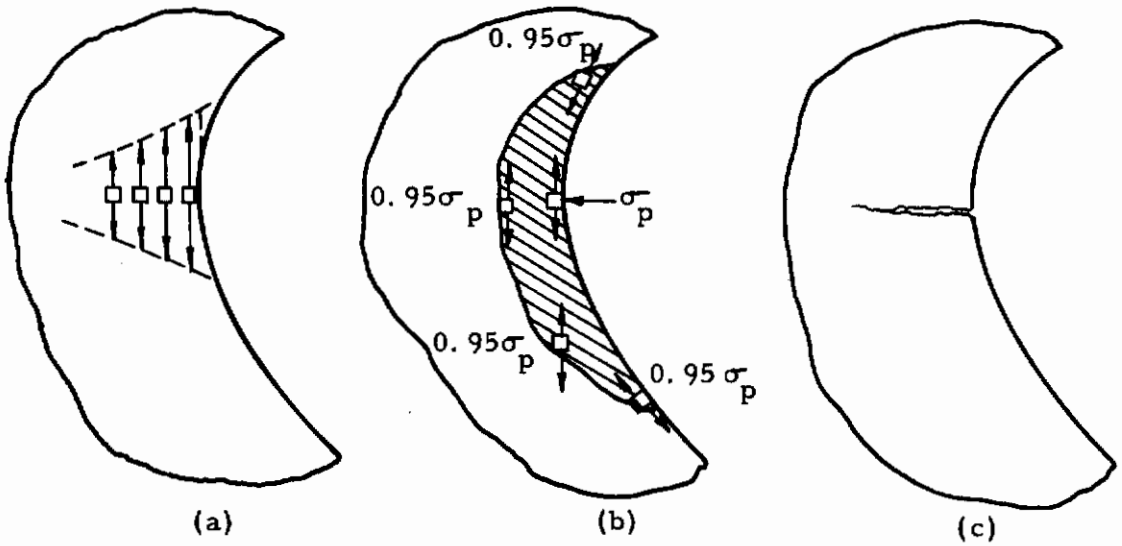

Specimen before cracking, showing stress gradient

Specimen before cracking showing volume subjected to more than 95% of maximum tensile stress

Specimen after cracking

Fig. 3-1 ILLUSTRATION OF PROPOSED FACTORS TO BE CORRELATED WITH FAILURE STRESS

Consider the case of a simple beam subjected to a uniform moment, and assume that the gage volume as well as the extreme fiber stress is identical for each, but the stress gradient vary. For sharp stress gradients, the stress will fall off rapidly as one proceeds into the interior of the specimen; these volumes will therefore make a smaller contribution to the overall fracture probability of the body. The net result is that, under the conditions quoted, the statistical failure theory will assign a higher survival probability to specimens having a higher gradient or, alternately, specimens subjected to a high gradient will be able to sustain a higher extreme fiber stress at the same fracture probability. This also becomes evident from Eq. 3-26, where the mean value of extreme fiber stress is seen to be inversely proportional to $V^{1/m}$ (assuming $\sigma_u = o$).

It is not definitely known whether the stress gradient in itself is a factor affecting failure since it is usually closely connected with effective size, and previous investigations have never attempted to segregate the independent effect of these two parameters upon the resulting fracture probabilities. The simplest way of studying the pure effect of stress gradient is to test pure bending specimens of rectangular cross section having the same gage volume but varying depths, hence varying stress gradients.

C. Effective Size

Effective size in a specimen subjected to a non-uniform stress distribution is defined as the size corresponding to a pure tensile specimen having the same probability of fracture under the same maximum stress.

If σ_p represents the maximum tensile stress anywhere in the specimen, the risk of rupture for a non-uniform stress field is given by Eq. 3-23. If V_{eff} is the effective or equivalent volume of a tensile specimen with the same risk of rupture,

$$V_{eff} = \frac{\int_V \phi \left[\sigma_p f(x, y, z)\right] \, dV}{\phi(\sigma_p)} , \qquad (3\text{-}31)$$

In general, the effective volume is a function of the failure stress and the distribution parameters. The effective volume of a beam of rectangular cross section under pure bending is

$$V_{eff} = \frac{V}{2(m+1)} \left(1 - \frac{\sigma_u}{\sigma_p}\right) , \qquad (3\text{-}32)$$

where V is the gage volume of the beam. The dependence on σ_p is eliminated if $\sigma_u = o$.

The application of Weibull's theory becomes very involved in cases of non-uniform stress distributions more complicated than those corresponding to pure bending; numerical or graphical methods would have to be employed for the solution of these problems. No attempt was made to carry our such an analysis for the ring specimens used here.

Instead, rough approximation to the effective size was sought on an empirical basis. This effective size was arbitrarily defined here as the volume of the specimen subjected to at least 95 per cent of its peak tensile stress. Figure 3-1(b) shows a shaded area around the point where failure originates. The tensile stress at every point in this area is greater than or equal to 95 per cent of the peak stress, σ_p, in the same area. For a two-dimensional stress distribution, this area is multiplied by the thickness of the specimen to give the effective volume of fracture as defined. This area is easily found using two-dimensional photoelastic models. For the case of a three-dimensional stress distribution, the through-thickness variation of the stress field must also be known for the computation of effective size.

4. SPECIMEN TYPES

The specimen types used in this Task consisted of dogbone-shaped specimens used in tension and pure bending tests, rings of different OD to ID ratios tested in diametral compression, a two-hole disk and a special theta-shaped specimen. A wide range of effective sizes and stress gradients was covered by these specimens. The range of effective size covered was about three decades; the stress gradient varied from 0 to 12.5 σ_p/in., where σ_p is the peak stress.

Significant parameters of the specimens used are tabulated in Table 3-I. Dimensions of the specimens are shown in Fig. 3-2, 3-3 and 3-4. The photoelastic patterns used to determine the volume under more than

Table 3-I

SIGNIFICANT PARAMETERS OF SPECIMENS USED IN STUDY OF NON-UNIFORM STRESS FIELDS

Specimen	Gage Length (in.)	Width (in.)	Thickness* (in.)		Volume Subjected to More Than 0.95σ_p		Stress Gradient (σ_p/in.)
			Plastics	Ceramics	Plastics	Ceramics	
5/16" Dogbone-Tension	1.000	0.312	0.250	0.312	0.0781	0.0976	0
1/4" Dogbone-Tension	.750	0.250	0.250	0.250	0.0469	0.0469	0
3/16" Dogbone-Tension	.500	0.187	0.250	0.125	0.0234	0.0117	0
Theta	1.50	0.100	0.250	-	0.0375	-	0
5/16" Dogbone-Bending	-	0.312	0.250	0.312	0.00195	0.00244	6.4 σ_p
1/4" Dogbone-Bending	-	0.250	0.250	0.250	0.00117	0.00117	8.0 σ_p
3/16" Dogbone-Bending	-	0.187	0.250	0.125	0.000585	0.000291	10.7 σ_p
3" Disk with two 3/4" Holes	-	-	0.250		0.00078		1.6 σ_p
3" x 2" Ring	-	-	0.250		0.000544		5.5 σ_p
3" x 1-1/2" Ring	-	-	0.250		0.000416		5.9 σ_p
3" x 1" Ring	-	-	0.250		0.000233		7.1 σ_p
3" x 1/2" Ring	-	-	0.250		0.000080		12.5 σ_p
0.24" x 0.24" Bar-Parallel Bending	2.00	-	-		0.00288		8.3 σ_p
0.24" x 0.24" Bar-Diagonal Bending	2.00	-	-		0.000144		5.9 σ_p

* The plastic specimens were all cut from 1/4" sheet stock. The ceramic specimens were varied in thickness to obtain a greater variation in volume.

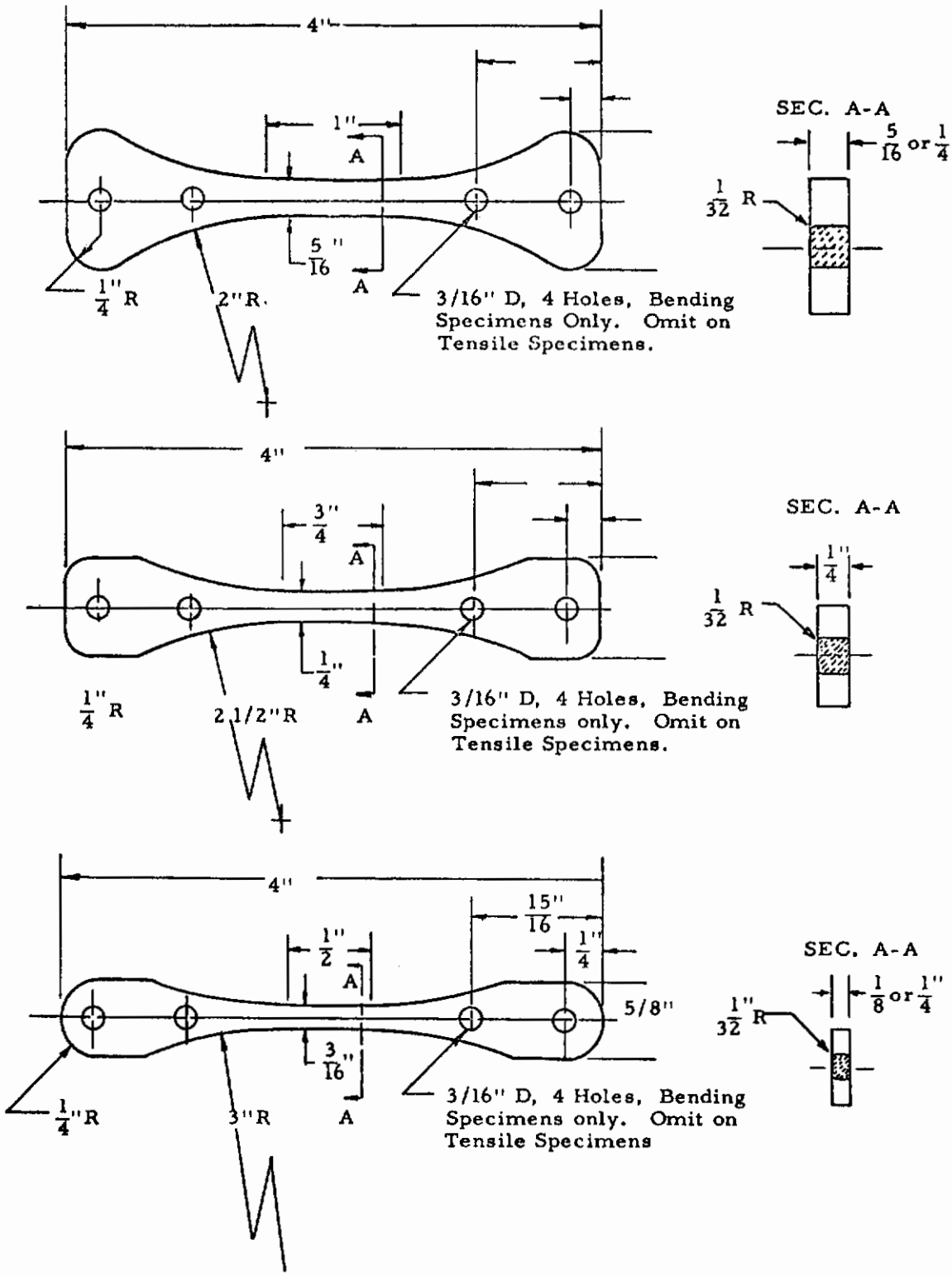

Fig. 3-2 DOGBONE USED IN TENSION BENDING TESTS

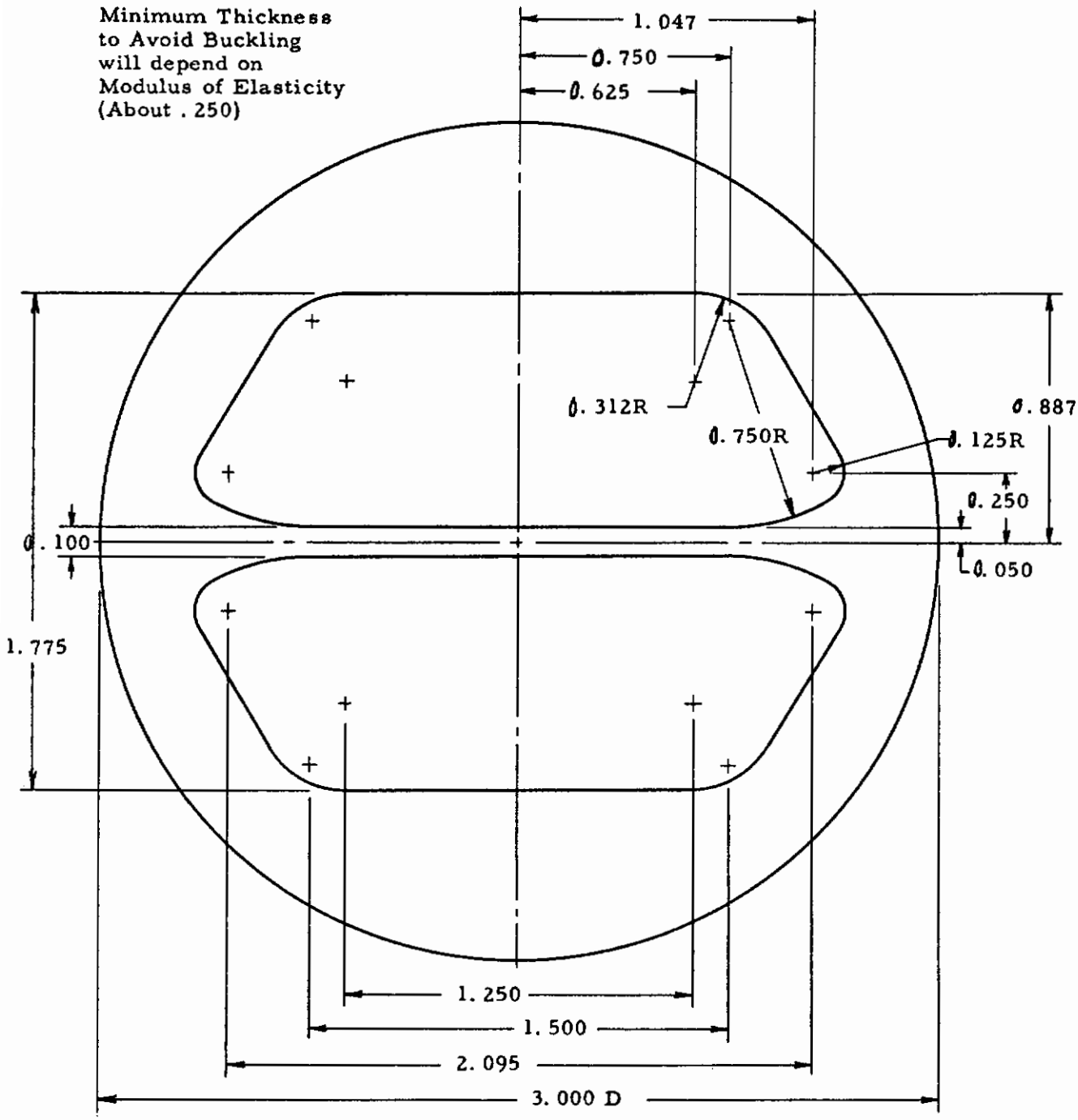

Fig. 3-3 THETA SPECIMEN GEOMETRY

(When a compressive load is applied perpendicularly to the bar direction, the bar will be subjected to uniform tension. Dimensions can be scaled linearly.)

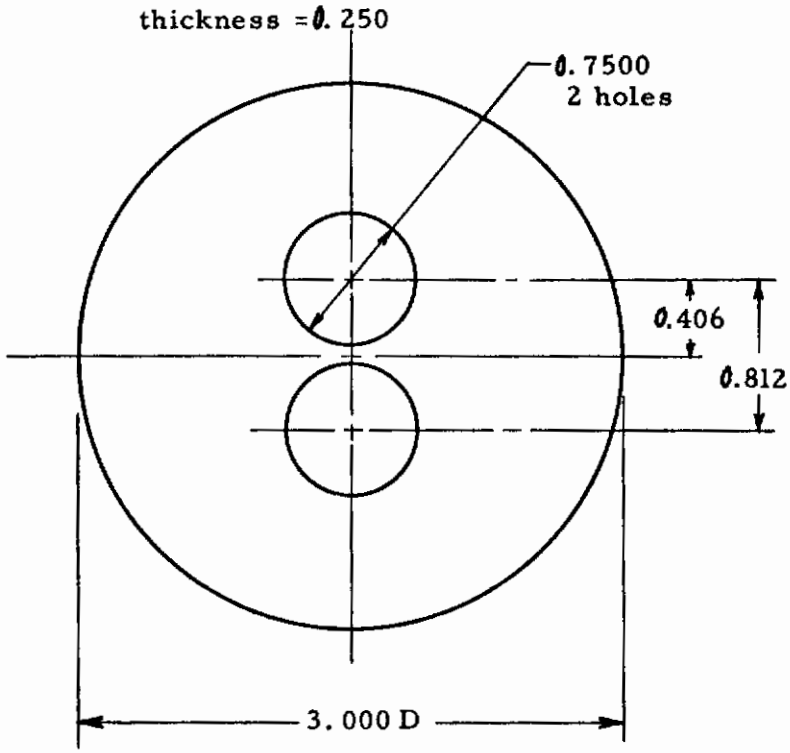

Fig. 3-4 DISK WITH TWO HOLES

(Under vertical diametral compression, failure will occur in the narrow strip between the holes.)

95 per cent of the maximum stress and the gradients in the rings and the two-hole disk are shown in Fig. 3-5.

5. THE THETA SPECIMEN

A. Need for a Special Design

The theta specimen design shown in Fig. 3-3 was developed with considerable effort and was added to the group of specimens for reasons that require explanation.

It is well known that one of the chief problems associated with the tensile testing of completely brittle materials is the difficulty of applying a truly axial load to obtain a uniform stress field in the test area. Many of the difficulties associated with this problem were treated in detail in the report presented for the work performed on Task 2 of this program.

Some of the reasons for this problem are illustrated and itemized in Fig. 3-6. The itemized factors are present regardless of the type of grips used on the specimen. From the simple column formula, it can be shown that the percent of increase in stress resulting from eccentricity is six times the ratio of the eccentricity to the diameter of a round rod and eight times the ratio of eccentricity to width for a square rod. Thus, eccentricity of a few thousands of an inch can produce an appreciable stress increase on one side of a tensile specimen and failures at lower loads than those corresponding to true axial loading. To circumvent all or most of these difficulties, various investigators have used disks, rings, briquettes and beams. All of these shapes have one thing in common: a non-uniform stress field.

While working with holes in disks to obtain non-uniform stress fields, the present investigators felt that a solution to this problem would be to develop a specimen shape that could be loaded vertically in simple compression and apply a truly axial uniform tensile stress to the central horizontal bar. Beside having a uniform tensile stress, the specimen would be simple to load, an important feature in high temperature testing. The dimensions of a specimen satisfying these requirements are shown in Fig. 3-3; because of its shape, it was called the theta specimen.

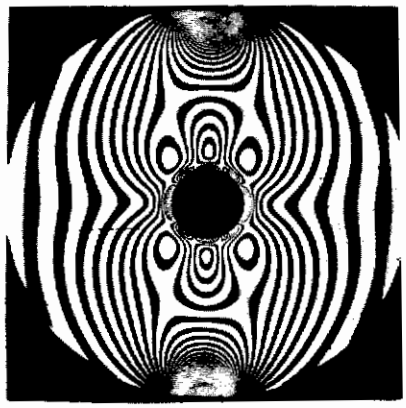

3" O.D. x 1/2" I.D. x 1/4" Thick

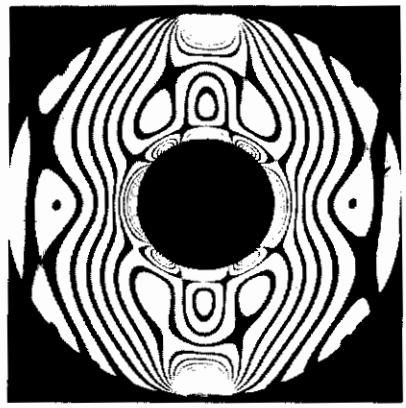

3" O.D. x 1" I.D. x 1/4" Thick

3" O.D. x 1-1/2" I.D. x 1/4" Thick

3" O.D. x 2" I.D. x 1/4" Thick

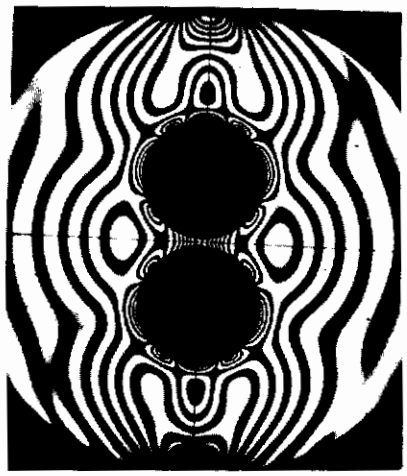

3" O.D. x 1/4" Thick with Two 3/4" Holes Separated by 1/16" Strip

Fig. 3-5 ISOCHROMATIC FRINGE PATTERNS OF FOUR RINGS AND TWO-HOLE DISK UNDER DIAMETRAL COMPRESSION

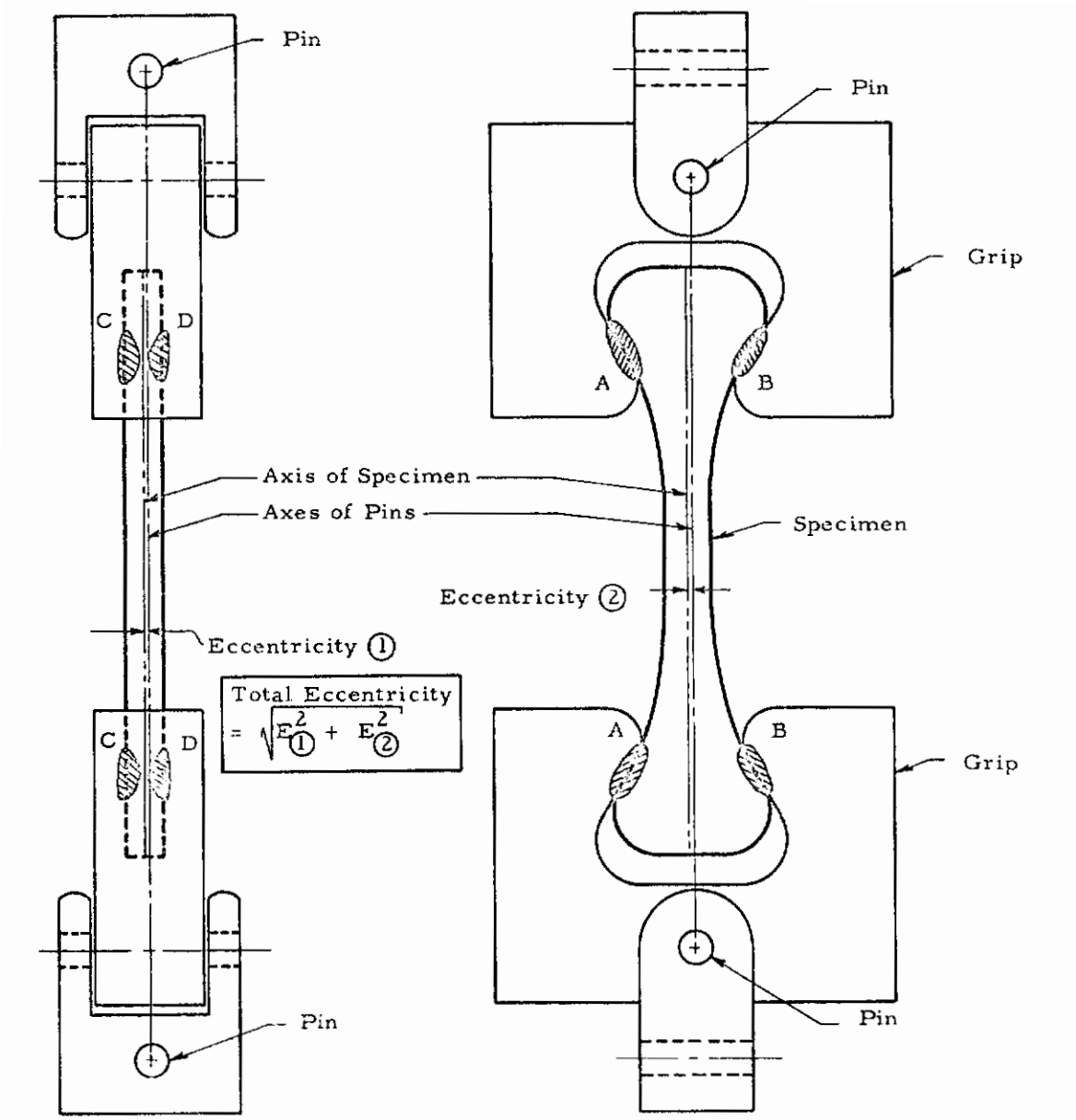

The eccentricity can be attributed to the following factors:

Unsymmetrical displacements in contact zones A and B } Least controllable and
Unsymmetrical displacements in contact zones C and D } probably most important
Unsymmetrical grip dimensions
Unsymmetrical specimen dimensions
Friction in the pin joints.

Fig. 3-6 UNIAXIAL TENSILE SPECIMEN AND GRIPS SHOWING ECCENTRIC LOADING FOR THE CASE WHERE THE SPECIMEN AXIS IS PARALLEL TO THE AXES OF THE PINS

B. Load-Stress Relationship

A photoelastic analysis was conducted to correlate the stress developed in the horizontal bar with the applied diametral load. Figure 3-7 shows isochromatic fringe patterns in the theta specimen under diametral loading. The patterns demonstrate clearly the desired features of the specimen, i.e., that the maximum tensile stress occurs in the bar, that the stress distribution in the bar is uniform and that the fillets at the ends of the bar do not produce an undesirable stress concentration. The symmetry of the pattern also shows that a simple alignment by eye is adequate. The stress in the bar determined from similar photoelastic patterns was found to bear the following relationship to load:

$$\sigma = K \frac{P}{Dt} = 16.4 \frac{P}{Dt} \tag{3-33}$$

where σ is the stress in the bar, P the applied load, D the diameter and t the thickness of the specimen.

Strains in the bar were measured and related to changes in vertical and horizontal diameters. The strain in the bar was measured by the moire method using grids of 1000 lines per inch. The moire pattern is shown in Fig. 3-8. The changes in horizontal and vertical diameters were measured by means of dial gages. The relationships

$$\epsilon = -0.585 \frac{\delta v}{D} = 1.293 \frac{\delta h}{D} \tag{3-34}$$

were established; where ϵ is the strain in the bar, δ_v and δ_h are the increments in the vertical and horizontal diameter, and D is the diameter of the model.

Thus, from load and deflection measurements one can determine stress and strain and hence the modulus of elasticity of the material. If the modulus of elasticity is known for the material and test conditions (e.g., loading rate, temperature, atmosphere) a single measurement of load or deflection will suffice for the determination of stress and strain in the bar.

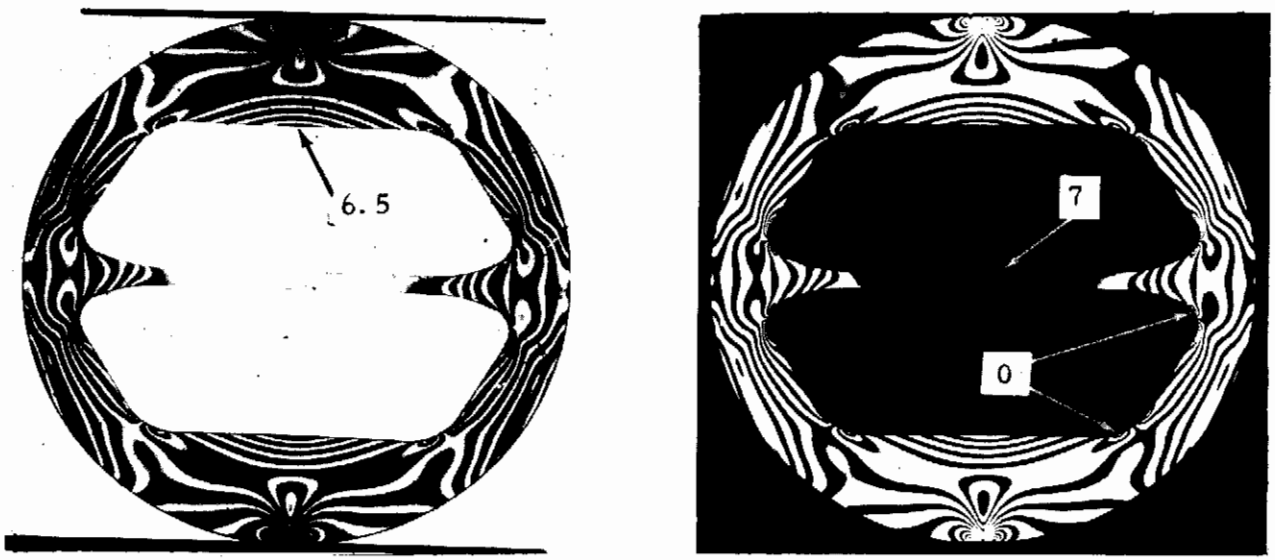

LIGHT FIELD

DARK FIELD

Fig. 3-7 PHOTOELASTIC PATTERNS OF THE THETA SPECIMEN UNDER DIAMETRAL COMPRESSIVE LOAD

(The numbers indicate fringe orders which, in general are proportional to the maximum shear stress, and on the boundaries and in the bar are proportional to the principal stress.)

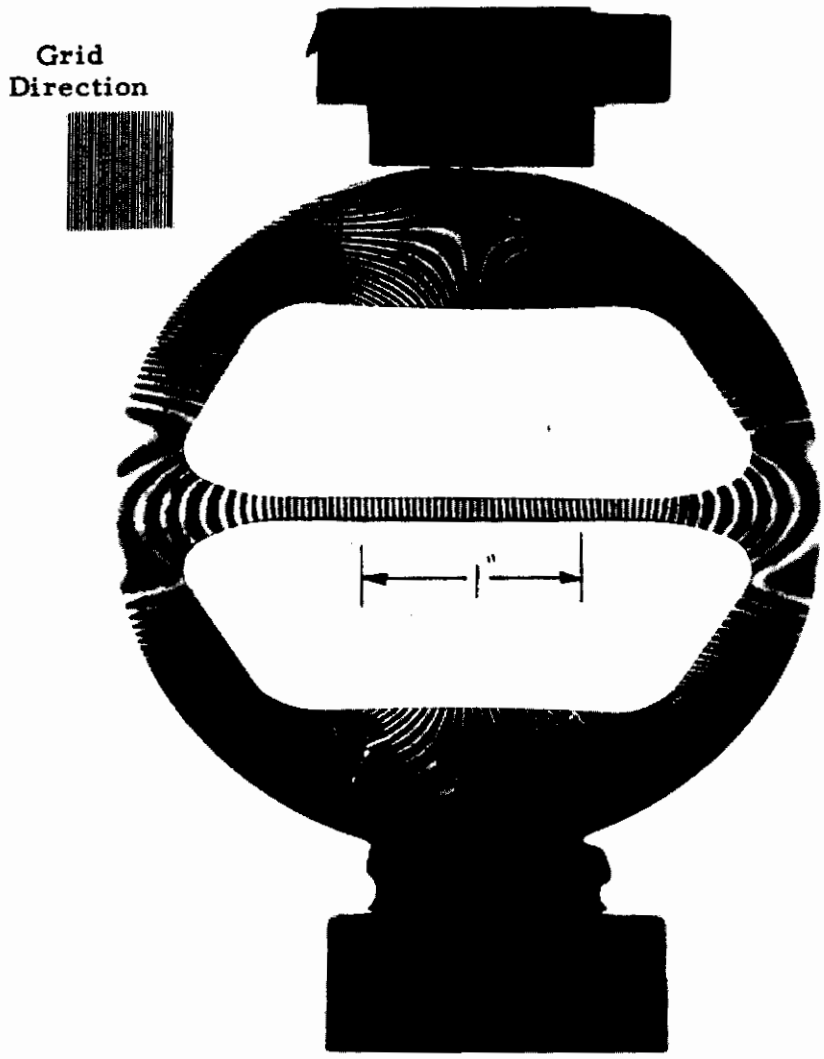

Fig. 3-8 MOIRE FRINGE PATTERN ON THETA SPECIMEN UNDER DIAMETRAL COMPRESSIVE LOAD

(The fringes represent lines of constant horizontal displacement. The incremental displacement between fringes is 0.001 in. The Strain in the bar in tenths of 1 percent is given by the number in 1 in.

Equations 3-33 and 3-34 will continue to hold for specimens of different sizes, provided their dimensions remain proportional to those shown in Fig. 3-3. (The thickness, t, can vary independently of all other dimensions.) There is a possibility, however, that the dimensional relationships of Fig. 3-3 cannot be strictly maintained. It is believed that the most important parameter affecting the load stress relationship is the ratio of bar width to specimen diameter (w/D). To measure this effect, a theta specimen with a wider-than-normal bar was made of CR-39. Load-fringe order relationships were determined in the original specimen and, also, after successive reductions, in bar width. The results are presented in Fig. 3-9 as a variation in stress ratio $K = \frac{\sigma}{P/Dt}$ using the dimensionless value of 30w/D as the abscissa. As the figure shows, the resulting relationship is almost linear. Geometric changes resulting from excessive deformations can also affect the load-stress relationship.

For the normal theta design of Fig. 3-3, the primary failure occurs in the bar. The photoelastic pattern of Fig. 3-6 is sufficient evidence of this fact and most CR-39 specimens tested failed with a single break in the bar. In some cases, however, the specimen shatters into many fragments at fracture, because of the sudden release of the elastic energy stored in the model. To obtain conclusive evidence of the sequence of failures, microflash photographs of Plexiglas specimens during fracture were obtained. Figure 3-10(a) shows completion of primary failure in the bar and incipient initiation of secondary fractures elsewhere in the specimen. Figure 3-10(b) shows another specimen after all primary secondary and tertiary failures have occurred. These photographs were taken with a microflash light source triggered by the disruption of a strip of conductive paint seen on the model. It should be remarked that the sequence of failures might change if the ratio of w/D is increased beyond a certain limit.

6. EXPERIMENTAL RESULTS

To study the effect of stress distribution alone on failure, all other factors (temperature, humidity, loading rate, batch of material) were maintained constant in the experiments. All specimens were tested in hard screw-type universal testing machines under constant deflection rate. As mentioned at the outset the present investigation was conducted on three preliminary model materials: CR-39 (Columbia Resin), Plexiglas and graphite.

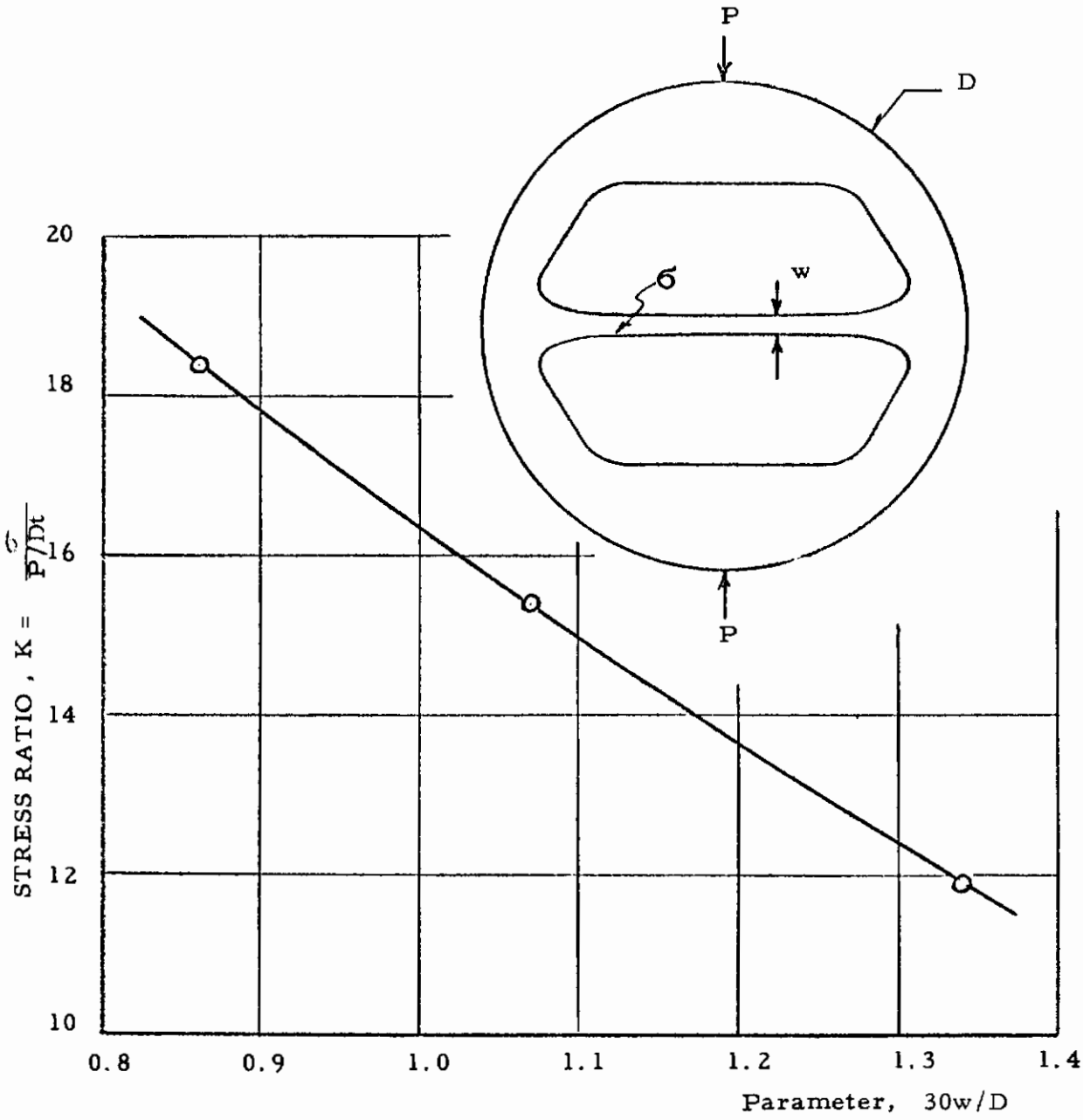

Fig. 3-9 STRESS-LOAD RELATION FOR GEOMETRIC VARIATIONS IN THE THETA SPECIMEN

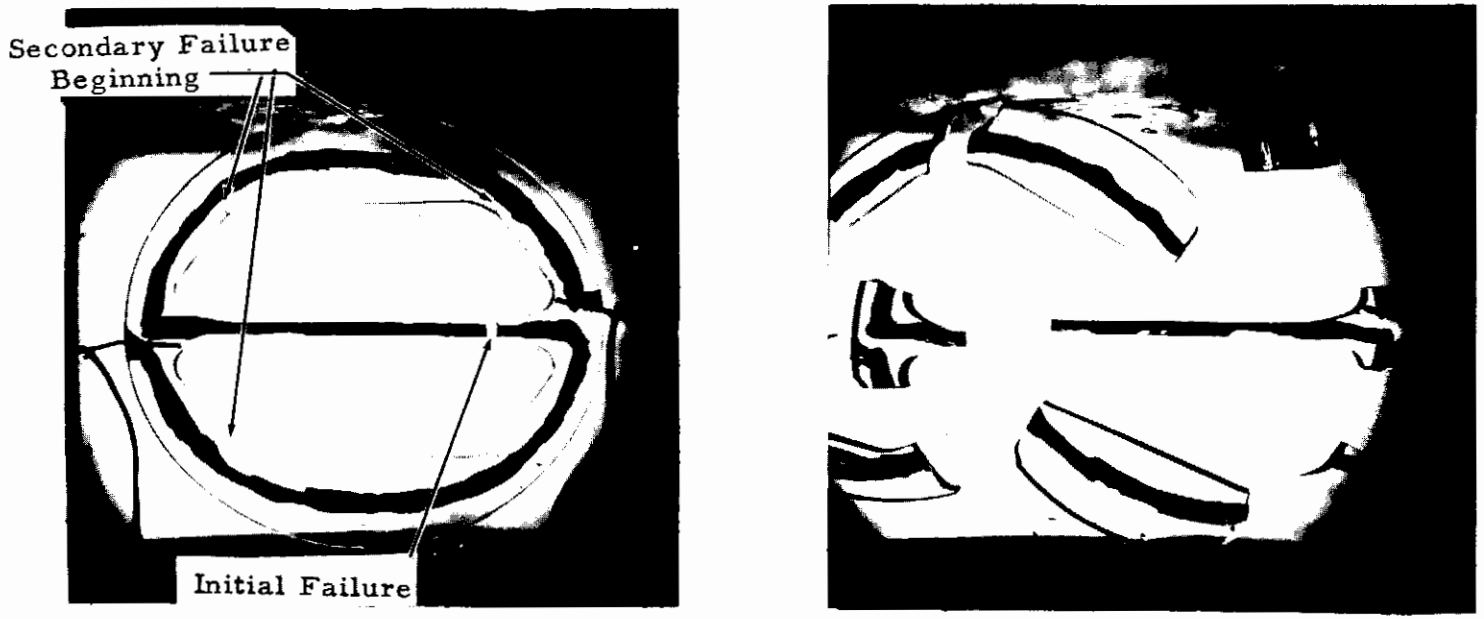

SHORTLY AFTER INITIAL FAILURE

AFTER ALL FAILURES

Fig. 3-10 TWO PLEXIGLAS THETA SPECIMENS AT DIFFERENT STAGES OF FAILURE DUE TO DIAMETRAL COMPRESSIVE LOAD

A. Columbia Resin (CR-39)

Reduced test results for thirteen types of specimen are presented in Table 3-II. Two additional types of specimen were added here. They were bars of square cross section (0.24 in. x 0.24 in.) loaded in pure bending with a gage length of 2 in. In one case, the beams were loaded so that the neutral axis was parallel to the top and bottom sides of the cross section, in the second case the beams were loaded so that the neutral axis would coincide with one diagonal of the cross section. In this manner, two greatly different volumes under high stress are obtained.

The mean failure stress was plotted against stress gradient in Fig. 3-11, and against the volume subjected to a tensile stress greater than 95 per cent of the peak stress in Fig. 3-12. It can be seen that stress gradient alone is not sufficient to explain the difference in failure stress from specimen to specimen. On the other hand, the effective size seems to be a dominant factor affecting failure stress. The points tend to fall on a shallow S-curve approaching asymptotically an upper and a lower limit for the stress. In the range of parameters considered, this curve could be approximated by a straight line. An approximate empirical equation of the following form can be derived for the limited range of sizes tested.

$$\sigma = A\, V_{95}^{-1/\alpha} \quad , \tag{3-35}$$

where V_{95} is the effective size as defined. From Fig. 3-12, it is found that $\alpha = 10.4$ and $A = 5,000$ and thus the empirical equation becomes

$$\sigma \cong 5,000\, V_{95}^{-1/10.4} \quad . \tag{3-36}$$

Experimental work with dogbone specimens subjected to pure bending and tension gave the following ratios for the mean fracture stresses:

$$\frac{(\sigma_m)_b}{(\sigma_m)_t} = 1.27 \text{ (5/16 in. dogbone specimens)}$$

$$= 1.26 \text{ (1/4 in. dogbone specimens)}$$

$$= 1.50 \text{ (3/16 in. dogbone specimens)}$$

Table 3-II

TEST RESULTS ON EFFECT OF NON-UNIFORM STRESS FIELDS FOR CR-39

Specimen Type	Number of Specimens	Stress-Load Relation	Stress, psi			
			Mean	Stand. Dev.	High	Low
5/16 in. Dogbone, Tension	9	σ = P/A	6,660	± 444	7,130	5680
1/4 in. Dogbone, Tension	10	= P/A	6,700	± 424	7,200	6160
3/16 in. Dogbone, Tension	10	= P/A	6,570	± 985	7,210	3860
Theta	15	= $K(\frac{P}{Dt})$	6,920	± 350	7,400	6280
5/16 in. Dogbone, Bending	9	= M/Z	8,480	±1376	9,740	5500
1/4 in. Dogbone, Bending	10	= M/Z	8,410	±1898	11,360	5670
3/16 in. Dogbone, Bending	9	= M/Z	9,860	±2126	13,220	6350
3 in. Disk with 2 holes	10	= $0.225\ (\frac{P}{wt})$	9,300	±1004	10,530	7310
3 in. x 2 in. Ring	12	= 10.52 P/(OD-ID)t	9,860	±1570	13,090	7740
3 in. x 1-1/2 in. Ring	13	= 6.45 P/(OD-ID)t	11,050	±2070	13,930	7010
3 in. x 1 in. Ring	7	= 4.67 P/(OD-ID)t	11,300	±1248	12,830	9560
0.240 in. x 0.240 in. Bar, Parallel Bending	33	= M/Z	8,190		9,550	5530
0.240 in. x 0.24 in. Bar, Diagonal Bending	16	= M/Z	12,210		16,350	7460

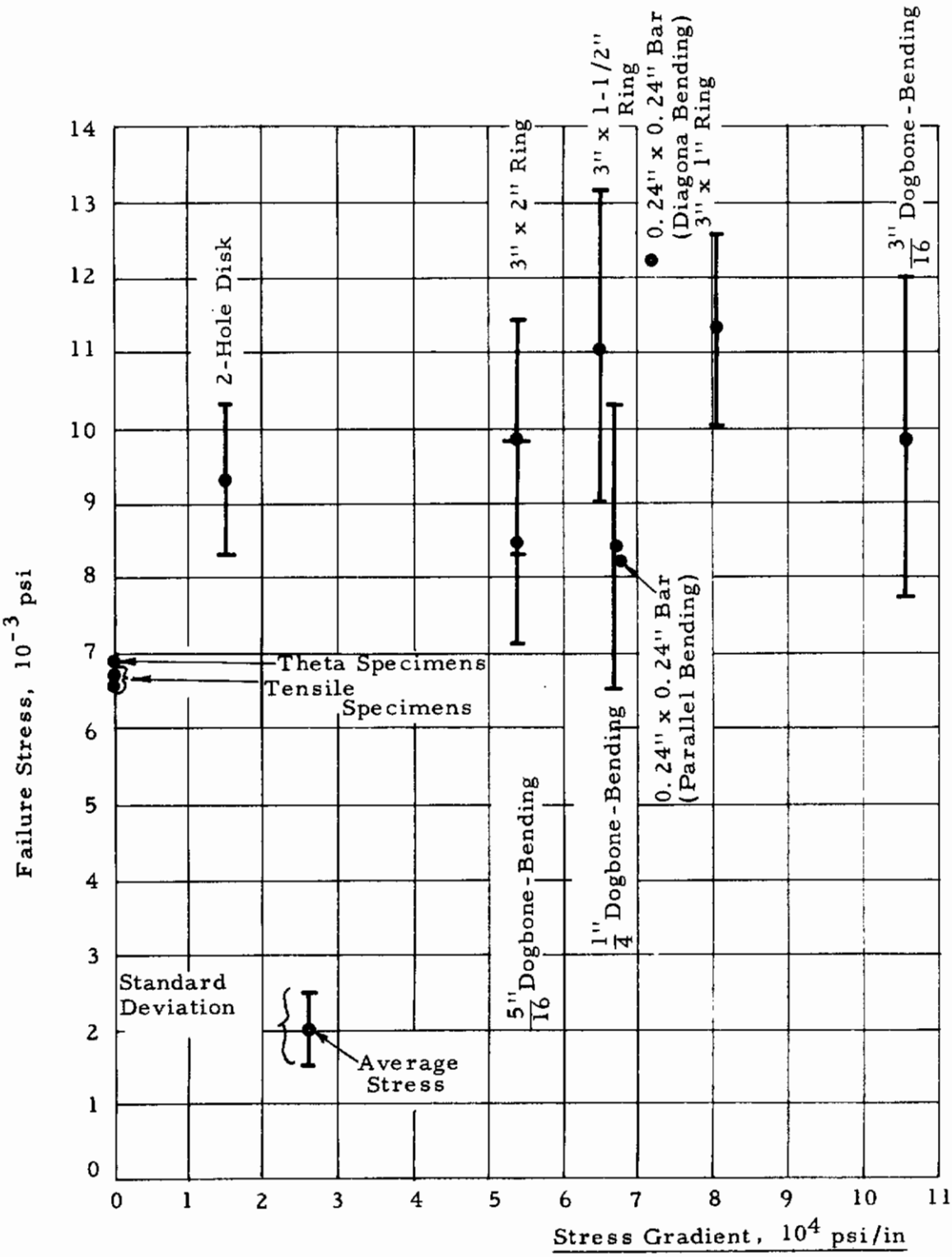

Fig. 3-11 FAILURE STRESS VS. MAXIMUM STRESS GRADIENT FOR VARIOUS CR-39 SPECIMENS

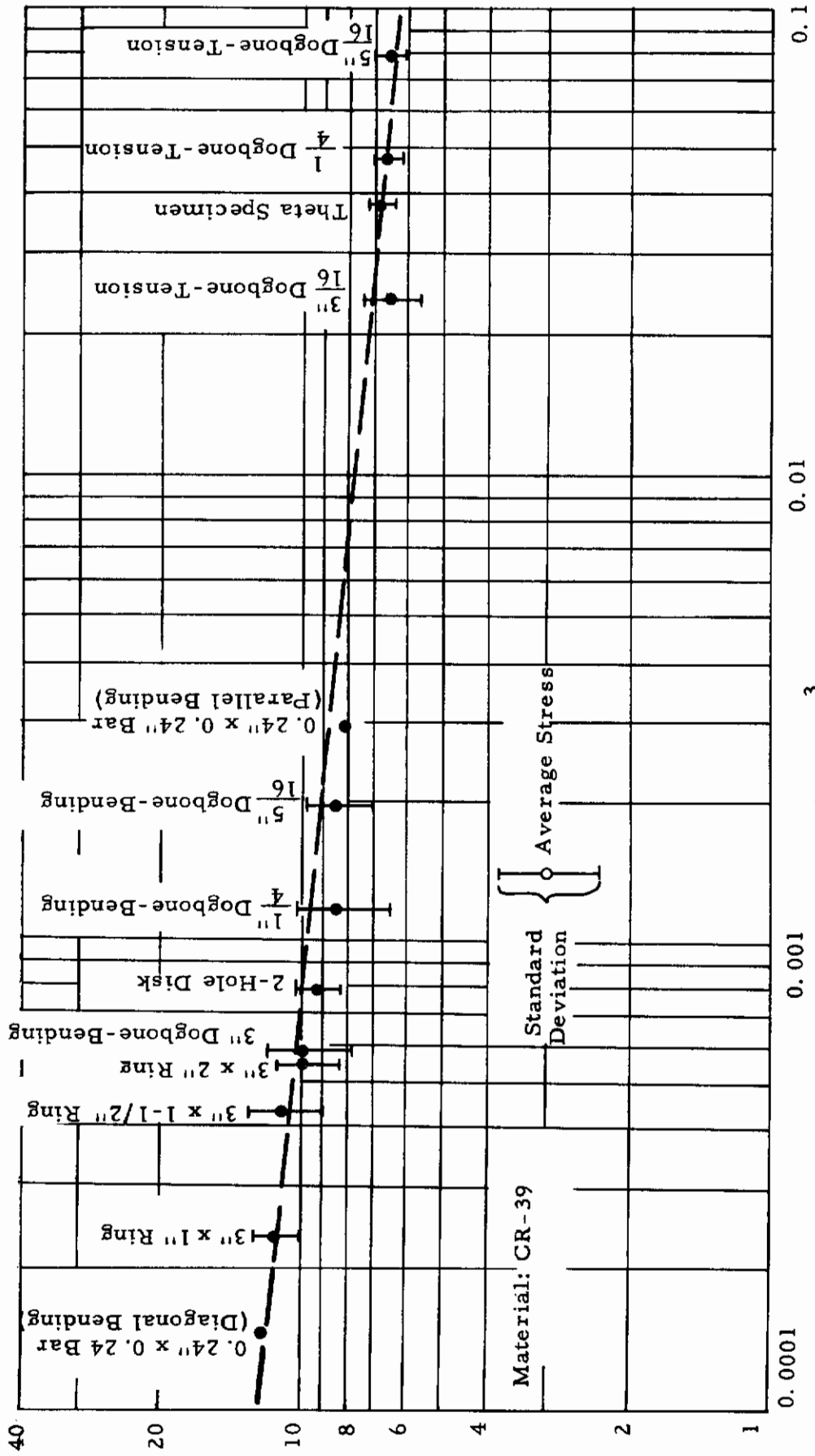

Fig. 3-12 FAILURE STRESS VS. VOLUME SUBJECTED TO MORE THAN 95% OF MAXIMUM TENSILE STRESS FOR CR-39

The average of these values is 1.34 and, from the predictions of the Weibull theory for the ratio of mean fracture stresses in pure bending and tension, as given by Eq. 3-27,

$$(2m + 2)^{1/m} = 1.34 \quad ,$$

from which

$$m = 10.8 \quad .$$

The agreement of this value with that of α is remarkable, although this may be, in part, coincidental.

Statistical analysis of experimental results of the theta specimen and the bars of square cross section indicated that surface flaws may influence failure appreciably. The fact that the "95 per cent volume" gives a good correlation with failure stress may also indicate that failure starts at the surface in most cases of non-uniform stress distribution and hence a surface layer qualifies as effective size of the specimen.

B. Plexiglas

Reduced test results for ten types of specimens are compiled in Table 3-III. The mean failure stress was plotted against the stress gradient in Fig. 3-13, and against the volume subjected to a tensile stress greater than 95 per cent of the peak stress in Fig. 3-14.

In this case, the correlation with stress gradient seems more meaningful than in the case of CR-39. As in the case of CR-39 the failure stress of rings is higher than that of beams having the same stress gradient. Also, the standard deviation tends to increase with increasing gradient (with the exception of the two-hole disk). It appears that the correlation would be more meaningful if specimens of one type only (rings or beams) were compared.

The scatter in Fig. 3-14 is fairly large. Again it would seem that an S-shape curve would best represent the results obtained, but a straight line was used for ease of comparison. The following approximate empirical formula for the limited range of sizes considered was derived from the figure.

Table 3-III

TEST RESULTS ON EFFECT OF NON-UNIFORM STRESS FIELDS FOR PLEXIGLAS

Specimen Type	Number of Specimens	Stress-Load Relation	Stress, psi			
			Mean	Stand. Dev.	High	Low
5/16 in. Dogbone, Tension	10	σ = P/A	7,840	± 890	9,400	6,540
1/4 in. Dogbone, Tension	10	= P/A	8,870	±1000	11,020	7,480
3/16 in. Dogbone, Tension	10	= P/A	7,800	±1430	10,130	6,030
Theta	15	= $K(\frac{P}{Dt})$	9,600	±1480	12,500	7,500
5/16 in. Dogbone, Bending	9	= M/Z	20,510	±1040	25,490	15,050
1/4 in. Dogbone, Bending	10	= M/Z	22,460	±5170	27,620	16,160
3/16 in. Dogbone, Bending	8	= M/Z	30,190	±8540	44,260	23,180
3 in. Disk with 2 holes	10	= $0.225(\frac{P}{wt})$	12,280	±3640	18,800	8,650
3 in. x 2 in. Ring	10	= 10.52 P/(OD-ID)t	23,620	±1530	25,610	20,870
3 in. x 1-1/2 in. Ring	10	= 6.45 P/(OD-ID)t	24,340	±1640	27,140	20,800

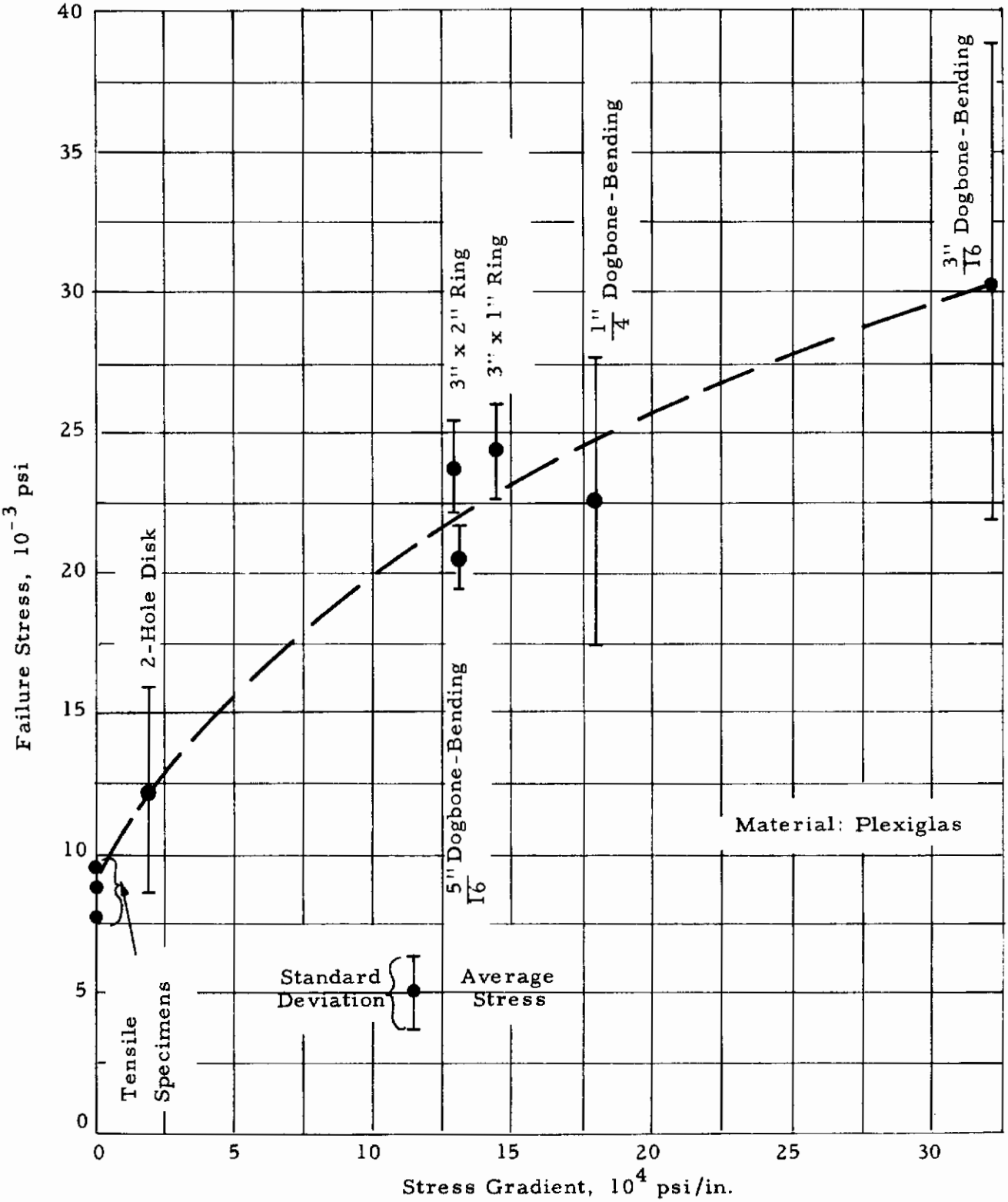

Fig. 3-13 FAILURE STRESS VS. MAXIMUM STRESS GRADIENT FOR VARIOUS PLEXIGLAS SPECIMENS

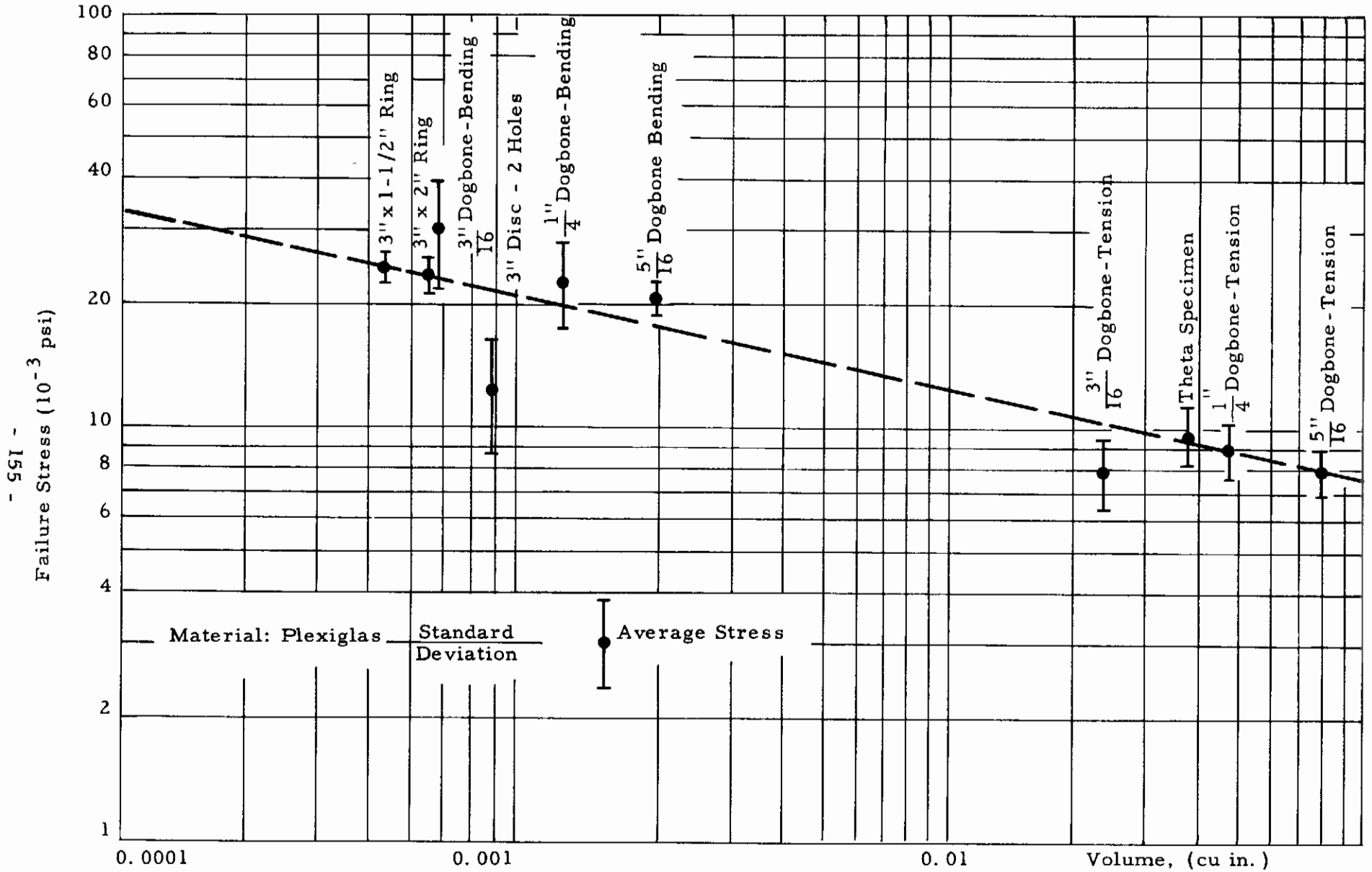

Fig. 3-14 FAILURE STRESS VS. VOLUME SUBJECTED TO MORE THAN 95 PERCENT OF MAXIMUM TENSILE STRESS FOR PLEXIGLAS

$$\sigma = A V_{95}^{-1/\alpha} = 4600 V_{95}^{-1/4.7} \qquad (3\text{-}37)$$

Tension and bending tests for the three dogbone specimens yielded the following ratios of failure stresses.

$$\frac{(\sigma_m)_b}{(\sigma_m)_t} = 2.62 \text{ (5/16 in. dogbone specimens)}$$

$$= 2.53 \text{ (1/4 in. dogbone specimens)}$$

$$= 3.86 \text{ (3/16 in. dogbone specimens)}$$

Ignoring the third value on account of its substantial deviation, the average of the first two series provides

$$(2m + 2)^{1/m} = 2.58$$

where,

$$m = 1.84 \ .$$

The large scatter obtained in the Plexiglas tests may be due in part to effect of suspected anisotropy.

C. Graphite

Reduced test results for six types of specimen are assembled in Table 3-IV. The mean failure stress was plotted against the stress gradient in Fig. 3-15. The correlation between the two quantities (stress and stress gradient) seems to be good mainly because most of the specimens used were of one type (ring) where gradient varies monotonically with effective size. A good correlation was also obtained between failure stress and volume subjected to more than 95 per cent of the peak tensile stress as shown in Fig. 3-16. The straight line approximation yields the empirical formula

$$\sigma = A V_{95}^{-1/\alpha} = 1300 V_{95}^{-1/7.9} \qquad (3\text{-}38)$$

for the limited range of sizes tested.

Table 3-IV

TEST RESULTS ON EFFECT OF NON-UNIFORM STRESS FIELDS FOR GRAPHITE

Specimen Type	Number of Specimens	Stress-Load Relation	Stress, psi			
			Mean	Stand. Dev.	High	Low
Theta	26	$\sigma = K \left(\frac{P}{Dt}\right)$	2030	± 550	2830	1000
3" Disk with 2 holes	10	$= 0.225 \left(\frac{P}{wt}\right)$	2740	±1300	4720	1190
3" x 2" Ring	10	$= 10.52\ P/(OD-ID)t$	3390	± 620	4170	2070
3" x 1 1/2" Ring	10	$= 6.45\ P/(OD-ID)t$	3400	± 440	4040	3140
3" x 1" Ring	10	$= 4.67\ P/(OD-ID)t$	3780	± 330	4210	3340
3" x 1/2" Ring	10	$= 3.93\ P/(OD-ID)t$	4400	± 380	5010	3870

The results of the theta specimen were analyzed statistically. The distribution curve for this series is shown in Fig. 3-17. The frequency or probability density curve shown in Fig. 3-18 was obtained by differentiating the distribution curve graphically. It is seen from this curve that the mode of the distribution is $\sigma_{mode} = 2100$ psi. The skewness of the distribution is typical of brittle materials. If the material is described by a single Weibull-type function, the parameters m, σ_u and σ_o can be found from Eq. 3-17, 3-18 and 3-19.

Following the graphical method of determination of the material function, log log $1/1 - S$ was plotted versus $\log \sigma$ in Fig. 3-19. The curve is concave upwards, which means that no single value of σ_u exists which would transform this curve into a straight line. This is also an indication of anisotropy (as Weibull defines it), i.e., that the probability of fracture under the same conditions of stress varies in different parts of the specimen.

A simple type of anisotropy is the so-called discontinuous anisotropy, in which the solid is assumed to be composed of two parts, V_1 and V_2, with two distribution function, S_1 and S_2 respectively, whose corresponding material functions are given by

$$\left(\frac{\sigma - \sigma_{u1}}{\sigma_{o1}}\right) \quad \text{and} \quad \left(\frac{\sigma - \sigma_{u2}}{\sigma_{o2}}\right)^{m_2} .$$

Then, if S_{12} is the combined distribution function

$$1 - S_{12} = (1-S_1)(1-S_2) , \tag{3-39}$$

yield,

$$y_{12} - y_1 = \log \left[1 + 10^{-(y_1 - y_2)}\right] \tag{3-40}$$

where

$$\left.\begin{aligned} y_1 &= \log\log \frac{1}{1-S_1} \\ y_2 &= \log\log \frac{1}{1-S_2} \\ y_{12} &= \log\log \frac{1}{1-S_{12}} \end{aligned}\right\} \tag{3-41}$$

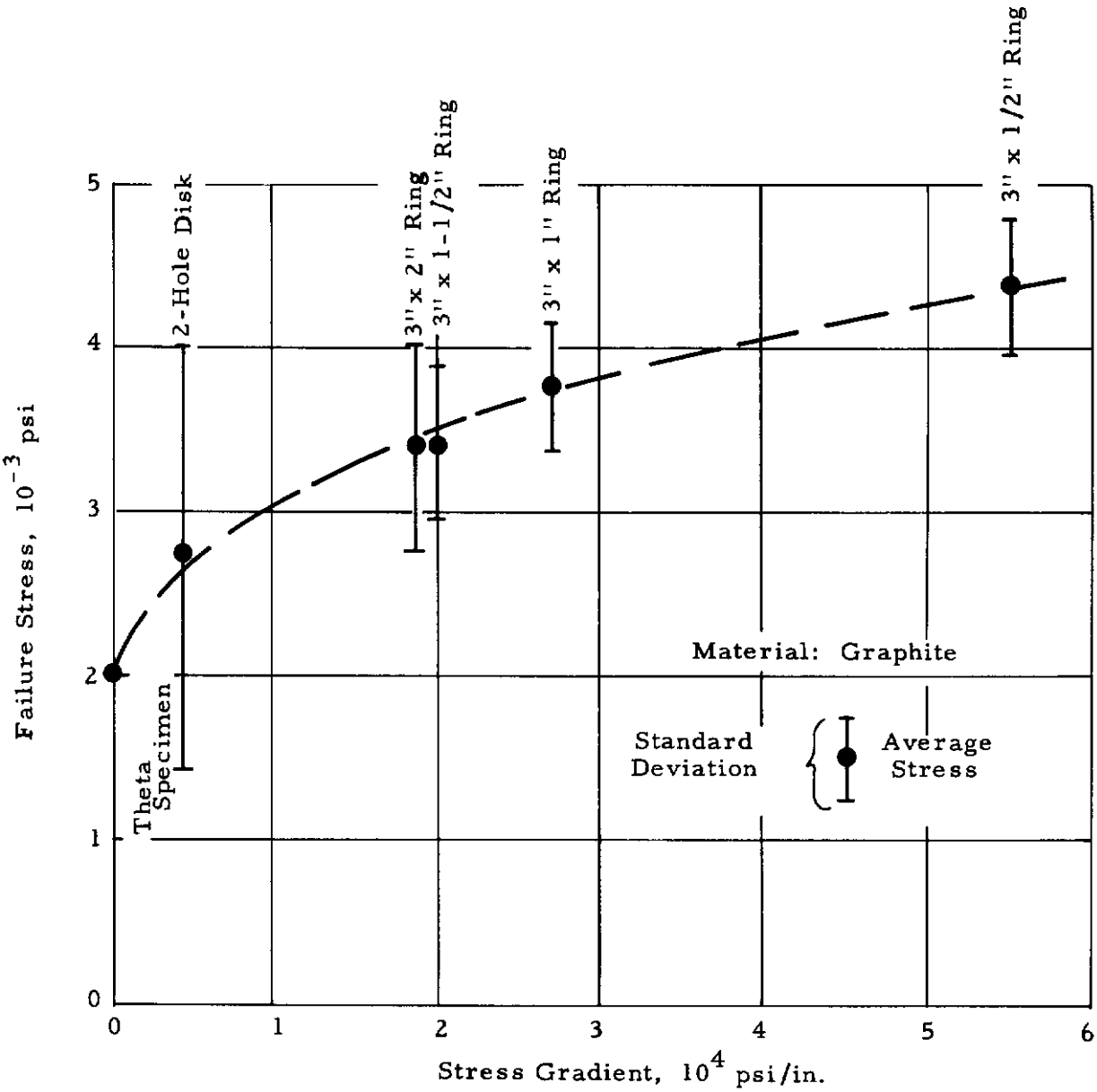

Fig. 3-15 FAILURE STRESS VS. MAXIMUM STRESS GRADIENT FOR VARIOUS GRAPHITE SPECIMENS

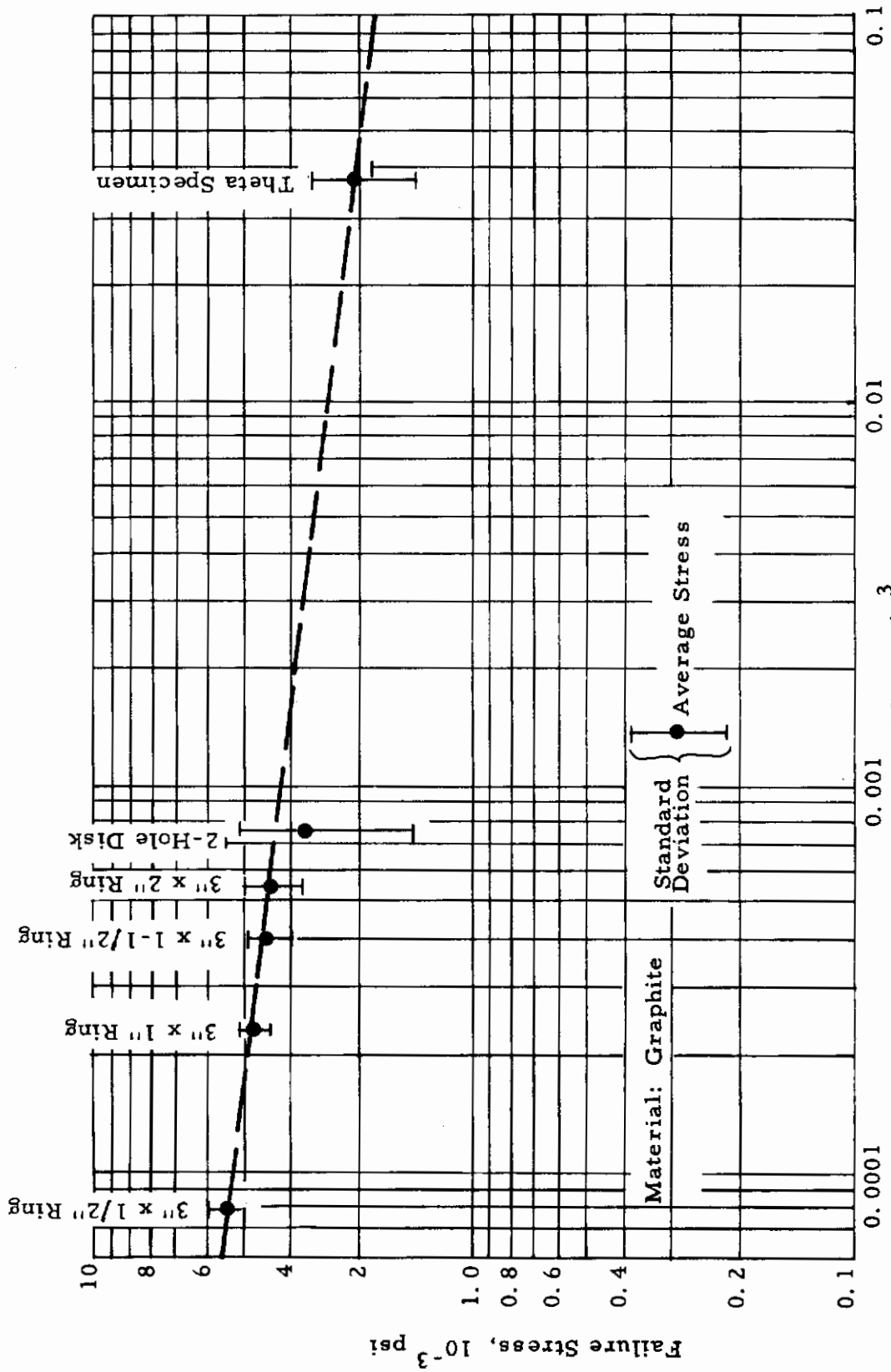

Fig. 3-16 FAILURE STRESS VS. VOLUME SUBJECTED TO MORE THAN 95% OF MAXIMUM TENSILE STRESS FOR GRAPHITE

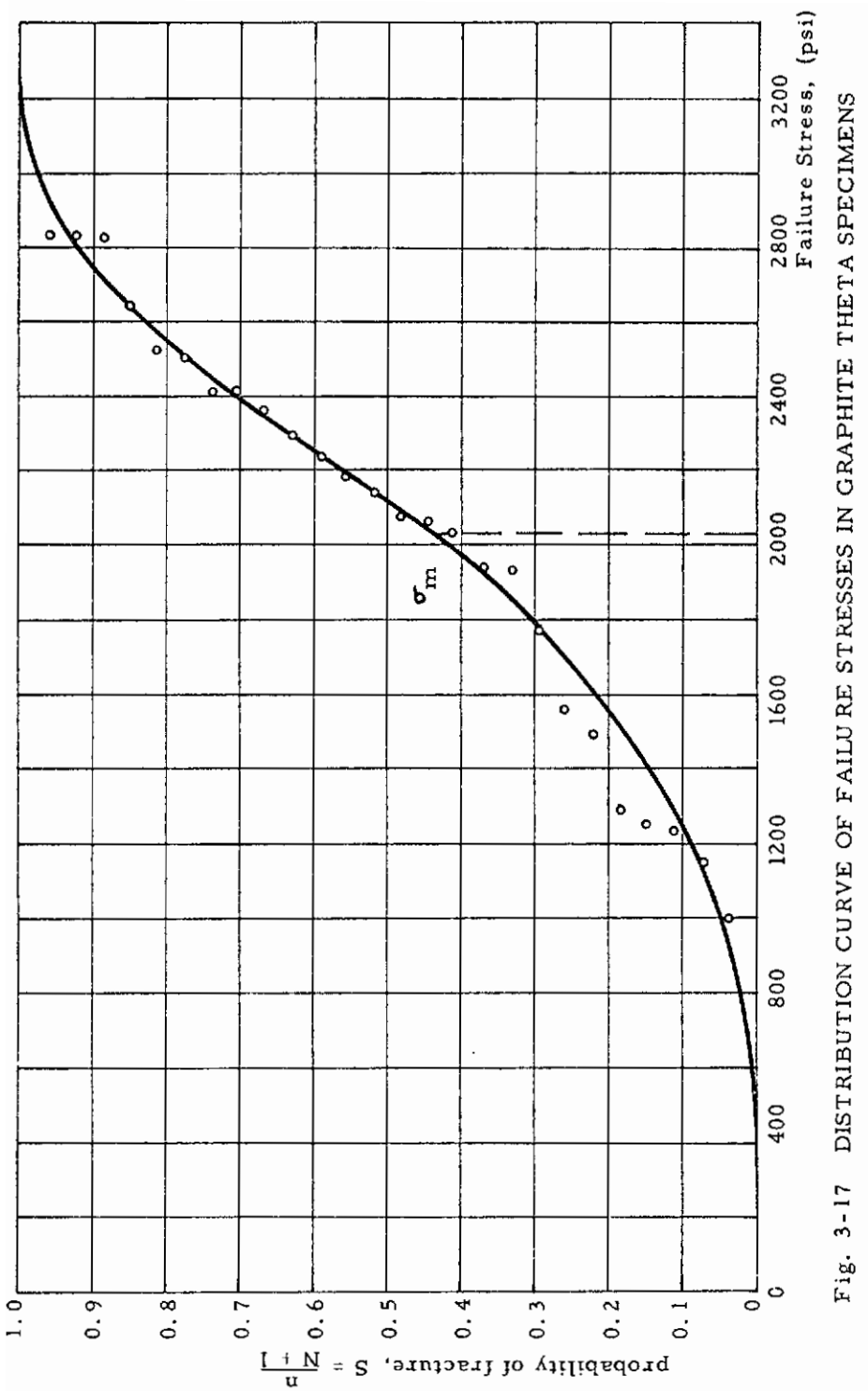

Fig. 3-17 DISTRIBUTION CURVE OF FAILURE STRESSES IN GRAPHITE THETA SPECIMENS

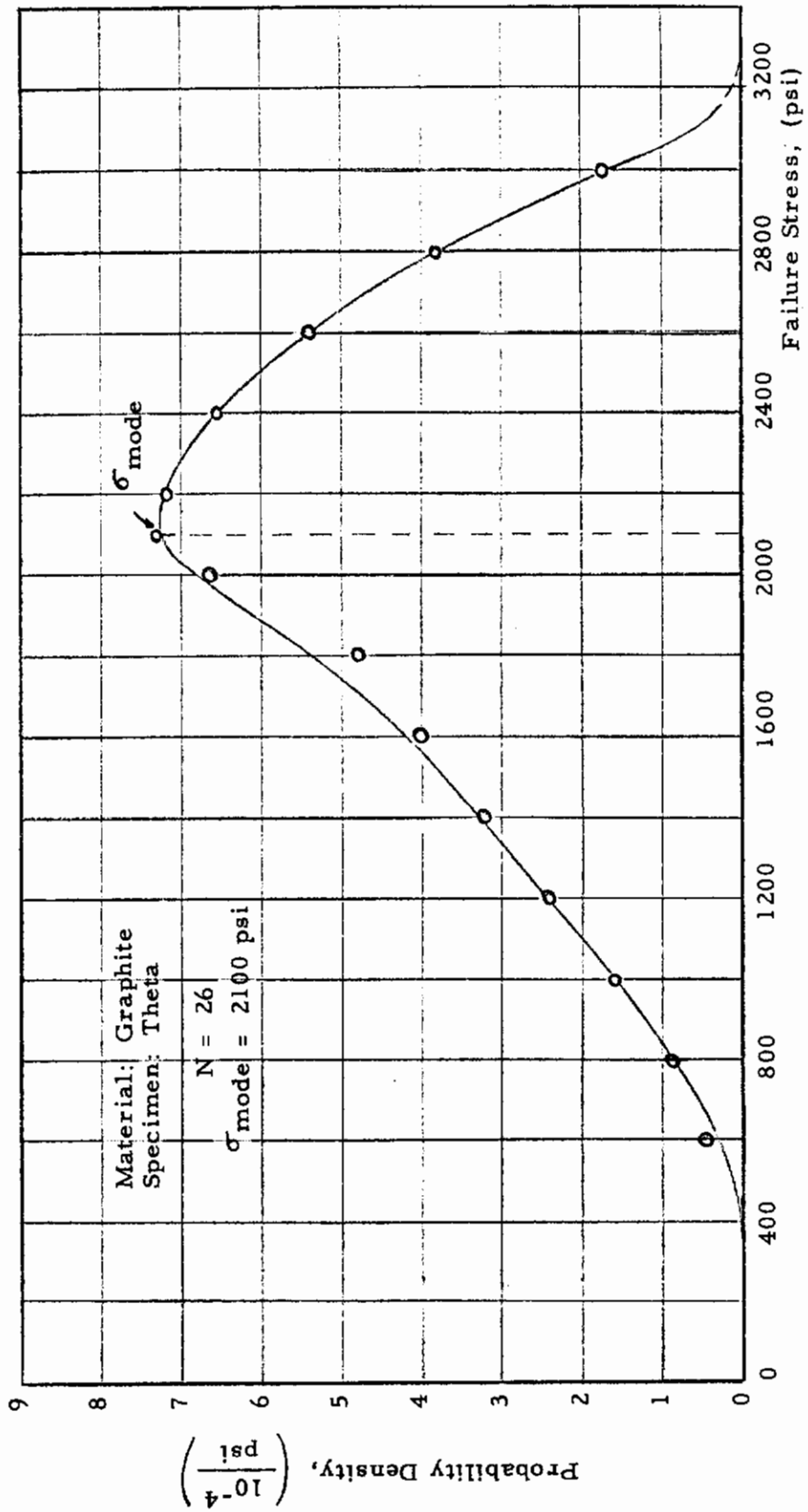

Fig. 3-18 PROBABILITY DENSITY CURVE OF FAILURE STRESSES IN GRAPHITE THETA SPECIMENS

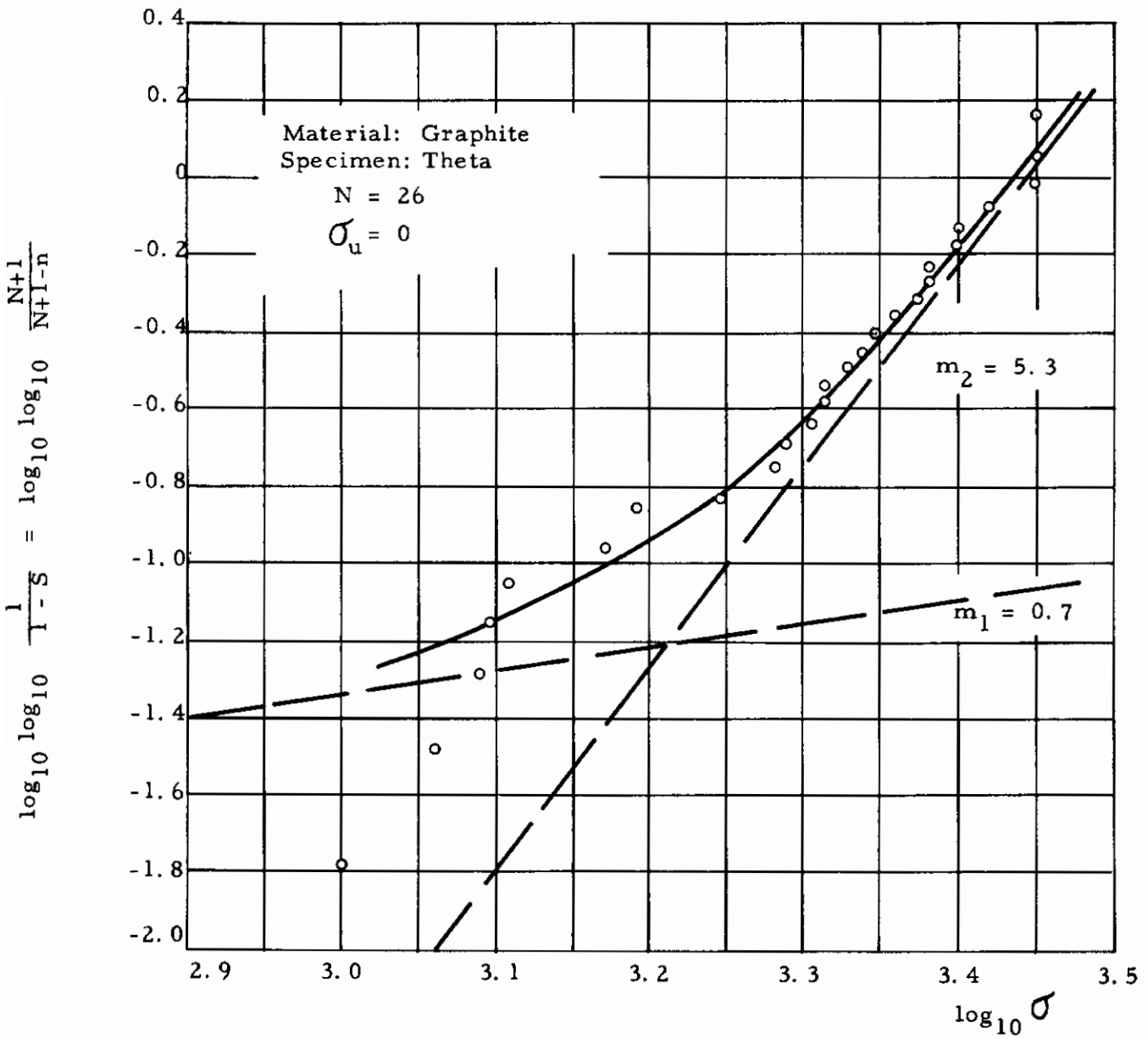

Fig. 3-19 GRAPHICAL DETERMINATION OF MATERIAL FUNCTION FOR GRAPHITE

Figure 3-20 shows a plot of $y_{12} - y_1$ versus $y_1 - y_2$.

In the system of coordinates of Fig. 3-19, y_1 and y_2 would appear as straight lines and y_{12} as a curve lying above these lines and approaching them asymptotically. In practice, y_{12} is obtained as the curve through the points and the asymptotes are found by trial and error from Eq. 3-40 as the two straight lines yielding a curve affording the best fit to y_{12}. In the present case, although the data do not appear satisfactory, two such lines were drawn in Fig. 3-19. The slopes of these lines are $m_1 = 0.7$ and $m_2 = 5.3$ which represent the exponents of the two material functions, provided that $\sigma_{u1} = \sigma_{u2} = o$. The first function is believed to apply to the surface layer of the specimen, the second to the interior. To determine the slopes of the asymptotes with confidence two or three sizes of specimens should be used.

D. Wesgo AL995

Figure 3-21 shows the variation of failure stress versus volume subjected to at least 95 per cent of the peak tensile stress. Using the straight line approximation,

$$\sigma \cong A V_{95}^{-1/\alpha} = 15,000 V_{95}^{-1/8} \qquad (3\text{-}42)$$

for the range of sizes considered here. Results on the Weibull constants are given in the Task 1 report.

7. CONCLUSIONS

Within the framework of the statistical theories of fracture proved eminently applicable to dealing with the strength criterion of brittle materials, full recognition is given such factors as the geometrical shape and volume of the body and the stress distribution existing in it. Further variables, naturally, are those which depend upon the material itself. These are, as commonly accepted, the flaw density constant and zero strength of the material, both of which are subject to variations with environmental conditions such as temperature. Recently an additional constant, the maximum fracture strength, has been suggested for inclusion into statistical failure theories.

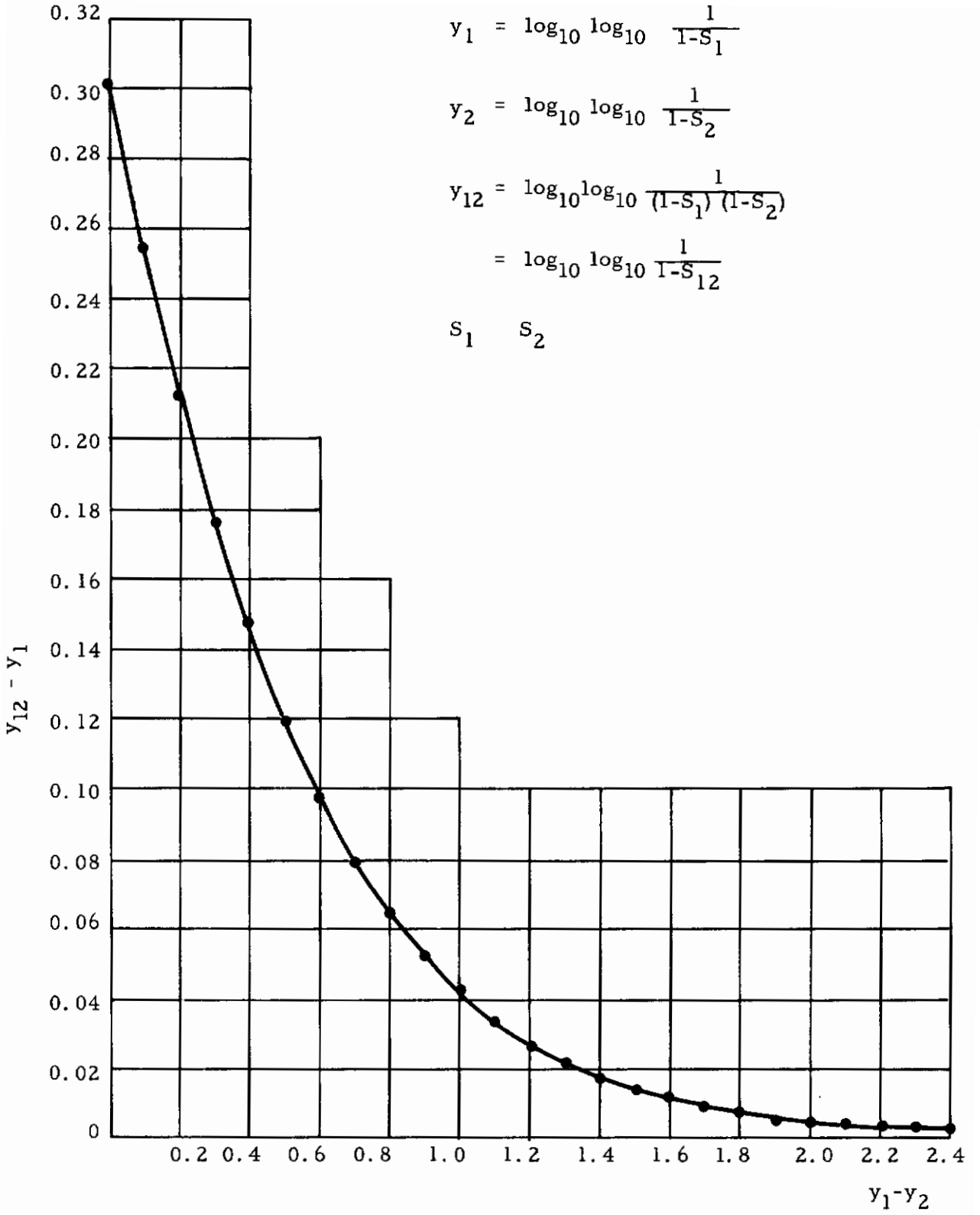

Fig. 3-20 DETERMINATION OF COMBINED DISTRIBUTION FUNCTION FROM TWO COMPONENT FUNCTIONS

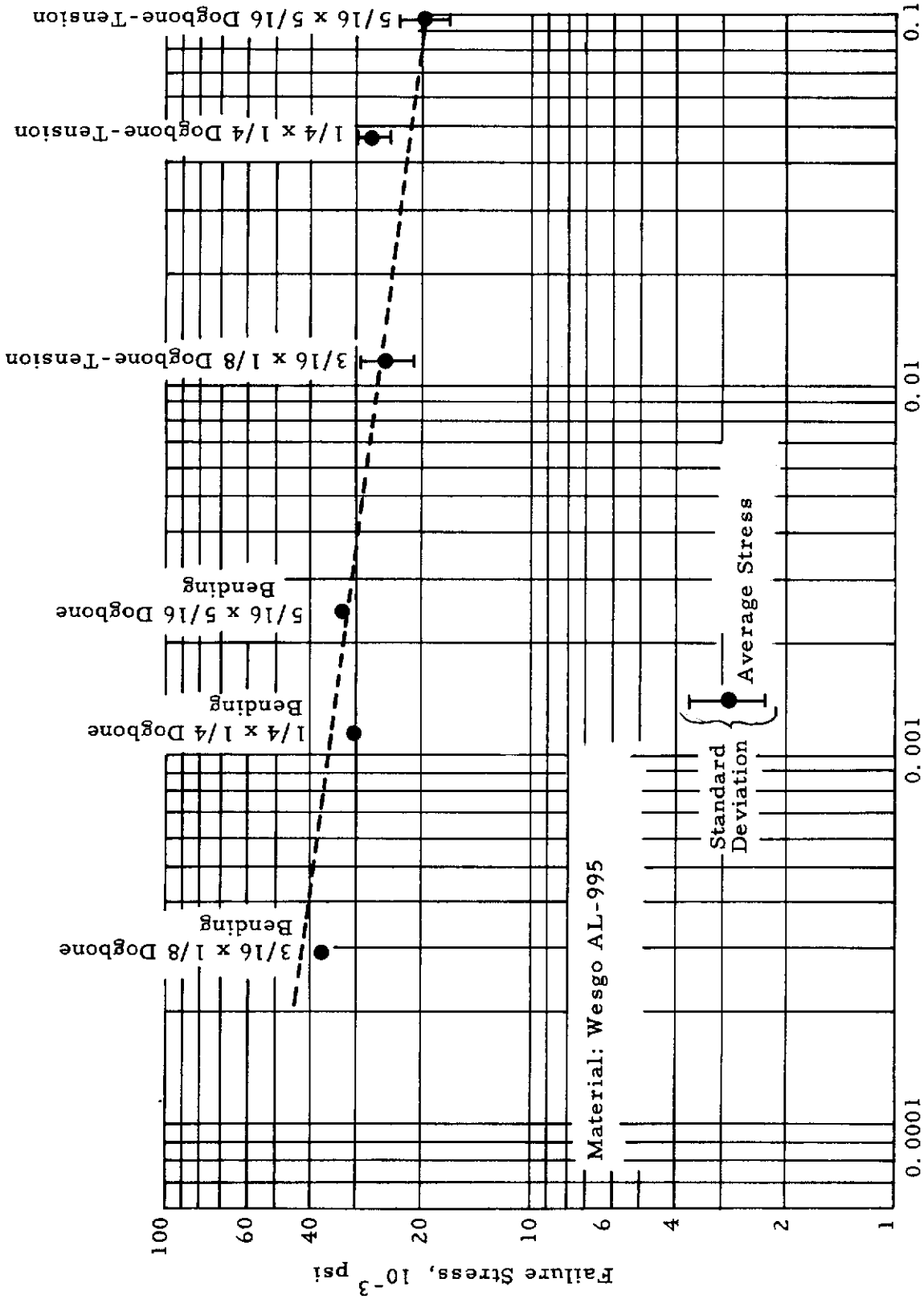

Fig. 3-21 FAILURE STRESS VS. VOLUME SUBJECTED TO MORE THAN 95% OF MAXIMUM TENSILE STRESS FOR WESGO AL-995

Existing theories, however, do not assume that the stress gradient at the point of fracture initiation has an independent effect upon failure, nor have experiments been carried out to investigate this problem. The current work, therefore, seeks to determine the parametric influence of stress gradient upon the fracture of brittle materials and, in a broader sense, to examine the effect of non-uniform stress field upon the statistical probability of fracture in bodies possessing no ductility.

A substantial part of the effort was devoted to the selection and investigation of specimen shapes giving the desired controllable variation of the parameters to be explored in this study. Tensile, bending and ring specimens were evolved, which allow for a variation of effective volumes over three decades, and for stress gradients ranging from 0 to 12.5 σ_p/in., where σ_p represents the peak stress occurring in the specimen.

A special shape, designated the theta-specimen was also developed when it became apparent that it would be extremely difficult to ensure the application of uniform tension in the brittle materials used. Under diametral loading, uniform stresses are generated in the central bar of this specimen, which is also the locus of maximum tensile stress and, therefore, the place of fracture initiation in the specimen. The theta shape is comparatively insensitive to small deviations of misalignment of the loading direction.

Statistical failure probabilities, based upon existing formulations, were derived for the shapes of tensile and bending specimens used in this work. Since large variations of effective size accompanied the variation of stress gradient, an additional criterion was postulated, as represented by the portion of the specimen volume subjected to more than 95 per cent of the governing tensile stress existing in the body.

Experiments were conducted on readily available and comparatively inexpensive brittle materials, such as Columbia Resin CR-39 (an amorphous brittle material), Plexiglas (an amorphous brittle polymer) and graphite. Weibull flaw density constants were obtained for each material, showing wide variations of properties. In addition, correlations were made regarding the individual influence of the stress gradient on the one hand, and

volume at high stress on the other, upon the fracture strength of the materials used. Good correlations were obtained for CR-39 and graphite between failure stress and the empirical 95 per cent-of-maximum-stress volume criterion. Graphite, when analyzed according to existing probabilistic fracture theories, appeared to exhibit a Weibull anisotropy, meaning that different parts of the specimen exhibit different failure probability constants. The most likely explanation for this is to assume that fracture initiation at the surface and the interior of graphite are governed by different material constants.

Experimental work on polycrystalline Al_2O_3 specimens was begun and some initial results are reported. This work is expected to be continued during the extension phase of this program.

8. CONTRIBUTING PERSONNEL

Contributions to the work reported herein were made by J. Anderson, J. Cistaro, I. M. Daniel, A. J. Durelli, S. Morse, T. Niiro, V. J. Parks, W. F. Riley and N. A. Weil.

In particular, the concept and development of the theta specimen, as well as the empirical criterion of 95 per cent of the maximum stress for defining the critical volume, is due to A. J. Durelli and V. J. Parks. Most of the theoretical derivations and experimental work were conducted by I. M. Daniel.

9. REFERENCES

3-1 Griffith, A. A., "The Phenomena of Rupture and Flow in Solids", Phil. Trans. Roy. Soc., 221A, 163 (1920); "The Theory of Rupture," Proc. of Int. Cong. of Appl. Mechanics, Delft, 1, 55 (1924).

3-2 Frenkel, J. I. and Kontorova, T. A., J. Phys., USSR, 7, 108 (1943).

3-3 Davidenkov, N., et al, J. Appl. Mech., 14, 62 (1947).

3-4 Weibull, W., "A Statistical Theory of the Strength of Materials", Ing. Vetenskaps Akad. Handl. 151 (1939); "The Phenomena of Rupture in Solids", Ibid. 153 (1939).

3-5 Weibull, W., "A Statistical Distribution Function of Wide Applicability", J. Appl. Mech. 18, 293-297, (1951).

3-6 Epstein, B., "Statistical Aspects of Fracture Problems", J. Appl. Phys. 19, 140-147, Feb. 1948.

3-7 Kies, J. A., "The Strength of Glass", Ballistics Branch, Mechanics Division, Naval Research Laboratory NRL Report 5098 (1958).

TASK 4 - EFFECT OF MICROSTRUCTURE

Principal Investigator: P. R. V. Evans
Armour Research Foundation

ABSTRACT

The fracture behavior of polycrystalline MgO and Lucalox has been studied under conditions of uniaxial compression in the temperature range 900° - 1900°C. In both oxides the fracture strength showed a marked temperature dependence and fracture was, in all cases, confined to intergranular cracking.

No truly ductile behavior was observed in either of these polycrystalline materials although metallographic evidence suggested that the possibility of obtaining ductility was greater in MgO than Lucalox. The fracture stress (σ_F) - grain size (d) data for Lucalox was subjected to a Petch-type analysis ($\sigma_F = \sigma_o + kd^{-1/2}$). The applicability of the Petch equation to this material was not established because of insufficient experimental data.

TASK 4 - EFFECT OF MICROSTRUCTURE

1. INTRODUCTION

Recent work by Stroh,[4-1] Cottrell[4-2] and Petch[4-3] on yield and fracture behavior of metals has lead to significant advances in the understanding of the mechanisms involved. These theories are based on dislocation concepts and have been able to account for the effect of such variables as grain size, impurity atoms and temperature. Indeed, in the case of iron and other body-centered cubic metals, many effects of alloying and metallurgical treatment of metals have been rationalized on this basis.

The success of these current theories dealing with the atomic mechanisms of cleavage fracture in metallic lattices has prompted an extension of this thinking to a study of fracture behavior in ceramic materials. This approach has been used in Task 4 to study fracture in polycrystalline Al_2O_3 and MgO and centers around the Petch equation relating fracture strength, σ_F and grain size, d, :

$$\sigma_F = \sigma_o + kd^{1/2} \qquad (4\text{-}1)$$

where σ_o represents the frictional stress on an unlocked dislocation and k is a constant directly related to the surface energy associated with the formation of the fracture surfaces. Equation 4-1 is particularly useful in studying fracture behavior since it separates the factors controlling σ_F into three components. Furthermore, the equation is based on a dislocation model for fracture and the parameters in the equation may therefore be interpreted in terms of this model.

In addition to studying the influence of d on σ_F over a broad range of temperatures, the experimental work was aimed at investigating the presence of a ductile-brittle transition temperature of the type observed in bcc metals. Previous work[4-4] has shown that ceramic single crystals do display a transition, but the manifestations of this transition are very

gradual, not accompanied by a change in the mechanism of fracture which remains cleavage throughout the entire range of temperature. In these latter respects their behavior differs from that of the bcc metals.

2. MATERIALS AND TEST SPECIMENS

The work was confined to a study of polycrystalline MgO and Al_2O_3 specimens of high density.

A. Polycrystalline MgO

All the MgO specimens tested were manufactured at ARF by hot pressing (see Chapter II for detailed description) and subsequently ground* to cylindrical shapes 1 x 1/2 in. diam. such that the end faces were square to within 0.001 in. of the specimen axis. The surface finish was smooth and reproducible. During both the centerless and surface grinding operations, water was used as a coolant. The chemical analysis of the hot-pressed MgO is given in Table 4-1. The relatively high carbon content is attributed to pick up from the graphite hot-pressing die and its incomplete removal during the subsequent decarburization treatment.

Dimensions of the MgO specimen were chosen with three considerations in mind: (1) The specimens should be stubby enough to avoid the possibility of elastic buckling. This requirement is amply satisfied, since elastic buckling is seldom of concern below "slenderness ratios" of 60; (2) The L/D ratio should be large enough to avoid any distortion of data by friction effects exerted at the specimen-platen interface (these effects, resulting in an apparent increase in compressive strength owing to the friction constraint, become significant only below L/D ratios of 2.0); and, (3) To satisfy the dimensional allowances of the available high-tempeaature testing machine which could accept specimens only up to 1-1/4 in. in height. The specimen size selected satisfied all of these requirements.

During the current program, all testing of MgO was restricted to a

* Carried out by Accurate Grinding Company, Chicago, Illinois.

hot-pressed material with a grain size of 0.027 mm. However, grain growth studies of this material were performed in order to provide specimens covering a range of grain diameters. The results of this work indicated that limited degrees of grain growth could be obtained by high temperature annealing in the vicinity of 1700°C while still retaining a relatively uniform grain size structure. Time did not permit tests to be carried out on these specimens. It is anticipated that these other grain size levels will be examined in the proposed extension of this program.

The specimen densities were within the range 99.4 - 99.7 percent of theoretical, the small amount of porosity being generally confined to the grain boundaries.

Table 4-1

CHEMICAL ANALYSIS OF HOT PRESSED MgO *

Element	Concentration ** (w/o)
C	0.018
Mg	Principal Constituent
Ca	0.5
Al	0.03
Fe	0.03
Si	0.02
Ti	0.004
Cr	0.0006
Cu	0.0003

* Carried out by Chicago Spectro Service Laboratory, Inc.

** With the exception of the carbon determination, the analysis is semi-quantitative.

B. Lucalox

The polycrystalline Al_2O_3 specimens were supplied by the General Electric Company, Cleveland, Ohio under the trade name Lucalox at three grain size levels, 0.005 mm, 0.03 mm and 0.1 mm. In the as-received condition the specimens were 1 x 1/2 in. diam. with the end faces square to the specimen axis to within 0.001 inch. During some preliminary tests it was discovered that the loading capacity of the compression testing unit was not adequate to produce fracture in these specimens. They were, therefore, centerless ground * to 3/8 in. diam. to reduce the cross sectional area and thus, the load at fracture. Although the height/diameter ratio for these specimens was now 2.7 compared to 2.0 for the MgO specimens, this difference in geometry was not thought to influence significantly, any comparison that might be made between the respective test data. The quantitative composition of the Lucalox is given in Table 4-II.

Table 4-II

SEMI-QUANTITATIVE ANALYSIS OF LUCALOX **

Element	Concentration (w/o)
Al	Principal Constituent
Fe	0.07
Mg	0.15
Ti	0.01
Mn	0.001
V	0.004
Na	0.08
Cu	0.0003
Ni	0.0015
Ca	0.04
Cr	0.002
Ga	0.003
Si	0.03

** Carried out by Chicago Spectro Service Laboratory, Inc.
* Carried out by Adolf Meller Company, Providence, Rhode Island.

The density of the Lucalox varied with grain size, approaching theoretical density for the 0.03-mm and 0.1-mm grain size and falling to about 97.22 percent of theoretical for the 0.005-mm material. Since porosity influences strength properties, its presence in the fine-grained samples certainly needs to be considered in the final analysis of the grain size - fracture strength test data.

All the grain size determinations carried out in this study were based on the formula:

$$D = \frac{1.075}{M}\sqrt{\frac{A}{N}}$$

where

D is the average grain diameter (cm)
M is magnification
A, area cm^2
N is the number of grains in area A.

Grain size determinations were performed on a series of selected samples. The values determined for the Lucalox specimens were in close agreement with the quoted figures of 0.005 mm, 0.03 mm and 0.1 mm. These latter figures have therefore been used in analyzing the Lucalox data.

Each specimen was carefully calipered to determine its actual diameter and cross sectional area prior to testing.

3. APPARATUS AND TESTING PROCEDURE

The high-temperature compression testing apparatus was built around an existing high temperature resistance furnace. A sectional view of the apparatus is given in Fig. 4-1 while the unit together with all the auxiliary equipment is illustrated in Fig. 4-2. Testing was carried out in a helium atmosphere and, with a tantalum heating element, the furnace was capable of temperatures up to 2200°C. The rate of heating and cooling of specimens was closely controlled by manual adjustment, this being necessary in the case of MgO which is particularly sensitive to thermal shock. It was also thought that controlled heating

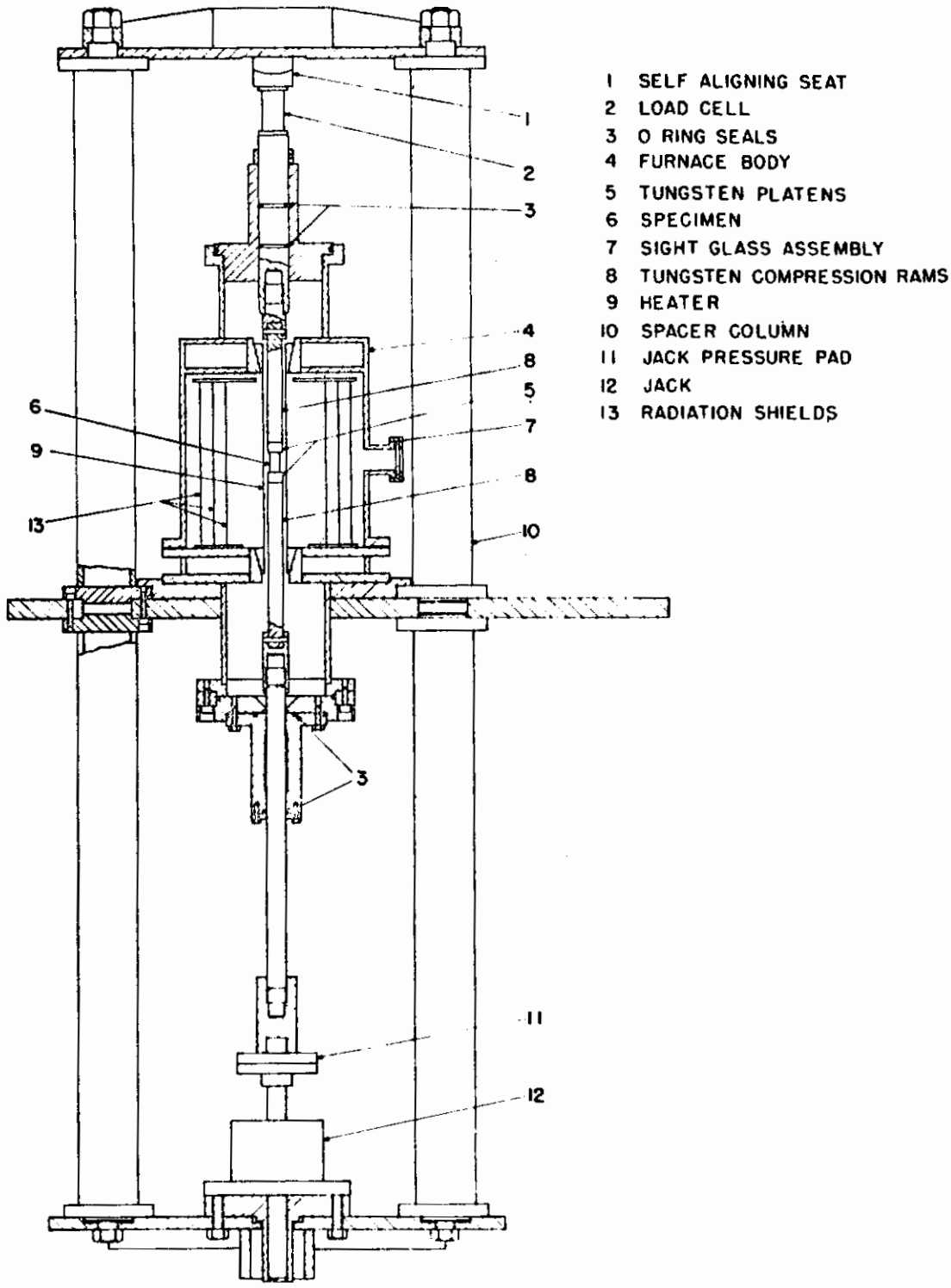

Fig. 4-1 HIGH TEMPERATURE COMPRESSION TESTING APPARATUS

Fig. 4-2 FULL VIEW OF COMPRESSION TESTING UNIT

(1) Framework of compression testing unit.
(2) Load cell
(3) Furnace body
(4) Transformer and electrical controls for heating furnace
(5) Motor drive
(6) Variable speed controller for motor drive
(7) Load cell instrument panel
(8) Tacometer
(9) Vacuum gage
(10) Speedomax recorder for load measurements

rates would tend to reduce the possibility of thermal cycling damage in the Lucalox rams used in the testing of Lucalox specimens. After some preliminary studies on MgO, the heating rate shown in Fig. 4-3 was used throughout the experimental work. While this heating rate was relatively rapid, it was found to induce no thermal shock damage in the test specimens.

The compression specimen was positioned in the uniform temperature zone of the furnace and the load applied through the bottom ram by a screw jack. The screw jack was driven by a 1/2-hp variable speed d-c motor through a 50:1 reduction gear. The load was measured by a resistance strain gage load cell which was directly recorded on a Speedomax recorder. The screw jack speed was held constant at 6.8×10^{-2} in./min resulting in a relatively constant strain rate of 6.8×10^{-2} in./in./min (1.13×10^{-3} sec^{-1}).

Two major problems encountered in building the apparatus and in carrying out the compression tests were (1) obtaining axial alignment of the rams and (2) selection of a suitable ram material that would withstand the extremely severe temperature-stress condition involved.

The alignment problem was overcome by improved engineering design.

After a series of preliminary experiments it was decided to try both tungsten and Lucalox as ram materials since both materials were commercially available in shapes suitable for this application. A set of 3/4-in. diam tungsten rams proved satisfactory for testing MgO up to 1600°C although the specimens did cause a small amount of localized deformation of the tungsten at the ram-specimen interface. The depth of penetration observed was about 0.0005 - 0.001 in. To avoid damaging the ends of the rams in this way, flat tungsten discs were always placed between the specimens and the rams. These discs were readily removed after each test, surface ground to yield a flat surface and re-used for further testing.

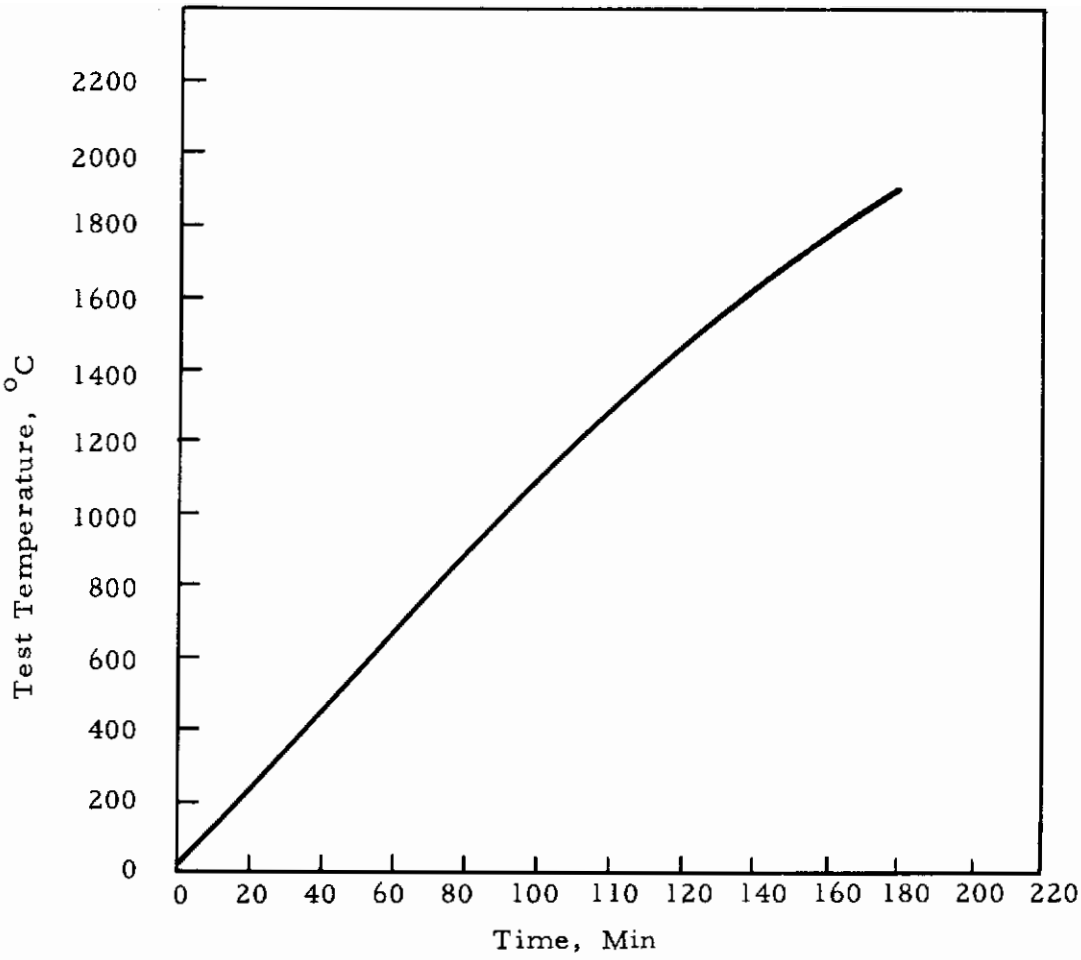

Fig. 4-3 RATE OF HEATING USED IN BRINGING COMPRESSION SPECIMENS UP TO TEST TEMPERATURE

Tungsten rams, even up to 1-in. diam, were found to be completely inadequate for the testing of Lucalox where even higher test temperatures were to be studied. It was therefore decided to use Lucalox rams for this phase of the work. Rods, 1-in. diam, were employed together with 1/4-in. thick discs which formed the working surfaces of the compression unit and thus reduced the possibility of damaging the rams. The rams were friction fitted into steel grips as illustrated in Fig. 4-4. Although this material has proved satisfactory, from a mechanical strength standpoint, it has suffered from the following disadvantages:

(1) The Lucalox discs crack during testing and a new set is required for each test run.

(2) The properties of Lucalox appear to deteriorate with use which results in the premature failure of the rams. Failure of the rams was generally associated with cracking in a direction parallel with the ram axis. To date, five Lucalox rams have had to be replaced.

Both these factors present problems since Lucalox is not an inexpensive material.

4. RESULTS AND DISCUSSION

A. Magnesium Oxide

The compression testing of hot-pressed polycrystalline MgO specimens was carried out in the temperature range 900 - 1600°C and has been confined to as pressed specimens having a grain size of 0.027 mm. The results obtained are summarized in Table 4-III and Fig. 4-5. Some typical autographic load-compression curves are given in Fig. 4-6 while a selected number of fractured specimens are shown in Fig. 4-7 through 4-9. The specimens deformed at 1600°C (Fig. 4-9), buckled during testing, suggesting that the loading was not entirely uniaxial. One possible explanation is that the onset of "plastic deformation" is accompanied by shearing along a preferred direction in the specimen. Further strain develops this localized shearing at the expense of other possible directions until fracture is ultimately reached. A similar effect has been observed with Lucalox (see Fig. 4-15).

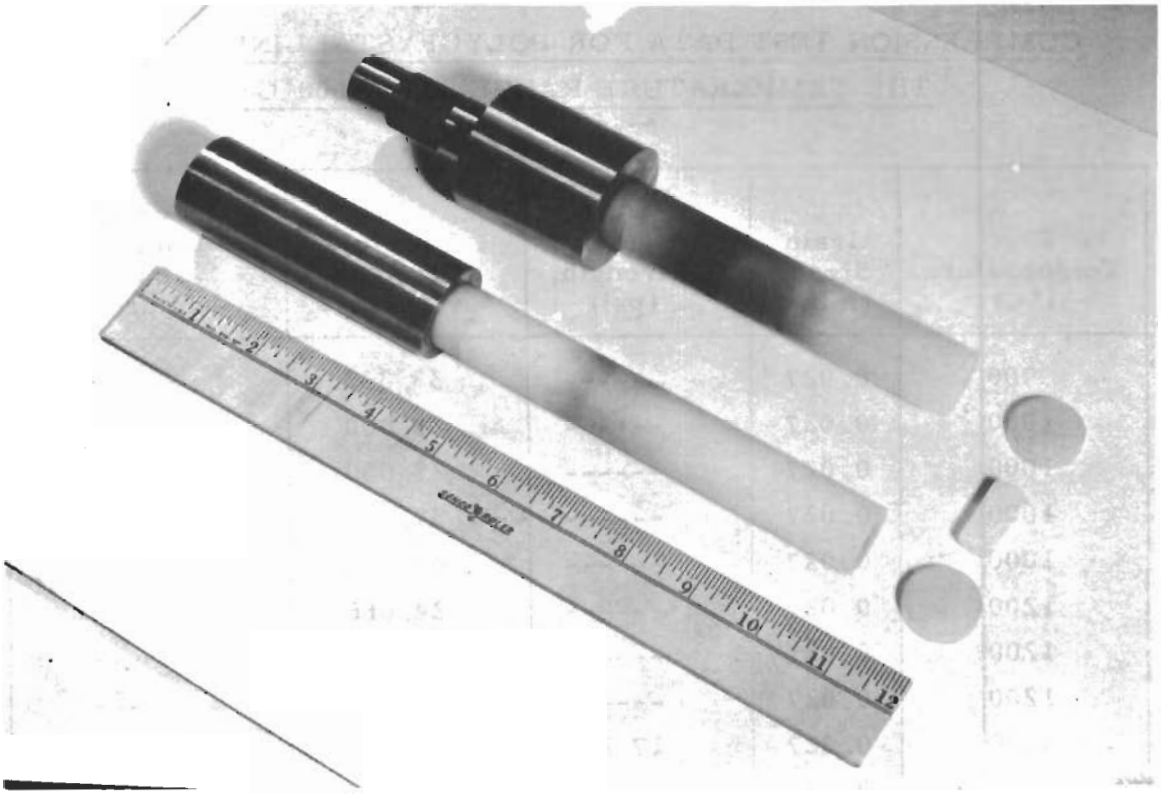

Fig. 4-4 LUCALOX RAMS, DISCS AND A COMPRESSION TEST SPECIMEN USED IN THE HIGH TEMPERATURE COMPRESSION TESTING EXPERIMENTS

Table 4-III

COMPRESSION TEST DATA FOR POLYCRYSTALLINE MgO IN THE TEMPERATURE RANGE 900 - 1600°C

Test Temperature, (°C)	Grain Size, (mm)	Yield Strength, (psi)	Fracture Strength, (psi)	Percent Ductility* in Compression
900	0.027	------	33, 333	---
1000	0.027	------	23, 000	---
1000	0.027	------	27, 000	---
1000	0.027	------	37, 000	---
1000	0.027	------	44, 556	---
1200	0.027	------	24, 666	---
1200	0.027	------	27, 390	---
1200	0.027	------	31, 840	---
1400	0.027	17, 222	20, 111	8.6
1400	0.027	17, 500	20, 000	7.8
1500	0.027	16, 944	18, 511	6.6
1500	0.027	18, 680	20, 000	7.4
1600	0.027	14, 667	17, 067	13.9
1600	0.027	------	14, 200	---

* Percent compression = $\frac{h_o - h_f}{h_o}$ where h_o and h_f are the original and final specimen heights respectively. The $h_o - h_f$ values were determined from the autographic recordings and not from a measurement of the specimens themselves.

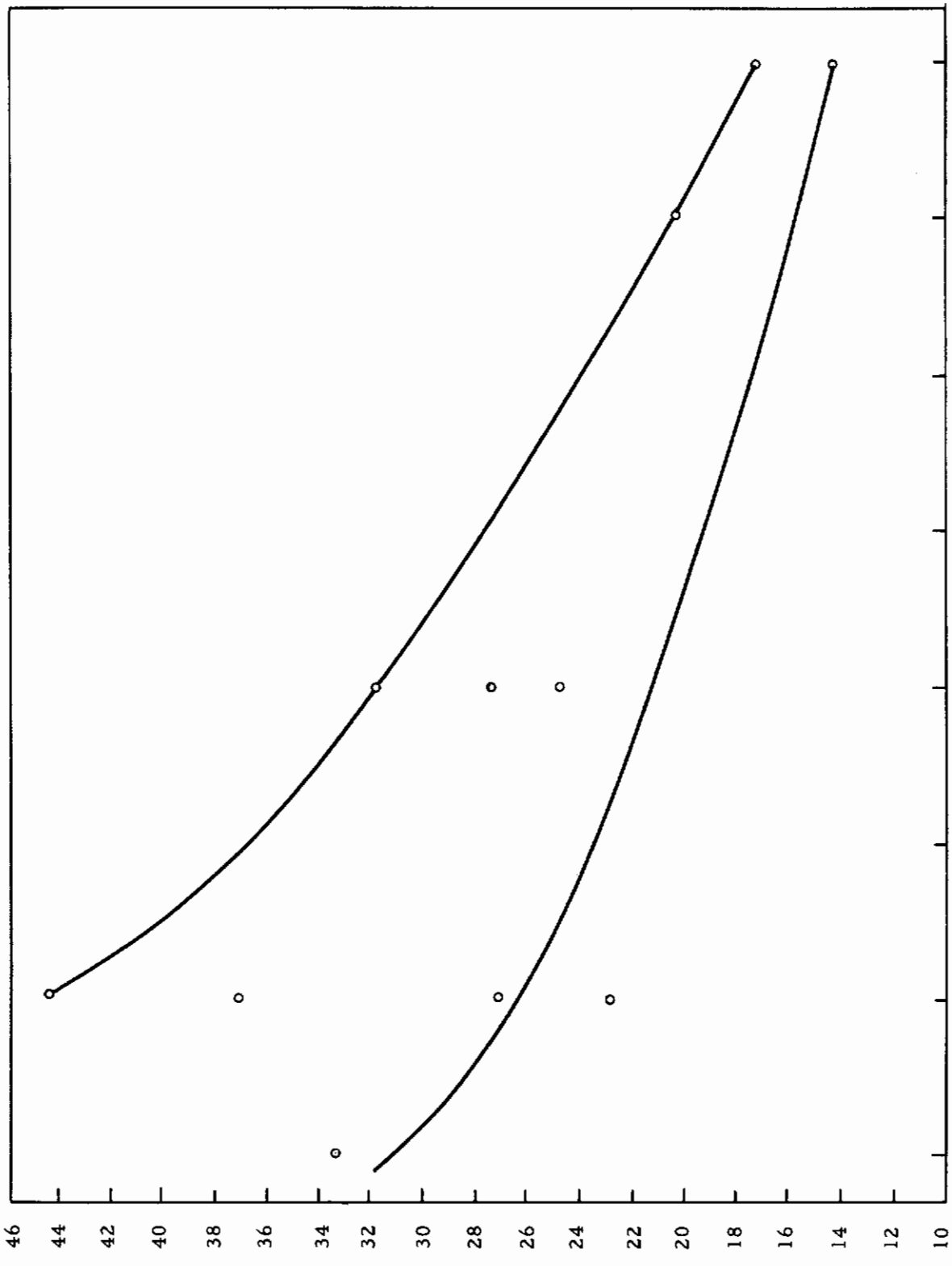

Fig. 4-5 VARIATION OF FRACTURE STRESS WITH TEMPERATURE FOR POLYCRYSTALLINE MgO

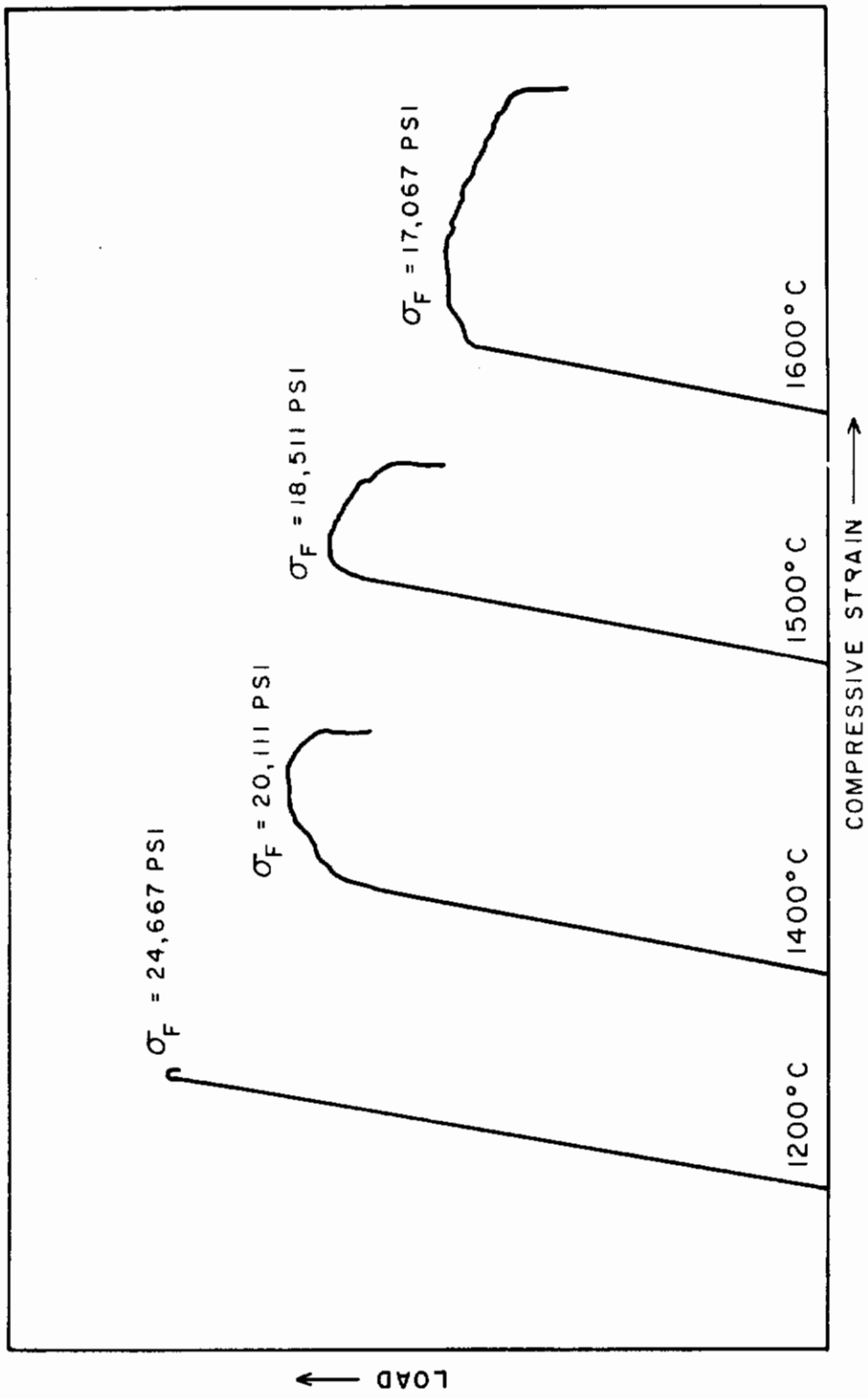

Fig. 4-6 AUTOGRAPHIC RECORDS OF POLYCRYSTALLINE MgO AT VARIOUS TEST TEMPERATURES

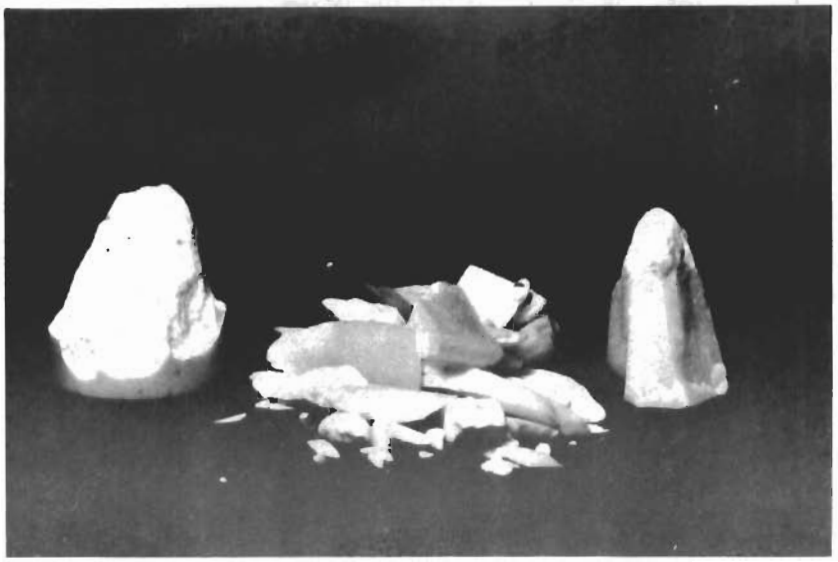

Fig. 4-7 POLYCRYSTALLINE MgO COMPRESSION SPECIMEN FRACTURED AT 1200°C

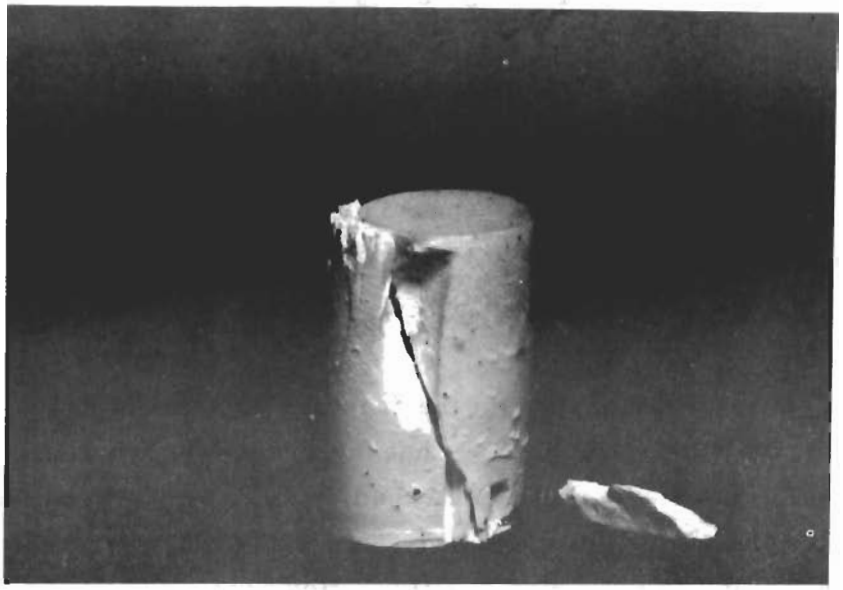

Fig. 4-8 POLYCRYSTALLINE MgO COMPRESSION SPECIMEN FRACTURED AT 1400°C
Grain Size = 0.027 mm

Fig. 4-9 POLYCRYSTALLINE MgO COMPRESSION SPECIMEN FRACTURED AT 1600°C
(Note Surface Blistering and Buckling of Specimen). Grain Size = 0.027 mm

Although the fracture stress-temperature data fall within a scatter band which becomes particularly wide at 1000°C (see Fig. 4-5), the strength of hot-pressed polycrystalline MgO exhibits a pronounced temperature dependence. The change in fracture strength with temperature was also accompanied by a marked change in fracture appearance as illustrated in Fig. 4-7 through 4-9.

The cause of the scatter in the fracture data is not known. The results do indicate a trend suggesting that the specimens produced during the latter stages of manufacturing at ARF had a greater fracture strength than those produced in the initial stages. The scatter may therefore be attributed to a variation in specimen quality. However, it is still not known why this effect should become particularly pronounced at 1200°C and below.

The autographic records in Fig. 4-6 indicate that, up to 1200°C, MgO is completely brittle while at 1400°C there is apparently evidence of plastic strain. The extent of this plastic strain shows a general increase

with increasing temperature. The extent to which this apparent plastic range represents truly plastic behavior, of the kind observed in metals, has not been determined as yet. The yield point measurements made in this temperature range, rather than being associated with creep or plastic flow, may represent the stress at which microcracks are formed. Further strain then results in the propagation of these cracks followed by ultimate failure.

Microscopic examination of specimens tested at 1400°C and 1600°C indicate that failure in this temperature range is entirely by intergranular fracture, as shown by the photomicrographs presented in Fig. 4-10 and 4-11. An examination of grain shape indicates that at 1400°C there is no evidence of plastic deformation of the grains while at 1600°C there are indications that individual grains are exhibiting some plasticity.

Surface blistering of specimens has been observed at 1400°C and above, increasing in severity with temperature. This is thought to be due to the presence of unstable impurities in the MgO; however the extent to which these blisters influence mechanical behavior is not known. Because of the severe surface blistering at 1600°C, tests were not carried out above this temperature.

B. Lucalox

The compression testing of Lucalox at three grain size levels was carried out in the temperature range 1600 - 1900°C. The fracture strength - grain size - temperature data are summarized in Table 4-IV and Fig. 4-12.

The results indicate that the strength of Lucalox is both temperature and grain size dependent. At 1600°C, an increase in grain size leads to a decrease in strength; this behavior is expected to occur from previous studies of the strength of polycrystalline solids. This trend is maintained by the 0.1-mm and 0.03-mm specimens up to 1900°C but not by the 0.005 mm specimens whose strength at this temperature falls below that of coarser grained material. Furthermore, the temperature dependence of strength for the 0.1-mm and 0.03-mm specimens is gradual while the loss of strength of the 0.005-mm material in this temperature range is quite precipitous.

Table 4-IV

COMPRESSION TEST DATA FOR LUCALOX IN THE TEMPERATURE RANGE 1600 - 1900°C

Test Temperature, (°C)	Grain Size, d (mm)	$d^{-1/2}$ ($mm^{-1/2}$)	Yield Strength, (psi)	Fracture Strength, (psi)	Percent Strain in Compression*
1600	0.005	14.3	----	39,910	--
1600	0.005	14.3	----	41,910	--
1600	0.03	5.78	----	39,270	--
1600	0.03	5.78	----	35,270	--
1600	0.03	5.78	----	35,630	--
1600	0.1	3.16	----	23,000	--
1600	0.1	3.16	----	21,180	--
1700	0.005	14.3	17,636	----	8.9
1800	0.005	14.3	12,730	----	16.2
1900	0.005	14.3	6,364	----	11.9
1900	0.005	14.3	5,818	----	20.4
1900	0.005	14.3	4,000	----	35.6
1900	0.03	5.78	----	22,636	--
1900	0.1	3.16	----	17,364	--
1900	0.1	3.16	----	14,545	--

* Does not represent ductility at fracture but the amount of compression the specimen received before the test was stopped.

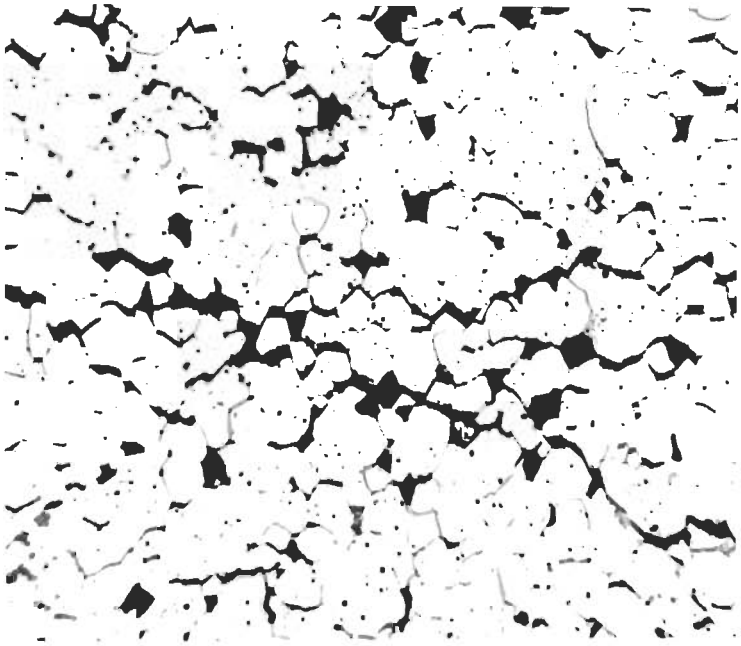

Fig. 4-10 PHOTOMICROGRAPH OF MgO SPECIMEN FRACTURED AT 1400°C X250

(Note profuse intergranular cracking)

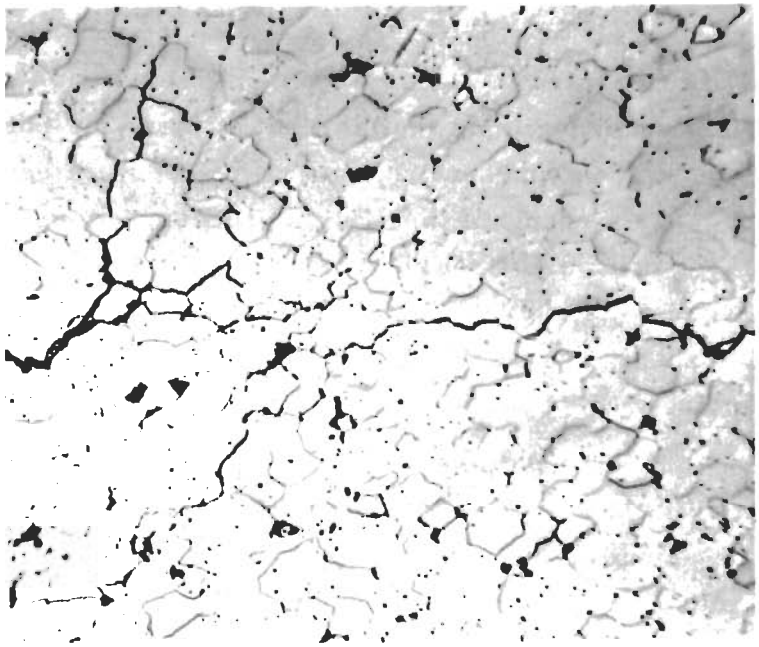

Fig. 4-11 PHOTOMICROGRAPH OF MgO SPECIMEN FRACTURED AT 1600°C X250

(Failure confined to intergranular cracking. There are indications that grains have undergone some plastic flow.)

This evidence clearly suggests that the mechanical behavior of the 0.005-mm specimens is significantly different from the other grain size materials tested. The reason for these differences is not clear, although the presence of an appreciable amount of porosity in the finest grain size specimens might partly account for the observed behavior.

At all test temperatures, the 0.1-mm and 0.3-mm specimens were completely brittle, while the 0.005-mm material did exhibit apparent ductility at 1800°C and above. This si demonstrated by the autographic records in Fig. 4-13 and the photographs of deformed specimens in Fig. 4-14 through 4-16. The load-compression curves suggest that at 1800°C and above the fine grained specimens first yielded and then plastically deformed in a manner similar to a ductile metal. However, as in the case of polycrystalline MgO, the true nature of this yield effect is not known. Two possibilities exist:

(1) Yielding was associated with the onset of gross plastic deformation within the bulk of the specimen as in the case of a ductile metal.

(2) Yielding represented the commencement of extensive grain boundary sliding resulting from the fact that at these temperatures the grain boundaries represent regions of weakness rather than strength. As a result of the sliding process, microcracks formed at the grain boundaries which, with increasing strain developed into intergranular fissures. Thus the stress at which yielding occurred probably represents the stress at which profuse intergranular cracking was initiated.

The experimental evidence tends to support the latter possibility. Metallographic examination of specimens deformed at 1900°C indicated that although the extent of deformation was not uniform (Fig. 4-17), extensive intergranular cavitation had developed in the heavily strained areas as shown in Fig. 4-18. In those regions restrained from flowing, i.e. adjacent to the compression rams, the microstructure showed little change (Fig. 4-19). In addition, there was no evidence of any change in grain

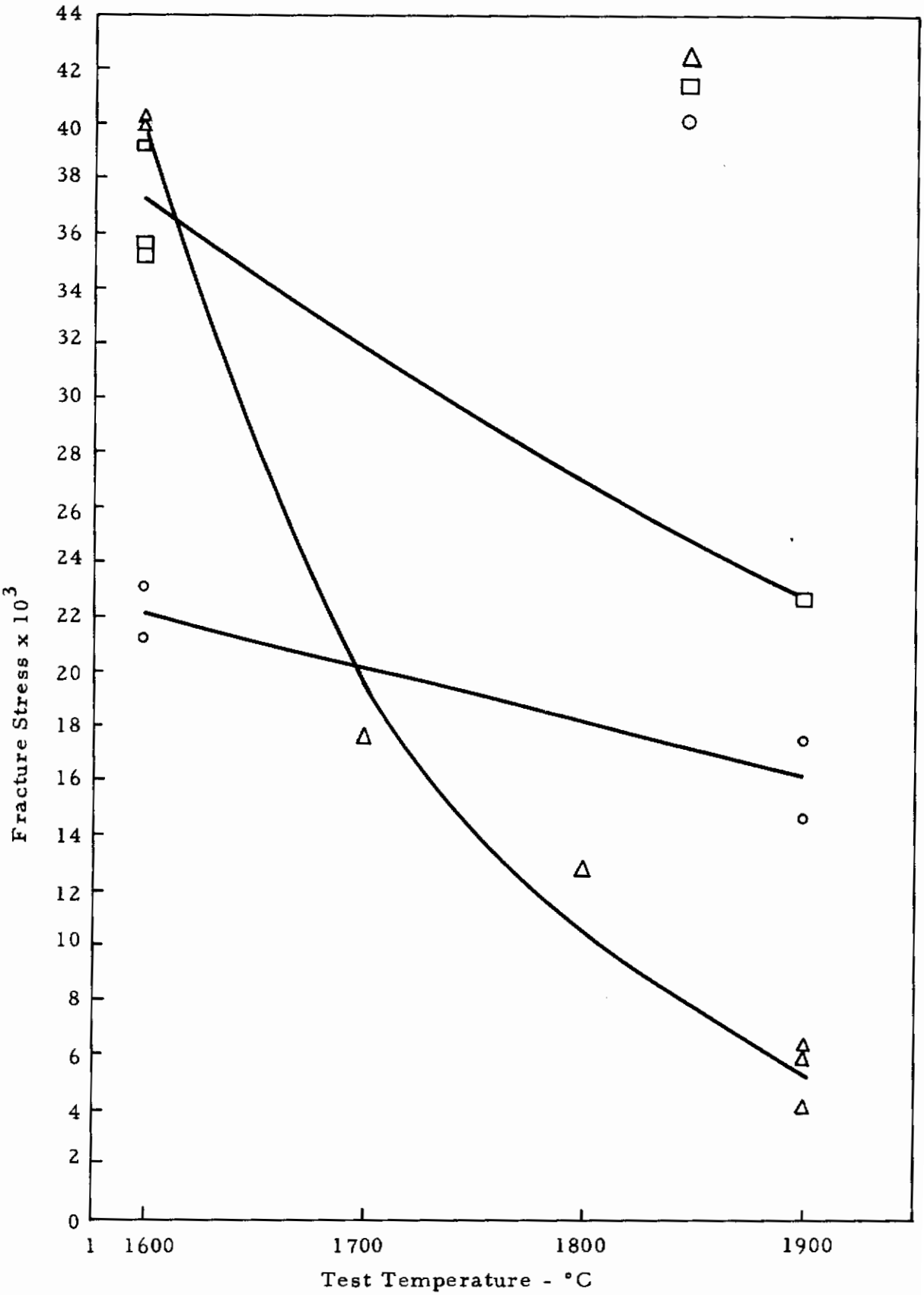

Fig. 4-12 VARIATION OF FRACTURE STRENGTH OF LUCALOX OF VARIOUS GRAIN SIZES WITH TEMPERATURE

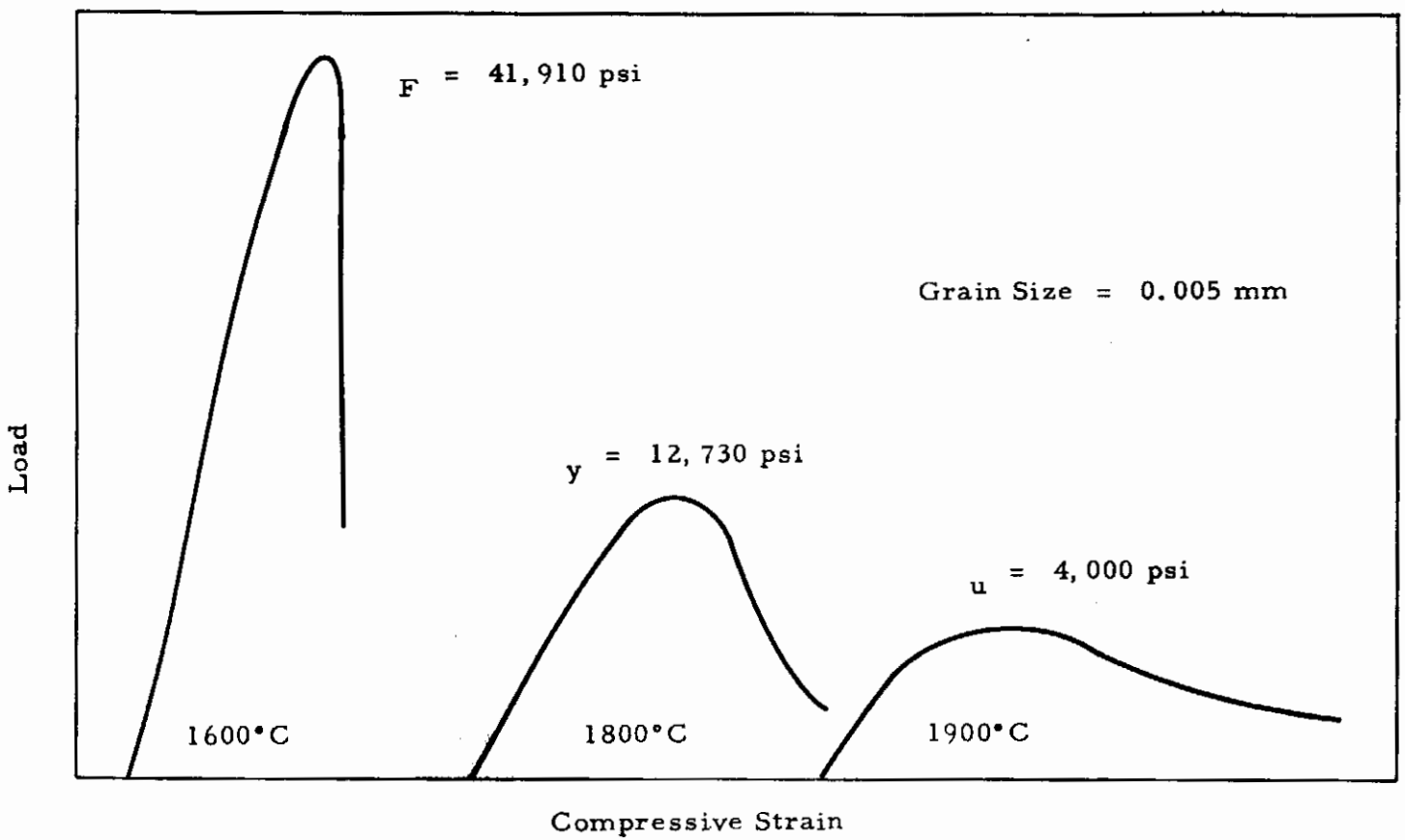

Fig. 4-13 AUTOGRAPHIC RECORDS OF LUCALOX AT VARIOUS TEST TEMPERATURES

Fig. 4-14 LUCALOX SPECIMENS BEFORE AND AFTER TESTING UNDER COMPRESSIVE LOADING AT 1600°C

Grain Size = 0.005 mm

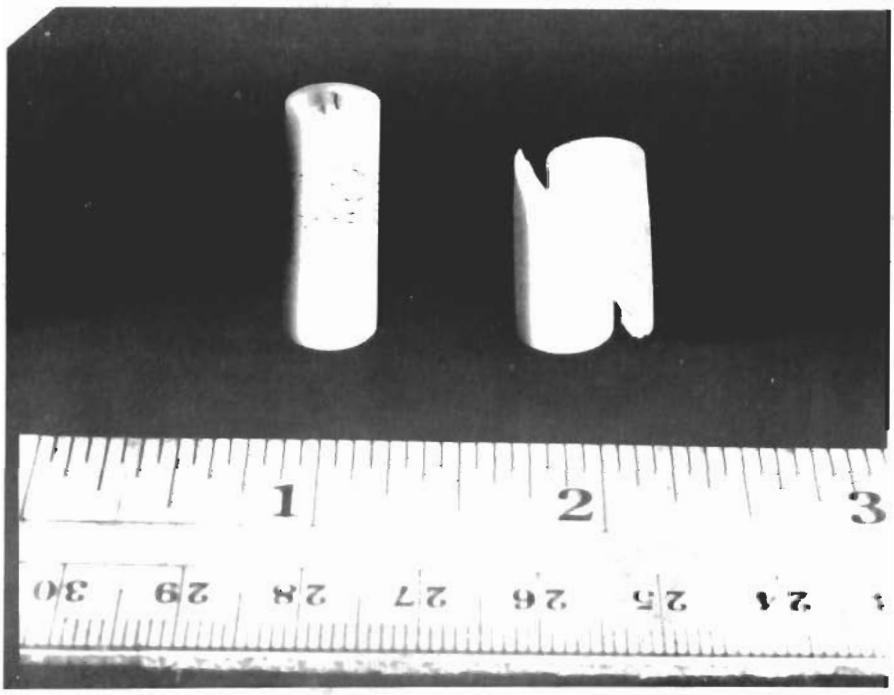

Fig. 4-15 LUCALOX SPECIMENS BEFORE AND AFTER TESTING UNDER COMPRESSIVE LOADING AT 1700°C

Grain Size = 0.005 mm

Fig. 4-16 LUCALOX SPECIMENS BEFORE AND AFTER TESTING UNDER COMPRESSIVE LOADING AT 1900°C Grain Size = 0.005

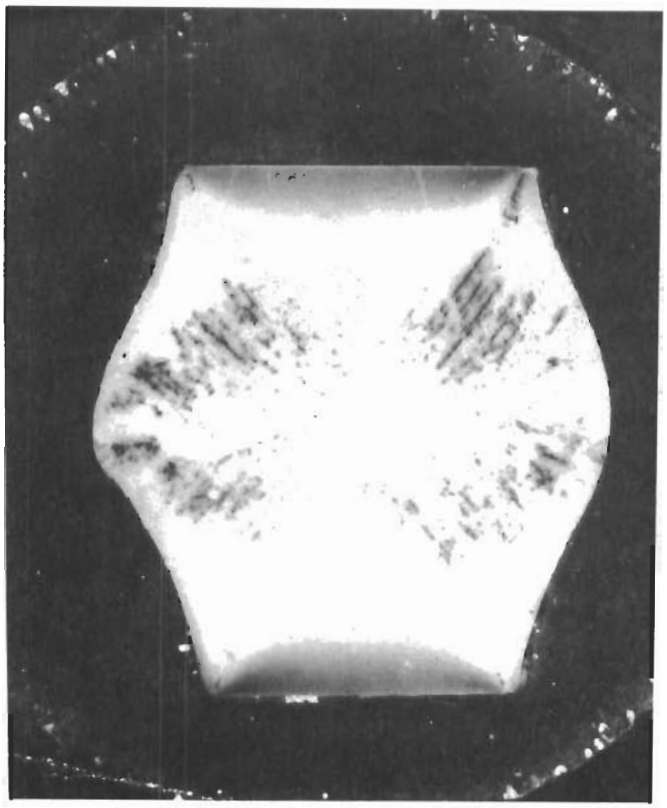

Fig. 4-17 CROSS SECTION OF GRAIN SIZE 0.005 mm LUCALOX COMPRESSED AT 1900°C X4

Compression axis vertical. Note non-uniform strain pattern.

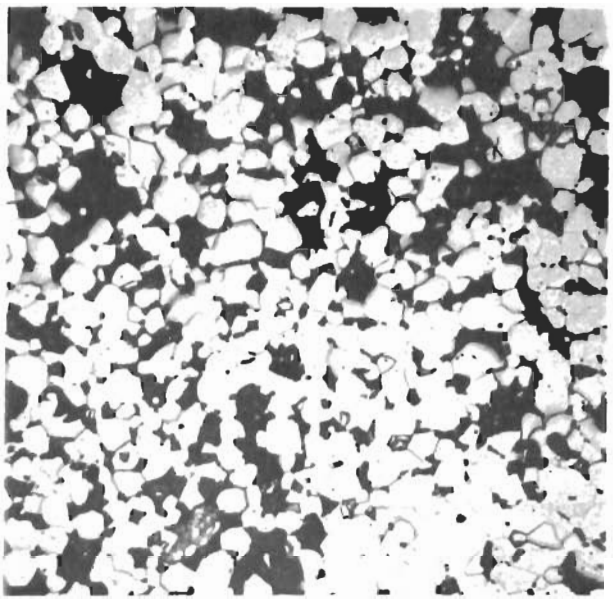

Fig. 4-18 PHOTOMICROGRAPH OF LUCALOX SPECIMEN (Grain size 0.005 mm) COMPRESSION TESTED AT 1900°C

(Note extensive intergranular fissuring accompanying deformation.)

Fig. 4-19 PHOTOMICROGRAPH OF ZONE NEAR COMPRESSION PLATENS IN LUCALOX SPECIMEN (Grain size 0.005 mm) COMPRESSED TESTED AT 1900°C X250

(Note absence of fissuring in this constrained zone.)

shape as a result of compression, which suggests that the grains did not undergo any appreciable plastic strain. It was concluded, therefore, that the deformation process and the observed ductility were associated with grain boundary sliding and intergranular fissuring similar to that observed in creep processes, rather than any gross deformation of the individual grains.

Examination of specimens exhibiting completely brittle behavior indicated that failure was due entirely to intercrystalline cracking.

The fracture stress data obtained at 1600°C and 1900°C has been subjected to a Petch-style analysis, and as indicated in Fig. 4-20, a linear relationship between the three grain size levels is not obtained. This, in some respects, is not surprising since the 0.005-mm material contains porosity and, as discussed, seems to be behaving quite differently from the other Lucalox specimens. At 1900°C, the fracture stress values plotted for the fine-grained material are probably not true values since deformation may be taking place by an entirely different mechanism at this temperature than that operative at 1600°C. The data is, therefore, inconclusive and some further tests at other grain size levels are required before the applicability of the Petch equation to Lucalox can be established.

It should be mentioned, in passing, that the Petch-type dependence of strength on grain size presupposes that the failure mechanism remains the same for the materials, which is patently not the case for the 5-μ grain Lucalox. Therefore, future work will also inquire into the grain size at which the failure mechanism changes from rigid cracking to intergranular fissuring by grain boundary sliding, and the variation of this critical grain size with testing temperature.

5. CONCLUSIONS

The present investigation has led to the following conclusions:

A. The fracture strengths in uniaxial compression of both polycrystalline MgO and Lucalox of high density show a marked temperature dependence in the range 900 - 1600°C and 1600 - 1900° respectively. This variation in strength is also accompanied by a change in the mode of fracture which showed a similar trend in both oxides.

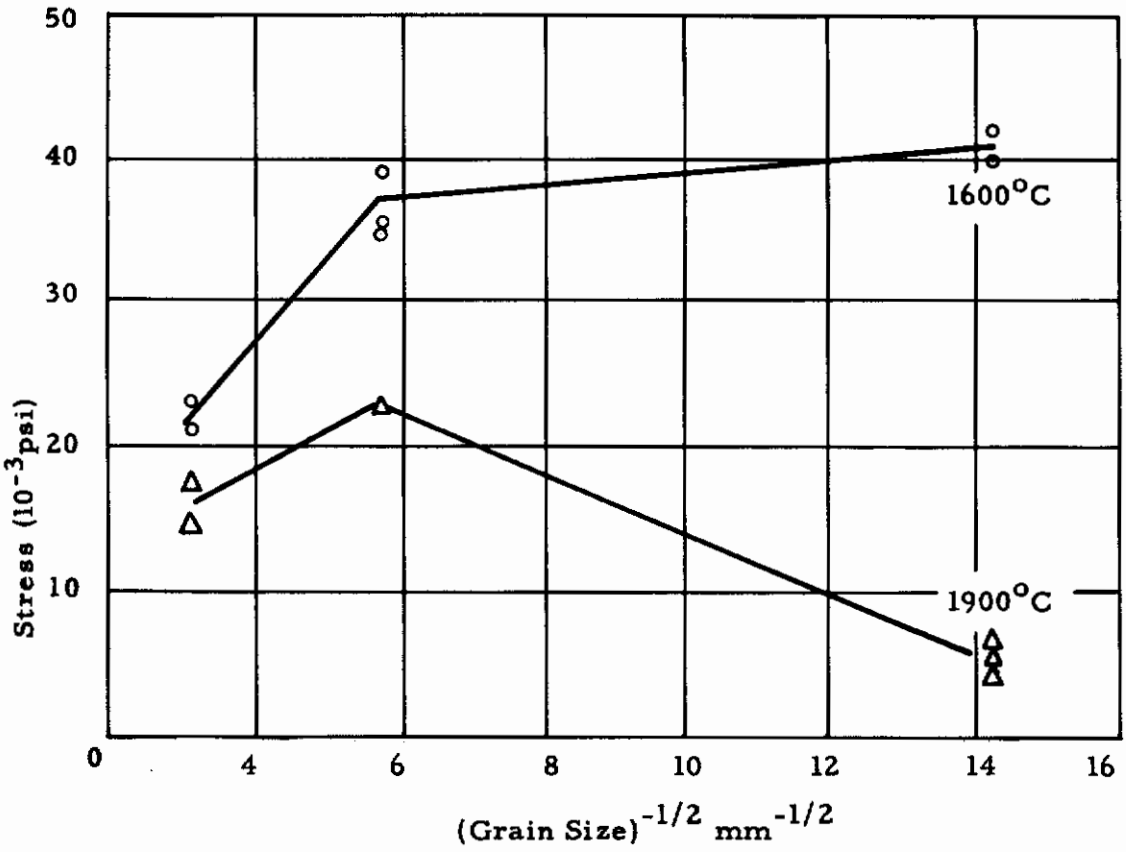

Fig. 4-20 PETCH-TYPE ANALYSIS OF THE FRACTURE STRESS-GRAIN SIZE DATA

B. The fracture strength of Lucalox, in general, increased with decreasing grain size. However, the fine grain material (0.005-mm grain size) did deviate from this behavior above 1600°C. This was attributed, in part at least, to the presence of porosity in this material.

C. A Petch-type analysis of the fracture stress (σ_F) - grain size, d, data obtained at 1600°C and 1900°C proved inconclusive because of the anomolous behavior of the fine-grained specimens and the absence of further σ_F - d data.

D. There was evidence of apparent ductility in both MgO at 1600°C and Lucalox at 1900°C. However, in the case of Lucalox, the ductility was traceable to a grain boundary sliding mechanism rather than gross plastic deformation of the bulk material. In polycrystalline MgO this mechanism may also have been operative although metallographic evidence did suggest that some true plastic deformation of the grains may also have occurred. It appears, therefore, that the possibility of obtaining true ductility is greater in polycrystalline MgO than Lucalox. This conclusion might reflect basic differences in the slip mechanisms and the crystallographic structures of these oxides.

E. At 1600°C, the fracture strength of Lucalox is approximately twice that of polycrystalline MgO of the same grain size. Lucalox is also considerably more brittle than MgO at this temperature.

F. Metallographic examination of fractured specimens of both MgO and Lucalox indicated that failure always occurred by intergranular fracture.

G. A hot-pressing technique was developed for producing ultra-high density polycrystalline MgO.

6. CONTRIBUTING PERSONNEL

Personnel contributing to this program include J. R. Dvorak, P. R. Evans, Henry Konjevich, and R. McGill.

7. REFERENCES

4-1 Stroh, A. N., Advances in Physics 6, 418 (1957).

4-2 Cottrell, A. H., Trans. AIME, 212, 192 (1958).

4-3 Petch, N. J., Fracture, John Wiley and Sons, New York, (1959).

4-4 Johnston, T. L, Stokes, R. J. and Li, C. H., 5th Technical Report Nonr-2456 (00) NR-032-451, July 1959.

TASK 5 - INTERNAL FRACTION MEASUREMENTS OF CERAMIC MATERIALS

Principal Investigator: P. D. Southgate
Armour Research Foundation

A B S T R A C T

The purpose of this program is to study the internal friction of ceramic materials, and to relate observed damping behavior to the pinning stresses and mobility of dislocations characterizing the materials studied. A highly refined experimental equipment has been constructed, which allows for accurate determinations of the internal friction in carefully supported specimens vibrating as free-free beams.

Experimental work to date has been confined to MgO single crystals. It was found that the amplitude independent component of dislocation damping is largely independent of temperature up to 500°C, in contrast to some theoretical predictions. Furthermore, the behavior of the amplitude dependent component also contradicts the predictions of the Granato-Lucke theory.

Annealing of dislocation damping occurs with increasing speed above 400°C and is a function of specimen purity. Complexes consisting of trivalent impurity-vacancy pairs exhibit a relaxation peak at 230°C (for 45 kc/s), at an activation energy of 0.63 + 0.02 eV. These complexes are created by a short anneal at above 1000°C; a lower temperature anneal causes them to dissociate until an equilibrium concentration is reached.

TASK 5 - INTERNAL FRICTION MEASUREMENTS OF CERAMIC MATERIALS

1. INTRODUCTION

Internal friction and the hardness of a material are two closely related quantities, the softer materials nearly always having the higher internal friction. The reason for this is straightforward: the mechanism inhibiting crack propagation, that of damping out of propagation energy by mobile dislocations, is exactly the same as that producing dynamic internal friction. Thus, a detailed study of internal friction mechanisms should give information on the way in which crack energy is dissipated, which may not be readily obtained from observations of crack propagation as such. In addition, the dynamic properties of other crystal imperfections govern hardening processes as well as participating in some dislocation damping mechanisms, and hence will be likely to affect the fracture mechanism of the material. Internal friction data may be analyzed to give values of several parameters associated with the motion of such imperfections, notably the activation energies.

Accordingly, the principal goal of research on this Task is to determine the nature of internal friction of ceramic oxides as influenced by temperature, surface treatment and the density of preexisting dislocations in the material. These results are then to be compared to existing theories or hypotheses, in order to relate the observed damping behavior with the mechanisms that can account for the mobilization of dislocations in the host lattice.

The investigation described here was conducted on single crystals of MgO of commercial origin, dislocations having been introduced into the specimens by room-temperature deformation. As was anticipated in the original proposal, the major portion of the period was spent in constructing the apparatus for internal friction measurements,

which is described in detail in Section 2 below. The results that follow are, at this time, limited in extent; it has not yet been possible to give a complete interpretation of the observed phenomena although some aspects of the experimental results obtained are fairly well understood.

Discussion of the theory of brittle fracture by Petch[5-1] postulates that, at least in metals, the criterion for crack propagation is that the damping force on an unlocked dislocation be less than the surface energy of crack formation, multiplied by a certain proportionality constant which depends on the length of the relevant slip plane and the elastic constants of the material. It is further assumed that the surface energy contains a term which depends on the stress required to unlock a dislocation from the pinning points, usually visualized as individual impurity atoms. If the type of fracture is to be temperature dependent, one would anticipate that dislocation damping, or unlocking, or both are likewise temperature-dependent quantities.

Internal friction measurements give data on both damping and unlocking. It is interesting to note that results to be presented here show very little temperature variation of either dislocation damping or unlocking, at least between room temperature and the range in which impurity precipitation occurs. For as-grown crystals, the observations are consistent with the concept that dislocations, as revealed by etch-pits, are not mobile at all. Recent electron micrographs[5-2] confirm this by showing the strong ball-and-chain type precipitation around such dislocations. Dislocations introduced from the surface during deformation, however, do remain mobile, and it is these which have been studied.

Measurements have been made in the range from 8 to 50 kc/s and from 30 to 1350°C. The maximum logarithmic decrement Δ measurable was of the order 10^{-3}, and the background damping from the support wires a few times 10^{-6}. Small changes of resonant frequency, and internal friction alone was studied. The temperature

variation of Δ has been analyzed in terms of three processes: amplitude independent dislocation damping, amplitude dependent damping ascribed to dislocation break-away, and a damping resulting from relaxation of associated vacancy-impurity pairs. In each case, the data raise important questions which cannot as yet be answered.

2. INTERNAL FRICTION APPARATUS

A. General Description

The materials which are to be measured have, at least at low temperatures, extremely low values of internal friction. This fact limits considerably the number of possible methods of measuring internal friction, since, in any system utilizing direct mechanical coupling between a transducer and the specimen, the damping of the transducer would probably mask that of the specimen. The electrostatically coupled system first devised by Bordoni[5-3] avoids this difficulty. For conducting specimens, a plate is placed a small distance from the specimen, and the drive potential (at the specimen resonant frequency) is applied between the plate and the specimen. If the mechanical drive is to be of the same frequency as the applied electrical signal, it is necessary also to apply a biasing voltage somewhat greater than the applied voltage. In addition, motion of the specimen will change the capacitance of the gap; hence, if this is made part of a high-frequency tuned circuit connected to an oscillator (36 mc/s in our case), a frequency modulated output proportional to the specimen displacement will be obtained.

Electrostative drive forces, for conducting specimens, arise directly from the uniform field between the specimen and the drive plate. In the case of a dielectric specimen, a uniform field produced by this arrangement would yield no attractive force, and an inhomogeneous field is required. This is produced by the grid shown in

Fig. 5-1. Two sets of bars are connected alternatively to wires across which the drive is applied. Near the surface of the grid, the field is very inhomogeneous and a dielectric specimen will be attracted toward it; the system works like a magnetic chuck as used on milling machines. Similarly, motion of the dielectric towards or away from the grid surface will change the capacitance between the two sets of bars. An approximate theory of the magnitude of the effect is given in Section 2E.

There are several ways of obtaining values for internal friction. The most desirable, giving an instantaneous meter-reading value, is to compare drive power with the oscillation amplitude which is excited. Unfortunately, this is not applicable to electrostatic drive systems since the drive efficiency cannot be determined accurately. The resonance width can be used to determine Q and this method has the advantage that each measurement is carried out at a fixed amplitude; however, it is susceptible to drift. The method chosen is that of plotting the free decay curve of the specimen. The output from the 36 mc/s oscillator is amplified and fed into a discriminator. After further amplification and mixing with a local oscillator the signal emerges at 2 kc/s with the decay envelope of the specimen oscillation. The signal is finally displayed on a logarithmic recorder, so that an exponential decay envelope appears as a straight line. Deviations from the exponential form, representing changes of internal friction with amplitude, can thus be readily detected.

A block diagram of the whole system is shown in Fig. 5-2. The drive generator is required to be of high stability so that the frequency may be held on the narrow specimen resonance, and so it consists of a main oscillator locked into a high-stability frequency meter oscillator. An oscilloscope displays the Lissajous figure of drive signal vs. specimen oscillation signal (before mixing) thus affording a sensitive means of detecting resonance.

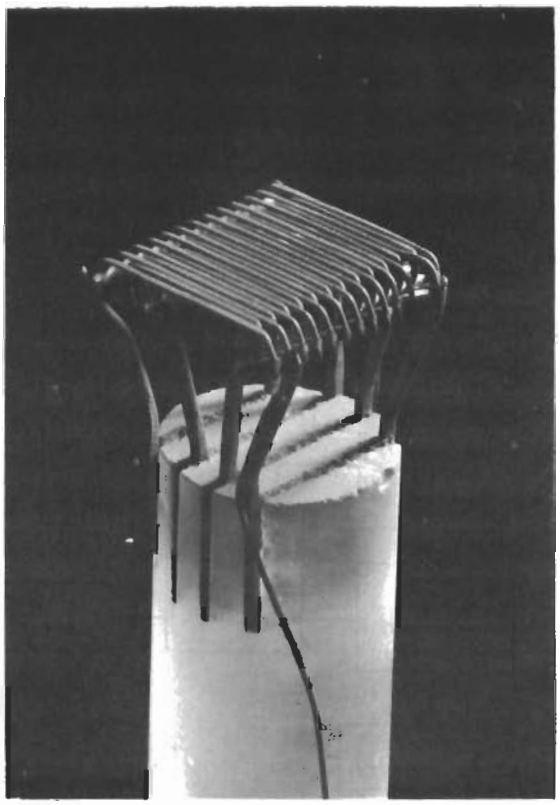

Fig. 5-1 PHOTOGRAPH OF DETECTING GRID

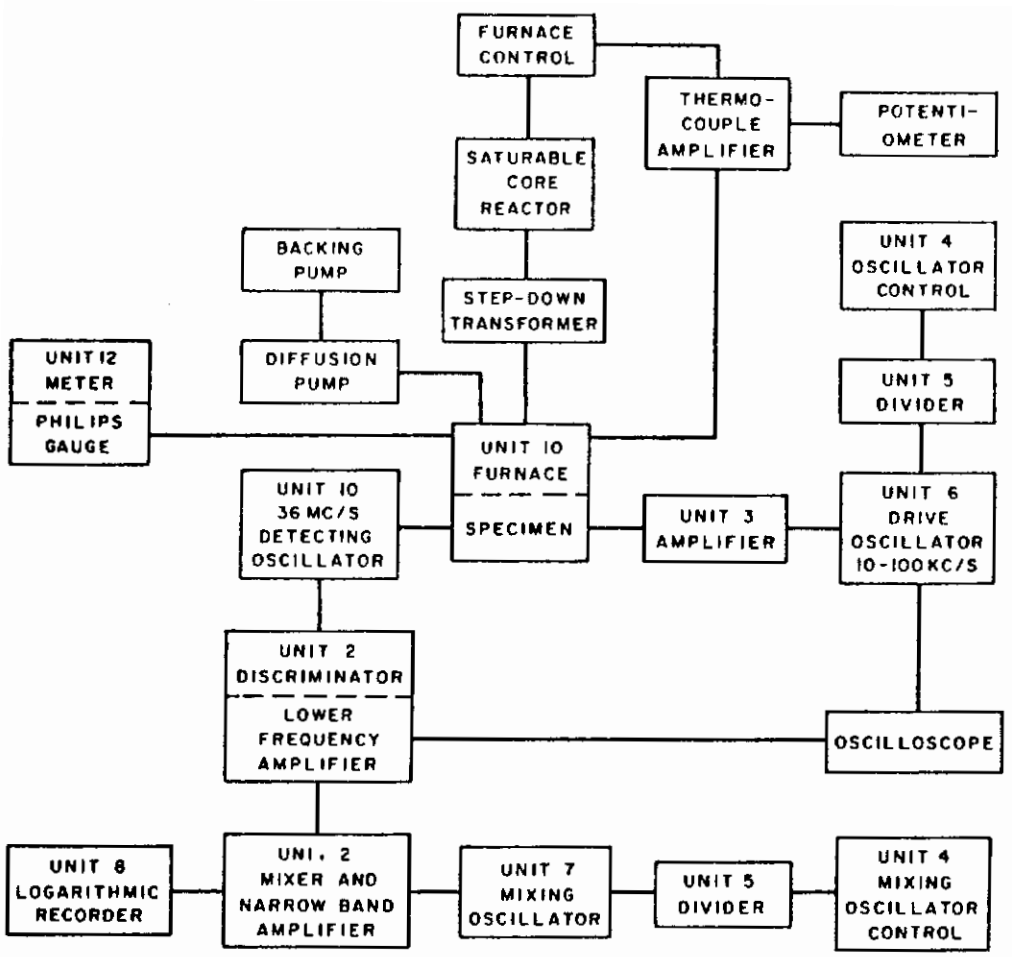

Fig. 5-2 BLOCK DIAGRAM OF APPARATUS

A general view of the apparatus is shown in Fig. 5-3. The majority of the electronic circuits are contained in the rack at the left. The X-Y oxcilloscope and the logarithmic recorder are on the bench. Further to the right appears the part of the apparatus containing the furnace, vacuum system, specimen and detecting oscillator ("the cart"), while the furnace supply rack is to the extreme right. The furnace is suspended by anti-vibration mounts; connection to the all-metal vacuum system is made via a flexible bellows tube.

B. Unit 1: Furnace and Specimen Support

The furnace is required to work in a vacuum, to reach temperatures in excess of 1500°C, and to have a very short time constant to facilitate quenching experiments. A molybdenum tube furnace will satisfy such requirements. The construction is seen in section in Fig. 5-4. The furnace body, which acts as the vacuum envelope, is highly polished on the inside to reflect heat and is surrounded by a water jacket. Further thermal insulation is provided by a thin cylindrical thermal shield within the body, which also helps keep the polished surface free of evaporated impurities. The heating tube consists of a 0.002-in. molybdenum foil wrapped into a tube and clamped by end-rings, being held in tension by the spring and bellows arrangement in the furnace top cap. Potential is applied between the top cap and the body, an interposed O-ring acting both as vacuum seal and electrical insulation. With an input of 7.5 v, 240 A, a temperature of 1400°C is attained.

The specimen is shown in Fig. 5-4 supported so that it is excited into flexural oscillation. The grid is held close to the center section of the side, and the specimen supported by two fine tungsten wires passing through holes drilled through the nodal points. Screw adjustments on the base-plate hold the wires in tension across the

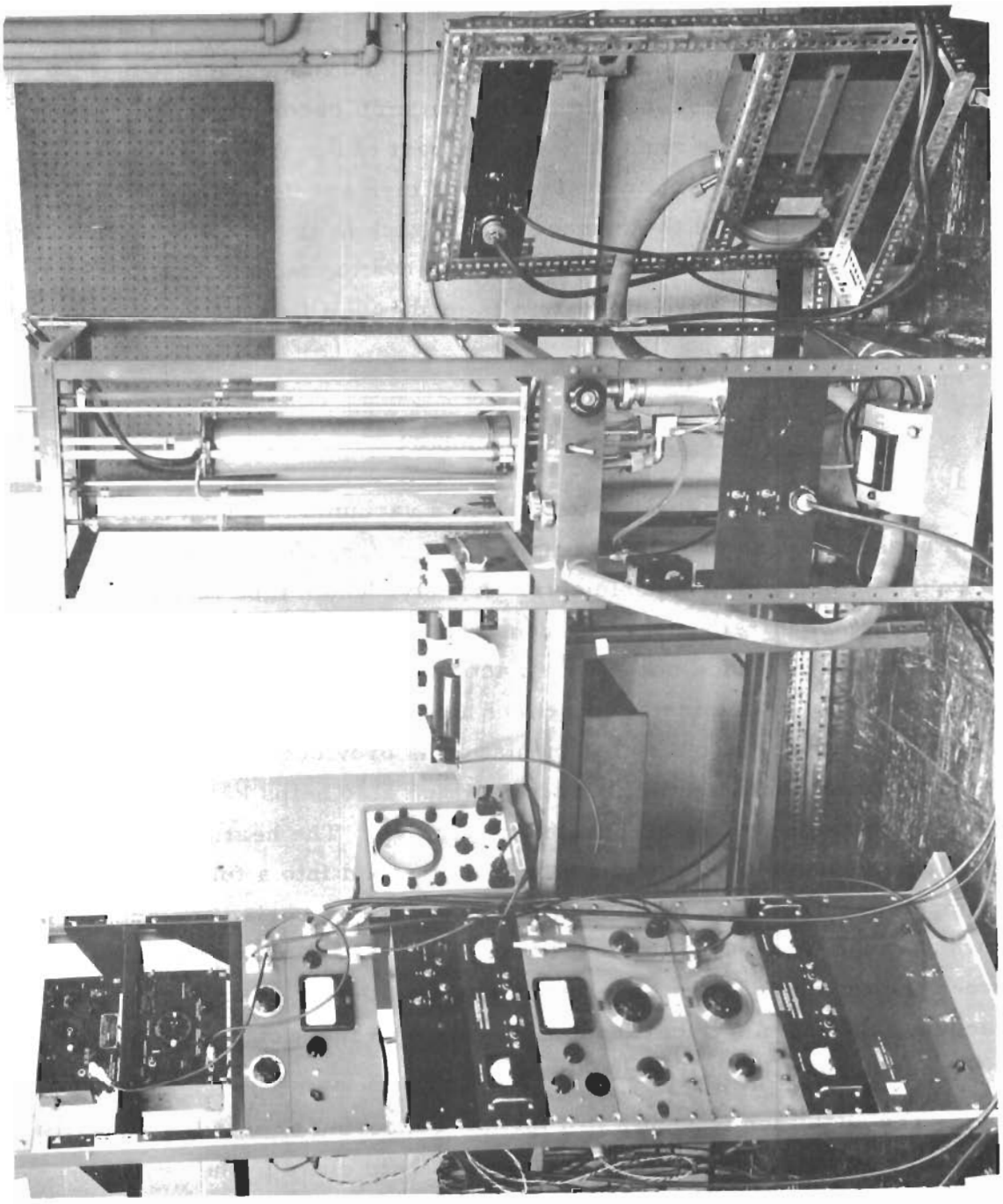

Fig. 5-3 GENERAL VIEW OF APPARATUS

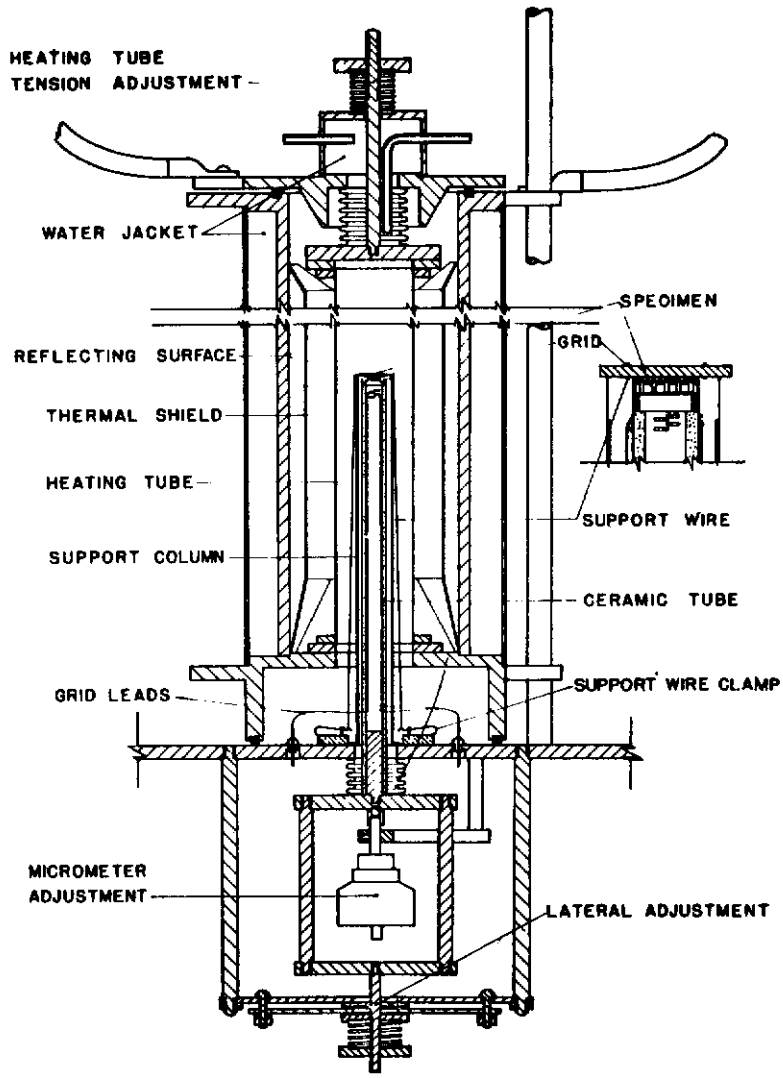

Fig. 5-4 SECTION OF FURNACE SHOWING SPECIMEN MOUNTING

top of a square-section tantalum tube. For conducting specimens, the tantalum tube is replaced by an insulating one of silica or alumina so that the specimen may be used as one drive electrode. The ceramic support for the grid passes up the center of this tube, and a micrometer screw and lateral adjustments beneath the base-plate allow setting-up and calibration adjustment of the grid-specimen gap to be made.

Fabrication of the grid is a matter requiring some care. Molybdenum wires 0.01-in. in diameter are laid parallel, being separated by 0.005-in. diameter wire. Alternate wires are then spot-welded to either of two pairs of tantalum cross-bars, and the ends of the grid wires cut off. After bending so that the two sets of cross-bars are not in contact with the wires, the grid is spot-welded to wires fixed into the end of the ceramic support rod. The assembly is then set in wax, leaving the face exposed so that it can be polished flat to remove slight distortions. Finally, the wax is melted away.

C. Electronic Circuits

Unit 2: Discriminator Amplifier

The circuit is shown in Fig. 5-5. The 36-mc/s input enters at a level of about 1 volt, is amplified by the 6AK5 tube and is fed directly into the Foster-Seeley discriminator circuit in the tube anode circuit. The discriminator out-put is filtered (560 Ω , 47 $\mu\mu$ F) and travels via SW 1/2, shorted, to the first amplifier tube. The meter in the cathode measured the d-c component of discriminator out-put, corresponding to the center frequency of the input signal. After filtering of low frequency components, the signal passes to a mixer 6AU6 tube, which has a large additional signal, 2 kc/s higher than the amplified signal, applied to the cathode through SK 3/2. The anode circuit has variable band-width centered on 2 kc/s. The subsequent amplifier has more filtering to remove the local oscillator signal and

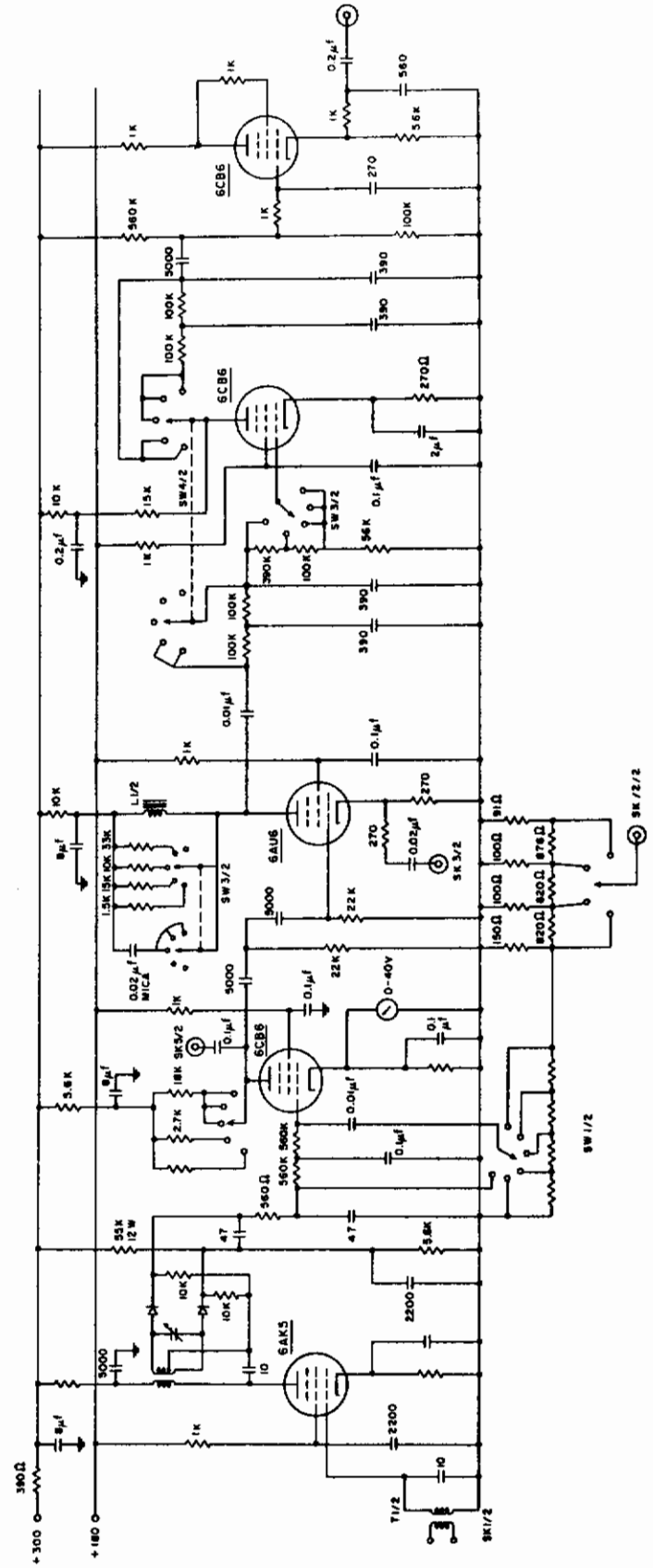

Fig. 5-5 DISCRIMINATOR AND AMPLIFIER

36 mc/s leakage. Alternately, SW 4/2 allows the amplifier to be used for a straight 1 to 10 kc/s amplification, since it would not be possible to filter out local oscillator signal well enough below 10 kc/s. The final output to the recorder is from a cathode follower.

The discriminator response curve as indicated by the meter for an RF input of 1 volt is shown in Fig. 5-6. The linear portion extends over 1.2 mc/s showing that the maximum frequency of mechanical oscillation that can be measured accurately using the d-c calibration is 600 kc/s. Undistorted decay curves will be obtained for higher frequencies, however. The overall gain of the lower frequency amplifier-mixer circuit from the grid of the first 6CB6 to the output is 1.3×10^4; the equivalent input voltage corresponding to noise and local oscillator break-through is 3μ V at 50 kc/s. The amplifier gain can be checked by the calibrating networks on SW 1/2, SW 2/2 using a monitored signal of the drive frequency from Unit 3. Changing the switch to the calibrating positions puts a filter circuit in which removes the a-c component of discriminator output while retaining the d-c bias so that the amplifier gain does not change.

Unit 3: Drive Amplifier

The circuit is shown in Fig. 5-7. The input, varying from 5 to 200 kc/s at a level of approximately 1 volt passes through one stage of untuned amplification before the final inductively loaded power stage. The tuning is broad and various bands are selected by SW 1/3. A maximum output voltage of 180 v rms can be obtained from the circuit: a voltage divider gives a small monitored output for Unit 2.

Unit 4: High Stability Generators

Two generators are required: one for the drive oscillator and the other for the mixing oscillator. The circuit of each generator is shown in Fig. 5-8. It is a modified frequency meter: government type

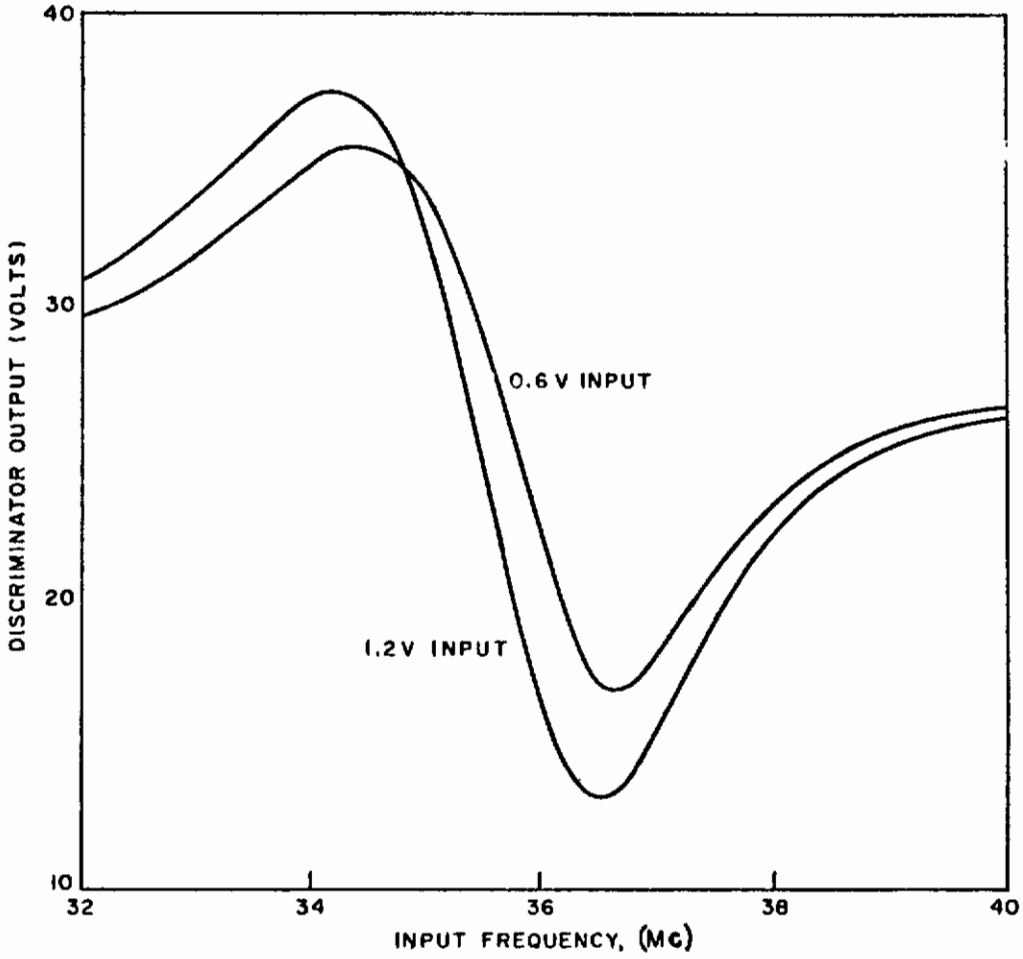

Fig. 5-6 DISCRIMINATOR CURVE

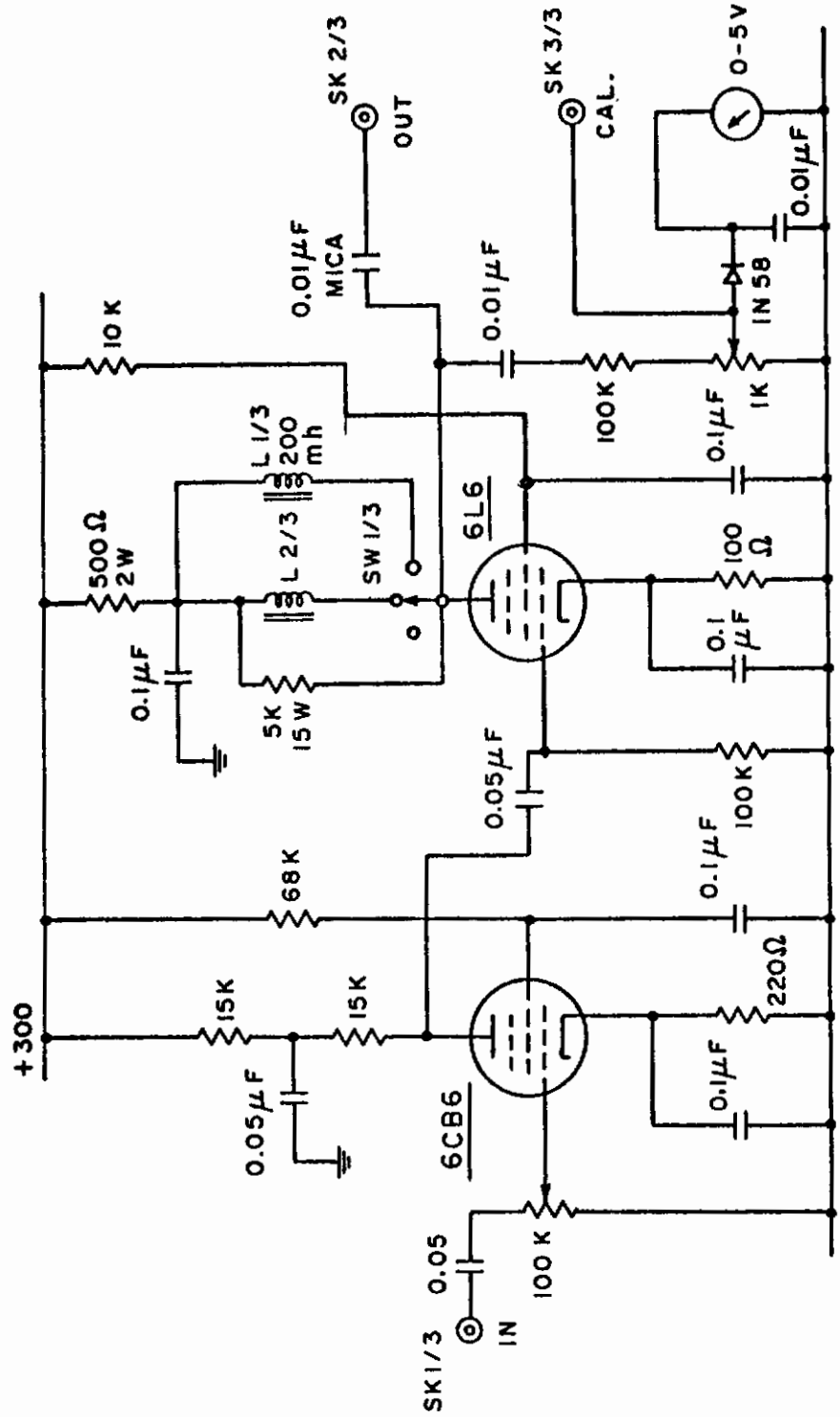

Fig. 5-7 DRIVE AMPLIFIER

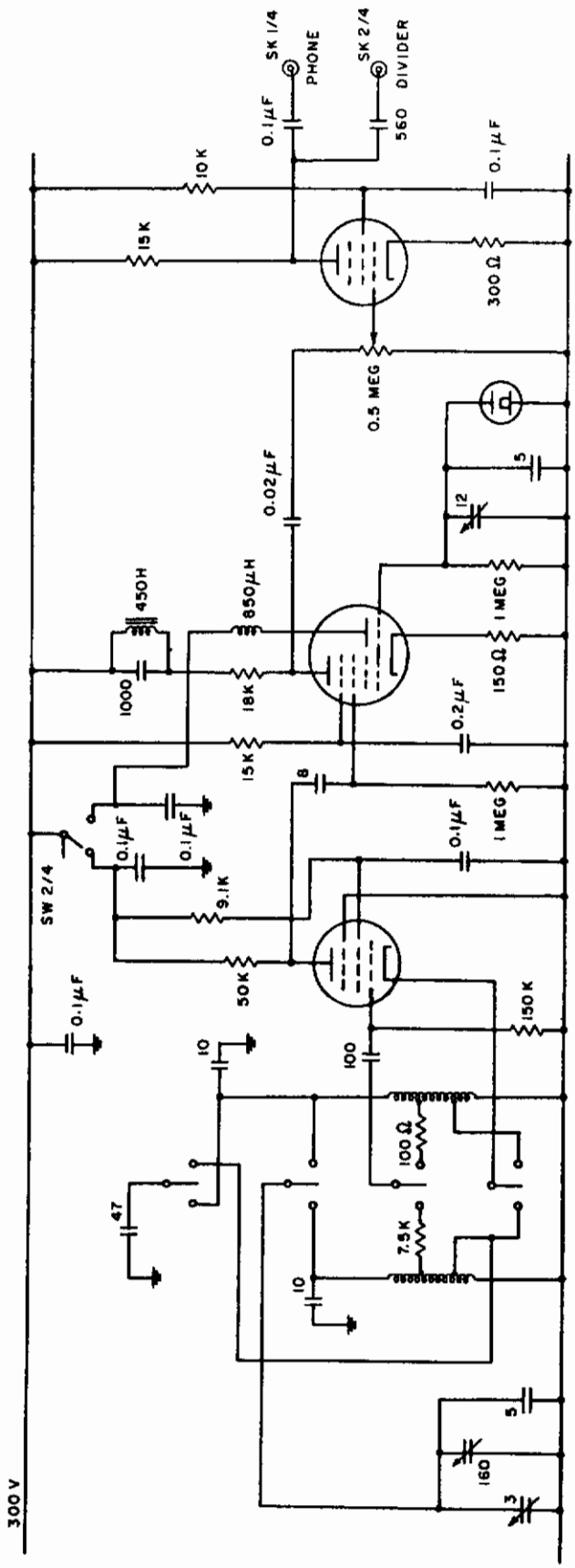

Fig. 5-8 HIGH STABILITY GENERATOR

BC221. The modification, in the anode of the VT 167 tube, allows the primary oscillator frequency rather than the beat frequency to be amplified, although the beat output is still retained for checking the variable oscillator frequency against the standardizing crystal. It is the short-term stability of this generator that is important. Beating the output against a crystal oscillator showed that the short-term stability at 120 kc/s was of the order 0.03 c/s, and that the drift over 10 minutes was less than 3 c/s. A 10-v change of the H. T. moved the frequency by 3 c/s. These shifts are sufficiently low for the purposes of these experiments. The generators are mounted on flexible supports to reduce frequency shift due to vibration or frame distortion.

Unit 5: Frequency Dividers

The frequency meters give a signal from 120 to 250 kc/s, and the range to be covered is 5 to 200 kc/s. Hence, frequency division is needed. The circuit is shown in Fig. 5-9; there is one such circuit for either generator. Two blocking oscillators are used. The first is triggered by the incoming sine wave from the frequency meters and converts the signal to a pulse train of the same frequency. The second is free running and locks into a submultiple of the input. Note that the connection is such that the second blocking oscillator is triggered not by the initial rise of the first but by the ringing return, the first transformer being slightly underdamped. This arrangement was found to be the most stable. Care has to be taken to set the free running frequency fairly close to a submultiple of the master oscillator frequency or irregular triggering will result. The triangular wave output from the grid was found to be most convenient for triggering the following oscillators.

Units 6 and 7: Locked Oscillators

Hewlett-Packard oscillators Type 200 GR are employed here. One is fed into the mixer circuit, SK 3/2 of unit 2, and the other to

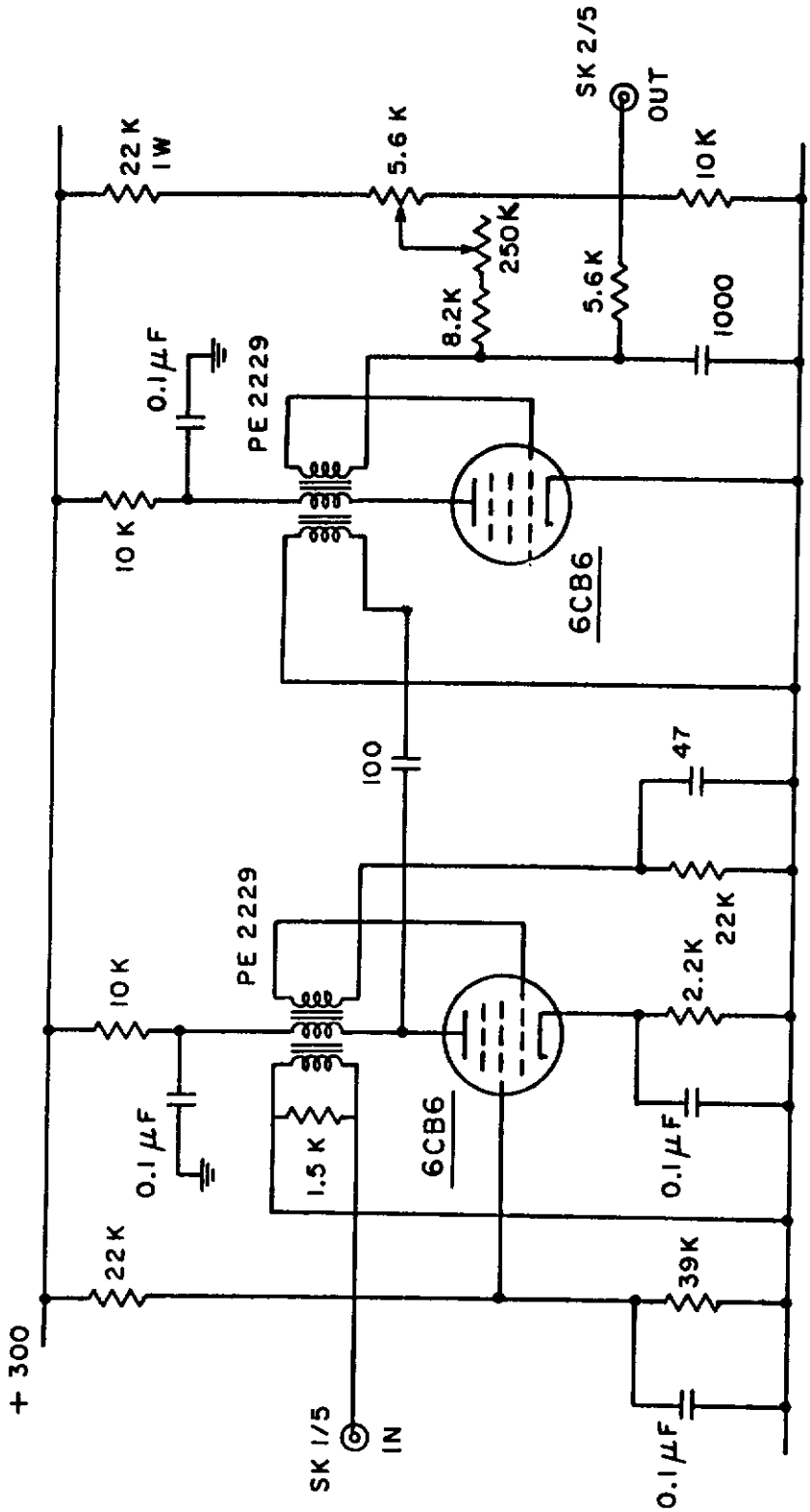

Fig. 5-9 FREQUENCY DIVIDER

the final drive output SK 1/3 of unit 3. The oscillators use a Wein bridge circuit which is not intrinsically very frequency-stable, but which can be readily locked to the output from unit 5 by a 3-$\mu\mu$ F capacitor connected to the grid of the first oscillator tube. Complete locking was obtained for $\pm$2 percent of dial setting.

Unit 8: Recorder

Checks on several commercially available logarithmic recorders showed the Bruel and Kjaer Type 2305 to be the fastest and most reliable. The maximum writing speed is 1000 db/sec; if one then takes 300 db/sec as being measurable, this limits the maximum log. decrement that can be measured to 5×10^{-3} at 10 kc/s and 5×10^{-4} at 100 kc/s. However, at these relatively high damping values, resonance-width measurements become sufficiently accurate to use, replacing decay-time measurements.

Unit 9: Cart and Detector Circuits

The cart circuits, shown in Fig. 5-10, consist of a-c supplies to the pumps and vacuum gauge, together with a water-pressure actuated switch to protect the furnace and diffusion pump.

The detector circuit is shown in Fig. 5-11. The 36 mc/s oscillator is loosely coupled to minimize fluctuations in frequency which are due to the tube, and has a small extra tuning capacitor in addition to that formed by the grid and leads. A cathode follower stage feeds the twin shielded lead to the discriminator-amplifier with a signal of about 1-v amplitude.

Unit 11: Furnace Control

This consists of a West Instrument "Gardsman" furnace supply unit. A saturable core reactor is controlled by a thermocouple in the furnace. The furnace is fed from these circuits through a step-down transformer: Jefferson type 248-171.

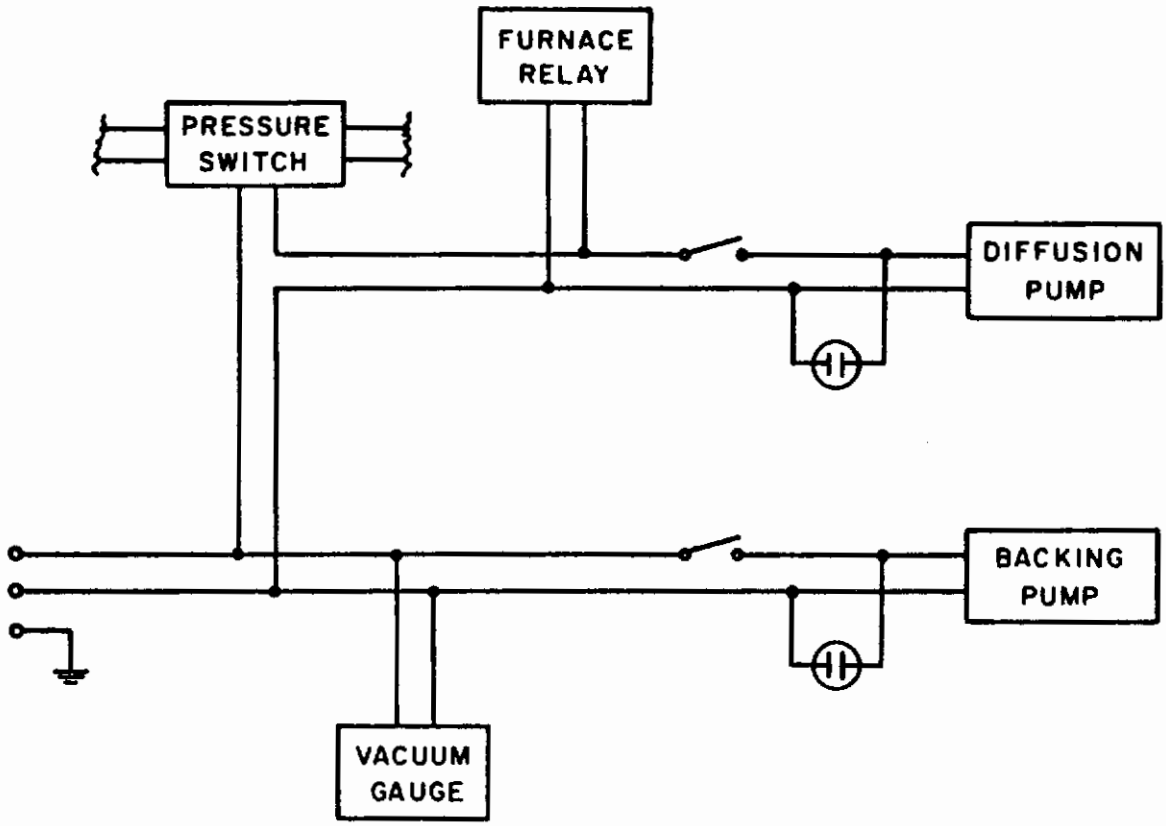

Fig. 5-10 CART CONNECTIONS

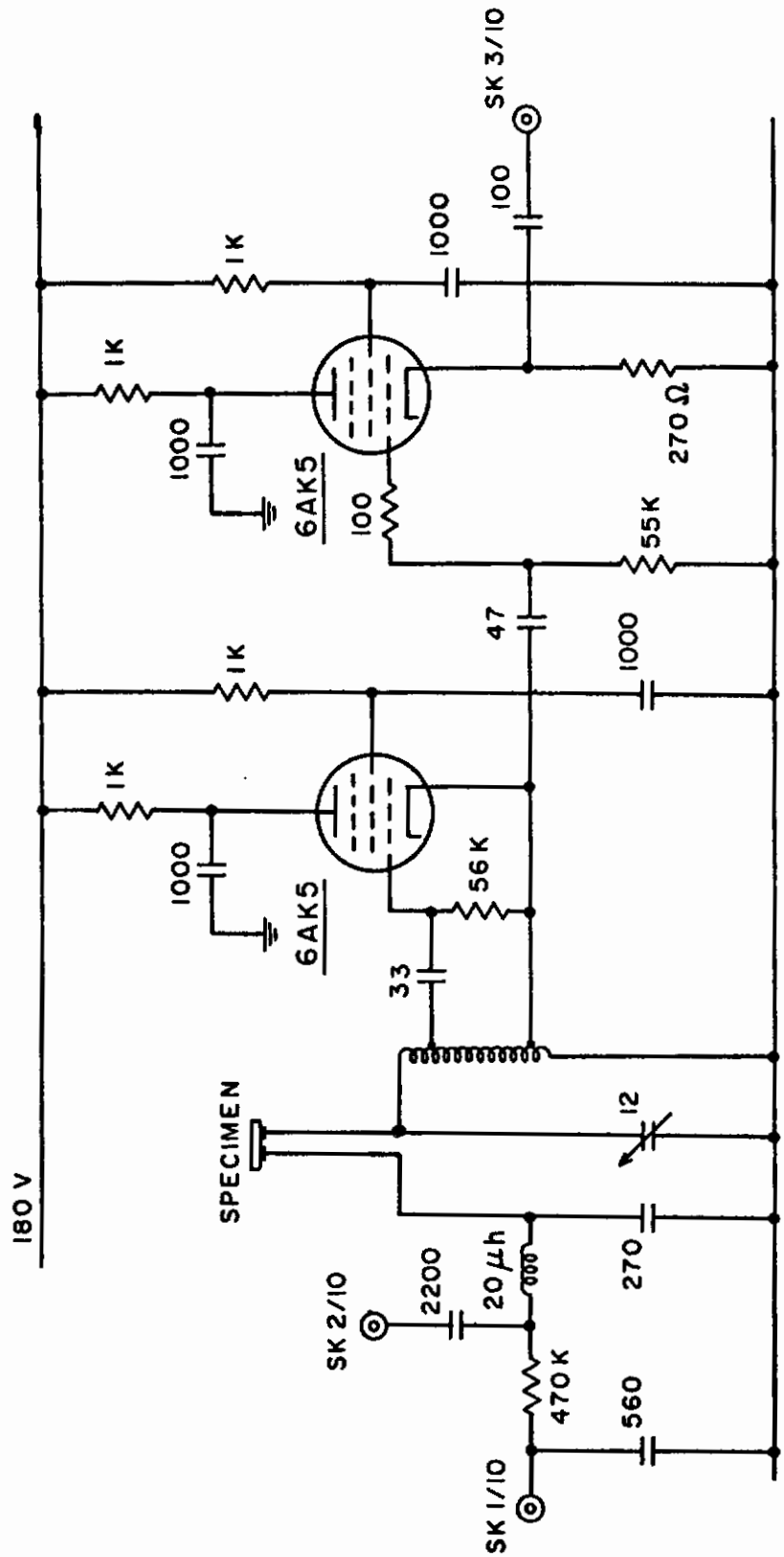

Fig. 5-11 DETECTOR CIRCUIT

Unit 12: Vacuum Gauge and Power Unit

A relatively simple (Veeco type DG-2) Philips vacuum gauge is being used to determine pressure levels in the test enclosure.

The power units are standard commercial units giving stabilized supplies of the following values: 250 v, 160mA; 180 v, 45 mA; 200 v to 800 v, 1 mA; and also 6.3-v heater supplies.

Unit 16: Plug Interchange

Figures 5-11 and 5-12 show this unit. It contains a switch which simultaneously cuts off the drive generator amplifier and the bias supplies, thus removing any interference which might otherwise occur in the recording of the specimen decay-curve. Capacitors can also be switched to slow down the shut-off rate of the bias voltage. This arrangement is needed since for some types of specimen mounting a rapid shut-off was found to produce bouncing of the specimen, with a consequent modulation of the decay curve. A further switch allows monitoring of either the specimen resonance or the frequency divider circuits.

D. Operation of System

To obtain reliable results, it is necessary to reduce the noise to the lowest level and, for the higher values of damping, to have a sufficient broad pass band. The narrowest band gives the greatest noise reduction, although its use would cause considerable error for logarithmic decrements greater than, say, 10^{-4} at 100 kc/s. It is also convenient to use broader bands if the specimen temperature drift is at all rapid, since otherwise the consequent change of frequency during decay can produce an effective change of amplifier gain.

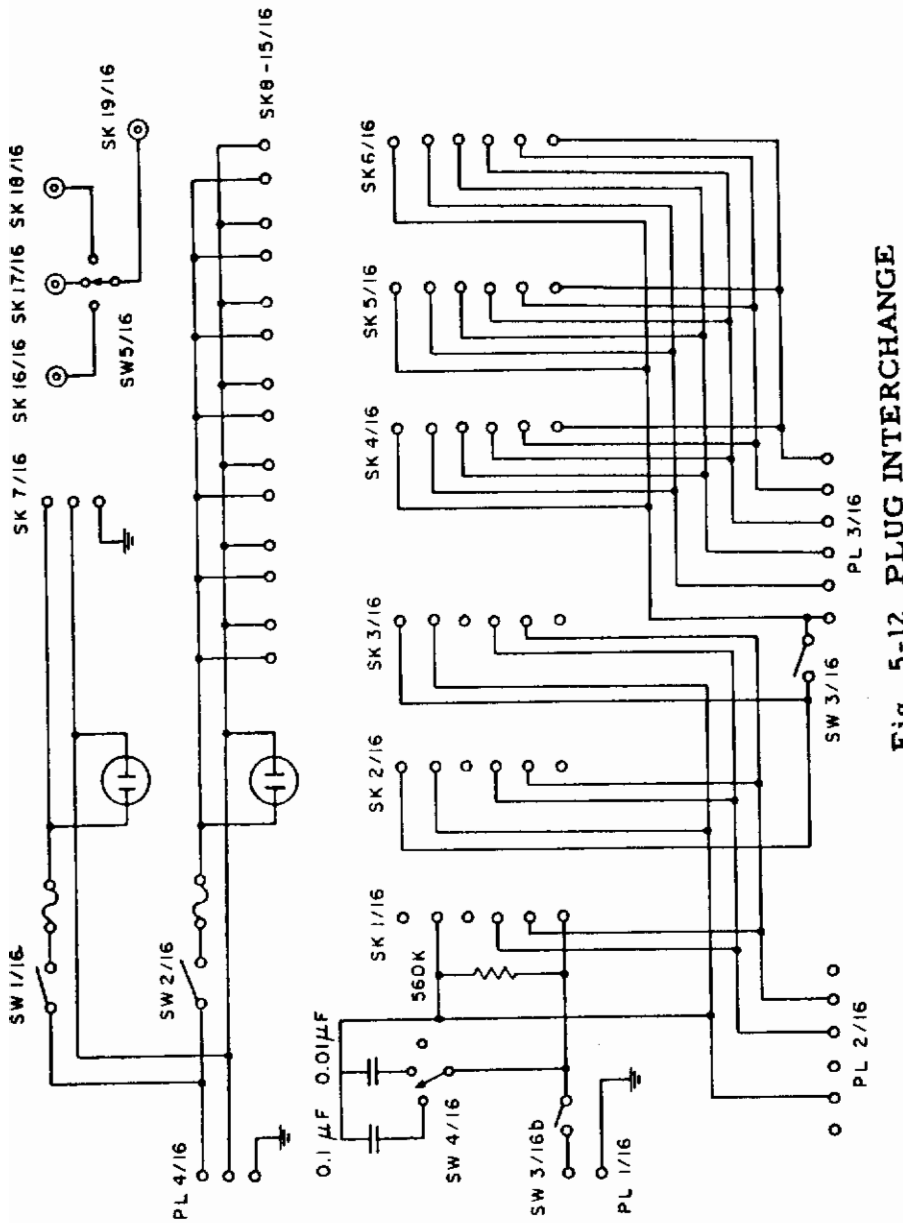

Fig. 5-12 PLUG INTERCHANGE

Fig. 5-13 shows the overall detector curve: Unit 2 meter reading plotted against gap width as read on the micrometer. At a gap width of 0.1 mm, the sensitivity is 5 microvolts per Angstrom. For a gap utilizing a plate and conducting specimen, the sensitivity is about ten times as great. Determination of absolute vibration amplitudes of a heated specimen is not easy, however, since relative movement of the grid wires can change the capacitance and hence produce an uncertainty in the gap width. It is proposed in the future to install a calibrating system.

It has been found necessary to support the specimen by wires passing through holes, to reduce the extraneous damping to a sufficient low value. Four-wire suspension, with the wires gripping either side, was found to be unsuitable. Even with the present system, occasional high values of damping are attributable to wire friction, probably occurring as the wire slips during heating. The background friction, however, with a specimen 20 x 4 x 2 mm, is only about 10^{-6}.

E. Grid Capacitance Change

An analytic form for the capacitance between the sets of grid wires for arbitrary spacing of the dielectric medium would be exceedingly complicated to compute. The argument that follows gives a value for the sensitivity of the system at a spacing which would represent a reasonable working point.

Smythe[5-4] obtained an equation, derived by a conformal transformation method, for the capacity in the fringing field between two sets of bars of width a and spacing g ; this is given by

$$\Delta C = \frac{n \epsilon_o w}{\pi} \left[\left(1 + \frac{a}{g}\right) \ln \left(\frac{4g + 3a}{2g + a} \right) - \frac{1}{4} \frac{a}{g} \ln \frac{a(4g + 3a)}{(2g + a)^2} \right] \qquad (5\text{-}1)$$

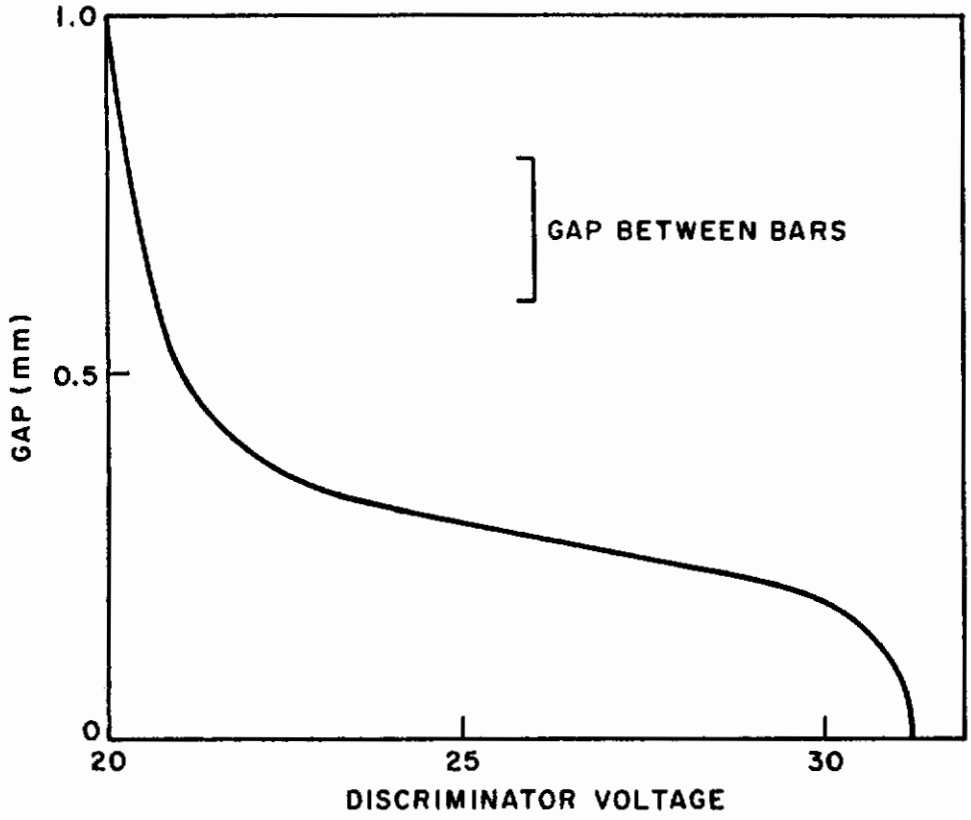

Fig. 5-13 OVERALL DETECTOR CURVE

where ϵ_o is the capacitance of free space, w is the breadth of the grid, and n is the number of gaps.

If we now assume that this fringing field is contined to the region above the grid plane, and that insertion of a medium of dielectric constant, K, in the region does not change the flux distribution below the plane, then the change in capacitance due to the medium will be

$$\delta C = (K - 1) C \qquad (5\text{-}2)$$

If the medium is moved away, it can safely be assumed that at a distance equal to the gap, g, the extra capacity due to the medium will be a fraction of δC, less than, say, one half. Thus, at some point between this spacing and contact, dC/dy will assume the value $\delta C/g$. This point will represent a useful working point.

Inserting values of

$$\begin{aligned} w &= 5 \times 10^{-3} \text{ m} \\ K &= 10 \\ a &= 5g \\ n &= 10 \\ g &= 10^{-4} \text{ m} \end{aligned}$$

into Eq. 5-1, solving for $\triangle C$, and setting $\delta C = g\, dC/dy$, one obtains from Eq. 5-2,

$$\left(\frac{dC}{dy}\right) = 1.3 \times 10^{-7} \text{ Fm}^{-1}$$

and

$$\frac{df}{dy} = \frac{1}{2} \frac{f}{C} \frac{dC}{dy} = 25 \text{ cycles per Angstrom displacement.}$$

3. PREPARATION OF SPECIMENS

Single crystals of MgO used in this study were obtained either from the Norton Company or from Semi-Elements, Inc., with maximum dimensions of the order of one inch. These crystals were cleaved or cut into several parallel specimens. Each specimen is identified by a number containing four digits; the first three digits represent the parent crystal and the last, the specimen itself. Table 5-I gives a spectrochemical analysis for four pieces, 102, 105, and 107 from Norton, and 108 from Semi-Elements. Number 111, mentioned later, also was obtained from Semi-Elements. In some cases, a very slight milkiness or yellow coloration of the crystal was visible.

Table 5-I

SPECTROCHEMICAL ANALYSIS OF SINGLE CRYSTAL MgO SPECIMENS

Specimen	Impurity, (ppm)						
	Al	Ca	Cr	Cu	Fe	Mn	Si
102	1000	600	100	2	600	40	10
105	600	1500	60	2	600	30	5
107	200	1500	60	2	600	40	5
108	200	200	80	2	400	30	5

Two types of specimen shape were used: a beam and a tuning-fork shape. These are shown in Fig. 5-14. The beam specimens were about 2-cm long, 4-mm wide, and were cleaved into sections 1.5 to 3 mm thick. They were used in the fundamental flexural mode of oscillation supported through 0.01-in. holes drilled ultrasonically through at the nodes ($0.224\,\ell$ from the end). The fundamental natural frequency of these varied between 20 and 50 kc/s, as obtained from the Rayleigh formula (valid for shallow beams):

$$f = \frac{9\pi}{8\sqrt{3}} \sqrt{\frac{E}{\rho}} \frac{d}{\ell^2} \qquad (5\text{-}2)$$

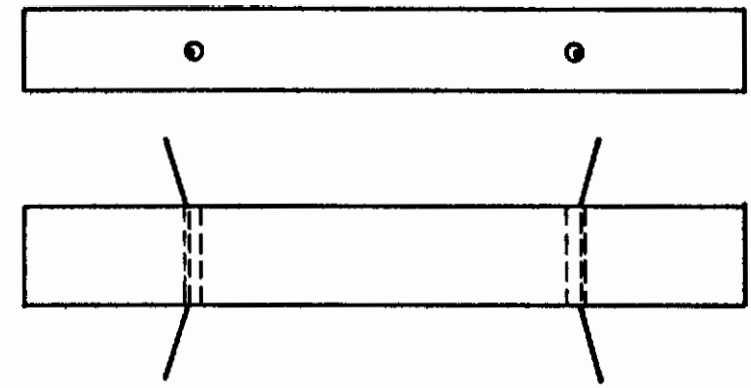

(a) BEAM

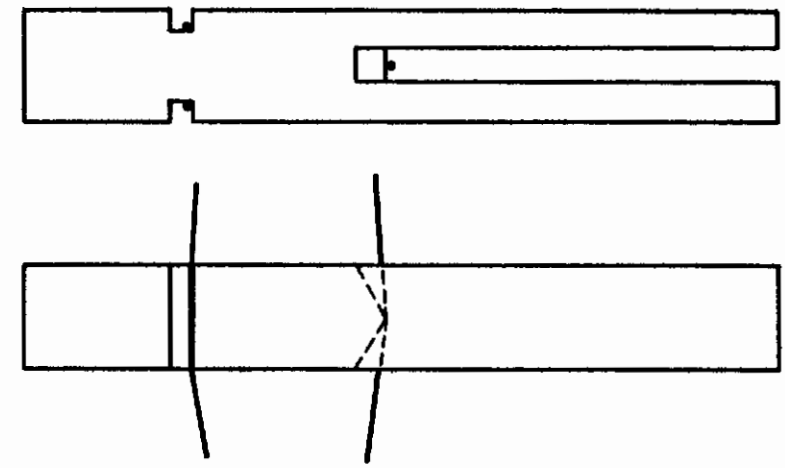

(b) TUNING FORK

Fig. 5-14 SHAPES OF SPECIMENS

The tuning-fork specimen was also about 2-cm long, and was cut to shape with a diamond wheel. Since it effectively consists of a pair of bars in fixed-free vibration, a much lower frequency can be obtained for a bar of given thickness. However, support difficulties are much greater; not only is the support weak due to the one-sided arrangement (allowing an exaggerated bouncing of the bar to occur), but the stem of the fork is not a true node. Hence, losses along the mounting wires are much greater than in the case of a straight bar.

Dislocations were introduced by bending at room temperature, using the method of Stokes[5-5]. Bars were cleaved slightly oversize, etched for 4 min in boiling orthophosphoric acid, being suspended by light end-clamps, and then washed immediately in boiling water. After sprinkling with 200-mesh silicon carbide, the bars were bent through an angle of several degrees (judged by eye) in a 3-point device which applied a constant load (lever, bucket and lead shot). Upon removal of the specimen the bend angle measured, and the procedure repeated to bend the specimen straight again. Yield stresses were quite consistent for all samples. Figure 5-15 shows a plot of applied moment versus beam thickness; the variation is, as expected, close to the square of the thickness.

Immediately prior to mounting in the apparatus, specimens were etched for about 1 hour in HCl + NH_4Cl. This is a slow, non-polishing etch, employed so that any small cracks, say around the support holes, would be opened up until the sides did not touch during specimen oscillation. Thus, excess damping due to the cracks would be eliminated without removing too much material. In addition, etch-pits on the deformed crystals revealed the slip line pattern, although the pits were usually too closely spaced to show the individual dislocations.

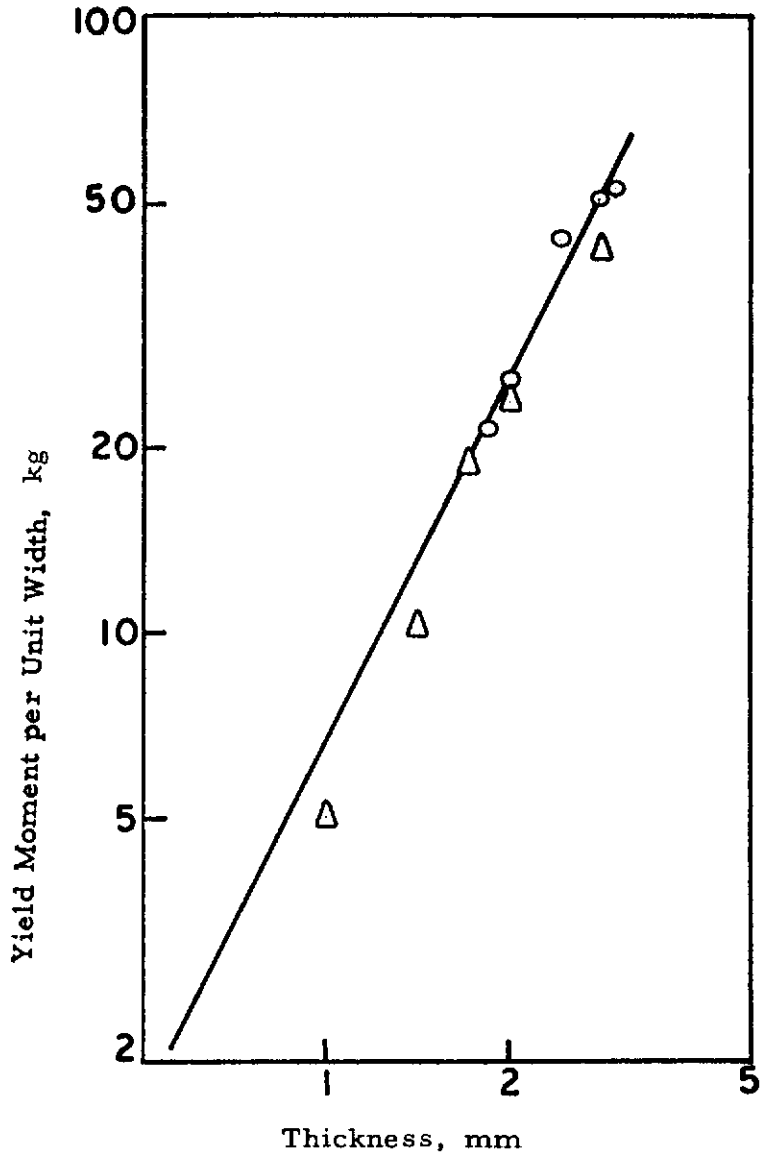

Fig. 5-15 YIELD MOMENT VS. BEAM THICKNESS FOR MgO SINGLE CRYSTALS AT ROOM TEMPERATURE

4. EXPERIMENTAL RESULTS AND DISCUSSION

A. Amplitude Independent Dislocation Damping

In general, the internal friction was found to be a function of amplitude of oscillation, increasing at the higher amplitudes. Figure 5-16 shows a typical curve. It is here tentatively assumed that this curve is composed of two more or less independent components; an amplitude independent part, Δ_I; and an amplitude-dependent component, Δ_H, which becomes effective above a certain amplitude. Thus,

$$\Delta = \Delta_I + \Delta_H \qquad (5\text{-}3)$$

Delta$_I$ is associated here with dislocation relaxation; Δ_H, which will be discussed in the following section is identified with breakaway.

Amplitude independent dislocation damping in deformed metals and semi-conductors usually shows a strong temperature dependence. At low temperatures, the Bordoni peak[5-6, 5-7], appears, due to thermal excitation across the Peierls force barrier, while at higher temperatures there is a rapid rise of damping[5-8, 5-9]. Reports on dislocation damping are not very numerous in ionic materials. Work in NaCl at room temperature[5-10, 5-11] has shown that the Granato-Lucke[5-12] theory successfully explains the annealing of dislocation damping by condensation of vacancies produced by plastic deformation or X-irradiation. At lower temperatures, results in other alkali halides[5-13, 5-14] have shown the importance of electronic and ionization processes in pinning dislocations. Except in the rather limited relaxation region, the temperature dependence of damping below room temperature was found to be small. A detailed investigation of the temperature dependence of damping in the alkali halides above room temperature has, however, yet to be made.

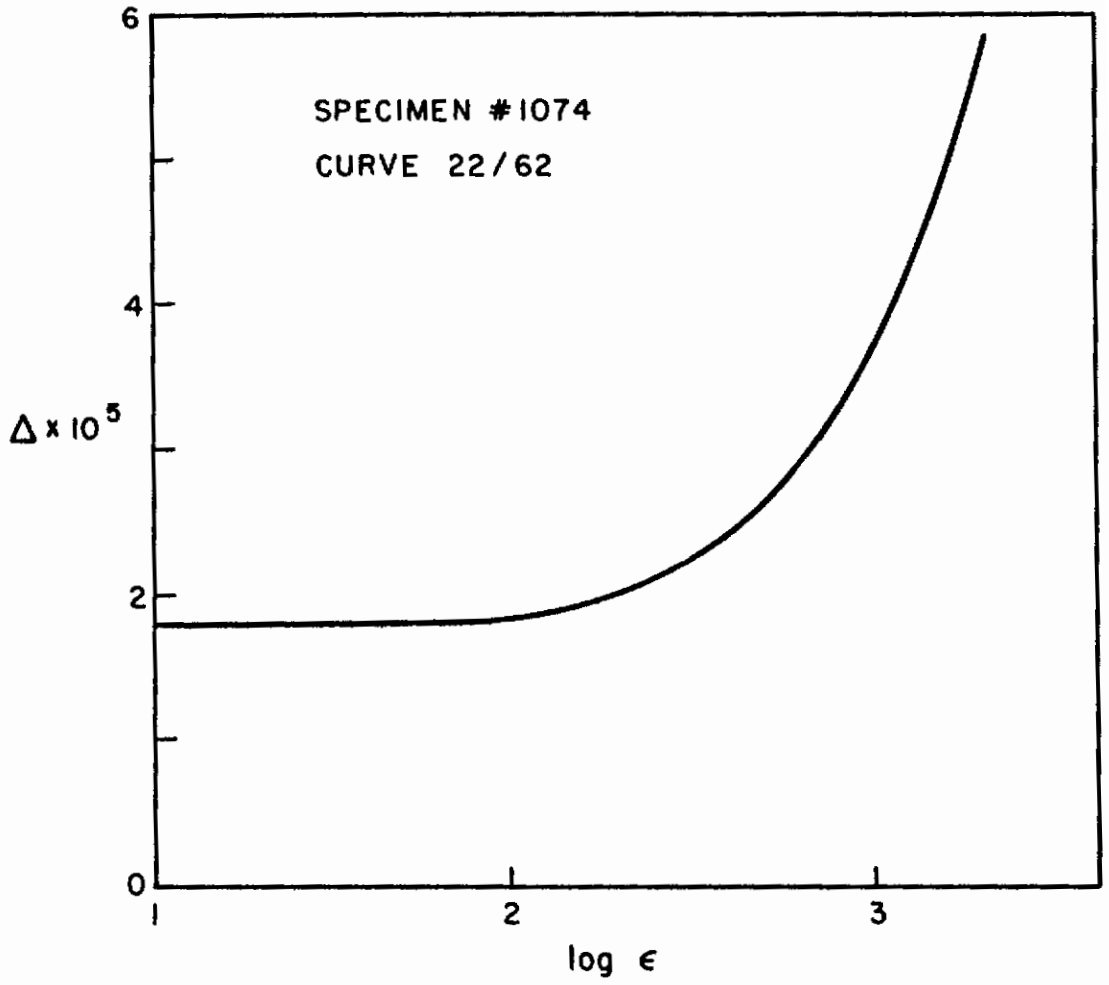

Fig. 5-16 AMPLITUDE DEPENDENCE OF LOG. DEC.

Results to date on MgO are interesting in that the temperature dependence of dislocation damping appears to be rather small. Typical curves are shown in Fig. 5-17 and 5-18, presenting sequential dislocation damping measurements taken during warm-up, anneal, and cooling for three specimens. The amplitude independent Δ_I is shown. It is evident that the curve shape is repeatable, varying only in a factor of proportionality for different anneals and original deformations. Above 400°C, annealing occurs too rapidly to allow accurate determination of the curve.

The Granato-Lucke theory of dislocation relaxation sets up the equation of motion for the dislocation as

$$A\frac{\partial^2 \xi}{\partial t^2} + B\frac{\partial \xi}{\partial t} - C\frac{\partial^2 \xi}{\partial y^2} = b\,\sigma\,, \qquad (5\text{-}4)$$

ξ being the dislocation displacement at y along its length, b the Burgers vector and σ the applied stress. B is a damping constant, and its temperature independence determines the variation of internal friction with temperature. Either the Seeger[5-7] or the Weertman[5-8] mechanisms of damping, however, give too rapid a temperature variation to fit the experimental curves. Attempts have been made to broaden the peaks produced by these mechanisms until a better fit is produced; however, it appears that unreasonably large variations of dislocation behavior within a given specimen are required to account for the curve in this manner. This situation points out the need to develop a new theoretical mechanism giving a temperature-independent B in ionic crystals. This line will be pursued in future work.

The kinetics of annealing also present an unsolved problem. It was hoped to extract an activation energy for the process by comparing anneal rates at different temperatures for similar crystals. Figure 5-19 shows the decremental damping as a function of annealing

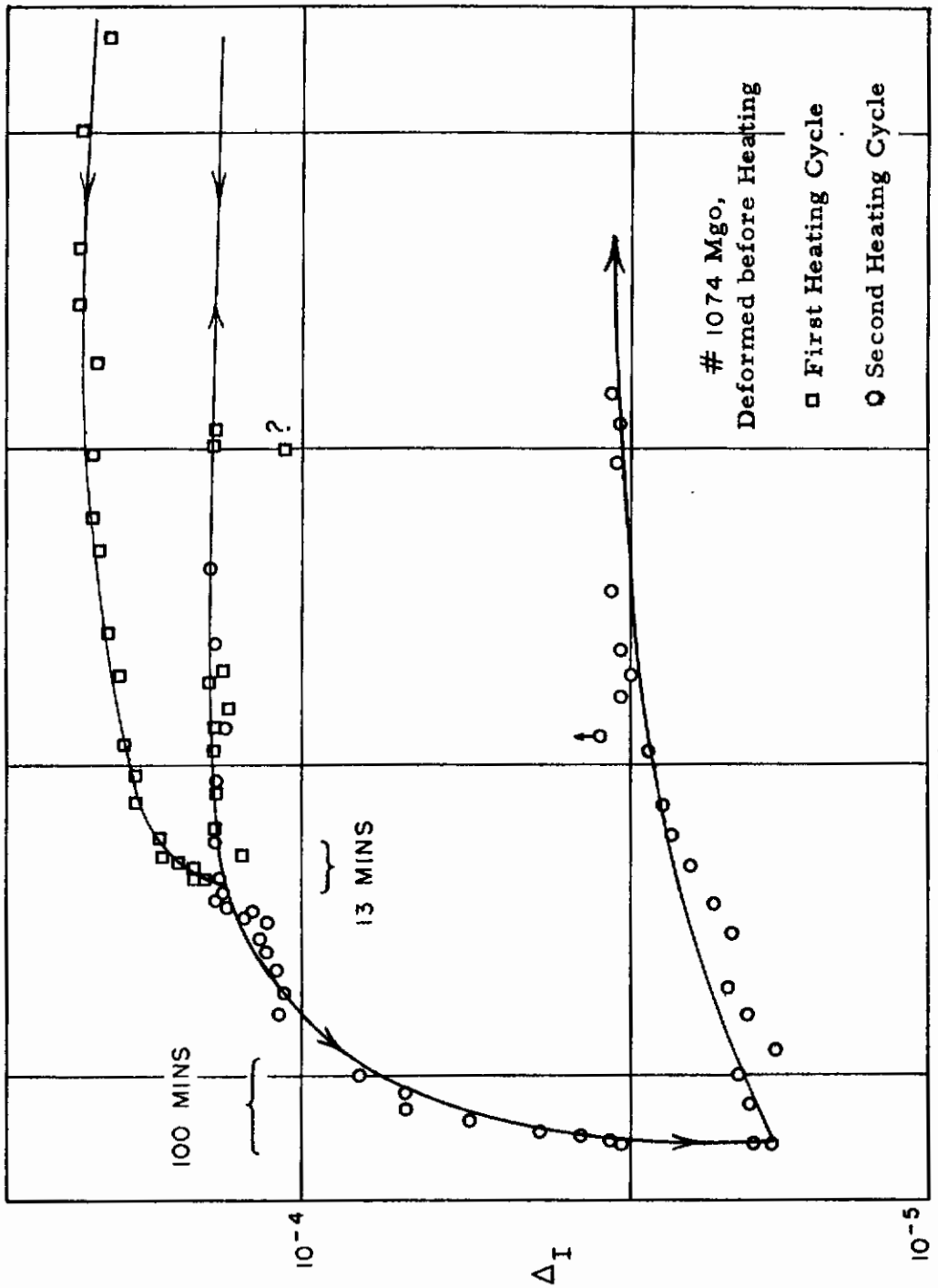

Fig. 5-17 DISLOCATION DAMPING IN A DEFORMED SPECIMEN

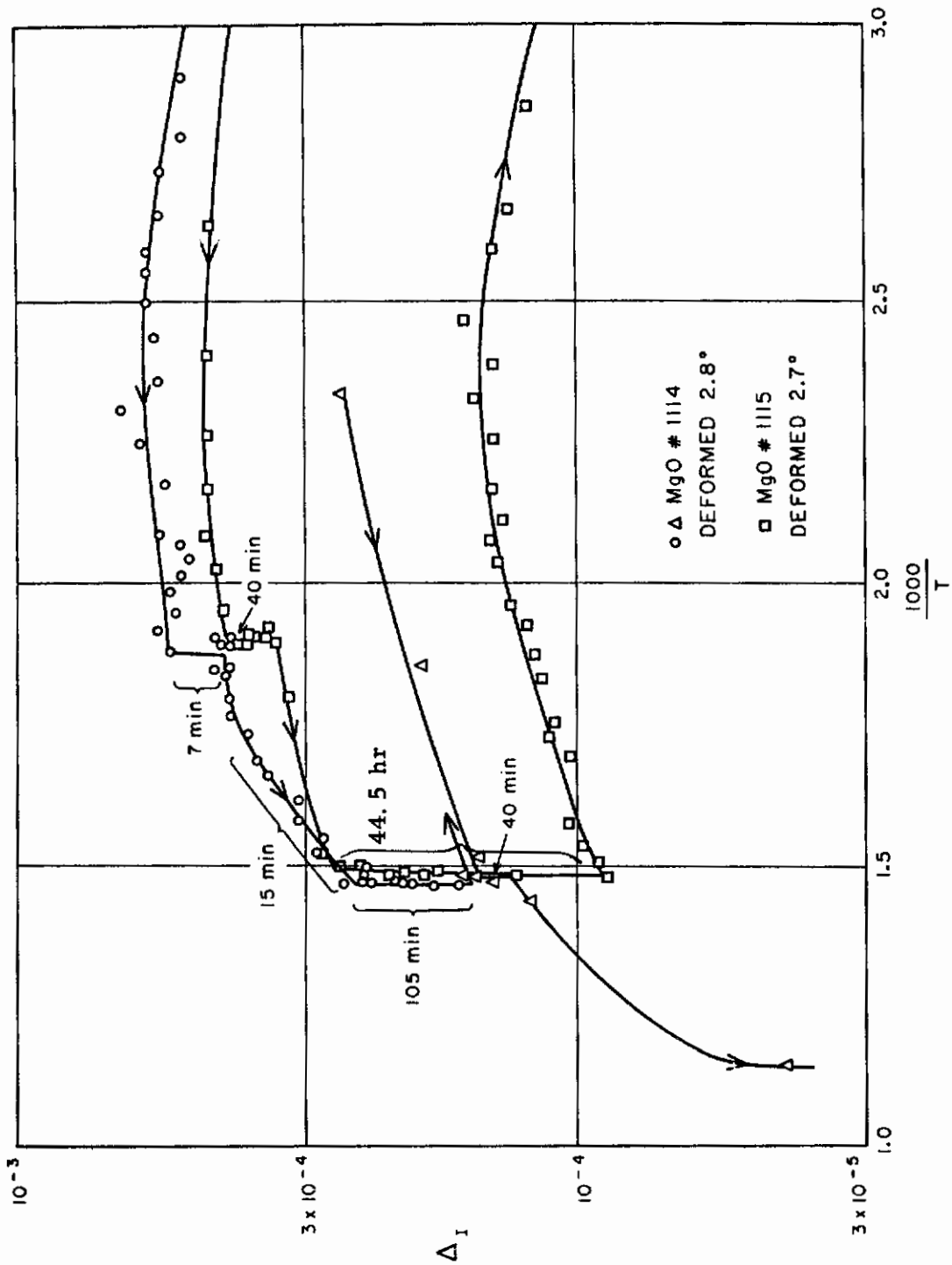

Fig. 5-18 DISLOCATION DAMPING IN A DEFORMED SPECIMEN

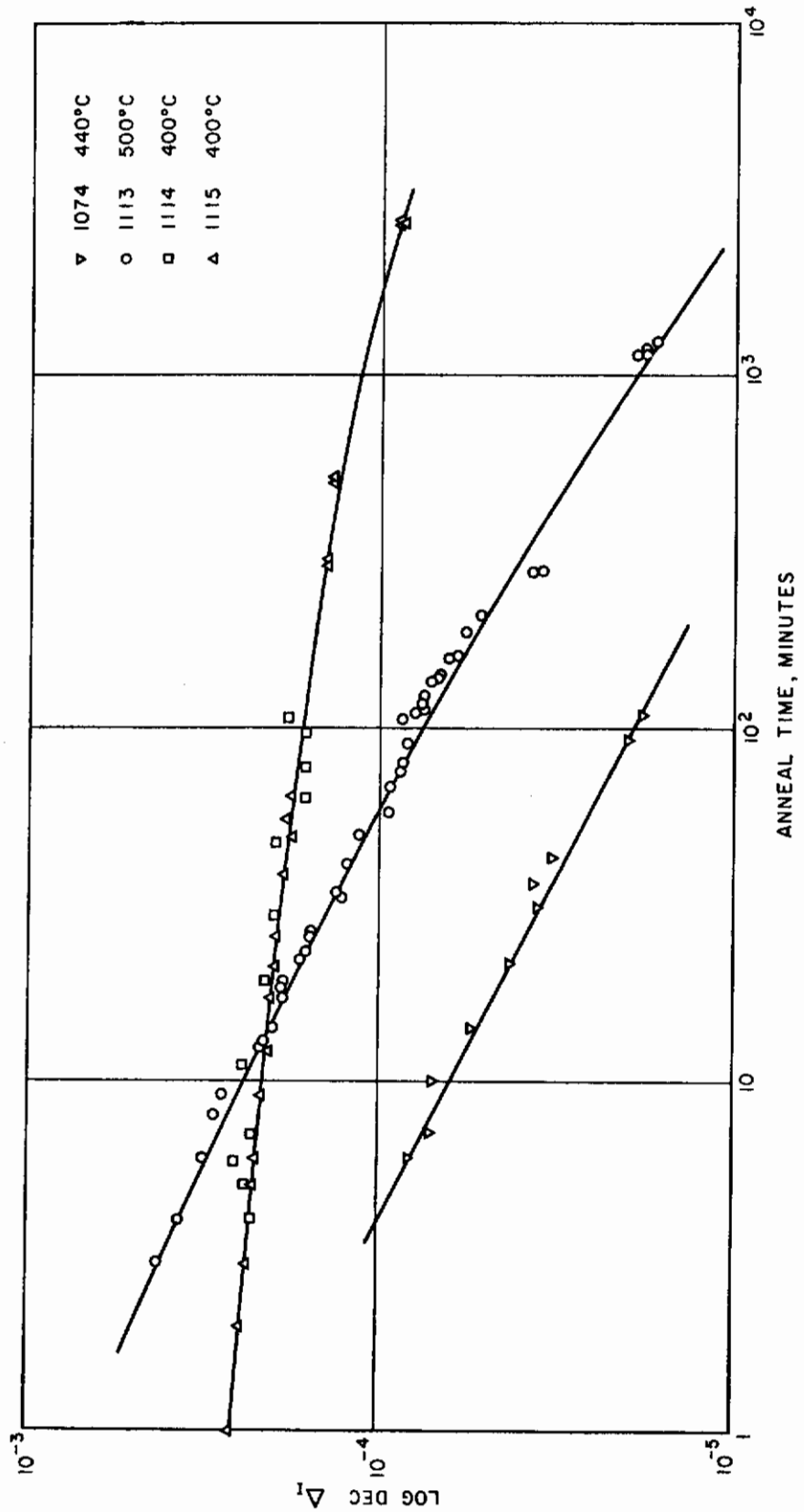

Fig. 5-19 ANNEALING OF DISLOCATION DAMPING FOR FOUR SPECIMENS

time for four specimens. Examination of the curves reveals that, if vacancy or impurity condensation is occurring, more than one process must be involved in the anneal, since an increase of temperature for a single process would shift the curve only to the left [5-9]; the observed increase of slope (on this log-log plot) between specimens 1115 at 400° and 1113 at 500° would not be produced. On the other hand, it is possible that dislocation recombination or interaction of some kind is occurring. In this case, the somewhat higher dislocation density of 1113 (deformed through twice the angle of 1115) might account for the higher slope. However, the slope of 1074 is almost as high as that of 1113 although it was annealed well below 500°C, and was bent through only 1.2°. Obviously more data are required. It should be noted that the curves can in no way be fitted to the formula of Granato[5-10]

$$\Delta_I = \text{const.}\ (1 - \beta\, t^{2/3})^{-4} \qquad (5\text{-}5)$$

since a plot of $\Delta_I^{-1/4}$ vs. $t^{2/3}$ deviates markedly from the linear for both 1113 and 1115.

Further anneal at 750°C caused a drop in Δ_I of the Norton crystal down to much the same values seen in the undeformed crystal. Figure 5-20 shows a comparison of the two crystals over the range 100°C to 600°C. A similar anneal in one of the purer Semi-Elements crystals, however, did not reduce Δ_I to the same low value. This indicated that impurity precipitation on dislocations is a likely mechanism producing the locking. Because of insufficient measurements, the kinetics of this precipitation cannot be evaluated at present.

B. Amplitude Dependent Dislocation Damping

Nearly all measurements show some amplitude dependence of Δ. Although it is present in undeformed specimens, its enhancement by plastic deformation indicates that it is almost certainly produced by dislocations. According to the Granato-Lucke theory[5-11],

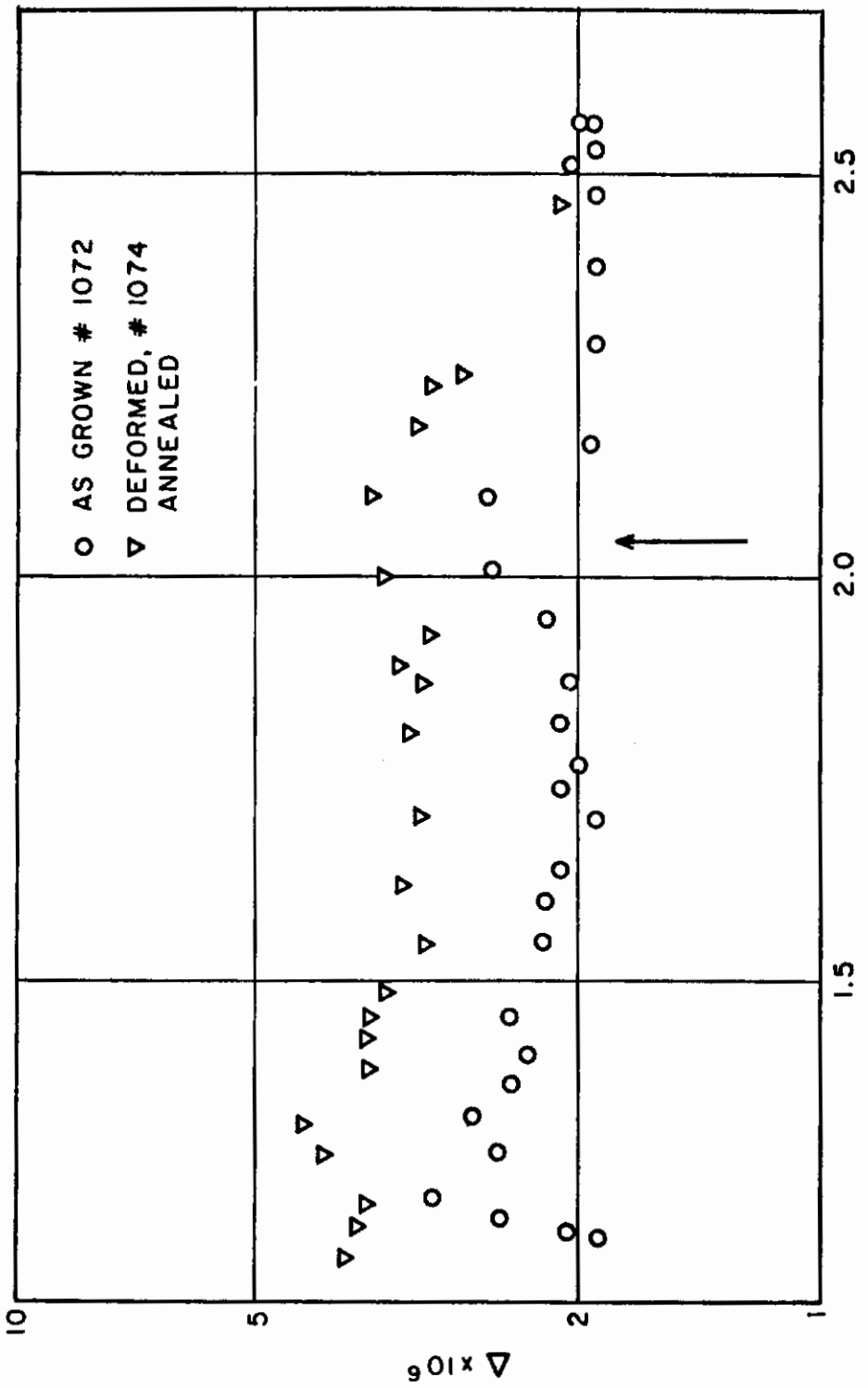

Fig. 5-20 TEMPERATURE DEPENDENCE OF DAMPING AFTER COMPLETE ANNEAL OF DEFORMED SPECIMEN

log ($\Delta_H \epsilon$) should be proportional to $1/\epsilon$, where ϵ is the strain amplitude. Figure 5-21 shows a plot for the amplitude dependence of damping, taken at different stages of anneal. Over three decades of $\Delta_H \epsilon$ are covered, and nowhere does a linear portion of the plot appear. This is contrary to reports on NaCl (5-11, 5-12), although a smaller range of amplitude was covered in the latter, possibly concealing the nonlinearity. The lack of fit of the MgO data to the formula makes it difficult to interpret, or even present, annealing data on dislocation break-away in a systematic fashion.

In the Norton specimens, annealing above 600°C removed amplitude dependence. However, it was observed that after a 5-min anneal at 1000°C, amplitude dependent damping reappeared in one specimen. It is suggested that impurity precipitates may have become redispersed by the anneal, partially freeing the formerly firmly locked dislocations.

C. Relaxation of Impurity-Vacancy Complexes

Lidiard[5-13] has discussed a form of dielectric relaxation in alkali halides which involves reorientation of vacancy-impurity pairs ("complexes"). Anion vacancies in an ionic lattice carry an effective negative change, and hence tend to become bound to positively ionized impurities. Figure 5-22 shows the situation when the vacancy is a nearest neighbor, which can then diffuse to one of four sites. The mechanical relaxation in MgO is similar to the dielectric relaxation, based on the fact that a stress in [100] will enhance the diffusional jumps shown in Fig. 5-22. The relaxation peak produced as a function of temperature in a specimen vibrating at 45 kc/s is shown in Fig. 5-23. The points are experimental, while the theoretical curve has the form

$$\Delta = \Delta_I + \frac{\text{const.}}{T} \cdot \frac{\omega\tau}{1+\omega^2\tau^2} \qquad (5\text{-}6)$$

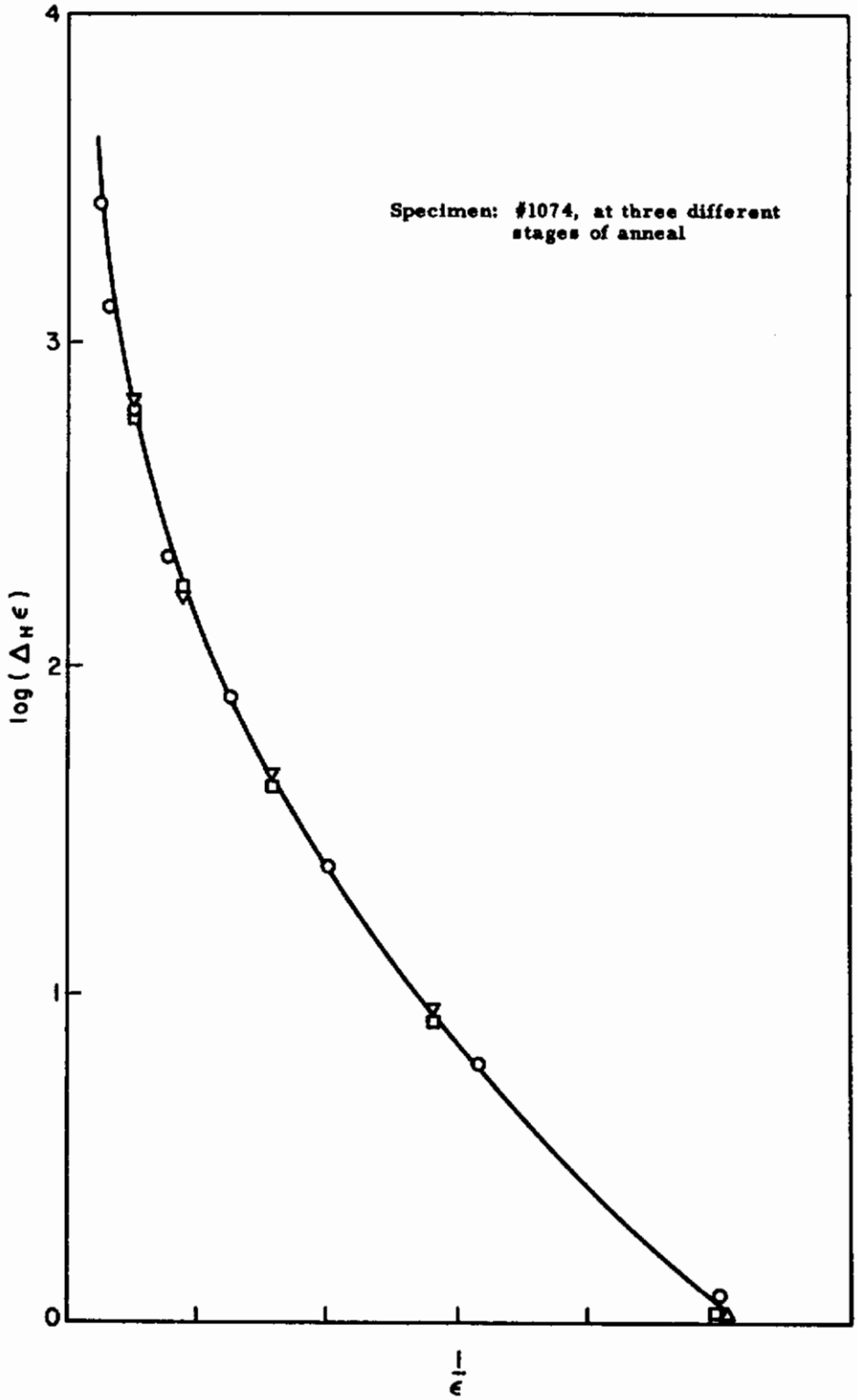

Fig. 5-21 CHECK ON GRANATE-LUCKE RELATION

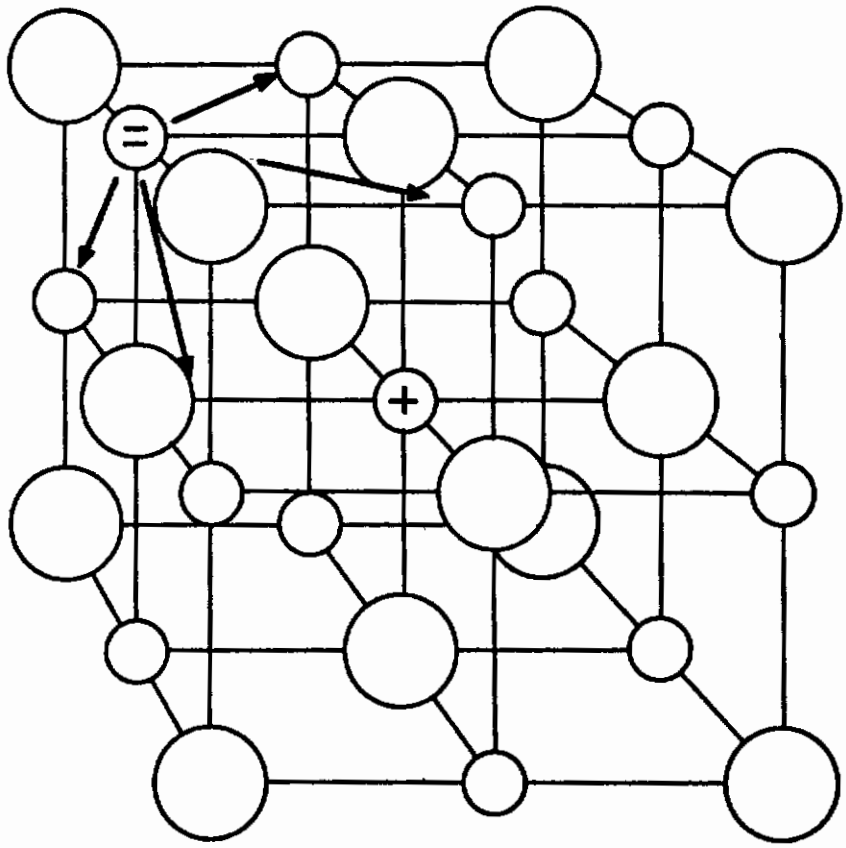

Fig. 5-22 GEOMETRY OF IMPURITY-VACANCY COMPLEX

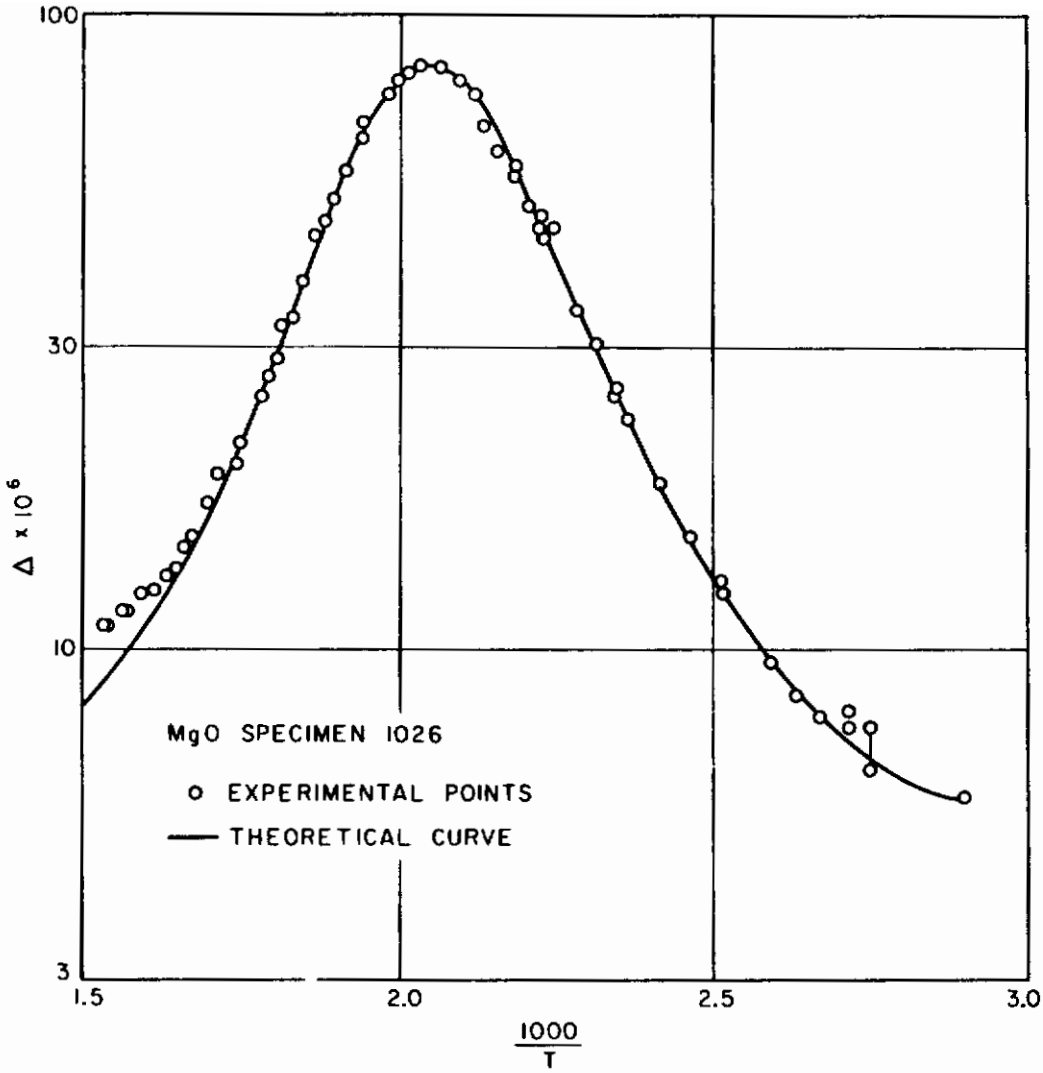

Fig. 5-23 RELAXATION PEAK OF COMPLEX AT 45 kc/s

Δ_I being a constant background damping and the relaxation time τ being put equal to $[\tau_0 \exp (H/kT)]$. From this curve we obtain $H = 0.62$ ev and $\tau_0 = 5 \times 10^{-12}$ sec. The peak has also been measured at a lower frequency in the tuning-fork specimen (Fig. 5-24) which was cut parallel to the previous specimen. As expected, the peak is of identical height and shape, although the background damping is greater. From the shift of the peak temperature the activation energy may also be derived using $\ln (\omega_1 / \omega_2) = \delta (H/kT)$. A value of 0.635 ev is obtained, in satisfactory agreement with the value from the peak shape. No independent estimates of vacancy migration energy are known, however, against which to check the values.

The peak does not attain its full height, or appear at all in some cases, until annealing at an elevated temperature is carried out. Five minutes at 1000°C was found to be adequate: indeed, the lower limit of annealing time requirement, although not explored during a few somewhat limited tests, appears to be less than one minute. This is quite consistent with diffusion, from the surface, of vacancies with an activation energy of about 0.62 ev. The reason for the reduced peak in as-grown crystals lies in the lower temperature anneal, during which the complexes dissociate. Several hours are required for this at 400°C, and during the normal process of crystal growth the cooling rate is indeed this slow. Some study has been made of the anneal characteristics; Fig. 5-25 shows a tentative anneal curve at 600°C. The initial Δ was 8.3×10^{-5} and the final, 3.4×10^{-5}; the linearity of the curve connecting the three intermediate points is not firmly established at this stage. A time constant of about 100 min is derived, which is longer than would be expected from the diffusion of vacancies to the surface with an activation energy of 0.62 ev, suggesting that some delaying process such as charge trapping may be occurring.

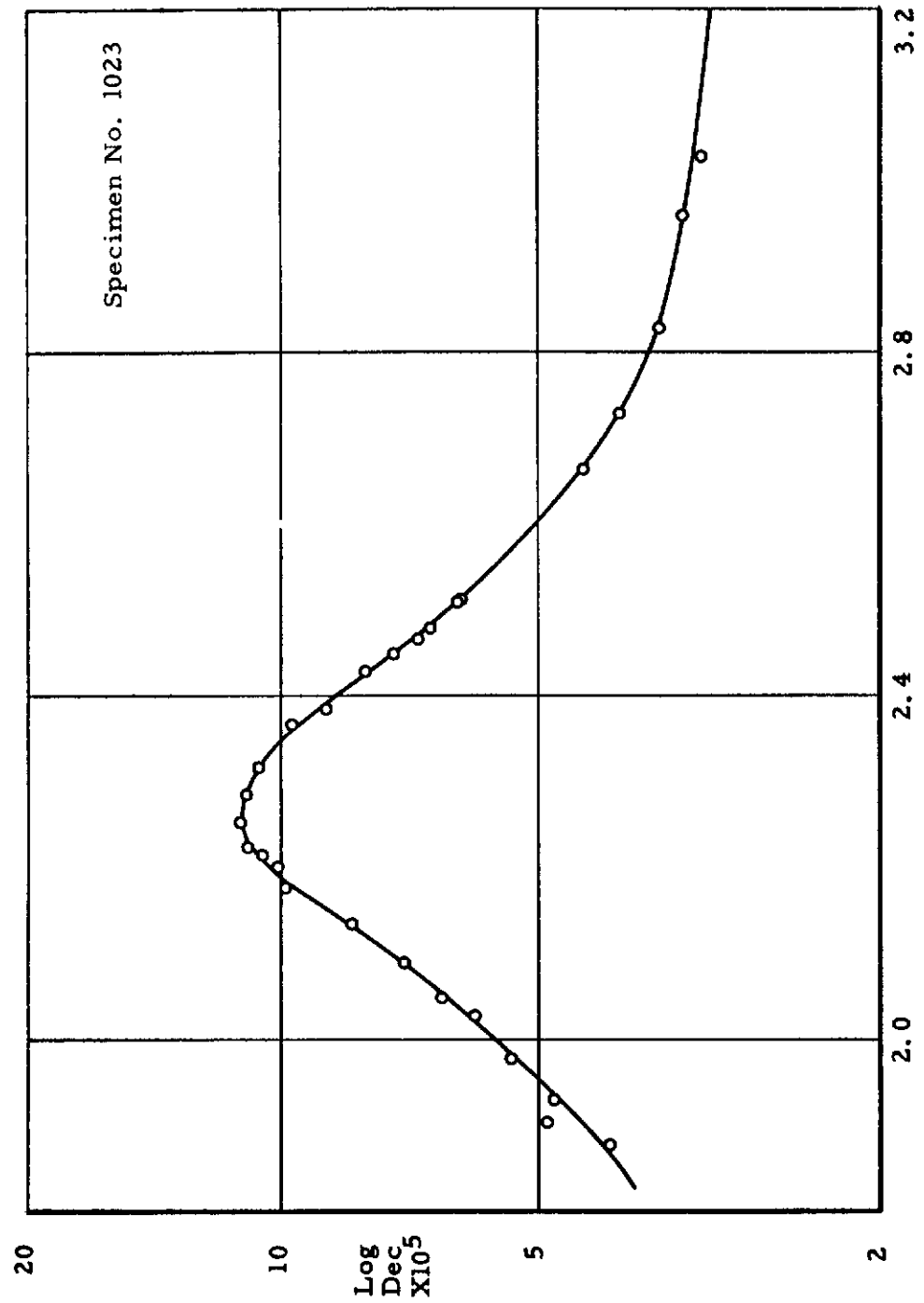

Fig. 5-24 RELAXATION PEAK OF COMPLEX AT 8.3 kc/s

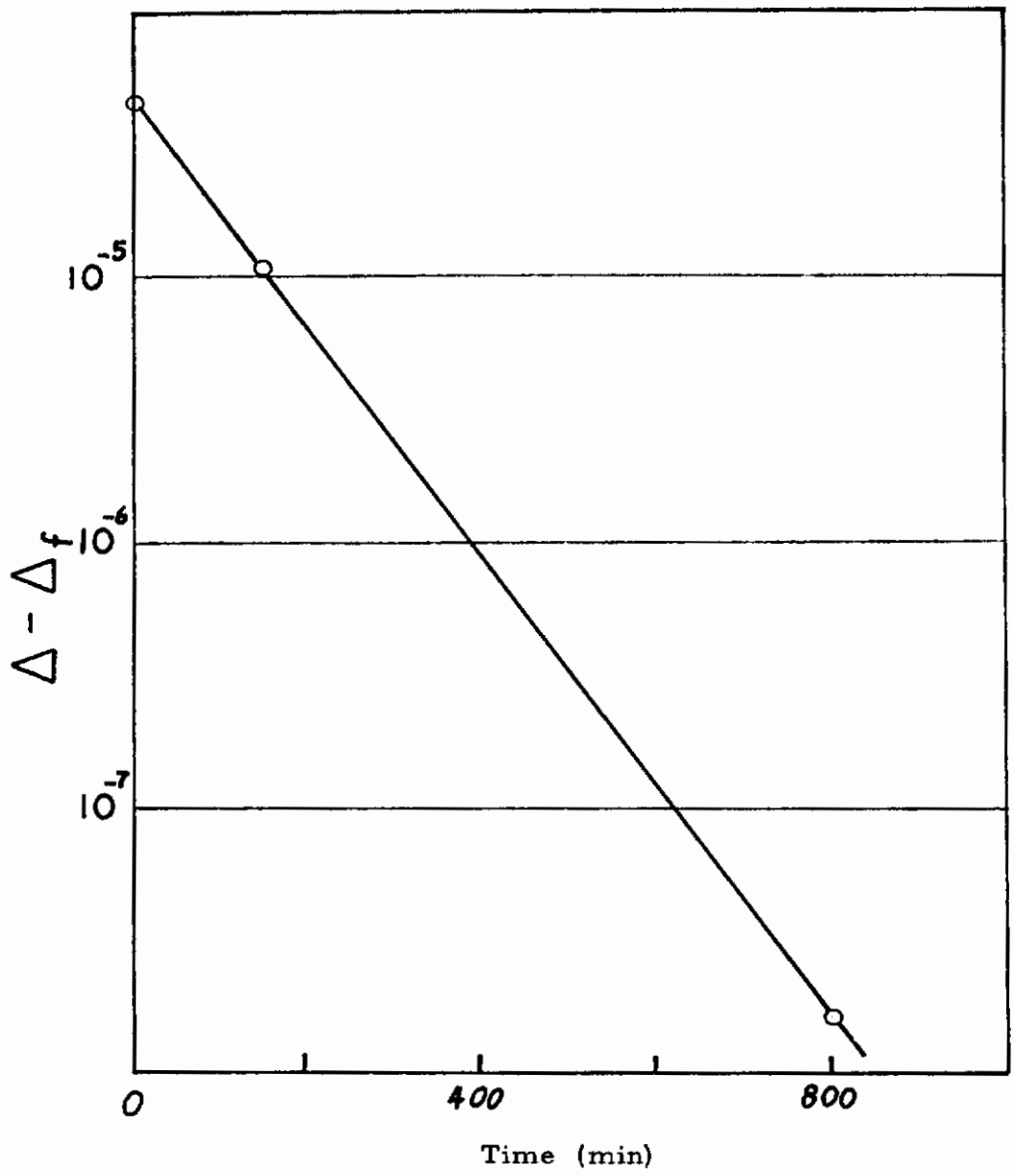

Fig. 5-25 ANNEALING OF RELAXATION PEAK OF COMPLEX

A surprising and interesting feature of the relaxation is the value of τ_o. Analysis of the geometry of the relaxation, following Lidiard,[5-13] shows that this would be expected to be 1/6 of the attempt period for vacancy jumps, i.e., h/6kT multiplied by an entropy factor exp (S/k), where S = (H/E) (dE/dT). Calculation gives a value 10^{-13}, significantly less than that derived from the relaxation peak. No discrepancy appears in the value of τ_o for dielectric relaxation in NaCl[5-14], and so one must search for some difference between the two cases. Two such differences come to mind. In the first place, charge compensation is not complete in MgO as in NaCl, since the effective negative charge of a magnesium vacancy is two while a trivalent impurity will carry only a single excess charge. Neutralization of the complex could be achieved by an extra trapped hole. For trivalent chromium, the epr spectrum of the complex has been studied by Wertz and Auzins[5-15]; however, there was no evidence of hole trapping. In either case, the nature of the complex will be affected by the charge disparity, and the binding will be somewhat weakened. The second difference is deduced from the shape of the relaxation curve, which fits a single activation energy. This indicates that the proportion of complexes would have a slightly different energy, and so distort the shape of the relaxation peak. Further study is required to discover the detailed nature of these differences and correlate them with the τ_o discrepancy.

Electron spin resonance spectra of two specimens have been taken in an endeavor to identify the impurities responsible for the peak. However, although there was a large difference in the heights of the relaxation peaks, hardly any significant differences between the spectra were visible. The spectra are dominated by the tall narrow lines of divalent manganese[5-16].

Table 5-11 shows the concentration of the various atomic species deduced from the epr spectra (within a factor of 3) compared

Table 5-II

ANALYSIS FROM ESR AND OPTICAL SPECTRA

	Specimen 1026	Specimen 1072
ESR Spectra		
Mn^{2+}	4×10^{-5}	4×10^{-5}
Fe^{3+} (cubic field)	8×10^{-5}	3.2×10^{-5}
Cr^{3+} (cubic field)	2.5×10^{-6}	4×10^{-6}
Cr^{3+} (100 field)	6×10^{-7}	5×10^{-7}
Cr^{3+} (110 field)	1.6×10^{-7}	-----
Optical Spectra		
Mn	4×10^{-5}	4×10^{-5}
Fe	6×10^{-4}	6×10^{-4}
Cr	1×10^{-4}	6×10^{-5}

with the spectrographic analysis ($\pm$50%). Specimen 1026 showed a 200° relaxation peak forty times the magnitude of that of 1072. It has been assumed that all the manganese was divalent, and the concentration of this has been equated in epr and spectrographic analysis. Discrepancies exist in the concentrations of both iron and chromium. In the case of chromium, the difference may be in the divalent chromium, and in the case of iron either in the divalent iron or the iron in a non-cubic field, the spectrum of which was not observed. In any case, the low concentration of chromium in the [110] directed field (specimen 1026) would be extremely unlikely to account for the mechanical relaxation peak observed. Differences between the concentrations of the species given in Table II for specimens 1026 and 1072 are, in fact, surprisingly small. A further anomaly was seen, however, in the fine structure of the Mn^{2+} spectrum. The ratio of

the strengths of the central line to the strongest satellite was 0.95 for specimen 1026 and 2.5 for 1072, whereas the theoretical ratio is 1.13. It is likely that the difference indicates a large concentration of some paramagnetic impurity, not observed in the epr spectrum due to either very large line width or location outside the range covered.

There is a possible relationship between the annealing of complexes and dislocation damping. Both annealing processes occur at a similar rate in a similar temperature range, and it is very likely that dislocations become pinned by the capture of vacancies which have been released from complexes. The concentration of complexes may be of the order of 10^{-5}, which would give one vacancy for every ten atom sites along a dislocation line (assuming a dislocation density of 10^{10} cm^{-2}), an adequate number to pin firmly the existing dislocations. The faster dislocation pinning seen in the more impure samples may well reflect the greater rate of vacancy production. Thus, reduction of the trivalent impurity concentration below a certain level could starve the lattice of vacancies and thus raise the temperature at which hardening of a deformed specimen occurred.

D. Higher Temperature Processes

Above 600°C, most of the damping due to dislocations introduced by low temperature deformation has been annealed out. A further peak is now seen near 860°C, as shown in Fig. 5-25 to 5-27. There is no indication as to the origin of this peak, although it seems rather broad to fit a simple relaxation mechanism. The previous deformation of specimen 1074 may account for the slightly greater peak height in this specimen, although the difference is very small. Heating to 1050°C has reduced the general background damping of specimen 1026, but the peak has been affected little, if at all.

Above this peak, a further rise of Δ occurs, which reduces on anneal. This is no larger in the deformed specimen than in the

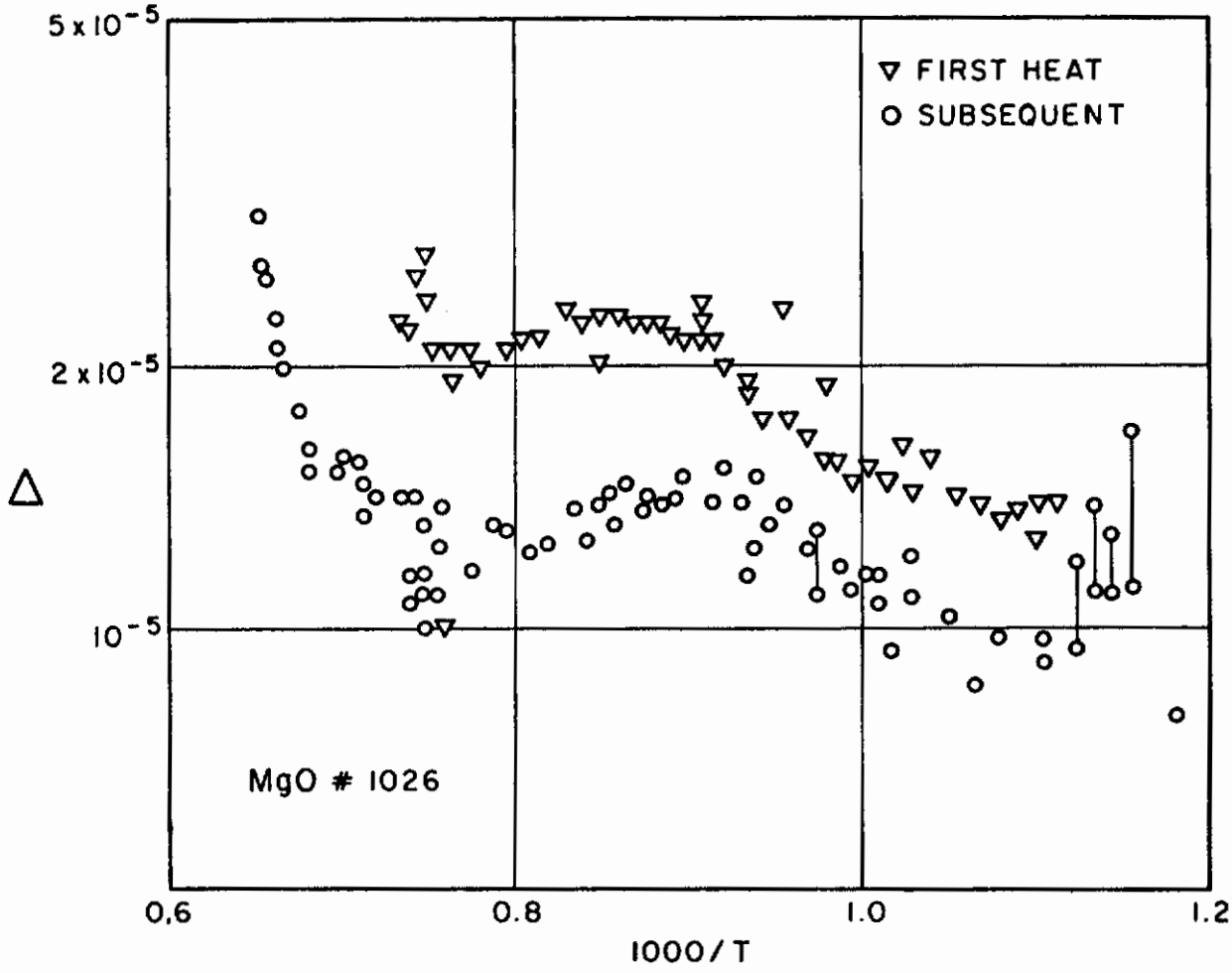

Fig. 5-26 HIGH TEMPERATURE BEHAVIOR OF SPECIMEN NO. 1026

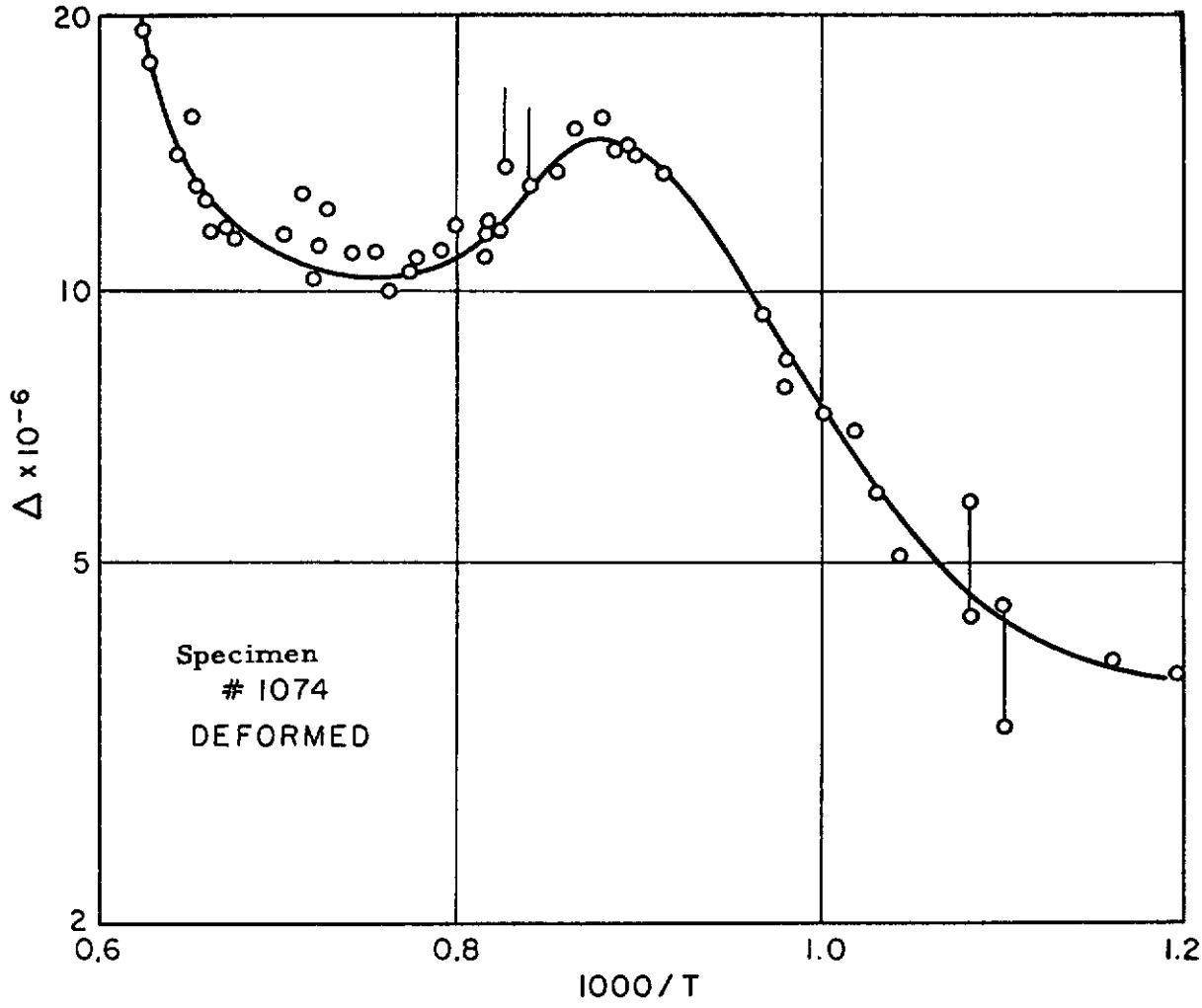

Fig. 5-27 HIGH-TEMPERATURE BEHAVIOR OF SPECIMEN NO. 1076

undeformed, and so cannot be due to unpinning of dislocations with an accompanying Weertman-type damping. More accurate data is required in this region.

5. CONCLUSIONS

Even though the work described here represents only the initial phase of the investigation on internal friction of MgO crystals, the following points have already been established as a result of research conducted on this Task:

A. Dislocation damping, both amplitude independent and dependent, can be created by deforming a specimen at room temperature. Between room temperature and 500°C the damping depends only slightly upon temperature. None of the existing theories of dislocation damping can satisfactorily explain the lack of temperature dependence.

B. Analysis of the amplitude dependent component shows that the derailed predictions of the Granato-Lucke break-away theory are not fulfilled.

C. Annealing of the dislocation damping occurs with increasing speed above 400°C, and is a function of specimen purity or dislocation damping. The law of anneal differs from that previously observed for sodium chloride.

D. Complexes consisting of trivalent impurity (iron?) vacancy pairs give a relaxation peak at 230°C (45 kc/s). The activation energy is 0.63 ± 0.02 ev. The value of the attempt frequency of relaxation is somewhat anomalous.

E. Complexes are created by a short anneal at above 1000°C, while anneals at lower temperatures cause them to dissociate until an equilibrium concentration is reached. It is not clear whether atoms or electronic processes govern the dissociation rate.

F. A small peak appears at 860°C, of much the same height in as-grown as in deformed samples. The origin is not yet known.

It is evident that more work, both experimental and theoretical, is required before a satisfactory picture can be formed of dislocation damping and its relation to vacancy equilibrium.

6. CONTRIBUTING PERSONNAL

In addition to the principal investigator, P. D. Southgate, contributors to this program have been D. K. Benson and S. A. Marshall.

7. REFERENCES

5-1 Petch, N. J., Phil. Mag. 3, 1089 (1958).

5-2 Venables, J. D., Phys. Rev. 122, 1388 (1961).

5-3 Bordoni, P. G., Nuovo Cimento 4, 177 (1947).

5-4 Smythe, W. R., Static and Dynamic Electricity, N. Y., McGraw-Hill (1950) p. 105.

5-5 Stokes, R. J., Johnson, T. L. Phil. Mag., 6, 9 (1961).

5-6 Bordoni, P. G., Nuovo Cimento, 4, 177 (1947).

5-7 Niblett, D. H., Wilks, J., Adv. in Phys. 9, 1 (1960).

5-8 Weertman, J., J. Appl. Phys. 28, 193 (1957).

5-9 Southgate, P. D., Proc. Phys. Soc. (Lond.) 76, 398 (1960).

5-10 Granato, A. Hikata, A. and Lucke, K., Acta Metall. 6, 470 (1956).

5-11 Granato, A. and Lucke, K., J. Appl. Phys. 27, 583 (1956).

5-12 Bauer, C. L., and Gordon, R. B., J. Appl. Phys. 31, 945 (1960).

5-13 Lidiard, A. B., Defects in Crystalline Solids: Phys. Soc., (Lond.) p. 261, (1955).

5-14 Haven, Y., J. Chem. Phys. 21, 171 (1953).

5-15 Wertz, J. E., and Auzins, P., Phys. Rev. 106, 484 (1957).

5-16 Low, W., Phys. Rev., 105, 793 (1957).

IV. FINAL REPORTS ON SUBCONTRACT TASK PROGRAMS

TASK 6 - EFFECT OF SURFACE ENERGY ON BRITTLE BEHAVIOR

Principal Investigator: Dr. N. J. Petch
University of Durham
Newcastle upon Tyne
England

ABSTRACT

Exploratory studies were carried out to determine the surface energy values associated with the fracture of brittle materials over a wide temperature range. The method of using pre-cracked thin plates has been selected as being the most reliable at moderate temperatures; the zero-creep technique, whose application to ceramic substances appears to be novel, will be applied at temperatures near the melting point of the material. In addition, studies were carried out on determining the lowering of surface energy from measurements of adsorption isotherms.

All necessary equipment required for experimental work has been constructed. Initial exploratory studies have been made with polycrystalline Al_2O_3 for all of the methods investigated. These studies were augmented by fractographic examinations, using electron micrographs of shadowed replicas taken from surfaces of fractured polycrystalline Al_2O_3 specimens.

TASK 6 - EFFECT OF SURFACE ENERGY

1. INTRODUCTION

In Griffith's[6-1] classical treatment of a completely brittle solid, the criterion for crack propagation was derived from the balance between the surface energy created and the strain energy released by the growth process. In this way, the stress σ_f for the growth of a crack of length 2c, in a solid of Young's Modulus E and surface energy γ_o was obtained as

$$\sigma_f = \left(\frac{2E\gamma_o}{\pi c} \right)^{1/2} \qquad (6\text{-}1)$$

If the solid is not completely brittle, plastic deformation occurs around the growing crack, but it has been supposed that the criterion for crack propagation can again be given by the energy balance. If this tenet is accepted, the stress required is still obtained from Eq. 6-1 except that the surface energy term, γ, now includes the plastic work associated with a unit area of the newly formed fracture surface.

An energy balance criterion for crack growth involves the tacit assumption that the crack is sufficiently sharp for the stress at the edge to produce separation of the atoms when the energy criterion is fulfilled. With cracks blunted by very easy plastic deformation this may not be so.

Thus, it seems that in the fracture of completely brittle solids the significance of the absolute surface energy is quite clear; when some plasticity is possible, the absolute surface energy in the crack growth criterion is replaced by an effective surface energy that includes a plastic work factor. If plastic deformation is very easy, the simple energy balance criterion for crack growth may well break down.

Because of the uncertainties involved, the principal aim of this research is to investigate the nature of the surface energy term in fracture mechanics, and to compare the results obtained with the predictions of presently existing theoretical formulations. The effort, quite logically, subdivided itself into three major phases: a review of the adaptability of

existing or proposed experimental methods for the determination of surface energy values, the determination of surface energy for various ceramic materials at different environmental conditions, and the comparison of data obtained with theoretical predictions. At its present stage, the work is concerned entirely with the absolute surface energy.

No completely reliable general method exists for the measurement of the absolute surface energy of a solid. The methods that have been used are summarized in Table 6-I.

Table 6-I

EXPERIMENTAL METHODS FOR
THE DETERMINATION OF SURFACE ENERGY

Methods giving absolute values of γ.	Methods giving relative values of γ.
Quantitative cleavage	Pendulum Sclerometer experiments
Fracture of a precracked thin plate	Energy balance of grinding
Energy balance for heat of solution	Energy balance of wear
Variation of solubility with particle size	Mutual grinding
Anator's method (90° contact angle for liquid in tube)	
Zero creep method	
Stable cracks, e.g., Roesler[6-4], Kies[6-7], Svensson[6-8]	
Limiting velocity of crack propagation, e.g. Shand[6-9]	

In the present work, experimental approaches were confined to the crack propagation and the zero creep method, described in Section 4, is necessarily applied near the melting point, but again no plastic deformation term comes into the determination. In Section 3 the effect of adsorption on the absolute surface energy is determined from measurements of adsorption isotherms and, finally, some fractography is described in Section 5.

2. CRACK PROPAGATION METHODS

A. Hertz Cracks

Roesler[6-4] has shown that stable conical-shaped cracks can be produced in glass and quartz. These are formed by pressing the flat end of a cylindrical indentor into a plane surface of the material. The crack grows with increase in load and also with time, but for a fixed load the size of the crack becomes approximately constant after about 15 minutes.

Roesler has calculated that the surface energy will be given by:

$$\gamma = k \frac{P^2 \sin \alpha}{4 \pi R^3 G} \qquad (6\text{-}2)$$

where P is the applied load, R is the radius of the base of the indentor (or crack), α is the half apex angle of the conical fracture surface, G is the rigidity modulus and k is a constant.

The calculation of the constant k is difficult. It is a strain energy minimization problem involving seventeen independent components of the displacement field. Roesler has calculated $k = 7.45 \times 10^{-3}$ for conical cracks of semi-included angle $\sin^{-1} 0.9285$, i.e. $\alpha = 68° 12'$.

To examine Roesler's method, we have repeated some of his measurements on glass. The value of α was verified as being $68.5° \pm 1°$. Roesler measured a value of $P = 1438 \times 10^6$ dynes for $R = 1$ cm. Equation 6-2 yields $\gamma = 4100$ ergs per sq cm. In the present work $P = 1392 \times 10^6$ dynes was obtained for $R = 0.85$ cm, giving $\gamma = 6200$ ergs per sq cm. This is reasonable agreement with Roesler, but both results appear to be a factor of about ten too large.

Experiments to produce conical cracks in polycrystalline Al_2O_3 or MgO have failed. Polycrystalline MgO blocks 1 in. x 1 in. x 3/4 in. were loaded by an 1/8 in. diameter indentor. The fracture load was 102 ton per sq in. at room temperature, the fracture occurring diagonally across the cube on an approximately plane surface. In liquid nitrogen, the fracture was again catastrophic although there was some semblance of an initial conical fracture surface. With Al_2O_3 specimens of a similar size, fracture was also catastrophic, although there was some semblance of an initial conical fracture surface. The specimens broke into many pieces; the central one of which was a rough triangular pyramid with its apex directly below the point of application of the indentor.

Because of the unlikelihood of producing stable conical cracks in polycrystalline MgO or Al_2O_3, and the debatable correctness of the existing mathematical interpretation, it was decided to abandon this line of investigation.

B. Quantitative Cleavage

The reasonable results obtained by Kuznetsov[6-3] with relatively crude apparatus suggested that γ MgO could possibly be evaluated using his technique. The apparatus used in the present investigation is shown diagrammatically in Fig. 6-1.

The method is as follows. A position of the tup is found, say x, such that cleavage of the crystal will not occur for a single impact with the wedge, but a repetition of the process of impacting from this same tup displacement three or four times will fracture the specimen.

Let us now denote the potential energy of the tup at the predetermined displacement x as U_o; this will then also be the value of kinetic energy at impact. After impact with the cleavage wedge, the rebound distance can be readily determined by means of photocell to within $\pm$ 0.05 mm; this, in turn, allows for the calculation of the rebound energy U_1. Thus, the energy U_2 dissipated in the system during the impact is given by $U_2 = U_o - U_1$.

If one assumes that the energy U_2 dissipated on impact remains constant for a series of single impacts, each with the tup initially at an identical

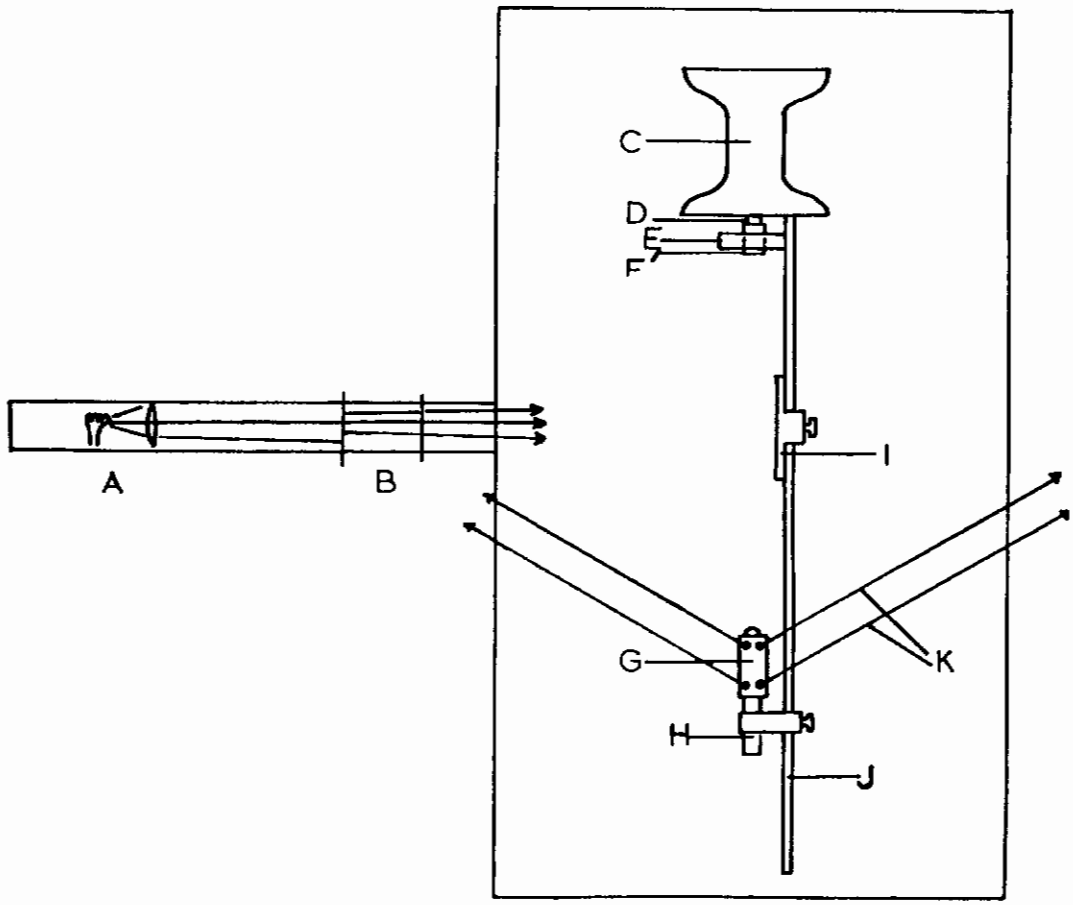

Fig. 6-1 QUANTITATIVE CLEAVAGE APPARATUS

A. Light Source	E. Wedge Support	I. Photo-Cell
B. Diaphragms	F. Cleavage Wedge	J. Scale
C. Anvil	G. Tup	K. Tup Supports
D. Crystal	H. Electro Magnet	

position x, then the difference in the rebound energies of two successive impacts, the second of which causes cleavage, will be due to the formation of the new surfaces. Thus, if two such impacts rebound with energies U_1 and U_1', respectively, then

$$2\gamma S = U_1 - U_1'$$

where S is the cross sectional area of the crystal.

It was found difficult to get sufficient sensitivity of the apparatus for an accurate determination of γ_{MgO}. A certain minimum energy of impact is needed to cause cleavage. The apparatus is most sensitive if the tup rebounds only a small distance, for in this part of the pendulum's arc a large lateral displacement is equivalent to a small change in kinetic energy. However, it is difficult to regulate the energy of impact causing cleavage to conform with the requirement of suitably small displacements. The use of a heavy tup does not help much in this regard, because it decreases the sensitivity of the apparatus on account of the change in kinetic energy with lateral displacement which is directly proportional to the weight of the tup.

For MgO and $CaCO_3$, (Fig. 6-2) we have found experimentally that the energy U_o necessary to cause cleavage varies approximately with the square of the cross sectional area of the crystal. Assuming that U_1 is a constant fraction of U_o, one can derive an expression for the sensitivity of the apparatus.

Let

R = length of pendulum

ℓ = lateral rebound distance

s = cross sectional area of crystal

h = vertical height moved through for a lateral rebound distance of ,

then

$$h = \frac{\ell^2}{2R} \qquad (6\text{-}3)$$

$$\frac{dh}{d} = \frac{\ell}{R} = \frac{\Delta h}{\Delta \ell}$$

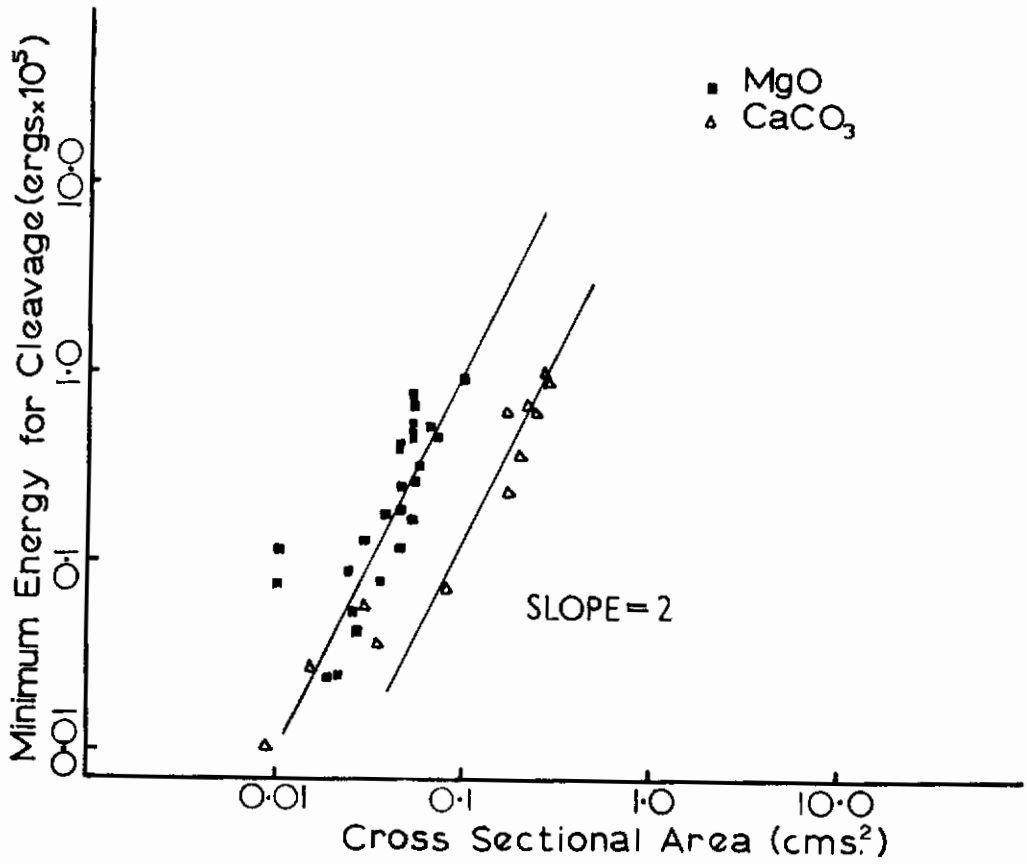

Fig. 6-2 MINIMUM TUP ENERGY FOR CLEAVAGE VERSUS CROSS SECTIONAL AREA OF CRYSTAL FOR MgO AND $CaCO_3$ CRYSTALS

Now $\Delta \ell$ is a measure of the sensitivity of the apparatus. Since $\Delta \ell = R\Delta h/\ell$ and $2\gamma S = mg\Delta h$, it follows that

$$\Delta \ell = \frac{2RS\gamma}{mg} \tag{6-4}$$

Now experimentally $S^2 \propto U_o \propto U_1 \propto \frac{\ell^2 mg}{R}$; therefore by direct substitution in Eq. 6-4

$$\Delta \ell \propto \left(\frac{R}{m}\right)^{1/2} \tag{6-5}$$

Thus, for maximum sensitivity, a long pendulum with a small mass is needed, but there are practical difficulties with very long lengths and very small masses. Also, at high impact velocities, the elastic waves set up can cause cleavage cracks to run perpendicular to the plane of the cleavage wedge and crushing of the crystal under the knife edge can occur. There are thus, limits to the values of R and m that can be used in practice.

Measurements of the surface energy of calcite with our apparatus gave 440, 535 and 820 erg per sq cm. Probably the lowest value is nearest to the true one, because imperfections in the cleavage will increase the apparent surface energy. These results are somewhat higher than those reported by Gilman[6-2] i.e., 220-280 erg per sq cm.

The value of 440 erg per sq cm corresponded experimentally with measuring a difference in rebound distance of only 0.8 mm. For MgO a single result indicated γ_{MgO} = 1250 erg per sq cm; the corresponding difference in rebound distance amounted to only 0.25 mm. Because of the uncertain accuracy and the limitations on the possibility of markedly increasing the sensitivity of the apparatus, it was decided to alter the original experimental procedure.

The technique is now being modified to allow the crystal to be partially cleaved before assembly in the apparatus and thus it may be possible to propagate the crack measurable amounts by only small impactive loads.

C. Precracked Thin Plates

The most promising technique is that of measuring the fracture stress of precracked thin plates. 5 x 2 x 0.1-cm plates of glass and polycrystalline Al_2O_3 have been pulled to fracture by attaching to the U-shaped jig shown in Fig. 6-3.

The initial work on glass showed that the breaking stress was independent of whether the crack was formed by ultrasonic drilling or was infinitely thin. This implies that the stress concentration at the tip of ultrasonically drilled cracks is sufficient to satisfy the maximum tensile strength criterion, so that the balance of net strain energy release with surface energy is the governing fracture criterion, i.e., Griffith crack propagation criterion,

$$\sigma_f = \left(\frac{2E\gamma}{\pi c}\right)^{1/2} \quad \text{, applies.}$$

One can thus calculate a value of γ for glass from the fracture stress of the precracked thin plates. Tests were performed with a range of crack lengths both in water and in paraffin oil. The results are shown in Fig. 6-4. A correction was applied to the breaking stress for the effect of a finite plate width where necessary, as suggested by Dixon(6-5).

The measured value of 1200 erg per sq cm in paraffin is near to the true surface energy of glass in a vacuum.

As can be seen, the surface energy values obtained in water appear dependent on the initial crack length. It seems probable that this is a static fatigue effect. Suppose that in water a crack can start to propagate at a low stress because of (say) adsorption. A short initial crack will then only have to grow a small amount to reach the critical size for continued propagation without adsorption. Thus, with a small crack, the observed fracture stress will tend towards the value characteristic of the surface energy for the adsorbed state, but with longer initial cracks, a greater amount of crack growth would be needed for this to happen and the observed fracture stress will tend towards the value characteristic of the true surface energy.

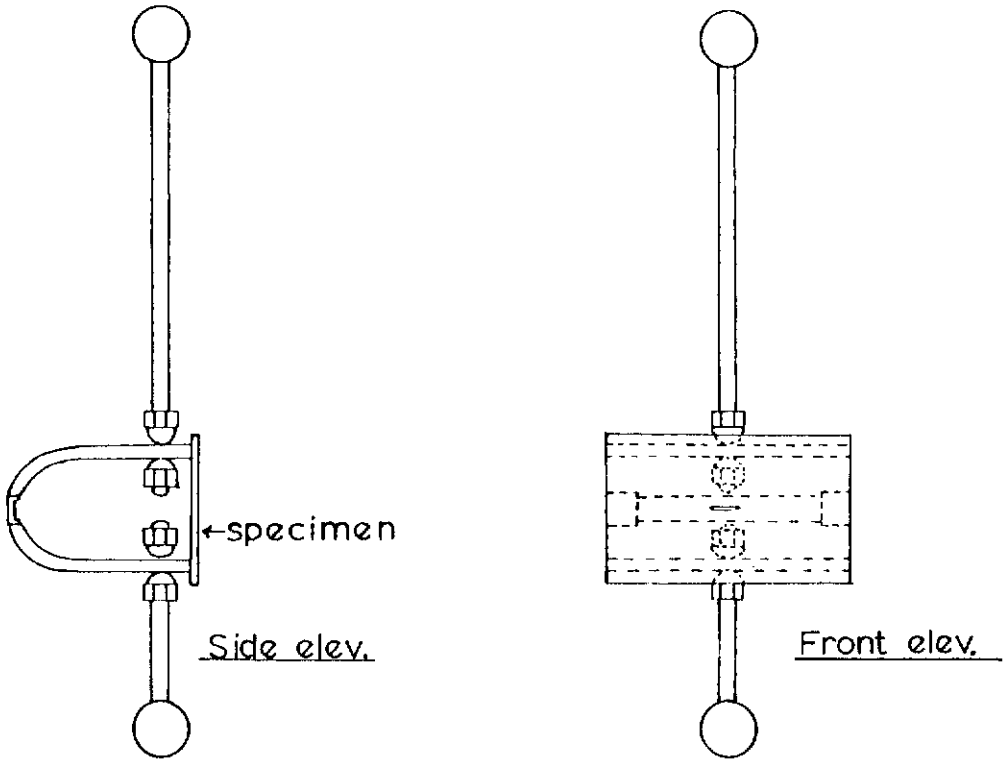

Fig. 6-3 U-SHAPED LOADING JIG FOR PRE-CRACKED PLATE SPECIMENS

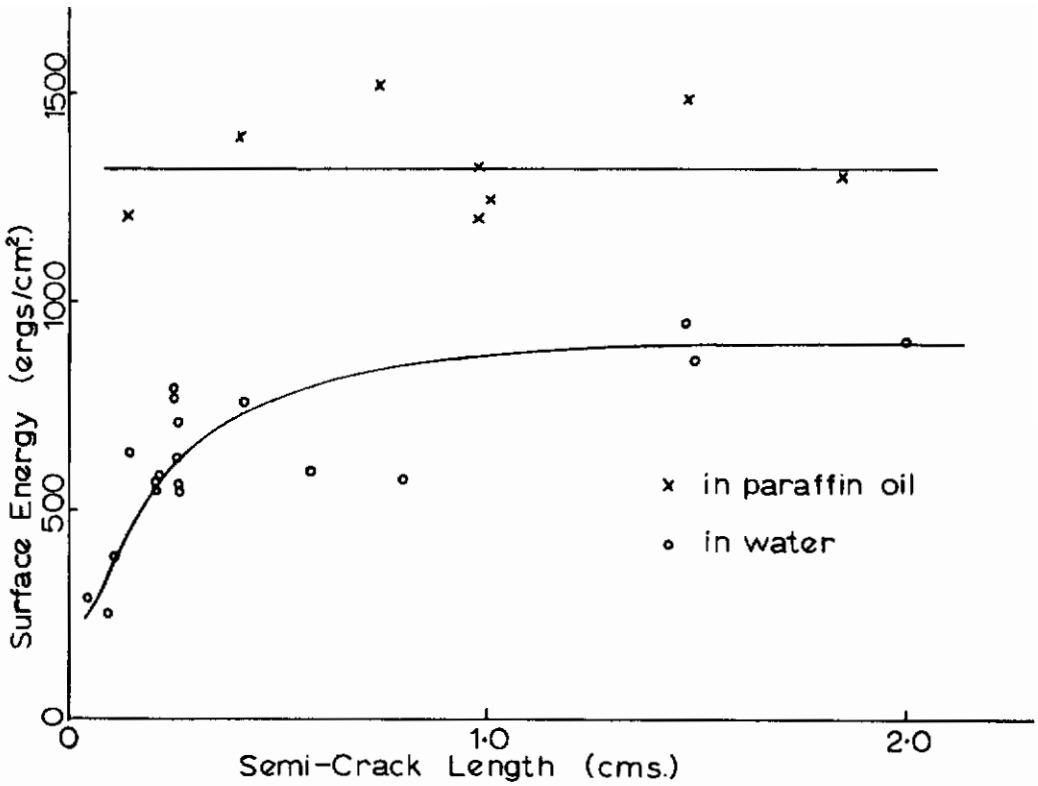

Fig. 6-4 CALCULATED SURFACE ENERGY OF GLASS FROM BREAKING STRESS DATA VERSUS PLATE THICKNESS

The surface energies obtained for polycrystalline Al_2O_3 are shown in Fig. 6-5(a). These values are generally of the right order of magnitude, but it will be seen that there is an apparent dependence upon thickness of the plate; the surface energy value decreasing as the thickness increases.

Figure 6-5(a) also shows that measurements in water at 20°C and in silicone at 100 and 150°C give lower surface energy values. The influence of water is probably a static fatigue effect and this is discussed further in Section 3. Some reduction in the surface energy with increase in temperature can be expected, but the decrease in the silicone oil measurements seems much too large to arise simply in this way.

One possible explanation of the apparent dependence of the surface energy on plate thickness is that there are some bending stresses present during testing. Strain-gauge measurements have now shown that this is in fact the case; and the U jig, which was fashioned after that used by Berdennikov[6-6], seems unsatisfactory. Probably in measurements on glass, which is of much lower modulus than Al_2O_3, the effect of bending is less, but this has not yet been checked experimentally.

The precise effect of bending on the crack propagation is not quite certain. It can hardly be so simple that the maximum fiber stress becomes all-important. It will be seen from Fig. 6-5(b) that the observed fracture stress is approximately proportional to 1 per plate thickness x crack length$^{1/2}$.

3. SURFACE ENERGY CHANGE IN POWDERS DUE TO ADSORBED GASES

Considerable investigation of the effect of water vapor and other atmospheric constituents on the fracture behavior of glass has not yet elucidated the true mechanism of the adsorption effect. Charles[6-10] has suggested that the delayed fracture of glass is due to stress corrosion at the tips of surface cracks in the specimens. Since any external medium which reacts chemically with the solid can, by a process of stress corrosion, deepen the crack and thereby weaken the solid, Charles, and Moorthy and Tooley[6-11], attributed the observed weakening in their glass specimens to geometrical changes brought about by stress corrosion of the surfaces.

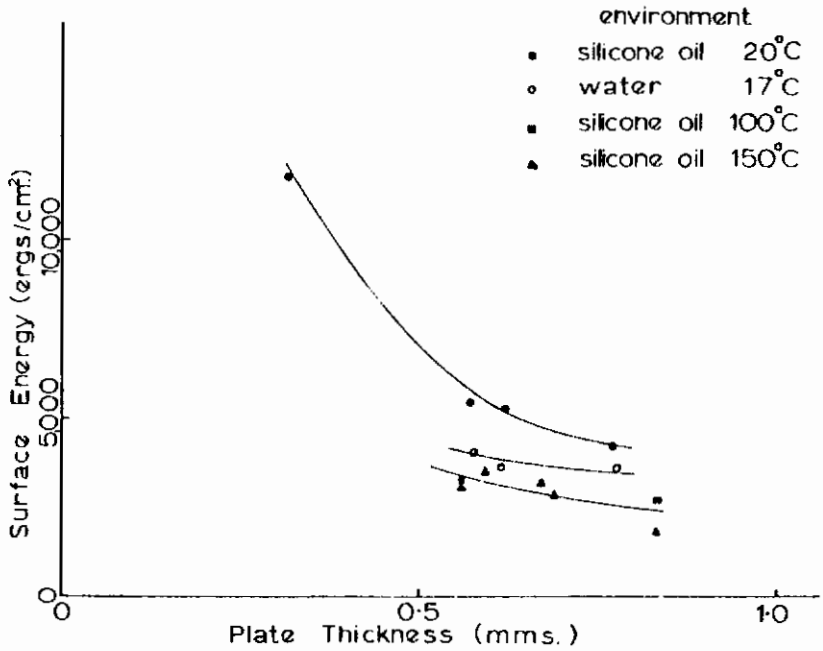

Fig. 6-5(a) CALCULATED SURFACE ENERGY OF Al_2O_3 FROM BREAKING STRESS DATA VERSUS PLATE THICKNESS

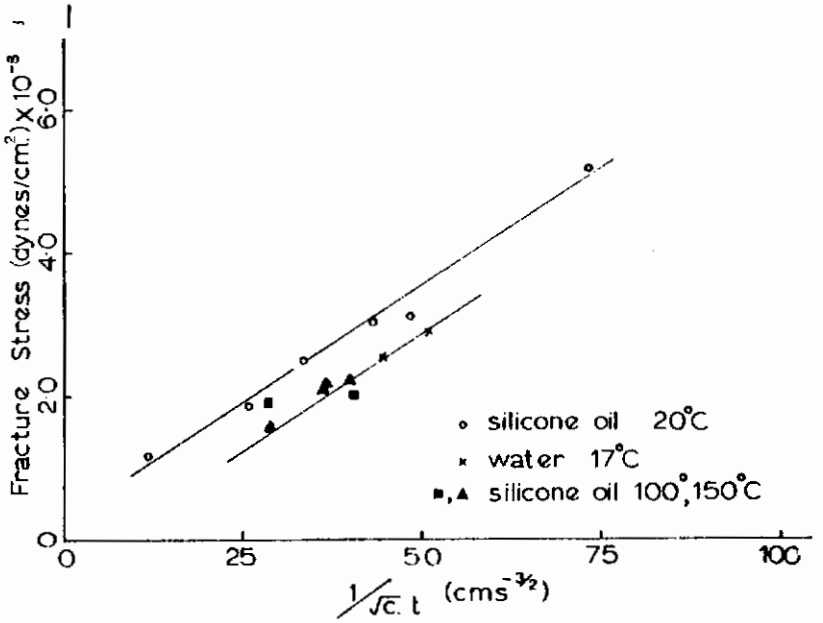

Fig. 6-5(b) FRACTURE STRESS OF PRECRACKED Al_2O_3 THIN PLATES VERSUS THE RECIPROCAL OF THE PRODUCT OF THE SQUARE ROOT OF THE SEMI-CRACK LENGTH AND THE PLATE THICKNESS

It was pointed out by Orowan[6-12] that the Griffith criterion, given in Eq. 6-1, might not be a sufficient condition for brittle fracture. Nevertheless, in deriving the sufficient condition from evaluation of the stress which has to be applied to break the bonds between atoms at the tip of the crack, he obtained the expression

$$\sigma_f = \left(\frac{E\gamma_o}{2c}\right)^{1/2} \tag{6-6}$$

which is little different from the Griffith condition.

Earlier, Orowan[6-13] had suggested that the fracture stress can be lowered, and delayed fracture effects introduced, by adsorption of atmospheric constituents on surface Griffith cracks in glass. This was then demonstrated[6-14] by cleavage experiments on mica, for which the surface energy was reduced from 4500 erg per sq cm to 375 erg per sq cm when tested in moist air. Jura and Harkins[6-15], meanwhile, demonstrated how graphical integration of the isotherm for adsorption of vapor at various pressures can be employed to calculate the lowering of surface energy by adsorption. It was subsequently demonstrated by Petch[6-16] that the actual decrease in fracture stress produced by adsorption was readily obtainable from the Langmuir isotherm, or by suitable integration of some other isotherm relevant to the adsorption process.

The surface energy lowering is given by Gibbs' adsorption equation

$$d\gamma = - \Gamma \, du \tag{6-7}$$

where $d\gamma$ is the change in surface energy produced by a change du in the chemical potential of the adsorbed phase and Γ is the number of molecules adsorbed per unit area.

If the adsorption takes place at temperature, T, from a gas at pressure, p, then

$$d\gamma = - G R T \, d(\log p) \tag{6-8}$$

where G is the number of gram-molecules of gas adsorbed at pressure, p, and temperature, T.

From the Langmuir isotherm,

$$G = G_s \frac{Ap}{1 + Ap} \tag{6-9}$$

where G_s is the number of moles adsorbed per unit area at saturation and A is a constant.

Substitution for G in Eq. 6-8 and integration gives

$$\gamma = \gamma_o - G_s \log (1 + Ap) \tag{6-10}$$

The lowered fracture stress can then be obtained from Eq. 6-1.

Schoening[6-17] has pointed out that, although the Griffith-Orowan equations indicate that the reduction of surface energy by adsorption of foreign molecules weakens the solid, a distinction must be made between the reduction of γ_o for an open surface and the reduction at the tip of a crack where adsorption takes place in a restricted space.

Delayed fracture phenomena have been observed in most non-metallic materials, including Al_2O_3, when a suitable reactive agent is present in the atmosphere. If, however, the contaminants are removed by baking and testing in high vacuum, the delayed fracture is almost entirely eliminated. Gurney and Pearson[6-18] have clearly demonstrated that water vapor and carbon dioxide are the main causes of delayed fracture in glass. Elimination of these constituents, either individually or together, produces a marked improvement in fracture behavior. Preston, Baker and Glathart[6-19] performed extensive experiments on the delayed fracture of a number of glasses and proposed that water vapor (perhaps modified by carbon dioxide) was primarily responsible for the weakening. The effect of water vapor was further examined by Schoening[6-17], who suggested that the strength of glass could be reduced by a factor of 0.57 on account of the lowering of surface free energy alone. The influence of gaseous adsorption on the rupture stress of glass fibers was also examined by Eischen[6-20], who postulated that the degree of reduction in breaking stress increased with the boiling point of the gas concerned.

Delayed fracture tests on sintered Al_2O_3 under normal atmospheric conditions, and also under high vacuum, after prior out-gassing at 350 ± 10°C for 48 hours in a vacuum of 10^{-5} torr in each instance have been carried out by Pearson[6-21]. His work clearly demonstrated that the delayed fracture effect can be largely eliminated by heat-treating and testing under high vacuum. This dependence of delayed fracture on atmospheric constituents suggests that the lowering of fracture stress due to adsorption on Al_2O_3 (and MgO) might be calculated from a determination of adsorption isotherms for carbon dioxide and water vapor.

Kipling and Peakall[6-22] have, in fact, examined the adsorption of water vapor on aluminum oxide but they employed material of high surface area (156 m^2/g) and determined gravimetrically the amount remaining adsorbed on the surface after 100 hours desorption at 25°C under a vacuum of 10^{-2} torr. When the loosely held physically adsorbed moisture had been removed they found that 3.43 milli-moles per g were still chemisorbed to give a surface equivalent to Gibbsite - $\gamma Al(OH)_3$.

A. Experimental Technique

Most of the adsorption measurements have been carried out on Al_2O_3 in the form of 1200-mesh crushed bauxilite (white fused Al_2O_3) obtained from Universal Grinding Wheel Company Limited. This material had a specific gravity of 3.94 and contained 99.00 per cent Al_2O_3, the major impurities being 0.3 to 0.4 per cent Na_2O, 0.05 per cent SiO_2, and 0.05 per cent Fe_2O_3, and was considered to give a closer approximation to the bulk material used in delayed fracture examinations than the more porous materials. Unfortunately, such a material has a comparatively low specific surface area and this imposed severe limitations on the sensitivity attainable in adsorption measurements.

A preliminary examination of the adsorption of carbon dioxide by alumina powder at -77°C was made using a sample of -150 +200-mesh powder supplied by Thermal Syndicate Limited and a helical silica spring McBain balance having a sensitivity of 16 cm/g. After out-gassing at 300°C under a vacuum of 10^{-1} torr for 18 hours, carbon dioxide was gradually admitted to the system. Even with a pressure of 700 torr carbon dioxide in the system,

the extension of the helical spring was estimated to be only about double the error of measurement, indicating a low surface area only of the order of 4 m^2/g.

It was realized that, even if the specific surface area was increased by employing finer powder, the sensitivity of this method would be insufficient to determine a full adsorption isotherm even if it were sufficient to measure the total adsorption at high pressures. The volumetric method of measuring adsorption has the advantage that quite large quantities of adsorbent may be used providing that variations in the "dead space" volume due to the actual volume occupied by powder are allowed for.

An apparatus was therefore assembled for the addition of measured amounts of gas at known temperature and pressure to an adsorption system containing the Al_2O_3 sample. A sketch of this apparatus is shown in Fig. 6-6; a picture of the completed equipment is presented in Fig. 6-7. The "dead space" volume of the adsorption portion was restricted by employing 2-mm bore capillary tube as far as possible in its construction. By means of a rotary pump and a single stage mercury diffusion pump the system could be evacuated to a pressure of $< 10^{-5}$ torr, as measured on an accurate McLeod gauge.

The "dead space" volume of the adsorption system without powder in the adsorption tube was calibrated at -77 and 20°C, after out-gassing at 330°C, by addition of measured quantities of carbon dioxide from the gas burette, and was found to be equivalent to about 20 cc of CO_2 at normal temperature and pressure (NTP, 20°C and 1 atm.) with the adsorption vessel at 20°C and containing one atmosphere of gas.

Adsorption isotherms were first carried out at -77°C using 1200-mesh bauxilite which had been out-gassed for at least 24 hours at 330°C under a vacuum of $< 10^{-5}$ torr. The amount actually adsorbed was calculated from the amount added by subtracting the calibrated volume of the "dead space" at the respective equilibrium pressure, allowing for the volume occupied by the powder of known density. The earlier determinations confirmed the fact that the powder had an extremely low surface area and the amounts adsorbed closely approached the lower limit of determination for the apparatus, the "dead space"

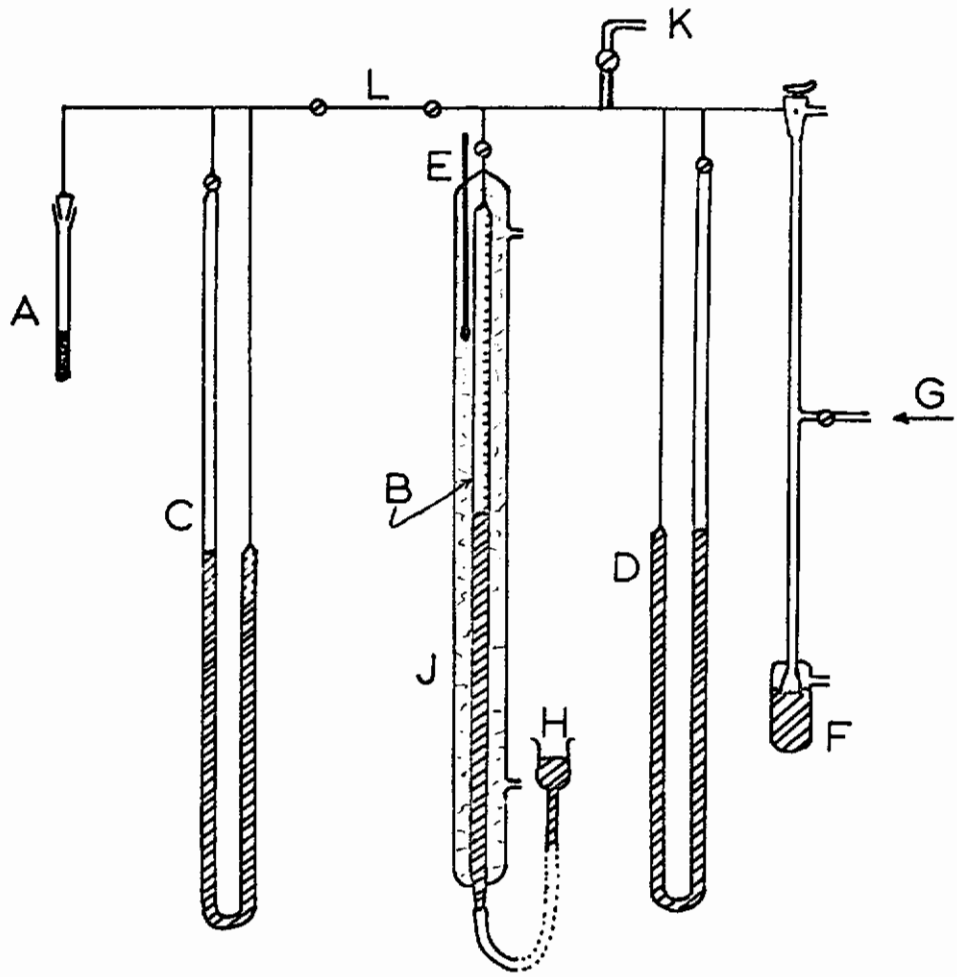

Fig. 6-6 DIAGRAMMATIC SKETCH OF ADSORPTION SYSTEM
(Capillary sections are represented by a single line.)

A. Adsorption vessel
B. Gas burette
C. Mercury manometer for equilibrium pressure measurements
D. Mercury manometer for gas collection
E. Thermometer
F. Mercury blow-off on gas collection system.
G. Gas inlet
H. Mercury reservoir for gas burrette
J. Water jacket for gas burette
K. Lead to McLeod gauge, cold trip, and diffusion and rotary pumps
L. Short length of capillary for controlled additions of gas

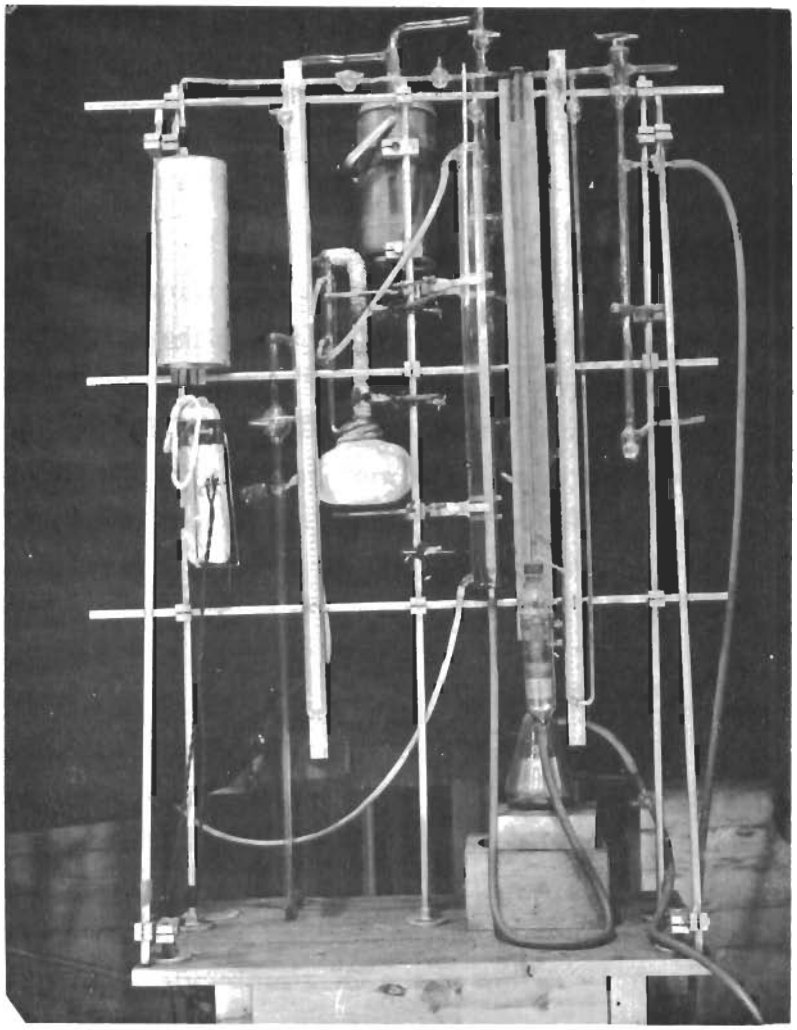

Fig. 6-7 GENERAL VIEW OF ADSORPTION SYSTEM

correction forming a considerable portion of the total amount added in each case. By increasing the weight of sample to 3.9 g, a reasonable adsorption curve was obtained which allowed determination of monolayer adsorption giving a specific surface area of 1.22 m^2/g.

Such low surface area obviously entails great difficulty in measuring the amount of adsorption prior to formation of a monolayer at ambient temperatures. Determination of an adsorption isotherm at 20°C served to confirm this, since the adsorption at 700 torr was only about 0.18 cc CO_2 (at NTP) per gram Al_2O_3.

The low adsorption was confirmed on examining the adsorption of carbon dioxide on a similar out-gassed sample of bauxilite by means of an accurate vacuum microbalance. Introduction of CO_2 at 0°C and 700 torr gave an apparent weight loss equivalent to 0.3 cc (CO_2) per g, indicating that the amount adsorbed is of the same order as the bouyancy correction for the balance. Under these conditions the amount of CO_2 adsorbed is less than 0.25 cc per g, which confirms the measurements carried out by the volumetric technique.

B. Discussion of Results

The curve for adsorption of CO_2 on the powdered bauxilite at -77°C, shown in Fig. 6-8, displays the normal characteristics of monolayer formation up to a pressure of 450 torr, followed by the build-up of multilayers at higher pressures. The amount of gas adsorbed to form a monolayer at this temperature allows calculation of the surface area of the sample from the known area of 17×10^{-16} sq cm of the CO_2 molecule. Despite the low surface area involved, the accuracy of measurements determined in this way was about $\pm$ 5 per cent, even though the total amount required to form a monolayer was only 0.27 cc (at NTP) per gram of Al_2O_3.

The amount of CO_2 adsorbed at ambient temperature is presented in Fig. 6-9. This is, of course, considerably less than that at -77°C; measurements therefore show a high degree of scatter. Desorption and adsorption curves were, however, found to be inseparable, and the results obtained were accurate enough to allow calculation of at least the order of the decrease in surface energy associated with the adsorption.

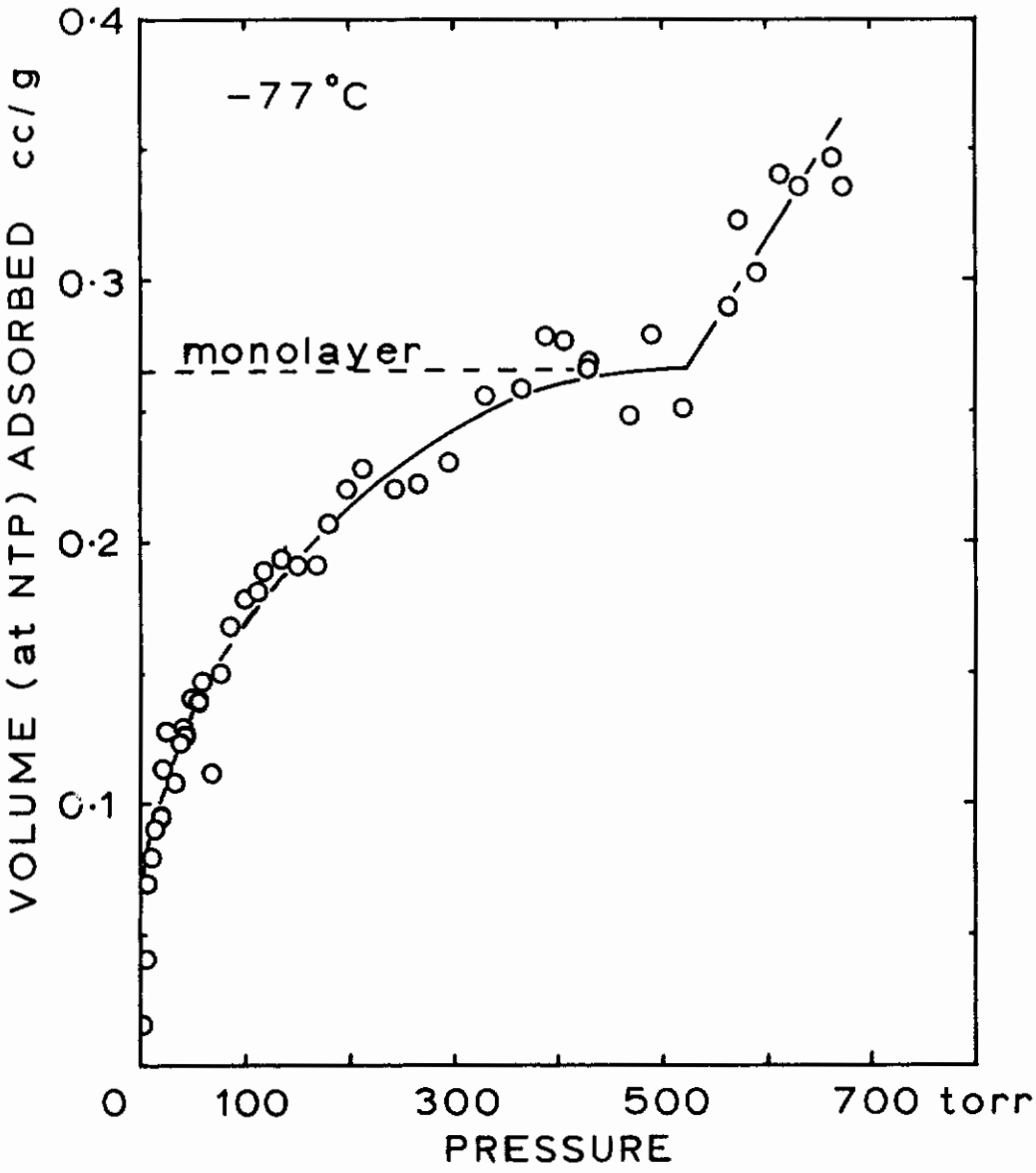

Fig. 6-8 CURVE FOR ADSORPTION OF CARBON DIOXIDE ON POWDERED BAUXILITE AT -77°C

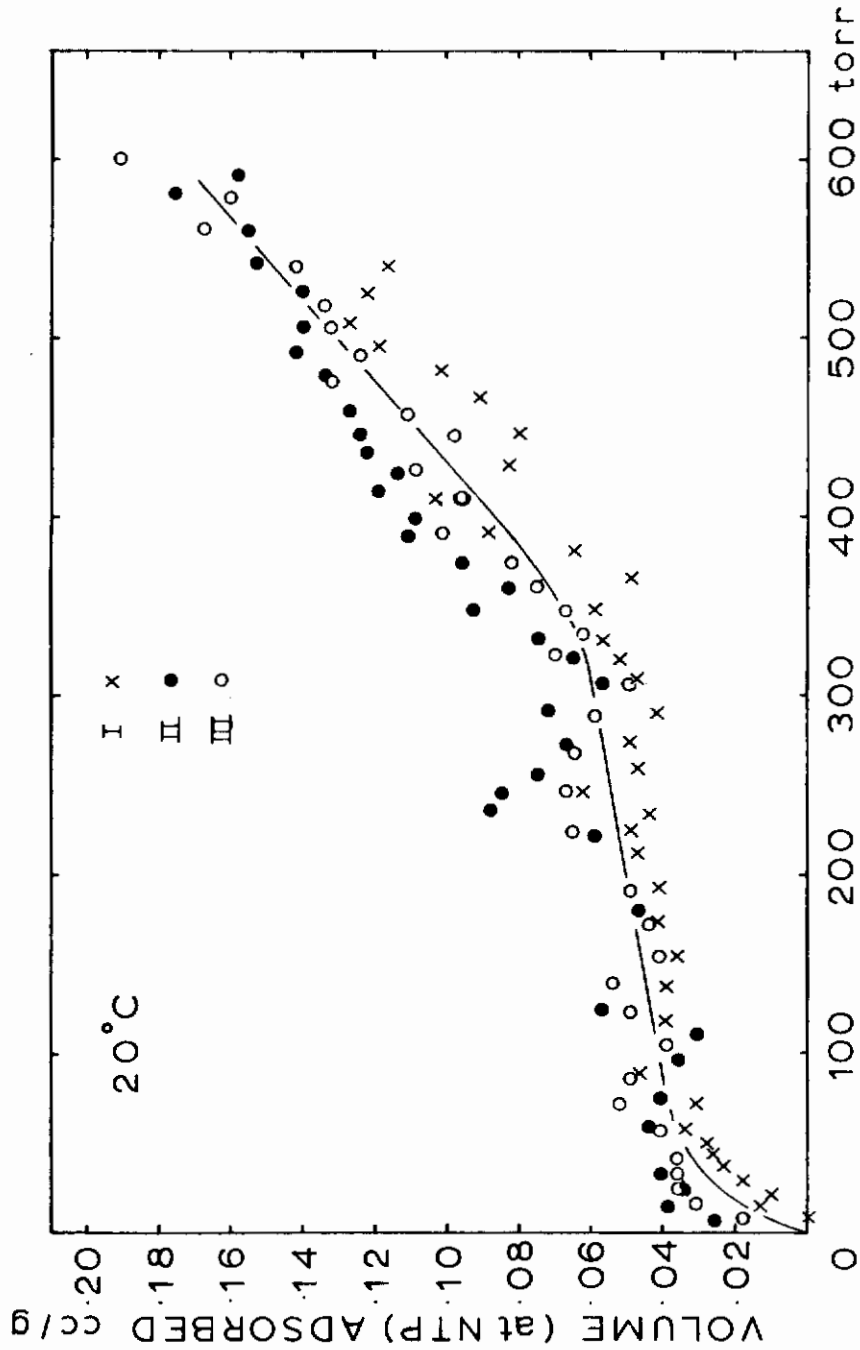

Fig. 6-9 RESULTS OF THREE SEPARATE DETERMINATIONS OF THE ADSORPTION OF CARBON DIOXIDE ON POWDERED BAUXILITE AT 20°C

A Langmuir plot of the results (Fig. 6-10) gives scattered points. Nonetheless, a linear relationship can be ascribed by means of the least squares method. The results shown in Fig. 6-9 for the adsorption of CO_2 at 20°C were treated in this way, allowing for the determination of the constants G_s and A in the Langmuir isotherm. The lowering of surface energy associated with adsorption of CO_2 at a partial pressure of 10 torr was then calculated from Eq. 6-10.

The results are shown in Table 6-II. It can be seen that although there is considerable variation, all the values of the lowering of surface energy are of the order of 1.0 erg per sq cm. Since the surface energy of Al_2O_3 in vacuo is normally considered to be in the region of 2000 erg per sq cm, this represents a negligible decrease resulting from the adsorption of CO_2.

Table 6-II

CHANGE IN SURFACE ENERGY FOR Al_2O_3 RESULTING FROM CO_2 ADSORPTION AT 20°C

Specimen	G_s (g mole cm^{-2})	A (cm^{-1})	$\gamma_o - \gamma$ at p = 10 torr, (ergs cm^{-2})
I	2.23×10^{-10}	0.159	0.80
II	3.06×10^{-10}	0.154	1.07
III	2.82×10^{-10}	0.178	1.13

It could be suggested that the out-gassing treatment employed was insufficient to expel any more firmly bound chemisorbed gas molecules from the surface of the powder. Nevertheless, the treatment was without doubt equivalent to that carried out by Pearson, who reported that it eliminated the delayed fracture effect in Al_2O_3. It would seem, therefore, that delayed fracture cannot be attributed to the lowering of surface energy caused by adsorption of CO_2.

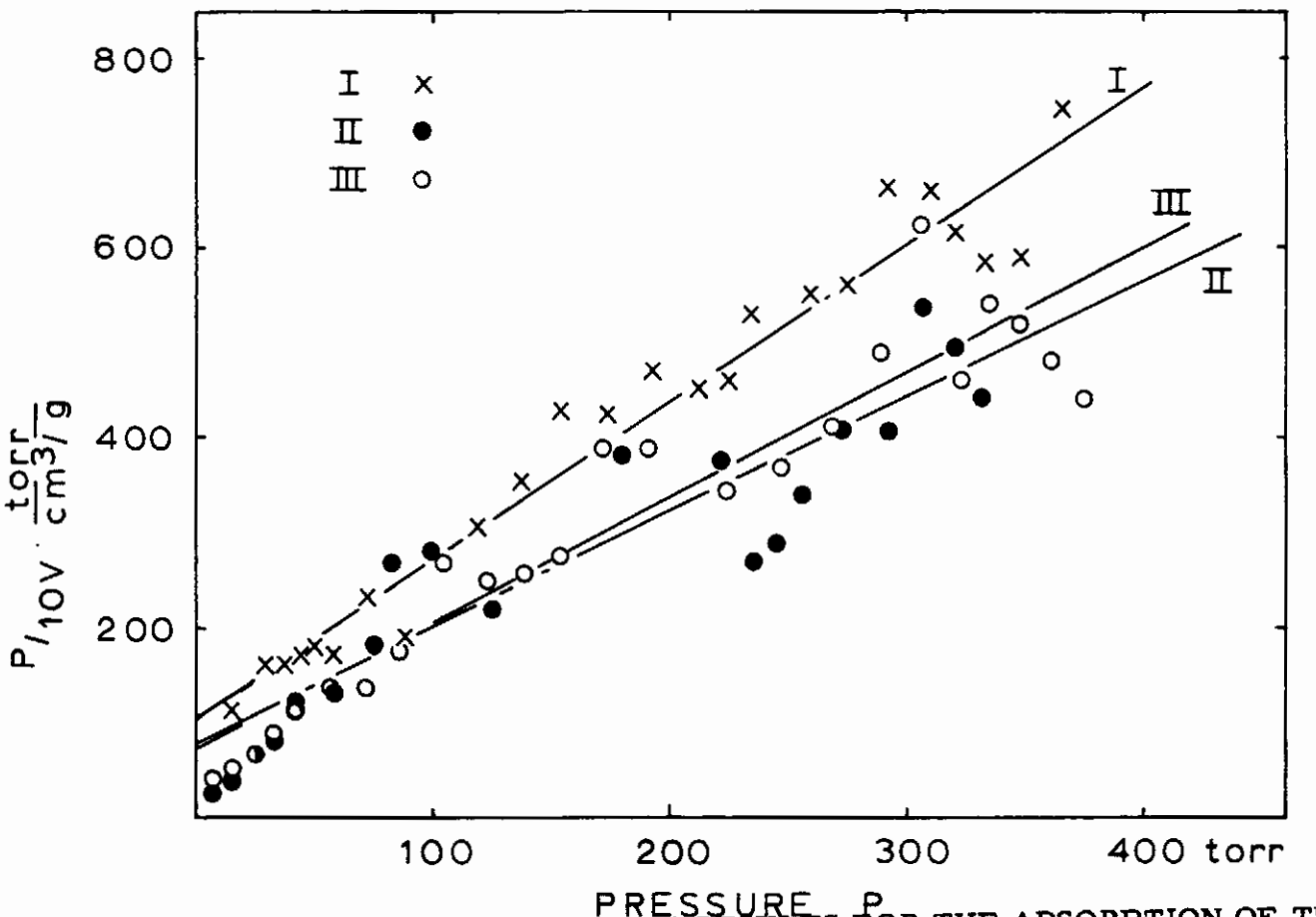

Fig. 6-10 LANGMUIR PLOT OF THE RESULTS FOR THE ADSORPTION OF THE CARBON DIOXIDE ON POWDERED BAUXILITE AT 20°C

It may be that the other atmospheric contaminant, water vapor, is in fact solely responsible for the delayed fracture effect. Schoening's results for the adsorption of water vapor on glass demonstrated that surface energy changes due to adsorption were sufficient to account for at least a considerable proportion of the reduction in fracture stress observed. For the same to be true for the adsorption of water vapor on Al_2O_3 there would have to be greatly increased adsorption compared with CO_2 — the number of moles of water adsorbed on glass at 10 torr is about 200 times the amount of CO_2 adsorbed on Al_2O_3 at this pressure. The Langmuir constant, A, would therefore be much higher.

Another feature of interest is the actual shape of the adsorption curves for CO_2 at 20°C. All three curves exhibit a stepped contour, the adsorption plateau occurring at much too low a pressure, and too small an amount adsorbed, to correspond to monolayer formation. If, in fact, it is a real effect it may be attributable to preferential adsorption on certain more favorable sites in the initial stages.

A sample of Al_2O_3 of higher specific surface area has been obtained. During continued phases of this work, we shall develop more accurate adsorption curves for carbon dioxide with the additional sensitivity thus available; in addition, we shall also examine the adsorption of water vapor on Al_2O_3 surfaces.

4. SURFACE ENERGY OF Al_2O_3 BY THE METHOD OF ZERO CREEP

The interface between two phases is characterized by an interfacial tension due to the excess of energy which exists at the interface. A reduction in surface area will therefore permit a body to lower its free energy; the corresponding work done will be equal to the reduction in surface free energy. It is to be expected then that a foil or thin wire, having a large surface area to volume ratio, will contract under the influence of its surface free energy when heated to temperatures approaching its melting point. By a judicious selection of weights which put the foil or wire into tension such that the contractive force of the surface free energy is exactly counterbalanced, will cause the wire to maintain its original length, affording a

method for the determination of the surface free energy[6-23] at very high temperatures. Because of its feature of arresting axial strains in the wire, the technique is designated as the zero creep method.

In obtaining the appropriate expression relating the balancing weight to the surface free energy[6-24], it is assumed that the resistance to extension under the influence of the weight comes from the surface and grain boundary tensions. By a virtual work argument, for a thin wire

$$w\, d\ell = \gamma_s\, ds + \gamma_b\, db \qquad (6\text{-}11)$$

where w is the balancing force, $d\ell$ the change in length, γ_s the surface energy, ds the change in surface area, γ_b the grain boundary tension and db the reduction in grain boundary area. If the grain boundaries lie normal to the wire axis and completely traverse the diameter, i.e., the wire is made up of a series of grains joined end to end and having the same diameter as the wire, then Eq. 6-11 leads to

$$w = \pi r \gamma_s - n \pi r^2 \gamma_b \qquad (6\text{-}12)$$

where r is the wire radius and n is the number of grains per unit length. Neglecting the grain boundary term would probably lead to an error of about 10 per cent. One may also assume that $\gamma_b/\gamma_s \approx 0.3$ or 0.4 as is frequently found to be the case. Alternately, the two energies may be separately determined by making measurements on specimens of different relative dimensions or different grain sizes.

The experimental approach involves determining the creep curves at constant temperature for a number of specimens subjected to different stresses. The creep strain is measured at various times until the strain rate at a given stress does not vary with time. The stresses are chosen so that both creep contraction and extension are observed. Then, by plotting the constant creep strain rate against stress, the stress corresponding to zero creep may be interpolated. The method has been used for surface energy determinations of copper[6-24], gold and silver[6-25], and nickel[6-26], with results which agree reasonably with those obtained by other methods.

The application of the technique to Al_2O_3 presents two problems, encountered only in a minor degree with the metals previously studied. These are that the temperatures involved are much higher (ca. 2000°C) and the preparation of Al_2O_3 in the form of thin wires is more difficult than is the case with ductile metals. Making reasonable assumptions for the quantities involved in Eq. 6-12 leads to the requirement that Al_2O_3 wires would need to be about 1 mm or less in diameter for the method to offer reliable results. Extruded wires of about 0.8-mm diameter, and of sufficient uniformity over lengths of a few centimeters, have been obtained and some preliminary experiments made in a borrowed furnace.

The preparation of the wires involves marking off a gauge length in a jig by drawing a fine steel wire lubricated with diamond paste over the surface to produce two small grooves 2 cm apart. The gauge length and the length of wire below the mid-point of the gauge length, which corresponds to the weight producing creep, are measured with a traveling microscope reading to 0.002 mm. During creep the rods are suspended through holes in the lid of an alumina crucible by attaching a small bead of alumina to one end, such that the bead does not pass through the hole in the crucible lid. The arrangement is shown in Fig. 6-11. The Al_2O_3 crucible and lid have internal dimensions 5-cm long and 3.5-cm diameter, allowing for up to 24 specimens to be contained in the crucible during any one run, with a maximum stress on any specimen of about 16,000 dynes per sq cm. Preliminary experiments at 2050°K have shown the feasibility of the method in that expansions and contractions of the gauge length of specimens has been observed.

In order that creep deformation may be detected in a reasonable period of time it is necessary that the temperature of testing be near to the melting point (2320°K). A graphite resistor furnace, similar in design to that used in the preliminary experiments and described by Davidson and Burwood[6-27], has been made for this purpose. The heating element is a graphite tube 8 in. long and 2-5/8 in. diameter, with a central bore which contains the Al_2O_3 crucible standing on an insulating refractory block. The tube is slotted, as shown in Fig. 6-12, to obtain the requisite length of electrical path; provision is made for the current to enter and leave at the lower end. This is

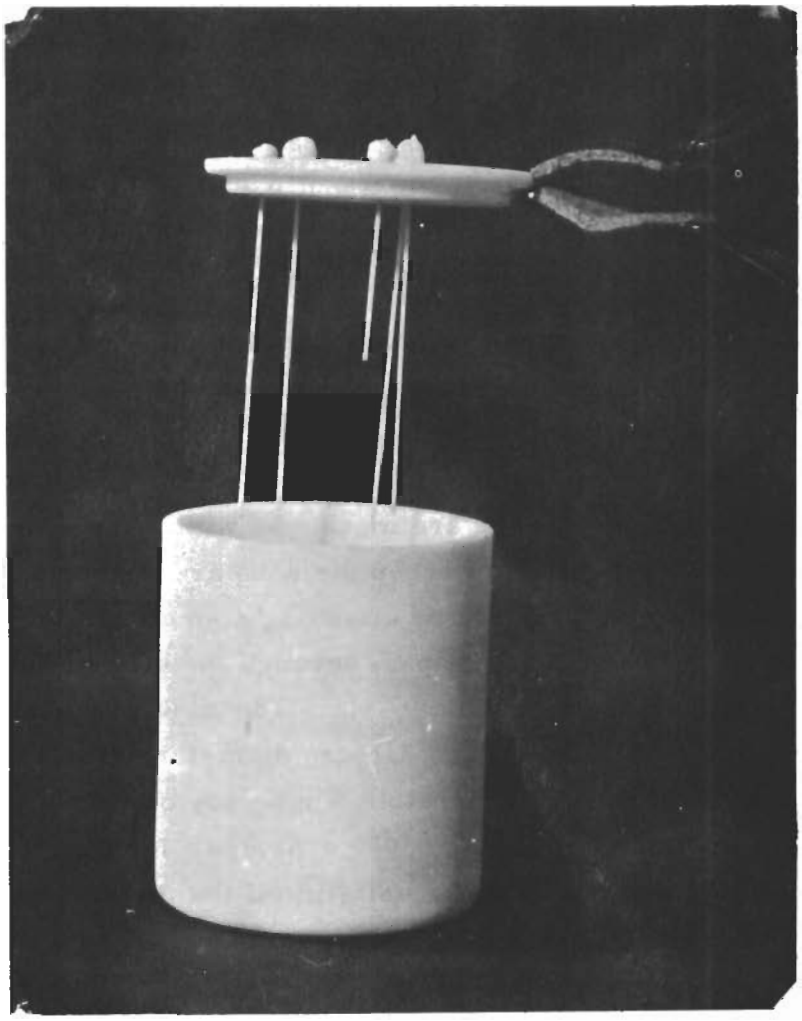

Fig. 6-11 GENERAL VIEW OF Al_2O_3 ROD ASSEMBLY USED

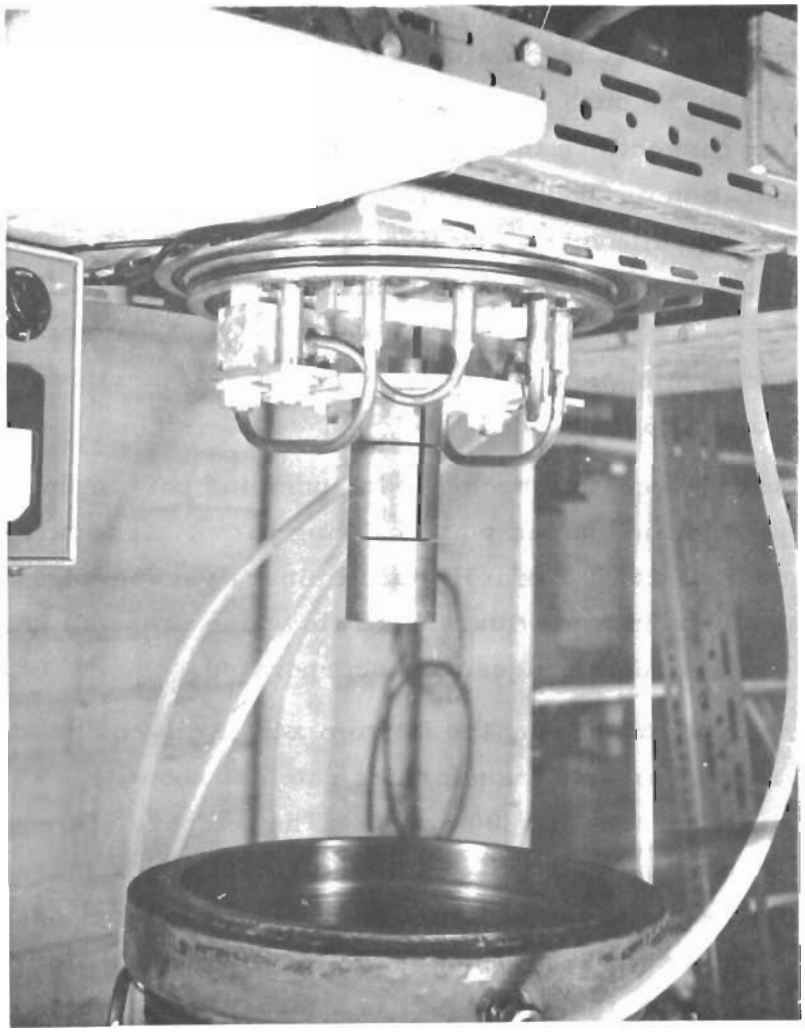

Fig. 6-12 HIGH-TEMPERATURE FURNACE, SHOWING GRAPHITE HEATER

achieved through two heavy copper water-cooled busbars, electrically insulated from the brass base by an aluminum silicate ceramic; the graphite tube is connected to the busbars by an interference fit. The insulated electrical and water connections through the brass base are made vacuum tight by the incorporation of O-ring seals. Reflection and redistribution of the heat from the graphite tube is by five radiation shields of sheets of 0.5-mm thick molybdenum, located and insulated by aluminum silicate ceramic and shown in Fig. 6-13. The whole is covered by a heavy water-cooled steel case with appropriate vacuum seals. The entire assembly installed in position is shown in Fig. 6-14.

The furnace is evacuated through 2 in. pumping port in the base by an appropriate size of diffusion pump and backing pump. The furnace has been designed to operate at 10^{-4} mm Hg; preliminary vacuum tests have indicated that this can be achieved with a leak rate which presents no problems. Appropriate traps and vacuum gauges are incorporated.

The power supply to the furnace is from a 27:1 oil-cooled step down transformer fed from a variable transformer rated at about 18 kVA at a maximum of 15 volts and a current of 1200 amps. The temperature control unit incorporates a photoelectric cell as the active element and is focussed on the graphite tube through slots in the radiation shields. The steel case is provided with water-cooled cells shown in Fig. 6-14, sealed with optical quality heat resisting glass; the photoelectric cell is attached to the outside of the cells. The temperature control unit, activated by a variable transformer, has been designed and is in the process of being constructed.

5. FRACTOGRAPHY

The fracture surfaces of the precracked thin plates described in Section 2 have been studied both optically, using cellulose acetate impressions viewed by transmitted light, and by means of electron microscopy. For the latter method, carbon replicas have been made from cellulose acetate impressions pre-shadowed at 45° with AuPd. Some difficulty is still being experienced because of the fragility of the replicas.

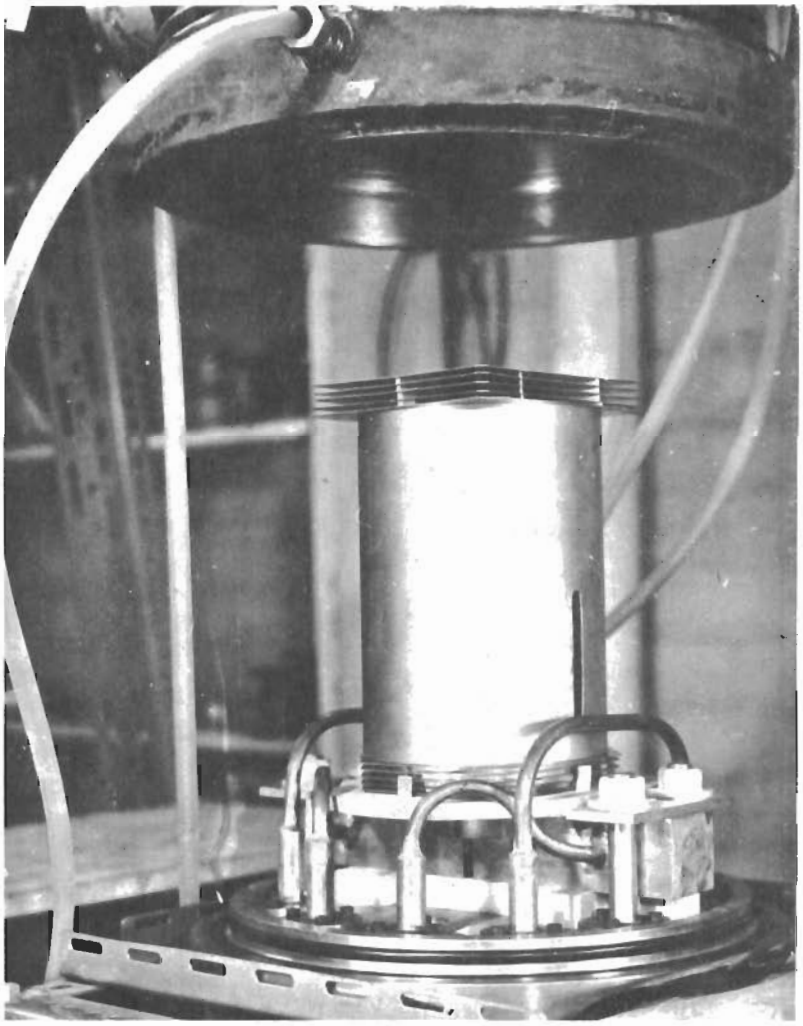

Fig. 6-13 HIGH-TEMPERATURE FURNACE WITH MOLYBDENUM SHIELDS IN PLACE

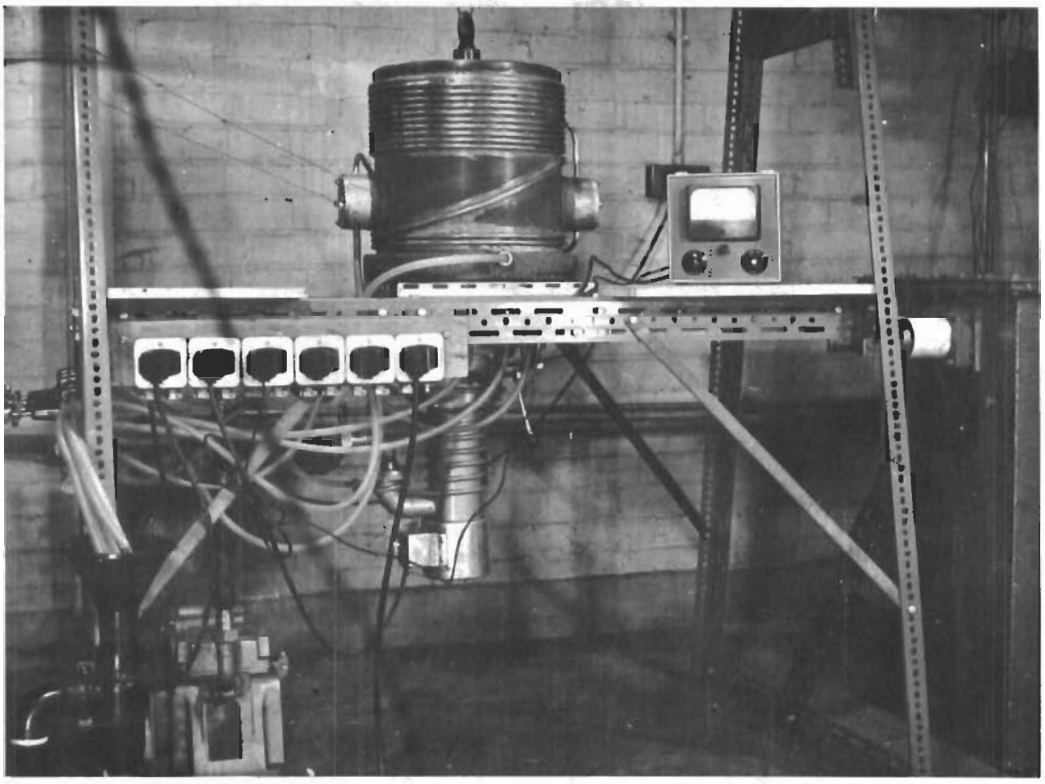

Fig. 6-14 GENERAL VIEW OF EXTERNALS
OF HIGH TEMPERATURE FURNACE

The fracture surfaces of Al_2O_3 broken in the temperature range 20 to 200°C appear identical, having a high proportion of grains showing smooth, flat surfaces, and many showing detailed surface markings.

Figure 6-15 shows a typical area of the fracture surface of polycrystalline Al_2O_3 broken at 20°C. Micropores can be seen, the step pattern joining two of these being a typical feature of the fracture surface. Figure 6-16 is a higher magnification of a part of the same area. Figure 6-17 shows the variation of fracture markings as influenced by the different grain orientation that exists in the polycrystalline Al_2O_3. In the lower left portion of this micrograph, as in others, one can readily see that a fracture facet which is forced to follow a line not along one of the easy parting planes does so in a stepwise manner. This indicates that, although the total area of surface created is greater, the total surface energy is less for this fracture path than for a straight path following the gross line of the facet.

Figure 6-18 shows the fracture surface remaining crystallographic across what is probably a grain boundary. It would appear that these two grains bear some simple crystallographic relation to one another. Figure 6-19 shows the appearance of typical serrated paths in the fracture facet, the single steps in the serrations being about 500 Å long in this instance. Lastly, Fig. 6-20 shows an area of conchoidal fracture adjacent to a grain more suitably oriented for cleavage. As can be readily seen by the presence of facets and river markings, the mode of fracture is a somewhat imperfect cleavage.

Textbooks on mineralogy suggest that Al_2O_3 can show perfect but interrupted cleavage on the basal plane and pseudo-cleavage on the $(10\bar{1}, 1)$ twin plane. For Al_2O_3 $(10\bar{1}1) \wedge (\bar{1}101) = 93° 56'$ and $(10\bar{1}1) \wedge (0001) = 57° 34'$.

A fractured single crystal of Al_2O_3 showing similar fracture surface markings to those seen in Figs. 6-15 to 6-18 has been examined by optical goniometry. Results are at present incomplete, but it appears that two reflections found correspond to $(10\bar{1}0)$ and $(11\bar{2}.2)$ planes, as shown in Fig. 6-21. Measurements on the electron micrographs show that, as near

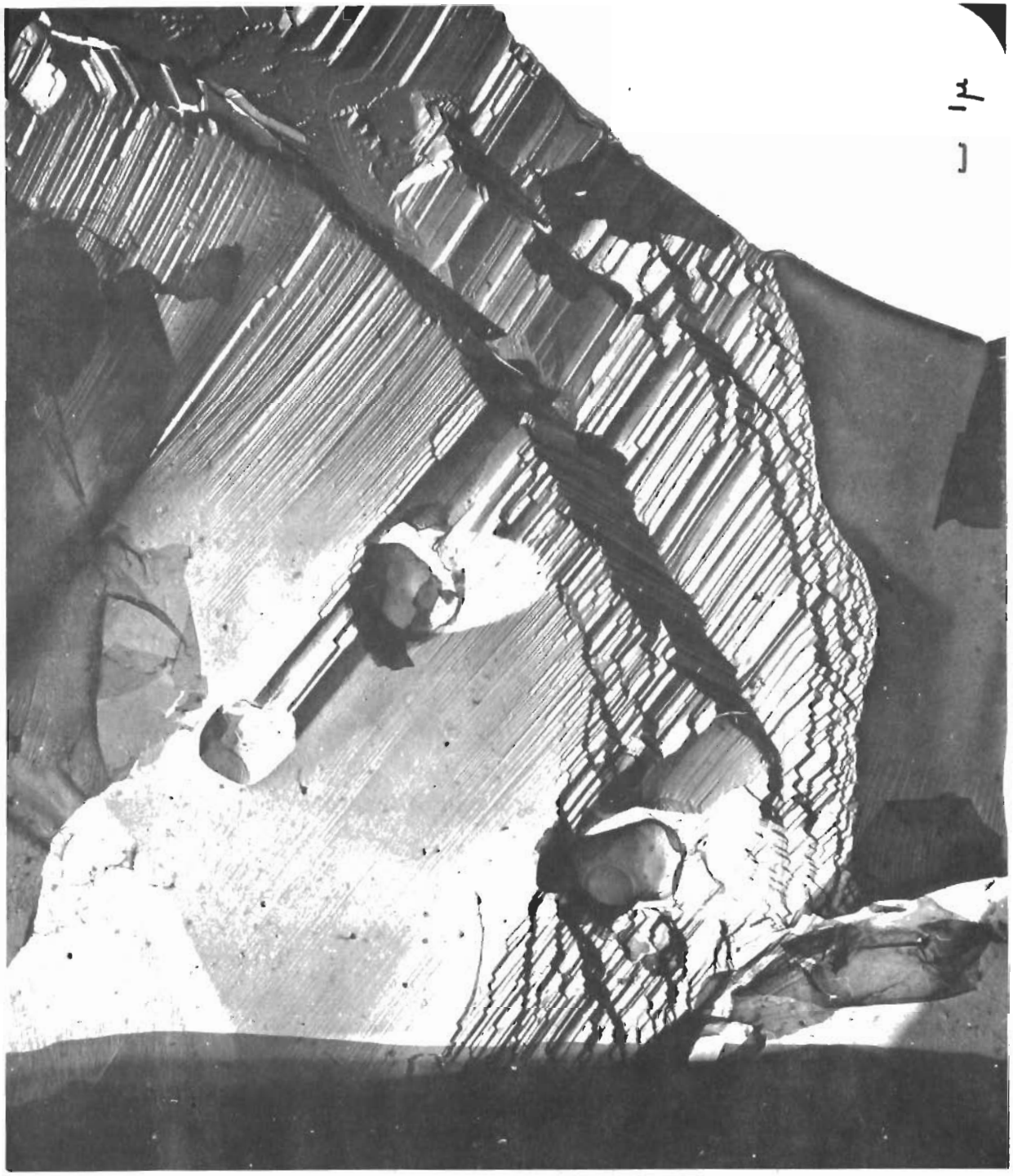

Fig. 6-15 ELECTRON MICROGRAPH OF Al_2O_3 THIN PLATE FRACTURE SURFACE
Carbon replica, X4800

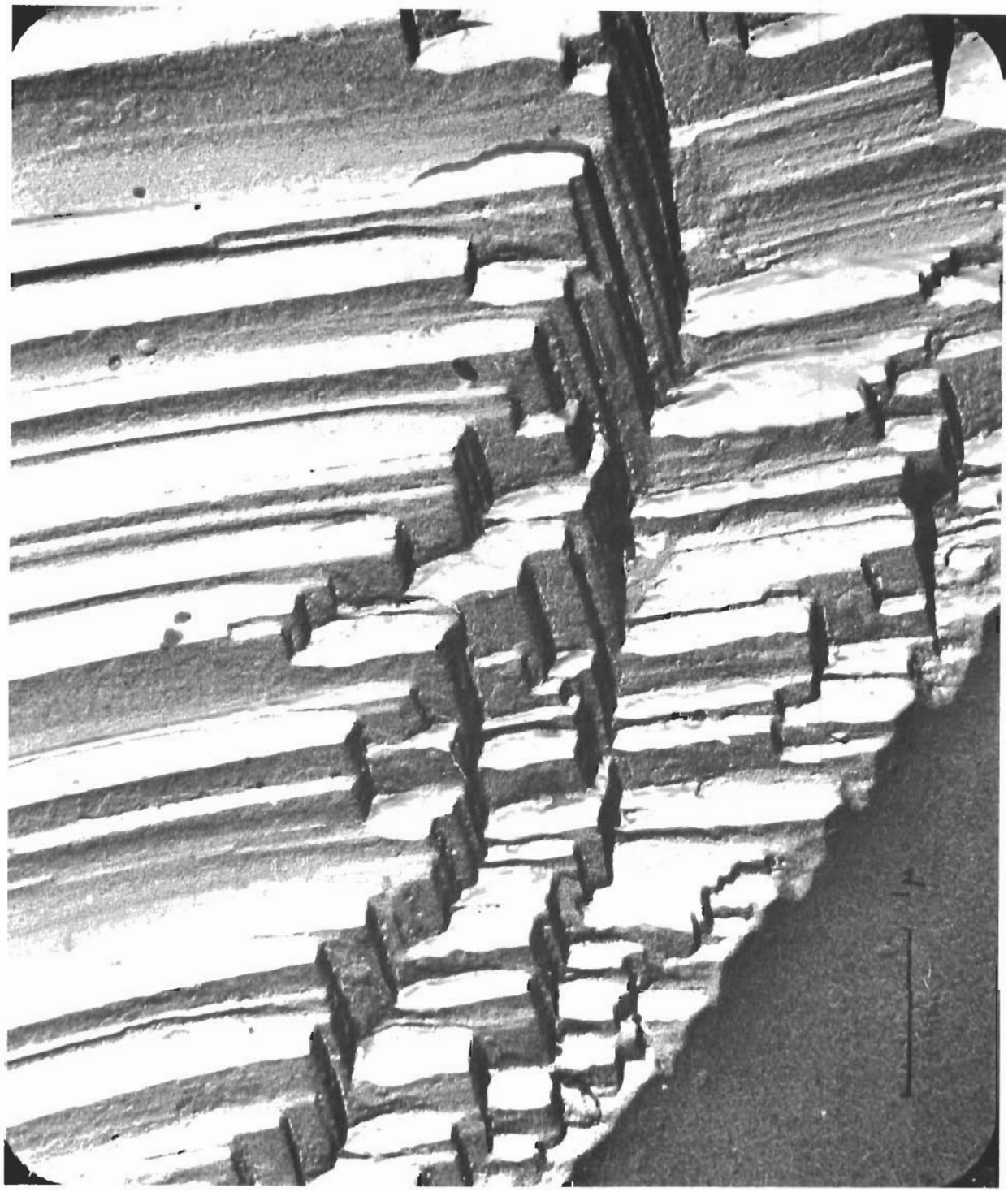

Fig. 6-16 ENLARGEMENT OF PART OF FIG. 6-15 X30,000

Fig. 6-17 EFFECT OF GRAIN ORIENTATION UPON FRACTURE SURFACE X24,000

Fig. 6-18 FRACTURE SURFACE PATTERN ACROSS GRAIN BOUNDARY X12,000

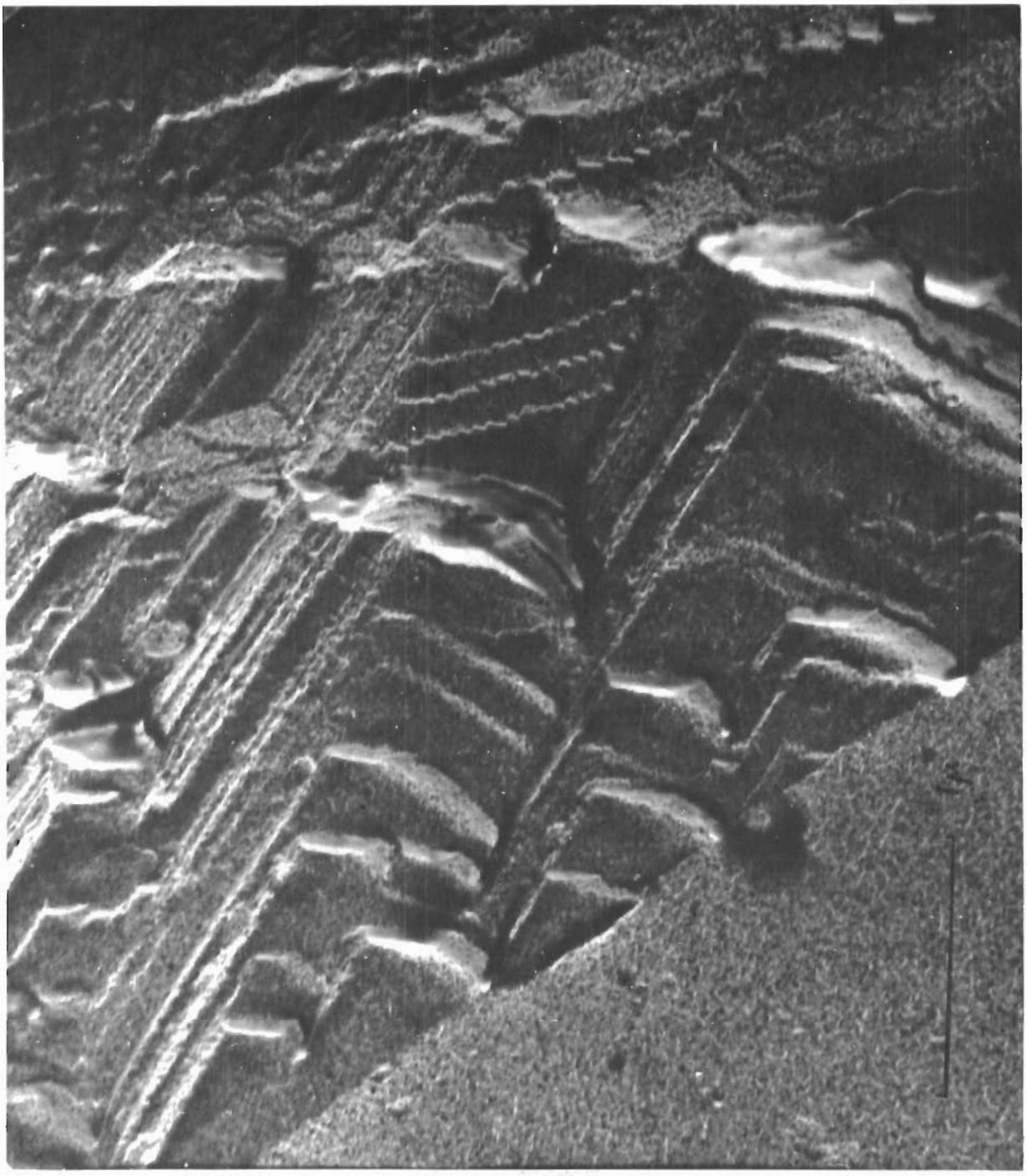

Fig. 6-19 HIGH MAGNIFICATION PICTURE OF SERRATED PATHS IN FRACTURE FACET X45,000

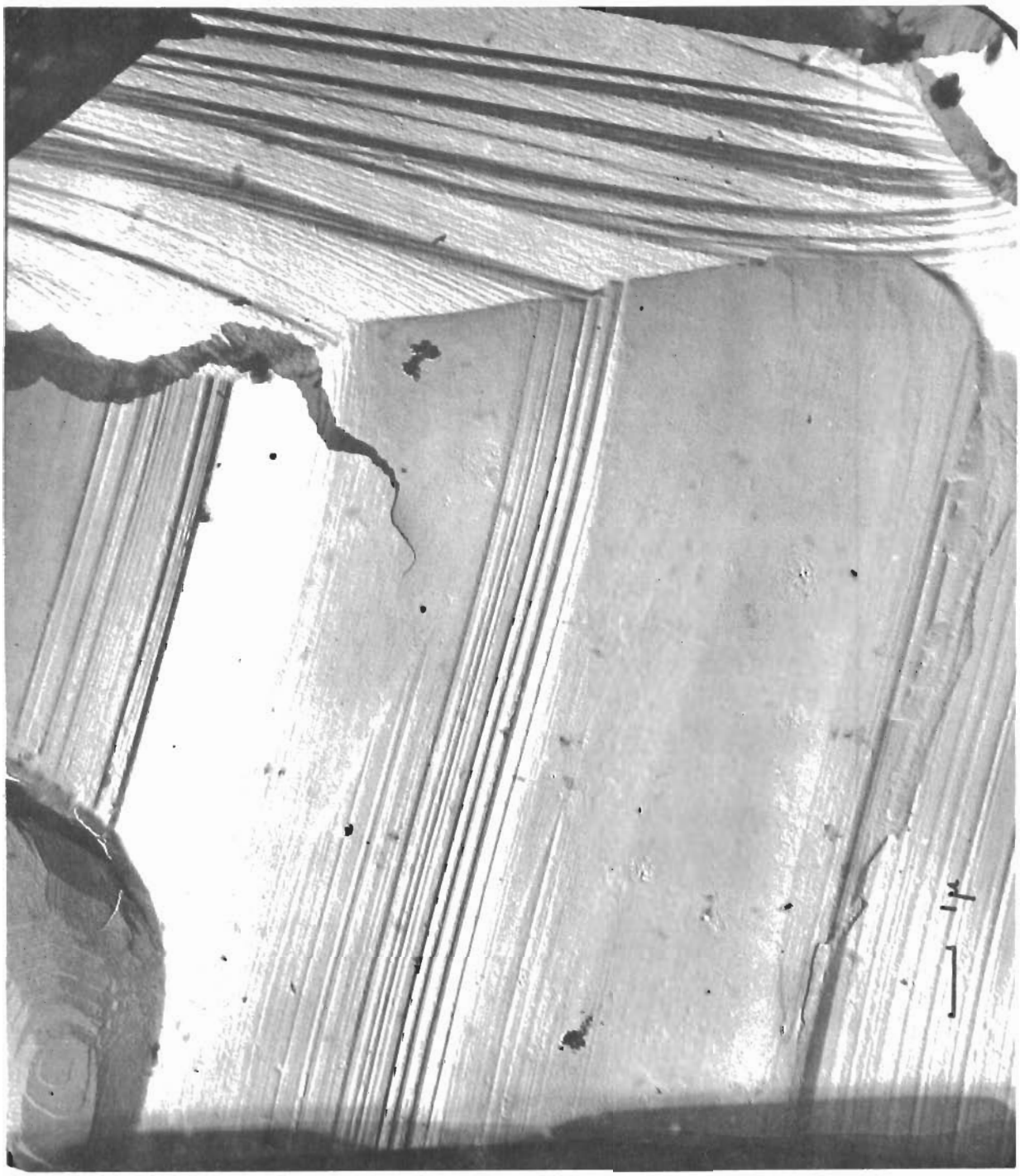

X12,000

Fig. 6-20 CONCHOIDAL FRACTURE MARKINGS

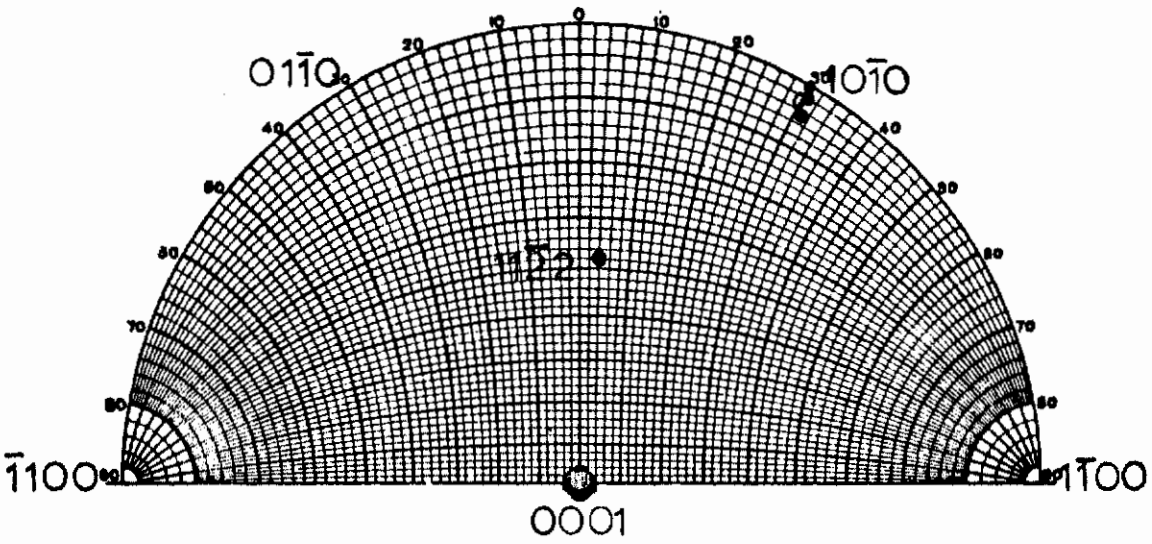

Fig. 6-21 ORIENTATION OF CLEAVAGE FACETS IN FRACTURE SURFACE OF POLYCRYSTALLINE Al_2O_3

as can be estimated, the cleavage steps meet at exactly 90°, and it is tentatively suggested that Al_2O_3 may show interrupted cleavage on (000.1), $\{10\bar{1}.0\}$ and $\{11\bar{2}.2\}$ planes.

Fractographic studies of this nature are a valuable aid in conjunction with the surface energy measurements, since they supply a means of studying the nature of the surface on which the measurements have been made.

6. CONCLUSIONS

A review has been made of all methods available for the determination of the surface energy associated with the creation of new surface in the fracture of polycrystalline ceramics. Of the various techniques reviewed, the crack propagation and zero creep methods were selected as offering the greatest reliability and reproducibility for the determination of surface energies. The former is useful at moderate temperatures, the latter at very high temperatures near the melting point of the material. In addition, adsorption techniques were developed for the determination of absolute surface energy values from adsorption isotherms, and some fractographic studies were carried out for the examination of the nature of fracture surfaces.

Work on crack propagation methods included an investigation of the applicability of Hertzian crack techniques, quantitative cleavage and the fracture of precracked thin plates for the determination of surface energies. For absolute surface energies, the precracked plate method is thought to hold out for the best good promise; however, grips that eliminate bending are needed for accurate measurements. These grips have been made, but have not yet been tested.

The Roesler and the impact cleavage methods have experimental and theoretical difficulties that considerably lower their accuracy. However, these methods may be useful at high temperatures, when difficulties in using the precracked plates may appear.

The lowering of the surface energy of Al_2O_3 by adsorption of CO_2 has been calculated from measurements of the adsorption isotherm. Because of a low specific surface, these measurements have been difficult, but there seems little doubt that the surface energy lowering in this case is

quite negligible. Measurements on the energy lowering from the adsorption of water vapor remain to be done. If these also indicate small energy changes, the explanation of delayed-fracture and of environment effects in terms of the lowering of surface energy by adsorption will have to be abandoned in this case.

The method of zero creep appears to be the only practical one for the direct determination of surface energy at very high temperatures. Its application to non-metallic bodies is believed to be novel. There are difficulties of specimen preparation, absent in the metal case. However, rods $\approx$ 1.0-mm diameter have been prepared and preliminary measurements suggest that application of the method to Al_2O_3 will be feasible. Construction of the special high-temperature furnace required has taken some considerable time, but, except for a few minor items, is now complete and it is expected that proper measurements will begin in a very short time.

All exploratory experimental studies to date have been confined to work with Al_2O_3. Satisfactory absolute surface energy measurements have not yet been achieved. Nevertheless, the method using precracked thin plates seems to have good promise at moderate temperatures. Removal of bending stresses from the testing jig used at present will be necessary; this is expected to be achieved with new grips that have been fabricated, but not yet tested. The method of zero-creep that yields absolute surface energy values at near the melting point has involved rather a large amount of equipment manufacture. This is all now practically ready. Some test of the method in a borrowed high-temperature furnace suggests that this technique should work satisfactorily.

The lowering of the surface energy of Al_2O_3 by the adsorption of CO_2 has been shown to be negligible. Measurements for water vapor have still to be carried out. If they should yield a similar result, surface energy lowering would seem to be eliminated as an explanation of delayed fracture and of environment effects in the case of Al_2O_3.

Fractography appears to be useful because of the information it gives about the surfaces used for measurement.

7. REFERENCES

6-1 Griffith, A. A., Proc. Internat. Congress App. Mechanics, Delft, 55, (1924).

6-2 Gilman, J. J., J. App. Phys., 31, 2208, (1960).

6-3 Kuznetsov, V. D., Surface Energy of Solids, H.M.S.O., (1957).

6-4 Roesler, F. C., Proc. Phys. Soc., B, 66, 981, (1956).

6-5 Dixon, J. R., Jour. Roy. Aero. Soc., 64, 141, (1960).

6-6 Berdennikov, Phys. Zeit. Sowjetunion, 4, 397, (1933).

6-7 Kies, U. S. Naval Res. Lab. Rep. No. 237.

6-8 Svensson, N. L., Proc. Phys. Soc., April 1961, 876.

6-9 Shand, E. B., J. Amer. Cer. Soc., 44, 1961, 21.

6-10 Charles, R. J., J. App. Phys., 1958, 29 (1549), 1554.

6-11 Moorthy, V. K. and Tooley, F. V., J. Amer. Ceram. Soc., 1956, 39, 215.

6-12 Orowan, E., Welding Journal Res. Suppl., 1955, 34, 157s.

6-13 Orowan, E., Nature, 1944, 154, 341.

6-14 Orowan, E., Z. Phys., 1933, 82, 835.

6-15 Jura, G. and Harkins, W. D., J. Amer. Chem. Soc., 66, 1356, (1944).

6-16 Petch, N. J., Phil. Mag., 1956 (viii), 1, 331.

6-17 Schoening, F. R. L., J. App. Physics, 1960, 31(10), 1779.

6-18 Gurney, C. and Pearson, S., Proc. Phys. Soc., 1949, 62B, 469.

6-19 Preston, F. W., Baker, T. C. and Glathart, J. L., J. Appl. Phys., 1946, 17, 162.

6-20 Eischen, G., Comptes Rendus, 1960, 250(12), 2194.

6-21 Pearson, S., Proc. Phys. Soc., 1956, 69B, 1293.

6-22 Kipling, J. J., and Peakall, D. B., J. Chem. Soc., 1957, Part 1, 834.

6-23 Sawai, I. and Nishida, N., Z. anorg. Chem., 1930, 190, 375.

6-24 Udin, H., Shaler, A. J., and Wulff, J., J. Metals, 1949, 1, 196.

6-25 Buttner, F. H., Udin, H., and Wulff, J., J. Metals, 1951, 3, 1209.

6-26 Hayward, E. R. and Greenough, A. P., J. Inst. Metals, 1959-60, 88, 217.

6-27 Davidson H., and Burwood, J., Engineering, Jan. 1954, 106.

TASK 7 - FRACTURE MECHANISMS

Principal Investigator: E. Orowan
Massachusetts Institute of Technology

ABSTRACT

The purpose of this research is to study the fracture mechanism of non-metallic materials, in order to obtain basic knowledge regarding the nature of crack initiation and propagation in brittle substances. During the current phase of the program a microscope stage and a high temperature testing machine have been built, the latter having a load range of 5000 lb at temperatures up to 4000°F.

The fracture mechanisms and cleavage surfaces of KCl crystals have been studied extensively at temperatures up to 600°C. Use of X-ray imaging methods disclosed the presence of kinking at the intersection of Gilman bands in MgO deformed at room temperature. The conversion of slip to kinking may be responsible for strain-hardening and crack initiation phenomena which has been heretofore attributed to the interaction of individual dislocations.

TASK 7 - FRACTURE MECHANISMS

1. INTRODUCTION

Much of the work concerned with the strength of brittle substances seeks to determine the parameters affecting two basic phenomena: crack initiation, and the propagation of fractures already nucleated. A good deal is understood about the factors affecting each phenomenon separately; while much remains to be done, the effects of grain size, porosity, surface energy, multiaxial stresses and speed of loading have been reasonably well determined. On the other hand, comparatively little attention has been paid to tying the information relating to crack initiation and its propagation together, to consider the overall mechanisms governing the fracture of brittle materials.

Although some high temperature refractories have limited ductility at the service temperature, they are almost completely brittle in a wide temperature range between room temperature and the service temperature. Brittleness in these materials is an inherent property which, in general, cannot be influenced effectively without modifying the composition or crystallographic structure of the material. All that can be done is to choose fabrication methods which prevent the formation of effective microcracks, suppress the formation of microcracks by plastic deformation under stress, or counteract the propagation of crack nuclei. The main possibilities of this nature are summarized in Table 7-I.

The purpose of the present work is to study the fracture mechanisms of non-metallic materials to obtain the basic knowledge required for the utilization of the possibilities described in Table 7-I for the production of high temperature refractories of reliably stable high mechanical strength and thermal shock resistance. In particular, this Task seeks to resolve the gap that exists currently between crack nucleation hypotheses on the one hand, and gross crack propagation and proliferation leading to fracture, on the other.

The materials studied fall into two categories; materials of practical importance as model refractories, and materials like alkali halides which have considerable ductility at relatively low temperatures and from which

Table 7-I

POSSIBLE METHODS FOR IMPROVING THE FRACTURE STRENGTH OF BRITTLE MATERIALS

General Method	Specific Approach	Remarks
Prevention of Inherent Cracks	Avoidance of formation of internal or surface crack in fabrication	Unreliable; subsequent surface damage can undo improvements obtained
	Remove exterior cracks by surface dissolution	As above; effective only for glasses and single crystals
Prevention of Plastic Crack Propagation	Increased yield stress	Hypothetical; effective only if crack nucleation is due to slip
	Changed deformation mechanism	Hypothetical; no method known
Increased Resistance to Crack Propagation	Residual skin compression	Effective in tempered glass and peened or nitrided metals; strength of multicrystalline refractories unaffected
	Fine grain structure	Very promising practical method
	Dispersed polyphase material	Potentially very promising method
	Composite material	Limited usefulness, extremely fine dispersion cannot be achieved mechanically
	Inclusion of limited voids	May be effective at very low porosity
Increased Density of Dislocation Sources	Highly localized pressure	Limited usefulness; ample dislocation sources already available
	Plastic deformation at elevated temperature, followed by suitable cooling	"Rheotropic embrittlement"; potential but limited practical importance

knowledge of plastic fracture mechanisms can be obtained more easily than from the majority of high temperature refractories.

The work proceeded in three directions. The first was the construction of a small testing machine which could be placed on the stage of a microscope for observing the specimen in ordinary or polarized light during deformation. This machine was constructed comparatively early, and various improvements have been added to it during the course of the program, among them an electric strain-gage dynamometer for measuring the load, and strain-gage extensometer for measuring or recording the deformation. The second line of work was the construction of a high temperature testing machine for tension, compression and (with an adapter) bending, for loads up to 5000 lb, and temperatures approaching 4000°F. The third line of work was the study of deformation and fracture of various single crystals, mainly MgO and KCl. Most of the work of the constructing of the high temperature testing machine was done by H. Keith; most of the crystal experiments by A. S. Argon.

2. THE MICROSCOPE STAGE TESTING MACHINE

Figure 7-1 is a photograph of the machine placed on the rotating stage of a polarizing microscope to which it is attached by clamps. The frame (1) is provided with dovetail-grooves in which plates carrying the stationary grip-holder (2) and the mobile grip-holder (3) can slide. The plate carrying the mobile grip-holder (3) is moved in the dovetail-guide by means of a threaded rod propelled by a toothed nut which is driven by the pinion (4). The gear ratio is high in order to be able to apply very small strains to specimens of low ductility; a revolution counter connected with the pinion shaft by bevel gears can be used as a rough measure of the strain applied. The strain can be measured accurately by an electric strain gage extensometer (not shown). The specimen is seen between the grip blocks, with the brass tubes into which it is cemented. The mobile grip holder (3) is connected with the dovetail plate by a strain gage dynamometer (5) which is a ring with a cylindrical inside and an octahedral outside surface, provided with 4 resistance gages. The thrust is transmitted from the pinion-driven toothed nut to the frame of the machine by a thrust ball-bearing.

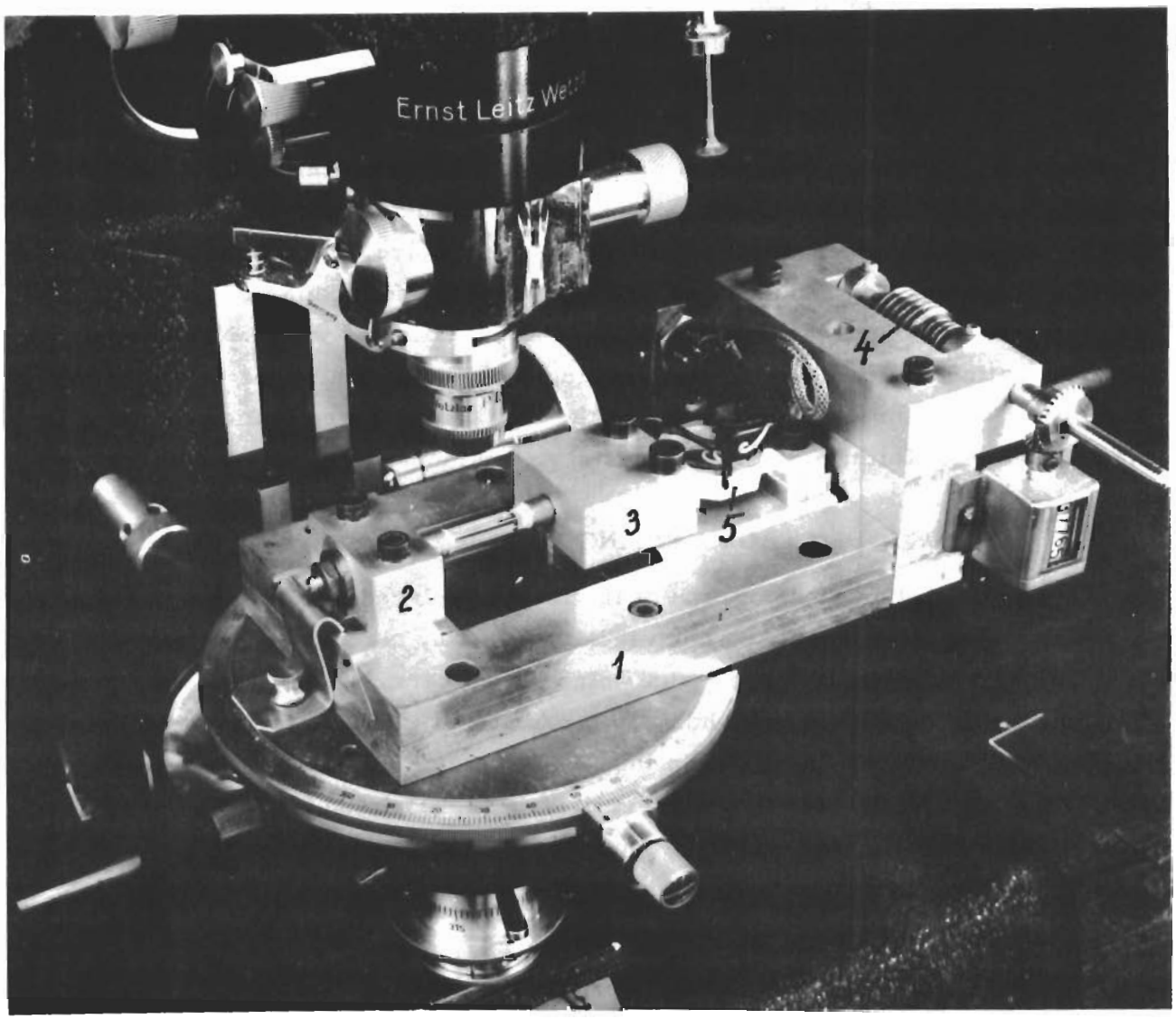

Fig. 7-1 VIEW OF MICROSCOPE STAGE TESTING MACHINE

In addition to the fixture shown in Fig. 7-1, adapters were made for the compression of specimens not provided with brass holders, and also for bending tests under four-point loading. The supports for the bending test are cylindrical surfaces covered with neoprene membranes of about 0.007 in. thickness; thus, concentrated pressure on the specimen is avoided without introducing too much elasticity in the machine.

3. THE HIGH TEMPERATURE TESTING MACHINE

The machine is designed for a maximum load of 5000 lb; the load is measured by dynamometers provided with sets of electric resistance gages. Frictional forces are held to less than 1 oz by the use of ball bearings, so that the machine can be used with sufficient accuracy for a load range of about 5 lb with suitable dynamometers. Like the microscope-stage testing machine, it has a threaded rod drive.

Heating of the specimen is accomplished with a tubular electric resistance heating element provided with two diametrally opposite lengthwise slots. This makes it possible to observe the specimen during the test; it also doubles the length of the current path and reduces by half the cross section, so that the heating current is halved. The heating element is made of tantalum sheet; for higher temperatures (up to nearly 4000°F) a tungsten heating element can be used. The heating element is surrounded by three sets of radiation shields (concentric cylinders around the tube, circular plates above and below). Heating element, radiation shields, specimen, and grips are in an evacuated steel vessel with water-cooled walls; the pulling rod is also water cooled. The power supply is a saturated core transformer of 25-KVA capacity.

Figure 7-2 shows a vertical and a horizontal section of the machine, and a vertical view. Figure 7-3 is a photograph of the machine showing the central part of the machine with the lower part of the vacuum vessel lowered, so that the radiation shield is visible; the lower grip is not inserted. This picture differs from the drawings in Fig. 7-2 in that the two balance weights for the removable lower part of the vacuum vessel have been joined together and the sprocket chains attached to the joined weight are led over two sprocket wheels, one with a hand-wheel, to opposite sides of the vessel.

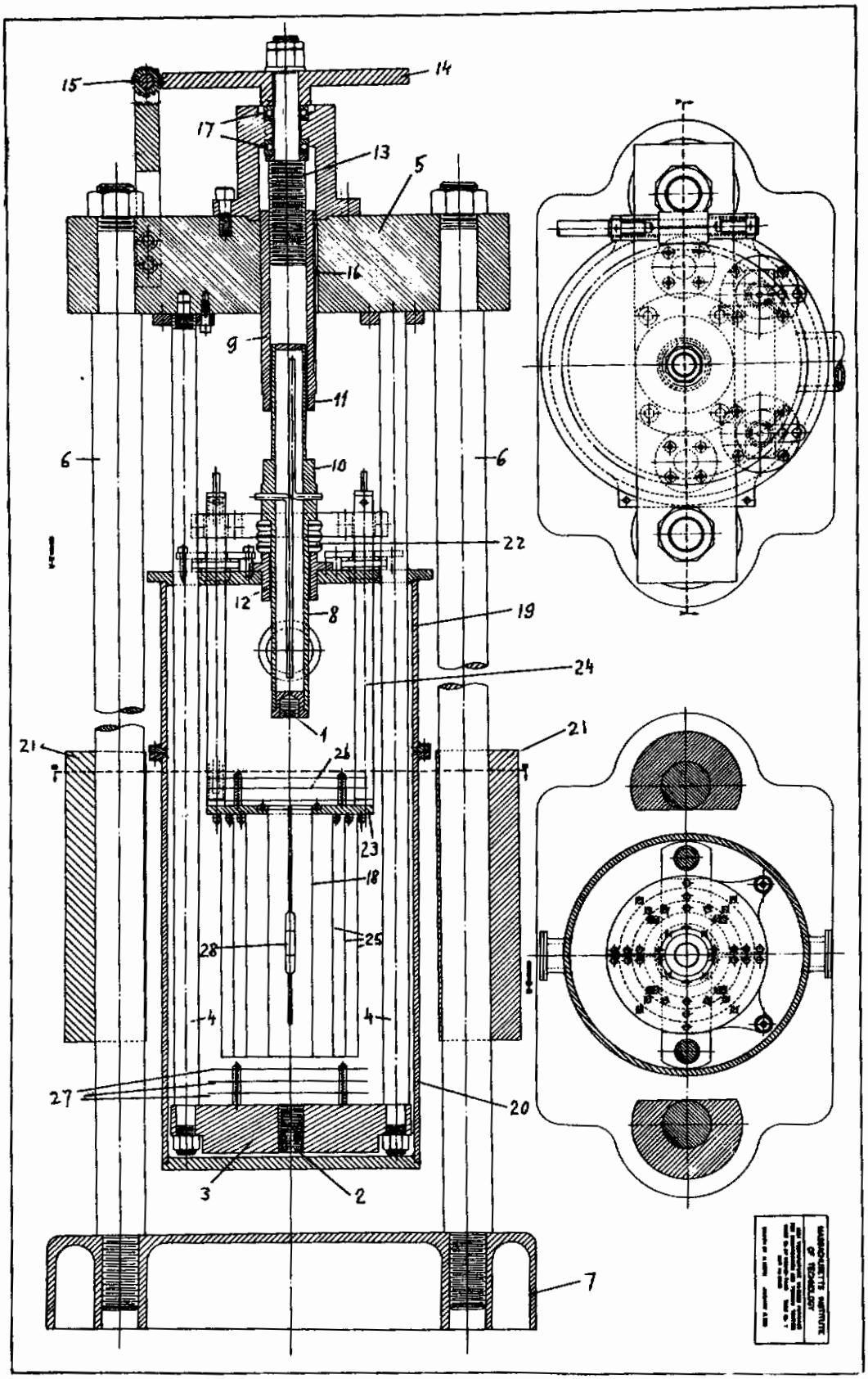

Fig. 7-2 HIGH-TEMPERATURE VACUUM FURNACE FOR USE WITH 5000 LB TESTING MACHINE

With reference to the numbering used in Fig. 7-2, the machine is built up on a frame consisting of a base (7), two vertical steel columns of 2-in. diameter, and a head-piece (5); its height is approximately 6 feet. Two steel columns (4) are suspended from the head-piece; their lower ends carry a heavy steel disc (3) with a central threaded hole (2) into which the lower (fixed) specimen grip is screwed. The upper grip is screwed into a threaded plug (1) closing the lower end of the lower part of the pulling (or compressing) rod (8). This hollow rod is water-cooled in a way seen in the drawing. It slides in the thick-walled tube (9) which is the upper part of the pulling rod and has an internal thread into which the threaded rod (13) engages. The tube is prevented from rotating by the key (16), so that it is lifted or lowered when the threaded rod is rotated by the pinion wheel (14) and the pinion (15). The pinion is supported on a swiveling block so that it can be disengaged if the pulling rod is to be moved rapidly.

The two parts (8) and (9) of the pulling rod are connected by a thin-walled tube or thin strips, the ends of which are screwed to (8) and (9) at the points (10) and (11), the connecting tube or strips (not shown in the drawing) carry the resistance gages and act as a dynamometer. The lower part (8) of the pulling rod is guided in the upper part by three vertical rows of steel balls in a single cage; similarly, the lower part of the rod is guided in the bushing (12) of the vacuum vessel by three rows of steel balls. In this way the friction is reduced, and the rod is guided with no perceptible play. Consequently, it can be used for compressing specimens as well as for pulling them, without danger of buckling at the sliding joint of the two parts (8) and (9).

The original plan was to seal the vacuum vessel at the bushing (12) by neoprene bellows (22) stiffened by wire ring. However, under vacuum all bellows made (by dipping from neoprene latex, with textile or steel wire reinforcements) had a tendency to instability by shear between neighboring corrugations; for this reason, the bellows were replaced by "Bellofram" rolling rubber diaphragms.

The vacuum vessel consists of a short upper and a long lower part bolted together by flanges with a sealing rubber O-ring between the flanges; its lower part can be lowered as shown in Fig. 7-3, by unbolting the connection and turning the hand-wheel shown in Fig. 7-4.

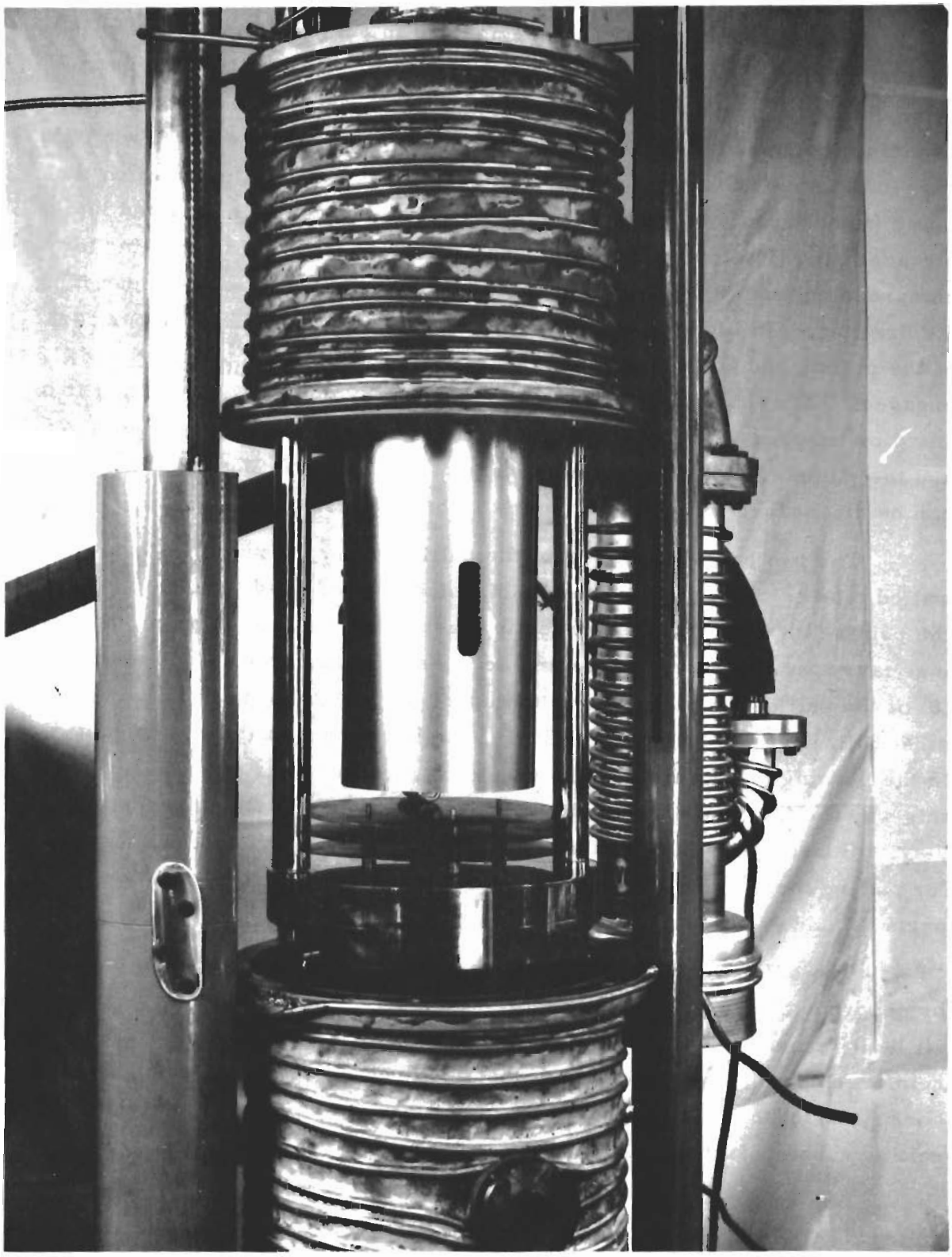

Fig. 7-3 VIEW OF CENTRAL PART OF HIGH-TEMPERATURE TEST FACILITY

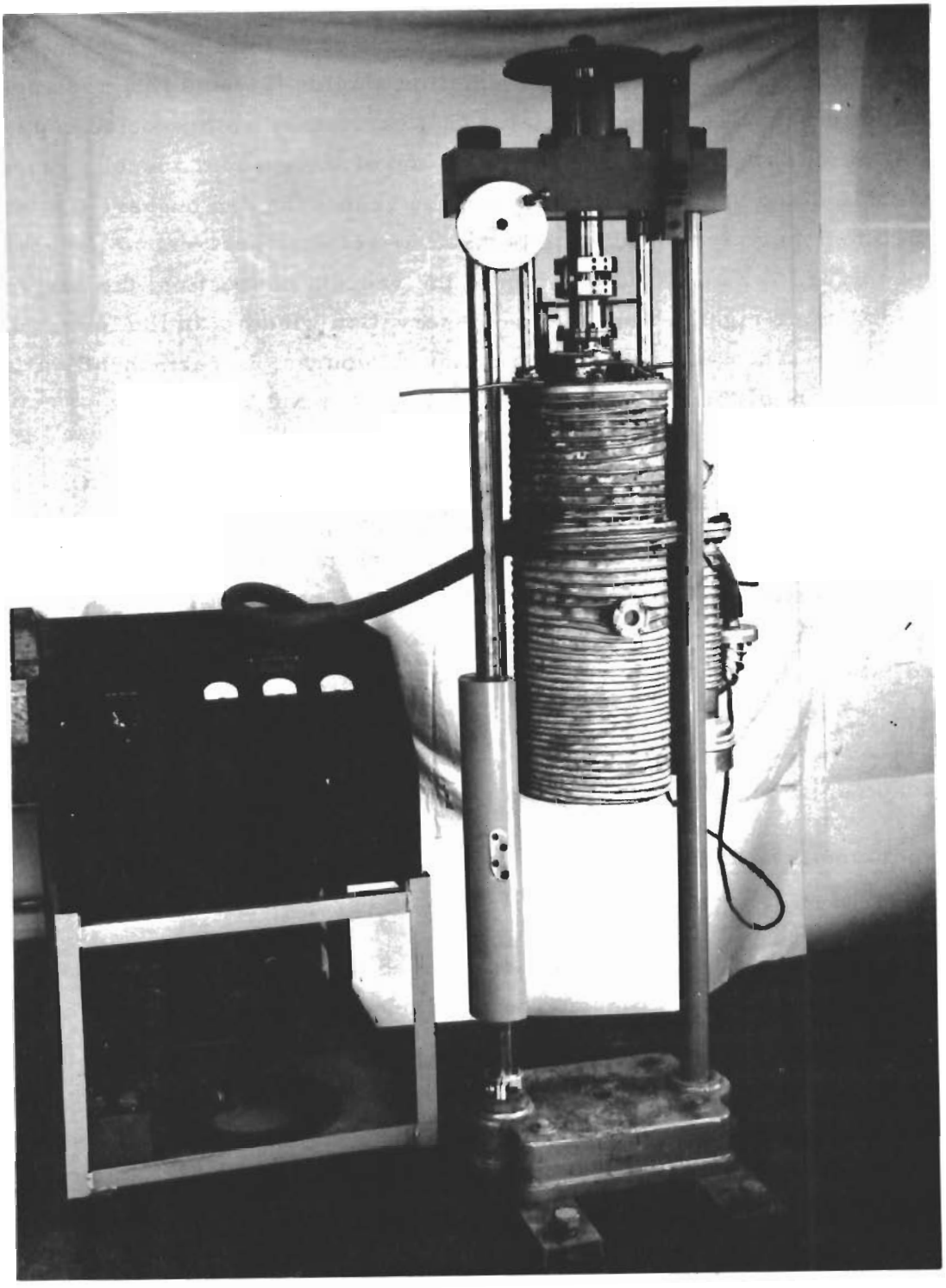

Fig. 7-4 OVERALL VIEW OF HIGH-TEMPERATURE TEST FACILITY FOR USE WITH 5000-lb TESTING MACHINE

The heating element (28), of tantalum sheet 60 mils thick and the upper horizontal and the cylindrical radiation shields (26) and (25) are supported by two heavy molybdenum plates (23) carried by water-cooled copper rods (24) which are introduced through the top of the vacuum vessel electrically insulated and vacuum sealed; above the vessel the two busbars (24) are bracketed together by an insulating bar. The vertical section and the vertical view in Fig. 7-2 show the position of the vacuum connection; the horizontal section (lower right) shows the two observation windows in the lower part of the vessel. The vacuum diffusion pump, of course, is permanently attached to the upper part of the vessel, as seen in Fig. 7-3 and 7-4.

4. EXPERIMENTS ON THE FRACTURE AND DEFORMATION OF NON-METALLIC SINGLE CRYSTALS

The single crystal work falls into two groups, the first with alkali halides (principally KCl), the second with MgO which, after the pioneering work of Gilman[7-1] and Stokes[7-2] has become a particularly attractive object of study independently of its practical use as a high temperature refractory. The main part of these experiments was made at room temperature, by microscopic x-ray methods; but they also included observations of cleavage surfaces after cleavage in a wide range of temperatures.

A. Experiments with Alkali Halides

a. Cleavage Experiments

Most of these experiments were carried out with KCl crystals made by the Harshaw Chemical Company; we are indebted to Professor A. Smakula of MIT, who kindly gave us several crystals, and also to our colleague Professor F. A. McClintock who gave us a large KCl crystal produced by Harshaw.

The crystals were cleaved with hammer and chisel at temperatures ranging from liquid nitrogen to about 600°C. The cleavage surfaces show three kinds of markings: tracks, stop-lines and worms. These will be discussed separately.

Tracks (trajectories, rivers, hackles). These are fine steps running approximately parallel to the direction of crack propagation. Figure 7-5 shows, as a composite micrograph, the entire cleavage face of a KCl crystal, cleaved

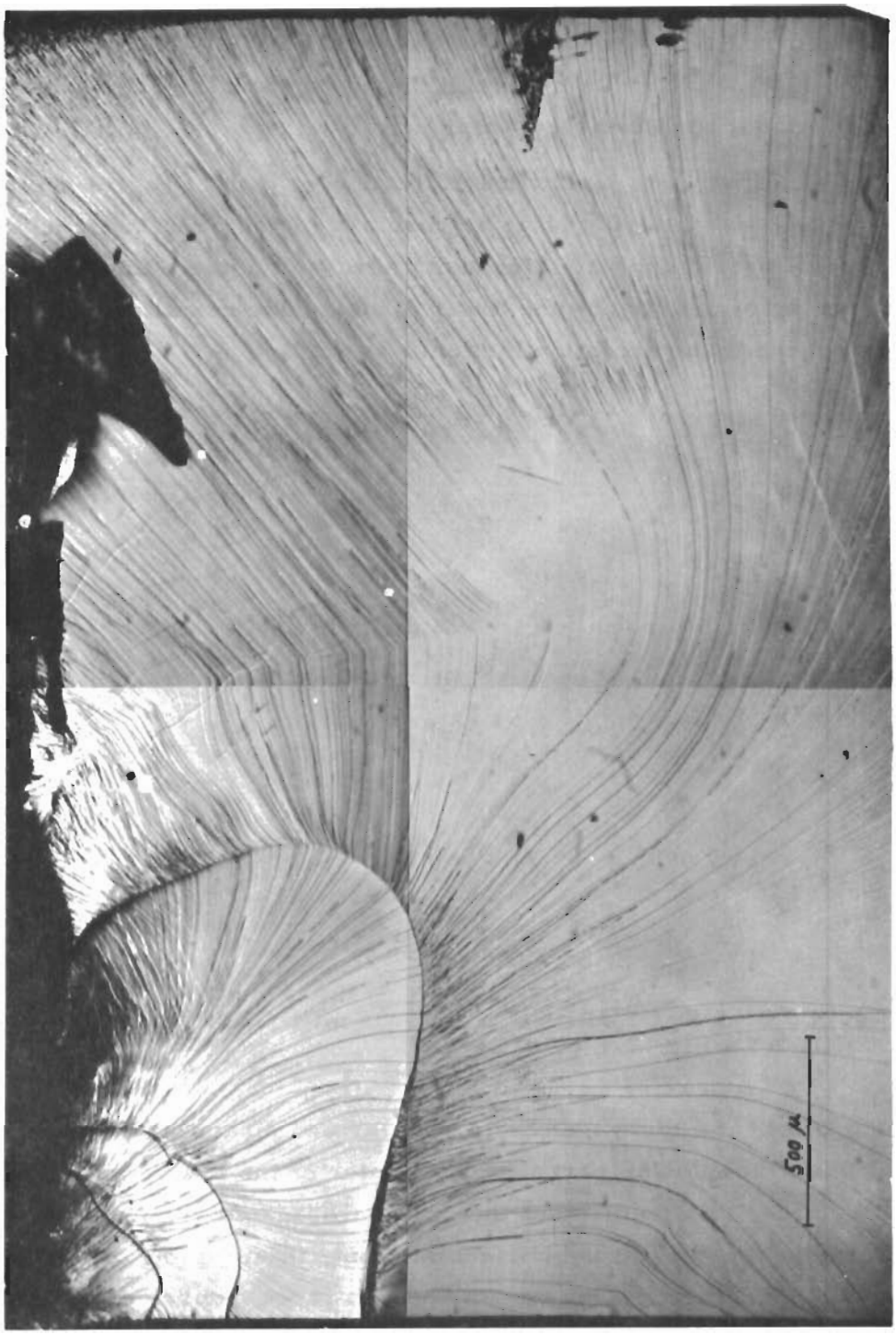

Fig. 7-5 FRACTURE SURFACE OF KCl CRYSTAL CLEAVED AT 400°C

at 400°C. The horizontal black strip at the top is the indentation of the chisel. The entire area is covered with more or less finely spaced tracks; at the upper left corner where the crack initiated they run at about 45° downwards and to the right. Near the middle of the photograph they become approximately horizontal, and then they swing upwards.

Figure 7-6 shows, at a higher magnification, a part of Fig. 7-5 (upside down). There are glittering shite segments along some of the tracks. They are due to the overlapping of neighboring cleavage planes, and the consequent undercutting of the step by the lower plane. The resulting crack under the step produces the bright reflection.

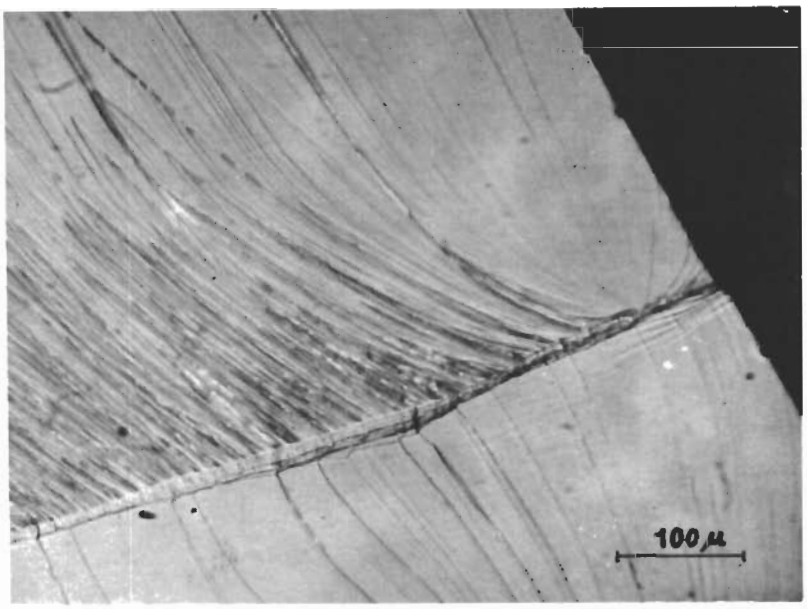

Fig. 7-6 PART OF FRACTURE SURFACE OF KCl CRYSTAL SHOWN IN Fig. 7-5 (400°C)

Tracks, i.e., new cleavage levels, appear and disappear during the propagation of the crack. The part near the center of the left vertical edge of Fig. 7-5 illustrates this point. As the crack propagated vertically downwards, it stopped at the dark broad horizontal front, interrupting the active cleavage planes. Cleavage is then re-started in a large number of neighboring planes, giving rise to very closely spaced tracks. Soon, however, groups of neighboring shallow steps join to a small number of large steps.

Figure 7-7 (cleavage at 400°C) shows details of how tracks merge. If both are of the "same sign" they join to form a single step the height of which is the sum of the heights of the two constituent steps. This occurs several times alone the largest step near the middle of the figure which increases in height as the crack propagated from right to the left. If the merging steps are equal in height but of opposite sign, they annihilate each other. This occurs in Fig. 7-7 at the nearly horizontal V-shaped junctions.

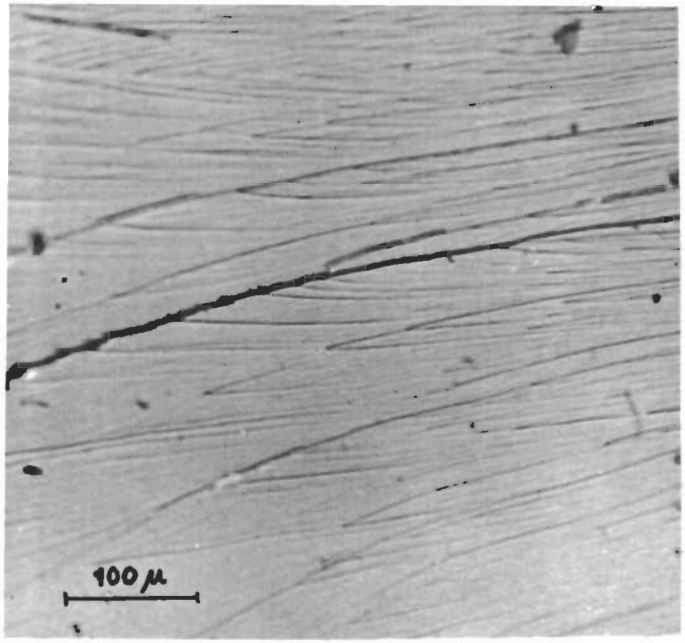

Fig. 7-7 CLEAVAGE TRACKS (RIVER MARKS) ON FRACTURE SURFACE OF KCl CRYSTAL (Cleaved at 400°C)

Figure 7-8 shows a cleavage surface produced in impact bending with a blunt instrument. The number of tracks is very small at the beginning but it increases so rapidly that finally the surface presents a fur-like appearance. The cause of this is not clear; the forking apart of cleavage planes at screw dislocations produced by plastic deformation may be a factor. Figure 7-9 shows details of steps with dislocation etch-pits in a crystal cleaved at 500°C. There is a clear tendency for rows of dislocation pits to accompany steps, giving evidence of plastic deformation where a lamella between neighboring cleavage planes is torn apart in the formation of a step.

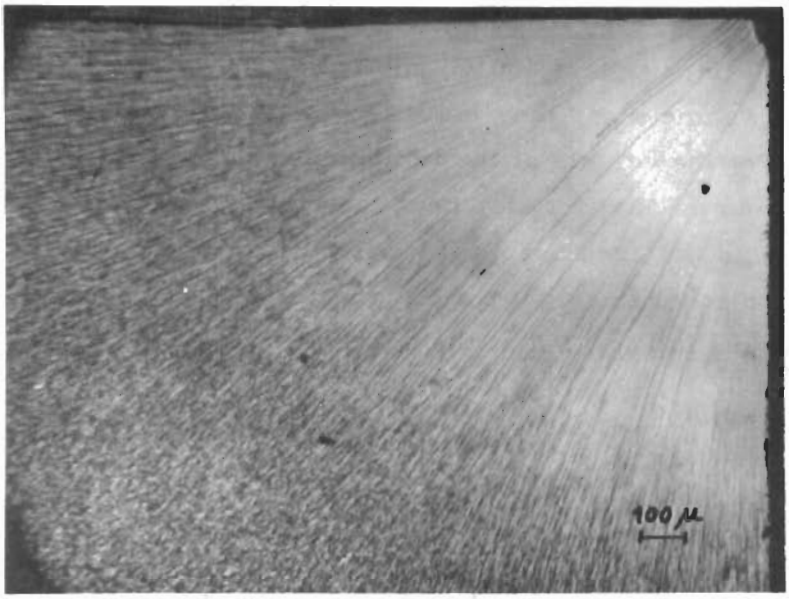

Fig. 7-8 FRACTURE SURFACE OF KCl CRYSTAL BENT BY IMPACT AT 200°C

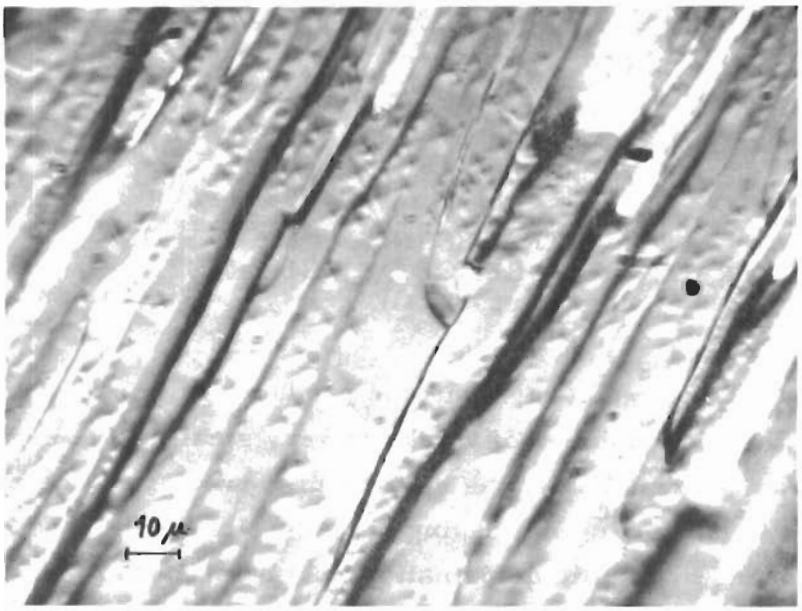

Fig. 7-9 CLEAVAGE TRACKS ON KCl CRYSTAL CLEAVED AT 500°C
Showing dislocation etch-pit distribution.

Stop Lines. The most conspicuous feature of Fig. 7-5 is the three concentric lines near the upper left corner of the picture. These are crack fronts where the crack propagation has temporarily stopped, due to either a drop of the load (the cleaving chisel may not follow the cleavage fast enough, or a drop of local stress due to bulging of the crack front), or due to reflected stress waves. Once the crack velocity has dropped, the yield stress may decrease below the cleavage strength and plastic deformation may be large enough to result in ductile fracture, as seen more clearly at higher magnification in Fig. 7-10. The direction of crack propagation, and that of the tracks, changes behind the stop line

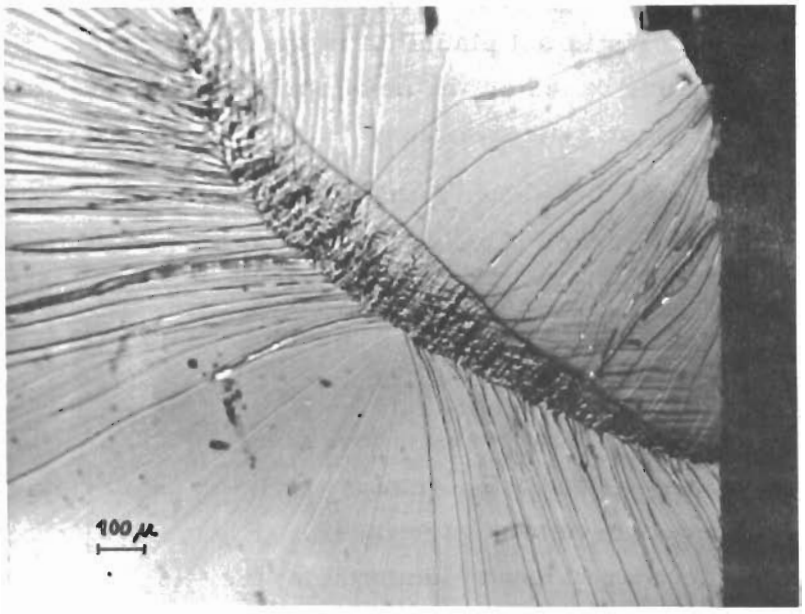

Fig. 7-10 ORIGIN OF CLEAVAGE FRACTURE RE-INITIATION AFTER EXTENSIVE PLASTIC DEFORMATION AT A FRACTURE-STOP FRONT

An interesting question is why ductile fracture changes again to cleavage fracture. Plastic deformation raises the yield stress; in general, it also raises the cleavage strength ("strain strengthening"). If the rise of the yield stress is greater, strain hardening may lead to cleavage fracture. However, this did not occur in the wide belt of ductile fracture in Fig. 7-10. The most plausible explanation is that plastic deformation produced a tri-axiality of tension which finally started cleavage fracture.

This explanation for the mechanism of stop lines and re-nucleation of cleavage was first advanced by Felbeck and Orowan (Weld. Journ. Res. Suppl. Nov. 1955) based upon observations in low carbon steel. This view finds support by the fact that stop lines in KCl do not occur at very low temperatures and become more and more marked as the temperature rises. The observation of the phenomenon in KCl is of interest because it has been suggested that the yield phenomenon in iron plays a decisive role in producing brittle fracture; according to the view mentioned, the yield delay (which is connected to the yield phenomenon) would give a chance for cleavage to occur before plastic deformation would take the upper hand. Since KCl, which shows no yield phenomenon, displays the stop line behavior as iron, the yield delay hypothesis is not plausible in the latter case. Both cases conform with the picture based on the development of triaxial tension at the crack tip after local plastic deformation.

Worms. Figure 7-5 shows a third feature of cleavage faces most clearly visible as light curved lines at the bottom of the bottom right quandrant. They are also present around the center of the upper edge of the figure in the form of light lines sloping at about 45° downwards and to the right. These lines have been termed "worms".

Worms are clearly observable above about 200°C and they are strongly marked above 400°C. Their most striking characteristic is that they do not match on opposite cleavage faces. Figure 7-11 shows this fact. The two cleavage faces are shown side by side; the illumination was chosen so that the worms appear mostly as sharp lines. Since they do not match, worms must have been formed after the crack has passed through, but before fracture was complete. This is in accord with the fact that worms become conspicuous only at higher temperatures when the yield stress becomes sufficiently low and pencil glide appears.

b. Plastic Crack Origination in KCl

In unpolished crystals fracture starts almost invariably at the surface, evidently at a surface crack of the Griffith type. In water-polished crystals, on the other hand, most surface cracks have been removed and

fracture starts, more often than not, in the interior. Figure 7-12 shows a cleavage surface with the crack origin which makes an angle of about 20° with the cleavage plane. Particularly in this case, the initiating crack does not seem to be an inherent flaw; it seems to have been produced by the preceding plastic deformation

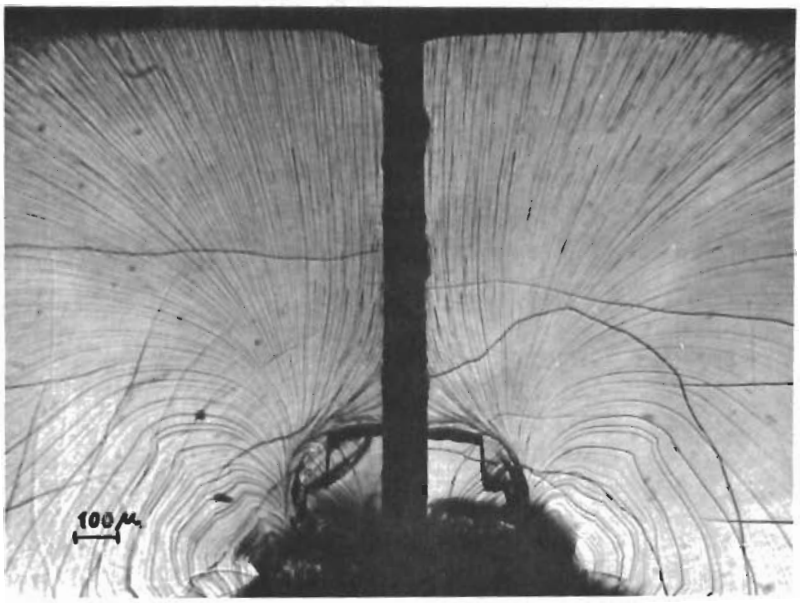

Fig. 7-11 FRACTURE SURFACE MARKINGS ON A KCl CRYSTAL CLEAVED AT 600°C
Note especially the wavy (worm) lines.

c. Pencil Glide in KCl

Figures 7-13 and 7-14 show slip bands in KCl deformed at 300°C, the latter being a case of extreme pencil glide. It has been known for a long time[7-16] that KCl shows a higher temperature slip both on the (110) and (111) planes, in the $[\bar{1}10]$ direction.

Figure 7-13 is interesting in that it shows two wide bands practically without slip markings. Examination of the crystal revealed that in these bands slip has taken place with a slip direction parallel to the plane of the figure. This has inhibited slip band formation with slip direction at an angle to the surface of the crystal, i.e., the formation of visible slip bands.

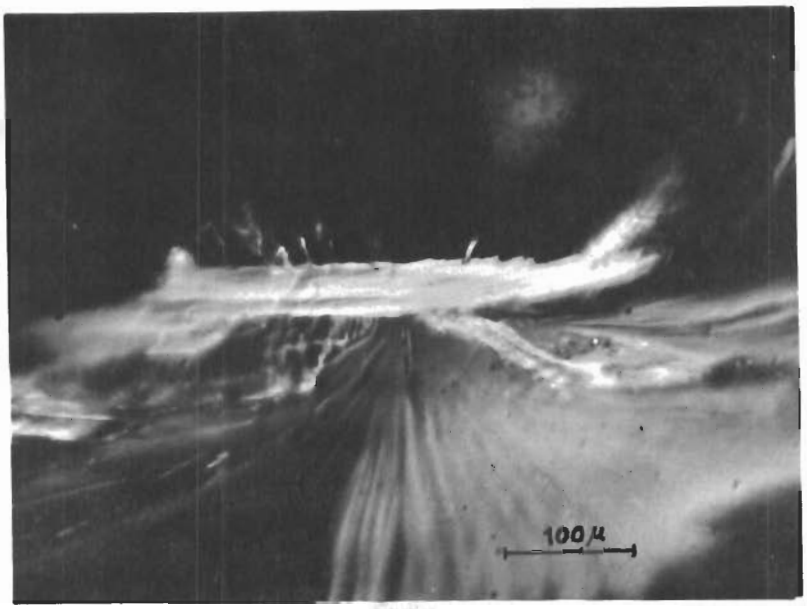

Fig. 7-12 INTERNAL FRACTURE ORIGIN IN A WATER POLISHED KCl CRYSTAL BENT AT 20°C. Plane of fracture origin makes an angle of 22° with the (100) cleavage plane.

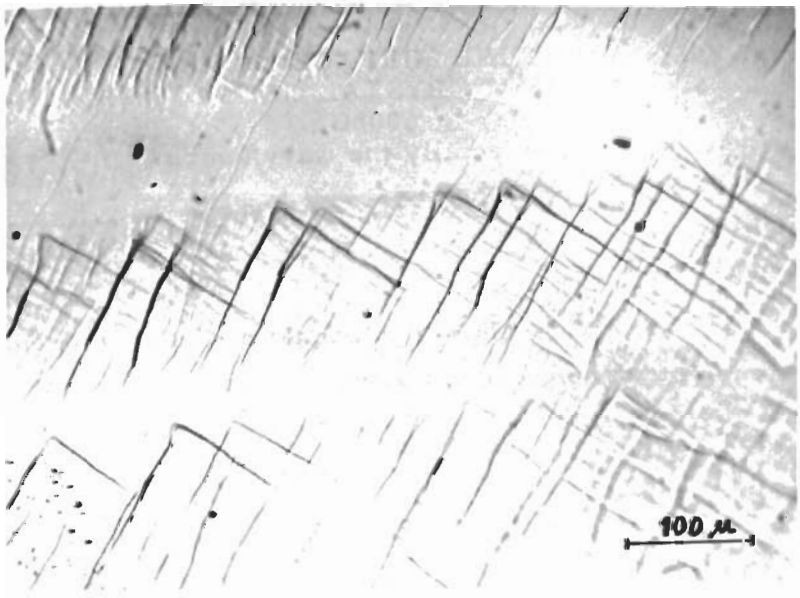

Fig. 7-13 SURFACE SLIP STEPS ON KCl CRYSTAL DEFORMED AT 300°C IN BENDING. The horizontal bands are (110) slip bands with the slip direction in the surface of the crystal.

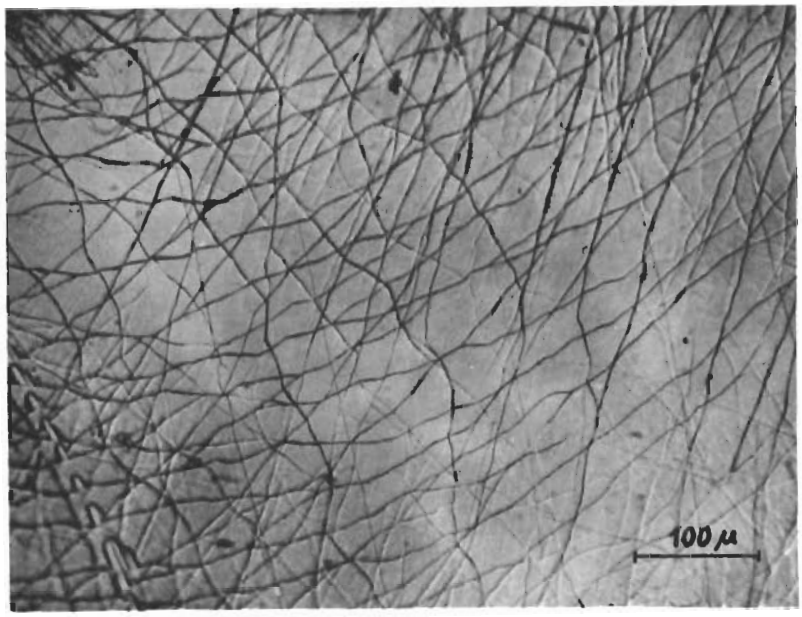

Fig. 7-14 A DIFFERENT AREA OF THE CRYSTAL SHOWN IN FIG. 7-13

B. Experiments with Magnesium Oxide

Magnesium oxide belongs to a group of crystals which can be obtained with a very low dislocation density. It was observed in LiF by Gilman[7-1], in MgO by Stokes and Johnston[7-2], in silicon iron by Low[7-3] that slip in such crystals occurs by the formation and gradual widening of bands very uniformly filled by dislocations; Gilman could show that the dislocations are produced by double cross slip multiplication. To avoid confusion, these bands will be called Gilman bands. They are certainly quite different from slip bands in the usual sense of the word which arise from slip lines at a later stage of the deformation.

Stokes and Johnston have observed that Gilman bands in MgO may suffer a parallel displacement where they are intersected by another band. Figures 7-15 and 7-16 are examples of this. The narrow vertical band in Fig. 7-15 has evidently suffered a counterclockwise shear by the operation of the wide horizontal band; this, however, might have been the result of a pure translation. In some cases, however, details of the intersection do not seem compatible with a simple translation (e.g., Fig. 7-16). In Fig. 7-17 the surface of an MgO crystal is seen that has been compressed in two stages and etched

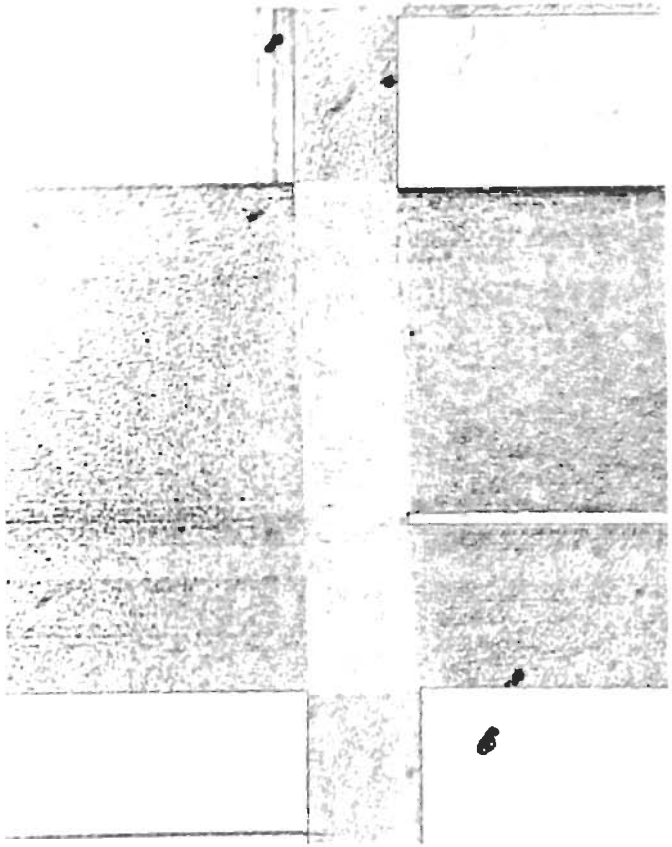

Fig. 7-15 CHANGE IN LATTICE ORIENTATION AT INTERSECTING SLIP BANDS (GILMAN BANDS) IN MgO CRYSTAL

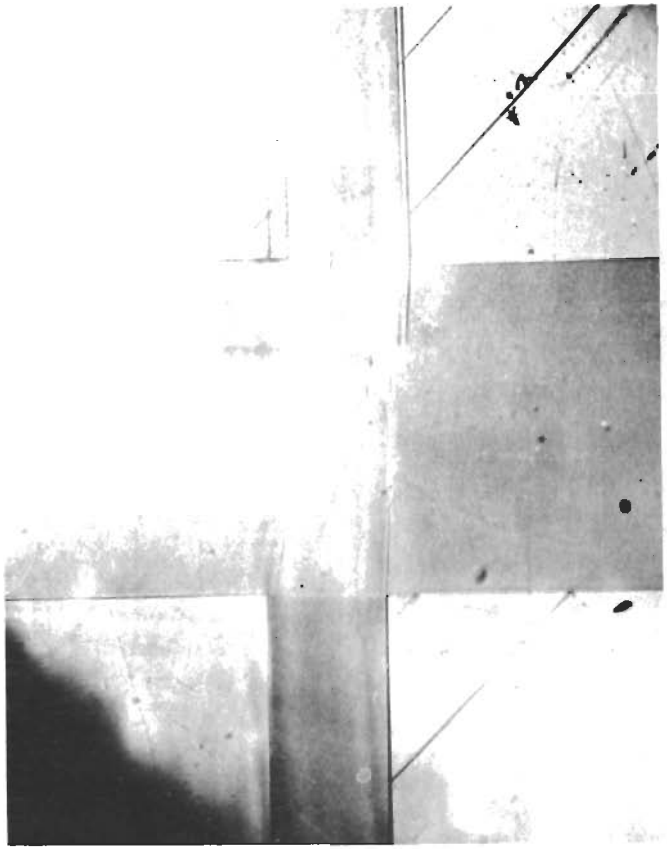

Fig. 7-16 CHANGE IN LATTICE ORIENTATION AT INTERSECTING SLIP BANDS IN DIFFERENT MgO CRYSTAL

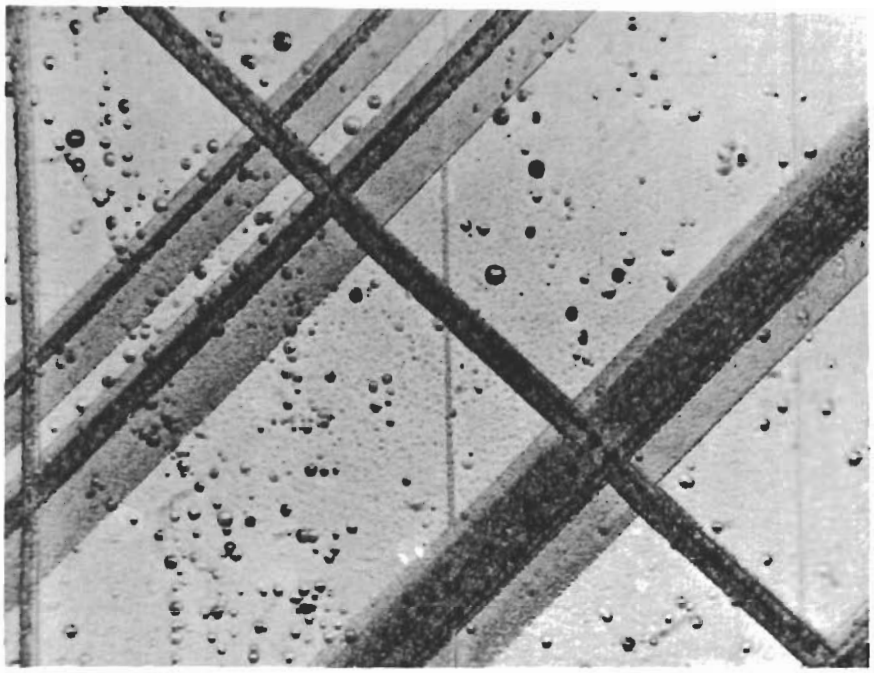

Fig. 7-17 STAGGERING OF DISLOCATION SLIP BANDS UNDER REACTIVATED FLOW IN MgO SINGLE CRYSTALS

after each compression. The strongly etched dark parts of the bands were the results of the first compression; the lighter part, those of second. The narrow dark band has been sheared by the three intersecting wide bands. The remarkable point is that the light lower edges of the three wide bands are sharply staggered at the intersection, while the dark cores of the wide bands must have progressed by different amounts above and below the intersections. This means that the deformation could not have been a simple translation which would not have permitted any staggering of the band edges. A similar picture of this same phenomenon is shown in Fig. 7-18.

To decide whether a non-translational deformation (lattice rotation) has taken place at the band intersections, x-ray images of the crystal faces have been prepared with the Berg(7-4) - Barrett(7-5) method. In this method a sufficiently divergent bundle of monochromatic x-rays falls on the face of the crystal to produce Bragg reflection at a suitable atomic plane. If the crystal is perfect and it is fully bathed in the x-ray beam, an image of uniform density of the crystal outlines is reflected. If, however, there is a volume of slightly different orientation in the crystal, the Bragg reflection is displaced, and the area corresponding to the disoriented volume on the

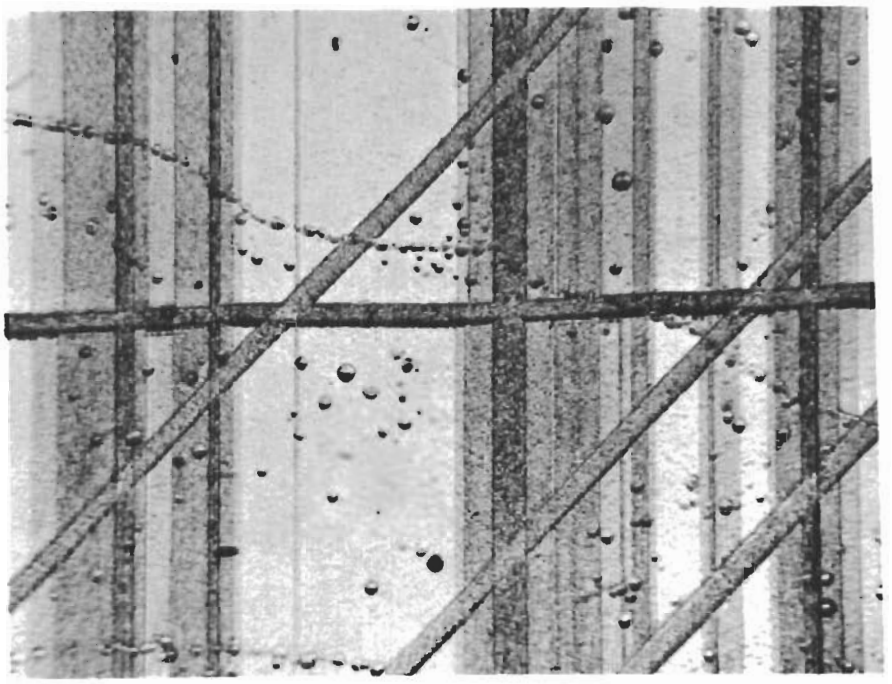

Fig. 7-18 SLIP-BANDS IN MgO UNDER REACTIVATED FLOW (As in Fig. 7-17)

film is lighter or completely white. The intersection already shown in the optical photograph of Fig. 7-16 is presented under transmitted polarized light in Fig. 7-19(a), and by the Berg-Barrett x-ray image in Fig. 7-19(b); an arrow in the latter points at the intersection shown in Fig. 7-19(a). These figures show that the intersection is broken up into three areas; in the x-ray image Fig. 7-19(b), the reflection from the central area can be found just beyond the lower left hand corner of the intersection, while the reflections from the top and bottom areas have been displaced by the same amount upward and to the right. The intersection itself is white on the x-ray image which shows the appearance of the x-ray film itself (not a print of the film). The Gilman bands are dark because the dislocations have reduced primary extinction and produced a mosaic effect.

Figure 7-20 shows a simple way in which the lattice can suffer a rotation at the intersection of slip bands. If the horizontal band operates first and then the vertical band becomes active, the shear produced by slip in the vertical band outside the intersection may arise partly or mainly by the operation of the slip planes of the horizontal band in the volume of intersection. In

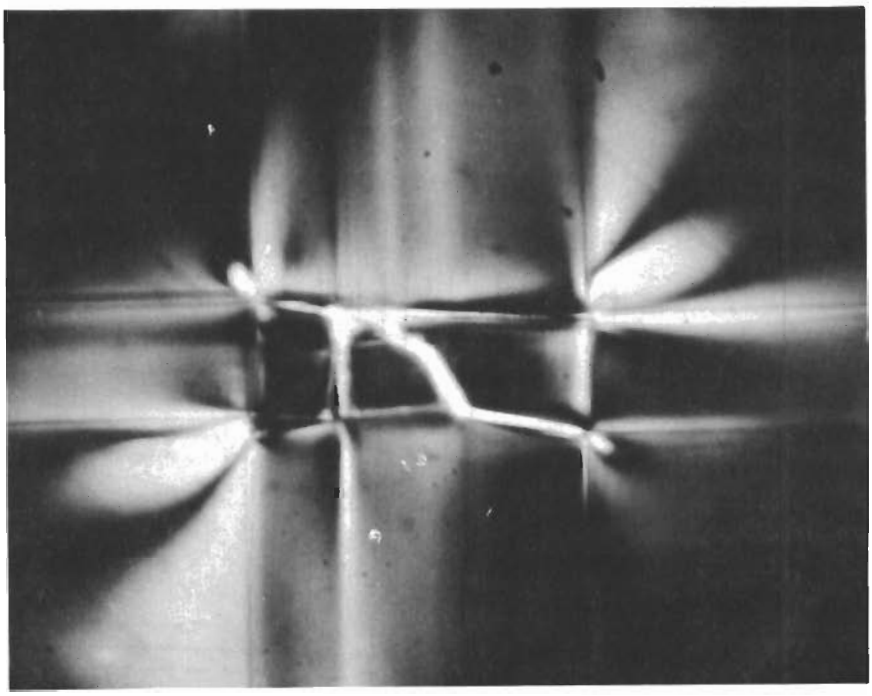

Fig. 7-19(a) AREA OF MgO CRYSTAL SHOWN IN Fig. 7-16 VIEWED UNDER TRANSMITTED POLARIZED LIGHT

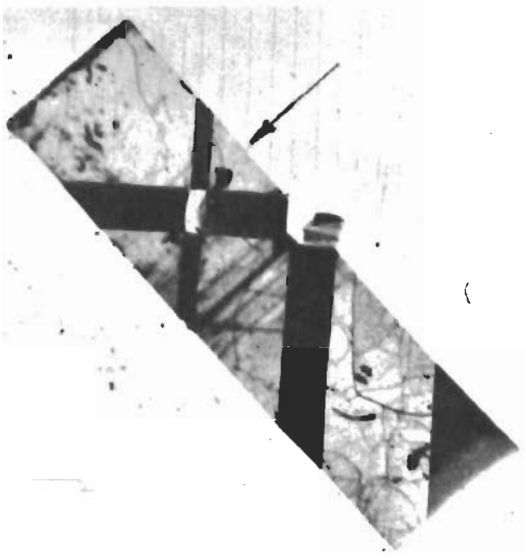

Fig. 7-19(b) BERG-BARRETT X-RAY IMAGE OF SAME AREA

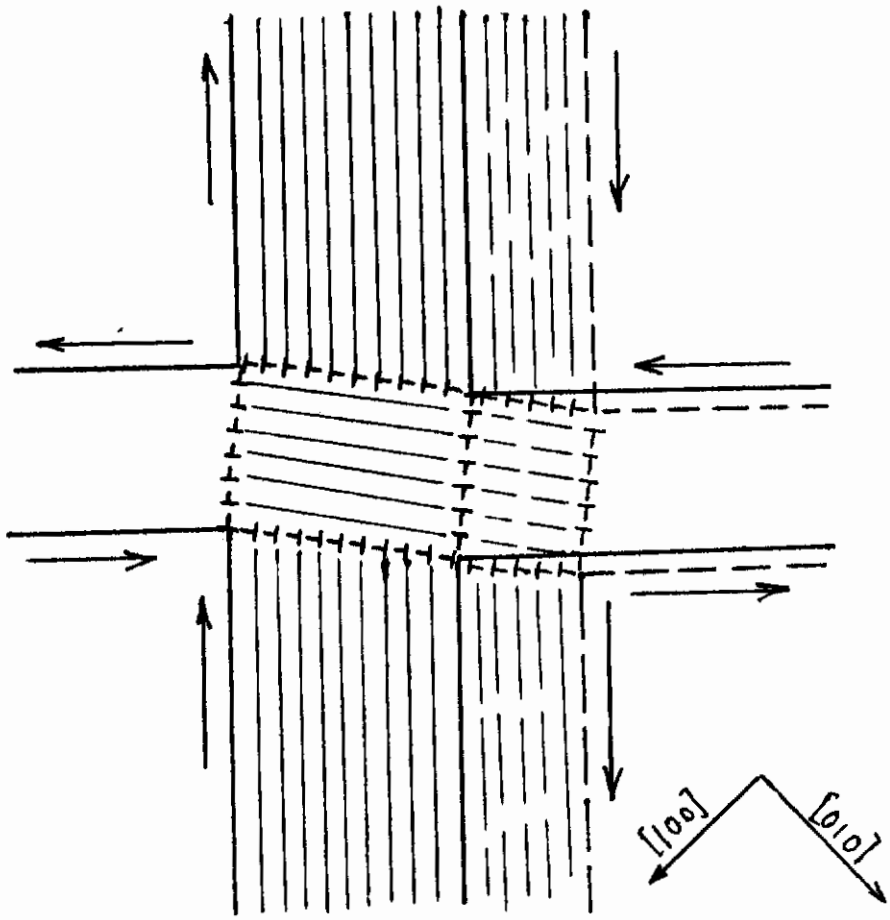

Fig. 7-20 SCHEMATIC REPRESENTATION OF LATTICE ROTATION AND DISLOCATION MOVEMENT DURING GROWTH OF INTERSECTING GILMAN BANDS

other words, the deformation in the vertical band may be due to slip outside the intersection, and to kinking[7-6, 7-7] plus slip in the intersection. Figure 7-20 shows, for simplicity, the case in which the deformation at the intersection is pure kinking. If the arrows indicate the direction of movement of the material adjacent to the slip bands, the termination of slip in the vertical band at the boundary of the intersection gives rise to the edge dislocations indicated in the drawing; at the boundaries of the kink (the vertical boundaries of the parallelogram surrounding the intersection) edge dislocations shown in the figure arise. The edge dislocations surround the parallelogram in the same sense of rotation. This is a consequence of the fact that the dislocations have arrived at the horizontal sides of the parallelogram coming from the outside, while the kink dislocations at the vertical sides have come from inside the volume of intersection. This is closely connected with the theorem of conjugate shear stresses and the corresponding theorem about the directions of shear on two perpendicular faces: in the irrotational case the edge dislocations on adjacent sides of the parallelogram would have opposite senses of rotation.

Evidently, the case shown in Fig. 7-20 can easily arise. When slip starts in the vertical band, the volume of the intersection is already filled with dislocations of the horizontal band; the shear in the vertical band can be as easily produced by slip on the horizontal planes as on the vertical planes, or perhaps more easily.

It seems to be the rule that a Gilman band behaves in a manner similar to Luders bands: deformation increases by the widening of the band, and no significant additional slip occurs inside the band. Experiments for investigating possible changes of orientation at slip band intersections in other crystals (first, in KCl) are in progress.

5. DISCUSSION

Conversion of slip into kinking takes place, according to x-ray evidence, probably in all intersections of Gilman bands in MgO, at least in those which are large enough to be explored by the Berg-Barrett method. The question is whether this phenomenon is to be expected more generally.

A. Asterism

Magnesium Oxide, like other crystals of the NaCl type, presents particularly favorable conditions for the process; every slip plane is intersected by a perpendicular slip plane with the slip direction normal to the line of intersection. However, there is a weighty reason for expecting the kink conversion process to occur very generally, fairly independently of the structure of the crystal. This is the general occurrence of asterism. Between 1925 and 1930 the phenomenon of x-ray asterism was in the center of attention in work on the plasticity of crystalline materials. Yamaguchi(7-8), Burgers(7-9), and Taylor(7-10) suggested that asterism would be due to the curvature of the lattice at the boundaries of slipped areas, i.e., at what is today called dislocations. This possibility disappeared when, on Taylor's suggestion, Starr(7-11) calculated the distortions at the tips of sheared cracks and found that the lattice curvature could not account for the observed asterism. Subsequently, Orowan and Pascoe(7-12) found that the asterism of an extended cadmium crystal was entirely the consequence of a slight macroscopic bending. However, this was not possible in the case of cubic single crystals such as those of aluminum.

Evidently, the kink conversion observed in MgO crystals gives rise to asterism, and a glance at Fig. 7-20 shows that the direction of lattice rotation produced by kinking is the same as that associated with x-ray asterism of the "microscopic" type (i.e., that which is not due to macroscopic bending). The only other way of explaining microscopic asterism of which one is aware at present is the small-scale local bending of slip lamellae into which the crystal breaks up ("flexural slip" of Polanyi(7-13)). This process is closely related to kinking; it may be regarded as a continuously distributed kinking.

Small but sharp kink bands embedded in a crystal grain filled with slip lines have been observed in aluminum by Cahn(7-14). According to Barrett and Levenson(7-15), slip and kinking contribute almost equally to the deformation of iron. In a polycrystalline material kinking could be understood as a consequence of constraints imposed upon slip by grain boundaries; in single crystals, however, the conversion of slip into kinking at band intersections seems to be the first possibility of understanding the occurrence of kinking as a sporadic local phenomenon.

B. Kink Conversion and Strain Hardening

A kinked band intersection is a prism enclosed by a low angle boundary; it is, therefore, an obstacle to further slip. Its resistance to dislocations approaching in the slip bands can be calculated by the summation of the stresses produced by the dislocations surrounding the prism. The interest of this point lies in the fact that, according to the discovery of E. Schmid[7-16], cubic metal crystals strain harden far more rapidly than crystals of hexagonal or tetragonal metals. The simplest interpretation of this is the assumption that the main factor in the strain hardening of cubic (in particular, of cubic face centered) metals is the intersection of slip bands with non-parallel slip directions. Accordingly, most theories of strain hardening in the 1950's were based on the assumption that dislocations on intersecting octahedral slip planes in cubic face centered crystals would fuse to give Lomer-Cottrell sessile dislocations which would be effective obstacles to slip. Sessile dislocations would lie along the line of intersection of the two slip planes; they could be identified in electron micrographs as straight dislocations in (110) directions. Such straight dislocation segments have not been observed frequently in electron micrographs; their conspicuous rarity raises doubts about the role of Lomer-Cottrell dislocations in strain hardening. It is of interest, therefore, that kink conversion at slip band intersections presents an alternative possibility of obtaining strain hardening by the operation of intersecting slip bands.

Schmid's observation that strain hardening is much more rapid in cubic crystals would be described today by saying that such crystals have a very short easy glide region (a few per cent shear strain), whereas hexagonal crystals may show easy glide over a range of shear strain exceeding 100 per cent. The absence of microasterism in cadmium crystals over a large strain range is a strong indication of an intimate connection between the cessation of easy glide and the beginning of lattice rotations. Since Lomer-Cottrell dislocations could hardly produce the observed asterism, the possibility that kink conversions rather than sessile dislocations are responsible for the strain hardening results from intersecting slip planes receives additional emphasis.

C. Bauschinger and Other Reversal Effects

It has been found recently that a strain reversal produces not only the classical Bauschinger effect but, in addition, a permanent lowering of the stress-strain curve. This could be due to the destruction of dislocation pile-ups and the building up of opposite pile-ups; however, it seems that this cannot account for the whole effect. Evidently, strain reversal in the vertical Gilman band in Fig. 7-20 could gradually remove the kinked volume at the intersection; insofar as such a reverse slip is possible in a band, a part of the strain hardening could be destroyed by reverse straining. In this connection the remarkable experiments of Polanyi[7-13] should be remembered, who found that the ability to undergo recrystallization can be destroyed by additional reverse deformation.

D. Kink Stresses and Fracture

Kinking gives rise to several types of internal stress. Mugge[7-6] already observed that disthene (kyanite) has a tendency to fracture along the kink plane and attributed this to the bending stresses in the sharply bent kink lamellae. Other types of internal stress may also arise. If ϕ is the angle between the active slip plane and the normal to the kink plane, t the thickness of the slip lamellae in the kink band, b the length of the Burgers vector, and n an integral number, the relationship $2t \tan \phi = nb$ must be satisfied to avoid tensile and compressive stresses parallel to the kink plane[7-7]. This demands a progressive change of the orientation of the kink plane with increasing kink strain (i.e., with increasing n). Such change of orientation can only be produced by high internal stresses because of non-fulfillment of this equation. The corresponding elastic strain may reach a magnitude between 1 and 2 per cent as measured from the birefringence observed; such stresses could easily induce crack formation. In the past, crack formation by plastic deformation has been attributed to dislocation reactions. As is seen in Fig. 7-19(a), the stresses due to kinking seem to offer a much more likely explanation for the initiation of cracks of the types observed.

6. CONCLUSIONS

(a) A microscope-stage testing machine was built for tension, compressing and bending.

(b) A high temperature testing machine for loads up to 5000 lb and temperatures up to about 4000°F was built.

(c) The cleavage mechanism of alkali halide crystals was studied.

(d) Kinking was observed by x-ray imaging methods at the intersections of Gilman bands in MgO. The conversion of slip to kinking at band intersections produces stresses which may be responsible for that part of strain hardening which so far has been attributed to individual dislocation reactions; they could also produce cracking of the types which were observed but could not be satisfactorily explained by individual dislocation reactions.

7. REFERENCES

7-1 Johnston, N. G. and Gilman, J. J., J. Appl. Phys. 31, 632, (1960).

7-2 Stokes, R. J. and Johnston, T. L., Phil. Mag. 4, 120, (1959).

7-3 Guard, R. W. and Low, J. R., Acta Met. 7, 171, (1959).

7-4 Berg, W., Naturwissenschaften, 19, 391, (1939) and Zeits. f. Kristallogr., 89, 286, (1934).

7-5 Barrett, C. S., Trans. AIME, 161, 15, (1945).

7-6 Mugge, O. Neues. Jahrb. f. Miner., 1, 71, (1898).

7-7 Orowan, E., Nature, 149, 643, (1942).

7-8 Yamaguchi, K., Sci. Pap. Inst. Phys. Chem. Res. Tokyo, 11, 151, 223, (1929).

7-9 Burgers, W. G. and Louwerse, P. C., Z. Physik, 67, 605, (1931).

7-10 Taylor, G. I., Trans. Faraday Soc., 24, 121, (1928).

7-11 Starr, A. T., Proc. Camb. Phil. Soc., 24, 289, (1928).

7-12 Orowan, E., and Pascoe, K. J., Nature 148, 467, (1941).

7-13 Polanyi, M., Zeits. f. Kristallogr., 61, 49, (1925).

7-14 Cahn, R. W. J. Lust. Metals, 79, 129, (1951).

7-15 Barrett, C. S. and Levenson, L. H., Trans. AIME, 137, 112, (1940).

7-16 Schmid, E. and Boas, W., Kristallplastizitat, J. Springer, Berlin, (1935).

TASK 8 - THE INFLUENCE OF IMPURITIES ON THE BRITTLE FRACTURE OF INORGANIC, NON-METALLIC CERAMICS

Principal Investigator: I. B. Cutler
University of Utah

ABSTRACT

The research work on this program is concerned with the effect of impurities upon the mechanical and physical properties of multicrystalline ceramic oxides. To segregate the effect of individual doping elements, methods were developed for the production of high purity Al_2O_3 and MgO bodies substantially superior to commercially available materials.

High purity powders prepared in this fashion were pre-sintered with impurities ranging from 0 to 10^4ppm. The optimum cold-pressing and sintering conditions for the attainment of maximum densities were determined, and methods were developed for the fabrication of test specimens of the desired shape. These were then used for the determination of grain sizes, density and modulus of rupture values.

Satisfactory post-sintered doping methods were also developed but time did not allow for detailed studies of specimens prepared by this technique.

TASK 8 - IMPURITY INFLUENCES

1. INTRODUCTION

The principal sim of this Task is to investigate the effect that carefully controlled quantities of impurities have upon the mechanical and physical behavior of high purity multicrystalline ceramics, represented in this program by Al_2O_3 and MgO. The effect of small quantities of impurities upon the properties of resulting ceramic bodies have been seldom explored before; investigations to date were oriented principally toward the exploration of the effect of doping constituents upon the transmissibility of electromagnetic radiation mainly in the infared region and the visible region in single crystals, or for the control of electrical properties[8-1].

The reasons for this lack of information are readily traceable to a single source: the difficulty of producing truly pure MgO or Al_2O_3. The most careful methods in current commercial use generally leave an impurity content of about 400-600 ppm even for single crystals; in the best polycrystals the impurity concentration is far higher (except for special laboratory applications where impurity levels as low as 100 ppm have been achieved[8-1] in multicrystalline Al_2O_3.) Impurities at these levels would tend to mask out any effect that doping constituents admixed in small quantities may otherwise have on the behavior of these oxides.

Excessive amounts of impurities generally segregate out at the grain boundaries and, by restricting the motion of dislocation glide bands across grain boundaries, would restrict the tendency for plastic flow in the material. Doping elements diffused uniformly through the crystal lattice are likely to act as a strong pinning mechanism, substantially raising the friction stress required to mobilize dislocations or vacancies. The general result of both of these mechanisms would be to restrain plastic flow while raising the strength of the host material: in one word, embrittlement.

This was confirmed by the recent work of Rosenberg and Cadoff[8-2] who found that the diffusion of a surface coating of Mg into pure LiF crystals caused a complete embrittlement of this inherently ductile material. Fracture occurred without noticeable macroscopic yielding (as compared to 3-10 percent over-all plastic strain in undoped LiF); at the same time the stress at fracture was increased from 1, 500 to 11, 000 psi. While this order-of-magnitude increase cannot be expected to occur with each doping element (since in this example a bivalent material was diffused into a monovalent host substance, raising the valence bonds of the lattice configuration), the general results are indicative of the strengthening/embrittling effect likely to accompany the addition of doping substances to otherwise pure ionic materials.

It is conceivable, however, that in inherently brittle materials some doping elements could exert a beneficial influence; this could be brought about if impurities restrict the dislocation glide paths to distances short enough so as to prevent the pile-up of sufficient number of dislocations to form incipient cracks. The result would then be analogous to the strength of enhancement attainable through a reduction in grain size. Also, if impurities can be made to act as a dislocation initiation source, the increased dislocation density nucleated from sites of impurity ions may impart a measure of ductility to otherwise wholly brittle materials.

In pursuing these research objectives, the primary need lay in the preparation of high-purity bodies of multicrystalline MgO and Al_2O_3 of suitable sizes to allow for the preparation of test specimens. The techniques developed for this purpose are described in Sections 2 and 3. A detailed investigation was then undertaken for methods that would allow for the successful doping of the resulting bodies in the pre-sintered and post-sintered state, as well as for the optimum pressing and sintering techniques required to yield

specimens of maximum attainable density. Research associated with this phase of the program is described in Section 4.

Rather complete results were obtained for the density, grain sizes and flexural strengths of pre-sintered specimens. Time, however, did not permit a statistical analysis of the data collected, nor could similar experimental results be developed for the specimens obtained by post-sintered doping techniques.

2. PREPARATION OF HIGH-PURITY Al_2O_3 POWDERS

Attempts were made to prepare a substantially pure Al_2O_3 starting from a number of reagent grade, thermally unstable salts. Aluminum chloride, aluminum sulfate, aluminum hydroxide, and aluminum nitrate are the salts that were used; the green and fired densities of bodies prepared by the various methods are shown in Table 8-IV. Aluminum oxide specimens that resulted from the decomposition of either the hydroxide or nitrate were observed to have unsatisfactory green and fired densities; approaches involving these compounds were therefore abandoned. The Al_2O_3 specimens prepared by the decomposition of the chloride or sulfate of aluminum were found to be satisfactory and very similar to each other. The sulfate proved more difficult to work with than the chloride. For this reason, $AlCl_3$ was selected as intermediate in the preparation of high-purity Al_2O_3 from metallic aluminum. The green densities of Al_2O_3 prepared by calcining $AlCl_3$ at 1250°C, determined as a function of calcining time, are presented in Table 8-V. It was found that three hours calcination at 1250°C gave essentially the same results as one hour calcination at 1300°C. It was decided to calcine the chloride at 1250° - 1275°C for four hours.

The feasibility of decomposing an alum rather than $AlCl_3$ to prepare a high-purity Al_2O_3 was also investigated. An excellent

high-density Al_2O_3 was prepared. The alum was obtained as the residue from the evaportion (to dryness) of a mixture made by adding reagent grade ammonium sulfate to the aqueous $AlCl_3$ solution. Calcination of the alum was accomplished under the same conditions as those used to decompose $AlCl_3$. A temperature of 1750°C for ca. two hours in a vacuum furnace resulted in the highest densities. It is believed that the use of a vacuum furnace for the introduction of impurities will be impractical since a number of the additives are volatile. The results given in Table 8-VI show that the Al_2O_3 prepared from the alum is slightly more dense than that prepared from $AlCl_3$. However, the product from the alum calcination was not considered sufficiently superior to that from the $AlCl_3$ to warrant the risk of contamination from the ammonium sulfate.

In the final procedure established for the preparation of high-purity alumina for use in this program, aluminum ingots 99.999 percent pure were cut into small pieces with a motor-driven saw. Iron deposited from the saw and other surface contaminants were removed from the pieces by means of an overnight wash in room-temperature hydrochloric acid.

The clean pieces of aluminum were then dissolved at ca. 100°C in reagent grade hydrochloric acid. This was done in Teflon beakers. The Teflon beakers were suspended in aluminum cooking pans which were then filled with oil. The acid solution was brought to a boil. Distilled water was sometimes added to the acid to speed the dissolution of the aluminum.

The resulting solution was dried at ca. 200°C to yield a residue of clean, white $AlCl_3 \cdot 6H_2O$ crystals. These crystals were calcined for four hours at 1250 to 1275°C. Particle sizes were found to be one micron or smaller in the calcined powder.

Table 8-I compares the purity of the Al_2O_3 prepared by this procedure with that of other available Al_2O_3 specimens. Tables 8-II and 8-III give results of spectrographic analyses by Harbison-Walker Company and Jarrell-Ash Company, respectively.

Table 8-I

COMPARATIVE SPECTROGRAPHIC ANALYSIS MADE AT THE UNIVERSITY OF UTAH

	Al	B	Ca	Cu	Ga	Fe	Pb	Mg	Ni	Si	Na	Ti	V
J. M. Standard Al_2O_3	M	0	0	0	0	0	0	0	0	4	0	0	0
ARF Al_2O_3 from $AlCl_3 \cdot 6H_2O$	M	0	0	0	0	0	0	0	0	0	0	0	0
Same but ground in mortar	M	0	0	0	0	0	0	0	0	0	0	0	0
Reagent grade	M	0	1	X	X	1	0	2	X	1	X	1	0
Linde Fine	M	0	2	0	0	2	1	2	0	2	0	1	tr
Linde Coarse	M	trace	2	0	0	0	2	1	0	3	0	1	0
Gulton MC	M	0	0	0	0	0	3	0	0	4	0	0	0
A-- 77 ARF*	M	0	0	0	0	0	0	0	0	7	0	0	0
A - 79 ARF*	M	0	2	0	0	3	0	0	0	0	0	0	0
Our MgO	tr	0	2	0	0	0	0	M	0	5	0	0	0
J. M. Standard MgO	tr	0	2	0	0	0	0	M	0	6	0	0	tr
J. M. Analysis of J. M. MgO	0	0	1ppm	1ppm	0	0	0	M	2ppm	1ppm	2ppm	0	0
J. M. Analysis of J. M. Al_2O_3	M	0	2ppm	2ppm	0	3ppm	0	1ppm	0	1ppm	5ppm	0	0

*These samples are difficult to arc and higher voltages were required to obtain vaporization; i.e., No. 4 really comparable to other samples.

Key: x = more than 1
1 = more than 2
2 = more than 3
3 = more than 4
4 = more than 5
6 = more than 7
trace = less than 7

Table 8-II

HARBISON-WALKER SPECTROGRAPHIC ANALYSIS OF THE HIGH-PURITY Al_2O_3

Impurity	Impurity Content, ppm		
	Sample 1 (unfired)	Sample 1 (fired)	Sample 2 (unfired)
Si	1.3	2.1	1
Fe	0.1 to 1	1	0.5
Mg	0.1 to 1	1.6	0.3

Table 8-III

JARREL-ASH SPECTROGRAPHIC ANALYSIS OF THE HIGH-PURITY Al_2O_3 and MgO

Impurity	Impurity Content, percent	
	Al_2O_3	MgO
Na	0.003	0.003
Mg	0.005	-----
Al	-----	0.006
Si	0.001	0.006
Ca	nil	< 0.001
Ti	< 0.002	nil
Cr	< 0.005	nil
Fe	0.003	0.003

Table 8-IV

GREEN AND FIRED DENSITIES OF Al_2O_3 PREPARED BY THERMAL DECOMPOSITION OF VARIOUS ALUMINUM SALTS

Condition			Al_2O_3 Density (g/cc)*			
Calcine Temp. °C	Green	Fired 1 hr. (1725°C)	$AlCl_3$	$Al_2(SO_4)_3$	$Al(OH)_3$	$Al(NO_3)_3$
1150	✓		1.53	1.31	1.79	1.47
		✓	3.48	3.59	2.43	2.56
1200	✓		1.68	1.84	1.72	1.50
		✓	3.67	3.78	2.33	2.58
1300	✓		1.75	1.84	----	----
		✓	3.72	3.77	----	----
1400	✓		1.87	1.68	1.99	1.61
		✓	3.59	3.37	2.24	2.94

* Theoretical density of Al_2O_3 is ca. 4.00 g/cc.

Table 8-V

GREEN DENSITY OF Al_2O_3 PREPARED BY CALCINATION OF ALUMINUM CHLORIDE AT 1250°C AS A FUNCTION OF CALCINING TIME

Calcination Time, hr	Green Density, (g/cc)
3	1.68
18	1.54
24+	1.84*
24+	1.77**

*Reagent grade aluminum chloride.

**Aluminum chloride prepared from metallic aluminum at this laboratory.

Table 8-VI

PERCENTAGE OF THEORETICAL DENSITY AS A FUNCTION OF FIRING TEMPERATURE AND TIME

Furnace Temperature, °C		Firing Time, hr	Percentage of Theoretical Density	
Gas Furnace	Vacuum Furnace		$AlCl_3 \cdot 6H_2O$, Calcined 3 hr at 1250°C	$Al(NH_4)(SO_4)$ Calcined 3 hr at 1250°C
1700	----	1	91.5	95.0
1750	----	1	94.0	94.2
1850	----	1	92.5	91.8
----	1750	2	95.2	96.2

Table 8-VII

RESULTS OF SINTERING MgO DERIVED FROM $MgCl_2 \cdot 6H_2O$

Sample	Calcination Temp. (°C)	Sintering Temp. (°C)	Sintered Bulk Density (g/cc)	Percent of Theoretical Density
A_1	500	1500	0.80	22.4
B_1	700		1.35	37.8
C_1	900		2.48	69.4
D_1	1100		2.40	67.2
A_2	500	1600	0.50	14.0
B_2	700		1.34	37.5
C_2	900		2.52	70.6
D_2	1100		2.28	63.8
A_3	500	1700	0.94	26.3
B_3	700		1.15	32.2
C_3	900		2.57	72.0
D_3	1100		2.50	70.0

3. PREPARATION OF HIGH-PURITY MgO

Considerable difficulty was encountered in the development of a suitable procedure for the preparation of sinterable, high-purity MgO powder. It was expected that high-purity MgCl could be obtained readily from the reaction of reagent grade hydrochloric acid with a commercially sublimed magnesium metal (estimated purity 99.99 percent). Therefore, preliminary sintering studies were conducted of reagent grade magnesium chloride. It was hoped that $MgCl_2 \cdot 6H_2O$ could be decomposed directly to a sinterable MgO. This possible procedure was investigated with different calcines of the chloride, but the results were disappointing, as shown in T Table 8-VII. On the other hand, MgO derived from $Mg(OH)_2$ exhibited excellent sinterability. Magnesium oxide derived from the hydroxide was found to have the following properties:

Pressed Bulk Density.....	2.3 g/cc
Fired Bulk Density.....	3.47 g/cc
Fired Linear Shrinkage.....	14 percent
Fired Volume Shrinkage.....	35.5 percent

Early results of hydrating MgO obtained from a low temperature (500°C) calcine of $MgCl_2 \cdot 6H_2O$ were encouraging. However, further work in that direction indicated that at calcining temperatures less than ca. 900° to 950°C, the hydrated chloride is not easily decomposed. Compounds such as $MgCl_2$ and Mg(OH)Cl are found mixed with the MgO product (Table 8-VIII).

The final procedure established for preparation of high-purity MgO circumvents these problems. Reagent-grade ammonium hydroxide is added to the chloride solution that results from the dissolution of the sublimed magnesium metal in reagent grade hydrochloric acid. This precipitates the hydroxide and leaves ammonium chloride in solution. The magnesium hydroxide is separated from the solution by filtration, washed with a dilute solution of ammonium

Table 8-VIII

X-RAY DIFFRACTION ANALYSES OF THE PRODUCTS FROM VARIOUS CALCINES OF $MgCl_2 \cdot 6H_2C$

Peak		MgO	$Mg(OH)_2$	MgOHCl	$MgCl_2$	$MgCl_2{\cdot}2H_2O$	$MgCl_2{\cdot}4H_2O$	$MgCl_2{\cdot}6H_2O$	$MgCl_2{\cdot}MgOH_2{\cdot}5H_2O$
$MgCl_2{\cdot}6H_2O{\cdot}NH_4OH$ 900°C		✓	✓	✓	✓			✓	
$MgCl_2{\cdot}6H_2O$ 500°C		✓	✓		✓	✓			
$MgCl_2{\cdot}6H_2O$	600°C	✓							
3 hr	700°C	✓							
	800°C	✓							
	600°C	✓		✓	✓			✓	
lump	700°C	✓		✓	✓			✓	
	800°C	✓							
	600°C		✓	✓	✓			✓	✓
hydrated	700°C	✓	✓						
	800°C	✓	✓						
$MgCl_2{\cdot}6H_2O$ 500°C/3hr plus H_2O Brucite 900°C $-H_2O$		✓	✓						
$MgCl \cdot 6H_2O$-brucite, 1000°C/ 3hr $-H_2O$		✓							

hydroxide in distilled water, and then dried in an oven. The dry powder is then calcined in an electric kiln at ca. 1050°C for 5 hours. Sintered Al_2O_3 crucibles were used to contain the powder. Table 8-I gives a comparative spectroscopic analysis of the MgO thus produced. In Table 8-IX, the effect of magnesium hydroxide calcine temperature on the sintering characteristics of the resulting MgO is given.

Table 8-IX

EFFECT OF $Mg(OH)_2$ CALCINING TEMPERATURE ON THE SINTERING CHARACTERISTICS OF MgO

(Sintering time, 1 hr)

$Mg(OH)_2$ Calcining Temperature (°C)	Time at Calcining Temperature (hr)	Percent Theoretical of Pressed Discs	Sintering Temp., (°C)	Percent Theoretical Density of Sintered Discs
900	3	65.1	1600	95.3
800	3	65.9	1600	93.3
700	3	65.9	1600	85.5
1000	3	60.4	1700	95.3
900	3	67.9	1700	96.4
900	1.5	66.5	1700	95.0
850	3	63.7	1700	95.3
800	3	67.9	1700	95.0

4. SPECIMEN PREPARATION

A. Pressing, Sintering and Cutting Operations

In the preparation of test prisms for modulus of rupture measurements, the high-purity powders are first cold-pressed into discs at a pressure of 20 tons/sq in. These discs are 2-9/16-in. diameter, and

ca. 3/16-in. thick. Distilled water is used as binder, 2 percent for Al_2O_3 and 5 percent for MgO. Disc-shaped filter paper is used against the die faces to avoid contamination of the material. Immediately after pressing, the discs are placed under vacuum in a desiccator and left for anywhere from 3 to 5 hours. This step was found necessary to prevent radial cracking of the discs during drying.

The dried discs are next fired in a gas-air kiln. Aluminum Oxide discs are fired at 1735°C (±20°C) for 8 hours. For MgO discs a 2-hour firing at temperatures from 1650° to 1740°C is used. Figure 8-2 gives temperature-time curves for the sintering of the MgO discs.

Once the discs are sintered, they are cut into test prisms with a diamond saw, following the layout presented in Fig. 8-1.

B. Doping Procedures

a. Pre-sintered doping of Al_2O_3

Generally, the impurity is added as the nitrate. A weighed quantity of the nitrate is dissolved in distilled water. This solution is mixed with the high-purity Al_2O_3 powder to produce a weight ratio of moisture to dry powder of 0.25. The mixture is then heated at 700 to 800°C for 1 hour to decompose the nitrate.

The procedure for addition of the titanium impurity is different in that the titanium oxide is added directly as a powder.

All powder mixtures are ball-milled overnight in plastic bottles using Lucite balls. The well-mixed powders may then be pressed into discs as previously described.

b. Pre-sintered doping of MgO

The procedure for doping MgO with impurities prior to sintering is essentially the same as that used for Al_2O_3. One important

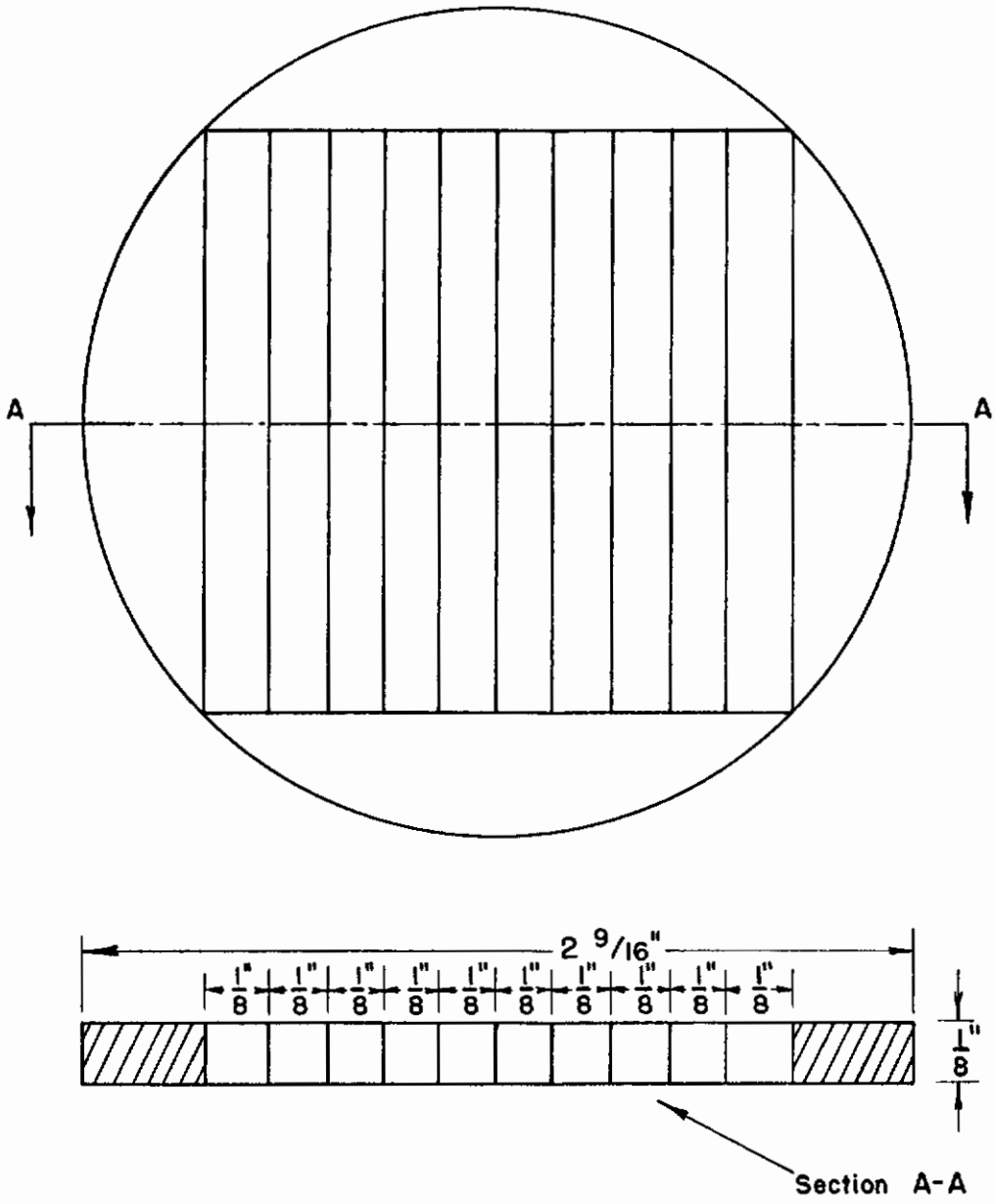

Fig. 8-1 PREPARATION OF TEST PRISMS

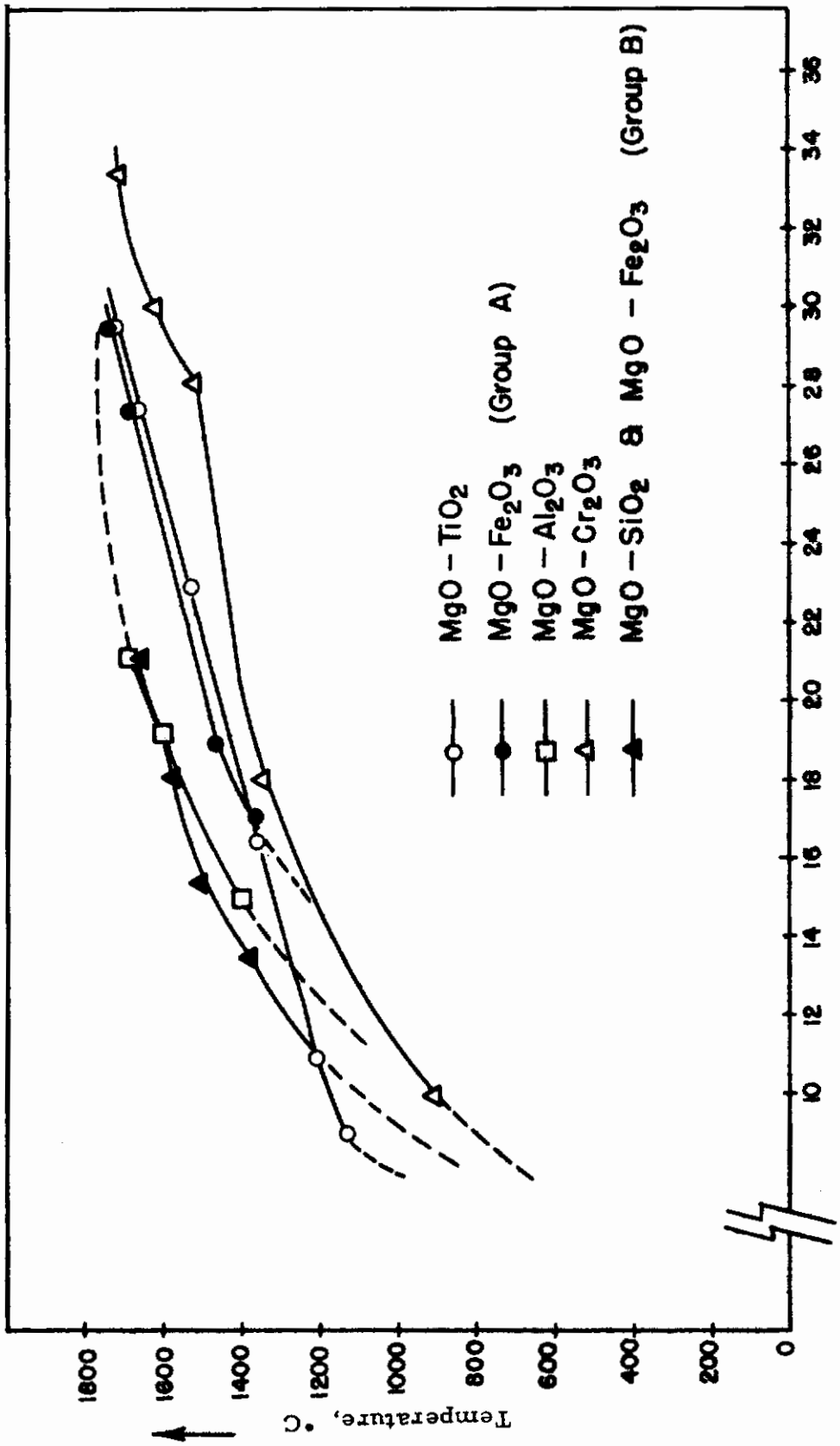

Fig. 8-2 FIRING SCHEDULE FOR MgO SPECIMENS DOPED WITH IMPURITY PRIOR TO SINTERING

exception is that the nitrates are dissolved in ethyl alchohol rather than distilled water. Also, SiO_2 as well as TiO_2 is added directly as the powdered oxide.

c. Post-sintered doping procedures

To diffuse impurities into a sintered test prism, the prism to be doped is rolled firmly in a moist (ca. 10 percent H_2O) powdered mixture of the impurity and the base oxide (Al_2O_3 for Al_2O_3 specimens, MgO for MgO specimens). The mixture contains 5-10 percent by weight of the impurity. The doping mixture forms a jacket around the specimen about 1/4-in. thick. Specimens thus encased are fired in a gas-air furnace at 1650°C. Firing times from 3 to 12 hours have been used. The sintered jacket is removed from the doped specimen by grinding. Great care must be exercised in the grinding operation to avoid breakage of the test piece.

5. EXPERIMENTAL WORK

Measurements made of pure sintered Al_2O_3 and MgO pieces and specimens doped with impurities before sintering include (1) density, (2) modulus of rupture at room temperature and 500°C, (3) microhardness, and (4) grain size. Time did not allow these measurements to be made on specimens doped after sintering.

Density measurements were made by means of a densitometer that weighs the sample in mercury to determine the volume. Results are tabulated in Table 8-X for the specimens of Al_2O_3 and in Table 8-XI for those of MgO. Table 8-XII shows the uniformity in density of prisms cut from typical high-purity Al_2O_3 discs. Note the uniformity of the ten prisms cut from one disc (mean deviation, 0.32 percent). Note also the specimens cut from a second and third disc have essentially the same densities as those cut from the first.

Table 8-X

AVERAGE FIRED DENSITIES OF Al_2O_3 SPECIMENS DOPED WITH IMPURITIES BEFORE SINTERING

Added Impurity	Amount Added Impurity, ppm	Density, g /cm^3	% Theoretical Density
None	0	3.74	93.4
Fe_2O_3	10	3.74	93.4
	10^2	3.73	93.0
	10^3	3.77	94.2
	10^4	3.80	95.0
TiO_2	10	3.68	92.0
	10^2	3.67	91.7
	10^3	3.72	92.9
	10^4	3.78	94.5
Cr_2O_3	10	3.68	92.0
	10^2	3.68	92.0
	10^3	3.70	92.5
	10^4	3.68	92.0
Na_2O	10	3.76	94.0
	10^2	3.76	94.0
	10^3	3.80	95.0
	10^4	3.78	94.5
MgO	10	3.81	95.2
	10^2	3.83	95.6
	10^3	3.82	95.5
	10^4	3.81	95.2

Table 8-XI

AVERAGE FIRED DENSITIES OF MgO SPECIMENS DOPED WITH IMPURITIES BEFORE SINTERING

Added Impurity		Amount Added Impurity, ppm	Density g /cm^3	% Theoretical Density
None		0	3.53	98.6
Fe_2O_3	Group A	10	3.53	98.6
		10^3	3.52	98.3
	Group B	10	3.51	98.0
		10^2	3.50	97.8
		10^3	3.49	97.4
		10^4	3.50	97.8
	Group C	10^2	3.52	98.3
		10^4	3.44	95.8
Al_2O_3		10	3.51	98.0
		10^2	3.53	98.6
		10^3	3.47	96.9
		10^4	3.46	96.6
TiO_2		10	3.50	97.8
		10^2	3.53	98.6
		10^3	3.52	98.3
		10^4	3.49	97.6
Cr_2O_3		10	3.54	98.9
		10^2	3.53	98.5
		10^3	3.48	97.1
		10^4	3.33	93.0
SiO_2		10	3.51	98.0
		10^2	3.50	97.8
		10^3	3.51	98.0
		10^4	3.47	96.9

Table 8-XII

FIRED DENSITIES OF TEST PRISMS CUT FROM TYPICAL Al_2O_3 DISCS

Specimen, (disc-prism)	Fired Density, (g/cm^3)
1-1	3.75
1-2	3.76
1-3	3.76
1-4	3.78
1-5	3.77
1-6	3.77
1-7	3.78
1-8	3.74
1-9	3.78
1-10	3.79
2-1	3.76
2-3	3.76
2-5	3.77
2-7	3.78
2-9	3.78
3-3	3.79
3-5	3.80
3-7	3.80

Modulus of rupture was determined by bending specimens in four point loading. A model TTC Instron tensile testing machine was used. For tests at elevated temperatures, a furnace was designed and constructed to be mounted in the Instron machine. Figure 8-3 is a schematic diagram of the furnace. Kanthal A-1 resistance elements are spaced over the length of the heating zone to give uniform heating. The bottom load bearing support pivots in both directions. The arrangement compensates for any warpage of the test bars. Sapphire rods are used at the contact points. The furnace construction is such that a series of specimens can be loaded in the furnace and tested at a given temperature. Test bars are pushed into the hot zone, loaded in the breaking device, broken, and the pieces removed to the opposite end of the furnace. The breaking load and the deflection are automatically recorded with the testing machine.

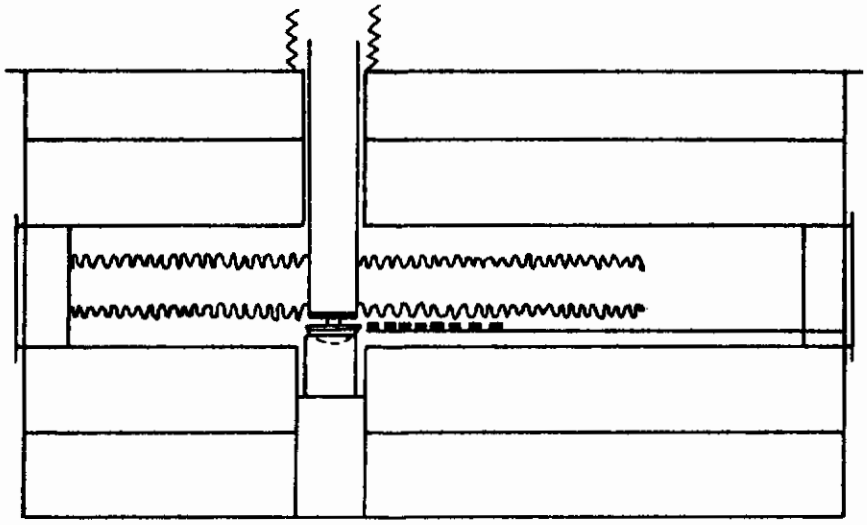

Side View Cross Section

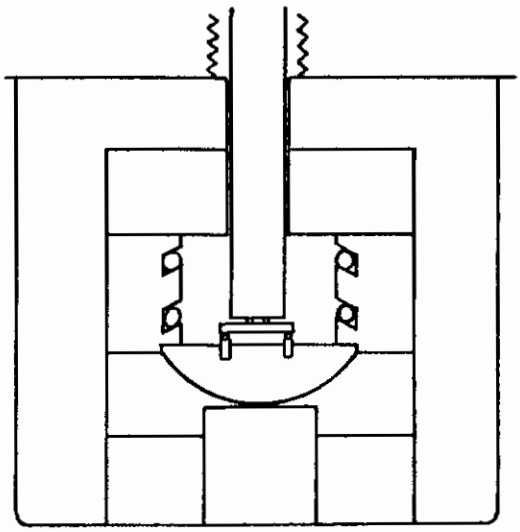

End View Cross Section

Fig. 8-3 DIAGRAM OF FURNACE

Measurements of modulus of rupture were made at 25 and 500°C. The test prisms were lapped smooth before they were tested. Results for Al_2O_3 specimens are summarized in Table XIII and Fig. 8-4 to 8-7. The data for MgO specimens are given in Table 8-XIV and Fig. 8-8 to 8-12.

Hardness measurements with diamond indenter showed no variation in the case of several series of doped Al_2O_3 specimens. As a result, hardness measurements were discontinued. It is planned to make similar measurements on the MgO samples at the first opportunity.

A microscope was used to measure grain size as a function of impurity content. These data are presented in Tables 8-XV for Al_2O_3 and 8-XVI for MgO. On another related project, some of the high-purity Al_2O_3 made in connection with this research was doped with various amounts of Na_2O impurity (added as β -Al_2O_3) ranging from 0 to 1000 ppm. Figures 8-17 to 8-20 are photomicrographs of the fired specimens. Figure 8-17 shows the specimen with no added Na_2O impurity, Fig. 8-18 that with 10 ppm, Fig. 8-19 that with 100 ppm, and Fig. 8-20 that with 1000 ppm. The surfaces of the specimens were flash etched at 1850°C.

Table 8-XIII

AVERAGE FIRED STRENGTHS OF Al_2O_3 SPECIMENS DOPED WITH IMPURITIES BEFORE SINTERING

Added Impurity	Amount Added Impurity, (ppm)	Modulus of Rupture, (10^{-3}psi) T=25°C				Modulus of Rupture, (10^{-3}psi) T=500°C			
		Ave.	Range	Standard Deviation	No. Broken	Ave.	Range	Stand. Deviat.	No. Broken
None	0	35.1	28.8-41.6	3.21	25	22.6	12.8-28.9	4.34	20
TiO_2	10	34.5	30.6-38.3	2.62	6	21.5	18.9-24.7	2.94	3
	10^2	30.5	27.7-32.4	1.82	6	18.2	13.3-23.1	2.84	9
	10^3	24.3	19.5-27.0	2.77	6	15.7	12.3-19.1	2.84	5
	10^4	13.3	8.6-17.0	2.82	8	13.4	8.9-15.1	2.94	6
Cr_2O_3	10	28.3	21.4-35.7	5.38	7	22.0	20.1-25.1	1.68	6
	10^2	25.6	19.2-37.2	6.02	10	22.3	19.1-25.4	2.36	6
	10^3	21.4	15.1-24.9	3.46	9	20.4	14.6-26.8	5.48	6
	10^4	30.6	22.4-34.8	3.68	9	19.6	13.8-24.4	5.09	6
Na_2O	10	30.8	28.8-38.3	5.90	7	23.6	13.7-29.6	5.62	6
	10^2	32.3	28.7-39.0	4.84	5	21.8	16.0-28.2	5.00	6
	10^3	27.8	21.6-34.1	4.24	6	21.5	16.1-28.6	4.84	12
	10^4	31.6	23.4-35.7	4.78	7	23.8	18.1-28.7	3.81	9
MgO	10	32.0	28.1-35.1	2.38	9	28.1	19.5-33.8	4.22	9
	10^2	32.7	25.9-42.9	5.68	9	30.3	25.0-35.4	3.87	7
	10^3	34.0	25.4-40.5	4.68	8	24.9	19.3-28.9	3.16	9
	10^4	30.8	19.4-40.9	7.28	9	24.1	19.5-34.7	4.62	9

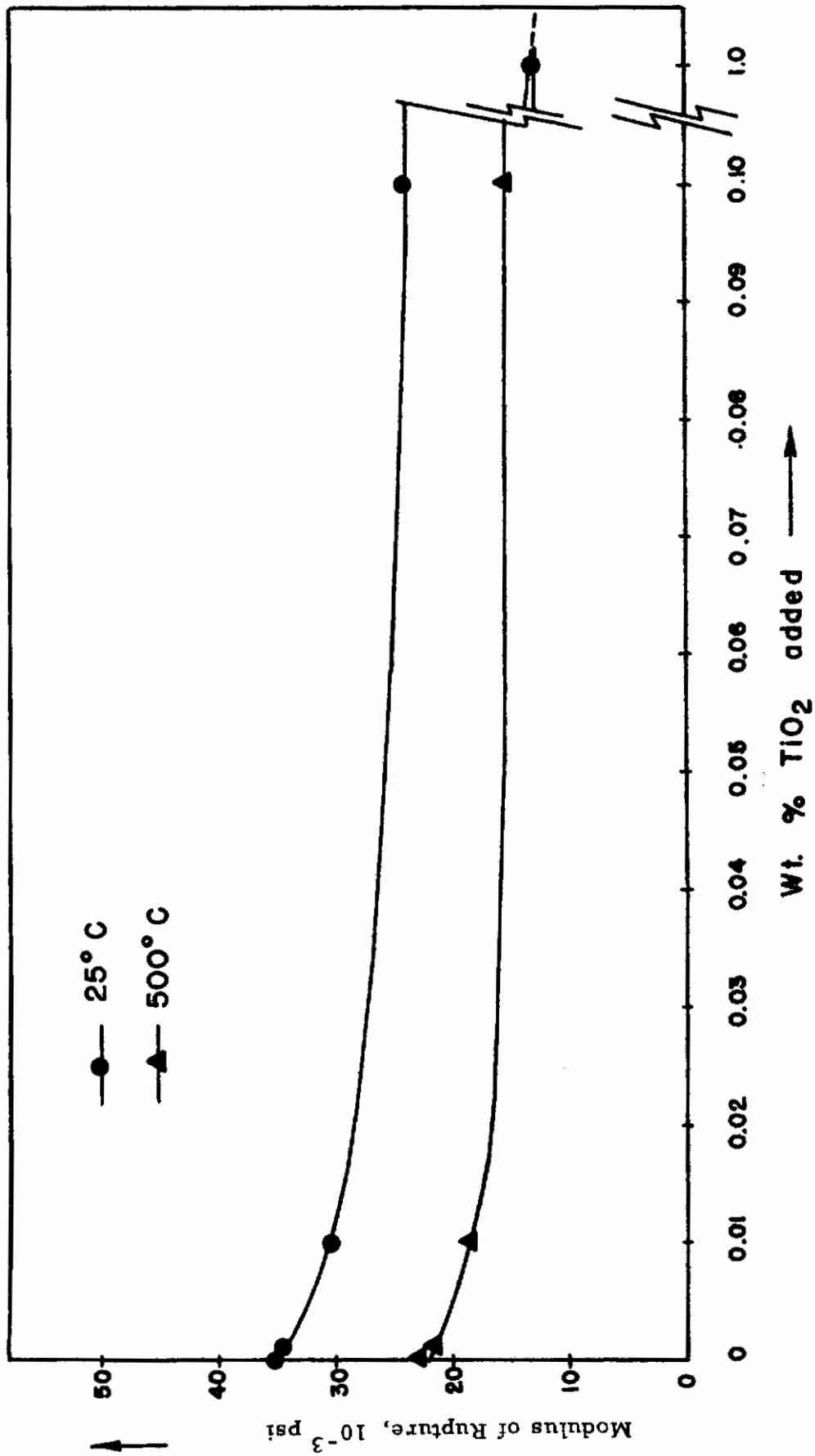

Fig. 8-4 STRENGTH OF Al_2O_3 AS A FUNCTION OF TiO_2 IMPURITY

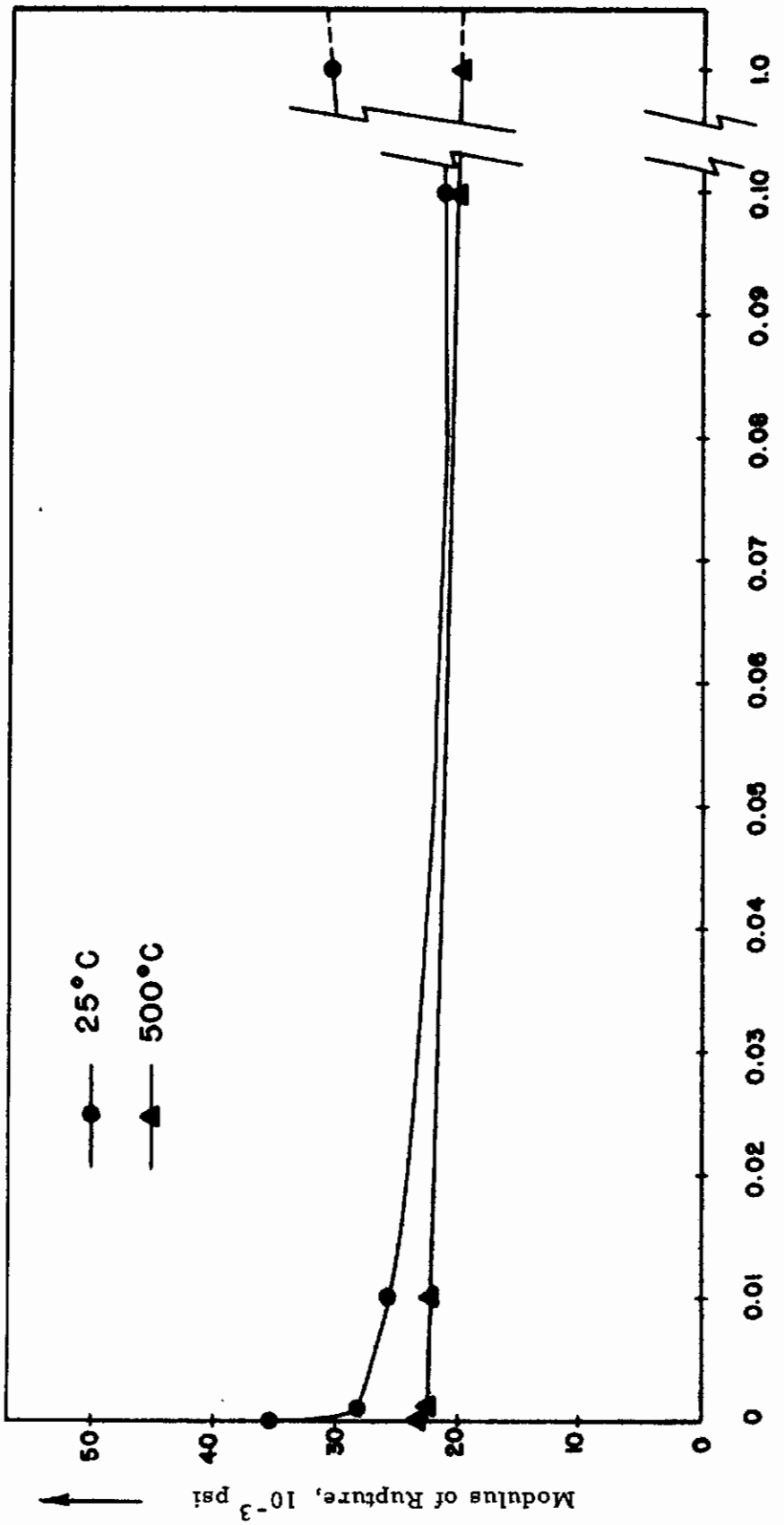

Fig. 8-5 STRENGTH OF Al_2O_3 AS A FUNCTION OF Cr_2O_3 IMPURITY

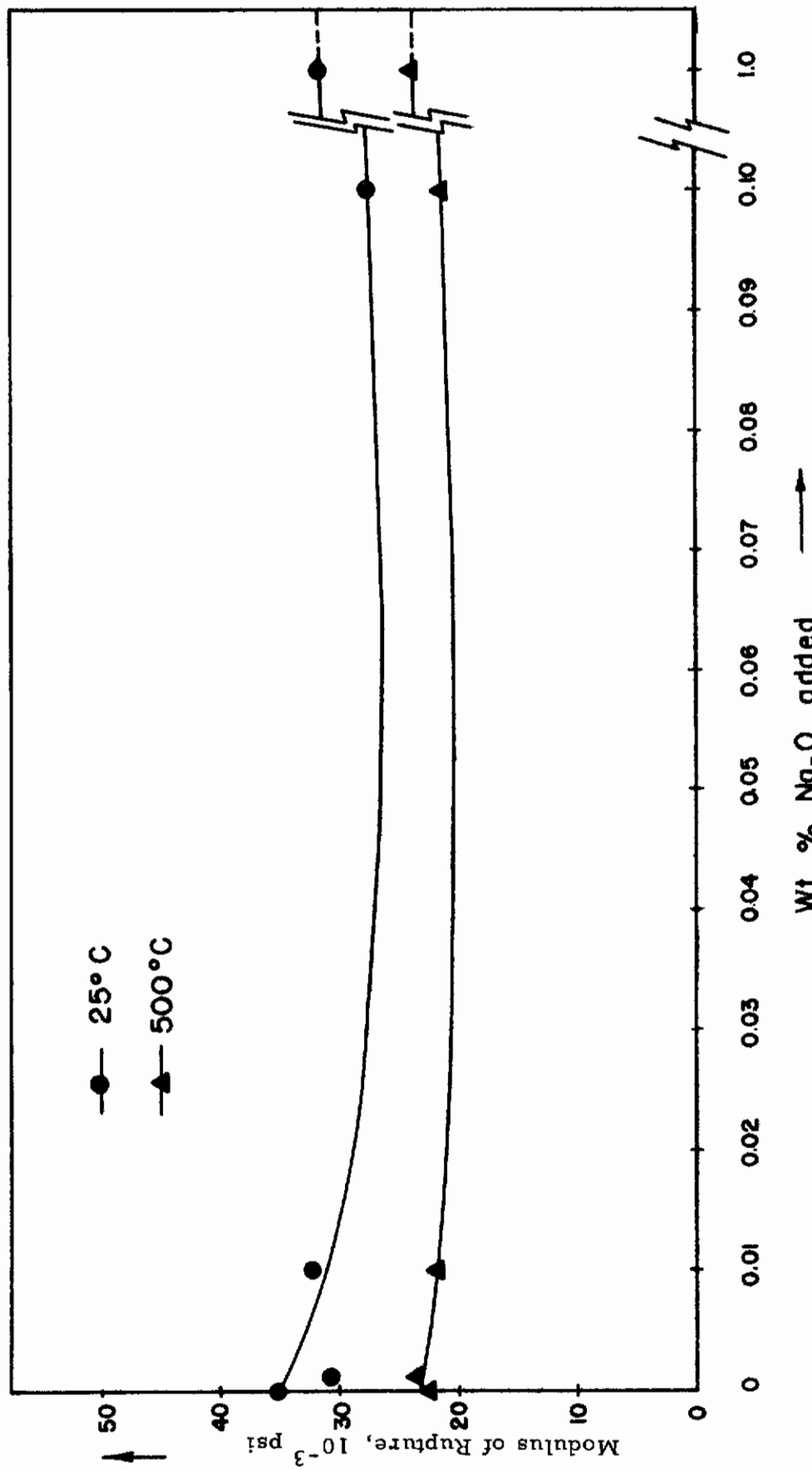

Fig. 8-6 STRENGTH OF Al_2O_3 AS A FUNCTION OF Na_2O IMPURITY

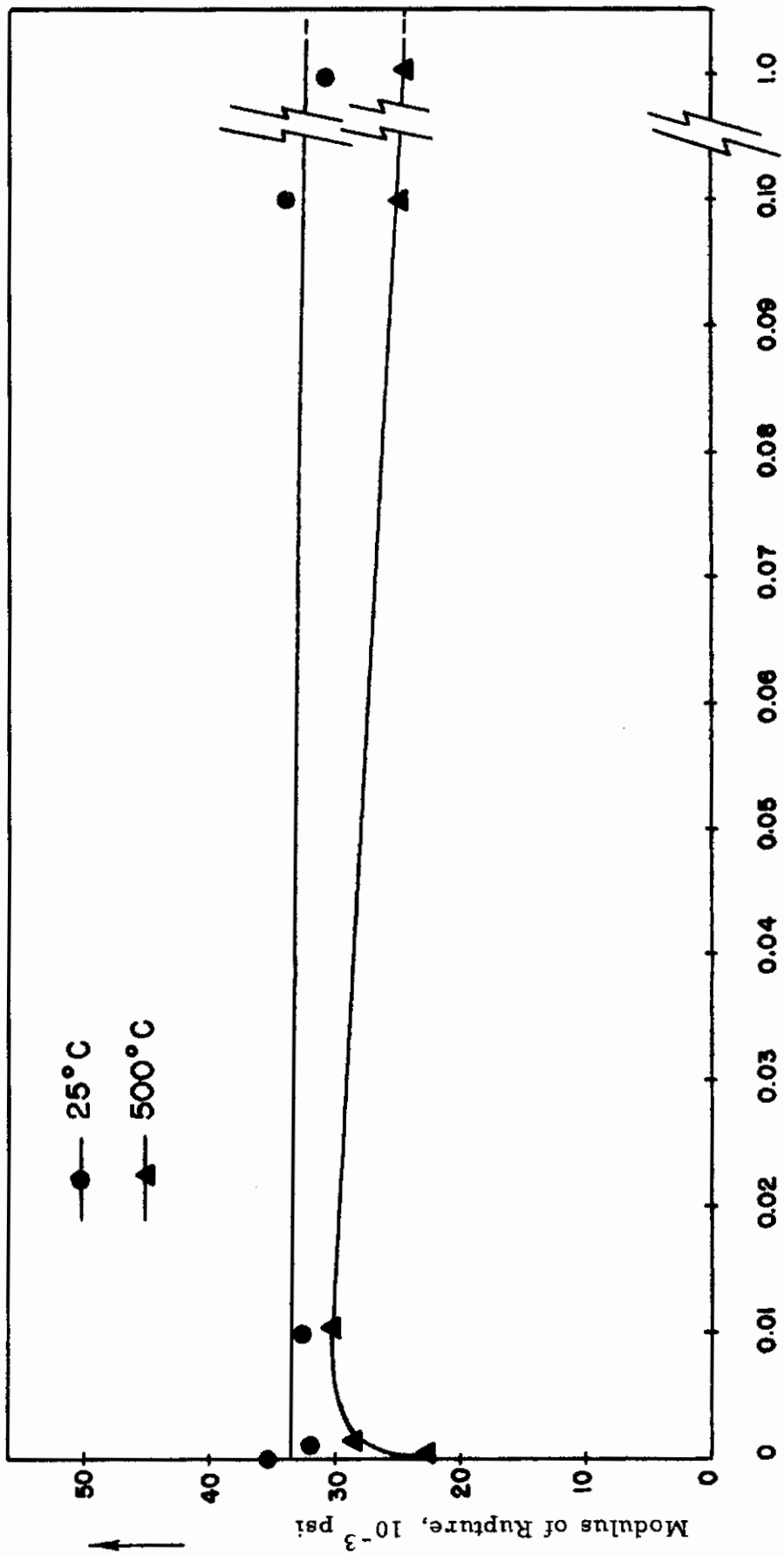

Fig. 8-7 STRENGTH OF Al_2O_3 AS A FUNCTION OF MgO IMPURITY

Table 8-XIV

AVERAGE FIRED STRENGTHS OF MgO SPECIMENS DOPED WITH IMPURITIES BEFORE SINTERING

Added Impurity		Amount Added Impurity (ppm)	Modulus of Rupture, (10^{-3}psi) T = 25°C				Modulus of Rupture, (10^{-3}psi) T = 500°C			
			Ave.	Range	Stand. Dev.	No. Broken	Ave.	Range	Stand. Dev.	No. Broken
None		0	15.8	11.9-18.3	2.16	6	22.2	18.8-25.8	3.33	5
Fe_2O_3	Group A	10	22.6	17.7-27.3	2.68	8	----	----	----	--
		10^3	21.3	19.7-26.1	2.32	9	----	----	----	--
	Group B	10	19.9	19.3-21.3	0.97	4	27.7	24.0-30.3	2.81	4
		10^2	17.8	19.3-24.4	4.79	3	16.8	13.8-21.5	4.08	3
		10^3	17.5	15.6-19.8	1.76	4	16.7	15.1-18.9	1.43	3
		10^4	14.4	10.5-19.3	3.55	4	15.3	13.9-16.6	1.91	2
	Group C	10^2	17.1	16.6-19.0	2.04	3	----	----	----	--
		10^4	10.4	9.4-11.0	1.42	3	----	----	----	--
Al_2O_3		10	21.0	18.6-26.4	2.96	6	24.7	14.9-32.5	2.96	4
		10^2	21.8	20.1-25.3	2.38	4	26.5	21.6-33.4	2.38	5
		10^3	19.8	19.7-19.8	0.71	3	21.4	13.3-26.7	0.71	4
		10^4	19.2	13.3-24.0	5.43	5	21.1	16.5-30.5	5.43	4
TiO_2		10	18.3	16.7-21.8	2.41	4	25.9	12.0-18.2	2.41	4
		10^2	21.8	17.7-26.2	3.52	4	26.8	21.7-25.0	3.52	3
		10^3	18.7	14.0-24.9	5.65	3	23.4	24.3-30.0	5.65	3
		10^4	13.9	12.3-15.2	1.46	3	15.0	21.8-28.7	1.46	3
Cr_2O_3		10	14.1	13.9-14.3	0.28	2	14.8	9.0-17.2	0.28	3
		10^2	13.1	9.0-19.0	4.01	3	22.8	18.9-24.6	4.01	4
		10^3	12.6	7.5-16.4	4.40	3	21.7	15.3-27.7	4.40	4
		10^4	7.9	6.2-17.5	2.39	3	10.1	8.9-11.3	2.39	2
SiO_2		10	20.6	16.8-24.1	1.54	4	31.3	30.7-31.9	0.72	3
		10^2	16.0	15.2-17.1	0.22	4	27.0	26.8-27.1	0.23	3
		10^3	18.4	15.6-23.4	2.75	4	29.2	24.4-32.3	4.21	3
		10^4	14.8	10.0-17.7	0.17	4	18.1	17.5-18.5	0.67	3

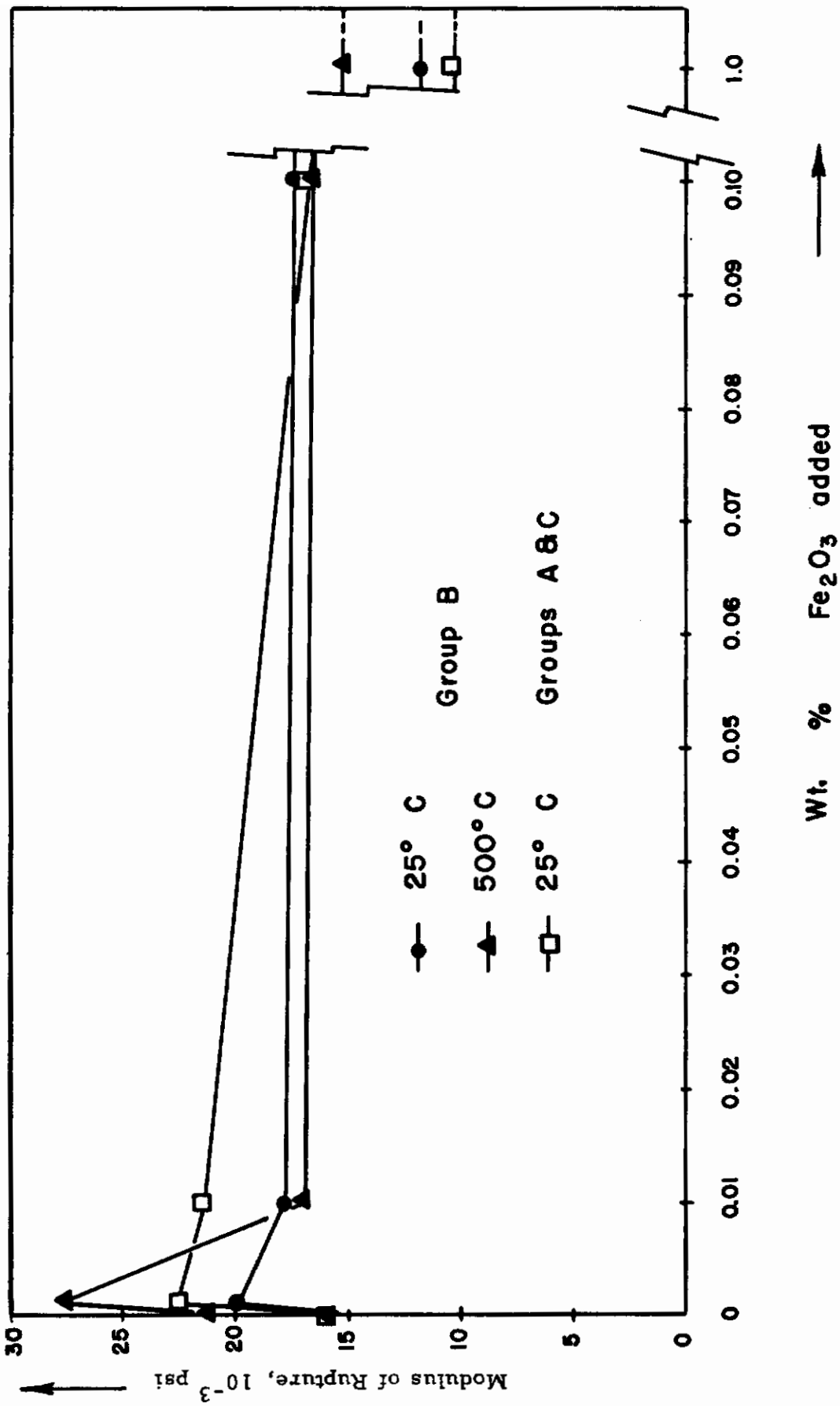

Fig. 8-8 STRENGTH OF MgO AS A FUNCTION OF Fe_2O_3 IMPURITY

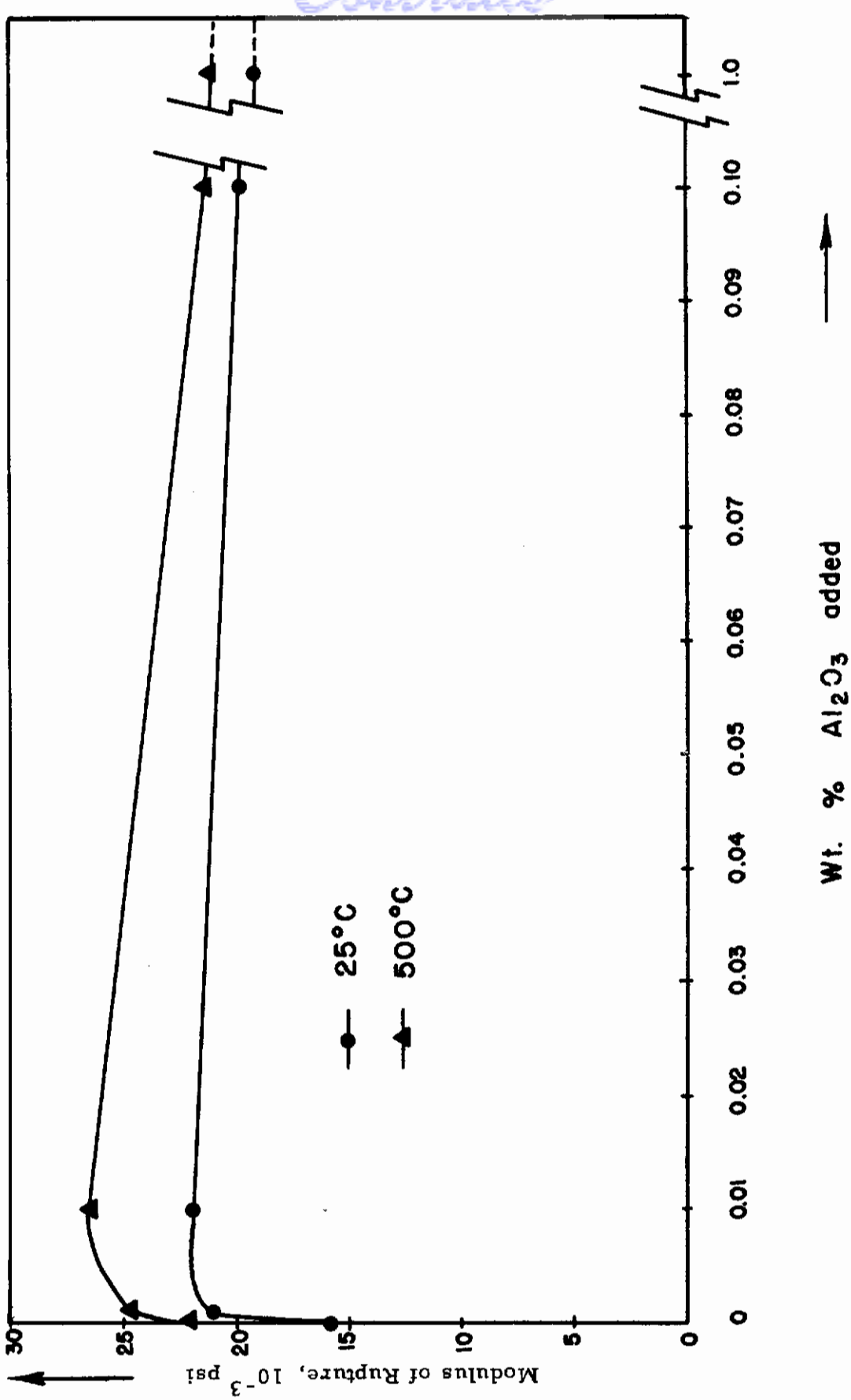

Fig. 8-9 STRENGTH OF MgO AS A FUNCTION OF Al_2O_3 IMPURITY

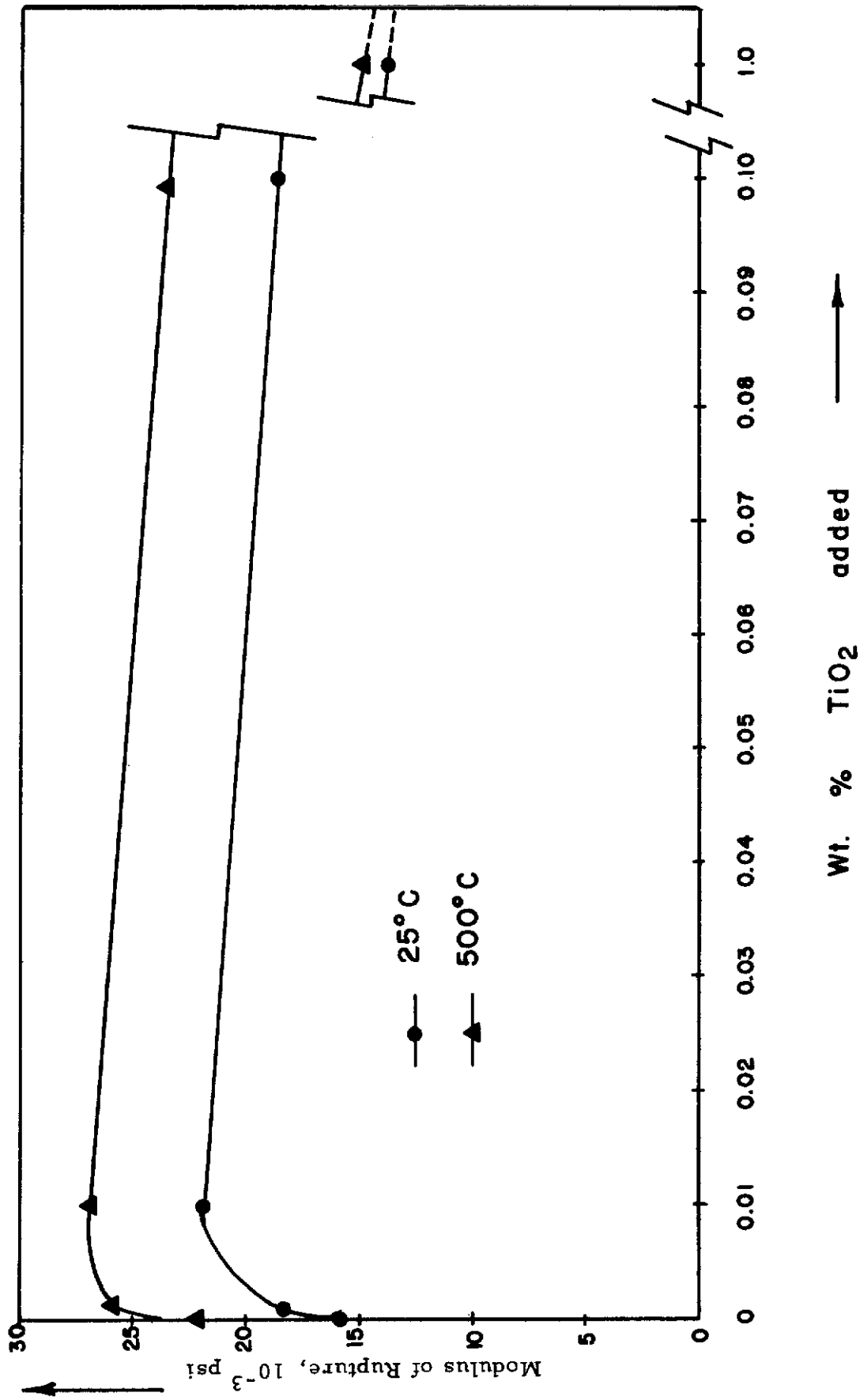

Fig. 8-10 STRENGTH OF MgO AS A FUNCTION OF TiO_2 IMPURITY

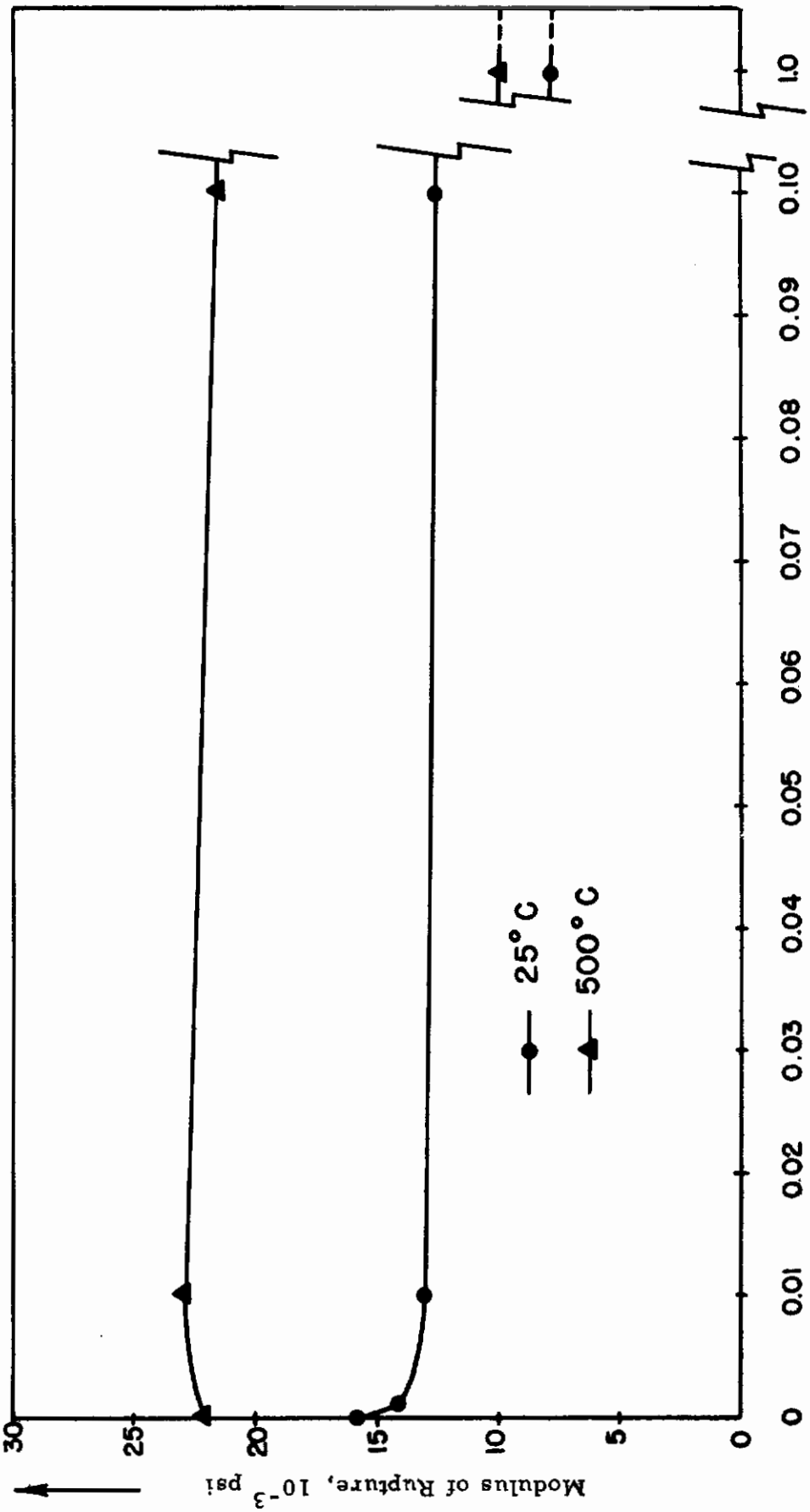

Fig. 8-11 STRENGTH OF MgO AS A FUNCTION OF Cr_2O_3 IMPURITY

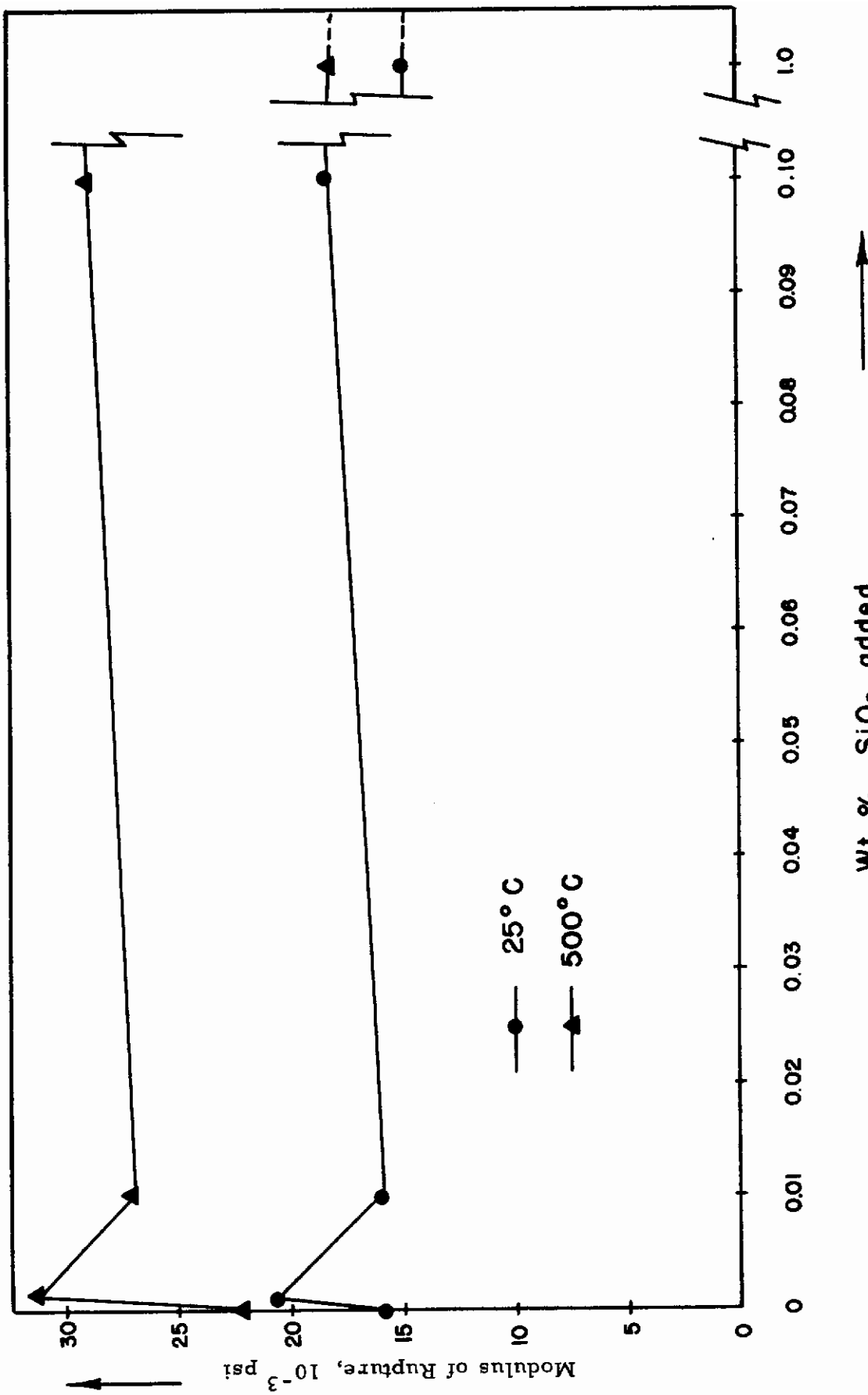

Fig. 8-12 STRENGTH OF MgO AS A FUNCTION OF SiO_2 IMPURITY

Table 8-XV

GRAIN SIZE OF FIRED Al_2O_3 AS A FUNCTION OF IMPURITY CONTENT

Amount Added Impurity, (ppm)	Average Grain Size (μ)				
	None	TiO_2	Cr_2O_3	Na_2O	MgO
0	16.6	----	----	----	----
10	----	17.5	15.7	15.9	14.2
10^2	----	18.0	15.5	12.7	16.3
10^3	----	20.8	16.3	15.1	11.8
10^4	----	49.0	16.6	16.7	13.0

Table 8-XVI

GRAIN SIZE OF MgO AS A FUNCTION OF IMPURITY CONTENT

Amount Added Impurity, (ppm)	Average Grain Size (μ)					
	None	Fe_2O_3	Al_2O_3	TiO_2	Cr_2O_3	SiO_2
0	52.3	----	----	----	----	----
10	----	19.1* 37.5**	21.9	16.1	59.7	36.9
10^2	----	43.2* 41.0**	26.0	17.4	59.7	46.1
10^3	----	40.0* 53.8**	25.6	20.0	30.1	38.2
10^4	----	61.2* 58.3**	23.2	44.5	1.63	15.3

* Groups A and C

** Group B

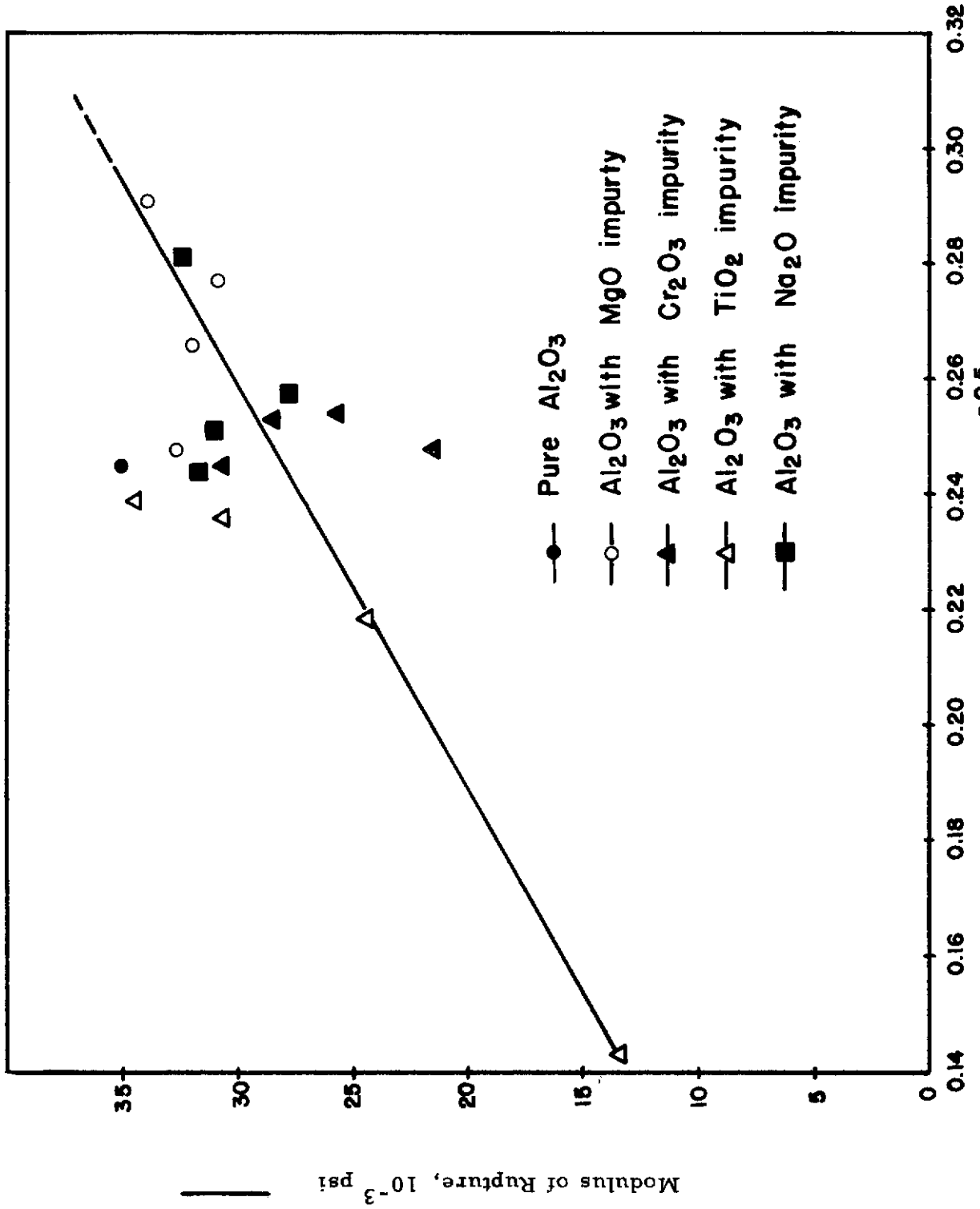

Fig. 8-13 MODULUS OF RUPTURE VS. (GRAIN SIZE)$^{-0.5}$ FOR PRESINTERED DOPED Al_2O_3

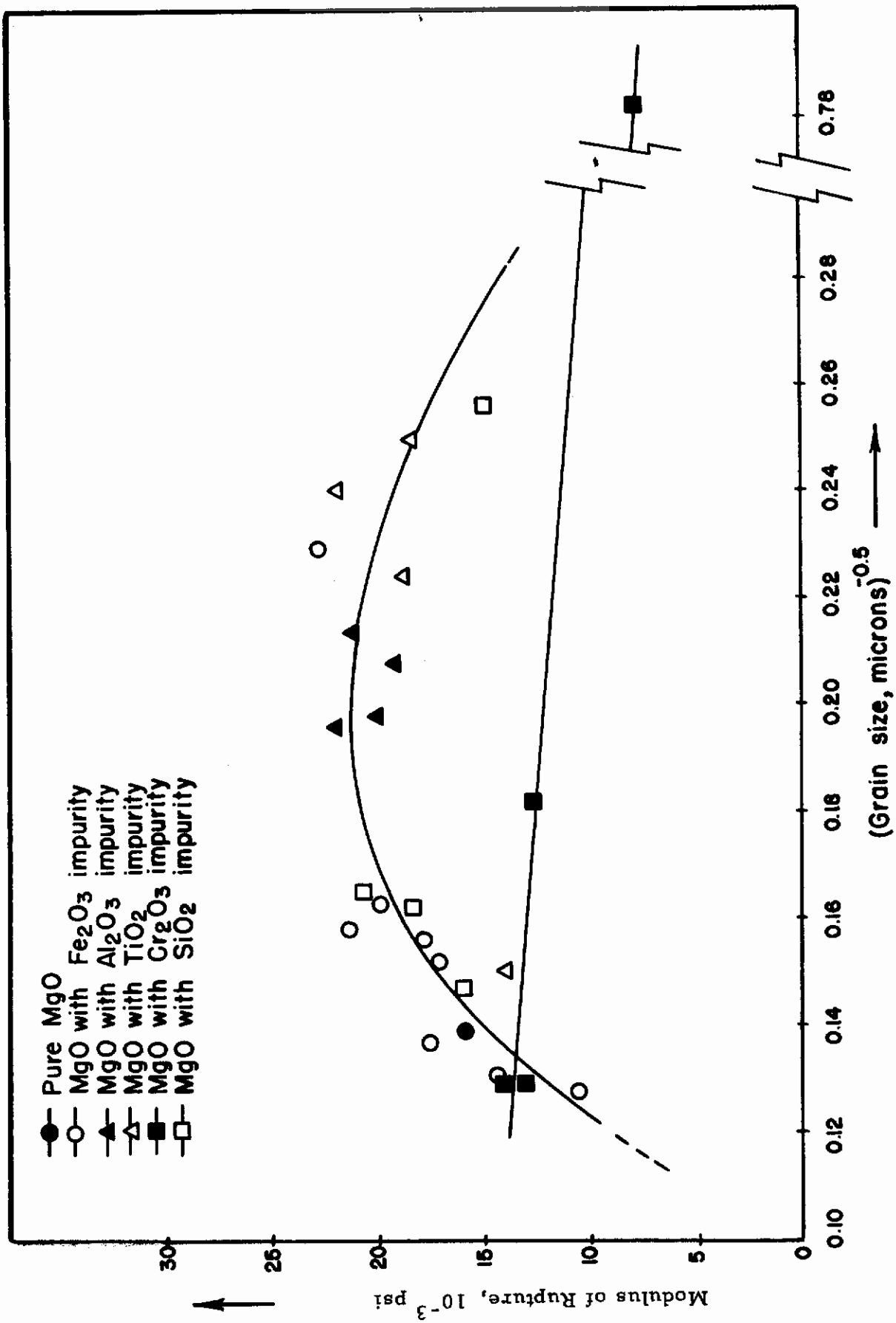

Fig. 8-14 MODULUS OF RUPTURE VS. (GRAIN SIZE)$^{-0.5}$ FOR PRESINTERED DOPED MgO

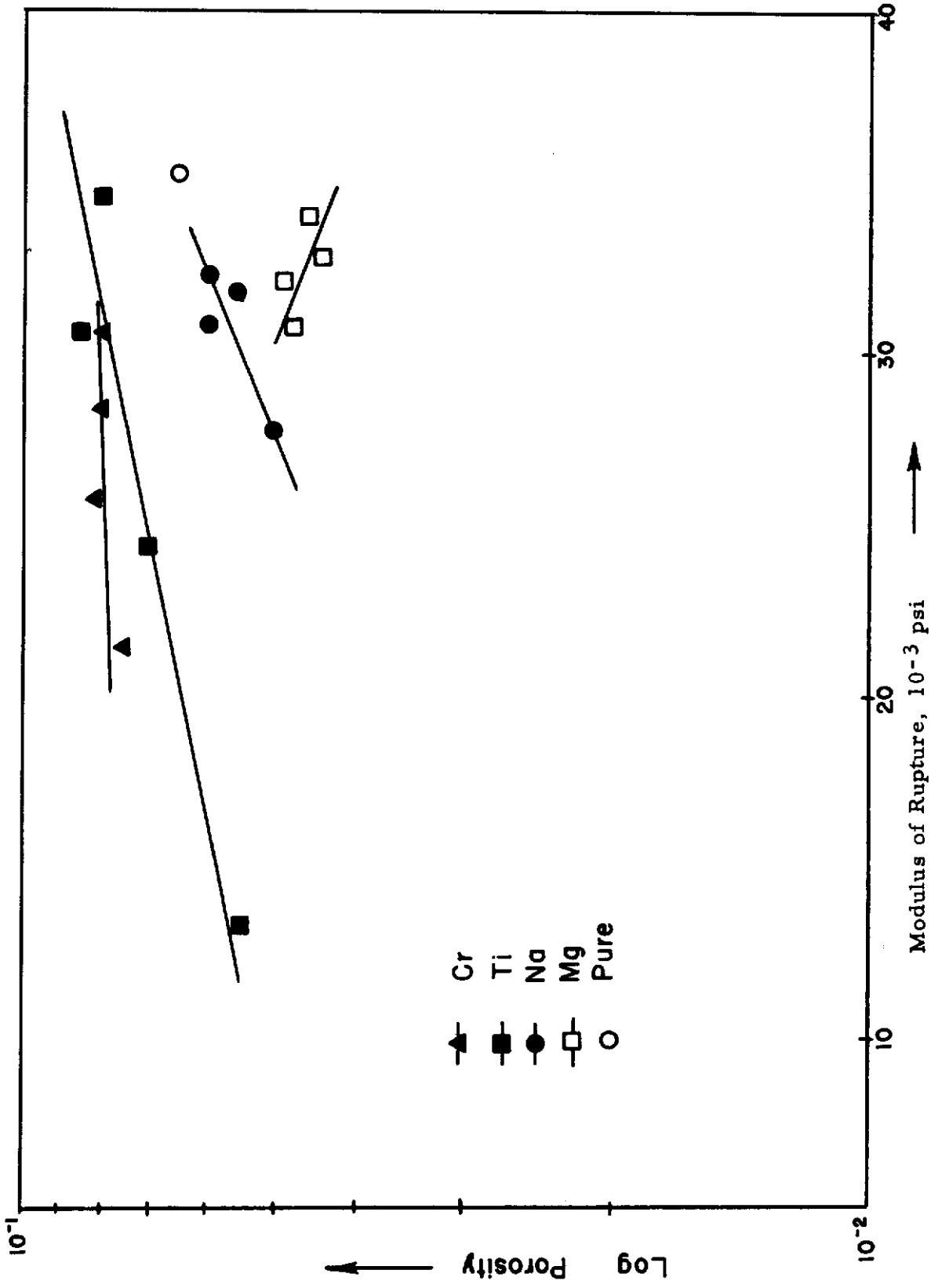

Fig. 8-15 LOGARITHM POROSITY VS. MODULUS OF RUPTURE, Al_2O_3 DOPED WITH IMPURITY PRIOR TO SINTERING

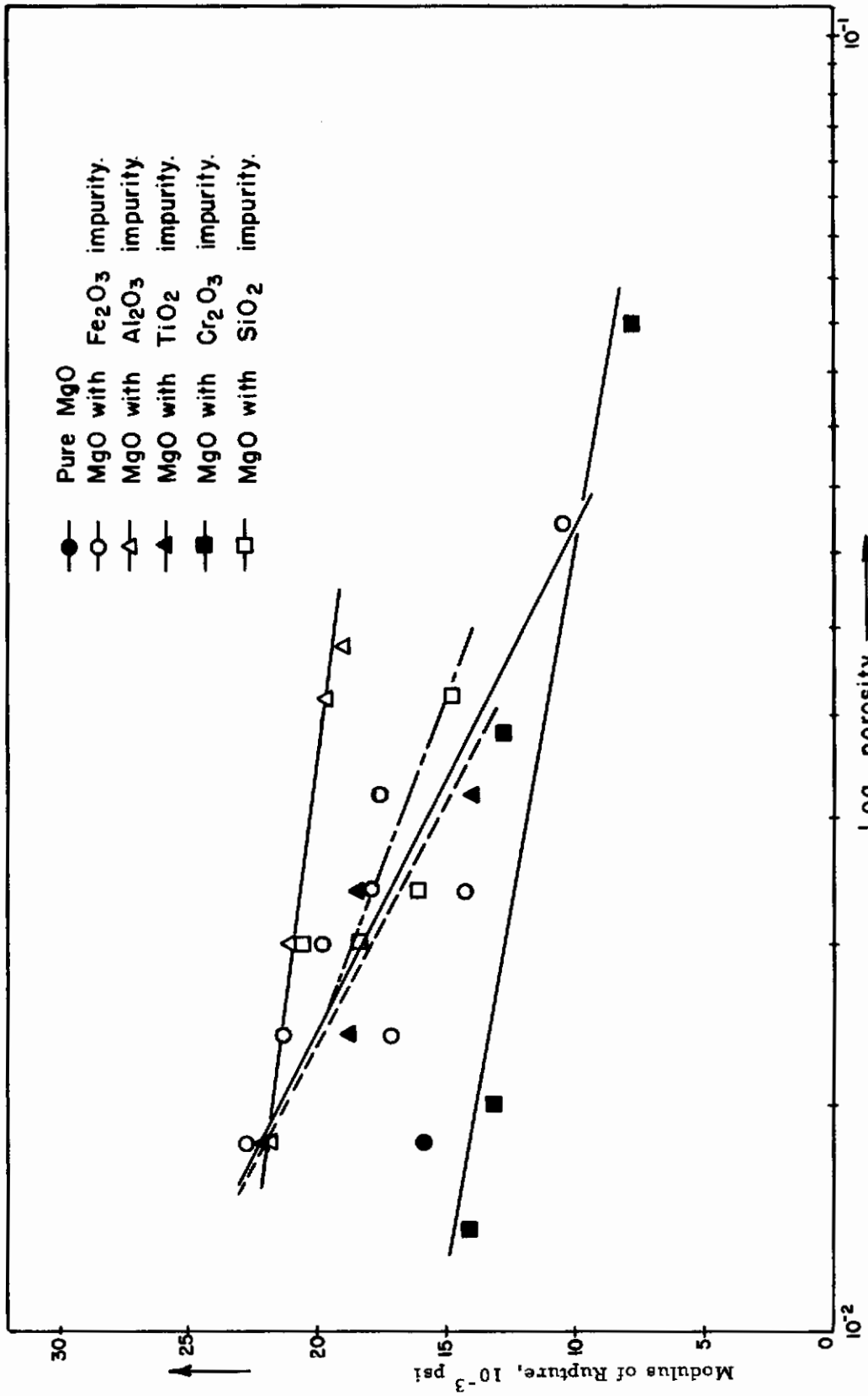

Fig. 8-16 LOGARITHM POROSITY VS. MODULUS OF RUPTURE FOR MgO DOPED WITH IMPURITY PRIOR TO SINTERING

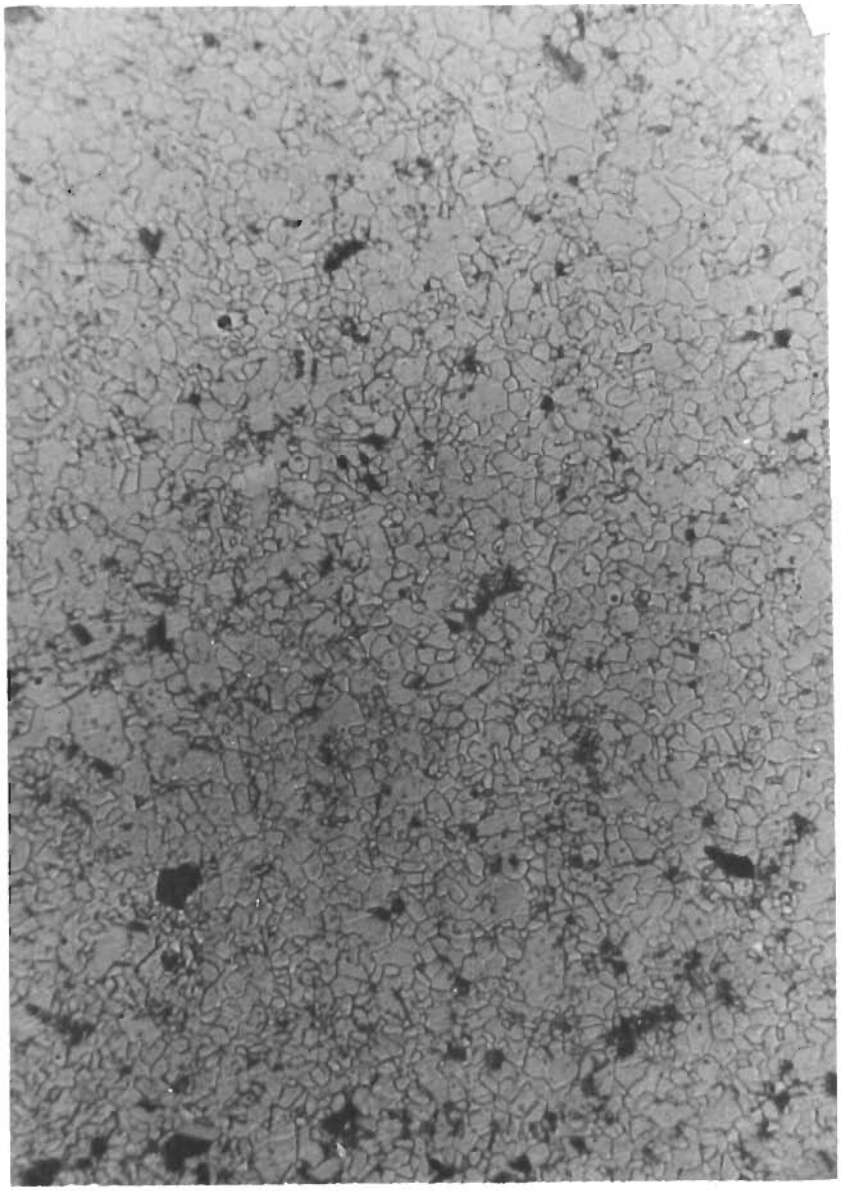

Fig. 8-17 Photomicrograph showing flash-etched surfaces of pressed and sintered high-purity Al_2O_3 doped prior to pressing with 0 ppm sodium oxide as β-alumina. (0.60 in. on the photomicrograph represents 100 microns on the actual surface.)

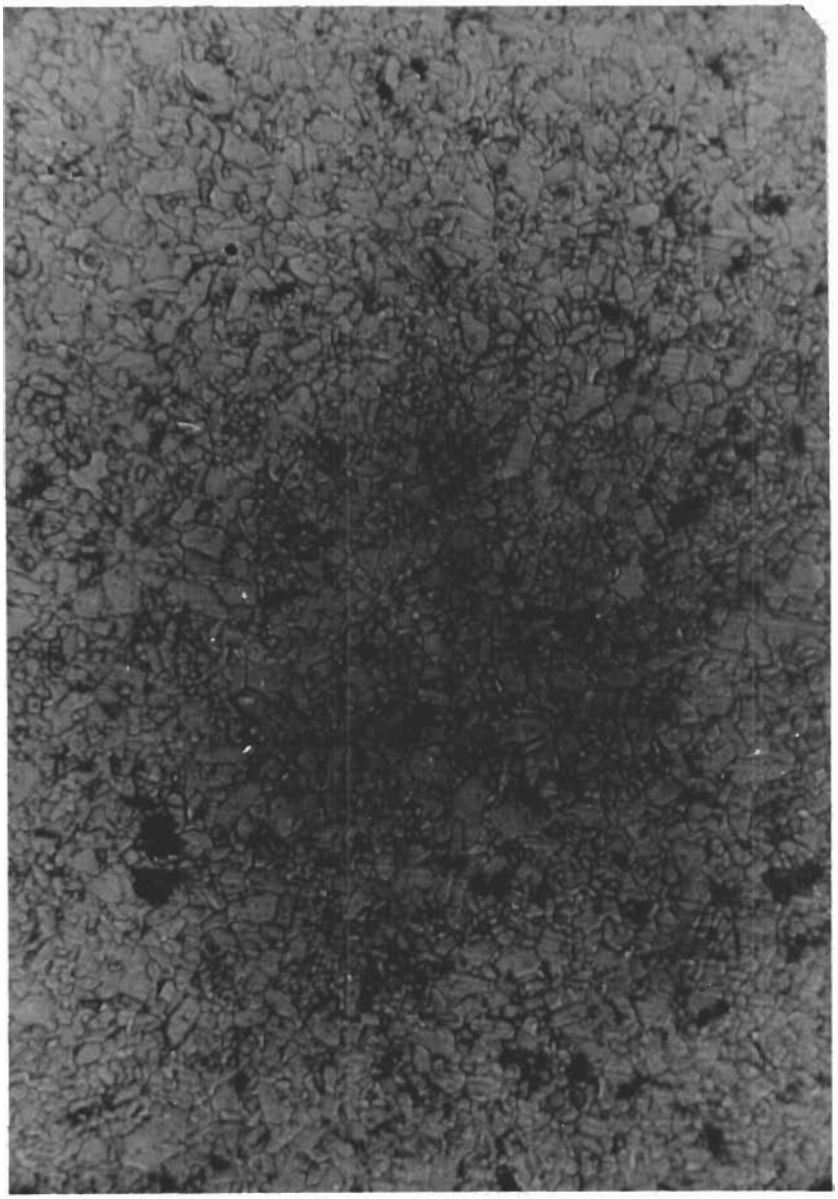

Fig. 8-18 Photomicrograph showing flash-etched surfaces of pressed and sintered high-purity Al_2O_3 doped prior to pressing with 10 ppm sodium oxide as β - alumina. (0.60 in. on the photomicrograph represents 100 microns on the actual surface.)

Fig. 8-19 Photomicrograph showing flash-etched surfaces of pressed and sintered high-purity Al_2O_3 doped prior to pressing with 100 ppm sodium oxide as β-alumina. (0.60 in. on the photomicrograph represents 100 microns on the actual surface.)

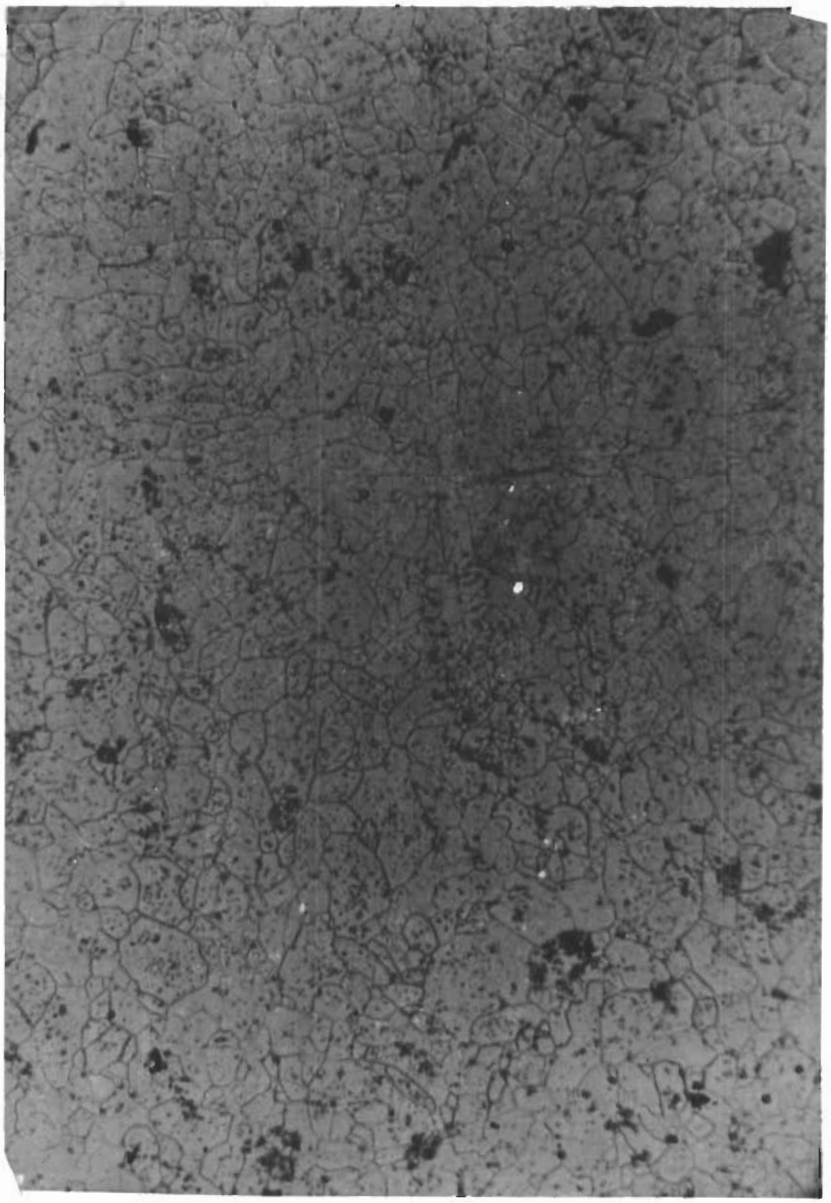

Fig. 8-20 Photomicrograph showing flash-etched surfaces of pressed and sintered high-purity Al_2O_3 doped prior to pressing with 1000 ppm sodium oxide as β-alumina. (0.60 in. on the photomicrograph represents 100 microns on the actual surface.)

6. DISCUSSION OF RESULTS

The results have not as yet been analyzed by statistical methods and it is impossible at this state in the investigation to point out a particular dependence of strength on impurity content that is independent of variations in porosity and crystal size. The data indicate that crystal size in the high purity Al_2O_3 is not altered markedly by impurities but porosity is an important factor. On the other hand, porosity did not change much in the magnesia samples and the crystal size appears to be a rather important variable.

Powder preparation of Al_2O_3 resulted in sintered specimens with large laminar pores. These originated with crystal clusters that were only partially crushed in the pressing operation. Pores in the MgO samples were all very small and of minor volume fraction. Compared to values reported in the literature, the strength of the sintered Al_2O_3 is low probably as a result of the porosity. The strength of the sintered MgO compares well with the better values quoted in the literature.

Of particular interest is the absence or exaggerated grain growth in the sintered Al_2O_3 specimens. Exaggerated grain growth occurs readily in commercial Al_2O_3 and was observed on the surfaces of specimens where commercial Al_2O_3 has been used as a setting sand (parting material). Early in the program this practice was discarded and exaggerated grain growth was eliminated. Bubble type, normal grain growth was observed in all samples of sintered alumina and magnesia on which strength data is reported here. It is interesting to note that only the specimens containing 1 percent TiO_2 showed a marked increase in grain size in the entire sintered alumina series. Wide variation of grain size were noted in the MgO series.

The curves representing the effect of impurities on the strength of sintered MgO are somewhat misleading. Pure samples were

fired with each series of doped specimens in the case of Al_2O_3 and hence difference in firing conditions were normalized by comparison with the pure specimens. The pure specimens were inadvertently left out of the firings of the doped MgO specimens. As a result, no valid comparison can be made between the pure and doped MgO specimens.

The effect of temperature on the strength of sintered and doped MgO and Al_2O_3 is not complete. Plans have been laid for strength tests at 1000°C for all specimens. It is not readily apparent why the strength at 500°C should be higher for MgO and lower for Al_2O_3 in comparison to room temperature strengths.

7. CONCLUSIONS

Research carried out on this program can be arranged into four distinct areas:

a. Preparation of suitable high-purity Al_2O_3 and MgO powders;

b. Establishment of satisfactory procedures for making pressed and sintered specimens for bend strength tests;

c. Development of techniques for doping the high-purity material with controlled quantities of selected impurities both before and after sintering, and

d. Measurement of the modulus of rupture (at room temperature and 500°C), density, and grain size in both doped and undoped specimens.

Work in the first area resulted in materials with purities substantially superior to any Al_2O_3 or MgO commercially available as shown in Tables 8-I to 8-III. Satisfactory specimens for bend strength tests were prepared by cold-pressing and sintering the pure or doped powders into discs, then cutting the discs into test prisms of the desired size and shape.

In the pre-sintered doping phase of this program, impurities were added either as oxides or as nitrates which were substantially decomposed to oxides. Amounts of impurities added prior to sintering ranged from 0 to 10^4 ppm. Apparatus for determining the modulus of rupture of test prisms at temperatures to 1100°C was developed on this project and is described in this report. Data presented for the high-purity Al_2O_3 and MgO both pure and doped with impurity before sintering include: modulus of rupture at 25° and 500°C, density, and grain size. Although satisfactory methods were developed for preparing specimens doped with impurities after sintering, time did not permit measurement of the modulus of rupture for such specimens.

8. REFERENCES

8-1 Atlas, L. M., and Nagao, H., "Control of Electrical Properties of Materials for High Temperature Radomes," WADC TR 59-300, October, 1960.

8-2 Rosenberg, R., and Cadoff, I., "Strengthening of LiF Crystals by Mg Diffused Surface Regions," Ann. Mtg. of AIME, St. Louis, February, 1961.

TASK 9 - STATIC FATIGUE: DELAYED FRACTURE

Principal Investigator: R. J. Charles
General Electric Research Laboratory

ABSTRACT

Experimental work conducted on this program has definitely established the presence of static fatigue in Al_2O_3, confirming previous investigators' findings. The reaction probably responsible for fatiguing action is the hydration of Al_2O_3 by water vapor. Delayed fracture is manifest either as a drop in strength at increased loading durations, or as an increase in fracture strength at increased strain rates.

The fatigue limit of sapphire appears to be 25 percent of its control strength at liquid nitrogen temperatures, and the variability of strength values is conspicuously less when the fatiguing process is permitted to operate than when it is prevented. Moreover, static fatigue appears to be a thermally activated process, unaffected by intrinsic material parameters such as grain size. The delayed fracture process in polycrystalline Lucalox appears to be similar in nature to that observed in sapphire, with fatiguing action persisting up to temperatures approaching 1000°C.

A theory of static fatigue has been formulated, and initial calculations were made for the surface energy value of intact sapphire and its hydration reaction product.

TASK 9 - STATIC FATIGUE: DELAYED FRACTURE

1. INTRODUCTION

Task 9 consists of a study of the corrosion processes which affect the long-term strength of single-crystal and polycrystalline aggregates of Al_2O_3 and MgO. The principal objective of this research program was to obtain information on the identity of the corrosion reactions, their mechanisms, and their total effect upon the rupture strength of these ceramics.

The most noticeable effect of delayed fracture, or "static fatigue", is the sharp dependence of observed strength upon the atmosphere present during the performance of the test. Another related effect is the decrease in resistance to failure with decrease in the rate of loading in certain atmospheres, i.e. the observed strength drops as the time of load application is extended. At zero rate of loading (dead-weight loading), the observed strength should be at a minimum, and times-to-failure under a given set of external conditions may be measured.

Much work along these lines has been done on inorganic glasses. Oxide glasses are nearly ideal materials for study of this nature because of their homogeneity, isotropy, and brittleness. Delayed fracture has been found to depend heavily on strain rate, temperature, pressure, atmosphere, surface condition, composition, and prior thermal history.

Very little work has been done, however, on crystalline oxides. Among the first references to the delayed fracture effect in crystalline oxides was that of Roberts and Watt,[9-1] who noted in 1949 that sintered alumina test specimens failed at 5 minutes and 120 minutes after loading in tension. Wachtman and Maxwell,[9-2] working in air with single-crystal sapphire, found a definite delayed fracture effect in most of the dozen samples tested at room temperature.

Williams,[9-3] working with a low density (3.84 g/cc) sintered alumina body, found times-to-failure in air as long as 10^5 seconds, depending on the stress level applied; however, the material appeared to be comparatively insensitive to cyclic fatigue at moderate frequencies of loading. Pearson,[9-4] also working with rather low-density sintered alumina, found that delayed fracture effects in ordinary atmospheric conditions could be largely eliminated by heating to about 350°C, cooling, and testing, all under a vacuum of less than 10^{-5} mm Hg. From this it was concluded that the effect was caused by an unspecified atmospheric attack acting on Griffith flaws in the stressed material.

All of the above investigations were done at room temperature. At other temperatures, Brenner[9-5] statically loaded sapphire whiskers at 1100°C and 1450° in dry H_2 and found no evidence of delayed fracture; these results were inconclusive, however, since the load was only one-third to two-thirds of the dynamic failure stresses, and load application periods were relatively short, not exceeding sixteen hours. However, later work in both hydrogen and oxygen atmospheres demonstrated fatigue in whiskers, with the time to fracture being exponentially related to the applied stress. Charles[9-6] has reported preliminary work on oxides including fused silica, granite, albite, spodumene, hornblende, sapphire, quartz, and magnesium oxide. This work included both crossbend tests on sapphire and compression tests on the other oxides, conducted in atmospheres of nitrogen-water combinations over a temperature range of -200°C to 240°C. It was shown that minimum strength values were obtained with a simultaneous application of stress and corrosive atmosphere. Atmospheres alone had little weakening effect on stress-free material, even MgO. Of great interest was the appearance of a definite strain-rate dependency of the failure stress.

It is clear from this brief review of the subject, that both polycrystalline and single crystal alumina exhibit a static fatigue in normal

atmospheres. It is not clear, however, whether MgO, either in single or polycrystalline form, exhibits behavior which may be characterized correctly as static fatigue. It seems[9-6] that MgO hydrates readily and that hydration with simultaneous plastic deformation can lead to low rupture strengths. It has been, however, the experience of these authors, and other,[9-7] that standard dead load tests on single crystal MgO specimens under ordinary conditions does not give evidence of static fatigue.

In view of these considerations, it was decided that the major effort of Task 9 should be directed towards a study of fatigue in alumina ceramics.

2. EXPERIMENTAL APPROACH

To determine whether or not a delayed fracture effect exists in a given material, it is generally useful to obtain "base level" or control data, gathered in the absence of fatigue, against which comparisons of failure strengths under environments conducive of static fatigue conditions may be made. The possibilities which exist for gathering base level data include the following:

a. Conducting experiments at low temperatures to inhibit the temperature-dependent kinetic factors which govern reaction rates.

b. Maintaining atmospheric conditions such that an atmospheric reaction cannot occur, i.e., vacuum inert atmospheres.

For a given group of specimens, with equivalent severity of surface notches or micro-cracks, destructive tests may be made under various conditions of load, time, and environment and the failure strength values compared against a maximum strength obtained under

either of the above two control conditions. In this manner the severity of fatigue may be estimated.

A. Dynamic and Static Testing

Obviously, if fatigue does not occur, the strength of a sample will be a function only of the applied stress level, but will be independent of the duration of loading. Conversely, if fatigue occurs, the failure strength or observed strength will be a complex function of the time of load application and the load changes, if any, during testing. Thus, in principle fatigue data can be obtained from tests at constant load or constant strain rate.[9-6] Both techniques were used in the experimental work described here.

B. Atmospheres and Temperatures

It is apparent that water vapor is one of the most influential atmospheres which cause fatigue in oxides. The raction is generally the formation of a hydrate. In the case of Al_2O_3, the specific hydrate formed is a function of temperature and pressure, with water or (OH^-) groups being lost as temperature increases.

Thus, if the hydration reaction is important in fatigue of alumina, one would expect to emphasize the delayed failure effects by conducting tests at moderate or low temperatures wherein mono- or multilayer absorptions of water vapor are readily obtainable. (i.e., the vapor pressure of water should be at least 0.4 times the saturation water vapor pressure for the temperature considered.) These considerations led to a selection of an experimental temperature range from about $-50^{\circ}C$ to about $200^{\circ}C$ for the detailed study of fatigue effects due to hydration.

It is conceivable that mechanisms dependent on the reduction of Al_2O_3 to sub-oxides by hydrogen could result in static fatigue. Such

a reduction reaction is known to result in the formation of alumina whiskers at high temperatures, and it is possible that similar mass transport processes may change micro crack geometries such that a stressed specimen may experience a time dependent failure. For these reasons it was considered necessary to perform further experiments with Al_2O_3 at temperatures in excess of 800°C in hydrogen atmospheres to determine whether or not a reduction reaction could lead to fatigue.

3. MATERIALS

The specimens used in this investigation were both single-crystal and polycrystalline Al_2O_3.

A. Sapphire

Al_2O_3 single crystals were obtained from the Linde Company, and consisted of random lengths of ground rod from which specimens of appropriate size were prepared. Diameter of these specimens was $0.070 \pm .0003$ inches. To insure that proper correlations between these specimens and the 0.125 inches specimens used throughout the other Tasks could be made, a number of these larger specimens were obtained and their bend strength values were compared with the .070 inch material. Correlations were exact within a few percent.

The use of sapphire presents certain special problems. The material itself is made by the Verneuil process, and is rarely completely free of the spherical air bubbles which are trapped during the process. Careful selection of specimens must be made to exclude such faulted material. Internal strains are to be expected due to the discontinuous manner in which material is added to the growing boule. Annealing after manufacture (details unavailable) is done to

help lessen the effect of these strains. And finally, the individualistic nature of each rod must be taken into account, for each rod experiences somewhat different conditions during its growth, such as temperature fluctuations and different seed stock. Because of these inherent sources of non-uniformity, it was decided to use numerous individual rods in each test and report the averages of results obtained, rather than try to compare the properties of individual rods under a given range of conditions.

Sapphire presents further problems because of its anisotropy. In bending, the effect of specimen orientation with respect to the optic axis is especially important; it has been reported [9-9] that loading parallel to the optic axis results in observed strengths nearly three times as high as loading perpendicular to the axis. It was decided to use one standard orientation throughout testing, with the load applied normal to the intersection of the neutral surface with the basal plane, which intersection was in turn perpendicular to the specimen rod axis [9-1]. This position corresponds to a maximum extinction position in polarized light when the rod axis is parallel to the vibration plane of one of the crossed polarizing prisms.

Boules grown by the Verneuil process as a rule do not have their optic axis parallel to the boule axis; similarly, the rods made from them have their optic axes tilted at some angle from the rod axis. The effect of the growth angle on mechanical properties is quite large, as seen by modulus of rupture values reported by Linde (Table 9-I; test conditions unknown). The angle is usually measured at ϕ, the angle between the optic axis (normal to the basal plane 0001) and the longitudinal rod axis. The preferred growth direction is near 60° according to the manufacturer. In order to check the orientations of samples received, a device was constructed to measure the values of ϕ for the samples by optical principles. Some

specimens were also oriented by X-ray techniques, partly as a check on the optical method. Figure 9-2 demonstrates the angular distribution of ϕ for some 200 samples checked to date. This distribution is similar to that of Wachtman and Maxwell[9-1, 9-10] whose "χ" is the complement of ϕ. Only these samples falling in a narrow zone around 60° were used in this investigation. It is of interest that some 10 percent of the off-the-shelf samples received from the manufacturer were rejected in this manner; this percentage of non-standard specimens could seriously affect the results of almost any testing program.

Table 9-I

MANUFACTURER'S ROOM-TEMPERATURE STRENGTH DATA FOR SAPPHIRE

ϕ, deg	Modulus of Rupture
30	100,000
45	78,000
60	65,000
75	94,000

All specimens were cleaned before testing to remove oil from the skin, dust, immersion oils, and other contaminants. The cleaning process consisted of a series of baths of toluene and acetone, interspersed and concluded with distilled water rinses. Specimens were dried and stored in cardboard until ready for use.

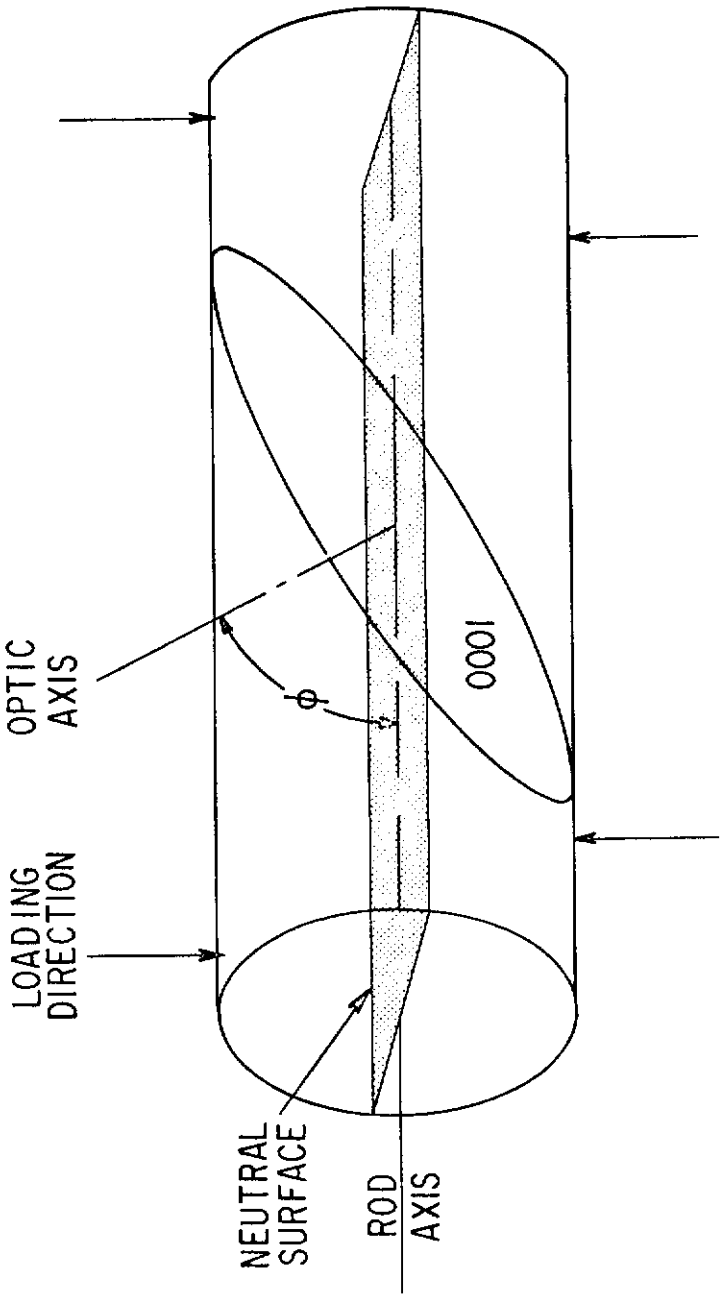

Fig. 9-1 LOADING METHOD FOR SAPPHIRE SPECIMENS

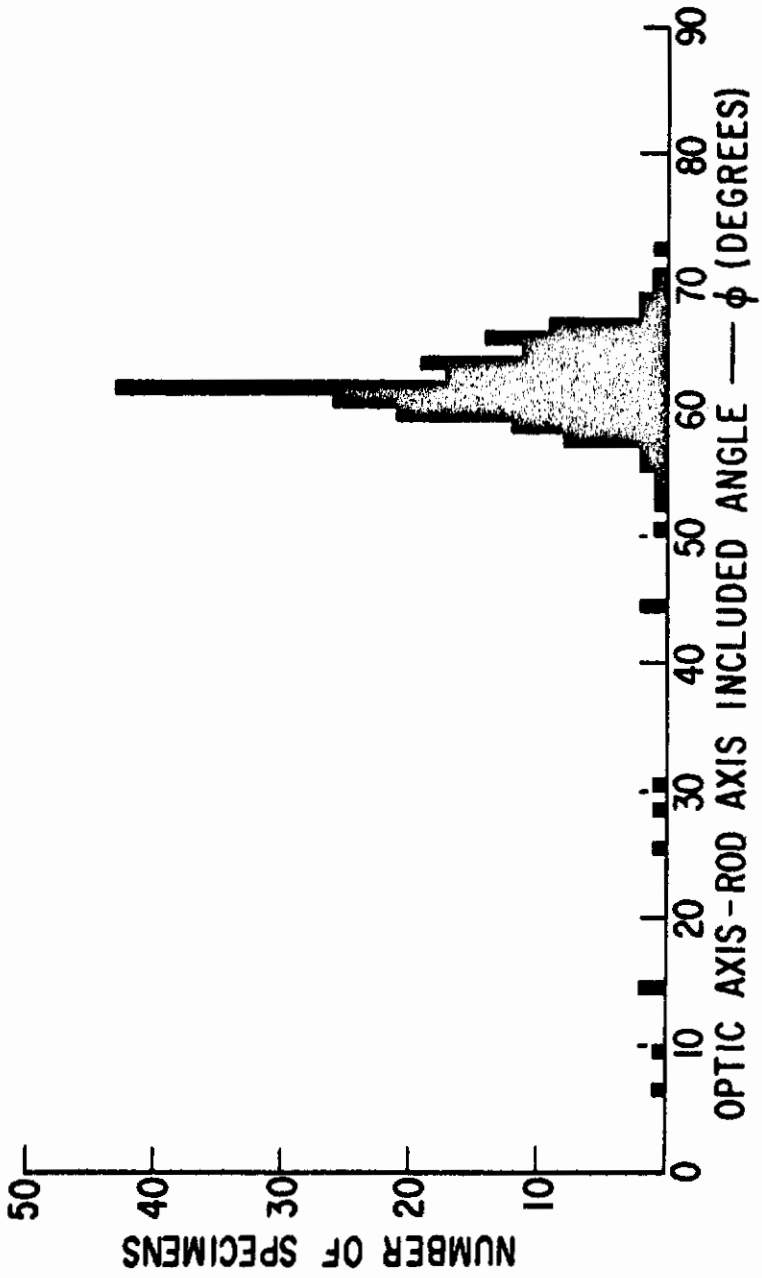

Fig. 9-2 VARIABILITY OF ϕ IN AS-RECEIVED LINDE SAPPHIRE

B. Polycrystalline Al_2O_3

Lucalox was used throughout the investigation. The type of testing done by this Task required a different specimen size and shape from the dog bone type. Therefore, polycrystalline samples were extruded to order, prefired, and finally sintered to the requisite degree of density and strength. In order to insure that the rod specimens used had the same surface grain size and strength characteristics as the specimens used in the other investigations, some preliminary work was done on the relationship between the density, grain size, and observed four-point bend strength of the material. Figure 9-3 shows the results of this preliminary work; each point represents twenty to thirty individual tests, performed at a constant strain rate of 1.4×10^{-2} min^{-1}, in air at room temperature. Density was measured by standard displacement methods.

Figure 9-3 shows that essentially full density is achieved above 30 micron grain size. The lower-density material may be likened to high-purity commercial Al_2O_3, with the reservation that the grain size is more uniform in the Lucalox Material used throughout the major portion of the work ranged 30-40 microns in grain size, with a corresponding strength of about 45,000 psi under the cited conditions. The microstructure (of the standard Lucalox) is presented in Fig. 9-4.

All polycrystalline material was tested in the as-fired condition. No particular preparation of the surface was made, other than the pretest cleaning by consecutive washes in toluene, distilled water, acetone, and distilled water, as before.

4. EXPERIMENTAL METHODS

The equipment and fixtures used in this investigation were designed to test the material in two ways, dynamic bending and static bending.

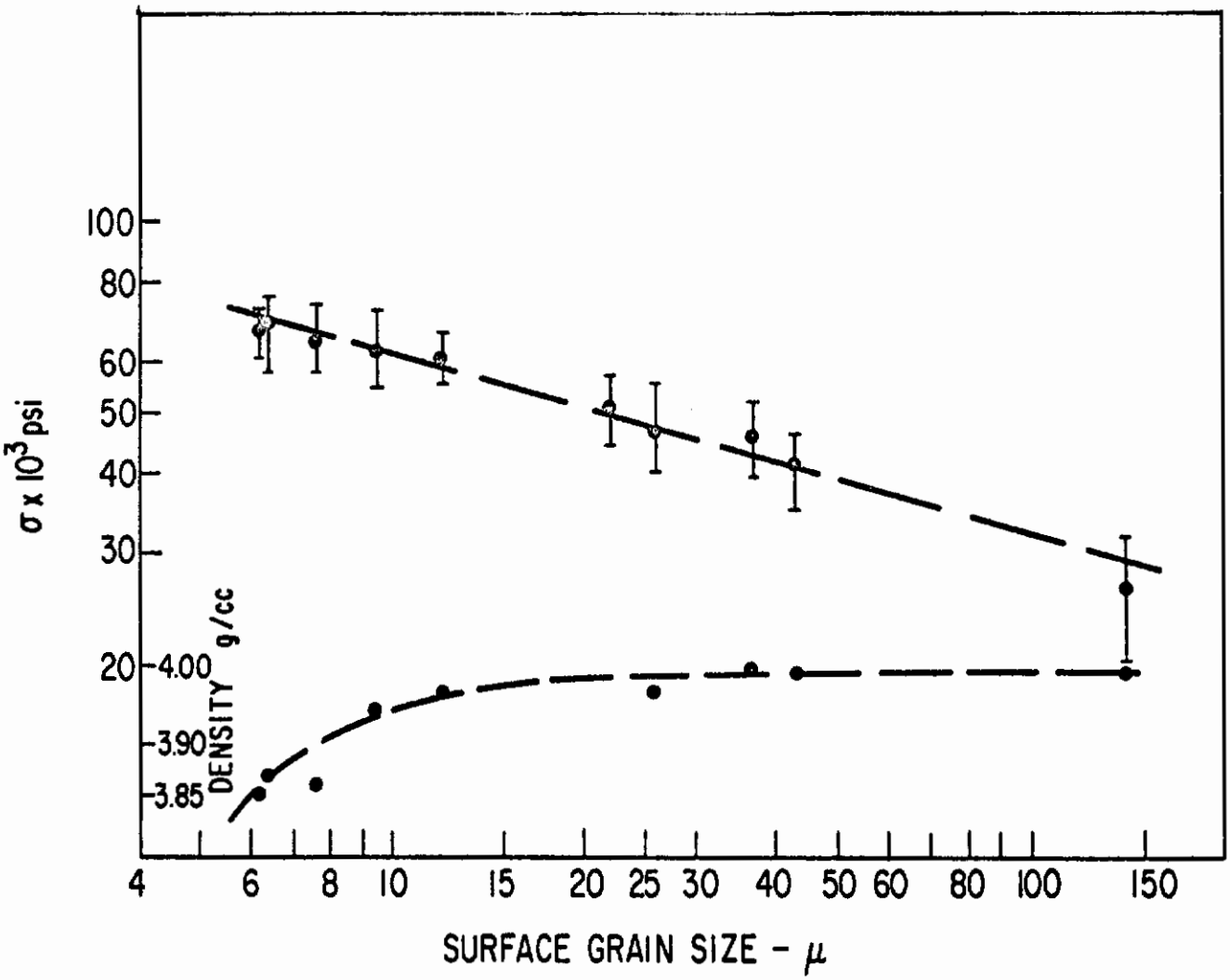

Fig. 9-3 EFFECT OF GRAIN SIZE ON STRE NGTH AND POROSITY OF LUCALOX

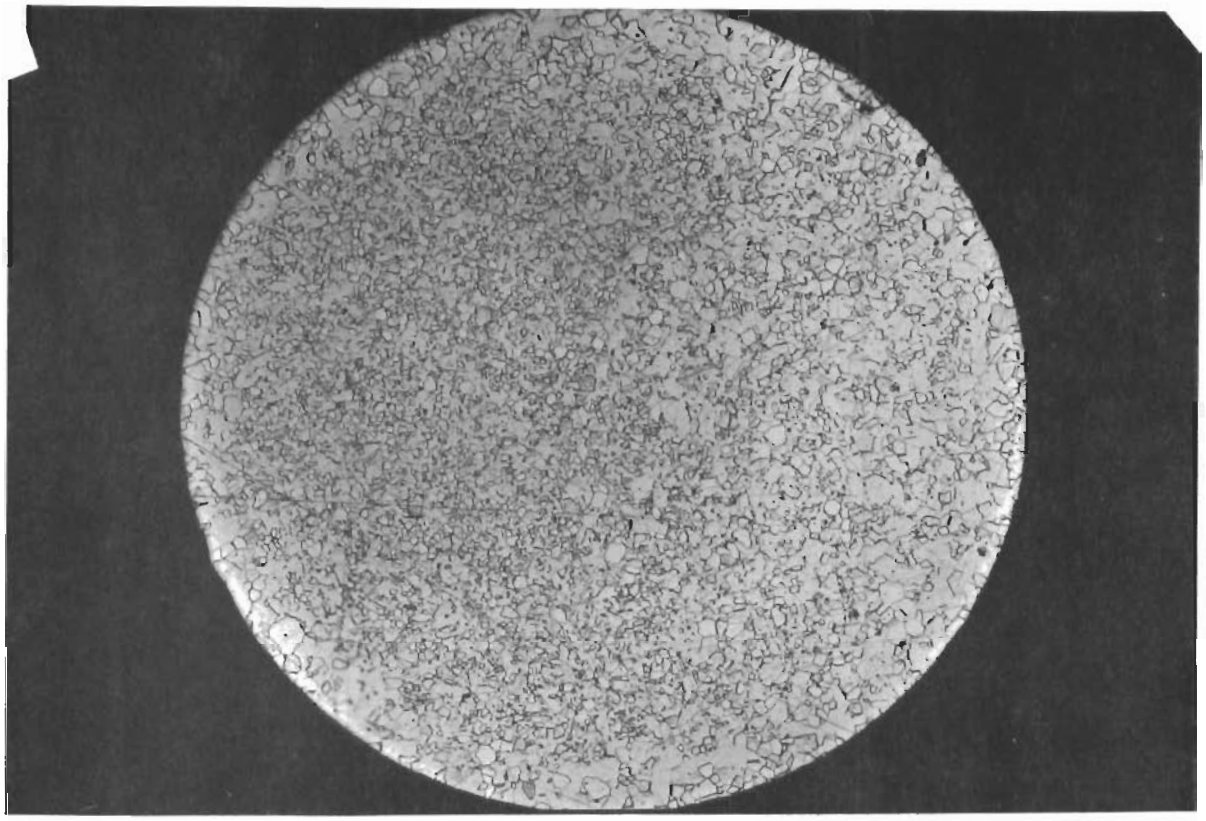

Fig. 9-4a

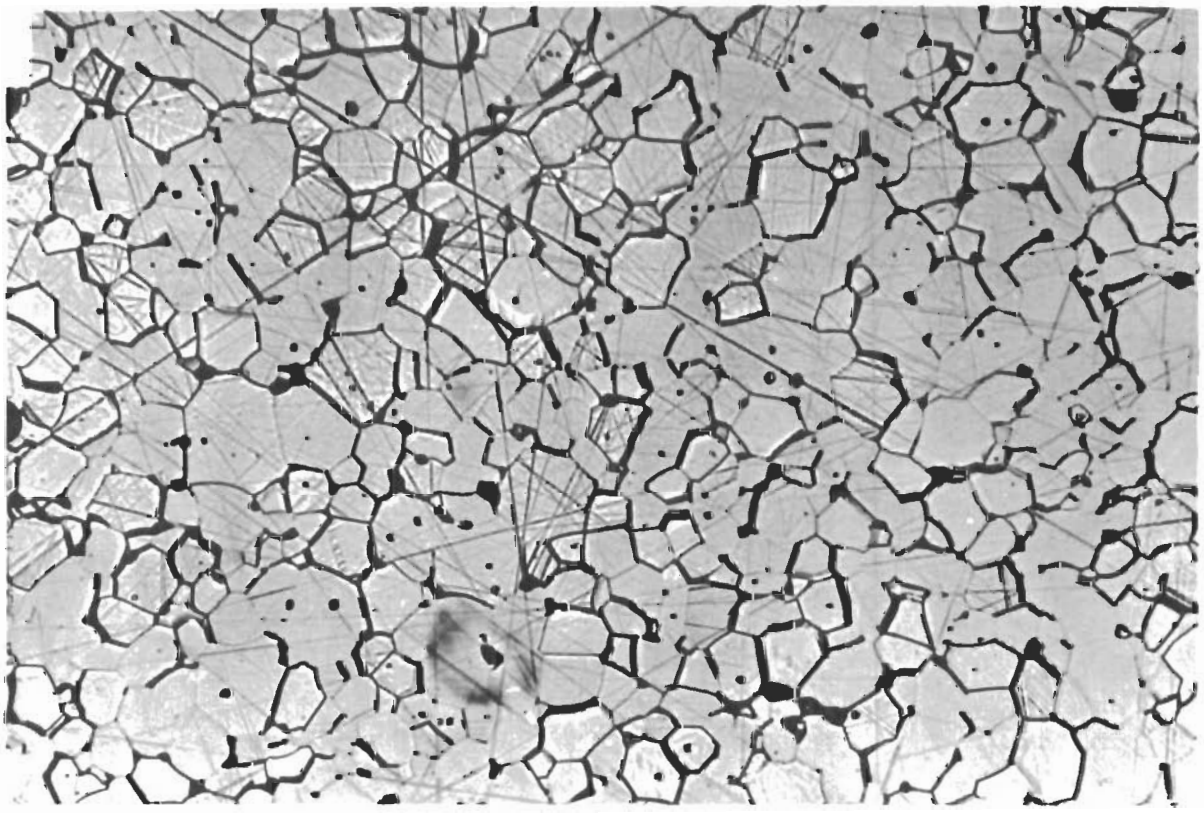

Fig. 9-4 MICROSTRUCTURE OF STANDARD LUCALOX TEST MATERIAL
(Average Surface Grain Size of 30-40 μ) (a) 75x, (b) 500x;
H_3PO_4 10 min. Overetching of grain boundaries has occurred in (b).

A. Dynamic Bending

Dynamic bending consisted of four-point bending with a constant strain rate applied to the gage section of the specimen. Four-point bending was selected because of the constant moment it exerts across the inner span. Because of the brittle nature of the specimens, and their small deflections prior to fracture, stresses were computed from the simple beam formula of $\sigma = Mc/I$.

An Instron testing machine was equipped to allow for dynamic tests at temperatures up to 1150°C in various neutral or reducing atmospheres. This consisted of a molybdenum bend fixture which could be used in air or encased within a stainless steel jacket for other atmospheres. A triple-wound Kanthal furnace surrounding the jacket provided heat for higher temperatures, and a Styrofoam case surrounding the jacket permitted low temperature tests using liquid nitrogen. Temperature in all cases was controlled by three chromel-alumel thermocouples within the bend fixture itself, and could be held to within $\pm$ 10°C of the nominal valve at all temperatures.

In view of the large number of tests required for the program, it was decided to construct a fixture to permit the simultaneous testing of up to twenty specimens per run. Figure 9-5 shows the multiple-specimen molybdenum loading fixture. Specimens are loaded at four points as the outer fixture moves past the inner one. Loading spans are 1.20 x 0.70 inches, respectively. Although subsequent modifications have been made, the principle of the apparatus remained unaltered. During tests involving sapphire, orientation was achieved by winding the specimens with three wraps of .010 in. nickel wire, and allowing the weight of the wire to keep the specimen oriented correctly. Effect of the wire on specimen strength appeared to be negligible; fracture seldom occurred at the point of wire contact.

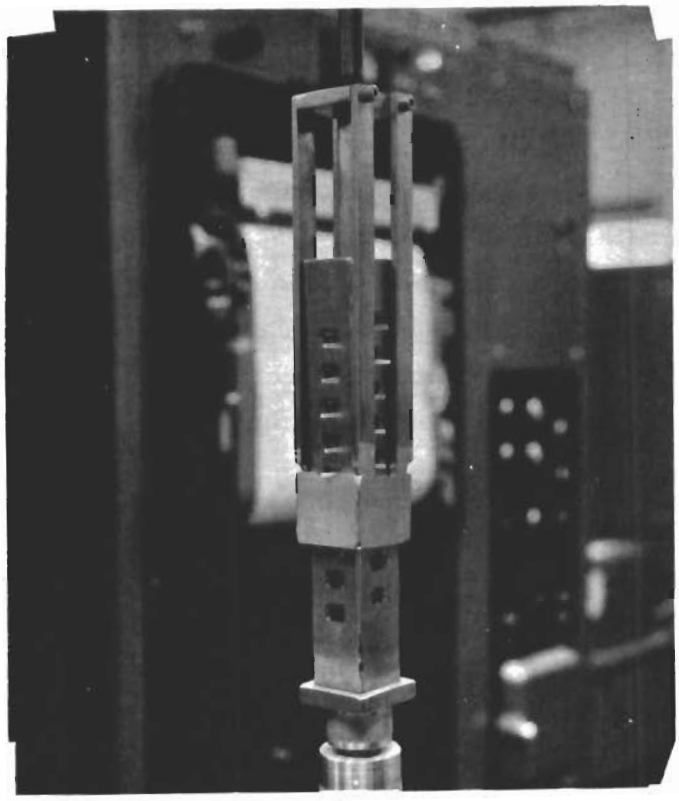

Fig. 9-5 MOLYBDENUM HIGH TEMPERATURE TEST APPARATUS

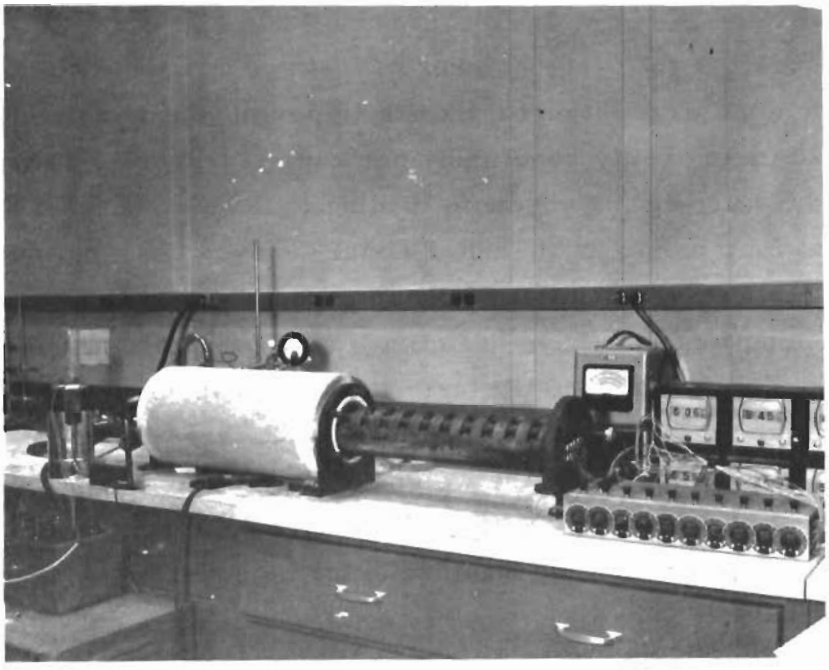

Fig. 9-6 LOW-TEMPERATURE AUTOCLAVE TEST APPARATUS

Vacuum atmospheres to 10^{-5} mm Hg were developed by means of a mechanical fore-pump and an oil diffusion pump, and were measured by a standard thermo-couple gauge. "Wet" hydrogen atmospheres and saturated air atmospheres were obtained by bubbling these line gases through several water bubblers and a detraining flask. Dry hydrogen atmospheres were produced initially by using commercial pure tank hydrogen. In later experiments dry hydrogen was procured by putting line hydrogen through oxygen, liquid nitrogen, and dessicant traps.

B. Static Bending

Static bending consisted of four-point bending, with the load being applied nearly instantaneously in the apparatus shown in Fig. 9-6. The heating jacket shown on the autoclave permitted the use of saturated steam atmospheres up to 200 psi. Ten specimens at a time can be tested in this fixture. A relay-contact system permits teimes-to-failure to be read directly from the series of clocks shown, to an accuracy of $\pm$ 5 seconds. A Styrofoam jacket permits testing in any atmosphere down to -150°C, using liquid nitrogen.

Weights may be adjusted to permit any desired stress level to be applied to the specimen. Outer and inner spans are 3.75 and 1.0 inches, respectively.

5. FATIGUE FAILURE THEORY

Charles and Hillig[9-8] have presented a theory of fatigue in which a material with the properties of an elastic continuum is considered to react chemically with its environment such that mechanical failure may be attributed to the alteration, by the dissolution or corrosion reaction, of the geometries of pre-existing flaws or cracks on the solid surface. The important point in this theory is that the reaction rate is dependent not only on local chemical conditions but also

on the local state of stress of the material. It is obvious, therefore, that the geometries of surface cracks would determine local instantaneous reaction rates. It is also clear that certain conditions of stress, temperature and environmental atmosphere may result in a continued enhancement of the stress concentrating ability of a given crack and thus lead to spontaneous crack propagation. Failure is thus dependent on time. The important conclusions of the above theory are illustrated in Fig. 9-7; the theoretical parameters governing fatigue may be obtained from experimental data plotted to represent a normalized fatigue curve. These parameters include the theoretical strength of the material, σ_{th}; an activation volume referred to a uniaxial stress, V^*; the surface energy, Γ, between the unreacted solid and its reaction products; the molar volume of the material, V_M; the initial length, L, of a critical flaw; the strength of the specimen in the absence of fatigue, S_N; and the limiting fatigue strength of the material in its environment, S_L.

Although the above theory was developed for an isotropic material it is intended, in the present work on alumina, to conduct fatigue experiments to determine whether or not a typical fatigue curve, as illustrated in Fig. 9-7 may be obtained. If such proves to be the case then the parameters listed above may have important meaning regarding the kinetics of the fatigue process in alumina.

6. EXPERIMENTAL RESULTS FOR SINGLE CRYSTAL ALUMINA

A. Base Level Strength of Sapphire

Table 9-II lists the liquid nitrogen and room temperature bend strengths of sapphire crystals in which the base planes exhibited two different orientations to the specimen axes.

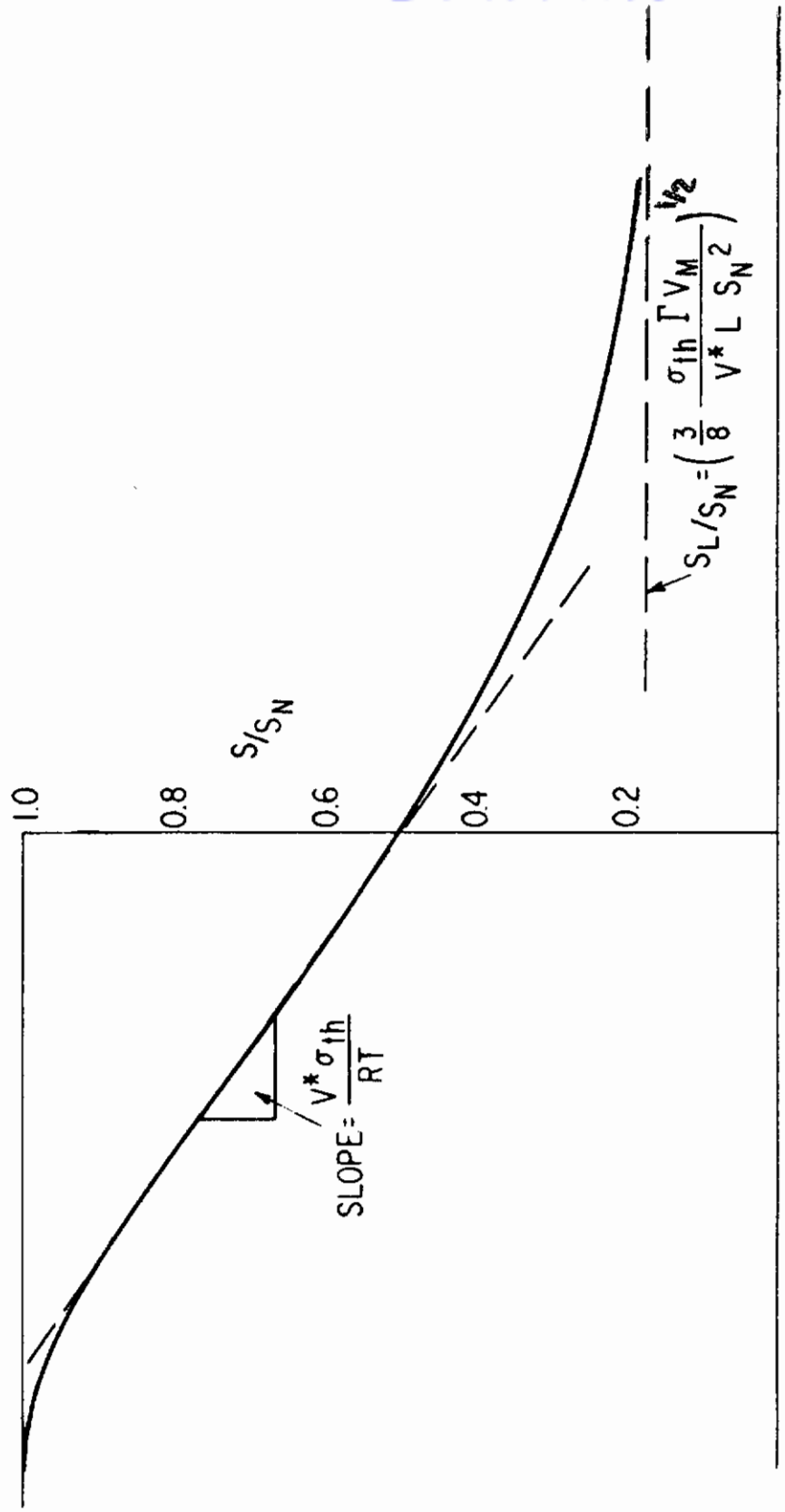

Fig. 9-7 THEORETICAL PREDICTION FOR STATIC FATIGUE: REF. 9-8

τ = time to failure

$\tau_{0.5}$ = time to failure at $S = S_N/2$

Table 9-II

EFFECT OF BASAL PLANE ORIENTATION AND TEMPERATURE ON OBSERVED BEND STRENGTH OF SAPPHIRE

Orientation	No. Tests	Temperature, °C	Atmosphere	Rupture Strength, psi
Zero-degree .070-in. diam.	10	25	Air	102,000
Zero-degree .070-in. diam.	20	-196	Liq. N_2	170,000
60° .070-in. diam.	9	25	Air	54,600
60° .070-in. diam.	11	-196	Liq. N_2	73,900
60° .125-in. diam.	11	25	Air	59,800
60° .125-in. diam.	9	-196	Liq. N_2	75,100

It will be noted that the strength of the zero degree rods is approximately twice that of the 60° specimens, in both test conditions. This shows a very real effect of the variation of the angle ϕ, as discussed earlier. The close correlation of strength of the two different sizes of specimens is also evident.

B. Constant Strain Rate Tests on Sapphire

Table 9-III lists the presently available data on the testing of sapphire rods in four point bending under various atmospheres and at various temperatures.

Table 9-III

CONSTANT STRAIN-RATE TESTS ON SAPPHIRE SINGLE CRYSTALS

$\dot{\epsilon}$ = 3×10^{-4} in./in./min
N = number of tests
σ = average failure stress $\times 10^{-3}$ psi
v = coefficient of variation

Temperature, °C		Sat. Air	Dry H_2	Wet H_2	Vacuum	Liq. N_2
-196	N					12
	σ					70.7
	v					11.3%
Room	N	18	15	14	18	
	σ	38.8	45.9	39.2	59.2	
	v	19.6%	9.4%	21%	12.5%	
200	N		14	12	11	
	σ		41.3	38.0	54.1	
	v		11.6%	14%	10.8%	
500	N				10	
	σ				48.1	
	v				12%	
850	N				12	
	σ				54.0	
	v				14%	

Results to date are insufficient to draw any conclusions but the limited results, plotted in Fig. 9-8, indicate that the single crystal results may parallel those obtained for the polycrystalline material (Fig. 9-12).

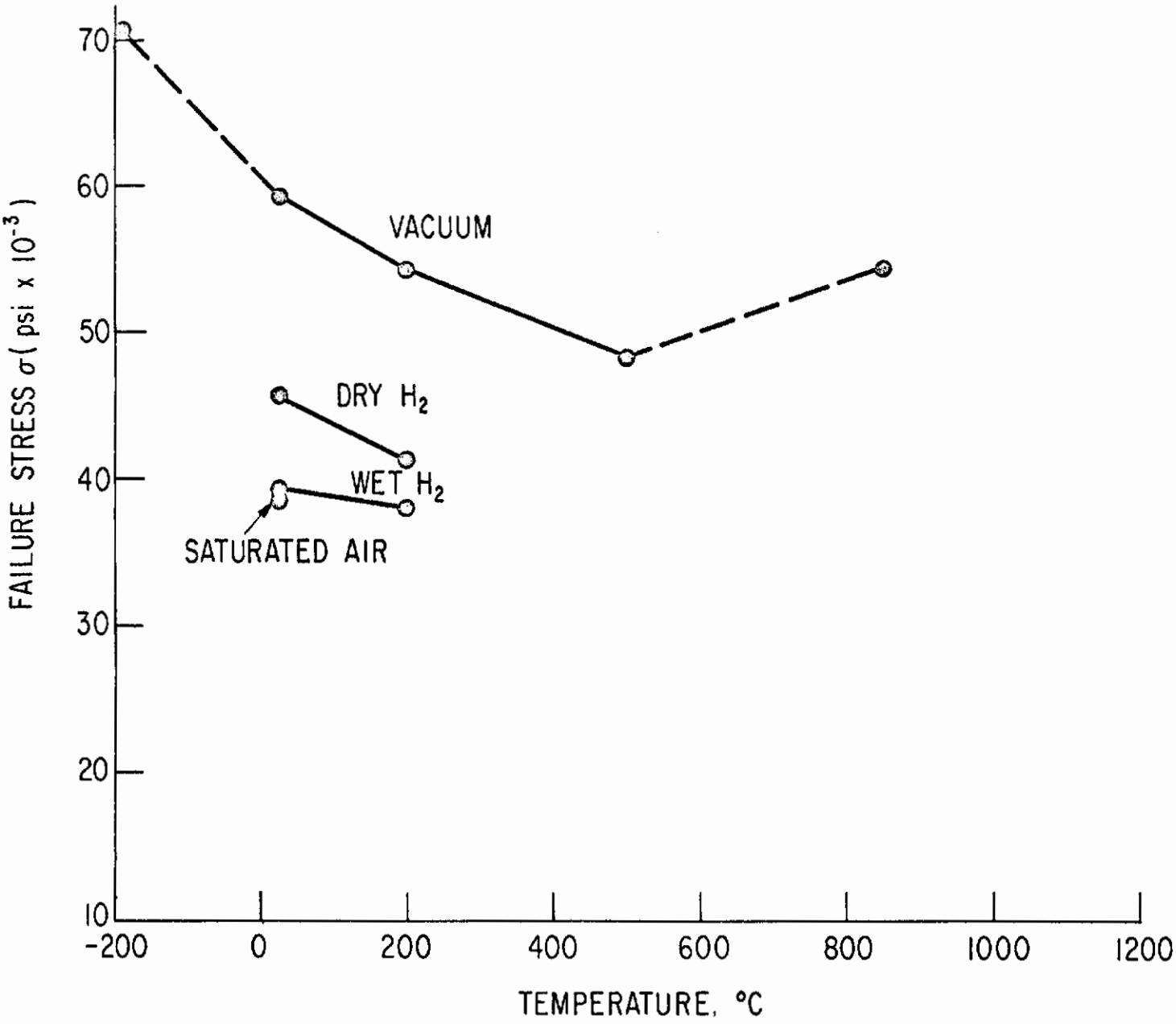

Fig. 9-8 ENVIRONMENTAL EFFECTS ON SAPPHIRE AT VARIOUS TEMPERATURES

Constant Strain Rate Tests at 0.31×10^{-4} min^{-1}.

C. Static Fatigue Tests on Sapphire

Table 9-IV lists the available data on the testing of sapphire specimens under static load. Figure 9-9 is a plot of the above data in the manner indicated by Fig. 9-7. Although no complete curve for any one temperature has as yet been determined for sapphire specimens, some estimates of the fatigue parameters, as outlined in a previous section, can be obtained from Fig. 9-9.

7. EXPERIMENTAL RESULTS FOR LUCALOX

A. Strength Versus Grain Size and Testing Rate

Figure 9-10 illustrates the effect of grain size and strain rate on the strength of the Lucalox alumina specimens selected as standard for this investigation. This figure also includes the strength-grain size dependence for tests at liquid nitrogen temperature. It is clear that a fatiguing effect is illustrated by these results for, in general, the strength of Lucalox tested at a strain rate of 2.7×10^{-4} min^{-1} is approximately 20 percent less than that tested at a strain rate of 1.4×10^{-2} min^{-1} and 30 percent less than the base level strength determined at a liquid N_2 temperature. Within the limits of accuracy of the data it would appear that although grain size affects the base level strength, it does not alter the fatigue effects that are observed.

Table 9-IV

STATIC FATIGUE DATA ON SINGLE CRYSTAL SAPPHIRE

Constant Stress, σ, psi	Conditions	No. Specimens Failing Within Indicated Time Decades, min									Most Prob. Time-to-Failure, min
		$10^{-2}<$	10^{-2}	10^{-1}	10^{0}	10^{1}	10^{2}	10^{3}	10^{4}	$<10^{4}$	
41,600	T = 198°C 200 psig steam	10									~ 0
23,500	As above	6		3		11	12	3			3
20,500	As above		1			4	14	7	2	7	90
18,400	As above		4	4		5	10	12	7	3	1000
16,800	As above						3	1	1	4	---
34,400	T = -35°C Sat. water vapor	2				15	5	5	3	6	7
39,000	As above					6	2	1			---
46,100	As above		1	3		1					~ 1 (tent.)
34,400	Room Temp. Sat. water vapor	8		1				1			

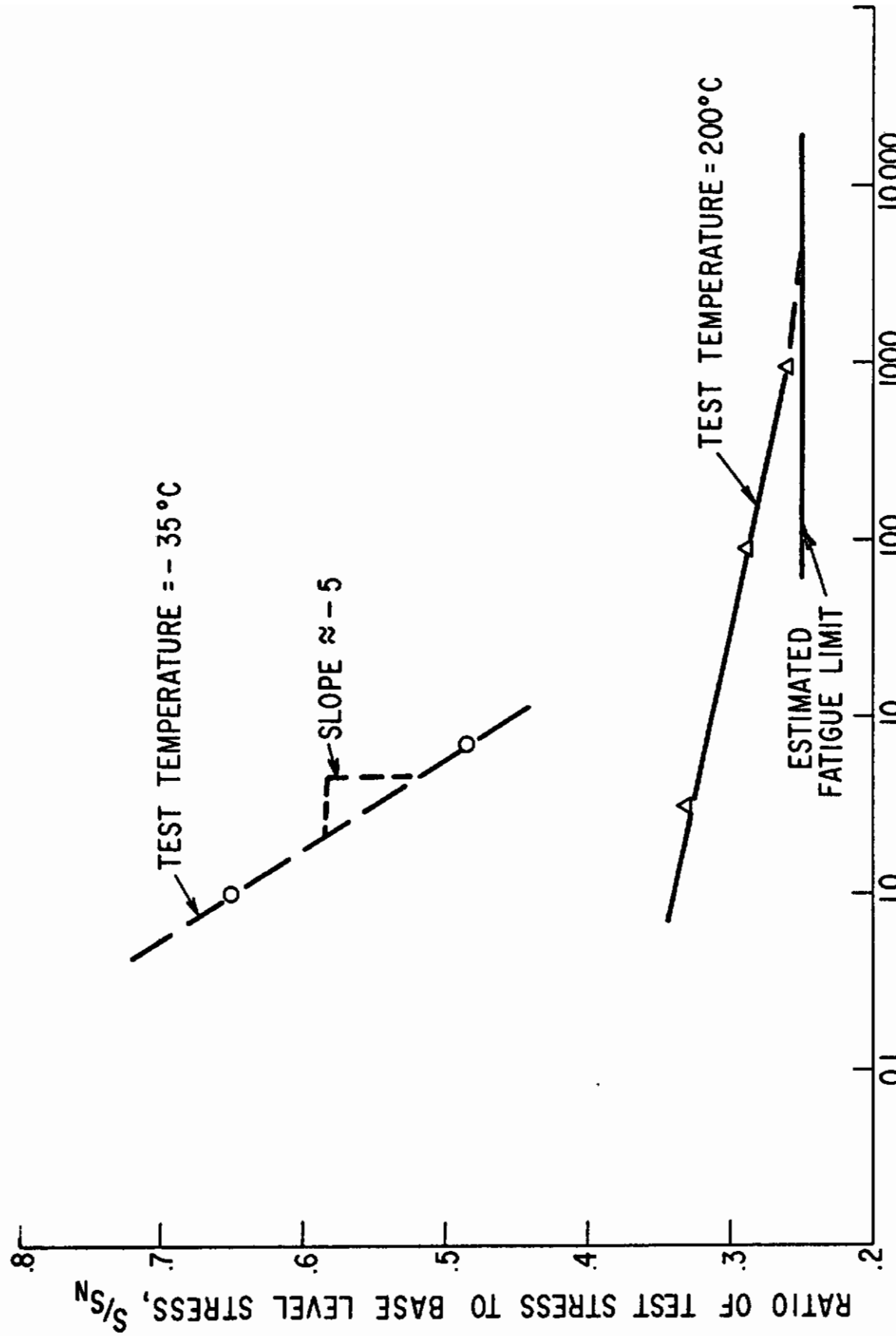

Fig. 9-9 STATIC FATIGUE OF SAPPHIRE AT VARIOUS TEMPERATURES

B. Constant Strain-Rate Tests on Lucalox

Table 9-V lists the results of constant strain rate experiments on the standard Lucalox specimens in various atmospheres and at various temperatures.

Figure 9-11 illustrates the normalized vacuum strength of Lucalox as a function of temperature and the normalized Young's Modulus of polycrystalline Al_2O_3 over the same temperature range. The similarity of the curves indicates that the fall off of strength of alumina in vacuum with increased temperatures may probably be attributed to the changes in theoretical strength as reflected by the changes in modulus with increased temperature.

Figure 9-12 illustrates the effect of dry hydrogen and wet hydrogen (saturated at room temperature) on the strength of alumina. It is evident, especially at the lower temperatures, that wet hydrogen fatigues Al_2O_3. This fatigue effect becomes less and less pronounced at increasing temperature, until at 1000°C no fatiguing action can be discerned.

It is difficult to explain the slight but observable fatiguing effect of dry hydrogen. At this time, the only plausible explanation appears to be the possible uncertainty of "dryness" within the testing chamber during test, althought the inlet hydrogen had a quoted dewpoint of about -60°C. Again, under dry hydrogen, the slight fatigue effect disappears at 1000°C.

C. Room Temperature Static Fatigue of Lucalox

Table 9-VI lists the presently available data for static fatigue (room temperature) on Lucalox. Data to date are insufficient to permit any conclusions to be drawn.

Table 9-V

CONSTANT STRAIN-RATE TESTS ON

STANDARD LUCALOX SPECIMENS

$\dot{\epsilon}$ = 3×10^{4} in./in./min

N = number of tests

σ = average failure stress x 10^{-3} psi

v = coefficient of variation

Temperature, °C		Sat. Air	Dry H_2	Wet H_2	Vacuum	Liq. N_2
-196	N				11	20
	σ				73.0	66.5
	v				12.3%	13.2%
Room	N	11	11	10	11	
	σ	46.5	52.3	44.9	65	
	v	5%	5.9%	6.8%	9%	
200	N		11	9	34	
	σ		48.4	42	57.2	
	v		7.8%	7.4%	12.8%	
350	N		10	19	12	
	σ		47.6	39	56.3	
	v		4.3%	8.9%	6.1%	
500	N		11	10	10	
	σ		50.4	43.4	56	
	v		9.2%	5.2%	6%	
700	N		10	9	12	
	σ		48.3	44	53.2	
	v		3.3%	10.2%	5.5%	
850	N		14	11	9	
	σ		51.4	47.5	50.5	
	v		6.1%	8.4%	8.5%	
1000	N		10	9	10	
	σ		50.8	52.7	47.2	
	v		10.3%	9.8%	14.4%	
1150	N				11	
	σ				42.0	
	v				13.6%	

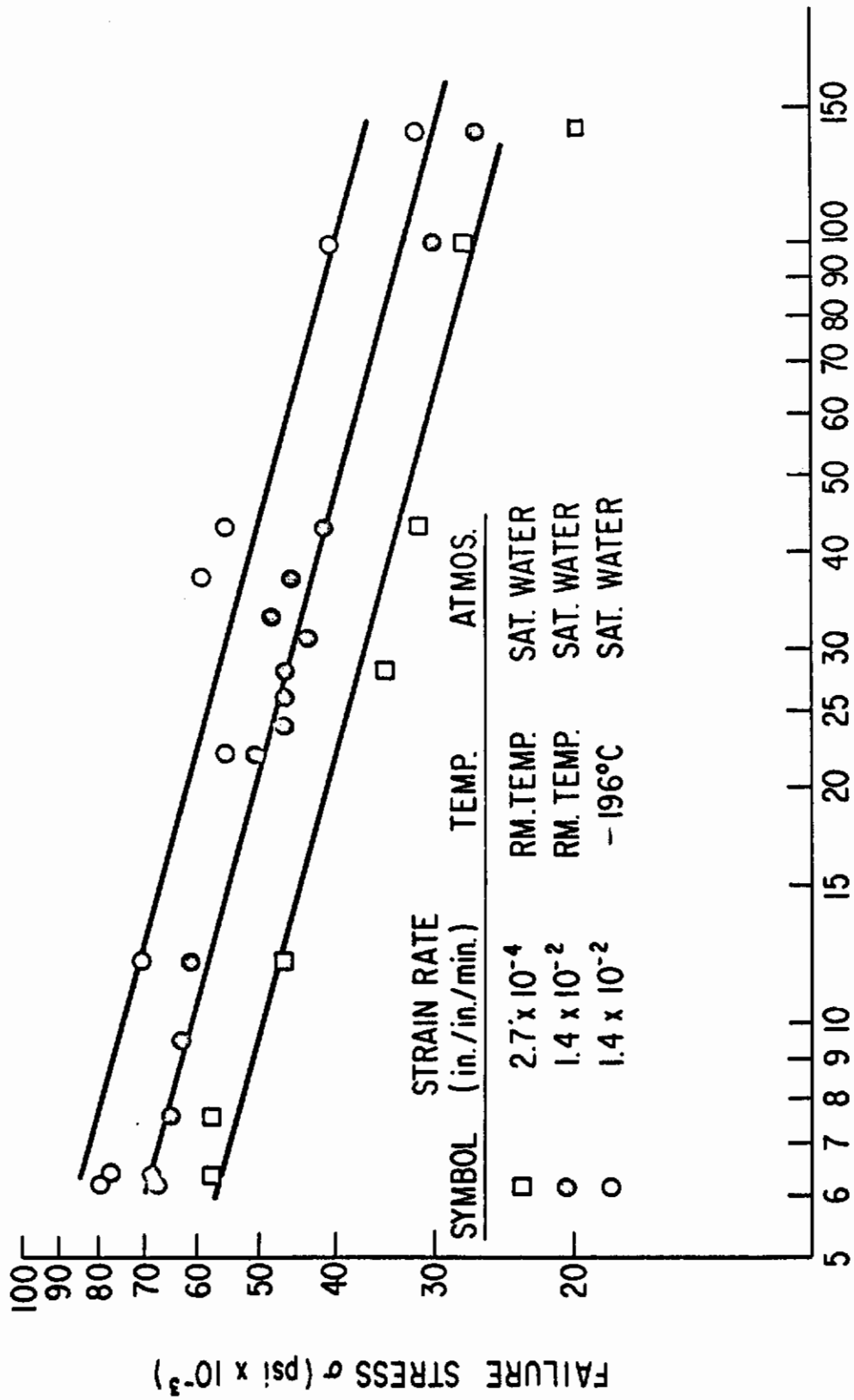

Fig. 9-10 EFFECT OF GRAIN SIZE AND STRAIN RATE ON STRENGTH OF LUCALOX

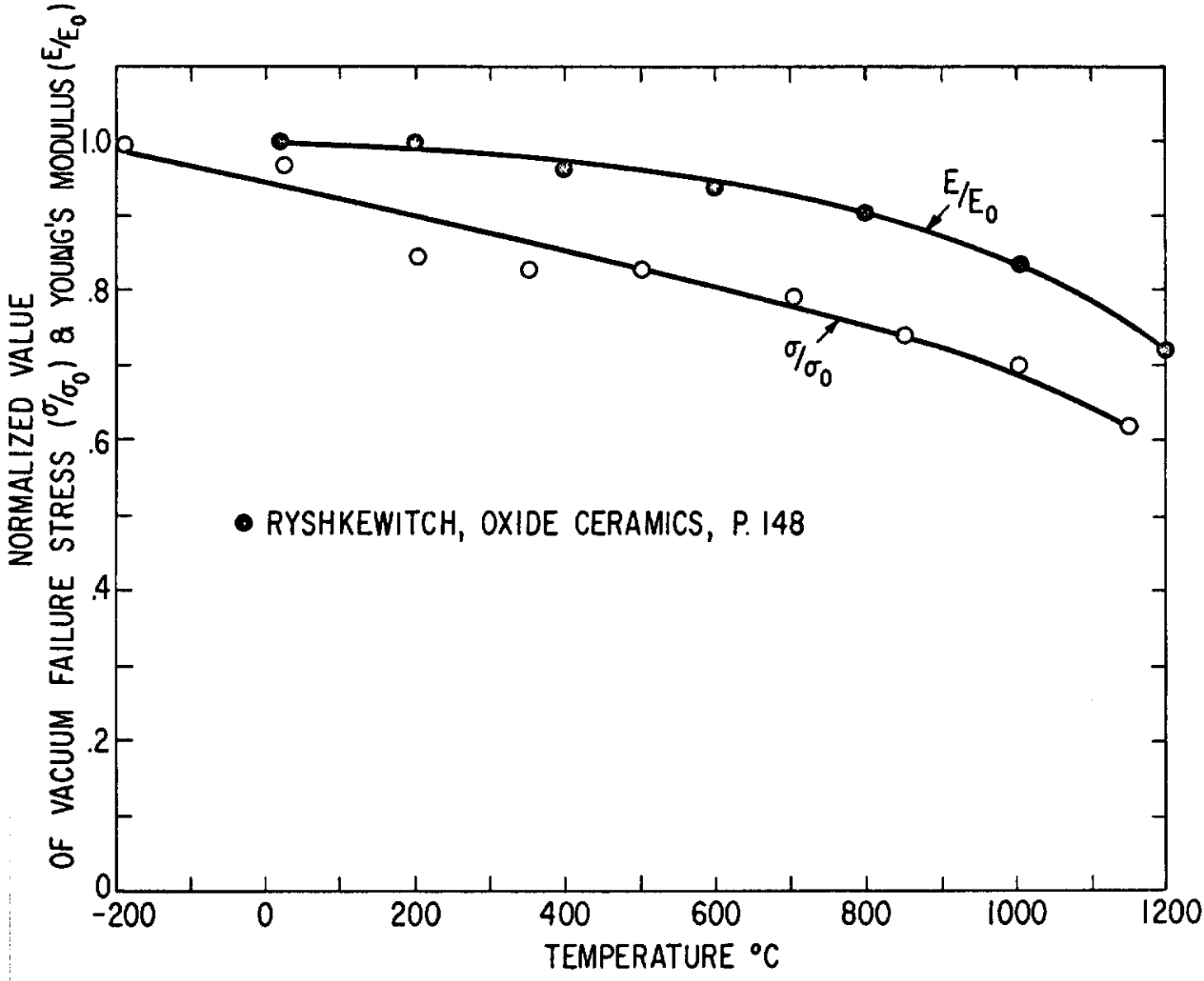

Fig. 9-11 NORMALIZED VACUUM STRENGTH AND MODULUS OF ELASTICITY OF Al_2O_3 AS FUNCTION OF TEMPERATURE

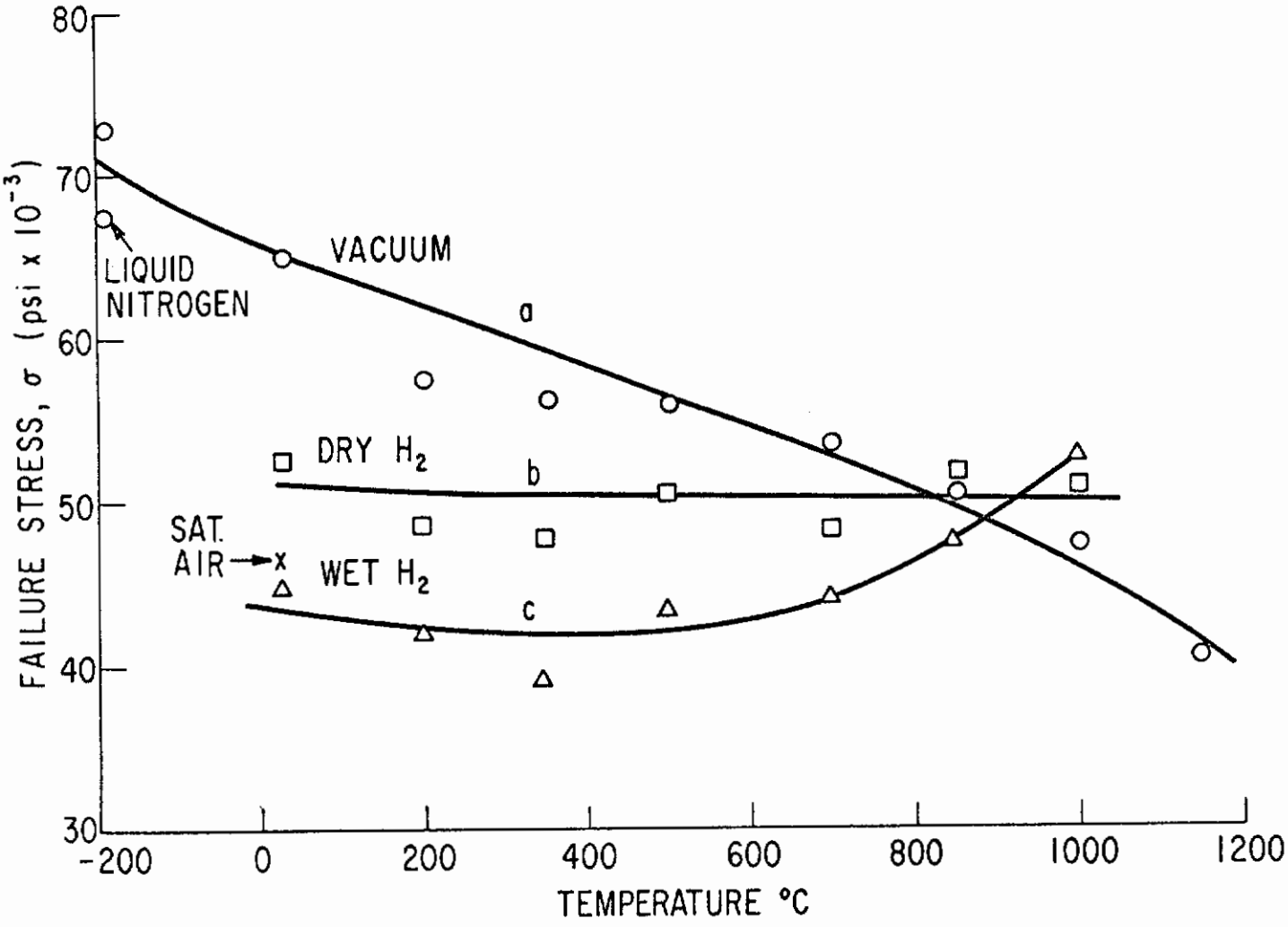

Fig. 9-12 TEMPERATURE-ENVIRONMENTAL EFFECTS ON THE RUPTURE STRENGTH OF STANDARD LUCALOX SPECIMENS

Table 9-VI

STATIC FATIGUE DATA ON STANDARD LUCALOX SPECIMENS

Constant Stress σ, psi	Conditions	No. Specimens Failing Within Indicated Time Decades, min.									Most Prob. Time-to-Failure, min
		10^{-2}	10^{-2}	10^{-1}	10^{0}	10^{1}	10^{2}	10^{3}	10^{4}	10^{4}	
55,100	Room Temp. Rough Vacuum (10mm Hg)	10	6	4	3	3	6	2	3		$\sim 10^{-1}$
48,000	As above			1			2	2	7		
44,100	As above							2	2		
48,500	Room Temp. Air, 20%RH	2		1	2	1	1				
48,500	198°C 200 psig steam	10									~ 0
41,600	As above	3	1	1	3	1					
29,600	As above							2	6		

8. CONCLUSIONS

The results reported in previous sections, while still incomplete, confirm and extend previous investigator's findings that Al_2O_3, both in single and polycrystal form, is subject to static fatigue. From these limited results a number of general conclusions may be made.

(a) The reaction responsible for fatigue is probably one in which water vapor from the atmosphere combines with the alumina to form one or more of the many possible hydrated states of Al_2O_3.

(b) As far as typical mechanical tests are concerned, the fatigue process in Al_2O_3 manifests itself in the same fashion as is observed for other materials (e.g., glass). Firstly, one observes delayed failure of alumina specimens at constant load in which the average failure time is a very strong function of the applied stress (Fig. 9-9). Secondly, the failure stress, at constant loading rate, increases with the absolute value of the loading rate (Fig. 9-12). Lastly, the coefficient of variation of failure stresses is considerably less when the fatigue process is permitted than when it is prevented; as illustrated by the data in Table 9-V, the coefficient of variation at liquid nitrogen temperature (fatigue process prevented) is around 13 per cent, whereas the mechanical tests under wet hydrogen (fatigue process permitted) generally show coefficients of variation of around 5 - 6 percent.

(c) The fatigue limit stress (S_L) for sapphire is about 0.25 S_N (Fig. 9-9) where S_N is the control strength of the material in liquid N_2, devoid of any weakening due to fatigue mechanisms. The ratio $S_L/S_N = 0.25$ for sapphire is slightly higher than that for the glasses[9-8] (i.e., 0.15).

(d) The fatigue reaction of sapphire is a thermally activated process. Its rate constant at room temperature sufficiently large so

that in a saturated water vapor atmosphere, only stresses near the fatigue limit will permit delayed failure times sufficiently long for easy measurement (i. e., greater than one second). As noted in Fig. 9-9, it was necessary to reduce the temperature to -35°C for static fatigue tests on sapphire to obtain satisfactory measurable delay times at stresses near one-half the base level stress.

(e) With an essentially inert gas (H_2) saturated with water vapor at room temperature, the fatigue reaction in Lucalox alumina is sufficiently strong to give evidence of fatigue up to temperatures approaching 1000°C (Fig. 9-12).

(f) As indicated by Fig. 9-10, the fatigue mechanism in Lucalox does not appear to be affected by the grain size of the material.

It is well to elaborate somewhat on this point for, within the initial planning of the overall program, great consideration was given to the manner in which the data obtained on the special samples required by Task 9 could be correlated with data on different samples used by other investigators in the program. The necessary correlation proves to be relatively simple and results from the following argument.

The intrinsic strength of a brittle ceramic body is subject to constitutional variables such as grain size and distribution, surface treatment, and the area of sample under stress as well as the variables introduced by test arrangements. As has been shown in the previous data, the intrinsic strength of an alumina specimen, of arbitrary preparation and shape, may be reduced if the environment permits a fatigue reaction. Prevention of this fatigue reaction by testing at reduced temperature, however, allows a measurement of the intrinsic or control strength of this specimen. Since the data already obtained (Fig. 9-9) indicates that the maximum reduction of the intrinsic strength of alumina by corrosion fatigue is approximately 75

percent one can, in principle, obtain the approximate fatigue limit stress of any specimen of alumina, tested in a water containing atmosphere, by first determining the control or base-level strength at low temperature.

Although the static fatigue data on single crystal sapphire, as illustrated in Fig. 9-9, is incomplete, some very rough estimates of the fatigue parameters identified in Fig. 9-7 may be made. The slope of the line joining the two points for fatigue experiments at $-35^{\circ}C$ is about -5, so that by reference to Fig. 9-7, $(V^*/RT)\sigma_{th} \approx 5(2.3)$. The modulus, E, of sapphire at this temperature is approximately 50×10^6 psi and thus one would estimate the theoretical strength, σ_{th}, of sapphire to be about E/5 or 10^7 psi. Converting to the desired units, the activation volume V^* (referred to a uniaxial stress), for the corrosion reaction resulting in fatigue, is about 0.5 cc/mole. This is a rough estimate but it corresponds well with typical values such as the activation volume for carbon diffusion in iron (referred to a hydrostatic stress) which is about 0.5 cc/mole, and the activation volume for alkali metal ion diffusion in silicate glasses (referred to a hydrostatic stress) which is about 4.0 cc/mole.

The fatigue limit for sapphire, S_L/S_N, is estimated as about 0.25 from Fig. 9-9, and utilizing an estimated molar volume of sapphire, V_M, of 25 cc's and an estimated critical crack length, L, of about 2 μ, the surface energy between the unreacted alumina and its corrosion product is calculated as about 50 ergs/cm^2. At this stage of the analysis of the corrosion reaction it is impossible to state whether or not this is even a reasonable value.

One further estimate of interest may be made to illustrate the object of some experiments presently underway. At the beginning of the static fatigue experiments on sapphire a single trial experiment on 10 samples was tried at room temperature in a saturated water

vapor atmosphere at a load corresponding to a S/S_N value equal to 0.48. When the load was applied failure of eight of the samples occurred almost instantly. We estimate the average failure time at one second. In Fig. 9-9 the average failure time for a load corresponding to $S/S_N = 0.48$ at $-35^{\circ}C$ is estimated at about 7 minutes. This data is sufficient to illustrate how a temperature dependence of the fatigue reaction may be made for, on an Arrhenius basis,

$$\log \frac{420}{1} = \frac{A^*}{2.3R}\left(\frac{1}{238} - \frac{1}{298}\right)$$

where A^* is an activation energy and R is the gas constant. The calculated value of A^* is thus equal to about 14 kcals/mole. Such a value is not unreasonable for a low temperature hydration reaction of an oxide.

The foregoing calculations are given primarily to illustrate the type of analysis the author desires to perform when full and complete experimental data on the delayed failure of alumina will have been obtained.

9. CONTRIBUTING PERSONNEL

Contributors to this task of the program include R. J. Charles, J. E. Burke and R. Shaw.

10. REFERENCES

9-1 Roberts, J. P. and Watt, W., "Mechanical Properties of Sintered Alumina", Ceramics and Glass, 10, 53, (1952).

9-2 Wachtman, J. B., Jr. and Maxwell, L. H., "Plastic Deformation of Ceramic-Oxide Single Crystals", J. Am. Cer. Soc. 37 (7), 291-99 (1954).

9-3 Williams, L. S., "Stress-Endurance of Sintered Alumina", Tr. Brit. Ceram. Soc. 35, 287-312 (1956).

9-4 Pearson, S., "Delayed Fracture of Sintered Alumina", Proc. Phys. Soc. (London) 69(B), 1293-96 (1956).

9-5 Brenner, S. S., in process.

9-6 Charles, R. J., "The Strength of Silicate Glasses and Some Crystalline Oxides", pp. 225-249 in Fracture, John Wiley and Sons, New York, (1959).

9-7 Clarke, F. P., private communication.

9-8 Charles, R. J., and Hillig, W. B., "The Kinetics of Glass Failure by Stress Corrosion", Symposium aur la Resistance Mechanique du Verre et les Moyens de l'Ameliorer, Florence, Italy, September, 1961.

9-9 Klassen-Nekhlyudova, M. V., as reported in Oxide Ceramics, E. Ryshkewitch, Academic Press, New York, 1960, p. 155; see also "Dependence of the Strength of Corundum Crystals on Crystallographic Orientation During Testing in Bend and Tension", Physical Properties of Synthetic Corundum, A Symposium, Trudy Inst. Krist. Akad. Nauk U.S.S.R., No. 8, 356 pp. (1953), pp. 215-224 (in Russian).

9-10 Wachtman, J. B., Jr., and Maxwell, L. H., "Plastic Deformation of Ceramic Oxide Single Crystals III", J. Am. Cer. Soc. 40 (11), 377-85 (1957).

TASK 10 - EFFECTS OF THERMAL-MECHANICAL HISTORY ON THE MECHANICAL PROPERTIES OF MAGNESIUM OXIDE CRYSTALS

Principal Investigator: R. J. Stokes
Honeywell Research Center

ABSTRACT

The principal objectives of this study are the determination of the mechanical behavior of ceramic oxide crystals as affected by their prior mechanical and thermal histories. It has been shown that the mechanical strength and ductility of MgO single crystals is determined singularly by the availability and operability of fresh dislocation sources. Such dislocation sources exist in all normally handled "as-received" material, which characteristically yield at a stress of about 10, 000 psi.

"Grown-in" dislocations, however, are locked very strongly; specimens carefully polished chemically to remove all surface sources withstand extremely high stresses without yielding. An anneal at 2000°C further increases the locking of grown-in dislocations.

The strength of as-received crystals sprinkled to introduce fresh dislocations, declines continuously with increasing temperature. However, crystals pre-annealed at 2000°C and sprinkled exhibit a local maximum in strength about 850°C--both as-received and pre-annealed crystals show a change in yield behavior to jerky flow about 600°C.

Mechanical pre-strain at high temperatures softens as-received crystals, but hardens crystals pre-annealed at 2000°C in the temperature range about 600°C.

Etch-pit studies reveal that an annihilation of dislocations by annealing begins above 800°C, confirming the recent findings of other investigators.

TASK 10 - EFFECTS OF THERMAL-MECHANICAL HISTORY

1. INTRODUCTION

The principal objectives of this task is to determine the mechanical and thermal histories. The study is concerned with two distinct areas; first, to compare the mechanical behavior of crystals containing only their grown-in dislocations with crystals containing controlled surface dislocations sources and, second, to determine the effect of heat treatment and past history on both of these extreme situations. Work to date has been concentrated exclusively on MgO crystals.

One of the most interesting properties of ionic solids of the rock salt structure is that under normal testing conditions, "Grown-in" dislocations appear to play no role in their plastic deformation. This was first reported in the etch-pit studies on LiF by Gilman and Johnston[(10-1)], and is true also for MgO. The dislocations which are generally responsible for plastic flow in ionic crystals get forced into the crystal during cleavage and later at points of mechanical contact. Gilman[(10-2)] has shown that the stress intensification factors associated with foreign particles under points of contact raise stresses beyond the theoretical shear strength of the lattice, and thereby inject dislocation loops into the surface of MgO by sprinkling with tiny hard particles of silicon carbide[(10-3)]. A consequence of these observations, established experimentally in the present work, is that there should be a marked increase in the mechanical strength of crystals once all surface dislocation sources have been eliminated. MgO is particularly suited for this kind of study since the crystals are very strong and may be cleaved at room temperature and manipulated carefully by hand without propagating slip dislocations deep into

their bulk. Certainly, surface dislocations are introduced, but they generally penetrate only a few microns and can be easily removed by a chemical polish. It will be shown that the presence of just one or two so-called "fresh" dislocation sources remaining at the surface has a striking effect on the strength, ductility and fracture behavior of magnesium oxide. In this respect mechanical history is a most significant factor.

Under special conditions "grown-in" dislocations can be made to move and initiate slip in LiF[10-2]. The special conditions consist of applying a high stress pulse to crystals which have been annealed between 300-400°C and quenched as quickly as possible. It is considered that the heat treatment evaporates impurities associated with "grown-in" dislocations and makes these dislocations effectively "fresh" and relatively easy to move under a high stress. Recent transmission electron micrographs have indicated that "grown-in" dislocations in magnesium oxide are likewise invariably associated with tiny precipitate particles strung along their length[10-4, 10-5]. May and Kronberg[10-6], following a study of the effects of heat treatment on the strength of magnesium oxide, concluded that softening by annealing and quenching was due to the the evaporation of impurities from the dislocations. In this respect thermal history may be an important factor in determining the mechanical behavior of magnesium oxide. However, before the true effect of heat treatment can be studied, it is necessary to eliminate any error due to variation in surface dislocation density. For this reason we have standardized two surface conditions and studied the effect of heat treatment on both (a) crystals polished and handled so carefully that only "grown-in" dislocations remain, and (b) crystals sprinkled with silicon carbide and pre-loaded at room temperature to introduce a high density of fresh surface dislocations.

Finally, we have considered other ways by which "grown-in" dislocations may become unlocked to provide sources for slip. One of these is currently under study and concerns the application of a fluctuating rather than a static stress to the crystal.

All of these studies have been conducted in terms of the stress-strain relationship under tension and bending, the etching behavior of individual dislocations and the fracture mechanism. It will be shown that the mechanical behavior following different mechanical and thermal histories can always be correlated with the density and distribution of available dislocation sources.

2. EXPERIMENTAL PROCEDURE

The essential feature of the experimental procedure was extreme care in handling during all phases of preparation to avoid the introduction of uncontrolled "fresh" dislocations. Tests to determine the mechanical properties of crystals containing grown-in dislocations only were conducted both under 3-point loading and simple tension in the Instron machine (loading rate generally .002 in. per min).

For the bending tests, single crystal beams were cleaved to the appropriate dimensions (1/4 in. x 1/8 in. x 1 in.) and chemically polished until no surface dislocations remained. This was determined by etching the polished crystals and examining them thoroughly for the sharp etch pits characteristic of "fresh" dislocations (see later). When satisfactory they were given a further final polish before testing. Unfortunately these tests suffered a limitation in that the crystals were generally so strong that crushing at the upper load point caused them to shatter prematurely. To overcome this limitation it was necessary to use a method of loading

which avoided contact in the gauge length. Four-point loading and simple compression offered no advantage, the only straight forward method available was simple tension.

A number of successful tension tests were performed on crystals into which reduced gauge sections, typically 3/8 in. long and .05 in. square, were machined either by ultrasonic or chemical reduction techniques. Chemical reduction was achieved by coating the grip ends of a specimen with a resistive plastic and immersing it in boiling acid for about 30 minutes. Following either method of reduction it was necessary to polish the whole crystal for a further 30 minutes to ensure the complete removal of surface dislocations. The crystals were mounted carefully in split grips with a single component thermal setting epoxy (Fullers Resiweld No. 105). This particular epoxy was very satisfactory: it was easy to apply, it wetted both magnesium oxide and steel and provided a very strong bond. The stress distribution during loading was assessed with stress birefringence techniques and was remarkably uniform throughout the gauge length.

The effect of heat treatment was studied only under bending. There were three types of tests. In the first, chemically polished crystals were annealed for 1/2 hr at various temperatures up to 2000°C and fast or slow cooled. Those maintained at 600°C, 800°C, 1000°C and 1200°C were fast cooled by removal from the air furnace, those at 1500°C and 2000°C were fast cooled in the helium atmosphere of a carbon furnace by switching the power off and increasing the gas flow rate. All specimens reached room temperature in 10-15 min.

In the second type of test, crystals were given a preliminary anneal at 2000°C for 1/2 hr, then sprinkled at room temperature, with silicon carbide and loaded until macroscopic yielding could just be detected. This introduced short slip band segments of "fresh"

dislocations into the crystal[10-3]. Crystals prestrained in this fashion were annealed at various temperatures for different behavior and dislocation density. The reason for the 2000°C preliminary anneal was two-fold; first it standardized the starting condition and second, it provided a clear background against which etching studies could be conducted with greater resolution (see later).

In the third type of test, crystals were sprinkled and preloaded at room temperature and then the deformation was continued at a higher temperature. Temperatures up to 1000°C could be reached with a small furnace placed around the specimen in the Instron. The specimen can slowly up to temperature and was allowed 1/4 hour at temperature to achieve equilibrium before loading. After a small amount of strain at the high temperature the test was recontinued later at room temperature.

A few tests have been conducted under fluctuating stress. To date these have been half cycle, i.e., tension-unload, and have been performed on conventional tension type specimens in the Instron.

In an attempt to understand the effects of heat treatment and restressing on the behavior of individual slip dislocations and slip bands, considerable use was made of etch pit techniques. There were many alternative procedures each giving a different type of information, dependent upon the stage selected for etching and whether an intermediate polish was used to erase old etch pits. For example, comparing an etched surface before and after annealing with or without an intermediate polish provided information on the effect of the anneal. Comparison could be made photographically or by cleaving a crystal in two and retaining one-half for reference. Similarly, etching before and after the final loading was used to identify the reactivated dislocation sources which contributed to the subsequent deformation.

During all annealing, polishing, handling and etching treatments, it was essential to support the specimens at their ends only, otherwise mechanical contact within the gauge length led to completely erroneous and non-reproducible observations.

3. THE STRENGTH OF CRYSTALS CONTAINING "GROWN-IN" DISLOCATIONS

A. Tension Tests

Tests were conducted on carefully polished crystals under both bending and simple tension. For convenience the tension tests will be described first. They are summarized in Fig. 10-1 and Table 10-I where the quoted stresses are absolute tensile stress, not resolved shear stress*. Table 10-I includes data on the specimen size, maximum stress supported and mode of deformation and fracture.

In all cases (excluding specimens 10 and 11) the specimens behaved absolutely elastically up to their maximum stress, the value of which could be extremely high. Under polarized illumination the gauge length of the crystals changed uniformly and gradually through the color spectrum as the stress birefringence increased. The highest stress value was measured on the bicrystal specimen, 109,000 psi. This particular specimen pulled out of the grips without yielding so probably an even higher value was possible. Five of the single crystal specimens (No.'s 2, 3, 4, 5 and 6) pulled out of the grips prematurely. It was found that their gauge length returned to complete extinction under crossed polaroids, indicative of zero residual stress and, therefore, elastic behavior under load.

* No significance should be attached to the modulus of the curves in the elastic region since the slope is purely arbitrary.

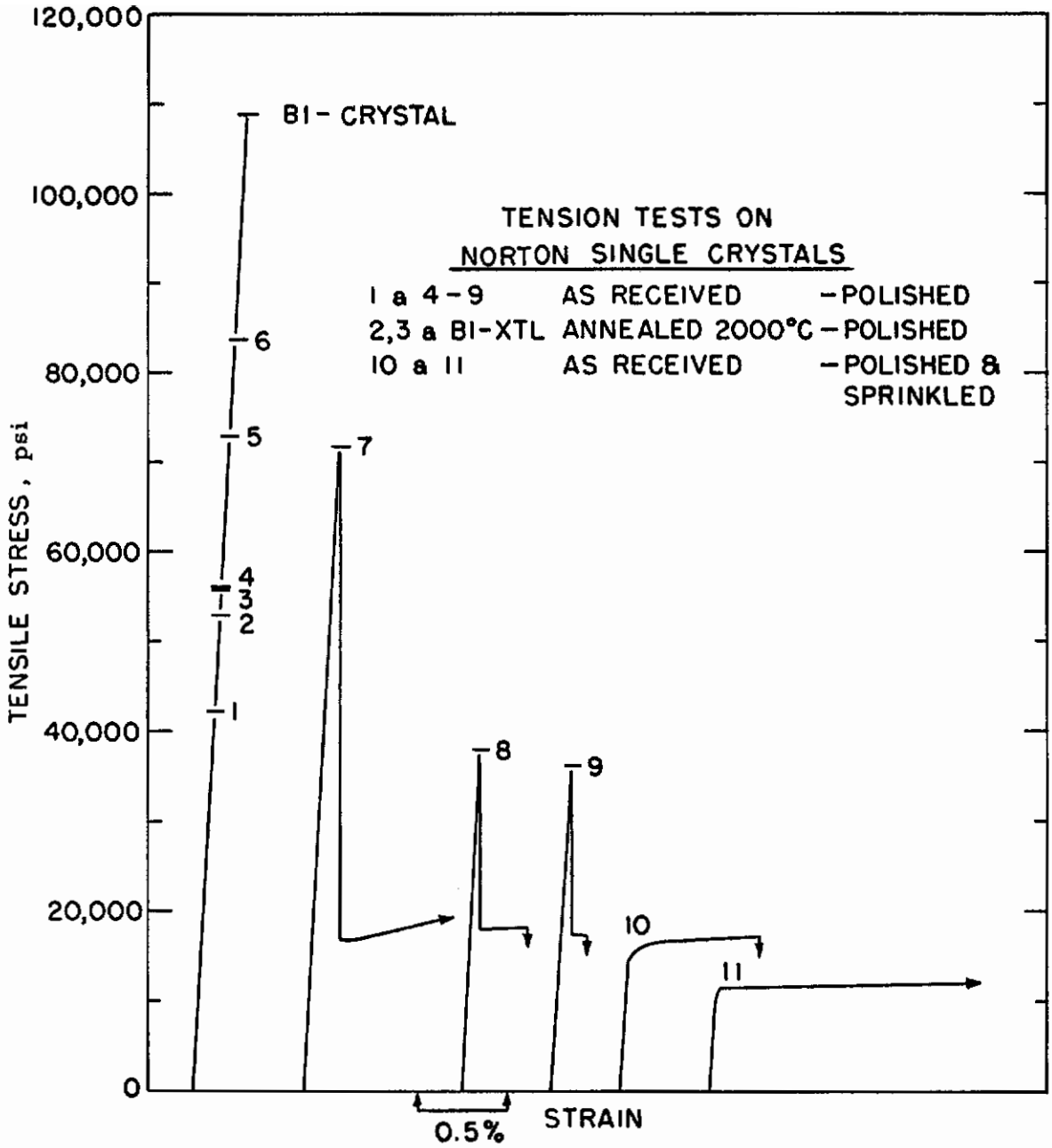

Figure 10-1 TENSILE PROPERTIES OF POLISHED MAGNESIUM OXIDE CRYSTALS.

Table 10-I

TREATMENT AND MECHANICAL BEHAVIOR OF MgO SINGLE CRYSTALS

Specimen No.	Cross-Sectional Area, (sq. in.)	Maximum Stress,(psi)	Mechanical Behavior
1	0.00625	42,300	Filled with slip. Fracture at slip intersection.
2**	0.00305	53,000	No slip. Pulled out of grips at 53,000 psi.
3**	0.0046	55,950	Do. at 55,590 psi.
4	0.00455	56,000	No slip. Fracture at surface flaw.
5*	0.00135	72,800	No slip. Pulled out of grips at 72,800 psi.
6*	0.0012	83,700	Do. at 83,700 psi.
7*	0.00175	71,700	Filled with slip. Yield at 16,700 psi. Fracture at slip intersection.
8	0.0046	37,950	Do. Yielded at 17,800 psi.
9	0.0040	36,260	Do. Yielded at 17,400 psi.
10	0.0045	17,500	Slip in crystal before test. Yielded. Fracture at slip intersection.
11	0.005	11,000	Slip sources introduced deliberately. Yielded. Fracture at slip intersection.
Bicrystal*	0.0018	109,000	No slip. Pulled out of grips at 109,000 psi.

*Chemically reduced gauge section.

**Annealed at 2000°C for 1/2 hr before test, slow cool.

Specimens 1, 7, 8, and 9 behaved elastically up to their maximum stress at which level they suddenly filled with a burst of slip on a number of intersecting planes. This was accompanied by a large stress drop. Specimen 1 fractured instantaneously due to slip band interaction and appeared completely brittle while the other three continued to deform plastically at a stress level of approximately 17, 500 psi. Specimens 8 and 9 fractured due to slip band intersection to leave the characteristic "line" source of fracture and specimen 7 was unloaded before fracture occurred.

It was impossible to determine exactly where slip originated in these four specimens. At first it was considered that the slip (as revealed by etching) started in the gripped area, where inevitable there was mechanical contact, and then ran down the gauge length. While this may or may not have been so for some specimens, in the case of specimen 9 the slip was confined entirely within the gauge length and must have originated there. It can be argued that the single source responsible for initiating slip (it would have been extremely coincidental if more than one was involved at the yield point) was a "grown-in" dislocation since, had it been a "fresh" dislocation, the curve would have been smooth and essentially similiar to that for specimen 11 as has been described elsewhere[10-7].

For comparison, specimens 10 and 11 illustrate the mechanical behavior of crystals containing fresh surface dislocations. Specimen 10 contained a few sources introduced by accident just before the test. It yielded smoothly at 15, 000 psi before it too fractured at a slip band intersection. Specimen 11 was deliberately sprinkled after polishing to introduce a high density of surface dislocations. It yielded smoothly at 11, 000 psi and was very ductile (hence the horizontal arrow in Fig. 10-1) in agreement with earlier observations on the tensile behavior on magnesia crystals[10-7].

Polishing a crystal so thoroughly that all fresh dislocation sources were eliminated therefore served to raise the strength considerably and change the yielding behavior. The obvious interpretation was that the "grown-in" dislocations were strongly locked either because of the impurity precipitate particles strung along their length or because they possessed the wrong Burgers vector to initiate glide on the $\langle 110 \rangle \{110\}$ system. There was apparently a considerable fluctuation in the stress required to unlock them since some crystals remained elastic up to 80, 000 psi and above, while others yielded at 36, 000 psi. This fluctuation may be due to the amount of impurity or the thermal history of the individual specimens. For the most part the crystals were received from the Norton Company and their thermal history and purity was unknown. Only three tension specimens (No. 's 2, 3 and the bicrystal) were given a heat treatment, this consisted of a 1/2-hr anneal at 2000°C followed by a relatively slow cool, taking a further 1-hr to reach room temperature. Significantly all three specimens deformed completely elastically. Whether a quench from the same temperature to isolate the dislocations from the impurity particles would result in a different behavior was not determined. However, bend tests to be described later indicated no difference.

It will be noted in Table 10-I that the four specimens to attain the highest strength, No. 's 5, 6, 7 and the bicrystal, were also the ones of smaller cross-section. The only significance attached to this observation was that it was a consequence of the statistical distribution of "grown-in" dislocations which could become active under stress; the smaller the stressed volume, the less the chance that slip would nucleate.

There was another important observation concerning the distribution of slip in carefully polished crystals as they yielded. Immediately after the yield drop, slip was found to have occurred in widely

spaced bands on intersecting planes all along the gauge length. Since slip originates at a single source, it was interesting to inquire how it could spread to form the systems observed at fracture. It should be remembered that when slip nucleated from a single fresh source, yielding occurred smoothly and the source gave rise to a single slip band which merely continued to get wider by the double cross-slip mechanism[10-8] at its edge[10-7]. The difference between these two situations must be ascribed to the stress level at which the single source began to operate. In the case of grown-in dislocations the stress level was very high: it is proposed that the initial burst of dislocations moved with such a high velocity that the concentrated stress pulse associated with them was able to trigger off other grown-in sources. Evidence that this could occur was obtained indirectly and is illustrated in Fig. 10-2 on a specimen undergoing bending; it can be seen that a slip band initiated slip on orthogonal systems at points where it intersected the grown-in substructure. No corresponding evidence could be obtained on the tension specimens; in general, the slip bands were too far developed to be able to determine their origin.

B. Bend Tests

The elimination of surface dislocations by polishing resulted in a very striking change in the fracture behavior of crystals undergoing bending as compared to those subjected to tension. The reason for this was that fresh dislocations were reintroduced along the line of contact with the central loading point on the beams, so that dislocations were able to move quite easily on the compression surface to promote local plastic deformation. The slip distribution then took the form shown in Fig. 10-3(a). Under load the neutral axis, as observed under polarized light, became further and further

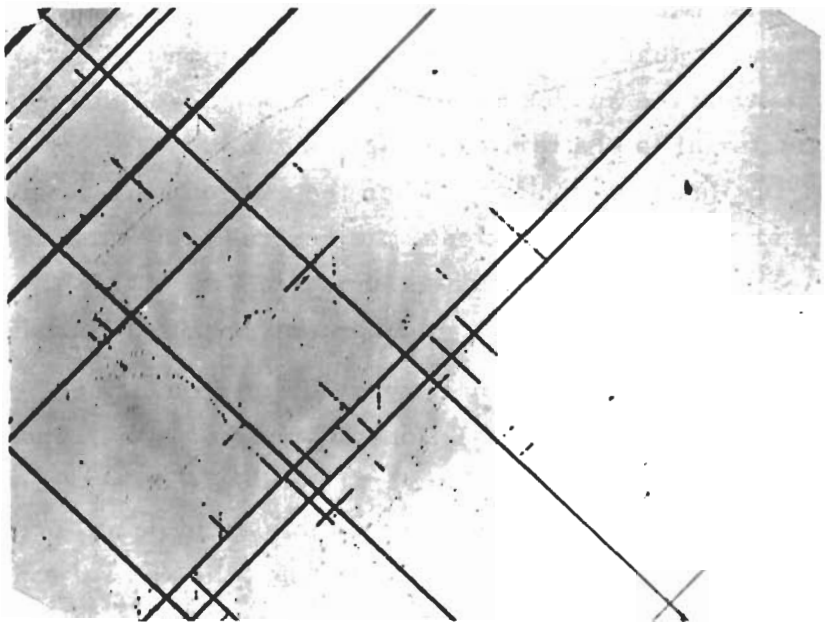

Fig. 10-2 NUCLEATION SLIP ON INTERSECTING SYSTEMS BY A PASSING SLIP BAND FOR SPECIMENS SUBJECTED TO TENSION (X75)

(Note slip origination where the passing slip band cuts across the substructure).

depressed toward the tension surface until, at a high stress, crushing occurred under the central load point and cracks started to propagate across the cross-section. Piecing the fragments together, it appeared that the bottom strain free region had burst out of the crystal and the sudden stress relaxation caused the remainder of the material to shatter. This action can be seen just starting in Fig. 10-3(a). By contrast, when the tension surface contained a number of fresh dislocations, the neutral axis remained along the center of the cross-section as shown in Fig. 10-3(b); fracture then eventually occurred by the mechanisms outlined elsewhere[10-7].

The stress-deflection curves obtained under such conditions were rather meaningless. Nonetheless they are included in Fig. 10-4 for the illustration of several points. The stress quoted in these curves was calculated from the elastic beam formula $\sigma = Mc/I$; this is obviously inaccurate when the neutral axis displaced and is provided only a means for comparison.

First, it will be noted that many of the curves showed an apparent plasticity before fracture. It is now known that this was due to deformation in the compression surface. Specimens 1 through 5, 9 and 10 all shattered in the manner described above and in this respect may be regarded as having deformed elastically up to the maximum stress similar to specimens 1 through 6 in Fig. 10-1. Specimens 6, 7 and 8 suddenly yielded when slip burst into the tension region and containued deforming at a lower stress similar to specimens 7, 8 and 9 in Fig. 10-1. Specimen 11 was sprinkled to introduce a high density of surface slip sources and showed a more conventional stress-deflection curve.

Fig. 10-4 also compares the behavior under bending of a number of polished crystals which have been subjected to different thermal histories. Within the accuracy of the technique it could be concluded that there was no difference between a fast (within 15 min)

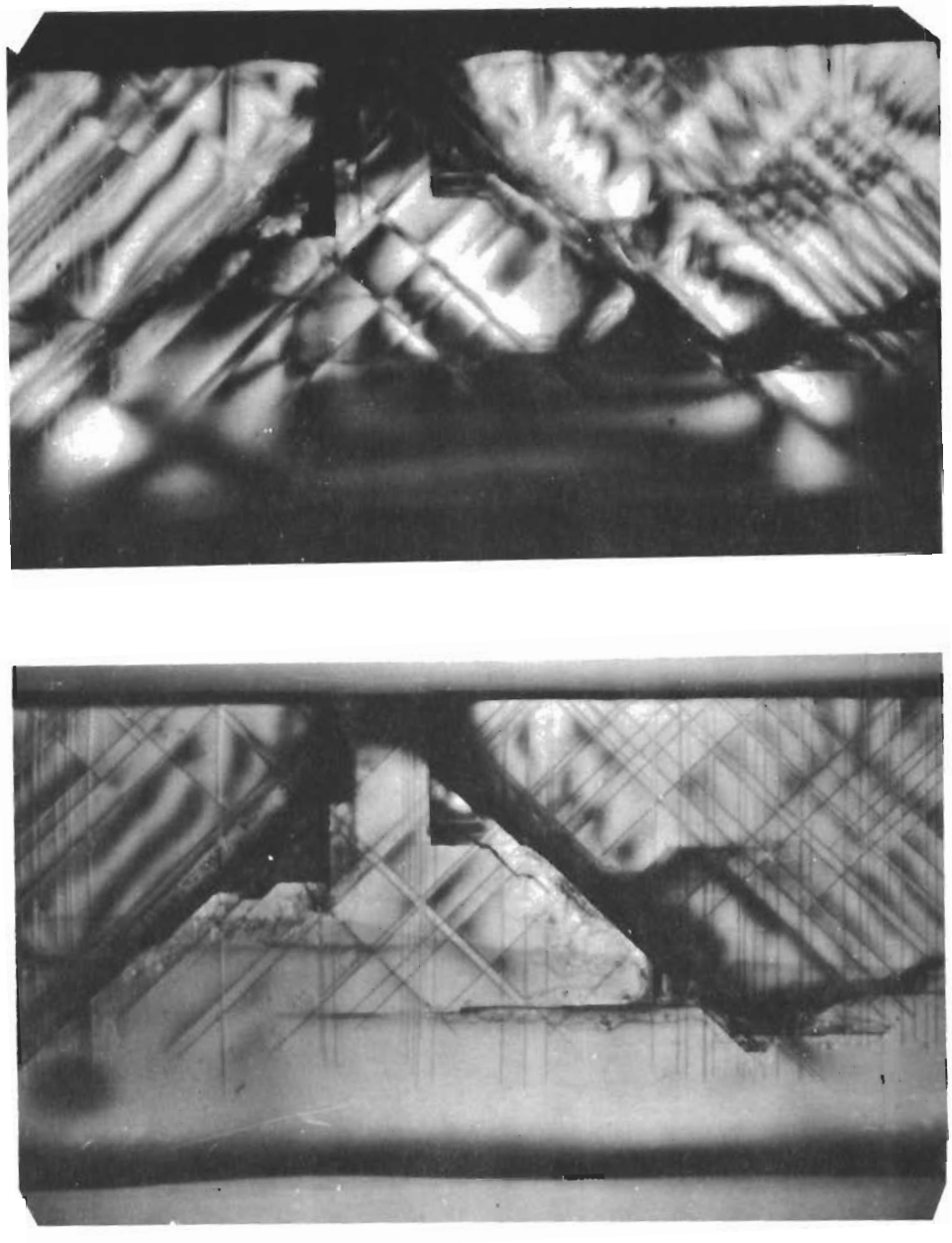

Fig. 10-3(a) SLIP DISTRIBUTION IN A POLISHED MgO CRYSTAL UNDER BENDING (X10)

Upper: Polarized Illumination Lower: Etched, Normal Illumination
(Note the horizontal crack just starting to run.)

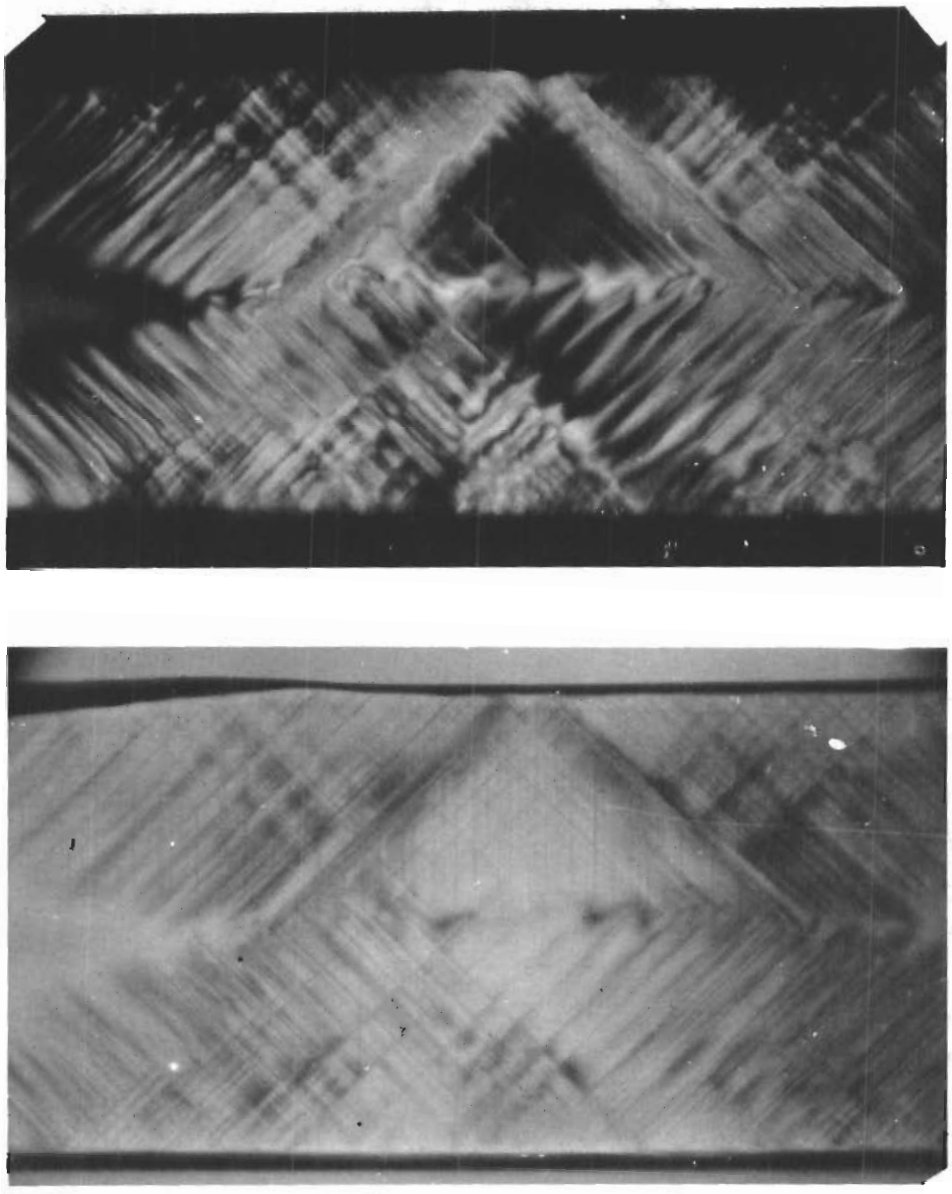

Fig. 10-3(b) SLIP DISTRIBUTION IN A POLISHED AND SPRINKED MgO CRYSTAL UNDER BENDING (X10)

Upper: Polarized Illumination Lower: Etched, Normal Illumination

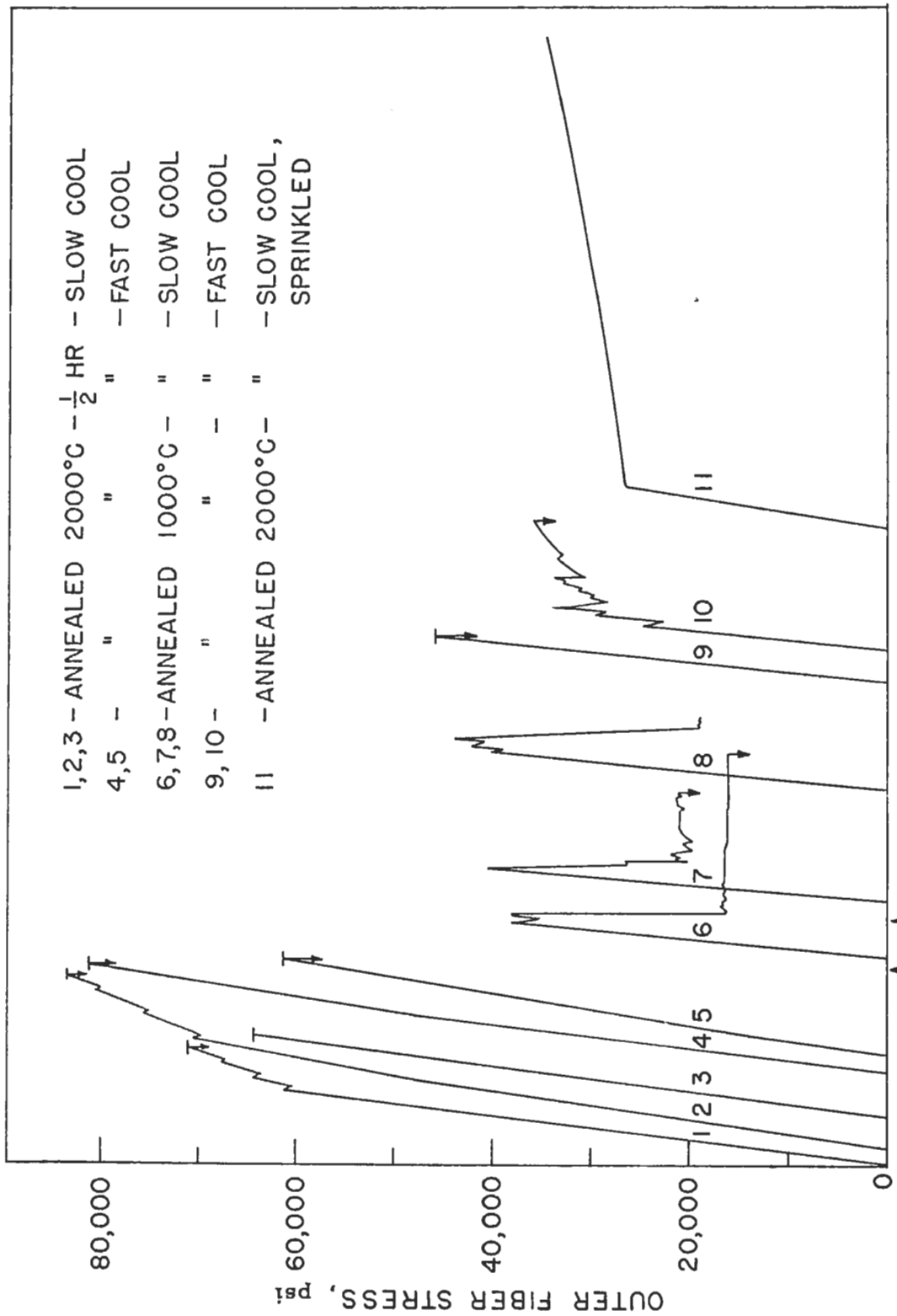

Fig. 10-4 BEND TESTS ON CAREFULLY POLISHED MAGNESIUM OXIDE CRYSTALS

and a slow (1 hr) cooling rate from 2000°C. On the other hand, fast cooling (within 2 min) from 1000°C gave curves different in form to those obtained by slow cooling (1 hr) from 1000°C. An explanation for these differences in terms of the locking of "grown-in" dislocations by impurities is not available at the moment.

C. Etch Pit Studies

Studies were made to determine the effect of heat treatment on the resulting microstructures, as revealed by etching. While there were quite distinct changes they could not be related simply to the mechanical behavior. They require a more detailed analysis in the future.

On etching magnesium oxide it was possible to distinguish between fresh dislocations, aged dislocations and "non-linear" defects. Fresh dislocations gave deep sharp conical pits of uniform size aligned in rows parallel with [100] or [110] directions, whereas aged dislocations were not so readily attached and left relatively smaller pits of varying sizes. Non-linear defects, which would include vacancy clusters, precipitate particles, etc., left shallow flat-bottomed pits.

Fig. 10-5 compares the microstructure following an anneal of companion Norton crystals at (a) 2000°C and (b) 1000°C. These were typical and could be developed essentially independent of the cooling rate from the respective temperatures. In Fig. 10-5(a) the only pits to be seen were those due to aged dislocations located in small angle boundaries, and a few isolated dislocations within the substructure against an exceptionally clear background. By contrast when the same starting material was annealed at 1000°C, (Fig. 10-5(b), the region between the small angle boundaries

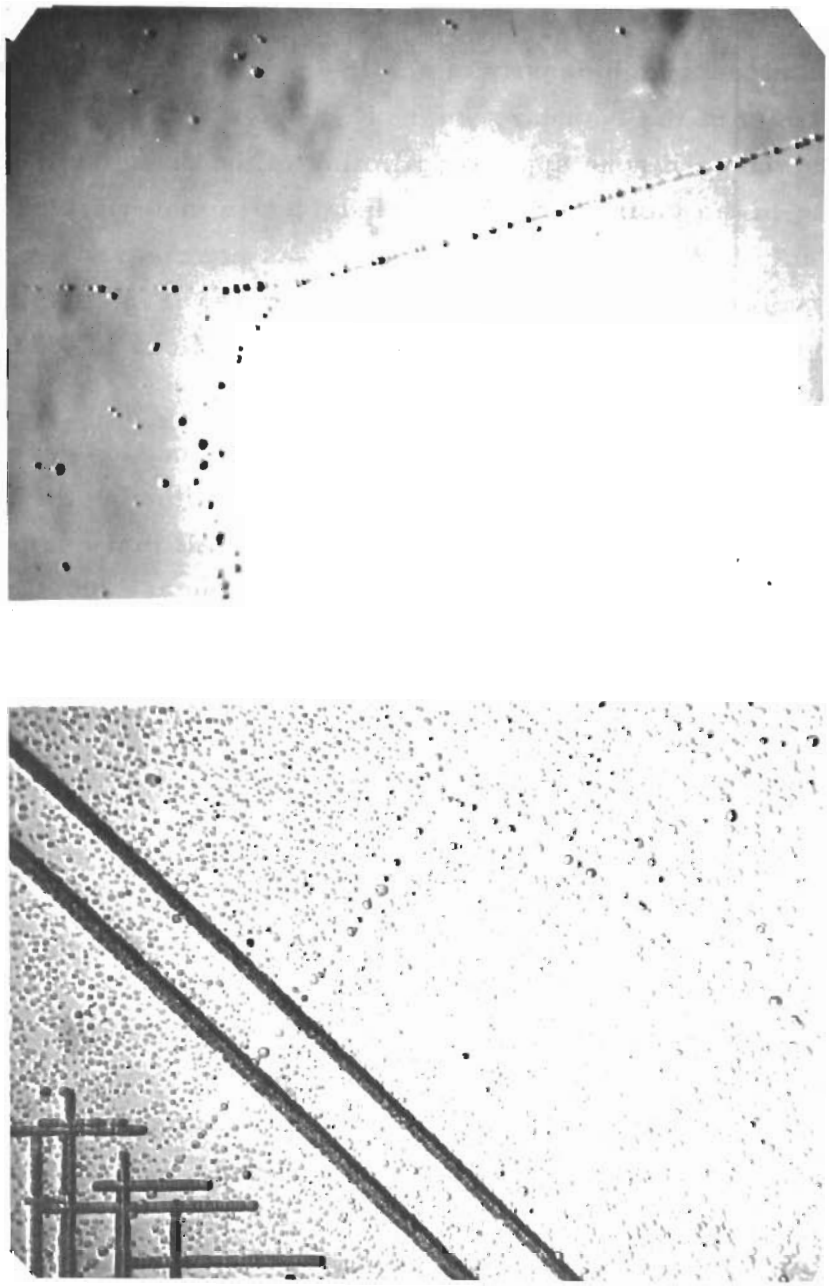

Fig. 10-5 APPEARANCE AND DISTRIBUTION OF ETCH PITS ON MAGNESIUM OXIDE (X250)

(a) Following a 1/2-hour anneal at 2000°C
(b) Following a 1-hour anneal at 1000°C

Note fresh dislocations at bottom left-hand corner of (b).

contained a high density of shallow pits except in the immediate vicinity of the boundary where there was a marked "denuded zone". The denuded zone appeared similar to the distribution of precipitate in the vicinity of grain boundaries in materials undergoing a precipitation reaction, although it was not clear why the microstructure was independent of cooling rate. Fig. 10-5(b) also includes some etch pits due to fresh dislocations in the bottom left-hand corner for comparison.

Etching crystals in the as-received condition generally led to a microstructure similar to Fig. 10-5(b) although the background density of shallow pits was not so high. All that can be concluded with certainty at this time is that annealing at 2000°C tends to clear up the background, presumably because the precipitating species was taken back into solution.

4. EFFECT OF HEAT TREATMENT ON PRE-STRAINED CRYSTALS

A. Bend Tests at Room Temperature

Tests to study the effects of heat treatment on prestrained crystals have been conducted under bending only. For the purposes of comparison the majority of tests have been run on specimens cleaved from the same large parent block. The specimens were annealed first at 2000°C for 1/2 hr with a fast cool, chemically polished and sprinkled with 325-mesh silicon carbide particles. They were then preloaded with a slight moment at room temperature, and annealed at various temperatures for different times. Next, they were reloaded at room temperature to determine the change in strength, fracture behavior and dislocation density. Typical results following a 1-hr anneal at various temperatures are included in Fig. 10-6 and 10-7. In Fig. 10-6 the flow stress ratio σ_2/σ_1 is plotted as a function of the annealing

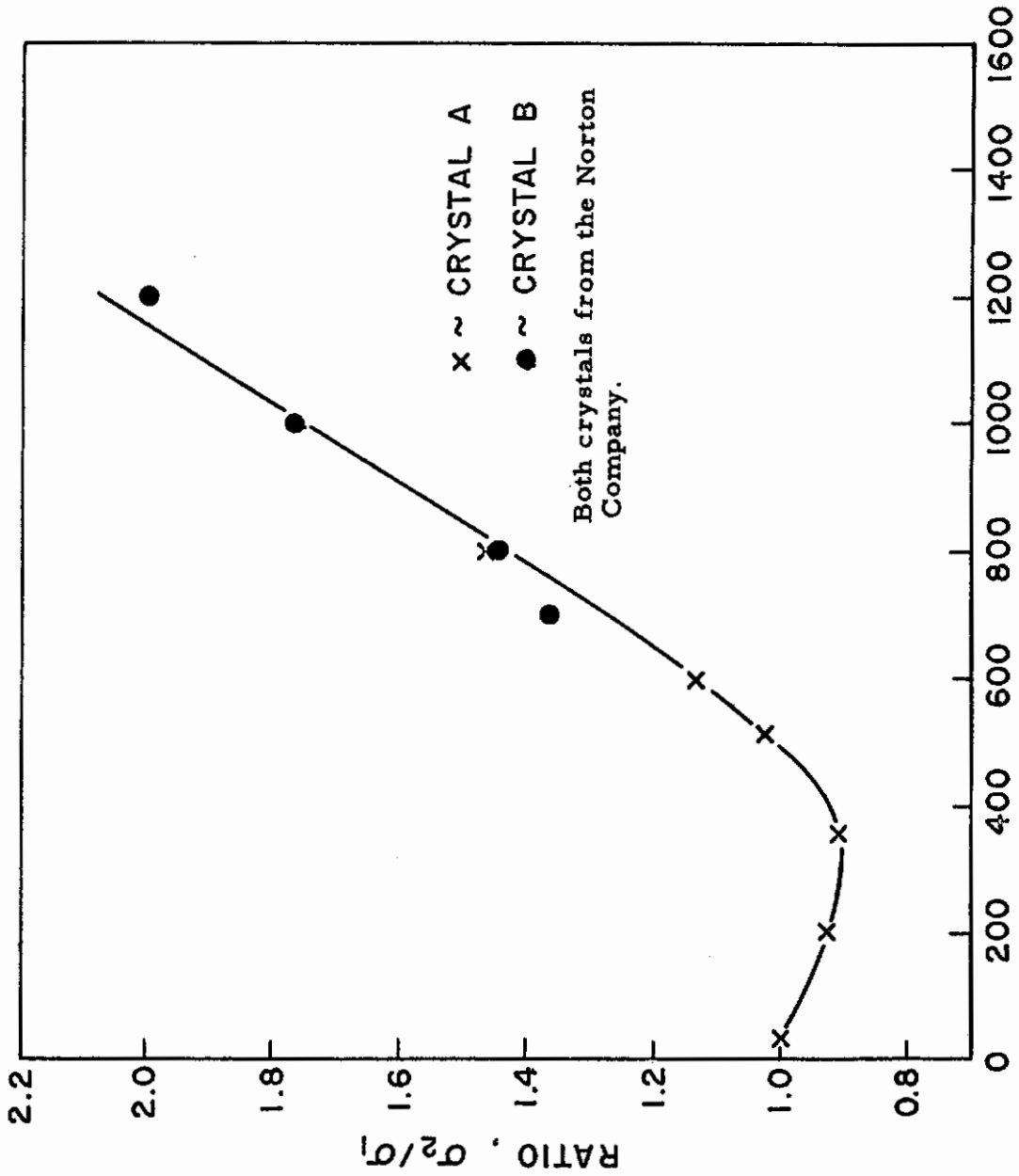

Fig. 10-6 EFFECT OF A 1-HR ANNEAL ON THE FLOW STRESS FOR SPRINKLED MgO CRYSTALS

σ_2 = Flow Stress After Anneal

σ_1 = Original Flow Stress

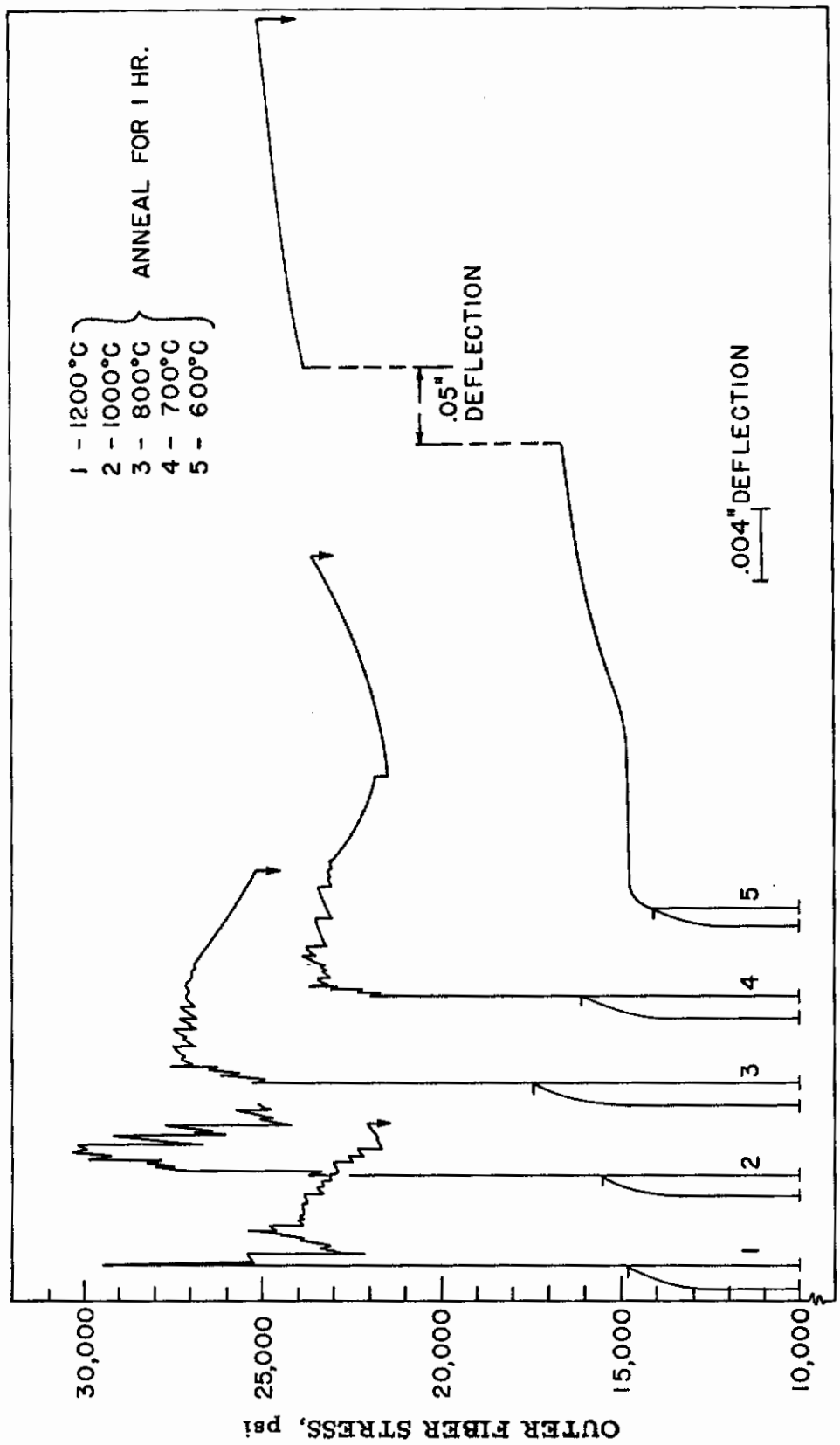

Figure 10-7 STRESS DEFLECTION CURVES FOR SPRINKLED MgO CRYSTALS BEFORE AND AFTER A ONE HOUR ANNEAL. CRYSTAL B.

temperature; σ_1 was the stress level at which preloading stopped and σ_2 was the stress level at which the first indication of renewed slip was observed in the tension region after the anneal. It should be noted that the value used for σ_2 was generally less than the stress required to promote macroscopic yielding. As Fig. 10-6 shows, the yield strength decreased slightly following an anneal at temperatures up to about 500°C. Above 600°C, the hardening was increasingly effective until at 1200°C the strength could be approximately doubled by annealing. Annealing for one hour (or even half an hour) at 1500°C or 2000°C raised the yield strength so high that slip could not be reactivated before the specimen fractured by crushing from the compression side as described in Section 3B.

Typical stress-deflection curves following a 1-hr anneal at 600, 700, 800, 1000 and 1200°C are included in Fig. 10-7. The preload stress level and deflection are included to the left of each curve. There were a number of interesting points:

(1) The curve following the 600°C anneal was significantly different from the others. There was virtually no strengthening, the curve was smooth and the ductility considerable. In addition, the complex fracture behavior and high slip band density were characteristic of magnesia crystals which had been sprinkled but not annealed at all[10-7]. Similar observations were made on crystals annealed at 200, 350, and 500°C and at 600°C for periods up to 16 hours.

(2) As the annealing temperature was raised above 600°C, the strength increased markedly, but the curves became jerky and the ductility decreased. After 1 hr at 700°C the curve levelled out and the specimen underwent hardening before fracture after considerable ductility. At 800°C the curve likewise became smoother but never levelled out. At 1000°C and 1200°C the yield drops were much more pronounced and the specimens were quite brittle. In all cases the specimens fractured from a characteristic line source due to slip band intersection[10-7, 10-9].

By varying the time of anneal at the different temperatures it was possible to get an over-all picture of the rate at which strengthening occurred. Rather than reproduce the curves in detail (the pattern was always the same as in Fig. 10-7) only the change in the flow stress ratio σ_2/σ_1, will be reported here. The ratios are plotted in Fig. 10-8 as a function of annealing time. It will be noted that the curves for 700, 800 and 1000°C could be grouped together and tended to level out at a value of 1.6. The curve for 600°C was lower and levelled out at 1.25. By contrast the curve for 1200°C was distinctly steeper and higher. In fact, after 2 hr, at 1200°C the slip in the tension region could not be reactivated even though the stress reached a value 2.5 times σ_1. Instead, the specimen fractured by crushing from the compression side as described earlier. This imposed a fundamental limit on this aspect of the study.

In all of the tests reported in this section the gauge length was viewed through the polarizing microscope during the final loading. It was confirmed that each of the yield drops contributing to the jerkiness on the curve corresponding with a burst of slip generally in the tension region of the crystal. A similar correlation was made with the slip band density determined by etch pit techniques. The number of yield drops corresponded exactly with the number of slip bands which could be seen to have reactivated under stress.

From these observations, it is possible to draw some general conclusions concerning the mechanical behavior of annealed prestrained crystals. First it is concluded that an anneal at 500°C or 600°C has only a minor effect on the stress required to move dislocations; the sources are easily reactivated, and their high density leads to smooth yielding. At 700°C the dislocations become more strongly locked and can be reactivated only one by one until the density of active sources is again high enough to produce a smooth stress deflection curve. At higher temperatures the locking is stronger and leads to sharp yield drops.

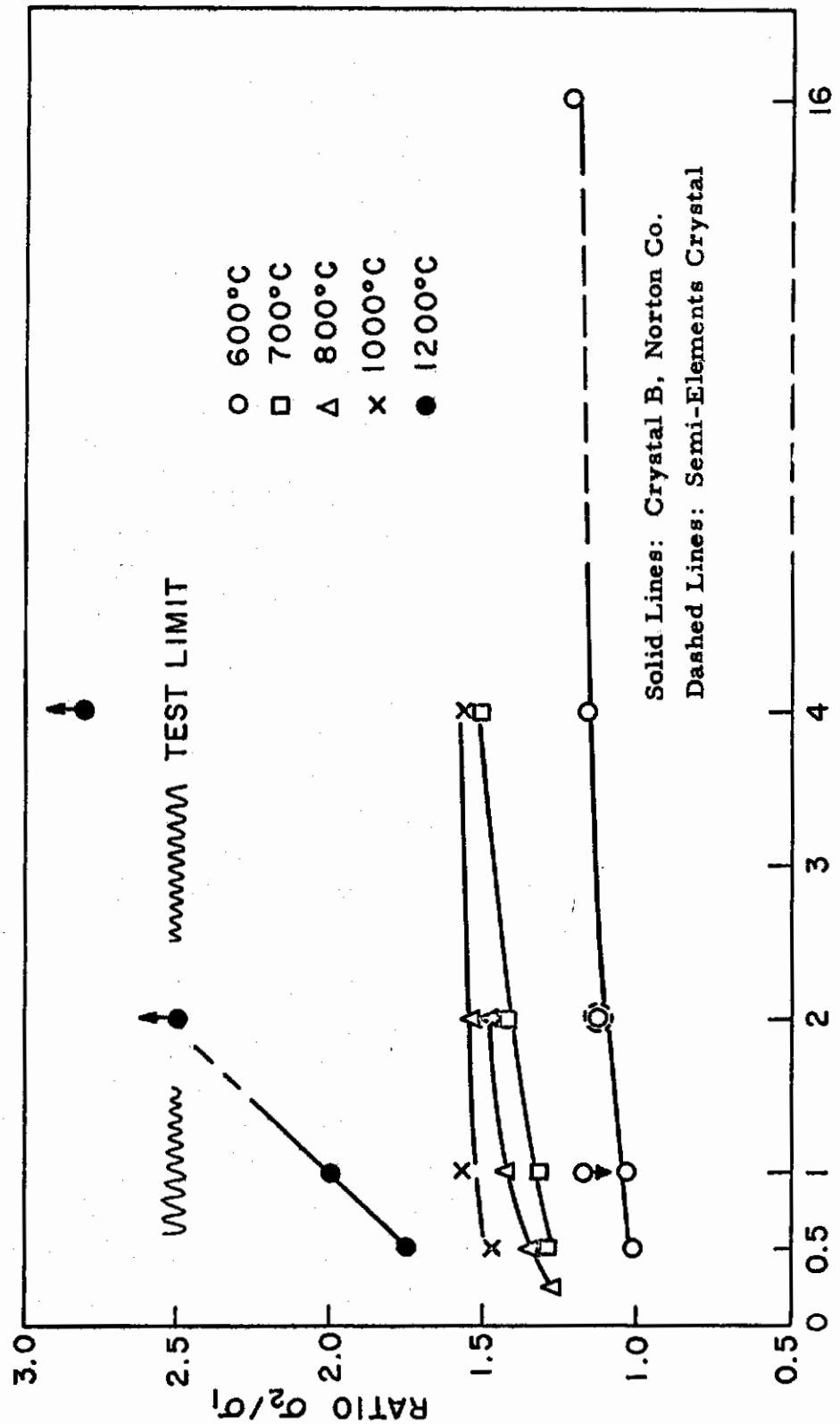

Figure 10-8 EFFECT OF HEAT TREATMENT ON THE FLOW STRESS RATIO FOR SPRINKLED MgO CRYSTALS.

It is important to note that the strengthening arises from dislocation locking and not from a change in microstructure for if a prestrained and annealed crystal was sprinkled to reintroduce fresh sources, then it became as soft and as ductile as before the anneal.

B. Bend Tests at High Temperatures

Again for the purposes of comparison the majority of tests have been run on a large number of crystals cleaved from the same block. In one series of tests specimens cleaved from a Norton Company single crystal were annealed first at 2000°C for 1/2 hr with a fast cool, while in another series, a Semi-Elements crystal was tested both as-received and after an anneal at 2000°C. The specimens were carefully polished, sprinkled with 325-mesh silicon carbide particles and preloaded at room temperature. The purpose of the preloading was to fill the tension region with fresh slip dislocations and also to measure the stress level σ_1 at which room temperature slip was occurring. Loading was continued at the high temperature for a period long enough to establish its yielding behavior; finally the test was completed at room temperature. A typical loading sequence of this nature is illustrated in Fig. 10-9.

As the test temperature was increased there was a marked change in yielding behavior. For the crystals pre-annealed at 2000°C (chiefly Norton Company) the stress deflection curves were smooth at test temperatures up to 400°C with a noticeable work hardening. At 500°C the plastic region of the curve was flat and smooth, and showed no work hardening. At 600°C the curve was also flat but very jerky. Above 700°C there was a large yield drop followed by considerable jerkiness as illustrated in Fig. 10-9(b) at 850°C. Essentially similar observations were

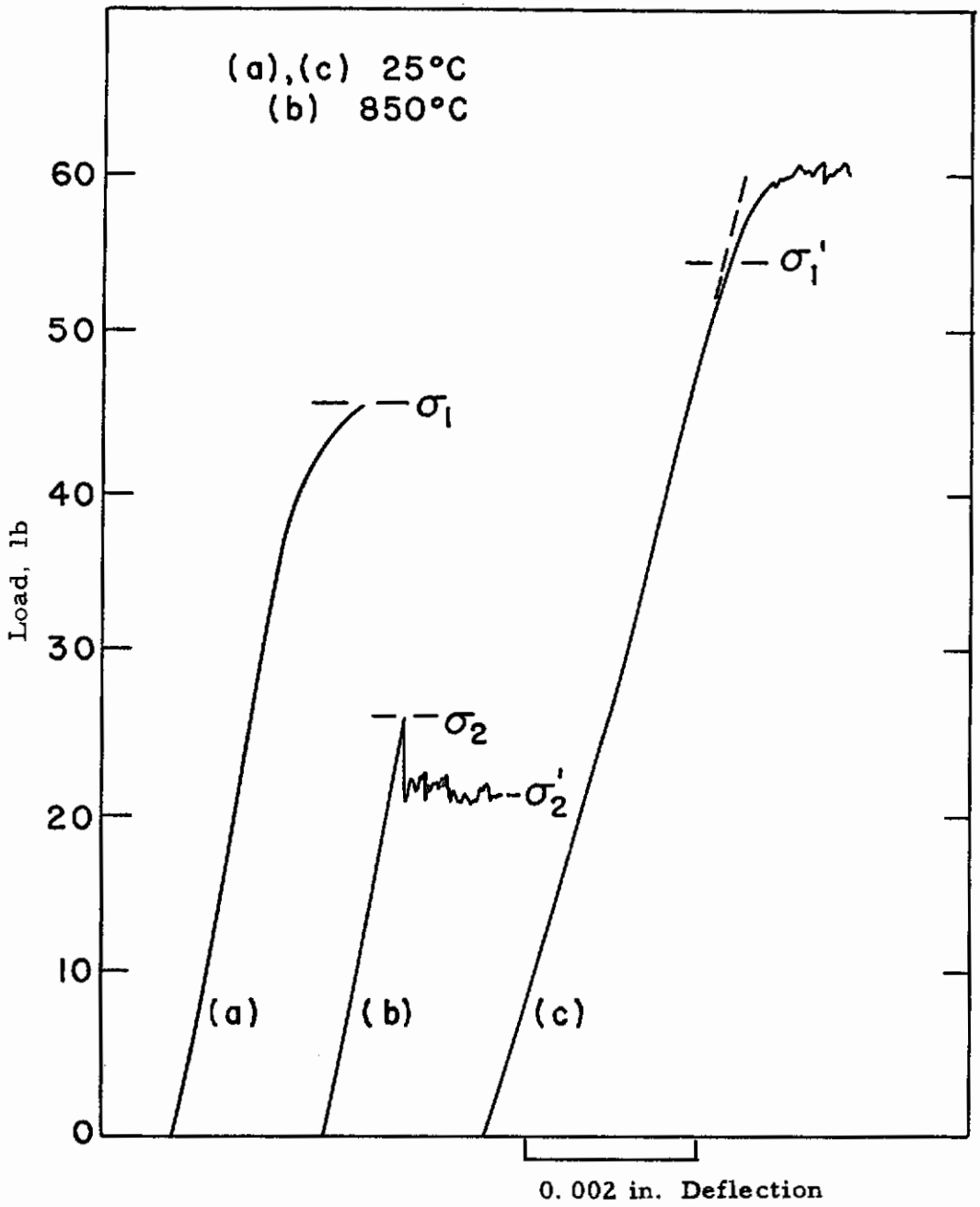

Figure 10-9 TYPICAL SEQUENCE OF BEND TESTS TO DETERMINE HIGH TEMPERATURE MECHANICAL BEHAVIOR.
MgO Crystals Preannealed at 2000°C

made on the (Semi-Elements) crystals except that the transition to jerky flow occurred 100°C higher. It was important to note that the transition in high temperature yielding behavior occurred between 500°C and 600°C, precisely the same temperature range wherein annealing started to produce an increase in room temperature strength as shown in Fig. 10-6.

The effect of temperature on the strength of MgO single crystals could be illustrated best by plotting the ratio of the flow stress at the high temperature (σ_1) to the flow stress at room temperature (σ_1) as a function of temperature. The use of the flow stress ratio, σ_2/σ_1 normalized the results and eliminated any variation in yield strength from specimen to specimen. As Fig. 10-9 shows, a different value of σ_2/σ_1 could be obtained depending upon whether the temperature was increased or decreased. These ratios are plotted in Figs. 10-10 and 10-11 for the Norton and Semi-Elements crystals respectively. Several interesting deductions can be drawn from an examination of these figures, as follows:

For increasing temperatures, the flow stress ratio passes through a minimum at approximately 500°C and a maximum at 850° C when both Norton and Semi-Elements crystals were given a preliminary anneal at 2000°C. The curve from Fig. 10-10 is replotted in Fig. 10-11 to show that the three points obtained on annealed Semi-Elements crystals lie right on the same curve. It was interesting to note that crystals tested under these conditions were equally as strong at 850°C as they were at 200°C.

The strength of as-received crystals decreased continuously with temperature. Comparing both temperature increase ratio curves in Fig. 10-11 it can be seen that as-received crystals were relatively stronger at temperatures up to 600°C, but above 600°C pre-annealed crystals were superior.

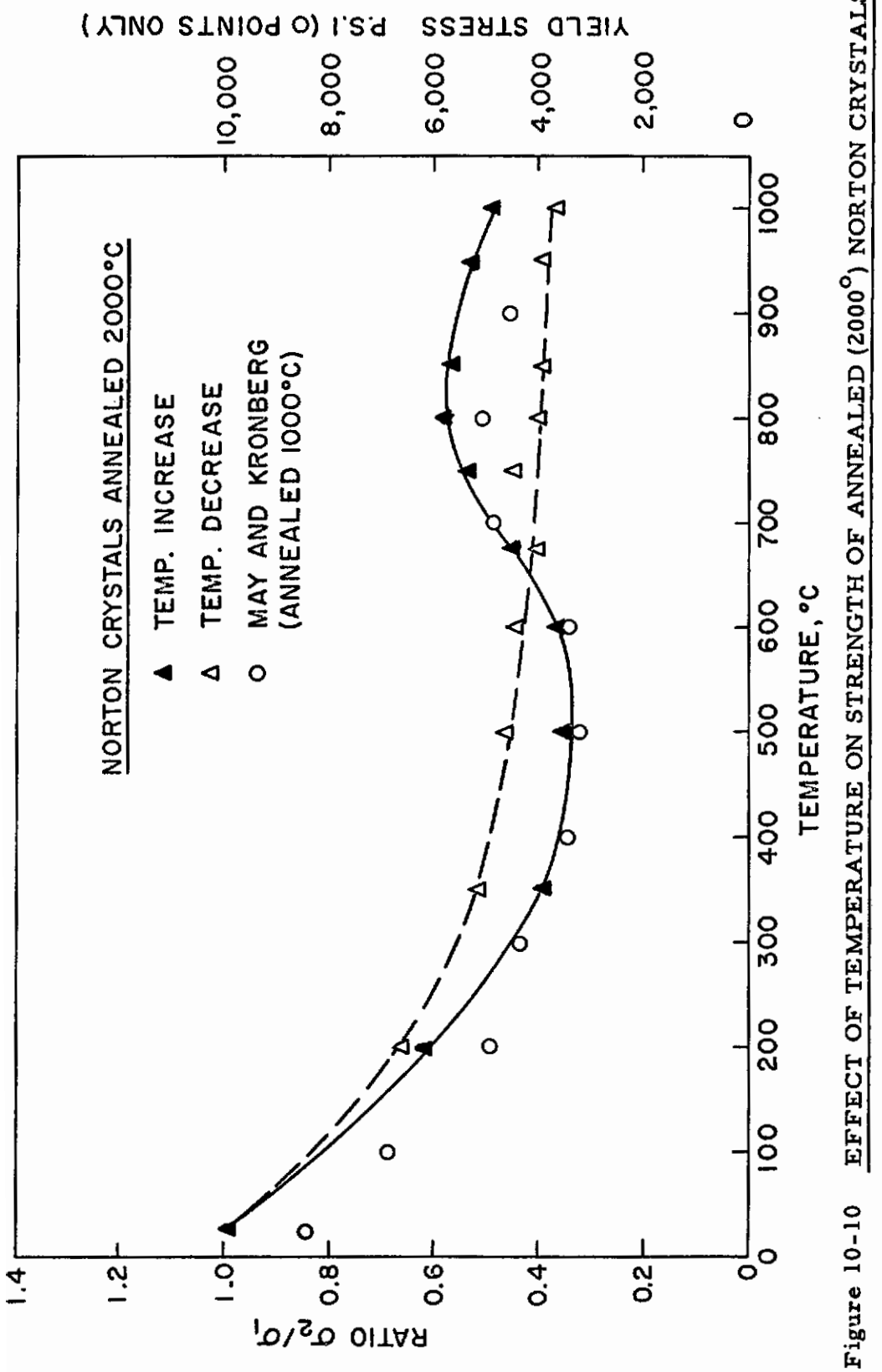

Figure 10-10 EFFECT OF TEMPERATURE ON STRENGTH OF ANNEALED (2000°) NORTON CRYSTALS.

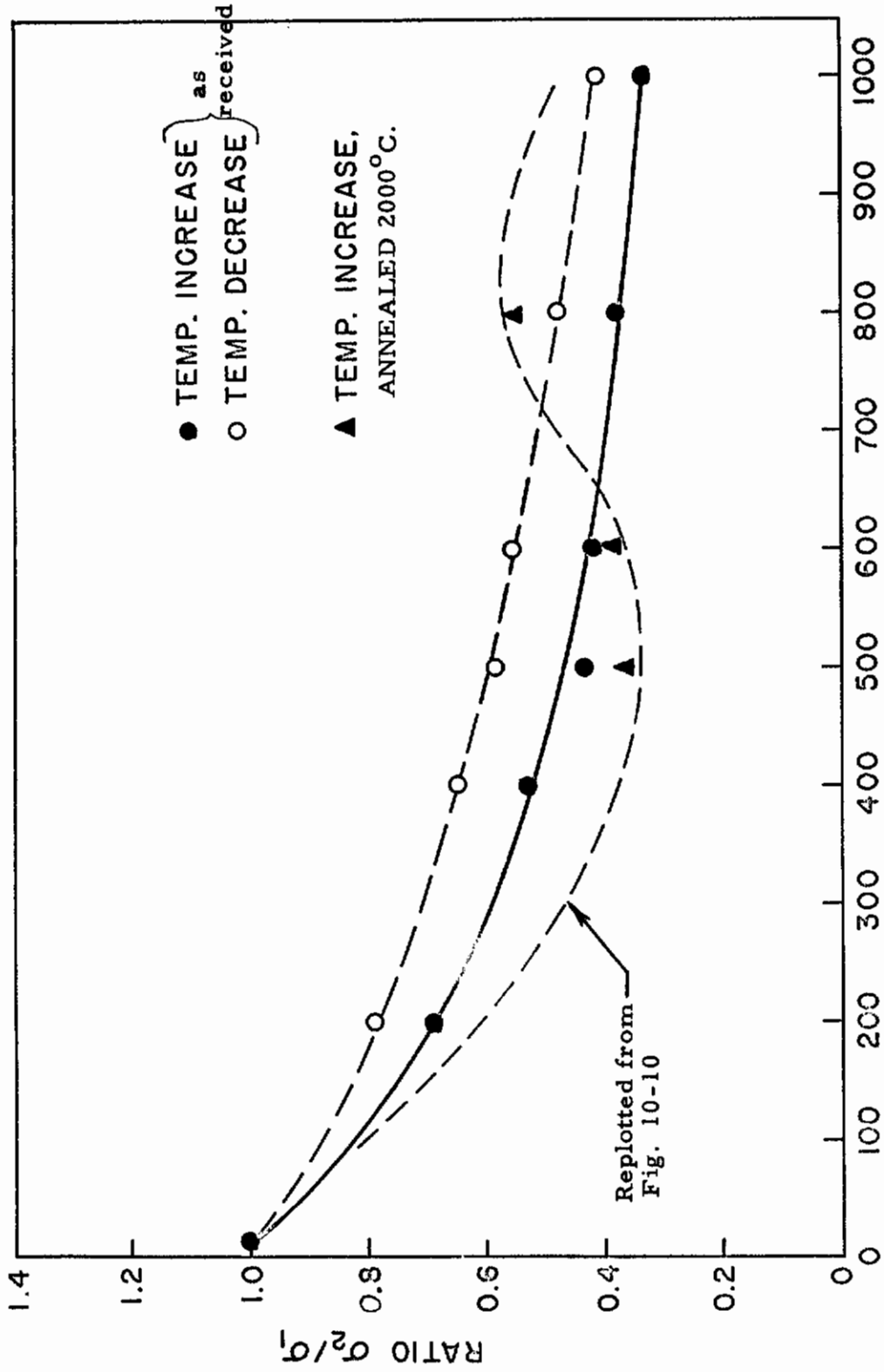

Figure 10-11 EFFECT OF TEMPERATURE ON STRENGTH OF AS-RECEIVED AND ANNEALED (2000°) SEMI-ELEMENTS CRYSTALS.

It is interesting to note that essentially similar observations were made by May and Kronberg[10-6], who compared the yield strength of as-cleaved crystals in three conditions, as-received, quenched from 1000°C, and slowly cooled from 1000°C. Both the as-received, quenched from 1000°C, and slowly cooled from 1000°C. Both the as-received and the slowly cooled crystals showed a gradually decreasing strength similar to as-received crystals in Fig. 10-11, whereas the quenched crystals showed a minimum and maximum in the strength curve at precisely the same temperatures measured on our annealed crystals in Fig. 10-10. May and Kronberg's results are plotted in Fig. 10-10 for comparison.

The purpose of the final test at room temperature was to determine whether or not the increased dislocation mobility and ease of cross slip during high temperature strain would produce a crystal softer and more ductile than before. A simple evaluation of this could readily be obtained by comparing the relative values of the flow stress ratio, σ_2/σ_1, on increasing and decreasing the temperature in Figs. 10-10 and 10-11. If σ_2/σ_1 on raising the temperature was less than on lowering it, then by definition the yield stress in the final room temperature test was less than the flow stress at the completion of the initial test. In this case the crystal was softened by the intermediate strain. If the values of the ratios were reversed, then the crystal was strengthened by the intermediate strain.

In Fig. 10-11 the flow stress ratio for decreased temperatures showed a continuous drop with rising temperature, but always maintained a value greater than that of the flow stress ratio for increased temperature ratio. Thus, the as-received Semi-Elements Crystals were always hardened by the intermediate high temperature strain. In Fig. 10-10 the situation was more complicated, the temperature decrease ratio also showed a continuous drop with temperature, but it intersected the inflected curve for the temperature

increase ratio at 700°C. Thus, crystals annealed at 2000°C were softened by intermediate straining at temperatures above 700°C. This is also illustrated in Fig. 10-9, where it can be seen that σ_1' is greater than σ_1 for intermediate straining at 850°C.

These results should be compared with the results of Section 3A where the consequences of annealing alone were described. There it was shown that intermediate annealing at temperature below 500°C led to softening but above 600°C resulted in hardening. These observations raise the question as to what extent the preliminary anneal at 2000°C influenced the results shown in Figs. 10-6, 10-7 and 10-8. Experiments in the future will be designed to clarify this point, since it obviously represents a most important aspect of thermal-mechanical history from the viewpoint of both experimental analysis and theoretical interpretation.

C. Etching Studies

In Section 3A it was shown that (pre-annealed) pre-strained MgO crystals became stronger upon annealing at temperatures above 600°C and that the strengthening was to be associated with the locking of dislocations. It is important both from the fundamental and technological point of view to understand the source of this strengthening. In this respect etch pit studies have been most stimulating although the observations and their interpretation remain incomplete and somewhat complicated. All etch pit studies have been conducted on the tension surface of crystals undergoing bending and have been limited chiefly to the emergent screw dislocations. At the outset it was clear that "fresh" and "locked" dislocations could be etched differently. "Fresh" screw dislocations were sharper, larger, more regular in size and more unsymmetrical than "locked" dislocation etch pits. The unsymmetry in fresh pits arises from the fact that screw dislocations intersect the surface

at 45°. The comparison may be made directly in Figs. 10-5 and 10-12 where fresh dislocations and locked dislocations have been placed side by side in the same crystal.

In one series of experiments crystals were prestrained at room temperature, annealed, etched, reloaded at room temperature and etched again. With this double etching procedure it was possible to determine to what extent the original fresh dislocations were reactivated after they had been annealed. Fig. 10-13 compares two crystals (a) annealed at 600°C and (b) annealed at 800°C.

In the crystal annealed at 600°C it was noted that: (a) the etch pits were equally as sharp and unsymmetrical as "fresh" screw dislocations, (b) slip during the second test continued from most of the slip band segments introduced in the prestraining (c) where slip had continued the original pits remained sharp indicating that the screw dislocations were still located in their original positions.

In the crystal annealed at 800°C it was noted that: (a) the etch pits were no longer as uniform in size, as sharp or as unsymmetrical as fresh dislocations, (b) slip had continued from only a few of the original slip band segments. In fact, the number of reactivated bands revealed by etching could be correlated accurately with the number of yield drops at the beginning of the stress deflection curve in Fig. 10-7.

These observations supported the proposal made earlier (Section 3A) that dislocations in slip band segments were only weakly locked by an anneal at 600°C but strongly locked by an anneal at 800°C.

The change in appearance of screw dislocation etch pits following an anneal at 800°C and higher was most significant and experiments were undertaken to determine the cause. The technique

consisted of placing fresh and "locked" dislocations side by side as in Fig. 10-12 and then etching deeper and deeper beneath the crystal surface to map the "locked" dislocation lines with the fresh dislocations acting as markers. The conclusion from this type of experiment was that the "locked" dislocations lay in the same $\{110\}$ plane as fresh dislocations but their rate of etching was retarded, thereby producing pits more symmetrical in appearance. This retardation could be explained by assuming that impurities had condensed onto the dislocation lines to lower their core energy.

In a second series of experiments crystals were prestrained, etched, annealed and etched again. Again annealing at temperatures below 600°C did not affect the slip bands but above this temperature both the location and density of dislocations was changed. This is illustrated in Fig. 10-14 following an anneal at 1200°C, where the lines of flat bottomed pits indicated that most of the dislocations had left their original position in the crystal. The small sharp pits within these lines represented the new location of the remaining locked dislocations.

We tentatively conclude on the basis of these etch pit studies that the effect of annealing was two-fold: first, many of the dislocations disappeared through climb and annihilation and second, those that remained had an associated impurity environment.

It is interesting to note that Groves and Kelly[10-5] have recently applied the electron transmission thin film technique to a study of the effects of annealing on dislocation loops in magneisum oxide. Their technique limits their study chiefly to the behavior of edge dislocation components. These authors show that the edge dislocation dipoles left behind dislocations as they move over slip planes at room temperature[10-8, 10-10] break up into a series of closed loops once the annealing temperature exceeds 700-800°C.

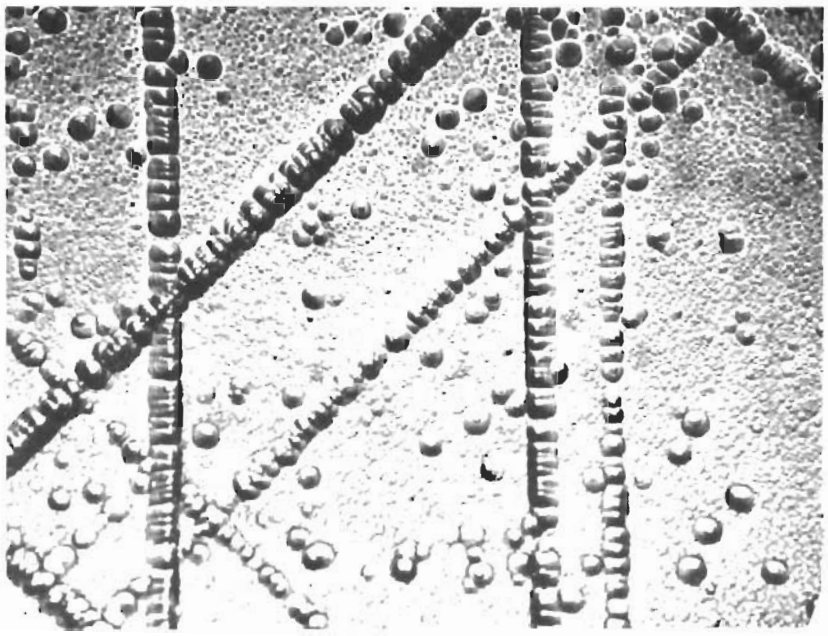

Fig. 10-12 APPEARANCE OF DISLOCATION ETCH PITS, (a) WHEN FRESH AND (b) AFTER AN ANNEAL AT 1200°C FOR 1 HOUR (X500)

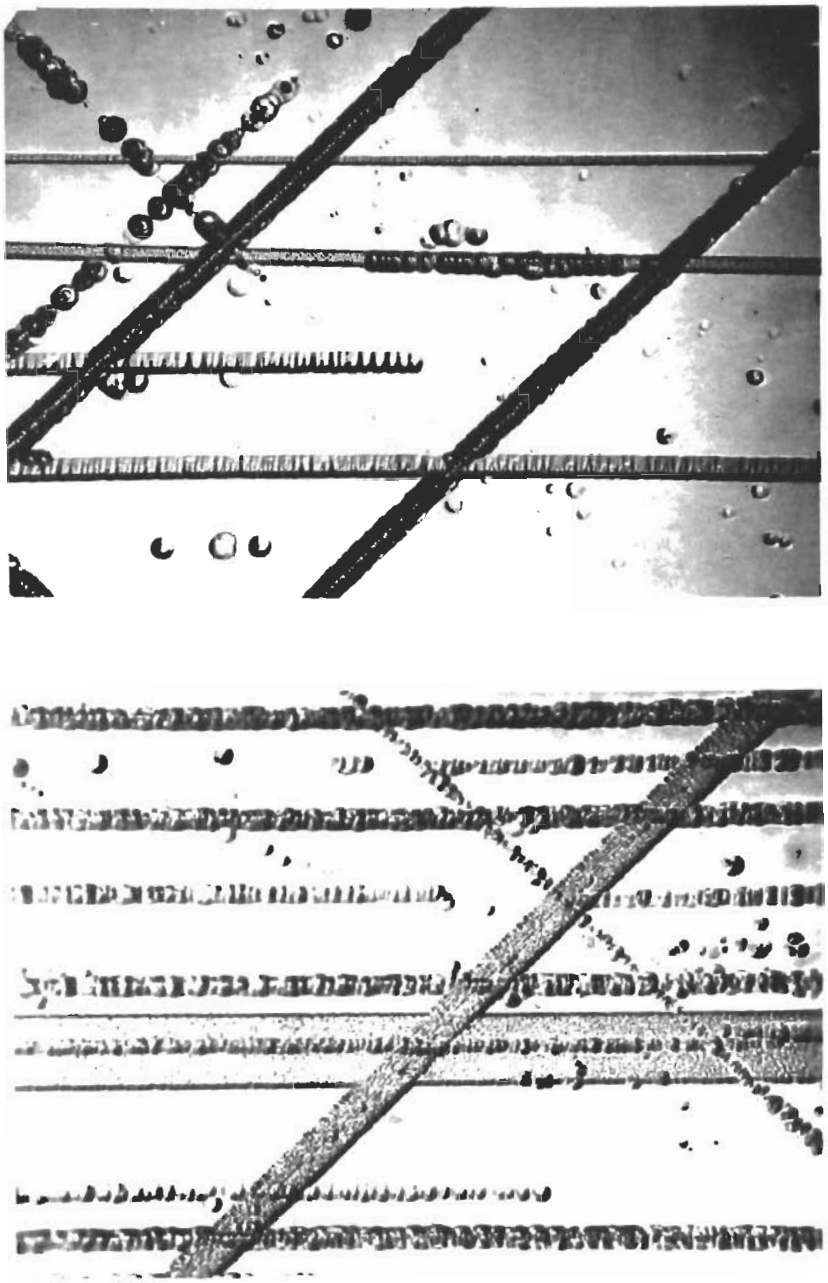

Fig. 10-13 THE REACTIVATION OF SHORT SLIP BAND SEGMENTS FOLLOWING AN ANNEAL (a) at 600°C, (b) at 800°C (X250)

Note: Difference in appearance of large pits between (a) and (b).

Such a change in dislocation structure would also be expected to contribute to the hardening observed after an anneal.

Finally, etch pit techniques were used to monitor the high temperature tests. While a detailed analysis was not completed there were some interesting preliminary observations; as follows:

The dislocation distribution in slip bands produced at high temperatures was very different from that at room temperature. Fig. 10-15 shows an example of slip at 600°C. The density of dislocations remaining in the slip bands was less than at room temperature, but there was a higher density of non-linear defects (identified by shallow bottomed pits) produced in the wake of dislocations.

When prestrained crystals were deformed at temperatures up to 500°C, the dislocations produced during the deformation at room temperature continued to move and contribute to the plastic deformation at the high temperature. The stress-deflection curves under these conditions were smooth (Section 3B). When prestrained crystals were deformed above 700°C only a few of the room temperature dislocations contributed to the high temperature plastic deformation. The stress deflection curves under these conditions were jerky (Section 3B).

From these observations it was concluded that the jerky flow exhibited at high temperatures (see for example Fig. 10-9) was again due to a dislocation locking phenomenon. It was tempting to conjecture that a similar mechanism was responsible for both dislocation locking during annealing and during high temperature deformation especially since the transition in mechanical behavior in both instances occurred in the same temperature range.

5. DISCUSSION AND CONCLUSIONS

The work described in the preceding sections may be summarized briefly as follows:

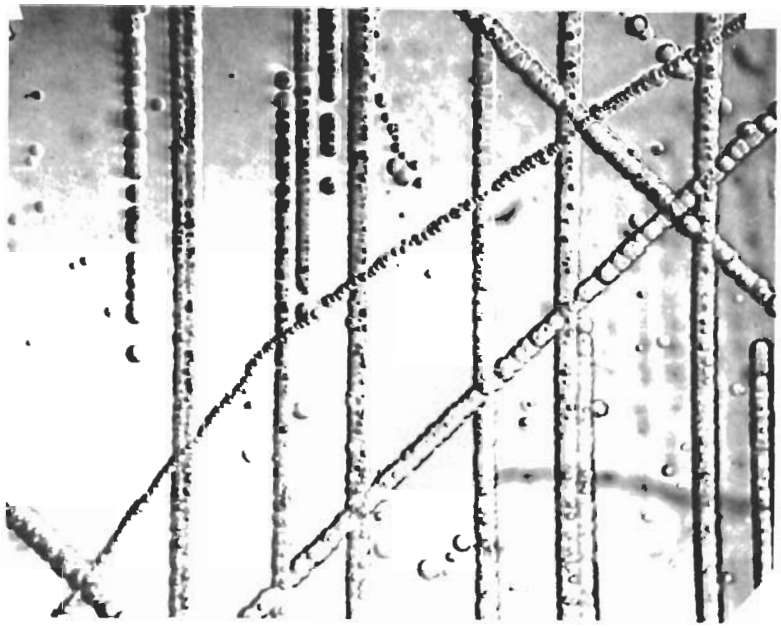

Fig. 10-14. EFFECT OF ANNEALING ON DENSITY AND DISTRIBUTION OF DISLOCATIONS. CRYSTAL-ETCHED BEFORE AND AFTER 2-HOURS' ANNEAL AT 1200°C (X500)

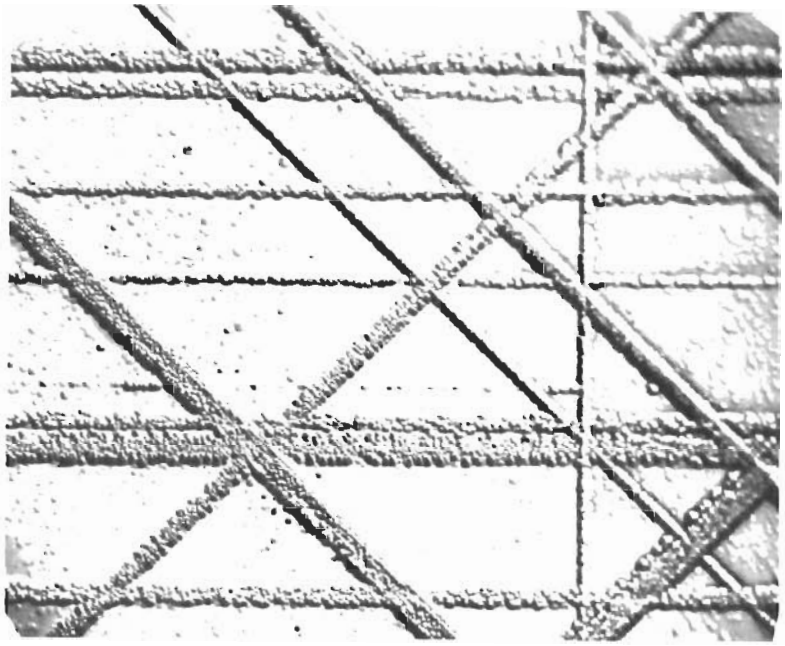

Fig. 10-15 SLIP BANDS PRODUCED IN AS-RECEIVED MgO CRYSTAL AT 600°C (X350)

Note the trail of flat-bottomed defects left behind the dislocations.

(1) "Grown-in" dislocations in as-received magneisum oxide crystals are locked very strongly and specimens may be subjected to extremely high stresses (50, 000 to 80, 000 psi in tension) without yielding. When crystals are annealed at 2000°C the grown-in dislocations seem to be locked even more strongly since one specimen has supported a tensile stress of 110, 000 psi without yielding. It is not presently clear to what extent heat treatment affects this behavior.

(2) Heat treatment does have an affect on the etching behavior of as-received crystals. An anneal at 2000°C eliminates the background of shallow flat-bottomed pits usually present and presumably due to clusters of point defects.

(3) Crystals which have been given a preliminary anneal at 2000°C and then sprinkled to introduce a few fresh surface dislocation sources normally yield around 10, 000 psi. After a further anneal at temperatures above 500°C the fresh dislocations become locked and the crystal hardens. The effectiveness of the looking increases as the temperature is raised and as the time at temperatures above 1000°C is lengthened.

(4) Crystals which have been given a preliminary anneal at 2000°C, sprinkled and preloaded at room temperature show a minimum and a maximum in their strength vs. temperature. The minimum occurs at 500°C and the maximum at 850°C.

(5) Crystals in the as-received condition, sprinkled and preloaded at room temperature show a continuous decline in strength with an increase in temperature.

(6) May and Kronberg[10-6] showed that crystals quenched from 1000°C also exhibited a minimum and maximum in strength, whereas crystals slowly cooled from 1000°C exhibited a continuous decline in strength with temperature.

(7) Both as-received and pre-annealed (2000°C) crystals show a change in yielding behavior when the test temperature is raised above 600°C. The curves become jerky and yield points develop.

(8) As-received crystals are softened by a high temperature prestrain. Crystals pre-annealed at 2000°C are hardened by a high temperature prestrain when the temperature exceeds 600°C

(9) Etch pits due to fresh dislocations are sharp and uniform in size and remain so following anneals at temperatures up to 600°C. Above 700°C the etch pits become less sharp and non-uniform in size due to a change in their etching rate. In addition, above 800°C many dislocations are annihilated by annealing.

At this time there is no simple mechanism which can account for all of these effects; indeed it seems likely that a number of different yet interdependent processes must be involved. One such process is that proposed by May and Kronberg[10-6] concerning the solution and precipitation of impurities in magnesium oxide. These authors suggested that impurities go into solution at temperatures around 850 to 1000°C and precipitate out below this temperature range. The minimum in the strength versus temperature curve in Fig. 10-10 is then attributed to the fact that impurities retained in solution following the quench from 1000°C start to precipitate out at 500°C. This leads to hardening which becomes more pronounced until the maximum at 850°C where they return into solution again. Unfortunately this solution and precipitation process alone cannot account for the increased room temperature strength of annealed crystals when the annealing temperature exceeds 1000°C (Fig. 10-6). It is possible that above 1000°C a second hardening process involving dislocation rearrangement by annihilation or climb, of the kind observed by Groves and

Kelley[10-5] may become more significant. Further experiments are necessary before any more definite conclusions can be drawn with regard to the processes occurring.

In conclusion, this work has shown that the mechanical strength and ductility of magnesium oxide single crystals and, as recent work in our laboratory on another project has shown, bicrystals is strictly determined by the availability and operation of dislocation sources. When dislocation sources are strongly locked, bicrystals are extremely strong as shown in Fig. 10-1, but should any slip occur in the vicinity of the boundary a crack immediately nucleates to fracture the specimen. One way to prevent this is to lock the slip sources by annealing. However, as the work described here has shown, fresh dislocation sources may be easily reintroduced by the slightest mechanical contact to the subsequent detriment of the mechanical strength. This poses an interesting problem for future consideration since it is obviously very important to learn how to prevent fresh dislocations either getting into or moving through crystals.

6. CONTRIBUTING PERSONNEL

The personnel contributing to this program were R. J. Stokes, K. H. Olsen and K. H. Vuori.

7. REFERENCES

10-1 Gilman, J. J. and Johnston, W. G., Dislocations and Mechanical Properties of Crystals, Wiley, P. 116 (1957).

10-2 Gilman, J. J., J. Appl. Phys. 30, 1584, (1959).

10-3 Stokes, R. J., Johnston, T. L., and Li, C. H., Trans. AIME, 215, 437, (1959).

10-4 Venables, J. D., Phys. Rev. 122, 1388 (1961).

10-5 Groves, G. W. and Kelly, A., Private communication.

10-6 May, J. E. and Kronberg, M. L., J. Amer. Ceram. Soc., 43, 525, (1960).

10-7 Stokes, R. J., Johnston, T. L., and Li, C. H., Phil. Mag. 6, 9, (1961).

10-8 Johnston, W. G. and Gilman, J. J., J. Appl. Phys. 31, 632 (1960).

10-9 Stokes, R. J., Johnston, T. L. and Li, C.H., Phil. Mag. 4, 920, (1959).

10-10 Washburn, J., Groves, G. W., Kelly, A. and Williamson, G. K., Phil. Mag. 5, 991, (1960).

TASK 11 - SURFACE ACTIVE ENVIRONMENTS

Principal Investigator: G. T. Murray
Materials Research Corporation

ABSTRACT

The prime objective of this Task of the program was to explore the embrittling effect of various environments upon the mechanical behavior of MgO single crystals. Extremely careful specimen preparation techniques were employed to avoid masking of the surface effects by extraneously induced conditions. Environments included the principal constituents of the atmosphere (O_2, N_2, CO_2 and H_2O) as well as A (used for control purposes).

Experiments were conducted at temperatures up to 600°C. Even after lengthy exposures at various temperatures, none of the environments were found to embrittle the MgO crystal, in contradiction to results previously reported in the literature. The only exception to this statement occurred for specimens exposed to air at 600° C for 160 hrs, or those exposed to steam at 350° C for 4.5 hrs. However, even these effects appear ascribable to the embrittling effect of surface precipitates formed, rather than to diffusion of gases into the host lattice.

TASK 11 - SURFACE ACTIVE ENVIRONMENTS

I. INTRODUCTION

It is widely recognized that certain non-metallic crystals, in particular those possessing ionic binding, exhibit considerable plastic flow prior to fracture. The extent of this plasticity is strongly dependent on surface condition and environment. For example, in the case of Na Cl, the most extensively investigated non-metallic material, embrittlement has been attributed to surface flaws, e.g., cleavage defects, residues, surface compound formation, and dissolved solutes [11-1, 2, 3]. For crystals free of surface flaws and residues it has been demonstrated [11-1] that the embrittlement incurred by short exposures to the ambient atmosphere is a result of the formation of a thin coherent $NaClO_3$ surface layer. The situation with respect to atmospheric embrittlement of MgO crystals is not so well defined. Several investigators [11-4, 5, 6] have reported that MgO crystals exhibit a significant loss in ductility on exposure to the ambient atmosphere, whereas other evidence [11-7, 8] could be found that refuted this point.

The present work was undertaken with the prime objective to investigate and understand the relation between surface treatment and ductility in MgO crystals, and the effect that various environments may have in modifying this relationship at various temperatures.

2. EXPERIMENTAL PROCEDURE

It became apparent early in the work that the surface preparation prior to exposure of the crystals to the gaseous media in question was all-important, and that variations in preparation might well account for some of the contradictions reported in the literature. Several factors of importance that have evolved during the course of this work and that of others [11-9, 10] are listed as follows:

(a) Cleavage cracks or steps can lead to an early fracture.

(b) Dislocation sources introduced during cleaving can promote ductility by decreasing the slip band spacing.

(c) Chemical polishing can remove cleavage effects but, as will be demonstrated later, surface residues, which often remain after normal chemical polishing operations, can lead to embrittlement.

(d) Extensive surface removal by chemical polishing can strengthen and reduce the plastic strain prior to fracture through the elimination of surface sources.

In order to examine the effect of a certain gaseous atmosphere on the ductility of the material it is necessary to eliminate the above embrittling or ductilizing effects. This can be done by testing a carefully chemically polished crystal after exposure to the gas of interest and compare the result to that obtained on a control specimen.

Early in the work specimens were prepared by cleaving and subsequent chemical polishing operations. These specimens yielded an average outer fiber strain at fracture in slow bend tests at room temperature of about 3%. However, there existed a large scatter in the results, presumably from the non-uniform distribution of surface sources that remained after polishing. The specimen preparation procedure that was finally evolved (suggested by the findings of Stokes [11-10]) and used for all data reported herein (except where noted), consisted of the following steps.

(a) Cleave as-received Semi-Element crystal blocks;

(b) Chemical polish in hot H_3PO_4 to remove cleavage defects (consists of 2 min. dissolution in H_3PO_4, boiling H_2O rinse, alcohol rinse and dry air steam);

(c) Sprinkle with 150 mesh carborundum powder to introduce a uniform surface distribution of dislocation sources;

(d) Prestrain plastically (in bending) to approximately 0.1% to expand the surface loops:

(e) Chemical polish again to remove possible surface cracks resulting from the sprinkling operation.

After the above treatment, some specimens were tested in three point bending (at various temperatures) as controls, others were exposed to various gaseous media and subsequently tested in an identical manner. Test temperatures at 350° C and below were attained with an oil bath. Above 350° C the specimens were heated in air with a radiant energy focusing heat lamp. Except where noted, all tests were conducted on a hard, continuous recording, constant (approximately 10^{-3} per min. on outer fiber) strain rate machine. Specimen dimensions were in the order of 0.085" x 0.100" x 0.650" gage length. For preliminary survey work in minimum of four specimens were tested for each surface condition studied. When an effect was found that was believed to be significant a minimum of eight specimens were employed to obtain the average result reported (outer fiber strain is reported in all cases).

3. RESULTS AND DISCUSSION

A. Control Specimens

Typical stress-deflection curves for specimens prepared by the carborundum sprinkling technique are shown in Fig. 11-1. These curves are characterized by a smooth and nearly horizontal plastic region. Tests on as-cleaved and cleaved chemically polished specimens showed more irregular curves and larger variations in fracture strain values.

B. Room Temperature Gaseous Exposure

(a) Ambient Air, O_2 , N_2 CO_2 and Argon

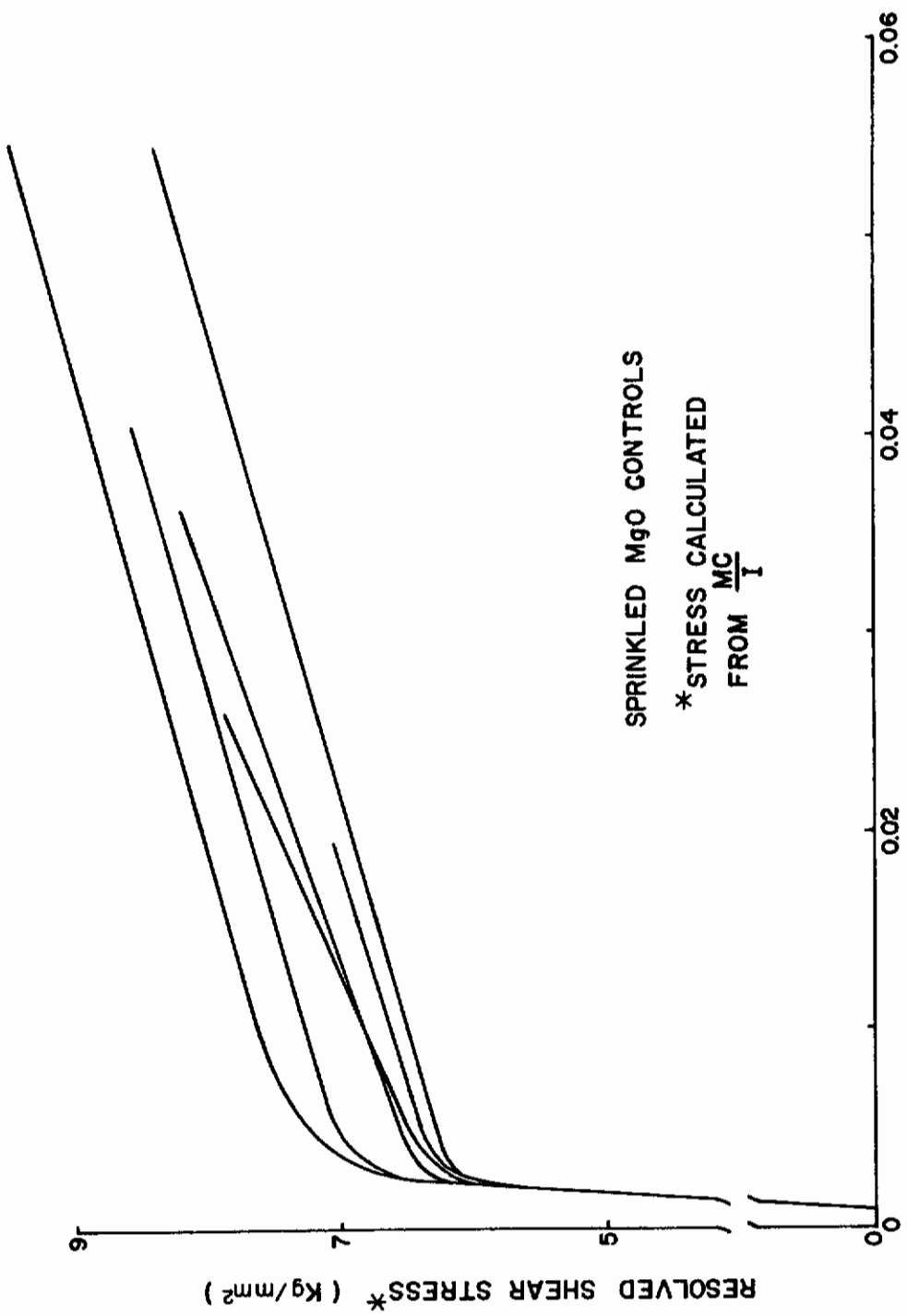

Fig. 11-1 STRESS DEFLECTION CURVES FOR SINGLE CRYSTAL MgO CONTROL SPECIMENS

Table 11-I

ROOM TEMPERATURE GASEOUS EXPOSURE

Atmosphere	Exposure Time, hr	Test Temp, °C	No. of Specimens	Average Strain %	Standard Deviation % Strain
Controls	0	25	12	2.8	1.2
Ambient Air	42	25	4	3.8	0.8
CO_2	212	25	4	2.6	1.7
Argon (controls)	112-188	240	7	5.5	1.8
Nitrogen	89-165	240	7	5.2	2.5
Oxygen	117-215	240	7	7.2	2.3
Controls	0	400	2	10.2	-
Ambient Air	14-139	400	7	10.0	2.3

The results obtained on specimens exposed for lengthy periods to these gases and then tested at various temperatures are compared to control specimen data in Table 11-1. Since the N_2, O_2 and A studies were conducted early in the work these specimens were prepared by cleaving and chemical polishing Norton material. Except for the ambient air and control specimen tests, all specimens were wrapped in lense tissue and carefully encapsulated in approximately one atmosphere pressure of purified reagent grade gases. After the exposure period the specimens were removed from the capsule with extreme care in order to prevent the introduction of fresh dislocation sources into the surface. It can be seen that none of these gases embrittled the MgO crystals at room temperature. The stress-deflection curves did not differ from those obtained on control specimens. Microscopic examination of the air, (O_2 , N_2 , A, and CO_2) exposed specimen surfaces showed them to be completely free of residue or compound formation. The CO_2 exposed specimens were of particular interest since tabulated data showed (see Fig. 11-2) that $MgCO_3$ could form at room temperature. However, this figure does not consider the rate of reaction, and one must conclude that longer aging period are required for $MgCO_3$ residue formation.

C. Moisture

Although air exposure did not show embrittlement, it is conceivable that embrittling ingredients other than O_2 and N_2 present in the air may contribute a loss of ductility. One has particular reason to suspect the moisture content of the atmosphere since calculations from thermochemical data show (Fig. 11-3) that the reaction

$$MgO + H_2O \rightarrow Mg(OH)_2$$

should proceed at room temperature at slight pressures of water vapor.

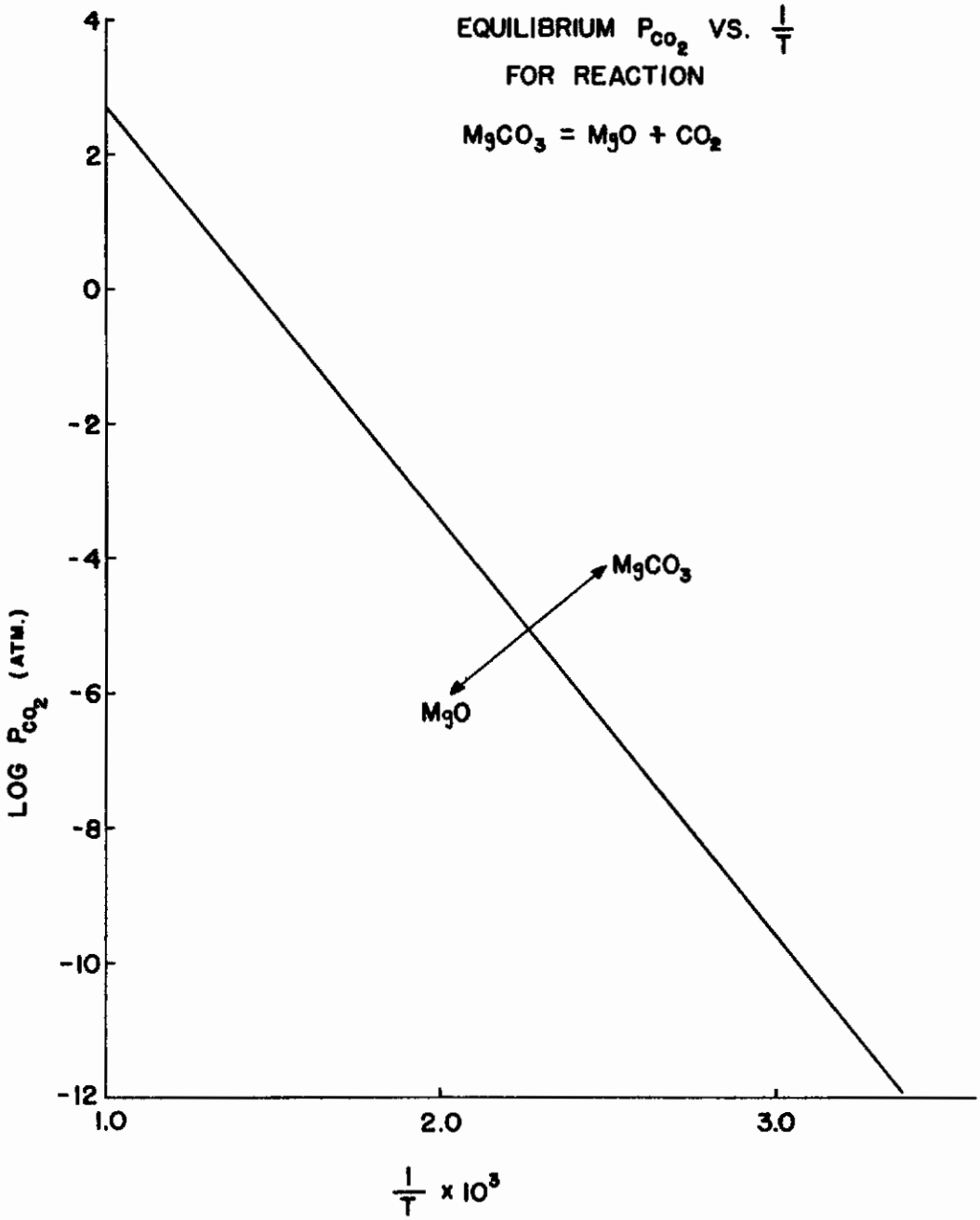

Fig. 11-2 EQUILIBRIUM CONDITIONS FOR $MgCO_3$ REACTION

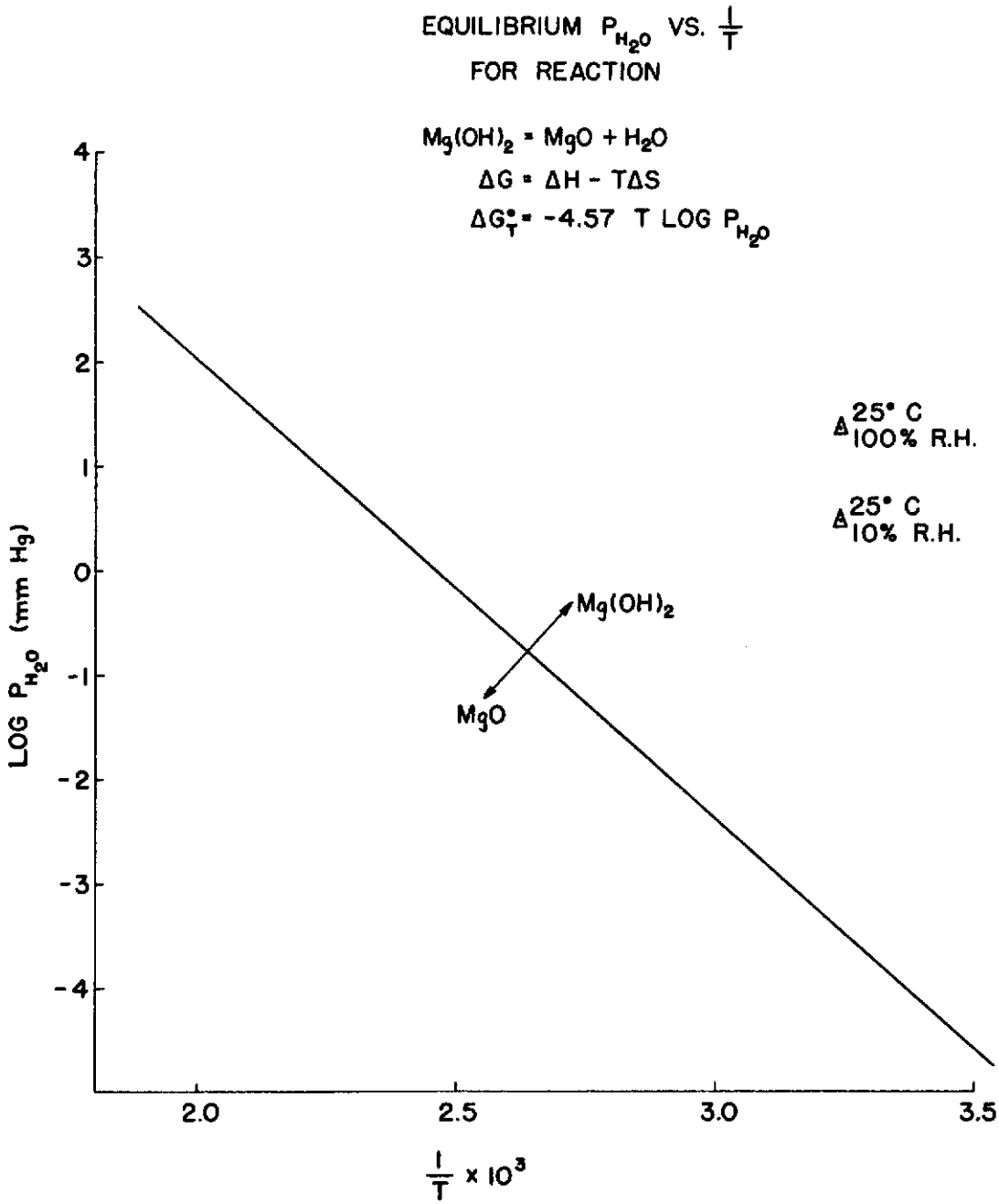

Fig. 11-3 EQUILIBRIUM CONDITIONS FOR $Mg(OH)_2$ REACTION

Specimens were exposed to saturated air in an air tight container for periods varying from 1 to 14 days while a set of control specimens were exposed to dry air in a dessicator. A third set of specimens was exposed for 4.5 hours to steam ($\sim$ 100°C) by placing them near the orifice of a boiling water container.

After about 4 days exposure to the saturated air one could begin to detect the formation of a surface precipitate by microscopic examination. This precipitate was quite profuse after a 14-day exposure, as shown in Fig. 11-4. The precipitate was even more marked after the steam exposure (Fig. 11-5). Precipitate formation could not be detected on the control specimens after the 14-day exposure.

The average values (4 to 8 specimens tested) of the strain at fracture at various temperatures for each surface condition are shown in Fig. 11-6. The 350° C test data show a definite embrittlement for the steam treated specimens (the scatter in the data was the order of ± 1.5% strain). The lower temperature measurements, however, do not show significant effects. One would suspect that the presence of a surface compound would shift the transition temperature upward and thus the embrittlement effect should show up at room temperature. However, a sharp transition is usually not observed in slow bend tests on ionic crystals [11-11] and this may tend to mask the effect at small strains. An alternate explanation is that the time at the 350° C test temperature could alter the adherency and/or structure of the surface precipitate so as to enhance the embrittlement. It is planned to check this possibility by heating steam exposed specimens for a short period at 350° C and subsequently testing these at room temperature.

The mechanism of this embrittlement has not been determined as yet. The stress-deflection curves for the steam specimens were no different in form from those aged in dry air, showing similar yield stresses but correspondingly lower fracture stresses than the latter.

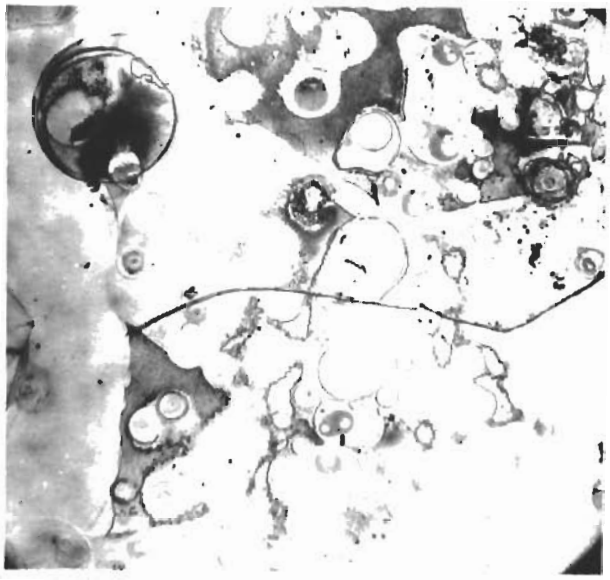

Fig. 11-4 PRECIPITATE ON MgO CRYSTAL AFTER 14 DAYS EXPOSURE TO WATER-SATURATED AIR Mag. X125

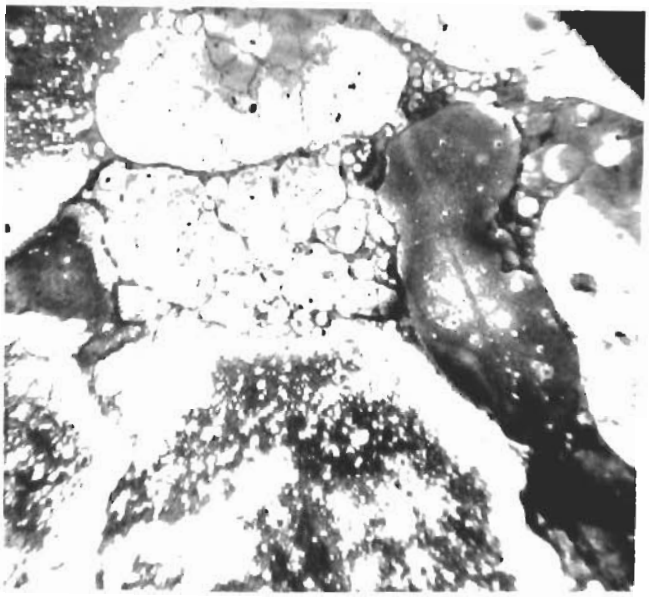

Fig. 11-5 PRECIPITATE ON MgO CRYSTAL AFTER 4.5 HR. EXPOSURE TO STEAM Mag. X50

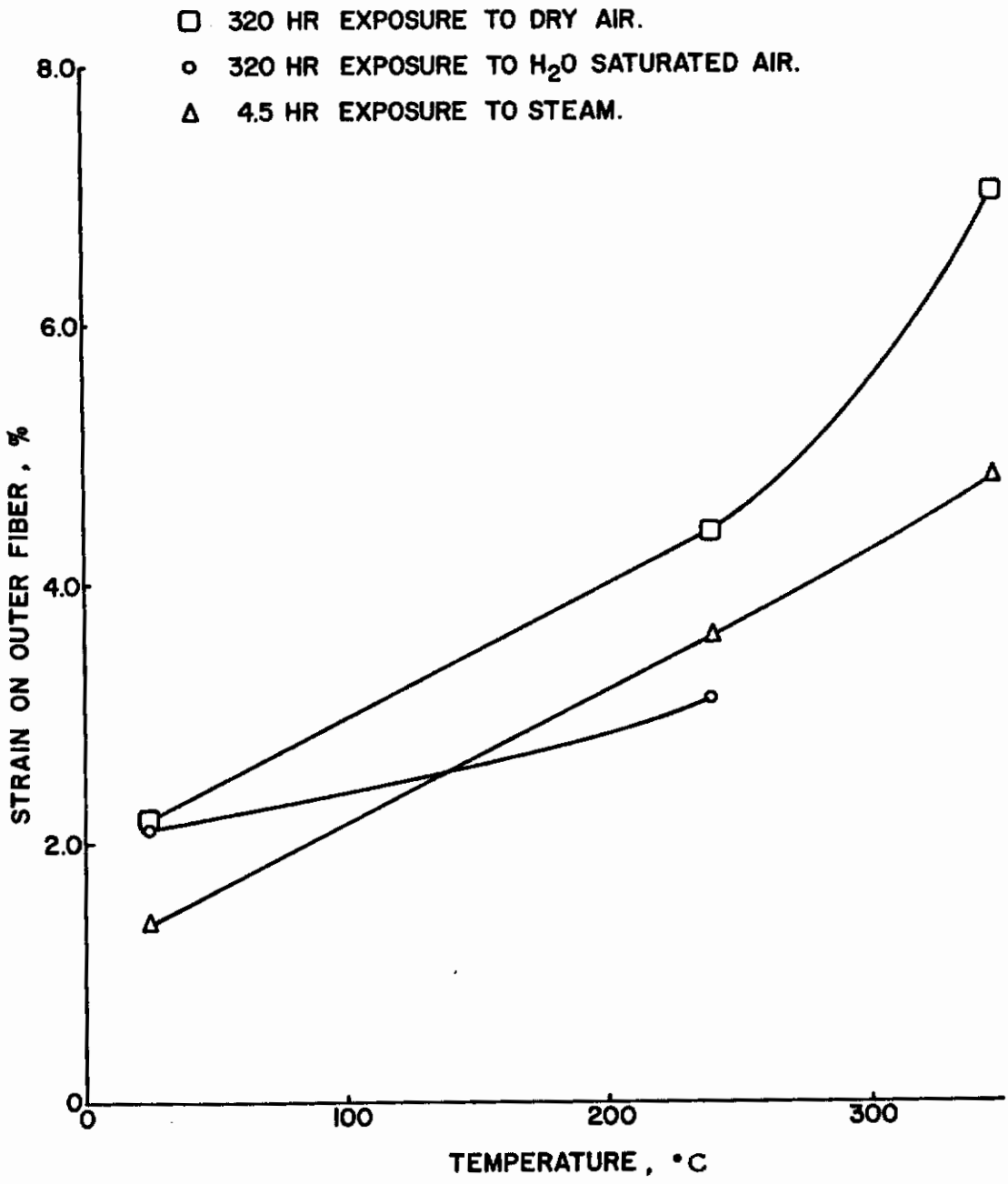

Fig. 11-6 EFFECT OF MOISTURE ON DUCTILITY OF MgO SINGLE CRYSTALS

Specimens exposed to water-saturated air were also tested at 350°C; however, this set of specimens exhibited an etch pit pattern (Fig. 11-7) on the bottom side that rested on a piece of filter paper. Apparently the continuous contact with water-soaked filter paper permitted a slow dissolution and concomittant etching of the dislocations that had been introduced by the pre-straining operation. (The water-saturated air exposed specimens used at the 25 and240°C test temperatures did not show this pattern, the difference presumably due to the placing of these specimens on lense tissue or other paper.) It was found that when this etch pit pattern was on the tensile side during the 350° C bend test the specimens were relatively brittle. However, when the pattern was on the compression side, the specimens were as ductile as the dry air aged specimens (the remaining three specimen sides showed the usual precipitate shown in Fig. 11-4). These results are summarized in Table 11-II. The stress-deflection curves for the dry air aged and the brittle tension side-etched specimens showed no difference in form other than that the tension side etched specimens exhibited a reduced strain at fracture and a correspondingly lower fracture stress (note the average stress values in Table 11-II). This leads one to suspect that the high dislocation density slip bands have been etched in such a manner as to form a notch, which gives rise to premature failure. Further experimentation is needed to clearly understand this phenomenon.

D. Elevated Temperature Gaseous Exposure

Specimens prepared in the usual manner were exposed to CO_2 (encapsulated) and air for 44 hours at 250° C and subsequently tested at room temperature. These specimens were supported in a jig such that only the ends came into contact with foreign objects. The results of these tests are summarized in Table 11-III. All specimens exhibited the same stress-deflection behavior and strain at fracture values commonly found for control specimens. No evidence of surface precipitate could be found.

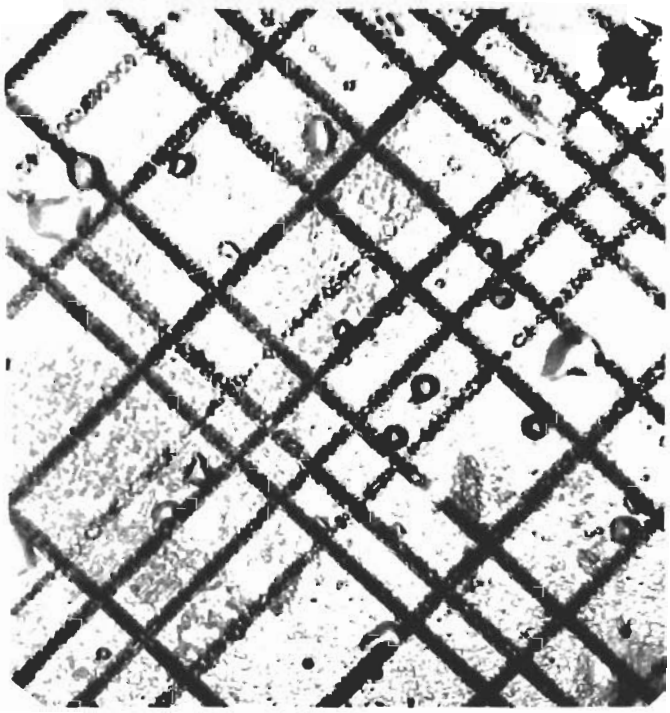

Fig. 11-7 ETCH PIT PATTERN ON MgO CRYSTAL AFTER 14 DAYS CONTACT WITH WATER-SOAKED FILTER PAPER X150

Table 11-II

BEND TESTS AT 350°C

Treatment	Resolved Yield Stress g/mm^2	Fracture* Stress g/mm^2	Average Strain %	Standard Deviation % Strain
326-hr exposure to dry air (8 specimens tested)	4600	8750	7.0	2.7
326-hr exposure to wet air; tension side etched (8 specimens)	4600	6750	2.6	1.5
326-hr exposure to wet air; comp. side etched (8 specimens)	3800	6900	7.6	0.8

* computed from $\frac{MC}{I}$ (resolved shear stress).

Table 11-III

CO_2 AND AIR EXPOSURE AT 250°C

Atmosphere	Exposure Time, hr	Test Temperature, °C	Average Strain, % 5 spec.
CO_2	44	25	3.8
Ambient Air	44	25	3.8

In view of the lack of embrittlement by various gaseous media on polished crystals it was decided to investigate the combination of surface defects and gaseous exposure. Cleaved and cleaved plus carborundum sprinkled surfaces were selected for initial exploration since these types of surface damage should be fairly reproducible from specimen to specimen. Since these specimens were quite brittle prior to gaseous exposure, eight specimens were tested for each condition examined. The results are listed in Table 11-IV. It can be seen that the 250° C air exposure showed an embrittlement only for the 250 mesh sprinkled specimens. The 150 mesh powder sprinkle reduced the ductility of the cleaved specimens, probably through the introduction of small cracks. The 250 mesh sprinkle enhance the ductility by introduction of surface sources, with less likelihood of crack formation. An air embrittlement effect in both the cleaved and 150 mesh sprinkled specimens could be masked by their low initial ductility. An interesting feature of this data is that both the sprinkling operation and the 250° C anneal reduced the yield and fracture stresses of the as-cleaved samples.

Pulliam [11-8] reported that air, O_2 and CO_2 embrittled crystals when exposure took place at 1000°C. In view of the absence of air embrittlement on polished specimens at 250° C in the present work it was decided to age at higher temperatures but to limit the exposure temperature to 600° C in order to avoid the 800° C

Table 11-IV

DEFECT SURFACE EXPOSURE TO AIR AT 250°C

Surface Condition	Treatment	Strain at Fracture % Avg. 8 Spec.	Standard Deviation % Strain	Resolved Yield Stress g/mm^2	Fracture Stress* g/mm^2
As-Cleaved	None-tested immediately	0.6	0.4	11,300	13,500
	Air-aged 250°C - 40 hr.	0.6	0.3	6,500	8,600
As-Cleaved Sprinkled	None tested immediately	0.3	0.2	8,500	10,500
150 Mesh	Air-aged 250°C - 40 hr.	0.6	0.3	6,000	7,350
As-Cleaved Sprinkled	None-tested immediately	1.2	0.2	7,500	9,500
250 Mesh	Air-aged 250°C - 40 hr.	0.5	0.4	6,400	8,000

* resolved shear stress - computed from $\frac{MC}{I}$.

"volume embrittlement" reported by Stokes [11-10]. The results of a series of room temperature tests after various air aging periods at 600°C are shown in Fig. 11-8 (8 specimens averaged for the 160 hr. point --- 4 specimens for each of the other points). These specimens showed a marked embrittlement after a 160-hr. exposure. In order to determine if this were a surface or volume embrittlement, another series of specimens were exposed for 160 hr. at 600° C and then tested after a small amount of the surface was removed by a chemical polish. These results are listed in Table 11-V. The average ductility increased as surface was removed indicating the embrittlement was primarily in the surface layers. The surfaces were examined microscopically after the 160-hr. exposure and found to contain a high density of small dark spots (Fig. 11-9). However, it is doubtful if the embrittlement is a result of surface compound formation since then the ductility should be completely restored after only a slight chemical polish, and such was not observed. Furthermore, a comparison of the stress-deflection curves (Fig. 11-10) if control, air aged, and air aged plus surface removal specimens show that dislocation pinning may be involved. Although no sharp yield points were observed, the aged specimens showed more irregular behavior and higher yield stresses than the control specimens. Experiments are now in progress to determine (a) if aged dislocations can be distinguished from fresh ones by the etching technique of Stokes [11-10] and (b) if embrittlement occurs after long aging periods in an inert gas.

E. Extraneous Effects

During the course of this study it was found that the specimen properties were extremely sensitive to handling procedures. In one case the cause of the observed embrittlement was traced to the presence of a surface residue that remained after the chemical polish; in another case to surface cracks on the specimen corners that

occurred by merely lightly touching the specimen to pyrex glass. These two types of embrittlement were examined more extensively and are described in the following.

a. Effect of Surface Residue

It was found that minute spots of residue often remained on the surface of some specimens after the normal chemical polish (Fig. 11-11). It could also intentially be formed by holding the specimen a few seconds in air between the H_3PO_4 and H_2O baths, or by immersion in a H_3PO_4 solution nearly saturated with MgO. This surface residue was removed (by scraping lightly with a razor blade) from several specimens and examined by X-ray diffraction. Two such powder specimens exhibited only MgO lines; however, one pattern showed numerous other lines that are believed to result from one or more phosphate compounds. It is believed that the residue usually consists of re-deposited MgO.

One group of specimens was allowed to form residue by air exposure after the H_3PO_4 bath, while another group was cleanly polished. The average values (four specimens for each condition) of the outer fiber strain obtained at fracture at two test temperatures are shown in Fig. 11-12. (These specimens were initially prepared according to the early cleave-chemical polish procedure.) The embrittlement by the residue is quite evident at the 400°C test temperature.

In an attempt to ascertain the mechanism of embrittlement by this surface residue, specimens were immersed in hot MgO-saturated H_3PO_4 which created a total surface coverage of residue. The specimens were then polished on each end in hot clean H_3PO_4 bath to leave a thin residue pattern near the specimen center, and placed in a three point jig such that the residue band was approximately 1.5 mm from the point of maximum bend. The jib was placed on a microscope such that the tension surface could be viewed during the bending process. Approximately 50% of these

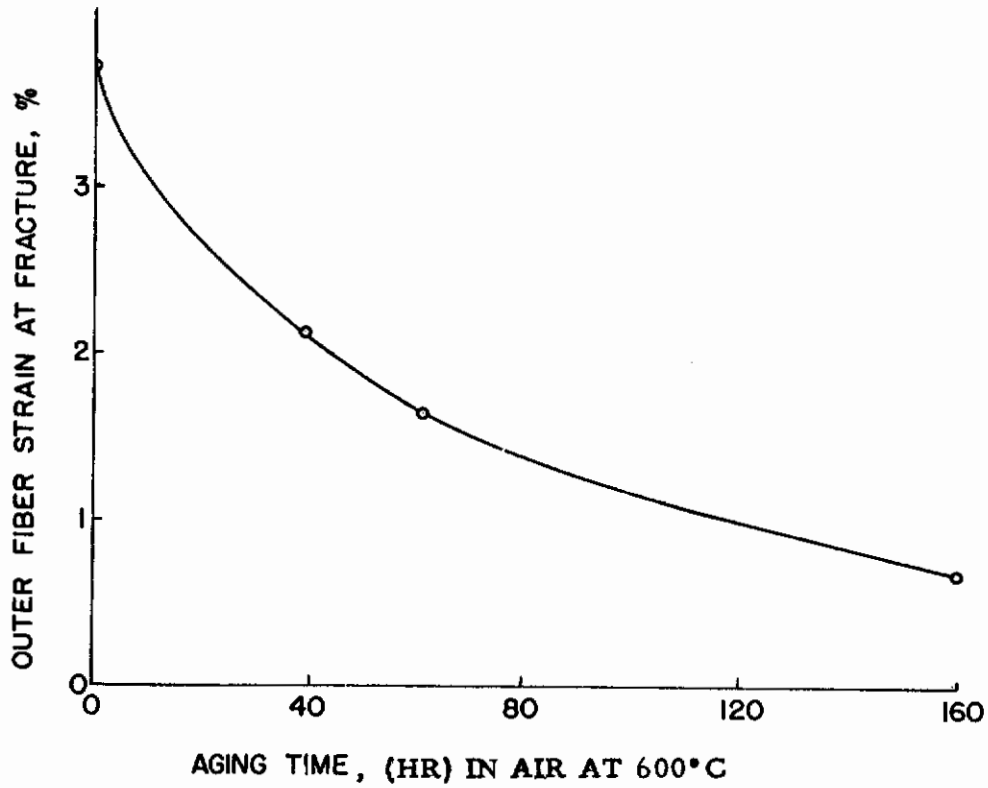

Fig. 11-8 EFFECT OF AGING AT 600°C ON DUCTILITY OF MgO SINGLE CRYSTALS

Table II-V

EFFECT OF SURFACE REMOVAL AFTER AIR-AGING AT 600°C

Treatment	Average Strain, % of 8 spec.	Standard Deviation, % Strain	Average resolved yield stress, g/mm^2
Aged in air 160 hr at 600° C none removed	0.9	0.8	8,900
Aged 160 hr, surface removed to 0.0025 in. depth	1.6	1.3	8,600
Aged 160 hr, surface removed to 0.005 in. depth	2.1	0.8	7,650

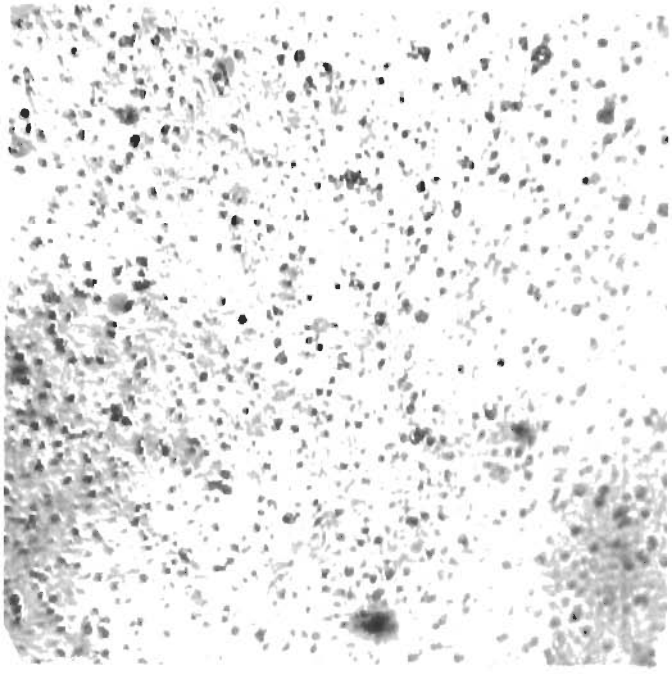

Fig. 11-9 SURFACE OF MgO CRYSTAL AFTER AIR-AGING 160 HR AT 600°C X500

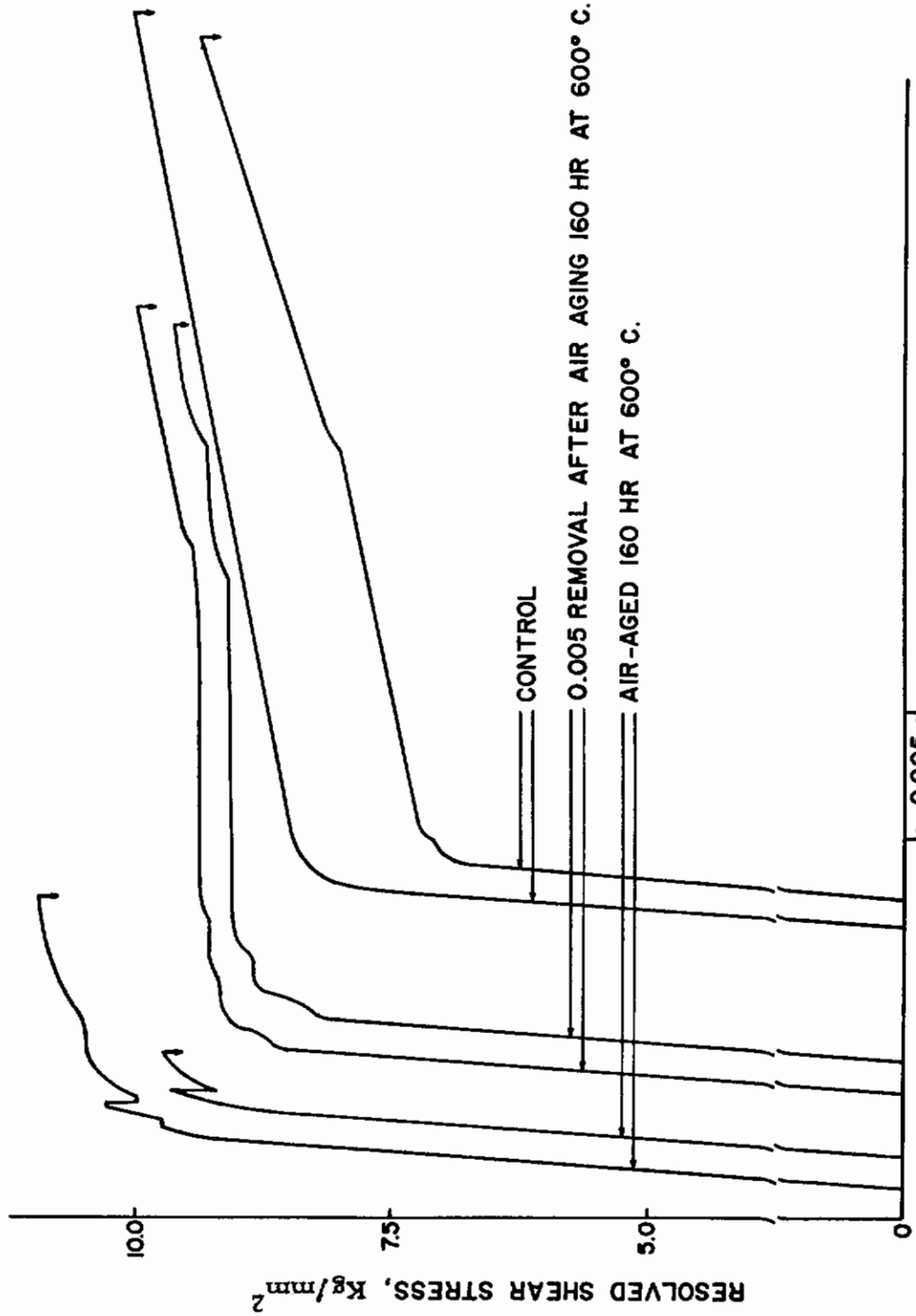

Fig. 11-10 STRESS-DEFLECTION CURVES FOR MgO CRYSTALS UNDER VARIOUS AIR-AGING CONDITIONS

specimens broke at or near the edge of the precipitate nearest the point of maximum bend. In all such cases slip bands could first be seen at the point of maximum bend and these grew in number spreading toward the residue region. It appeared that fracture occurred shortly after the first slip bands intersected the residue. Some of the other specimens broke at the point of maximum bend while a few broke at points not related to either the residue or maximum bend regions. The possibility that residue acts as a notch is being considered and further experiments have been planned.

b. Pyrex Glass Contact

In elevated temperature experiments specimens were encapsulated unprotected with a minimum of specimen movement during encapsulation. When control specimens showed embrittlement, it was decided to determine the extent of a possible glass reaction or handling defects. It was found that cracks could be introduced into the specimen corners by sliding the specimen through a short segment of pyrex tubing or by merely allowing one end of the specimen to fall onto the pyrex from a distance of the order of 5 mm. An example of these cracks are shown in Fig. 11-13. Some cracks were microscopically visible without the aid of an acid etchant, but it was necessary to etch to show all existing cracks.

4. CONCLUSIONS

The effect of various structure-sensitive parameters is most readily revealed by ductility measurements near the brittle-ductile transition temperature. For MgO crystals tested at slow strain rates ($\sim 10^{-3}$/min. in bending) this transition is in the vicinity of room temperature. (Faster strain rates would elevate the transition temperature but would probably reduce the extent of the effect and thus the sensitivity of detection.)

Fig. 11-11 RESIDUE FORMED ON MgO CRYSTAL FOLLOWING CHEMICAL POLISH X600

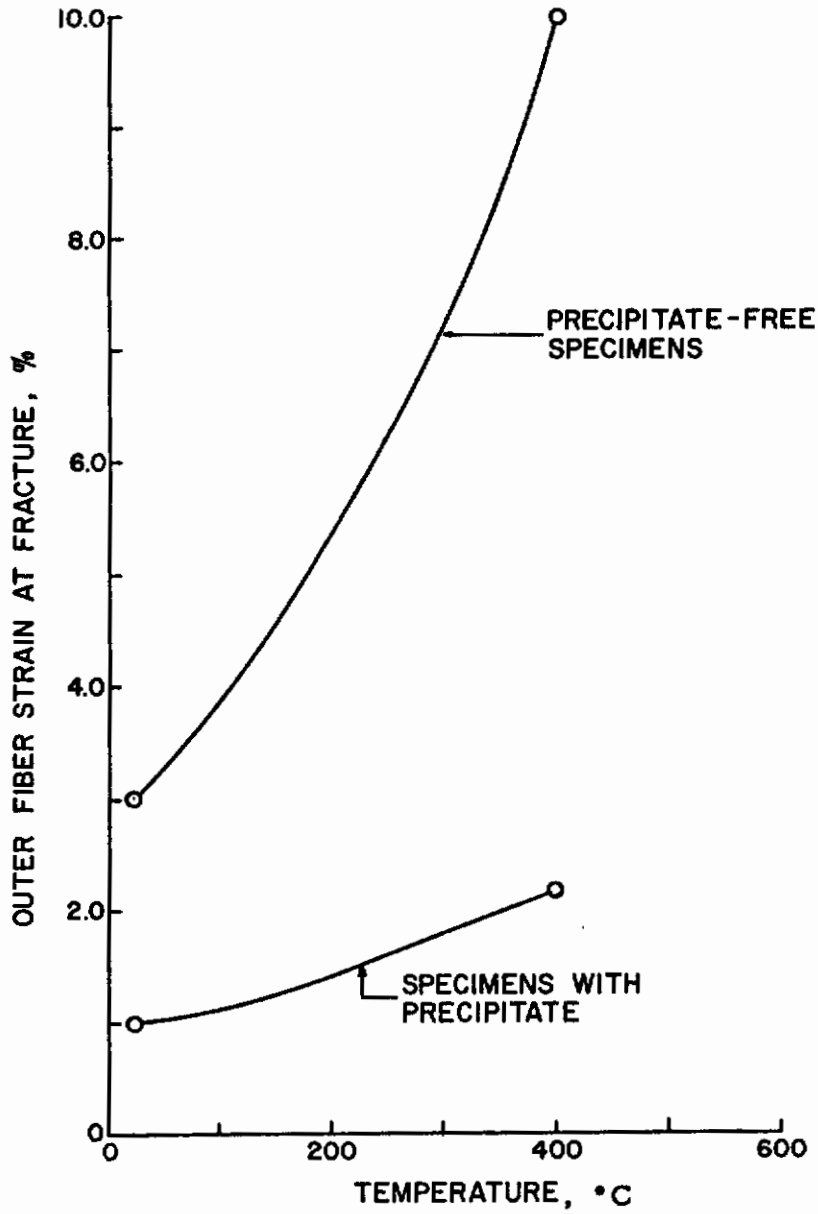

Fig. 11-12 EFFECT OF RESIDUE FORMED ON MgO CRYSTAL AFTER CHEMICAL POLISHING

Fig. 11-13 CRACKS ON EDGE OF MgO CRYSTAL AFTER CONTACT WITH PYREX TUBE X600

$Mg(OH)_2$ decomposes at this temperature and it is possible that the decomposition itself could play a role. The tension side etch pit embrittlement found at the 350°C test temperature is an entirely different phenomenon and is believed to be related to notch formation.

Probably the only embrittlement of real practical significance found in the present work is that for air aging at 600°C. The stress-deflection curves and the surface removal tests strongly suggest that gaseous atoms have diffused into the surface layers and locked dislocation sources. This effect is worthy of further study.

The work described has been largely of an exploratory nature and little effort has been devoted to the study of mechanisms involved. The more experience one gains with MgO crystals the more appreciative one becomes of the extreme notch sensitivity of this material. With the possible exception of the 600°C air embrittlement, it is not unrealistic to consider all other embrittlement phenomena found to be connected with the presence of notches. Thus, surface residues, compounds [11-12], etched slip bands, cleavage steps and microcracks could all act as notches and cause premature failure. It is planned to carefully evaluate this possibility in future studies of the various mechanisms of interest.

5. REFERENCES

11-1 Class, W.H., Machlin, E.S. and Murray, G.T., Trans. AIME, 221 769 (1961).

11-2 Stokes, R.J., Johnston, T.L. and Li, C.H., Trans. AIME, 218, 655 (1960).

11-3 Aerts, E. and Dekeyser, D., Acta Met., 4 557 (1956).

11-4 Parker, et.al., J. Am. Ceram. Soc., 41 161 (1958).

11-5 Stearns, C.A., J. Appl. Phys., 31 2317 (1960).

11-6 Lad, R.A., Stearns, C.A., and Del Duca, M.G., Acta Met., 6 610 (1958).

11-7 Thompson, D.S., and Roberts, R.J., J. Appl. Phys., 31 433 (1960).

11-8 Pulliam, G.R., WADC TR 59-261, Sept., 1959.

11-9 Stokes, et. al., Eighth Tech. Report, Contract NONR 2456(00), June, 1960.

11-10 Stokes, R.J., Task 10, This report.

11-11 Murray, G.T., J. Am. Ceram. Soc., 43 330 (1960).

11-12 Marsh, D.M., Phil. Mag., 1197 (1960).

APPENDIX A - ANELASTIC PHENOMENA IN POLYCRYSTALLINE OXIDE CERAMICS

ABSTRACT

An internal friction apparatus which vibrates a polycrystalline ceramic rod in flexure at low frequencies was constructed. The apparatus was designed to permit static loading of the specimen in tension while it is vibrated. Using this equipment the variation of internal friction, Q^{-1}, with T, vibration amplitude, static load, and time in a Morganite Al_2O_3 rod has been briefly examined. The temperature variation of Q^{-1} of this oxide is unlike that of Chang's pure Al_2O_3 by not having a sharp grain boundary relaxation peak, and by showing plastic behavior at a lower temperature.

The dependence of Q^{-1} on vibration amplitude (which may be transposed into a strain amplitude and a corresponding stress) resembles that of metals and single crystals in that the rate of increase of Q^{-1} with amplitude rises sharply above a certain critical value. However, the activation energy of the anelastic process in the alumina ceramic suggests a diffusion rather than a dislocation mechanism. In some cases, this diffusion process can be shown to be the same as that responsible for creep. Where this is true, measurements of Q^{-1} vs amplitude may be used to establish, for any desired temperature, the critical stress above which creep rates will increase rapidly.

Static load experiments were rendered somewhat ambiguous by concomitant frequency changes; indirect evidence suggests that the increased stress does enhance a broad peak which probably represents a spectrum of grain boundary relaxation processes.

APPENDIX A - ANELASTIC PHENOMENA IN POLYCRYSTALLINE OXIDE CERAMICS

1. INTRODUCTION

Measurements of internal friction, Q^{-1}, in single crystals of non-metals (Al_2O_3, MgO) have been and are presently being carried out as a means of studying dislocation motion and its interactions with impurities and defects. Such measurements have also been made on polycrystalline metals, not only in connection with dislocation studies but also to observe such phenomena as grain boundary slip and the precipitation of new phases. However, it has only been recently that damping has been measured in polycrystalline refractory oxides. Wachtman[A-1] and Chang[A-2] have shown that if Q^{-1} is plotted as a function of specimen temperature for pure Al_2O_3 or BeO, a peak, which may be attributed to grain boundary slide, appears at some temperature above 800°C. The temperature location of this maximum point was found to be sensitive to the vibration frequency of the specimen, and its temperature shift with changing frequency may be used to calculate an activation energy for the sliding process. Chang found for Al_2O_3 that the resulting energy was about 2×10^5 cal per mole, similar to the value he obtained from creep experiments with the same Al_2O_3. Unlike the common situation with metals, impurities introduced into the pure oxides created new peaks on the low temperature side of the original maximum.

In the case of oxides, therefore, impurities tend to lower grain boundary viscosity, a phenomenon which is the reverse of their expected influence on dislocation motion. In the light of this result and the coincidence between the activation energies of self diffusion and grain boundary relaxation, Chang came to the reasonable conclusion that the slip process in his samples was more closely allied to diffu-

sion than to the movement of dislocations. Another result of Chang's work was the observation that while relaxation peaks induced by Cr and La had much lower activation energies than that of the pure Al_2O_3; these impurities did not lower the activation energy of steady state creep. From this it may be inferred that the relaxation processes involving these two cations were not important for creep of the ceramic as a whole.

It is evident from this abbreviated account of Chang's work with polycrystalline oxides that the familiar internal friction technique may have important application in the study of structural ceramics. These materials are generally polycrystalline, and they are commonly subjected to temperatures at which ionic diffusion may be rapid. It is, therefore, likely that the same processes which promote damping are in part responsible for fatigue in a ceramic exposed to stress in a high temperature environment. Consequently, measurements of the stress or time variation of Q^{-1} in heated ceramic specimens might provide a rapid means of estimating resistance to fatigue at various temperatures. One objective of this program was to build an apparatus suitable for this purpose; i.e., one which could determine Q^{-1} in a statically loaded ceramic specimen. Another objective was to measure the temperature variation of Q^{-1} in a commercial high (99.7%) Al_2O_3 ceramic.

2. APPARATUS

Unlike dislocation mechanisms in single crystals, grain boundary relaxation processes are best observed at low frequencies. This eliminates the necessity for heating specimens to very high temperatures, and also allows relatively simple and inexpensive equipment to be used. Chang and Gensamer[A-3] have described an apparatus in which a specimen bar is driven into free flexural vibration. The oscil-

latory motion is detected and recorded by a linear variable differential transformer whose core is fastened to the specimen. This basic design was used in the apparatus shown in Fig. A-1, the major departure from the Chang and Gensamer equipment being the position of the rigid specimen mounting. In Fig. A-1, the rigid mount is at the top of the bar, necessitating a heavy framework or cage to support the massive block to which the specimen is clamped. All of these subsidiary supports are possible sources of unwanted damping and could have been eliminated by the simple expedient of clamping the specimen at the bottom as Chang and Gensamer did. Nevertheless, the inverse positioning was made necessary by the requirement that the specimen be loaded in tension in some of the internal friction experiments.

Static loading was accomplished by a system consisting of a long threaded pendulum and weights which were attached to the free lower end of the specimen bar. Theoretically, the loading of the bar could be increased without changing the frequency of vibration by moving the weights a sufficient amount to compensate for displacement of the center of oscillation. A clamping device at the bottom of the supporting cage permitted the specimen to be immobilized while weights were being moved or changed.

Specimens were in the form of 6 x 1/4-in. round rods of Morganite 99.7% Al_2O_3 tapered at the middle to form a gage section measuring approximately 0.080 x 0.25 in. at the thinnest point. These bars were fastened with a heat-curing epoxy cement (Emerson and Cuming Eccobond Paste #88) into threaded steel bushings. The bushing at the top was then screwed into a water-cooled fitting on the heavy steel block, and the lower one was fitted into a short section of the pendulum. The purpose of the threaded bushings was to facilitate specimen removal from the apparatus; if the Al_2O_3 rods had been cemented directly into the steel block, lower background damping levels would

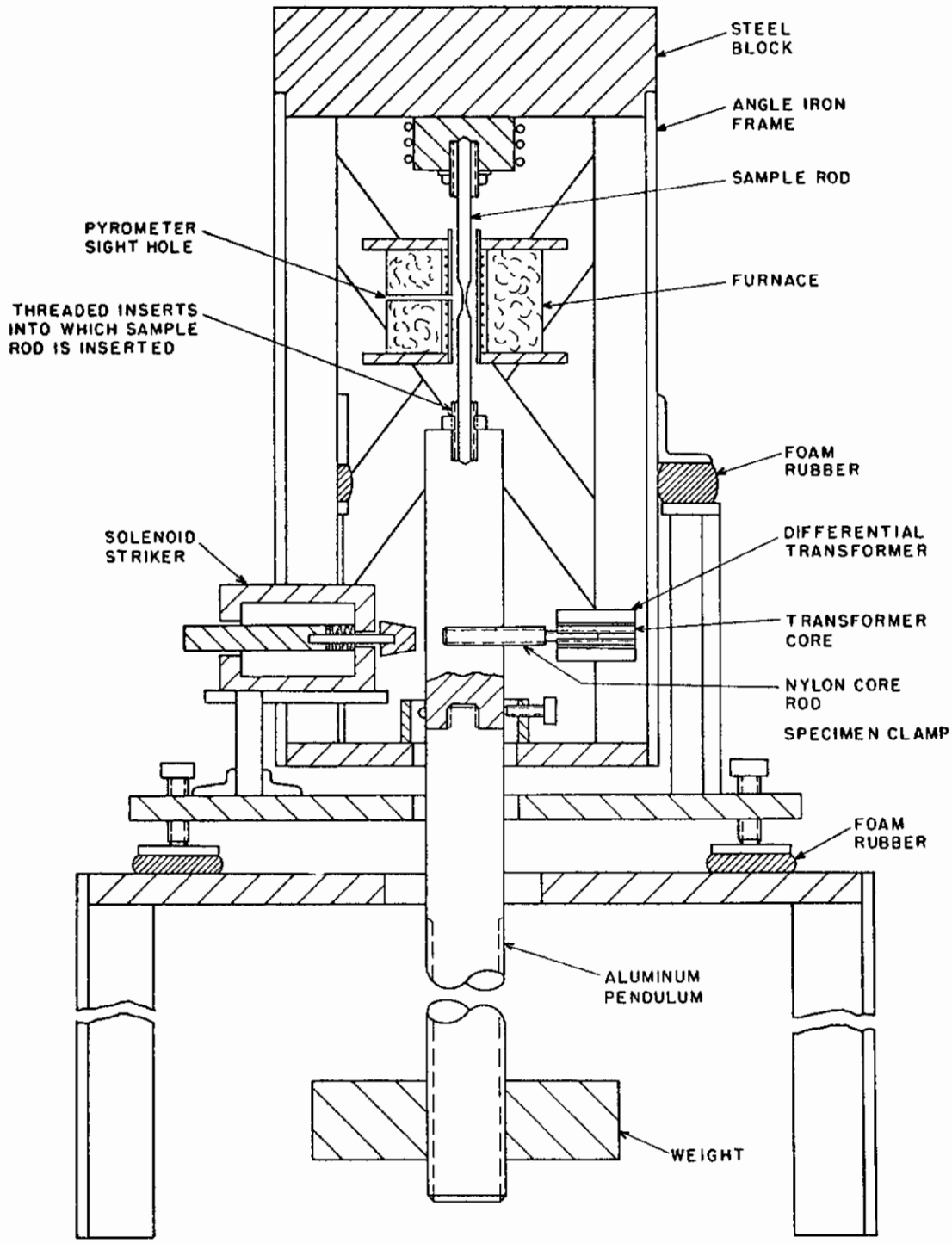

Fig. A-1 SECTION THROUGH INTERNAL FRICTION APPARATUS (FURNACE AND DIFFERENTIAL TRANSFORMER SUPPORTS NOT SHOWN)

undoubtedly have been obtained. Attempts were made to reduce damping at the thread contacts by coating them with Duco cement and by using a lock nut and deformable copper washer. Nevertheless, despite these precautions, it is likely that most of the instrument damping had its source in the supposedly rigid mounting of the specimen bar.

The sample rod was driven into free vibration by a blow from the core of a solenoid. Heating was provided by a platinum-wound furnace having two small holes drilled from the outside into the combustion tube. One hole served as a pyrometer sight port while the other contained a thermocouple whose junction rested about a millimeter from the gage section of the Al_2O_3 rod. The entire apparatus was fitted with a hood to permit introduction of different gaseous atmospheres.

To measure damping, the oscillating output from the differential transformer was first demodulated and then recorded by an oscilloscope whose trace was photographed. After correction for the width of the oscilloscope beam trace, Q^{-1} was calculated from the amplitude change on the photographs by means of:

$$\log \text{dec} = \frac{1}{n} \ln \frac{A_m}{A_{m+n}} \qquad \text{(A-1)}$$

and

$$Q^{-1} = \log \text{dec} / \pi , \qquad \text{(A-2)}$$

where A_m and A_{m+n} are the amplitudes of the mth and m + nth oscillations, n is the number of cycles between A_m and A_{m+n}.

The logarithmic decrement and internal friction are not entirely characteristic of damping processes that occur in the specimen. Thus,

$$Q^{-1} = \frac{dE}{2\pi E} \qquad \text{(A-3)}$$

where dE is the energy loss per cycle and E is the total energy of the moving system. Therefore, if the total energy E is raised by increasing either the mass of the pendulum bar or its amplitude, the experimental value of Q^{-1} will be lowered even though the specimen does not change its damping characteristics.

For a given distance, L_1, of the center of oscillation from the gage section (pivot point) the total energy E, of equation A-3 is approximately:

$$\dot{E}_1 = \frac{A_1^2}{2L_1} (m_1 g + K), \qquad \text{(A-4)}$$

where A_1 is the amplitude of the center of oscillation, K is the spring constant of the Al_2O_3 specimen (the force required to produce unit deflection of the specimen at unit length from the gage section) and m_1 is the mass of the pendulum system. Increasing the mass to m_2 may cause L_1 and A_2 to be changed to L_2 and A_2, and raises E_1 to E_2.

To determine changes in specimen damping caused by increasing load, the total energy of the system must be normalized to a constant value. This may be done by multiplying experimental values of Q^{-1} obtained for each load increment by the factor E_2/E_1. If the system is arranged so that L and A remain constant when the mass is increased (i.e., the pendulum weights are moved to retain constant frequency), E_2/E_1 simplifies to:

$$\frac{E_2}{E_1} = \frac{m_2 g + K}{m_1 g + K} \qquad \text{(A-5)}$$

3. EXPERIMENTAL RESULTS

Internal friction experiments, all of them largely exploratory, were primarily concerned with the variation of Q^{-1} in Morganite Al_2O_3

rods with temperature, vibration amplitude, load, and (under constant load) time.

A. Temperature Variation of Q^{-1}

Figure A-2 shows three curves obtained from the same Morganite Al_2O_3 rod by varying the static load from one lb (a) to four lb (b) to 19.4 lb (c). Aside from the resulting rise of tensile stress on the specimen, this variation also caused the frequency to change from 30 to 5 to 2.6 cps. The geometry of the pendulum was such that at constant angular amplitude, the increase of weight also entailed an increase in the energy of the system (E) in the ratio 1:3.2:4.7. To permit direct comparison of the internal friction values corresponding to these three load conditions, experimental results were multiplied by the appropriate energy ratios before being plotted in Fig. A-2.

Deferring discussion of the obvious load or frequency effects to a later section, it is apparent from Fig. A-2 that curves A, B, and C for Morganite Al_2O_3 bear little resemblance in shape to curve D represented by Chang for pure Al_2O_3. The most important point of departure is the large relaxation peak which culminates at about 1100°C for Chang's Al_2O_3 and which is quite absent from the less pure Morganite specimen. In contrast, the latter shows a rapid and continued temperature increase of Q^{-1} above 850° to 1050°C depending on the specimen load. On the assumption that this rise reflects an exponential increase in rate of some anelastic process, plots of log Q^{-1} vs $10^3/T$ were prepared for the segments of curves A, B, and C above 1000°, 900°, and 1075°C. The resulting curves A and B of Fig. A-3 show a gradual change of slope from almost zero at the lowest temperatures to a fairly linear segment which corresponds to an activation energy (U) of about 70 kcal per mole. This behavior suggests a transition from essentially elastic behavior to an anelastic mechanism having U equal to 70 kcal per mole.

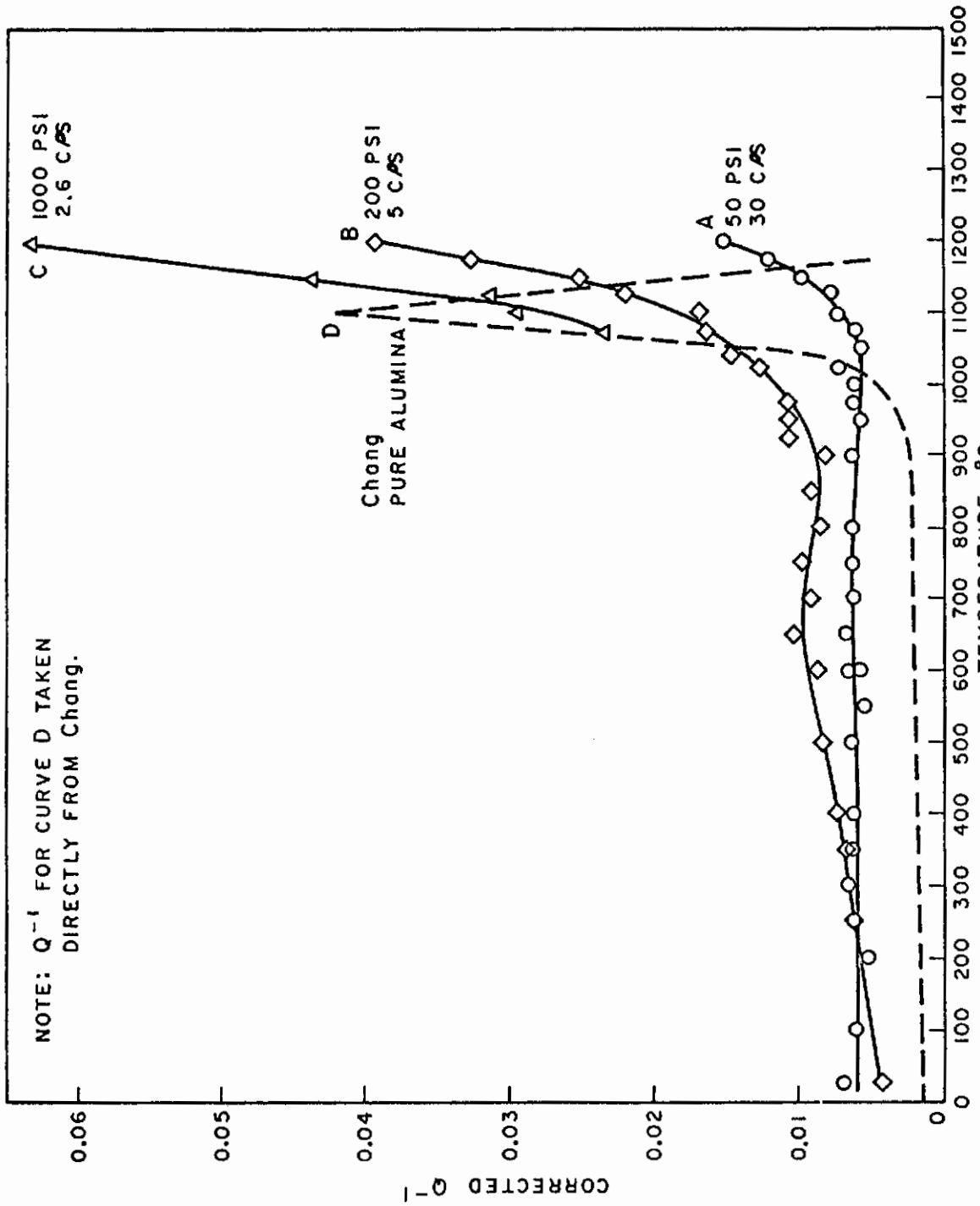

Fig. A-2 TEMPERATURE VARIATION OF INTERNAL FRICTION

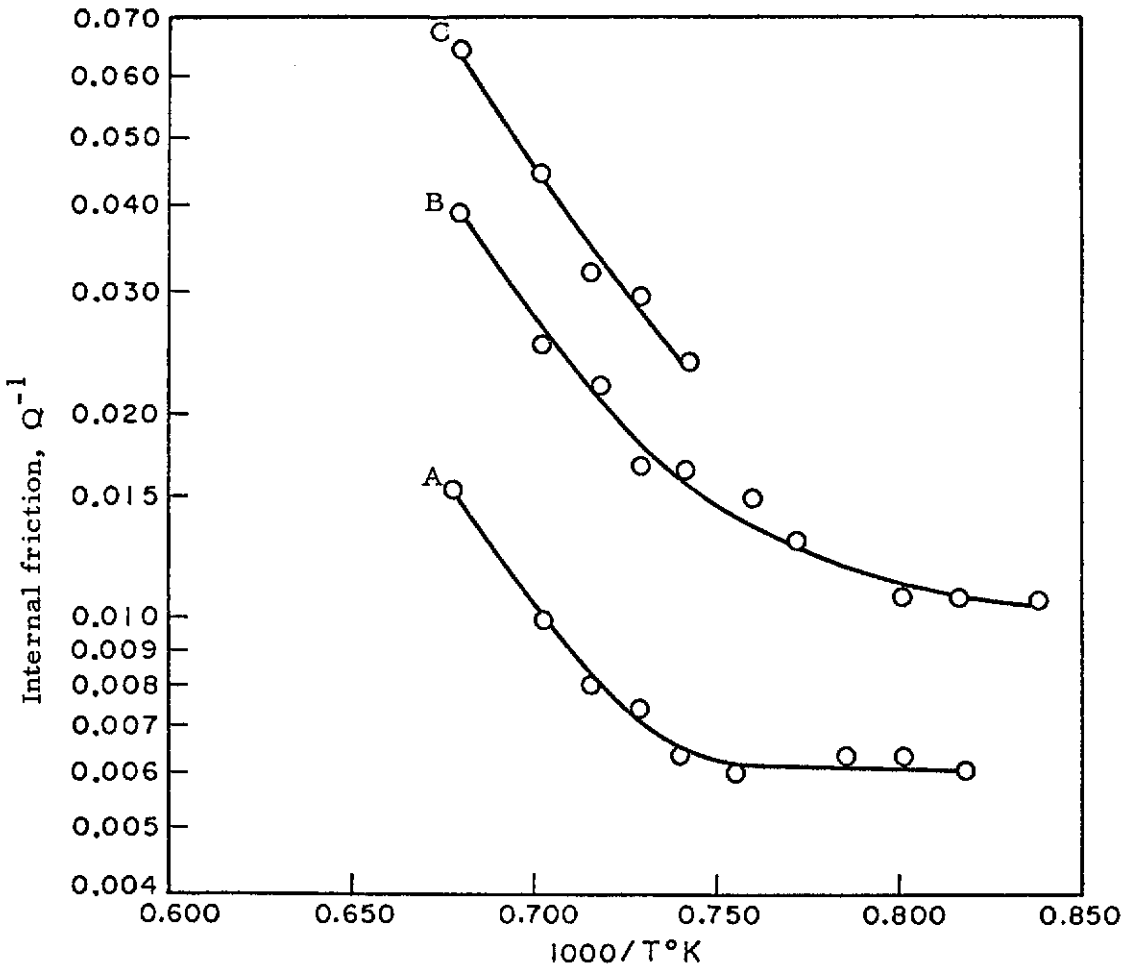

Fig. A-3 ARRHENIUS PLOTS OF CURVES A, B, AND C OF FIG. A-2

B. Variation of Q^{-1} with Vibration Amplitude

Both metals and ionic single crystals characteristically show a sudden rise of Q^{-1} as the vibration amplitude exceeds a critical value. The cause of this effect is well known, and consists of a release of dislocations from pinning sites (impurities, lattice defects) and the consequent increase in the lengths and vibration amplitudes of the unpinned sections. The precedent of these observations suggests the possibility of similar behavior in ceramics; therefore measurements of Q^{-1} were made with varying vibration amplitude at a series of four temperatures. Since the amplitude of the vibrating bar depends on the distance from the pivot point, it would be preferable to replace it with a term of more general interest; i.e., the maximum tensile strain at the gage section, or with the aid of the elastic modulus, the stress producing this strain. This calculation is rendered somewhat difficult by the varying thickness of the gage section of the specimens used in this program. However, photoelastic analysis of a plastic model quickly revealed the strain pattern and greatly simplified the problem. By this means it was estimated that a deflection of 0.001 inch at the differential transformer core caused a maximum tensile strain of about 8×10^{-6} in./in.

Results of Q^{-1} vs deflection measurements at the four temperatures are shown in Fig. A-4. Both the 1150° and 1210°C curves show the discontinuous increase of Q^{-1} previously described as a sign of dislocation unpinning. These discontinuities occur at maximum tensile strains of approximately 28×10^{-6} and 17×10^{-6} in./in., and if the elastic moduli of Al_2O_3 at 1150° and 1210°C are taken as 40×10^6 and 38×10^6 psi,[A-4] the tensile stresses causing these strains are 1100 psi and 650 psi. The fact that the critical stresses are different at the two temperatures demonstrates that the anelastic process in question has an activation energy. If s_1 and s_2 are the magnitudes of the stresses at temperatures T_1 and T_2:

$$U\,(\text{electron volts}) = \frac{1.72 \times 10^{-4} \ln s_1/s_2}{1/T_1 - 1/T_2} \qquad (A\text{-}6)$$

= 3.2 electron volts or about 74 kcal per mole.

Considering the scatter of experimental points in Fig. A-4, this value for the activation energy is in surprisingly good agreement with that obtained from Fig. A-3.

C. Variation of Q^{-1} with Load

When weights are suspended from the free end of the specimen two major effects are produced: the rod is subjected to an additional tensile stress, and the vibration frequency is reduced. Specifically, the three curves of Fig. A-2 were determined under loads of 1, 4, and 19.4 lb, which corresponds to tensile stresses on the gage section of 50, 200, and 1000 psi, and frequencies of 30, 5, and 2.6 cps. Figure A-2 shows that the main effect of increasing the load is to lower the temperature at which plastic behavior initiates. Another effect is to create a low broad peak culminating at about 650°C which probably represents the operation of one or more relaxation processes.

The temperature displacement noted above may be used to calculate a third value for the activation energy of the predominant mechanism of plasticity. In this case, s_1 and s_2 of equation A-6 may be replaced either by the frequencies (or the stresses) corresponding to curves A and B of Fig. A-2, and T_2 and T_1 (870° and 1050°C) are the temperatures at which Q^{-1} first rises rapidly. When the frequencies (30 and 5 cps) are introduced into equation A-6, U is about 60 kcal per mole; whereas, if the stresses are used instead, U is appreciably lower. The fairly close agreement between 60 kcal per mole and the previously calculated values of 70 and 74 kcal per mole, establishes that the temperature displacement for the onset of plastic behavior is caused by the frequency rather than the stress change. This result is confirmed by the relative invariance of Q^{-1} with load in experiments conducted at 1200°C at constant frequency.

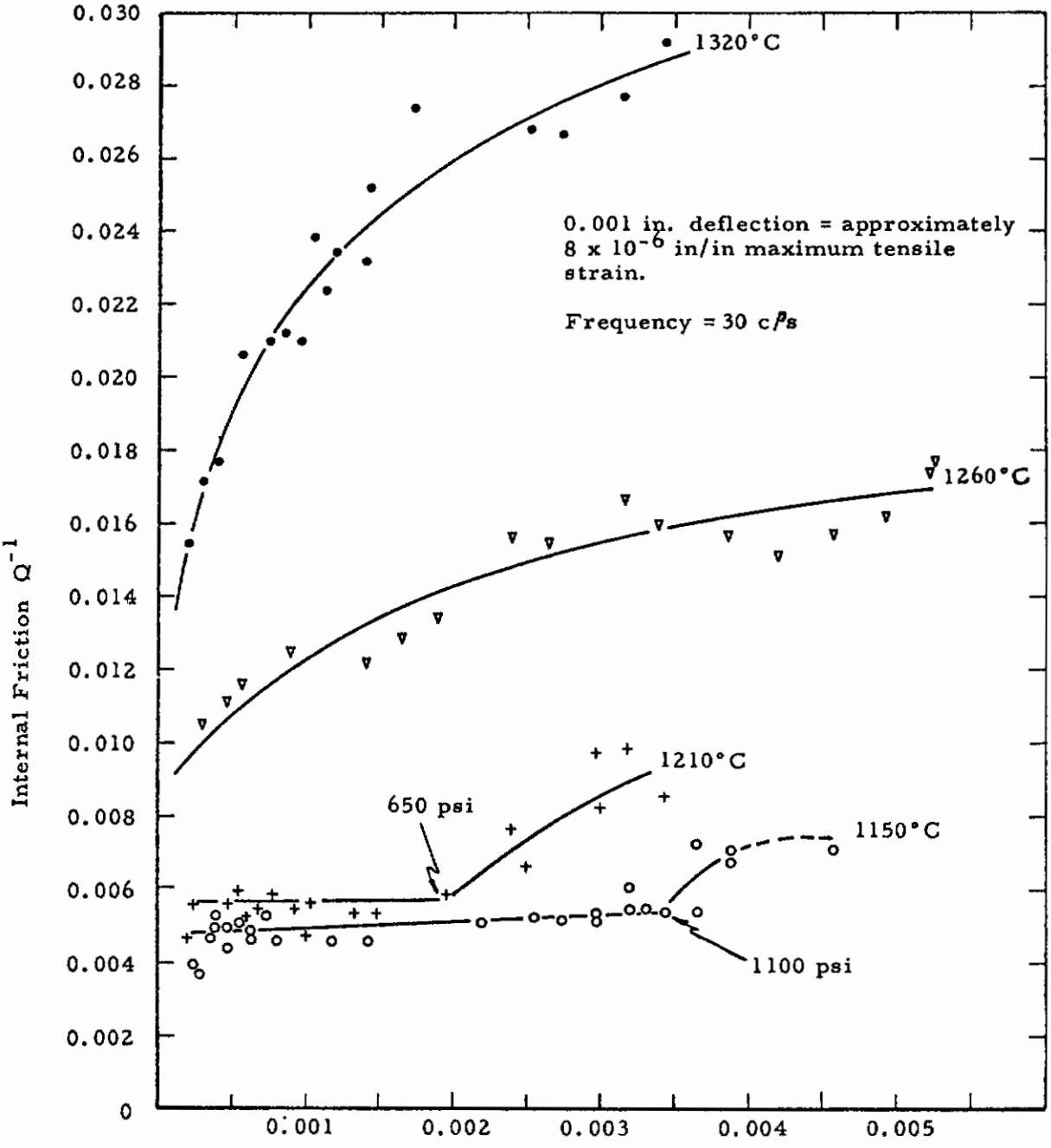

Fig. A-4 AMPLITUDE VARIATION OF Q^{-1}

No direct experimental data are available at present for determining whether the relaxation peak of curve B (Fig. A-2) originates from the increased stress or from the lowered frequency. However, indirect evidence based on the elastic modulus will be presented in a later section in support of stress as the causative agent.

D. Variation of Q^{-1} with Time at Constant Load

Under the action of corrosion processes, failure of Al_2O_3 can take place at lower than normal stresses[A-5]. These processes are accelerated by water vapor which is present while the stress is being applied. The region of extremely high strain at the tips of minor flaws greatly increases the local chemical reactivity, thereby accelerating the processes which lead to growth of the flaw. These changes might be reflected in a rise of Q^{-1} for a specimen subjected to a constant load in a moist atmosphere. Because of lack of time, only a few probing experiments could be carried out at 150°, 980°, and 1300°C in a superheated steam atmosphere, under stresses of 1000, 1000, and 400 psi respectively. None of these trials revealed any significant change of Q^{-1} over time intervals ranging from 20 to 98 minutes. Since the specimen did not fail during any of these exposures, it is not known at present whether corrosion damage was actually appreciable but was not detected by the internal friction apparatus, or whether the stress-temperature-time intervals studied formed a region in which only very little fatigue occurred.

4. DISCUSSION

By comparing the Q^{-1} vs T curves of single crystal and polycrystalline Al_2O_3, Chang was able to demonstrate convincingly that

his relaxation peak at 1100°C is due to a grain boundary slip process. If, moreover, Chang's measured activation energy of 200 kcal per mole is compared with values of 140 and 230 kcal per mole assigned by Kuczynski, Abernathy, and Allen [A-6] to the self diffusion of Al and O ions, the slip appears to be caused by a diffusion-like mechanism.

These relationships are not so clear for the Morganite Al_2O_3 used in the present program. Only a broad low relaxation peak occurs in curve B and there is no sign of Chang's maximum at 1100°C. The sharp rise of Q^{-1} above 1000°C is not reversed at higher temperatures, and therefore represents only a progressive rise of plasticity which would also occur in a single crystal, probably at a higher temperature. Another point of difference between pure and Morganite Al_2O_3 is the lower activation energy (60-74 kcal per mole) calculated for plastic processes in the latter than for the relaxation mechanism of the former. This depression of U is undoubtedly caused by the 0.3% of siliceous and alkaline earth impurities in the Morganite which not only lower the energy required to create and move oxide ion vacancies, but in some cases (e.g., Mg^{2+}) are themselves very mobile. One concomitant of the reduced activation energy is the initiation of plastic behavior in Morganite at an appreciably lower temperature than in Chang's pure Al_2O_3; note that above 1100°C, curve D of Fig. A-2 returns to values of Q^{-1} near those of much lower temperatures. This does not occur for the less pure Al_2O_3 of curve A. The same result is produced by doping pure Al_2O_3 with La or Cr ions. Moreover, these ions, like the impurities in Morganite, act to lower the high relaxation peak at 1100°C. In pure Al_2O_3, this peak is probably caused by a single relaxation process, possibly the oscillation of O^{2-} ion vacancies near the grain contacts where both the stresses and stress gradients are at a maximum. The presence at the contacts of a glassy phase or of high concentrations of impurities tends to divide

the single diffusion process into a spectrum of mechanisms of lower activation energy whose relaxation times form a broad band of values. The consequence of this degeneration of one into many processes is to flatten out a high narrow relaxation peak into a low broad one such as occurs in curve B of Fig. A-2.

The sensitivity of Q^{-1} to the stresses arising from flexural vibration has its origin in the strain energy which these stresses develop in the specimen. Strain energy like its thermal counterpart, can contribute to the reservoir needed to activate an anelastic process. The lower the temperature, the more the deficit of thermal energy must be made up from the strain source; consequently, as shown in Fig. A-3, there is an inverse relationship between the temperature and the minimum strain required to initiate the rapid rise of Q^{-1}.

Nevertheless, the effects produced by both energy sources are not entirely alike: whereas Q^{-1} rises exponentially with increasing temperature (Fig. A-2), it tends to level off with increasing strain. These results imply that strain energy is only effective in activating a limited number of ions which have already obtained a certain fraction of their total required activation energy from the thermal reservoir.

If it can be demonstrated that the damping process which is being activated by strain is also active in fatigue, the measurement of Q^{-1} vs strain amplitude (or of the corresponding flexural stress) might have an interesting engineering application. In this case, discontinuities such as occur in curves A and B of Fig. A-3 signify that a certain critical stress is required to initiate the fatigue process. Moreover, this stress decreases with rising temperature (and with falling frequency). Internal friction measurements of the type outlined in this report, can therefore provide a very rapid method of estimating this critical stress and its variation with temperature

and frequency - using a single specimen for the entire set of measurements.

As previously noted, the applicability of this procedure depends on the coincidence of the friction and fatigue process. In this regard, Chang found that for pure Al_2O_3 the activation energies of the 1100°C relaxation peak and of steady state creep were about the same. This was not true for the new peaks introduced by the presence of La and Cr ions; apparently the motion of these impurities contributed to Q^{-1} but they did not influence the creep process. Therefore, before Q^{-1} vs amplitude curves can be used to predict critical creep stresses, it will be necessary to compare the activation energy of the dominant friction mechanism with that obtained from a creep experiment.

Stress effects produced by a constant load on the specimen should for the most part be similar to those resulting from the oscillating stresses generated by vibration. Unfortunately, most of these effects were masked by frequency changes and unequivocal results were only obtained at 1200°C for stresses ranging from 430 to 850 psi. In this region Q^{-1} was found to be essentially invariant, which is in accord with the tendency of Q^{-1} in curves A and C of Fig. A-3 to level off at higher stresses.

Another possible stress effect is the development of the broad maximum at 650°C in curve B of Fig. A-2. According to Zener[A-7], Q^{-1} at the peak of a relaxation process (neglecting background effects) is given by:

$$\frac{1}{2} \cdot \frac{M_U - M_R}{M_U M_R} \qquad \text{(A-7)}$$

where M_U and M_R are respectively the dynamic and static elastic moduli of the specimen. Consequently, any change of the elastic moduli caused by a variation of temperature or stress can produce a corresponding change in the height of a relaxation peak. In the present

case, the heavier load of curve B (as compared to A) not only increases the stress, but by lowering the frequency, also displaces the relaxation peak to a lower temperature. Incomplete data in Reference A-4 show that the rates of temperature change of M_U and M_R are very similar below 900°C, indeed, if any change of $M_U - M_R$ occurs, it appears to be in the direction of an increase with rising temperature. This would lead to an intensification of the relaxation peak at higher frequencies, which is just the reverse of the observed results. On the basis of this very indirect and very slim body of evidence, therefore, the enhancement of the 650°C relaxation peak of curve B (Fig. A-2) appears to arise from the effects of stress.

5. CONTRIBUTING PERSONNEL

Laboratory work on the construction of the internal friction apparatus and its application to the study of Morganite Al_2O_3 specimens was carried out by John W. Stuart and Leon M. Atlas, with valuable suggestions from P. D. Southgate. The photoelastic analysis of stresses in plastic models and the application of these results to the Al_2O_3 specimens was performed under the direction of S. A. Bortz.

6. REFERENCES

A-1 Wachtman, J. B., Jr., WADC Tech. Report 57-526 (1957).

A-2 Chang, R., "High Temperature Creep and Anelastic Phenomena in Polycrystalline Refractory Oxides" J. Nuclear Materials 2, 174-181, (1959).

A-3 Chang, L. C., and Gensamer, M., "Internal Friction of Iron and Molybdenum at Low Temperatures" Acta Metallurgica 1, 483, (1953).

A-4 Hruz, F. M., Appendix I "Mechanical Property Survey of Refractory Nonmetallic Crystalline Materials and Intermetallic Compounds" WADC Tech. Report 59-448 (January 1960).

A-5 Charles, R. J., "Static Fatigue; Delayed Fracture", Task 9 of Final Report of "Studies of the Brittle Behavior of Ceramic Materials" Contract No. AF 33(616)-7465, Task No. 73500, (November 1961).

A-6 Kuczynski, G. C., Abernathy, L. and Allen, J., "Sintering Mechanisms of Aluminum Oxide" Chapt. 21 in "Kinetics of High Temperature Processes", W. D. Kingery, Ed., Tech. Press of M. I. T. and J. Wiley and Sons (1959).

A-7 Zener, C., "Elasticity and Anelasticity of Metals" University of Chicago Press, Chicago (1942).